COMBATING BACTERIAL INFECTIONS THROUGH BIOMIMETIC OR BIOINSPIRED MATERIALS DESIGN AND ENABLING TECHNOLOGIES

EDITED BY: Gianluca Ciardelli, Ipsita Roy, Jochen Salber, Antonia Nostro and Aldo R. Boccaccini

PUBLISHED IN: Frontiers in Bioengineering and Biotechnology

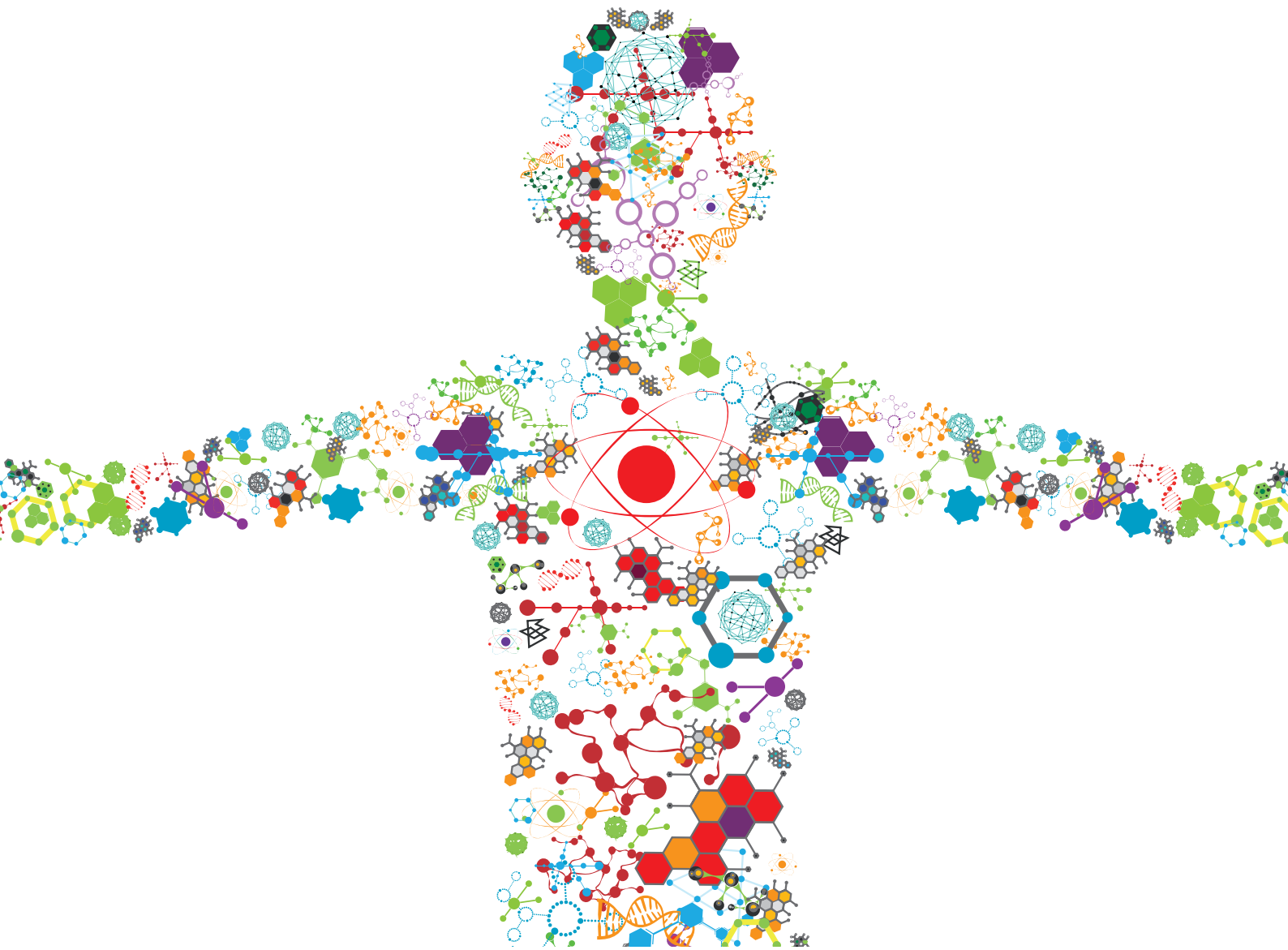

frontiers Research Topics

frontiers

ISSN 1664-8714
ISBN 978-2-88974-244-8
DOI 10.3389/978-2-88974-244-8

About Frontiers

Frontiers is more than just an open-access publisher of scholarly articles: it is a pioneering approach to the world of academia, radically improving the way scholarly research is managed. The grand vision of Frontiers is a world where all people have an equal opportunity to seek, share and generate knowledge. Frontiers provides immediate and permanent online open access to all its publications, but this alone is not enough to realize our grand goals.

Frontiers Journal Series

The Frontiers Journal Series is a multi-tier and interdisciplinary set of open-access, online journals, promising a paradigm shift from the current review, selection and dissemination processes in academic publishing. All Frontiers journals are driven by researchers for researchers; therefore, they constitute a service to the scholarly community. At the same time, the Frontiers Journal Series operates on a revolutionary invention, the tiered publishing system, initially addressing specific communities of scholars, and gradually climbing up to broader public understanding, thus serving the interests of the lay society, too.

Dedication to Quality

Each Frontiers article is a landmark of the highest quality, thanks to genuinely collaborative interactions between authors and review editors, who include some of the world's best academicians. Research must be certified by peers before entering a stream of knowledge that may eventually reach the public - and shape society; therefore, Frontiers only applies the most rigorous and unbiased reviews.
Frontiers revolutionizes research publishing by freely delivering the most outstanding research, evaluated with no bias from both the academic and social point of view. By applying the most advanced information technologies, Frontiers is catapulting scholarly publishing into a new generation.

What are Frontiers Research Topics?

Frontiers Research Topics are very popular trademarks of the Frontiers Journals Series: they are collections of at least ten articles, all centered on a particular subject. With their unique mix of varied contributions from Original Research to Review Articles, Frontiers Research Topics unify the most influential researchers, the latest key findings and historical advances in a hot research area! Find out more on how to host your own Frontiers Research Topic or contribute to one as an author by contacting the Frontiers Editorial Office: frontiersin.org/about/contact

COMBATING BACTERIAL INFECTIONS THROUGH BIOMIMETIC OR BIOINSPIRED MATERIALS DESIGN AND ENABLING TECHNOLOGIES

Topic Editors:
Gianluca Ciardelli, Politecnico di Torino, Italy
Ipsita Roy, The University of Sheffield, United Kingdom
Jochen Salber, Ruhr-University Bochum, Germany
Antonia Nostro, University of Messina, Italy
Aldo R. Boccaccini, University of Erlangen Nuremberg, Germany

Citation: Ciardelli, G., Roy, I., Salber, J., Nostro, A., Boccaccini, A. R., eds. (2022). Combating Bacterial Infections Through Biomimetic or Bioinspired Materials Design and Enabling Technologies. Lausanne: Frontiers Media SA.
doi: 10.3389/978-2-88974-244-8

Table of Contents

05 ***Editorial: Combating Bacterial Infections Through Biomimetic or Bioinspired Materials Design and Enabling Technologies***
Gianluca Ciardelli, Aldo R. Boccaccini, Ipsita Roy, Antonia Nostro and Jochen Salber

08 ***Physical and Antibacterial Properties of Peppermint Essential Oil Loaded Poly (ε-caprolactone) (PCL) Electrospun Fiber Mats for Wound Healing***
Irem Unalan, Benedikt Slavik, Andrea Buettner, Wolfgang H. Goldmann, Gerhard Frank and Aldo R. Boccaccini

19 ***Potential of Manuka Honey as a Natural Polyelectrolyte to Develop Biomimetic Nanostructured Meshes With Antimicrobial Properties***
Elena Mancuso, Chiara Tonda-Turo, Chiara Ceresa, Virginia Pensabene, Simon D. Connell, Letizia Fracchia and Piergiorgio Gentile

32 ***Amphiphilic Cationic Macromolecules Highly Effective Against Multi-Drug Resistant Gram-Positive Bacteria and Fungi With No Detectable Resistance***
Sudip Mukherjee, Swagatam Barman, Riya Mukherjee and Jayanta Haldar

51 ***Response of Human Macrophages to Clinically Applied Wound Dressings Loaded With Silver***
Patrícia Varela, Lennart Marlinghaus, Susanna Sartori, Richard Viebahn, Jochen Salber and Gianluca Ciardelli

64 ***Activated Polyhydroxyalkanoate Meshes Prevent Bacterial Adhesion and Biofilm Development in Regenerative Medicine Applications***
Sheila Piarali, Lennart Marlinghaus, Richard Viebahn, Helen Lewis, Maxim G. Ryadnov, Jürgen Groll, Jochen Salber and Ipsita Roy

78 ***Evaluation of Nisin and LL-37 Antimicrobial Peptides as Tool to Preserve Articular Cartilage Healing in a Septic Environment***
Ziba Najmi, Ajay Kumar, Alessandro C. Scalia, Andrea Cochis, Bojana Obradovic, Federico A. Grassi, Massimiliano Leigheb, Meriem Lamghari, Iraida Loinaz, Raquel Gracia and Lia Rimondini

95 ***Assessment of Growth Reduction of Five Clinical Pathogens by Injectable S53P4 Bioactive Glass Material Formulations***
Eline G. J. Thijssen, Nicole A. P. van Gestel, Raymond Bevers, Sandra Hofmann, Jan Geurts, Inge H. M. van Loo and J. J. Arts

104 ***Bioactive Dental Adhesive System With* tt*-Farnesol: Effects on Dental Biofilm and Bonding Properties***
Diana Leyva del Rio, Neimar Sartori, Nichole Barton Tomblin, Jin-Ho Phark, Vanessa Pardi, Ramiro M. Murata and Sillas Duarte Jr.

115 ***Toward a Closed Loop, Integrated Biocompatible Biopolymer Wound Dressing Patch for Detection and Prevention of Chronic Wound Infections***
Andrew C. Ward, Prachi Dubey, Pooja Basnett, Granit Lika, Gwenyth Newman, Damion K. Corrigan, Christopher Russell, Jongrae Kim, Samit Chakrabarty, Patricia Connolly and Ipsita Roy

127 ***Chemical Modification of Bacterial Cellulose for the Development of an Antibacterial Wound Dressing***
Isabel Orlando, Pooja Basnett, Rinat Nigmatullin, Wenxin Wang, Jonathan C. Knowles and Ipsita Roy

146 ***The Open Challenge of* in vitro *Modeling Complex and Multi-Microbial Communities in Three-Dimensional Niches***
Martina Oriano, Laura Zorzetto, Giuseppe Guagliano, Federico Bertoglio, Sebastião van Uden, Livia Visai and Paola Petrini

163 ***Antibacterial Composite Materials Based on the Combination of Polyhydroxyalkanoates With Selenium and Strontium Co-substituted Hydroxyapatite for Bone Regeneration***
Elena Marcello, Muhammad Maqbool, Rinat Nigmatullin, Mark Cresswell, Philip R. Jackson, Pooja Basnett, Jonathan C. Knowles, Aldo R. Boccaccini and Ipsita Roy

179 ***Synergistic and Antagonistic Effects of Biogenic Silver Nanoparticles in Combination With Antibiotics Against Some Pathogenic Microbes***
Kawther Aabed and Afrah E. Mohammed

193 **In situ** ***Forming Hyperbranched PEG—Thiolated Hyaluronic Acid Hydrogels With Honey-Mimetic Antibacterial Properties***
Jeddah Marie Vasquez, Ayesha Idrees, Irene Carmagnola, Aa Sigen, Sean McMahon, Lennart Marlinghaus, Gianluca Ciardelli, Udo Greiser, Hongyun Tai, Wenxin Wang, Jochen Salber and Valeria Chiono

frontiers in Bioengineering and Biotechnology

EDITORIAL
published: 16 December 2021
doi: 10.3389/fbioe.2021.818643

Editorial: Combating Bacterial Infections Through Biomimetic or Bioinspired Materials Design and Enabling Technologies

Gianluca Ciardelli[1]*, *Aldo R. Boccaccini*[2]*, *Ipsita Roy*[3]*, *Antonia Nostro*[4]* and *Jochen Salber*[5,6]*

[1]Department of Mechanical and Aerospace Engineering, Politecnico di Torino, Turin, Italy, [2]Institute of Biomaterials, University of Erlangen Nuremberg, Erlangen, Germany, [3]Department of Materials Science and Engineering, The University of Sheffield, Sheffield, United Kingdom, [4]Department of Chemical, Biological, Pharmaceutical and Environmental Sciences, University of Messina, Messina, Italy, [5]Salber Laboratory, Centre for Clinical Research, Department of Experimental Surgery, Ruhr-Universität Bochum, Bochum, Germany, [6]Department of Surgery, Universitätsklinikum Knappschaftskrankenhaus Bochum GmbH, Bochum, Germany

OPEN ACCESS

Edited and reviewed by:
Hasan Uludag,
University of Alberta, Canada

***Correspondence:**
Gianluca Ciardelli
gianluca.ciardelli@polito.it
Aldo R. Boccaccini
aldo.boccaccini@fau.de
Ipsita Roy
i.roy@sheffield.ac.uk
Antonia Nostro
anostro@unime.it
Jochen Salber
Jochen.Salber@ruhr-uni-bochum.de

Specialty section:
This article was submitted to Biomaterials, a section of the journal Frontiers in Bioengineering and Biotechnology

Received: 19 November 2021
Accepted: 06 December 2021
Published: 16 December 2021

Citation:
Ciardelli G, Boccaccini AR, Roy I, Nostro A and Salber J (2021) Editorial: Combating Bacterial Infections Through Biomimetic or Bioinspired Materials Design and Enabling Technologies. Front. Bioeng. Biotechnol. 9:818643. doi: 10.3389/fbioe.2021.818643

Keywords: biomimetic polymers, *in vitro* models, surface functionalisation, bioactive ceramic, antibacterial activity, bioinspired biomaterials, drug-free, antibacterial composites

Editorial on the Research Topic

Combating Bacterial Infections Through Biomimetic or Bioinspired Materials Design and Enabling Technologies

An essential cornerstone of modern medicine for the implementation of curative surgical or interventional therapies and for the treatment of microbial, bacterial and fungal infections was the discovery and development of antibacterial (antibiotics) and fungicidal (antifungals) agents that could be applied systemically either orally or parenterally (intravenously). In addition, improving hygiene in hospitals before, during and after invasive procedures (working aseptically) has significantly reduced the number of postoperative infections. With the introduction of antibiotics and antifungals, it was discovered almost simultaneously that these substances lead to ineffectiveness in various microbes or strains of these microbes (Ventola, 2015). In other words, certain subpopulations of microbes developed resistance to these newly introduced antimicrobial agents as a result of a natural evolutionary process with increasing drug use and spread. In this way, a kind of race developed between the development of new antimicrobials, especially antibiotics and the development of resistance of microbes, especially bacteria, to these agents. In the course of the further development of medicine with new therapeutic possibilities such as the steadily increasing implantation of foreign materials (such as catheters, stents, joint endoprosthesis and many more) as well as technical possibilities to perform increasingly complex operations (e.g., limb reconstructions, transplantations, etc.) or life-sustaining, intensive medical therapies on a daily basis, the use and consumption of antibiotics and antimycotics also increased (Charani et al., 2017).

However, not only in human medicine, but also in other areas, increasingly larger quantities of antimicrobial agents and antiseptic disinfectants were used and in many cases misused. This attitude has led to a steadily growing number of resistant bacterial and fungal species. New development and approval of effective antimicrobial agents has not kept pace with this drastic development (Hutchings et al., 2019). With the increasing use of foreign materials (biomaterials, wound dressings, implants, endoprosthesis) in patients and the growing number of patients with chronic wounds, another phenomenon has been discovered, the biofilm formation of bacteria and fungi on foreign body surfaces or on necrotic or immune-compromised host tissues. As part of the complex biofilm formation process, microbes create a survival

habitat in which they can evade the influence of the host's own immune system, largely protect themselves from the effects of applied antibiotics and antifungals, and even develop resistance to these agents (Idrees et al., 2018).

All this led to the consideration not only of the development and approval of new antibiotics and antifungals as a target-oriented strategy, but also to look for other alternative and complementary strategies. Just as the first so-called classical antibiotic penicillin was produced by a fungal culture (i.e., by nature itself), there is an almost inexhaustible repertoire of natural substances such as antimicrobial peptides (AMPs), biofilm-degrading enzymes, inorganic ions and principles such as anti-adhesive surface modifications or morphologies for the prevention of bacterial adhesion and thus biofilm formation or surface-active destruction of microbes (Amin Yavari et al., 2020). All this led to the fact that today we are in the so-called antimicrobial resistance (AMR) crisis. This is where our Research Topic *Combating Bacterial Infections Through Biomimetic or Bioinspired Materials Design and Enabling Technologies* comes in, to harness the natural potential of antimicrobial strategies for modern medicine. As is often the case when exploring new ways to solve an existing problem, such as foreign body-associated infections, biofilm formation and resistance to classical antibiotics, new challenges are brought to light. This includes the proof of efficacy of new alternative strategies and filling gaps in understanding of the interaction of complex multimicrobial aggressors with the host. In addition, modelling of these complex interactions and preclinical testing of these new compounds and/or strategies *in vitro* is required. This will ensure that the biofilms can be prevented or removed, and the microbes killed without at the same time harming the host cells and thus the host itself. In this research topic, a review is devoted to illustrate these challenges (Oriano et al.). In addition, further 13 original papers highlight various strategies for combating biofilms and clinically relevant bacterial strains, some of which are highly resistant, in an alternative-complementary manner.

Reactive oxygen species (ROS) in general and hydrogen peroxide in particular are generally considered to be potential antimicrobial agents. Clinically, dilute aqueous hydrogen peroxide solutions have been widely used in the cleansing of heavily contaminated soft tissue wounds or in the sanitation of bony implant regions in the case of periprosthetic joint infections (PJI). Here, the detrimental effect on the local host cells, whose physiological functioning is extremely important for healing, was disregarded for a long time. This does not mean that hydrogen peroxide or other ROS are unsuitable, because even certain defense cells (e.g., phagocytes) in the human body make use of them, but in a clever, intelligent way. In the article by Vasquez et al. it is shown how the antimicrobial effect of honey can be cleverly imitated by material engineering to release defined hydrogen peroxide concentrations locally (e.g., in wounds) to kill bacteria without damaging the host cells. In another original work, Mancuso et al. combined Manuka honey (MH, polyanionic), which is recognized as having antimicrobial activity, with poly-(allylamine hydrochloride) (polycationic) as a LbL coating using electrospun PCL meshes as a substrate to generate a biocompatible, antimicrobial, and multilayer nanocoating on the PCL mesh. Among other things, the authors were able to show that the LbL technique can be used as an effective means for the production of complementary antimicrobial medical devices.

In connection with open bone fractures, penetrating contaminants and thus bacteria, surgeons are faced with the major problem of eliminating bacterial entry, preventing bacterial adhesion and thus biofilm formation on the implants and especially at the implant-bone interface, replacing lost bone substance and at the same time supporting fracture healing and bone regeneration, in addition to acute bone fracture treatment with temporary force-bearing implants (intramedullary nails, plate-screw systems, etc.). This is where the work of Marcello et al. comes in and reported for the first time the synthesis of a novel dual-substituted hydroxyapatite (HA) containing selenium (Se) and strontium (Sr) and its combination with two types of polyhydroxyalkanoates (PHAs) differing in molecular chain length (short-chain, scl; medium-chain, mcl). From this, the authors prepared novel antibacterial composite materials for bone regeneration without using antibiotics. Modification of the PHA matrix with the antibacterial Se- and bone regenerative Sr-containing HA resulted in an increase in the mechanical strength of both scl- and mcl-PHA films while decreasing the deformability of the materials. These newly developed composite materials possess high antibacterial activity against *Staphylococcus aureus* 6538P and *Escherichia coli* 8739. In an interesting paper by Thijssen et al., the authors approached the problem of chronic osteomyelitis from a translational, clinically practical perspective. They optimized the handling properties of a clinically used bioglass-based antimicrobial bone substitute $S_{53}P_4$ (Bonalive®) to facilitate its use by orthopedic surgeons. The authors tested these new injectable putty formulations on five different clinically relevant germs and investigated the influence of the binder components poly(ethylene)glycol (PEG) and glycerol on the antibacterial properties of the bioactive glass $S_{53}P_4$. The authors critically discussed the results previously presented in the literature as well as their own.

Monovalent silver (Ag^+) ion releasing systems continue to be a clinically used strategy to prevent bacterial adhesion to implant surfaces or to combat bacteria in the wound area. Due to their concentration-dependent toxicity to mammalian cells, nanoparticulate silver release systems in particular represent an interesting solution. Aabed and Mohammed showed in their article that biogenic AgNPs capped and reduced by biomolecules such as carbohydrates and proteins result in safe, inexpensive and stable Ag^+-releasing nanoparticles that could be useful in antimicrobial drug formulations. Nevertheless, it is important to critically investigate the use of alternative, complementary antimicrobial strategies such as the application of inorganic ion-releasing nanoparticles (Ag^+ in this case) with respect to their mechanism of action. It is important not only to understand their microbe-killing effect, but also to shed light on their eukaryotic toxicity and immunomodulatory properties. In another contribution to this topic Varela et al. addressed this issue and investigated various clinically used wound care materials that can release silver ions with respect to cytocompatibility and immunomodulation *in vitro*. In particular, subchronic and chronic wounds with often severe microbial colonization and complex

inflammatory status, which is individually dependent on the overall health of the affected patient, represent a major challenge and socioeconomic burden. This is a significant market for the medical device industry and there are now many high-tech products on the market. Therefore, it is not surprising that basic experimental research is viewed critically by the industry. This critical bench-to-market-to-clinic-and-back discussion is tremendously important to better understand and optimize the efficacy of current antimicrobial wound dressings and their investigations.

The enormous importance of the topic "chronic wounds and antimicrobial wound dressings" is also illustrated by the fact that three additional research articles are dedicated to this topic within the scope of this special edition. The work by Ward et al. describes for the first time a novel mcl-PHA/graphene composite wound patch that can detect the presence of infection with *Pseudomonas aeruginosa* PA_{14}, an important wound pathogen, in real time. In addition, a closed-loop control algorithm was outlined that will be further developed to create a system that can dynamically control the concentration of antimicrobial agents (such as silver ions, but also others) in a wound bed to actively kill *P. aeruginosa* in response to infection. Orlando et al. have presented for the first time a promising strategy for using bacterial cellulose as a wound dressing with tailored properties. Its intrinsic hydrogel-like nature can provide a high level of moisture for dry wounds and great biocompatibility, while the eco-friendly functionalization performed can ensure inhibitory activity against various bacterial species. In addition, this versatile method can also be applied to other polysaccharides to provide them with intrinsic antibacterial properties while improving their wound healing properties.

Essential oils represent another group of substances that may have anti-microbial as well as anti-inflammatory properties. Here, too, it is crucial how such substances are formulated, applied and released. Unalan et al. combined peppermint essential oil (PEP) with poly (ε-caprolactone) (PCL) in electrospun fiber mats for use as cytocompatible and antimicrobial wound dressings. Leyva Del Rio et al. used tt-farnesol, a natural sesquiterpene alcohol found in propolis, as a potential antimicrobial and anti-biofilm agent in dental adhesive systems. Formulation of this agent was shown to suppress both the production of extracellular insoluble polysaccharides (EIPs) and the bacterial viability of *Streptococcus mutans* biofilm. However, the authors also critically discussed that the addition of tt-farnesol to the complex composition of the dental adhesive system altered its physical and binding properties.

Two other research papers investigated the usability of AMPs. While Najmi et al. investigated the use of the antimicrobially active peptides Nisin and LL-37 to prevent septic articular cartilage degeneration, Piarali et al. dealt with the development of electrospun PHA meshes modified in a single step with a combination of the AMP Amhelin and the biofilm degrading enzyme Dispersin B. Both works were able to demonstrate antimicrobial (and biofilm-disruptive) efficiency while maintaining biocompatibility considering application and environmental conditions.

Amphiphilic cationic macromolecules (ACMs) represent another promising way to attack bacteria and fungi, including highly resistant strains, and their polymicrobial biofilms. For example, Mukherjee et al. demonstrated that their polyetheleneimine-based ACMs are highly active against MRSA and *Candida albicans* without damaging mammalian cells in the required therapeutic window.

In all cases, Nature itself is the inspiration. More specifically, *Combating Bacterial Infections Through Biomimetic or Bioinspired Materials Design and Enabling Technologies* invites the reader to learn about breakthrough contributions from leading scientists in the areas of i) Biomimetic polymers and hybrids with antibacterial activity, ii) Bioactive ceramics and glasses that prevent bacterial growth, iii) Design of unfavorable surface topographies and chemical functionalisation for bacterial colonization, and iv) 2D and 3D *in vitro* testing of antibacterial activity and eukaryotic biocompatibility.

AUTHOR CONTRIBUTIONS

JS wrote the initial editorial text version. GC, AB, IR, and AN made a comprehensive proofread, a careful reference check, and added comments. Finally, all changes and reviewer suggestions were inserted by JS, with regards to content finally checked by GC, AB, AN and IR and submitted by JS.

REFERENCES

Amin Yavari, S., Castenmiller, S. M., van Strijp, J., and Croes, M. (2020). Combating Implant Infections: Shifting Focus from Bacteria to Host. *Adv. Mater. (Deerfield Beach, Fla.)* 32 (43), e2002962. doi:10.1002/adma.202002962

Charani, E., Tarrant, C., Moorthy, K., Sevdalis, N., Brennan, L., and Holmes, A. H. (2017). Understanding Antibiotic Decision Making in Surgery-A Qualitative Analysis. *Clin. Microbiol. Infect.* 23 (10), 752–760. doi:10.1016/j.cmi.2017.03.013

Hutchings, M. I., Truman, A. W., and Wilkinson, B. (2019). Antibiotics: Past, Present and Future. *Curr. Opin. Microbiol.* 51, 72–80. doi:10.1016/j.mib.2019.10.008

Idrees, A., Varela, P., Ruini, F., Vasquez, J. M., Salber, J., Greiser, U., et al. (2018). Drug-free Antibacterial Polymers for Biomedical Applications. *Biomed. Sci. Eng.* 2 (1). doi:10.4081/bse.2018.39

Ventola, C. L. (2015). The Antibiotic Resistance Crisis: Part 1: Causes and Threats. *P T* 40 (4), 277–283.

Conflict of Interest: The authors declare that the research was conducted in the absence of any commercial or financial relationships that could be construed as a potential conflict of interest.

frontiers in Bioengineering and Biotechnology

ORIGINAL RESEARCH
published: 26 November 2019
doi: 10.3389/fbioe.2019.00346

Physical and Antibacterial Properties of Peppermint Essential Oil Loaded Poly (ε-caprolactone) (PCL) Electrospun Fiber Mats for Wound Healing

Irem Unalan[1†], Benedikt Slavik[2†], Andrea Buettner[2†], Wolfgang H. Goldmann[3], Gerhard Frank[1] and Aldo R. Boccaccini[1†]*

[1] Department of Materials Science and Engineering, Institute of Biomaterials, Friedrich-Alexander-University Erlangen-Nuremberg, Erlangen, Germany, [2] Chair of Aroma and Smell Research, Department of Chemistry and Pharmacy, Friedrich-Alexander-University Erlangen-Nuremberg, Erlangen, Germany, [3] Department of Physics, Institute of Biophysics, Friedrich-Alexander-University Erlangen-Nuremberg, Erlangen, Germany

OPEN ACCESS

Edited by:
Anderson Oliveira Lobo, Federal University of Piauí, Brazil

Reviewed by:
Edvani Curti Muniz, Federal University of Piauí, Brazil
Xin Zhao, Hong Kong Polytechnic University, Hong Kong

***Correspondence:**
Aldo R. Boccaccini
aldo.boccaccini@ww.uni-erlangen.de

†ORCID:
Irem Unalan
orcid.org/0000-0002-4729-0012
Benedikt Slavik
orcid.org/0000-0002-6237-8012
Andrea Buettner
orcid.org/0000-0002-6205-5125
Aldo R. Boccaccini
orcid.org/0000-0002-7377-2955

Specialty section:
This article was submitted to Biomaterials, a section of the journal Frontiers in Bioengineering and Biotechnology

Received: *31 July 2019*
Accepted: *06 November 2019*
Published: *26 November 2019*

Citation:
Unalan I, Slavik B, Buettner A, Goldmann WH, Frank G and Boccaccini AR (2019) Physical and Antibacterial Properties of Peppermint Essential Oil Loaded Poly (ε-caprolactone) (PCL) Electrospun Fiber Mats for Wound Healing. Front. Bioeng. Biotechnol. 7:346. doi: 10.3389/fbioe.2019.00346

The aim of this study was to fabricate and characterize various concentrations of peppermint essential oil (PEP) loaded on poly(ε-caprolactone) (PCL) electrospun fiber mats for healing applications, where PEP was intended to impart antibacterial activity to the fibers. SEM images illustrated that the morphology of all electrospun fiber mats was smooth, uniform, and bead-free. The average fiber diameter was reduced by the addition of PEP from 1.6 ± 0.1 to 1.0 ± 0.2 μm. Functional groups of the fibers were determined by Raman spectroscopy. Gas chromatography-mass spectroscopy (GC-MS) analysis demonstrated the actual PEP content in the samples. *In vitro* degradation was determined by measuring weight loss and their morphology change, showing that the electrospun fibers slightly degraded by the addition of PEP. The wettability of PCL and PEP loaded electrospun fiber mats was measured by determining contact angle and it was shown that wettability increased with the incorporation of PEP. The antimicrobial activity results revealed that PEP loaded PCL electrospun fiber mats exhibited inhibition against *Staphylococcus aureus* (gram-positive) and *Escherichia coli* (gram-negative) bacteria. In addition, an *in-vitro* cell viability assay using normal human dermal fibroblast (NHDF) cells revealed improved cell viability on PCL, PCLPEP1.5, PCLPEP3, and PCLGEL6 electrospun fiber mats compared to the control (CNT) after 48 h cell culture. Our findings showed for the first time PEP loaded PCL electrospun fiber mats with antibiotic-free antibacterial activity as promising candidates for wound healing applications.

Keywords: peppermint essential oil, poly (ε-caprolactone), electrospinning, antibacterial activity, wound healing

INTRODUCTION

Human skin, the largest organ in the integumentary system, provides a robust barrier to protect the body against physical, chemical, thermal, surgical, and bacterial damages (Priya et al., 2008). The injury of human skin occurs by acute and chronic wound effects such as trauma, burns, ulcers, or diabetes. Wound dressings play a crucial role in treating these injuries by protecting the wound

from the external environment, providing suitable moisture and facilitating the wound healing process (MacNeil, 2008). Further, antibacterial wound dressings are required to reduce the risk of bacterial infection during the wound healing process. Many reports have been published on the antibacterial effects of wound dressings containing antibiotics (Howell-Jones et al., 2005) and metal ions such as silver, zinc, and copper (Juby et al., 2012; Mahltig et al., 2013; Kędziora et al., 2018). Moreover, in recent years the combination of synthetic biomaterials and biological molecules based on plant-derived compounds has started to be used widely for wound healing approaches (Ramos-e-Silva and Ribeiro de Castro, 2002; Dhivya et al., 2015). Although the use of phenols and essential oils (EOs) as natural active agents is rather novel in combination with engineered biomaterials for biomedical applications (Sadri et al., 2015; Li et al., 2018; Jaganathan et al., 2019), there is increasing interest for this kind of substances in medicine, considering the fact that EOs have been used by humans for thousands of years to obtain therapeutic effects (Silva and Fernandes Júnior, 2010).

EOs based on plant extracts, such as peppermint, cinnamon, lemon, and clove essential oil, have been applied to accelerate the wound healing process since ancient times due to their various therapeutic benefits like antibacterial activity, inflammatory, and antioxidation potential (Prabuseenivasan et al., 2006; Bakkali et al., 2008). However, the volatility, low stability, and high sensitivity to environmental factors have limited the usage of EOs in wound healing applications (El Asbahani et al., 2015). In the last decade, however, research has focused on EOs-biomaterial incorporation to exploit the therapeutic properties of EOs (Bilia et al., 2014; Rijo et al., 2014; Zhang et al., 2017). One commonly considered EO is peppermint (PEP) essential oil. PEP is mostly derived from the leaf of the *Mentha piperita* (Lamiaceae) and it is composed of L-menthol, menthone, methyl acetate, and limonene, which exhibit antibacterial activity (McKay and Blumberg, 2006; Kligler and Chaudhary, 2007).

Electrospinning is a cost-effective, versatile, and well-established method to produce flexible, highly porous, nano- or micro-size, and continuous fibrous structures (Sill and von Recum, 2008). Keeping the stability of chemical structures and enhancing biological properties by incorporation of synthetic and natural polymers are further advantages of the electrospinning method (Martins et al., 2008). Various biodegradable and biocompatible polymeric materials such as poly(*ε*-caprolactone) (PCL), poly (L-lactic acid) (PLLA), poly (lactic-co-glycolic acid) (PLGA), collagen, chitosan, gelatin, and their copolymers have been investigated for fabricating fibrous materials (Sell et al., 2010; Mogoşanu and Grumezescu, 2014; Sun et al., 2016). Among these, PCL is the most commonly used biocompatible, low-cost, biodegradable, linear-aliphatic polyester for fiber electrospinning fabrication (Abedalwafa et al., 2013). It can be easily processed in combination with natural polymers and biomolecules to enhance antibacterial and biological properties. Also, PCL exhibits relatively high mechanical properties (Croisier et al., 2012). The development of PCL fibers by electrospinning using "benign" (non-toxic) solutions has been also investigated (Liverani and Boccaccini, 2016). In recent years, combinations of EOs and PCL have been investigated as wound dressing materials in several studies. For instance, Suganya et al. (2011) fabricated PCL and polyvinyl pyrrolidone (PVP) nanofiber mats containing herbal drug from *Tecomella undulata* by electrospinning technique. Their work revealed that incorporation with EO led to strong antibacterial properties against several bacteria strains, such as *P. aureuginosa*, *S. aureus,* and *E. coli*. According to Shao et al. (2011), green tea phenols (GTP)-loaded poly(ε-caprolactone)/multi-walled carbon nanotubes (PCL/MWCNTs) composite nanofibers displayed low cytotoxicity for osteoblast cells whereas high inhibition effect was observed for Hep G2 tumor cells. Jin et al. (2013) reported that human dermal fibroblasts (NHDF) proliferation was increased during 9 days of cell culture with the addition of four different plant extracts separately. In another study, Karami et al. (2013) produced thymol loaded 50/50 PCL/poly(lactic acid) (PLA) hybrid nanofibrous mats for wound healing. *In vivo* rat wound healing results indicated that the wound-closure percentage was 92.5% after 14 days compared to 68% for gauze bandages as a control. More recently, Amiri and Rahimi (2019) developed PCL electrospun nanofibers containing cinnamon oil nanoparticles, and their results revealed the positive effect of controlled cinnamon oil release in drug delivery and tissue engineering applications.

The aim of the present study was to fabricate various concentrations of peppermint oil loaded PCL electrospun fiber mats intended for antibiotic-free wound healing applications and to characterize their morphology, physical properties, and antibacterial activity. In this sense, we investigated the effect of various PEP concentrations (1.5, 3, and 6% v/v) on morphology, average fiber diameter, contact angle (wettability), *in vitro* degradation, antibacterial activity, and cell viability of PCLPEP electrospun fiber mats. The combination of PEP and PCL in fibrous structures for biomedical applications has not been investigated before, to the best of the authors' knowledge.

MATERIALS AND METHODS

Materials

PCL (Mw = 80,000), PEP essential oil (purified by triple-distillation), standard menthol, and fetal bovine serum (FBS) were purchased from Sigma-Aldrich (Darmstadt, Germany). Glacial acetic acid (GAA, VWR, Darmstadt, Germany) was used as a solvent. Phosphate-buffered saline (PBS, biotech grade, pH 7.4) and dichloromethane (DCM) were obtained from VWR (Darmstadt, Germany). The microorganism strains of *S. aureus* (ATCC25923), and *E. coli* (ATCC25922) were used in our laboratory. Luria-Bertani (LB) agar and lysogeny broth (LB) medium were supplied by Carl Roth GmbH (Karlsruhe, Germany). Dulbecco's modified Eagle's medium (DMEM), penicillin/streptomycin (PS), and trypsin/EDTA were purchased from Thermo Scientific (Schwerte, Germany). NHDF cell line was obtained from Translation Research Center (TRC), Erlangen. All reagents and solvents were of analytical grade.

Methods

Preparation of Electrospinning Solutions

The preparation of electrospinning solutions is illustrated in **Figure 1**. PCL solution (20 w/v%) was dissolved in GAA overnight under constant stirring at room temperature to

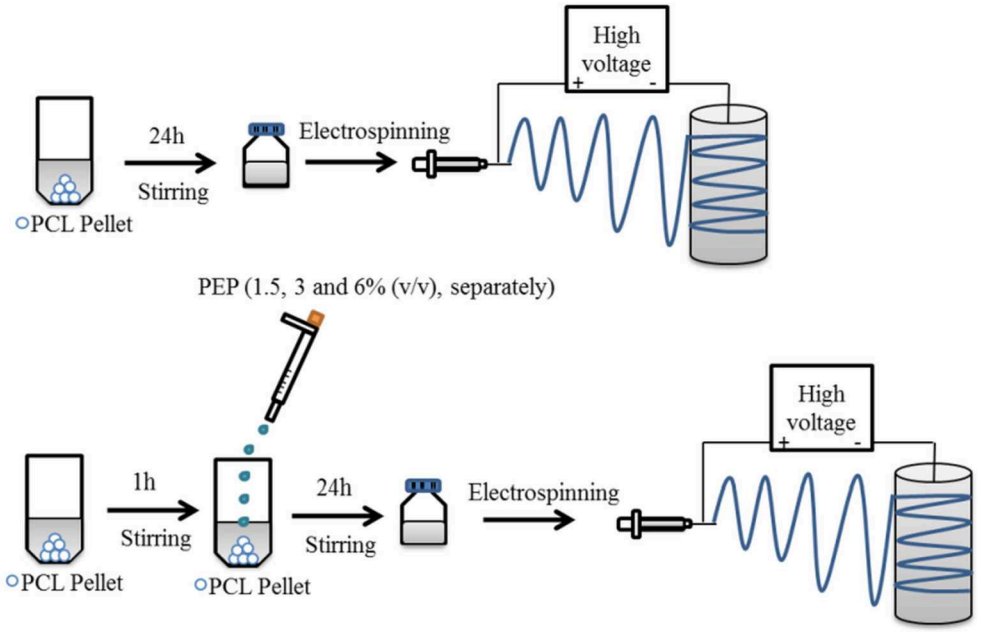

FIGURE 1 | Schematic illustration for the preparation of electrospun fiber mats with and without PEP.

fabricate pure PCL electrospun fiber mats. For the PEP loaded PCL solutions, various concentrations of PEP [at 1.5, 3, and 6% (v/v), namely PCLPEP1.5, PCLPEP3, and PCLPEP6] were added separately into the polymer solution. The prepared solutions were stirred overnight at room temperature to yield a homogenous solution. The polymer and PEP concentrations were adjusted to the optimum electrospinning parameters.

Electrospinning Process

Electrospinning was carried out under defined and constant ambient conditions [temperature (T): 25°C and relative humidity (RH): 40%] by using a commercially available setup (EC-CLI, IME Technologies, Netherlands). Each electrospinning solution was loaded separately into a 3 ml plastic syringe equipped with a 23G needle. The solutions were fed at 0.4 ml/h. An aluminum sheet wrapped around a rotating drum, used as the collector, was placed at a distance of 11 cm from the needle tip to the collector. Electrospun fiber mats were collected by applying a voltage at +14 kV in the needle, and at −1 kV in the target. Further, the gas shield accessory with nitrogen flux was set at 8 ml/min for optimization of the Taylor cone. The obtained samples were stored at 4°C in the dark until further analysis.

Characterizations

Surface morphology and average fiber diameter

The morphology of the electrospun fiber mats was characterized using a scanning electron microscope [SEM, ETH: 2 kV, Everhart-Thornley detector (SE2), AURIGA base 55, Carl Zeiss]. The samples were coated with a thin layer of gold (Q150T Turbo-Pumped Sputter Coater/Carbon Coater, Quorum Technologies) before SEM observations. The average diameter and diameter distribution of electrospun fibers was estimated from the SEM micrographs via Image J analysis software (NIH, USA). The average fiber diameter was measured randomly at 50 different points for each sample.

Raman spectroscopy analysis

Raman spectra of the electrospun fiber mats and peppermint oil were analyzed using a μRaman spectrometer (LabRAM 800, HORIBA, Jobin Yvon) operating with a He-Ne laser source with an excitation wavelength of 633 nm. A microscope objective 50x/0.75 and a 1.800 line/mm spectrometer grating was used to record the spectra.

Wettability

The wettability of the electrospun fiber mats was measured by using a contact angle measuring device (DSA30 CA Measurement setup, Kruess GmbH) by the sessile drop method. The sample was pasted on a glass slide before the test, and an 8 μl droplet of de-ionized water was pipetted onto the surface of fiber mats for each measurement. Three measurements were taken at different locations of the same mat, and the average value was obtained.

In vitro degradation

In vitro degradation experiments were carried out as described previously (Agnes Mary and Giri Dev, 2015). Briefly, the electrospun fiber mats were cut into 3 ×3 cm^2 pieces, which had an initial weight of around 30 mg. The samples were immersed in 10 ml of phosphate-buffered saline (PBS, pH 7.4) solution for 1, 3, 7, and 14 days at 37°C and 120 rpm. At each time interval, samples were taken out from the PBS and rinsed three times

with de-ionized water prior to drying at 37°C for 3 days. The morphology of samples was analyzed by SEM. The weight loss of electrospun fiber mats was calculated as follows (1):

$$Weight\ loss\ (\%) = \frac{(Wi - Wd)}{Wi} x100 \quad (1)$$

where wi and w_d are the initial and dry weight of mats, respectively. All degradation tests were carried out in triplicate.

Peppermint oil content in PCL electrospun fiber mats

The total PEP content in PEP loaded electrospun fiber mats was analyzed by determining the menthol content by means of gas chromatography-mass spectrometry (GC-MS) using a GC 7890A and MSD 5975C (Agilent Technologies, Waldbronn, Germany) equipped with a DB-FFAP capillary column (30 m × 0.25 mm, film thickness 0.25 μm; Agilent Technologies, Santa Clara, CA). Firstly, the calibration curve was prepared from pure undiluted menthol at various concentrations (between 0.623 and 107 μg/ml) then, the solutions were injected into the GC-MS system. The concentration of menthol was calculated using the peak area (concentration = 916066 x peak area, $R^2 = 0.9959$). After obtaining the menthol calibration curve, the electrospun fiber mats (∼10 mg) were submerged in DCM (20 ml) for 2 h. Subsequently, the volatile fraction of PEP extraction was isolated by means of the solvent-assisted flavor evaporation technique (SAFE) (Engel et al., 1999). The volatile fraction in DCM was dried over sodium sulfate and then was filtered. The final volume was reduced to 100 μl using Vigreux- and microdistillation at 50°C (Bemelmans, 1979) Then, 1 μl of each sample was taken for the GC-MS measurements. The oven temperature was programmed at 40°C for 2 min and was then heated up at 8°C/min to 240°C and held for 5 min. Helium was used as carrier gas with a flow rate of 1 ml/min. Mass spectra were recorded with selected ion monitoring(SIM) mode (m/z ratio 71).

Afterwards, the percentage of encapsulation efficiency was calculated as follows (2):

$$Encapsulation\ Efficiency\ (EE)\ (\%) = \frac{m_a}{m_t}\ x\ 100 \quad (2)$$

Where, m_a and m_t are the actual and theoretical amounts of PEP in the electrospun fiber mats, respectively.

Antibacterial Assay

The antibacterial activity of PCL and PCLPEP electrospun fiber mats was determined on *S. aureus* (Gram-positive) and *E. coli* (Gram-negative) bacteria. Firstly, the bacteria strains were incubated in lysogeny broth medium at 37°C for 24 h, and the optical density (OD) of the bacteria population was calibrated (600 nm, Thermo Scientific™ GENESYS 30™, Germany) to reach the value of 0.015, according to turbidity measurements of bacterial cultures. To assess the antibacterial activity of electrospun fiber mats, the samples were weighted (30 mg) and were sterilized by UV irradiation for 30 min prior to the experiment. Then, the samples were placed into a tube with 20 μl bacteria suspension, which was measured with the OD, in 2 ml broth medium. The samples were incubated at 37°C for various times (3, 6, 24, and 48 h). The OD value of the samples was measured at 600 nm after each incubation time interval, and relative bacterial viability was calculated as follows:

$$Relative\ bacterial\ viability\ (\%) = \frac{sample_{OD}}{control_{OD}} x100 \quad (3)$$

The lysogeny broth medium and bacterial cell suspension in lysogeny broth medium were used as blank and control. Three parallel experiments were performed for each sample.

WST-8 Cell Viability Assay

The cell viability of NHDF cells was analyzed on the PCL, PCLPEP1.5, PCLPEP3, and PCLPEP6 fiber mats. Firstly, NHDF cells were cultured in DMEM supplemented with 10% (FBS) and 1% penicillin/streptomycin solutions in 75 cm^2 cell culture flasks (Nunc, Denmark). Counted cells were seeded into 24-well plates at a density of 50,000 cell/well and incubated at 37°C in a humidified incubator with 5% CO_2 for 24 h. Prior to cell culture experiment, the nanofiber mats were fixed on CellCrownTM 24 inserts (ScaffdexOy, Tampere, Finland) and sterilized by UV light irradiation for 30 min. After 24 h incubation, the samples were immersed in a 24-well plate without touching the cell and incubated for further 48 h. After culturing the cells for 48 h, the viability of the cells was analyzed by a WST-8 cell counting assay kit (Sigma Aldrich) (with 5% WST-8 reagent in DMEM for a period of 2 h at 37°C). Finally, the absorbance of the obtained dye was measured at 450 nm using a spectrophotometric plate reader (PHOmo, anthos Mikrosysteme GmbH, Germany). The percentage of cell viability was calculated as follows:

$$Cell\ viability\ (\%) = \frac{Ab.\ of\ control - Ab.\ of\ test\ sample}{Ab.\ of\ control - Ab.\ of\ blank} x100 \quad (4)$$

The absorbance of cell plus culture medium and WST-8 reagent were used as a control and blank. All samples were measured six times.

Statistical Analysis

The statistical analysis of the data was carried out using one-way analysis of variance (ANOVA) with Origin (OriginLab, Northampton, MA, USA). To evaluate the statistically significant difference between groups, Bonferroni's test was applied, and $p < 0.05$ was considered to be significant.

RESULTS

Surface Morphology and Diameter Distribution of Electropsun Fibers

Electrospun PCL and PCL fibers loaded with various amounts of PEP [1.5, 3, and 6% (v/v), namely PCLPEP1.5, PCLPEP3, and PCLPEP6] were fabricated by electrospinning method. Electrospinning processing parameters were optimized at a flow rate of 0.4 ml/h, the voltage of 15 kV and distance of 11 cm to reduce the number of beads on the fiber and fabricate homogenous, smooth fibers. All prepared mats were coded as shown in **Table 1**. **Figure 2** illustrates that the morphology of the electrospun fiber mats was smooth, uniform, and bead-free.

TABLE 1 | Sample composition, sample label, average fiber diameter, and loading efficiency of electrospun fiber mats.

Sample code	PCL (w/v %)	PEP (v/v %)	Average fiber diameter (μm)	Encapsulation efficiency (EE) (%)
PCL	20	–	1.6 ± 0.1	–
PCLPEP1.5	20	1.5	1.1 ± 0.2	36 ± 14
PCLPEP3	20	3	1.0 ± 0.2	39 ± 10
PCLPEP6	20	6	1.0 ± 0.2	43 ± 7

This result indicates no PEP aggregation on the fiber surface and that the incorporation of PEP in the PCL solution did not affect the fiber morphology. Additionally, the average fiber diameters of PCL, PCLPEP1.5, PCLPEP3, and PCLPEP6 fiber mats were 1.6 ± 0.2, 1.1 ± 0.2, 1.0 ± 0.2, and 0.9 ± 0.2 μm, respectively (**Table 1**). The distribution of fiber diameters indicates that the addition of PEP led to a slight decrease in fiber diameter as compared to neat PCL (**Figure 1**). However, increasing PEP concentration from 1.5 to 6% (v/v) did not significantly affect the average fiber diameter.

Raman Spectroscopy Analysis

The spectra of the Raman spectroscopy analysis of PEP and electrospun fiber mats are shown in **Figure 3**. As was reported in previous studies, menthol, menthone, and 1,8-cineole are the main components of PEP (Reverchon et al., 1994; Rohloff, 1999). Therefore, it was important to investigate the presence of such compounds in the fibers. The Raman spectrum of PEP exhibits peaks at 2870, 1457, and 769 cm^{-1}, as illustrated in **Figure 3a**. The band at 2870 cm^{-1} is assigned to terpenoid vibrations of the PEP (Schulz et al., 2004). The other strong peaks at 1457 and 769 cm^{-1} correspond to CH_3/CH_2 bending of menthol and the ring deformation mode of menthol, respectively (Rösch et al., 2002; Jentzsch et al., 2015). As presented in **Figure 3b**, the typical peaks of PCL at 2916 and 2864 cm^{-1} can be related to the asymmetric and symmetric vibrations of the CH_2 group. Further, the band for C=O vibration of the ester group was observed at 1721 cm^{-1} (Wesełucha-Birczyńska et al., 2015). These PCL peaks are evident in PCLPEP1.5, PCLPEP3, and PCLPEP6 electrospun fiber mats, whereas the bands of PEP only appeared in PCLPEP3 and PCLPEP6 (**Figures 3c–e**). Likewise, the typical band of PEP at 769 cm^{-1} did not appear in the Raman spectrum of PCLPEP1.5, PCLPEP3, and PCLPEP6. This could be attributed by the overlap with the PCL peaks.

Wettability

Figure 4 shows the contact angle values of PCL, PCLPEP1.5, PCLPEP3, and PCLPEP6 electrospun fiber mats. The average contact angle of PCL electrospun fiber mats was 104 ± 8°, whereas the PEP addition slightly decreased the contact angle to 98 ± 5°. However, no significant differences between PEP loaded PCL electrospun fiber mats, PCLPEP1.5 (100 ± 6°), PCLPEP3 (99 ± 5°), and PCLPEP6 (98 ± 5°) were found.

In vitro Degradation

An *in vitro* degradation study of electrospun fiber mats was conducted to evaluate the effect of PEP addition on PCL degradation in PBS. The morphology of electrospun PCL, PCLPEP1.5, PCLPEP3, and PCLPEP6 fiber mats after immersion in PBS for 14 days is illustrated in **Figure 5**. SEM images revealed that the fiber morphology was slightly degraded compared to the original structure. However, the overall fibrous morphology of samples mostly remained during the degradation study. **Figure 6** shows the weight loss percentage of electrospun PCL, PCLPEP1.5, PCLPEP3, and PCLPEP6 fiber mats. The results demonstrated that the addition of PEP slightly increased the degradation rate compared to PCL electrospun fiber mats on 1d. However, there were no statistical changes among PCLPEP1.5, PCLPEP3, and PCLPEP6.

Peppermint Oil Content in PCL Electrospun Fiber Mats

The main compound of PEP, menthol, was identified by GC using retention index and comparison with standard menthol (**Figure 7**). The actual amount of menthol in the pure PEP was 297 mg/ml. Besides, the encapsulation efficiency of PEP in PCL fiber mats was investigated by GC-MS spectroscopy. **Table 1** shows the influence of the different concentrations of PEP on the percentage of encapsulation efficiency. The PEP encapsulation efficiency increased from 36 ± 14 to 43 ± 7% at PEP concentrations of 1.5 to 6 (v/v %). The results indicate that increasing PEP concentration has led to increased encapsulation efficiency.

Antibacterial Assay

The antibacterial activity of PCL, PCLPEP1.5, PCLPEP3, and PCLPEP6 electrospun fiber mats was tested with *Staphylococcus aureus* as gram-positive bacteria and *Escherichia coli* as gram-negative bacteria, separately. As presented in **Figure 8**, the relative bacterial viability of samples was investigated at 3, 6, 24, and 48 h. During the 48 h incubation, PCLPEP1.5, PCLPEP3, and PCLPEP6 exhibited decreased bacterial viability compared to PCL electrospun fiber mats. Additionally, the antibacterial activity was enhanced with an increase of PEP concentration in PCLPEP1.5, PCLPEP3, and PCLPEP6. The PCLPEP6 composition showed the lowest bacterial viability (*S. aureus*; 50 ± 3% and *E. coli*; 70 ± 2%) at 24 h incubation.

WST-8 (Cell Viability) Assay

The viability of NHDF cells was investigated to assess the biocompatibility of PCL, PCLPEP1.5, PCLPEP3, and PCLPEP6 fiber mats after 48 h of incubation, as shown in **Figure 9**. The results demonstrated that the cell viability of all fiber mats was increased compared to the control. However, there was no significant difference between each other. Our results thus indicated that PEP loaded PCL electrospun fiber mats exerted no toxic effects on NHDF cells.

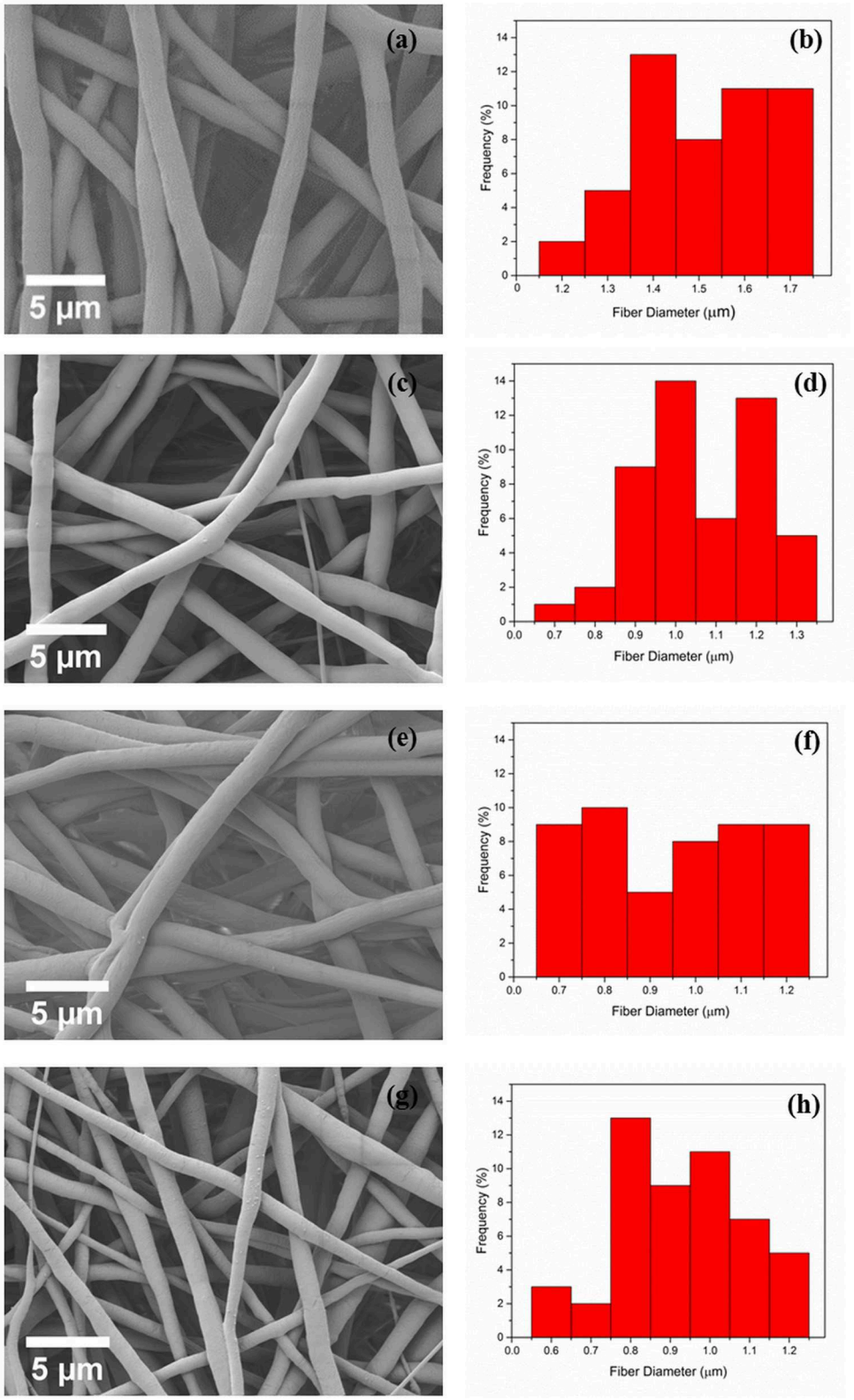

FIGURE 2 | The morphology and fiber diameter distribution of PCL **(a,b)**, PCLPEP1.5 **(c,d)**, PCLPEP3 **(e,f)**, and PCLPEP6 **(g,h)** electrospun fiber mats, respectively.

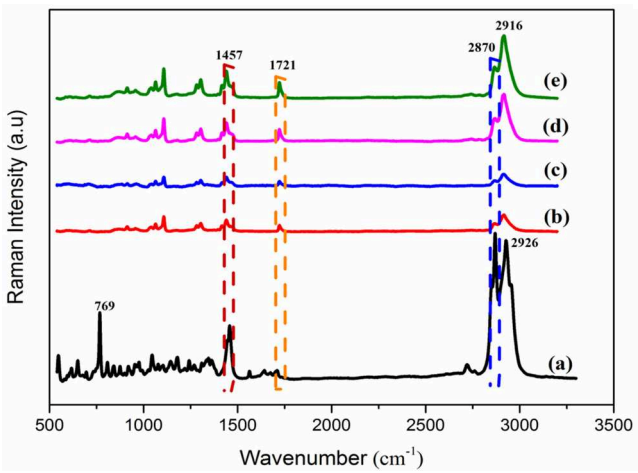

FIGURE 3 | The Raman spectra of pure PEP **(a)**, PCL **(b)**, PCLPEP1.5 **(c)**, PCLPEP3 **(d)**, and PCLPEP6 **(e)** electrospun fiber mats.

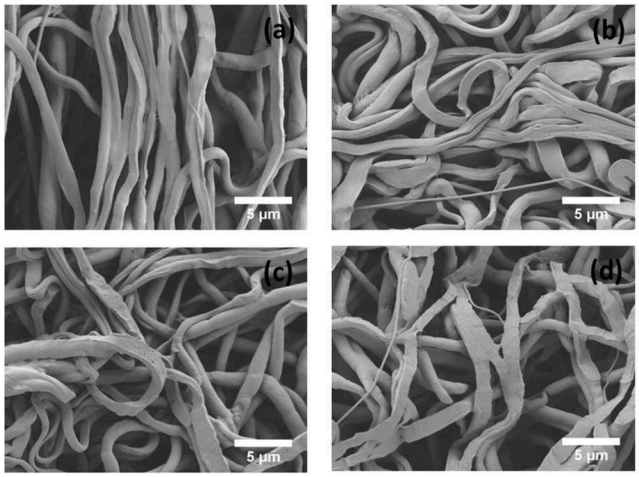

FIGURE 5 | SEM images of PCL **(a)**, PCLPEP1.5 **(b)**, PCLPEP3 **(c)**, and PCLPEP6 **(d)** electrospun fiber mats after 14 days incubation in PBS at 37°C.

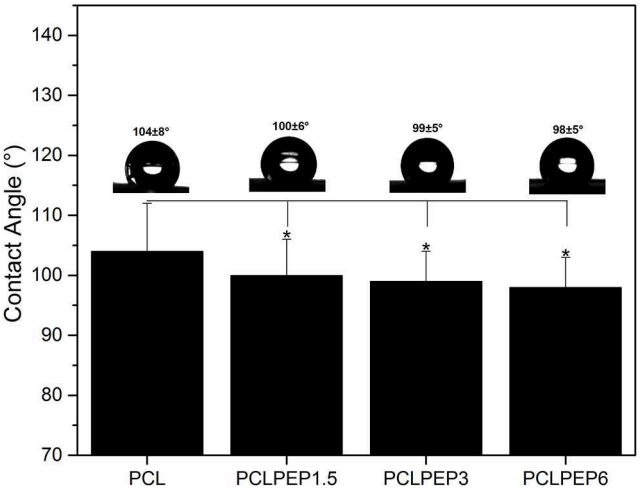

FIGURE 4 | Water contact angle of PCL, PCLPEP1.5, PCLPEP3, and PCLPEP6 electrospun fiber mats ($n = 3$, sample in triplicate,*$p < 0.05$).

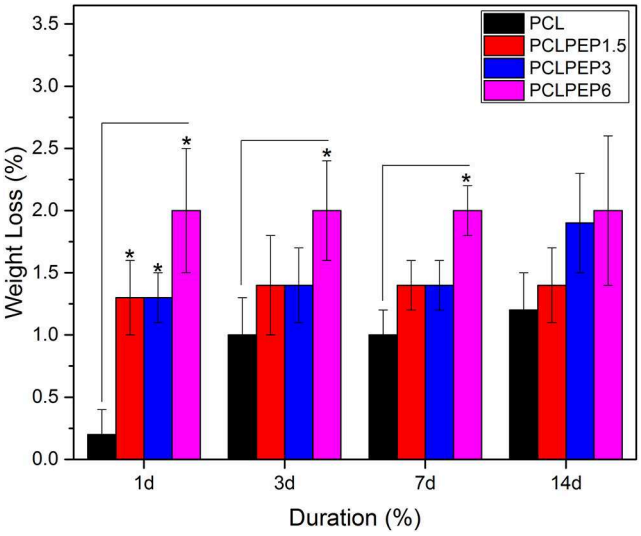

FIGURE 6 | Weight loss percentage of PCL, PCPPEP1.5, PCLPEP3, and PCLPEP6 electrospun fiber mats incubated in PBS at 37°C for 1, 3, 7, and 14 days ($n = 3$, sample in triplicate,*$p < 0.05$).

DISCUSSION

EOs for antibiotic-free wound healing applications represent an emerging area of interest, which exploits the antibacterial activity, anti-inflammatory and antioxidative properties of EOs. This study investigates the various concentration of PEP loaded into electrospun PCL fiber mats in term of physical properties and antibacterial activity. Very few studies have reported on the electrospun fiber system incorporated with peppermint oil for wound healing applications. For instance, Liakos et al. (2015) fabricated homogenous, and bead-free cellulose/peppermint oil electrospun composite fibers for wound dressing; our results resemble their findings. In a related study, Jaganathan et al. (2019) reported on smooth and uniform electrospun polyurethane (PU) fibers of 635 nm ± 105 nm diameter using an electrospinning method adding PEP and copper sulfate ($CuSO_4$) for wound dressing applications.

Data obtained in this study indicated that the average fiber diameter slightly decreased with the addition of PEP from 1.6 ± 0.2 to 0.9 ± 0.2 µm (**Table 1**). This could be due to the plasticizer effect of the essential oil (Mori et al., 2015). In this regard, PEP might be acting as a plasticizer, altering the order between single polymer chains and resulting in the decrease of solution viscosity. Further, the addition of PEP may increase the solution conductivity, which decreases the fiber diameter. Many studies have investigated that various electrospinning parameters such as polymer concentration, solution viscosity, flow rate of the polymer solution and solution conductivity affect the

fiber morphology and fiber diameter and the solution of EO is expected to have an effect on these (Sill and von Recum, 2008; Bhardwaj and Kundu, 2010). According to Rieger et al. (2016), cinnamaldehyde (CIN) incorporation in chitosan/poly (ethylene oxide) nanofiber mats strongly decreased the solution viscosity (from 2.5 to 0.8 Pa s). In another study, Mani et al. (2018) reported that polyurethane composites containing neem oil showed a smaller fiber diameter due to the increase in the conductivity of the polymer solution. Similarly, Uslu et al. (2010) fabricated hybrid nanofibers based on poly (vinyl alcohol)/poly (vinyl pyrrolidone)/poly (ethylene glycol) incorporated with aloe vera. It was found that hybrid nanofibers exhibited a decreased diameter with increased electrical conductivity. The fact that PEP addition to PCL had no significant effect on PCL fiber morphology is important for applications, taking into account the need of developing a robust method for the reproducible production of fiber mats.

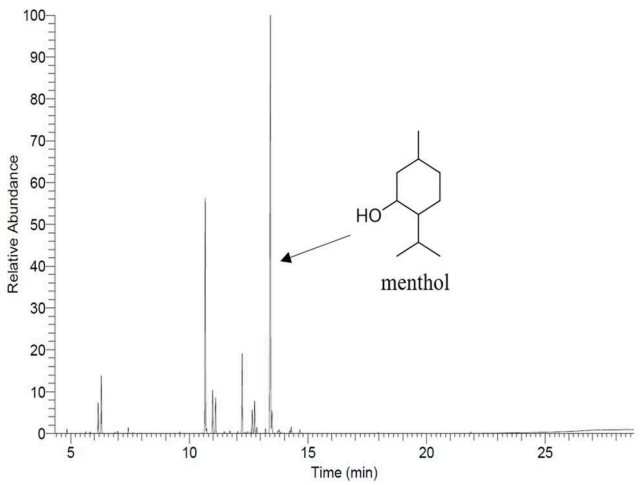

FIGURE 7 | Gas chromatography profile of menthol showing it as a main component of PEP.

Based on the findings in this study, the addition of PEP slightly decreased the average contact angle (**Figure 4**). This result might be due to the chemical structure of PEP that includes an oxygenated group, which can interact with the H_2O molecule. In a similar study, Jin et al. (2013) fabricated PCL nanofibers incorporated with four different essential oil extracts, namely *Indigofera aspalathoides* (IA), *Azadirachta indica* (AI), *Memecylon edule* (ME), and *Myristica andamanica* (MA). Their results indicated that the addition of essential oil decreased the contact angle value compare to pure PCL (Jin et al., 2013), which is in agreement with our results. In another study, findings of Agnes Mary and Giri Dev (2015) indicated that PCL electrospun matrices comprising aloe vera (AV) had lower contact angle values when the AV concentration increased.

In general, the degradation rate of biopolymers depends on crucial factors such as crystallinity, hydrophilicity, molecular weight, morphological structure, pH, and temperature (Göpferich, 1996). As illustrated in **Figure 6**, the weight loss percentage of electrospun fiber mats slightly increased with the addition of PEP. This result might be attributed to the reduction of intermolecular forces between the PCL chains due to the addition of PEP. Furthermore, the wettability results (**Figure 4**) indicated that addition of PEP slightly reduced the contact angle value, which could also affect the degradation rates. In a similar study, Agnes Mary and Giri Dev (2015) found that the degradation of PCL fibers containing Aloe vera (AV) degraded faster due to the increase of the hydrophilicity of fibers (Agnes Mary and Giri Dev, 2015). In another study, Sadri et al. (2015) reported that the amount of green tea extract increased the degradation of

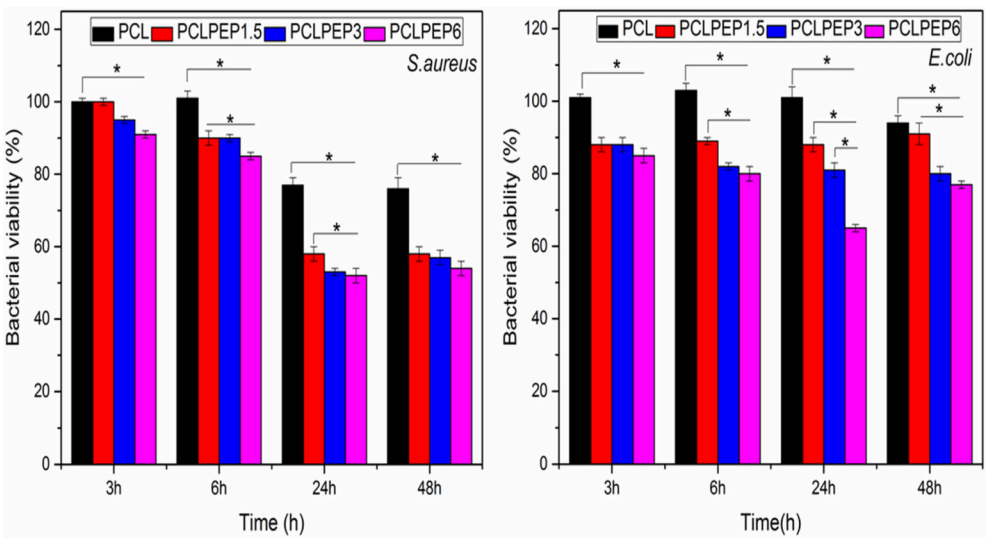

FIGURE 8 | Relative bacteria viability of *S. aureus* (Gram-pozitive) and *E. coli* (Gram-negative) on the different type of electrospun fiber mats (PCL, PCLPEP1.5, PCLPEP3, and PCLPEP6) after 3, 6, 24, and 48 h incubation ($n = 3$, sample in triplicate,*$p < 0.05$).

chitosan/polyethylene oxide polymeric nanofibers (Sadri et al., 2015).

On the other hand, the encapsulation efficiency of PEP in PCL electrospun fiber mats was investigated. **Table 1** shows the effects of the various initial amounts of PEP on encapsulation efficiency. Increasing the initial PEP amount resulted in an overall increase in the amount of PEP encapsulation in the electrospun fiber mats. Similarly, Tampau et al. (2017) investigated the influence of different polymer and carvacrol concentrations on the encapsulation efficiency and found that the encapsulation efficiency increased from 15 to 75% at 5 to 15 wt% carvacrol ratio. Balasubramanian and Kodam (2014) fabricated different concentrations of lavender essential oil encapsulated in polyacrylonitrile (PAN) nanofibers for antibacterial applications. It was revealed that the encapsulation efficiency of fibers ranged from 25.8 to 32.4%. Moreover, the encapsulation efficiency increased with increasing lavender oil concentration in the fibers. In another study, Tavassoli-Kafrani et al. (2018) reported that the encapsulation efficiency of gelatin nanofibers incorporating at different ratios of orange EO increased as the concentration of orange oil increased.

The antibacterial activity of the PEP loaded PCL electrospun fiber mats was tested with *S. aureus* and *E. coli* bacteria. PEP is known to be a potent antimicrobial against a variety of microorganisms by interacting with their cell membrane (McKay and Blumberg, 2006; Kligler and Chaudhary, 2007). Our results indicated that the addition of PEP reduced the bacteria viability for both bacteria strains, as shown in **Figure 8**. Recently, Li et al. (2018) reported that eugenol loaded PCL/gelatin(Gel) electrospun membranes exhibited increasing antibacterial properties with increasing the concentration of eugenol. Moreover, the present samples exhibited better bacterial inhibition toward *S. aureus* than *E. coli*. Gram-negative bacteria such as *E. coli* consist of a double membrane and the outer membrane has a lipopolysaccharide layer which prevents penetration of antibacterial compounds (Hammer et al., 1999; Burt and Reinders, 2003; Burt, 2004). Therefore, PEP loaded electrospun fiber mats could be less effective in their action against *E. coli*. Wen et al. (2016) found similar results for cinnamon oil incorporated PLA (polylactic acid) electrospun nanofibrous film.

Data presented here indicated that there were no significant differences ($p < 0.05$) in the cell viability of the electrospun mats in comparison with the control (**Figure 9**). The *in vitro* cell viability results demonstrated that PCL, PCLPEP1.5, PCLPEP3, and PCLPEP6 electrospun fiber mats exerted no cytotoxic effect on NHDF cells. In agreement with our results, Tang et al. (2019) reported that peppermint and chamomile loaded gelatin nanofibers did not change NIH-3T3 fibroblast cell viability. In another study, Hajiali et al. (2016) investigated the antibacterial activity and biocompatibility of alginate-lavender nanofibers. The cell viability of lavender incorporated alginate nanofibers was 91%. It was stated that the addition of lavender oil did not affect cell viability of human foreskin fibroblast (HFF-1) cells compared to the control group.

Given the large number of studies emerging on the use of EOs in different polymers, the relative antibacterial effectiveness of electrospun fibers incorporating different EOs should be investigated.

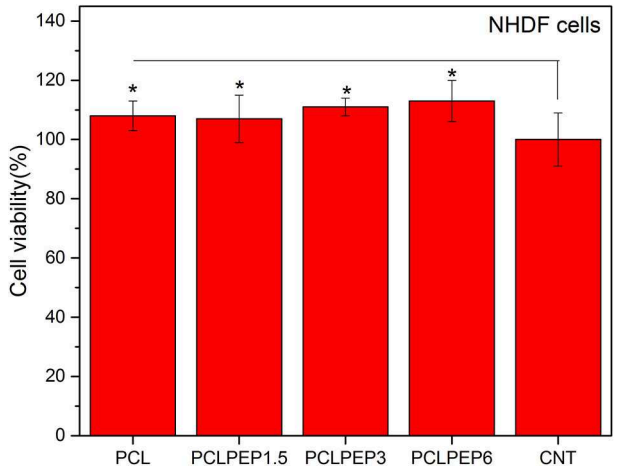

FIGURE 9 | The cell viability of PCL, PCLPEP1.5, PCLPEP3, and PCLPEP6 electrospun mats in comparison with control (CNT) ($n = 6$,*$p < 0.05$).

CONCLUSION

In this study, electrospun PCL fibers at different concentrations of PEP [1.5, 3, and 6 (v/v)%] were developed and characterized. The fibers were smooth and uniform under optimum electrospinning parameters. The morphological analysis showed that the average fiber diameter was reduced from 1.6 $\pm$ 0.1 to 1.0 $\pm$ 0.2 μm when loading PEP. The presence of PEP was confirmed by Raman spectroscopy and GC-MS analysis. Furthermore, the antibacterial activity of PCLPEP electrospun fiber mats was evaluated against both bacteria strains (*S. aureus* and *E. coli*). Our results showed that bacterial inhibition was effective on PEP loaded PCL electrospun fiber mats, especially PCLPEP6. Moreover, the cell viability and antibacterial assay results indicated that the addition of PEP did not induce cytotoxicity, although it led to high antibacterial activity. Consequently, PEP loaded PCL electrospun fiber mats have potential for applications in antibiotic-free bacterial infection treatment as wound healing materials.

DATA AVAILABILITY STATEMENT

The raw data supporting the conclusions of this manuscript will be made available by the authors, without undue reservation, to any qualified researcher.

AUTHOR CONTRIBUTIONS

IU and ARB conceived the presented idea. IU fabricated the samples and performed the experiments, analyzed the data, and wrote the manuscript. BS and IU performed the Gas Chromatography-Mass Spectroscopy analysis and collected the

data. WG helped carry out the antibacterial activity assay. GF assisted with Raman Spectroscopy measurements. ARB was involved in the planning and supervision of the project. All authors discussed the results, provided critical feedback and contributed to the final manuscript.

FUNDING

IU was funded by the Deutscher Akademischer Austauschdienst (DAAD) program of Research Grants – Doctoral Programmes (Section ST21, 91652927).

REFERENCES

Abedalwafa, M., Wang, F., Wang, L., and Li, C. (2013). Biodegradable poly-epsilon-caprolactone (PCL) for tissue engineering applications: a review. *Rev. Adv. Mater. Sci.* 34, 123–140.

Agnes Mary, S., and Giri Dev, V. R. (2015). Electrospun herbal nanofibrous wound dressings for skin tissue engineering. *J. Text. Inst.* 106, 886–895. doi: 10.1080/00405000.2014.951247

Amiri, S., and Rahimi, A. (2019). Poly (ε-caprolactone) electrospun nanofibers containing cinnamon essential oil nanocapsules: a promising technique for controlled release and high solubility. *J. Indus. Text.* 48, 1527–1544. doi: 10.1177/1528083718764911

Bakkali, F., Averbeck, S., Averbeck, D., and Idaomar, M. (2008). Biological effects of essential oils–a review. *Food Chem. Toxicol.* 46, 446–475. doi: 10.1016/j.fct.2007.09.106

Balasubramanian, K., and Kodam, K. M. (2014). Encapsulation of therapeutic lavender oil in an electrolyte assisted polyacrylonitrile nanofibres for antibacterial applications. *RSC Adv.* 4, 54892–54901. doi: 10.1039/C4RA09425E

Bemelmans, J. M. H. (1979). "Review of isolation and concentration techniques," in *Progress in Flavour Research*, eds D. G. Land and H. E. Nursten (London, UK: Applied Science Publisher), 79–88.

Bhardwaj, N., and Kundu, S. C. (2010). Electrospinning: a fascinating fiber fabrication technique. *Biotechnol. Adv.* 28, 325–347. doi: 10.1016/j.biotechadv.2010.01.004

Bilia, A. R., Guccione, C., Isacchi, B., Righeschi, C., Firenzuoli, F., and Bergonzi, M. C. (2014). Essential oils loaded in nanosystems: a developing strategy for a successful therapeutic approach. *Evid. Based Complement. Altern. Med.* 2014:651593. doi: 10.1155/2014/651593

Burt, S. (2004). Essential oils: their antibacterial properties and potential applications in foods-a review. *Int. J. Food Microbiol.* 94, 223–253. doi: 10.1016/j.ijfoodmicro.2004.03.022

Burt, S. A., and Reinders, R. D. (2003). Antibacterial activity of selected plant essential oils against *Escherichia coli* O157:H7. Lett. Appl. Microbiol. 36, 162–167. doi: 10.1046/j.1472-765X.2003.01285.x

Croisier, F., Duwez, A. S., Jérôme, C., Léonard, A. F., Van Der Werf, K. O., Dijkstra, P. J., et al. (2012). Mechanical testing of electrospun PCL fibers. *Acta Biomater.* 8, 218–224. doi: 10.1016/j.actbio.2011.08.015

Dhivya, S., Padma, V. V., and Santhini, E. (2015). Wound dressings–a review. *Biomedicine* 5, 24–28. doi: 10.7603/s40681-015-0022-9

El Asbahani, A., Miladi, K., Badri, W., Sala, M., Addi, E. A., Casabianca, H., et al. (2015). Essential oils: from extraction to encapsulation. *Int. J. Pharm.* 483, 220–243. doi: 10.1016/j.ijpharm.2014.12.069

Engel, W., Bahr, W., and Schieberle, P. (1999). Solvent assisted flavour evaporation–a new and versatile technique for the careful and direct isolation of aroma compounds from complex food matrices. *Eur. Food Res. Technol.* 209, 237–241. doi: 10.1007/s002170050486

Göpferich, A. (1996). Mechanisms of polymer degradation and erosion. *Biomaterials* 17, 103–114. doi: 10.1016/0142-9612, 85755-3

Hajiali, H., Summa, M., Russo, D., Armirotti, A., Brunetti, V., Bertorelli, R., et al. (2016). Alginate–lavender nanofibers with antibacterial and anti-inflammatory activity to effectively promote burn healing. *J. Mater. Chem. B* 4, 1686–1695. doi: 10.1039/C5TB02174J

Hammer, K. A., Carson, C. F., and Riley, T. V. (1999). Antimicrobial activity of essential oils and other plant extracts. *J. Appl. Microbiol.* 86, 985–990. doi: 10.1046/j.1365-2672.1999.00780.x

Howell-Jones, R. S., Wilson, M. J., Hill, K. E., Howard, A. J., Price, P. E., and Thomas, D. W. (2005). A review of the microbiology, antibiotic usage and resistance in chronic skin wounds. *J. Antimicrob. Chemother.* 55, 143–149. doi: 10.1093/jac/dkh513

Jaganathan, S. K., Mani, M. P., and Khudzari, A. Z. M. (2019). Electrospun combination of peppermint oil and copper sulphate with conducive physico-chemical properties for wound dressing applications. *Polymers* 11:586. doi: 10.3390/polym11040586

Jentzsch, P., Ramos, L., and Ciobotă, V. (2015). Handheld Raman spectroscopy for the distinction of essential oils used in the cosmetics industry. *Cosmetics* 2, 162–176. doi: 10.3390/cosmetics2020162

Jin, G., Prabhakaran, M. P., Kai, D., Annamalai, S. K., Arunachalam, K. D., and Ramakrishna, S. (2013). Tissue engineered plant extracts as nanofibrous wound dressing. *Biomaterials* 34, 724–734. doi: 10.1016/j.biomaterials.2012.10.026

Juby, K. A., Dwivedi, C.:, Kumar, M., Kota, S., Misra, H. S., and Bajaj, P. N. (2012). Silver nanoparticle-loaded PVA/Gum acacia hydrogel: synthesis, characterization and antibacterial study. *Carbohydr. Polym.* 89, 906–913. doi: 10.1016/j.carbpol.2012.04.033

Karami, Z., Rezaeian, I., Zahedi, P., and Abdollahi, M. (2013). Preparation and performance evaluations of electrospun poly (ε-caprolactone), poly (lactic acid), and their hybrid (50/50) nanofibrous mats containing thymol as an herbal drug for effective wound healing. *J. Appl. Polym. Sci.* 129, 756–766. doi: 10.1002/app.38683

Kędziora, A., Speruda, M., Krzyżewska, E., Rybka, J., Łukowiak, A., and Bugla-Płoskońka, G. (2018). Similarities and differences between silver ions and silver in nanoforms as antibacterial agents. *Int. J. Mol. Sci.* 19:444. doi: 10.3390/ijms19020444

Kligler, B., and Chaudhary, S. (2007). Peppermint oil. *Am. Fam. Physician* 75, 1027–1030. Available online at: https://www.aafp.org/afp/2007/0401/p1027.html

Li, Z., Zhou, P., Zhou, F., Zhao, Y., Ren, L., and Yuan, X. (2018). Antimicrobial eugenol- loaded electrospun membranes of poly (ε-caprolactone)/gelatin incorporated with REDV for vascular graft applications. *Colloids Surf. B Biointerfaces* 162, 335–344. doi: 10.1016/j.colsurfb.2017.12.004

Liakos, I., Rizzello, L., Hajiali, H., Brunetti, V., Carzino, R., Pompa, P. P., et al. (2015). Fibrous wound dressings encapsulating essential oils as natural antimicrobial agents. *J. Mater. Chem. B* 3, 1583–1589. doi: 10.1039/C4TB01974A

Liverani, L., and Boccaccini, A. R. (2016). Versatile production of poly (epsilon-caprolactone) fibers by electrospinning using benign solvents. *Nanomaterials* 6:75. doi: 10.3390/nano6040075

MacNeil, S. (2008). Biomaterials for tissue engineering of skin. *Mater. Today* 11, 26–35. doi: 10.1016/S1369-7021, 70087-7

Mahltig, B., Soltmann, U., and Haase, H. (2013). Modification of algae with zinc, copper and silver ions for usage as natural composite for antibacterial applications. *Mater. Sci. Eng. C* 33, 979–983. doi: 10.1016/j.msec.2012.11.033

Mani, M. P., Jaganathan, S. K., Khudzari, A. Z., Rathanasamy, R., and Prabhakaran, P. (2018). Single-stage electrospun innovative combination of polyurethane and neem oil: synthesis, characterization and appraisal of blood compatibility. *J. Bioact. Compat. Polym.* 33, 573–584. doi: 10.1177/0883911518792288

Martins, A., Reis, R. L., and Neves, N. M. (2008). Electrospinning: processing technique for tissue engineering scaffolding. *Int. Mater. Rev.* 53, 257–274. doi: 10.1179/174328008X353547

McKay, D. L., and Blumberg, J. B. (2006). A review of the bioactivity and potential health benefits of peppermint tea (*Mentha piperita* L.). *Phytother. Res.* 20, 619–633. doi: 10.1002/ptr.1936

Mogoşanu, G. D., and Grumezescu, A. M. (2014). Natural and synthetic polymers for wounds and burns dressing. *Int. J. Pharm.* 463, 127–136. doi: 10.1016/j.ijpharm.2013.12.015

Mori, C. L., Passos, N. A. D., Oliveira, J. E., Altoé, T. F., Mori, F. A., Mattoso, L. H. C., et al. (2015). Nanostructured polylactic acid/candeia essential oil

mats obtained by electrospinning. *J. Nanomaterials* 16:33. doi: 10.1155/2015/439253

Prabuseenivasan, S., Jayakumar, M., and Ignacimuthu, S. (2006). *In vitro* antibacterial activity of some plant essential oils. *BMC Complement. Altern. Med.* 6:39. doi: 10.1186/1472-6882-6-39

Priya, S. G., Jungvid, H., and Kumar, A. (2008). Skin tissue engineering for tissue repair and regeneration. *Tissue Eng. B Rev.* 14, 105–118. doi: 10.1089/teb.2007.0318

Ramos-e-Silva, M., and Ribeiro de Castro, M. C. (2002). New dressings, including tissue-engineered living skin. *Clin. Dermatol.* 20:715. doi: 10.1016/S0738-081X00298-5

Reverchon, E., Ambruosi, A., and Senatore, F. (1994). Isolation of peppermint oil using supercritical CO2 extraction. *Flavour Fragr. J.* 9, 19–23. doi: 10.1002/ffj.2730090105

Rieger, K. A., Birch, N. P., and Schiffman, J. D. (2016). Electrospinning chitosan/poly (ethylene oxide) solutions with essential oils: correlating solution rheology to nanofiber formation. *Carbohydr. Polym.* 139, 131–138. doi: 10.1016/j.carbpol.2015.11.073

Rijo, P., Matias, D., Fernandes, A., Simões, M., Nicolai, M., and Reis, C. (2014). Antimicrobial plant extracts encapsulated into polymeric beads for potential application on the skin. *Polymers* 6, 479–490. doi: 10.3390/polym6020479

Rohloff, J. (1999). Monoterpene composition of essential oil from peppermint (Mentha× piperita L.) with regard to leaf position using solid-phase microextraction and gas chromatography/mass spectrometry analysis. *J. Agric. Food Chem.* 47, 3782–3786. doi: 10.1021/jf981310s

Rösch, P., Kiefer, W., and Popp, J. (2002). Chemotaxonomy of mints of genus Mentha by applying Raman spectroscopy. *Biopolymers* 67, 358–361. doi: 10.1002/bip.10099

Sadri, M., Arab-Sorkhi, S., Vatani, H., and Bagheri-Pebdeni, A. (2015). New wound dressing polymeric nanofiber containing green tea extract prepared by electrospinning method. *Fibers Polym.* 16, 1742–1750. doi: 10.1007/s12221-015-5297-7

Schulz, H., Baranska, M., Belz, H. H., Rösch, P., Strehle, M. A., and Popp, J. (2004). Chemotaxonomic characterisation of essential oil plants by vibrational spectroscopy measurements. *Vib. Spectrosc.* 35, 81–86. doi: 10.1016/j.vibspec.2003.12.014

Sell, S. A., Wolfe,P. S., Garg, K., McCool, J. M., Rodriguez, I. A., and Bowlin, G. L. (2010). The use of natural polymers in tissue engineering: a focus on electrospun extracellular matrix analogues. *Polymers* 2, 522–553. doi: 10.3390/polym2040522

Shao, S., Li, L., Yang, G., Li, J., Luo, C., Gong, T., et al. (2011). Controlled green tea polyphenols release from electrospun PCL/MWCNTs composite nanofibers. *Int. J. Pharm.* 421, 310–320. doi: 10.1016/j.ijpharm.2011.09.033

Sill, T. J., and von Recum, H. A. (2008). Electrospinning: applications in drug delivery and tissue engineering. *Biomaterials* 29, 1989–2006. doi: 10.1016/j.biomaterials.2008.01.011

Silva, N. C. C., and Fernandes Júnior, A. (2010). Biological properties of medicinal plants: a review of their antimicrobial activity. *J. Venom. Anim. Toxins Trop. Dis.* 16, 402–413. doi: 10.1590/S1678-91992010000300006

Suganya, S., Senthil Ram, T., Lakshmi, B. S., and Giridev, V. R. (2011). Herbal drug incorporated antibacterial nanofibrous mat fabricated by electrospinning: an excellent matrix for wound dressings. *J. Appl. Polym. Sci.* 121, 2893–2899. doi: 10.1002/app.33915

Sun, X., Zheng, R., Cheng, L., Zhao, X., Jin, R., Zhang, L., et al. (2016). Two-dimensional electrospun nanofibrous membranes for promoting random skin flap survival. *RSC Adv.* 6, 9360–9369. doi: 10.1039/C5RA23034A

Tampau, A., González-Martinez, C., and Chiralt, A. (2017). Carvacrol encapsulation in starch or PCL based matrices by electrospinning. *J. Food Eng.* 214, 245–256 doi: 10.1016/j.jfoodeng.2017.07.005

Tang, Y., Zhou, Y., Lan, X., Huang, D., Luo, T., Ji, J., et al. (2019). Electrospun gelatin nanofibers encapsulated with peppermint and chamomile essential oils as potential edible packaging. *J. Agric. Food Chem.* 67, 2227–2234. doi: 10.1021/acs.jafc.8b06226

Tavassoli-Kafrani, E., Goli, S. A. H., and Fathi, M. (2018). Encapsulation of orange essential oil using cross-linked electrospun gelatin nanofibers. *Food Bioprocess Technol.* 11, 427–434. doi: 10.1007/s11947-017-2026-9

Uslu, I., Keskin, S., Gül, A., Karabulut, T. C., and Aksu, M. L. (2010). Preparation and properties of electrospun poly (vinyl alcohol) blended hybrid polymer with aloe vera and HPMC as wound dressing. *Hacet. J. Biol. Chem.* 38, 19–25. Available online at:http://www.hjbc.hacettepe.edu.tr/site/assets/files/2605/38_1_19-25.pdf

Wen, P., Zhu, D. H., Wu, H., Zong, M. H., Jing, Y. R., and Han, S. Y. (2016). Encapsulation of cinnamon essential oil in electrospun nanofibrous film for active food packaging. *Food Control* 59, 366–376. doi: 10.1016/j.foodcont.2015.06.005

Wesełucha-Birczyńska, A., Świętek, M., Sołtysiak, E., Galiński, P., Piekara, K., and Błażewicz, M. (2015). Raman spectroscopy and the material study of nanocomposite membranes from poly (ε-caprolactone) with biocompatibility testing in osteoblast-like cells. *Analyst* 140, 2311–2320. doi: 10.1039/C4AN02284J

Zhang, W., Ronca, S., and Mele, E. (2017). Electrospun nanofibres containing antimicrobial plant extracts. *Nanomaterials* 7:42. doi: 10.3390/nano7020042

Conflict of Interest: The authors declare that the research was conducted in the absence of any commercial or financial relationships that could be construed as a potential conflict of interest.

frontiers in Bioengineering and Biotechnology

ORIGINAL RESEARCH
published: 04 December 2019
doi: 10.3389/fbioe.2019.00344

Potential of Manuka Honey as a Natural Polyelectrolyte to Develop Biomimetic Nanostructured Meshes With Antimicrobial Properties

Elena Mancuso[1], Chiara Tonda-Turo[2], Chiara Ceresa[3], Virginia Pensabene[4], Simon D. Connell[5], Letizia Fracchia[3] and Piergiorgio Gentile[6]**

[1] Nanotechnology and Integrated Bio-Engineering Centre (NIBEC), Ulster University, Newtownabbey, United Kingdom, [2] PolitoBIOMed Lab, Department of Mechanical and Aerospace Engineering, Politecnico di Torino, Turin, Italy, [3] Department of Pharmaceutical Sciences, Università del Piemonte Orientale A. Avogadro, Novara, Italy, [4] School of Electronic and Electrical Engineering and School of Medicine, University of Leeds, Leeds, United Kingdom, [5] School of Physics and Astronomy, University of Leeds, Leeds, United Kingdom, [6] School of Engineering, Newcastle University, Newcastle upon Tyne, United Kingdom

OPEN ACCESS

Edited by:
Aldo R. Boccaccini,
University of Erlangen Nuremberg, Germany

Reviewed by:
Senentxu Lanceros-Mendez,
University of Minho, Portugal
Liliana Liverani,
University of Erlangen Nuremberg, Germany

***Correspondence:**
Elena Mancuso
e.mancuso@ulster.ac.uk
Piergiorgio Gentile
piergiorgio.gentile@ncl.ac.uk

Specialty section:
This article was submitted to Bionics and Biomimetics, a section of the journal Frontiers in Bioengineering and Biotechnology

Received: 01 July 2019
Accepted: 06 November 2019
Published: 04 December 2019

Citation:
Mancuso E, Tonda-Turo C, Ceresa C, Pensabene V, Connell SD, Fracchia L and Gentile P (2019) Potential of Manuka Honey as a Natural Polyelectrolyte to Develop Biomimetic Nanostructured Meshes With Antimicrobial Properties. Front. Bioeng. Biotechnol. 7:344. doi: 10.3389/fbioe.2019.00344

The use of antibiotics has been the cornerstone to prevent bacterial infections; however, the emergency of antibiotic-resistant bacteria is still an open challenge. This work aimed to develop a delivery system for treating soft tissue infections for: (1) reducing the released antimicrobial amount, preventing drug-related systemic side effects; (2) rediscovering the beneficial effects of naturally derived agents; and (3) preserving the substrate functional properties. For the first time, Manuka honey (MH) was proposed as polyelectrolyte within the layer-by-layer assembly. Biomimetic electrospun poly(ε-caprolactone) meshes were treated via layer-by-layer assembly to obtain a multilayered nanocoating, consisting of MH as polyanion and poly-(allylamine-hydrochloride) as polycation. Physicochemical characterization demonstrated the successful nanocoating formation. Different cell lines (human immortalized and primary skin fibroblasts, and primary endothelial cells) confirmed positively the membranes cytocompatibility, while bacterial tests using Gram-negative and Gram-positive bacteria demonstrated that the antimicrobial MH activity was dependent on the concentration used and strains tested.

Keywords: electrospinning, layer-by-layer assembly, Manuka honey, manofunctionalization, soft tissue regeneration

INTRODUCTION

Skin and soft tissue infections (SSTIs) are the most common bacterial infections, encompassing a variety of pathological conditions that involve skin and underlying subcutaneous tissue, fascia, and muscles (Esposito et al., 2017). In the USA alone, they account for ∼10% of hospital admissions, and they are the most significant cause of morbidity and mortality among hospitalized patients, posing considerable diagnostic and therapeutic challenges (Miller et al., 2015). Moreover, the aging population and the higher number of critically ill patients are playing a crucial role on the incidence of SSTIs, which have increased meaningfully over the past two decades (Tun et al., 2018). The antibiotics has been the cornerstone to prevent bacterial infections. However, several drawbacks, associated with their adoption, have posed serious issues toward their efficacy: (i)

bacterial resistance following the release of each new drug, (ii) lack of wide spectrum action, and (iii) reduced function because of the biofilm layers formed by some bacteria (Zhang et al., 2013; Maxson and Mitchell, 2016). For minimizing SSTIs consequences, including the huge financial burden they cause onto the healthcare services and the significant societal costs (Zimlichman et al., 2013), the development of novel and more effective antimicrobial strategies has revealed of paramount importance. Many studies report the importance to inhibit the growth of bacteria in the early biofilm formation stage, thus preventing the infection from starting (Roy et al., 2018). In this regard, the use of technologies at the nanoscale, to develop antibacterial surfaces and coatings, has received great attention within the scientific community, as promising frontier to reduce SSTIs (Pfalzgraff et al., 2018).

Among the nanotechnologies, layer-by-layer (LbL) electrostatic assembly provides to develop multilayered nanocoatings, based on the alternating exposure of a charged substrate to solutions of positively and negatively charged polyelectrolytes (PEs), where a rinsing step is generally included to prevent cross-contamination of the PE solutions. LbL method is an inexpensive and environment friendly, versatile, and simple technique that allows to achieve desired properties and fine control of the coating thicknesses by adjusting the deposition cycle conditions (Gentile et al., 2015a). Furthermore, the driving force of LbL assembly being electrostatic interaction, almost any type of charged specie (e.g., organic molecules or biological macromolecules) can be incorporated into any LbL-treated surfaces (e.g., sheets, fibers, etc.) (Richardson et al., 2015; Ferreira et al., 2019). Within this study, the authors demonstrated that the main advantage of LbL assembly was the relatively small amount of loaded biomolecules/drugs needed to achieve effective concentrations. This has been reported in previous works, where meshes were functionalized with LbL assembly to impart a cascade of nanostimuli and to control the adhesion, proliferation, and differentiation of stem cells with the consequent formation of new bone matrix (Gentile et al., 2017) as well as to effectively deliver the metronidazole drug from oral implant (Gentile et al., 2015b).

Numerous antibiotic-based coatings, constructed via the LbL assembly technique and intended for the development of antibacterial implants, have been investigated so far, given the long-acting stability of LbL film surfaces in comparison to other functionalization techniques (Kruk et al., 2016; Park et al., 2018). However, it has been found that the effect of antibiotics may decrease with time, since antibiotic-resistant bacteria may potentially develop (Li and Webster, 2018). Therefore, the emergency of antibiotic-resistant bacteria remains a big challenge also with the use of LbL assembly method. As an alternative, heavy metals, such as iron, silver, and copper, have been considered as promising PEs for multilayer assembly (Séon et al., 2015; Zhu et al., 2018). However, their high loading has been shown to cause tissue toxicity and impaired wound healing (Guthrie et al., 2012), and bacteria may develop a resistance to metal-based nanoparticles as reported for the silver (Zahin et al., 2019). Moreover, the incorporation of antibacterial peptides and enzymes has also emerged as interesting approach for SSTIs (Pfalzgraff et al., 2018), but their lack of stability during the LbL preparation has limited their application (Zahin et al., 2019).

In the last decade, the antimicrobial activity of different natural compounds has been reported in the literature. As example, chitosan is a well-known biomaterial, obtained from the deacetylation of chitin, produced from the exoskeleton of arthropods, that possesses hemostatic, antioxidant, antitumoral, and bactericidal behavior (Kumar, 2000). Furthermore, oregano, a worldwide used culinary herb, showed antimicrobial and antioxidant properties due to the presence of thymol and flavonoids respectively (Zinoviadou et al., 2009). An alternative natural-based agent, the honey, was proposed in this work in the virtue of its ancient antibacterial properties. Honey has been used to treat infected wounds by indigenous cultures around the globe before bacteria were discovered to be the cause of infections (Molan, 2001). Although some honey varieties have demonstrated to have beneficial effects into infected sites, most modern research has focused on a particular type produced in New Zealand from the nectar of the *Leptospermum scoparium* shrub, called Manuka honey (MH) (Minden-Birkenmaier and Bowlin, 2018). This honey contains the constituents of other honey varieties, but its unique component, methylglyoxal, acts as an additional antibacterial agent (Cokcetin et al., 2016).

The increasing prevalence of data supporting honey's effectiveness as a natural broadband antibacterial agent has encouraged researchers in exploring MH as a wound treatment (Armstrong, 2009) or incorporated in tissue-engineered hydrogels (Bonifacio et al., 2018), demonstrating that MH could significantly reduce the rate of infections on biomaterials and promote fibroblast migration and collagen deposition. In addition, MH could enhance tissue–material integration/regeneration and accelerate healing of the surrounding site (Minden-Birkenmaier and Bowlin, 2018). However, the undesirable cytotoxic effects of high concentrations of honey and its uncontrolled release over time represent two of the greatest hurdles in the development of honey-containing tissue-like substitutes (Sadeghi-Aliabadi et al., 2015). The LbL-assembly approach allows the incorporation of MH with a subsequent and more efficient controlled release of honey from the nanolayers. This strategy offers solutions to the current warning about the potential toxic effects of high honey concentration on myofibroblasts and local mesenchymal-stem cells (Du Toit and Page, 2009). Moreover, the main advantage of this approach is the relatively small amount of honey loaded to achieve a therapeutic outcome, preventing both bacteria resistance and drug-related systemic side effects.

In this work, nanostructured honey-based coatings were deposited on biomimetic electrospun poly(ε-caprolactone) meshes via LbL technique to obtain discrete nanoscale layers to incorporate and to control the MH release with minimal interaction with the biomaterial substrate. After the LbL optimization to achieve appropriate MH release kinetics, the nanocoating was characterized by morphological and physicochemical analyses to evaluate the multilayered deposition while by biological and antibacterial behavior to study the MH efficiency.

MATERIALS AND METHODS

Materials

Poly(ε-caprolactone) (PCL; Mw = 82 kDa), poly(sodium4-styrenesulfonate) (PSS; Mw = 70 kDa), 1,6-hexanediamine (ED), chloroform (≥99.9%), formic acid (≥95%), and sodium acetate buffer solution were purchased from Sigma-Aldrich, UK. Poly(allylamine hydrochloride) (PAH) was supplied from Alfa Aesar, UK, while medical-grade MH (400 mg/kg of methylglyoxal) was purchased from ManukaGuard®, USA. Ultrapure water was obtained by a Milli-Q® Integral system (Merck, Italy). All materials and chemicals were used without further purification.

Electrospun Membranes Preparation

PCL membranes were fabricated using an electrospinning system (Linari Engineering Srl, Italy). Process and solution parameters were optimized to fabricate defect-free nanofibers with dimensions in the hundreds of nanometers scale. Briefly, PCL pellets were solubilized using a chloroform and formic acid solution (70:30 *v*/*v*) to obtain a 12% *w*/*v* concentration of the PCL solution. For each membrane, 0.6 g of PCL was solubilized in 3.5 ml of chloroform for 1 h under stirring, and then, 1.5 ml of formic acid was added and mixed for 20 min. The spinning process was performed at room temperature, and the spinning parameters were set as voltage of 20 kV, syringe flowrate of 1.5 ml/h, and nozzle–collector distance of 20 cm.

Electrospun Membranes Functionalization

PCL electrospun membranes (size of 10 × 10 cm and thickness of ≈200 μm) were aminolyzed by dipping into ED solution (0.06 g/ml) for 10 min at 20°C, to graft—NH_2—to get a positive charge on the surface and then abundantly washed in deionized water and left drying for 24 h. PSS (5 mg/ml), PAH (5 mg/ml), and MH (15, 30, 60, and 120 mg/ml) solutions were prepared by dissolving the PEs in sodium acetate buffer solution (pH 5.3–5.5). The ζ-potentials of these solutions was measured by laser Doppler electrophoresis (Zetasizer Nano, Malvern Instrument, USA). For the LbL assembly, aminolyzed membranes were dipped first into the polyanionic solutions (MH) for 15 min, followed by a washing step in sodium acetate buffer solution for 5 min to remove any unbound PE material. The membranes were then soaked in the polycationic solution (PAH) for 15 min followed by a washing step using the same conditions described before. This dipping process was repeated for eight cycles for creating 16 nanolayers. The samples were left to dry overnight, coded as MH_1.5, MH_3, MH_6, and MH_12, the membranes functionalized using different concentrations of MH (1.5, 3, 6, and 12% *w*/*v*, respectively) in sodium acetate buffer solution (pH 5.3–5.5), while the membrane coated with PSS and PAH as was coded with PSS/PAH (used as control).

Physicochemical Characterization

Quartz crystal microbalance analyses (QCM-D) were performed with a QSense Explorer device equipped with an open module (Q-Sense, Sweden). Changes in frequency (Δf) and energy dissipation factor (ΔD) were monitored at its fundamental resonance frequency (5 MHz) and odd overtones (3, 5, 7, 9, 11, 13). Gold-coated sensors (QSX301, Q-Sense, Sweden) were used and cleaned following manufacture's instruction before use. Immediately after cleaning, a gold-coated sensor was placed in the open module, and 400 μl of ED solution was gently poured on the sensor surface using a micropipette. After 10 min, the ED solution was removed, and 400 μl of sodium acetate buffer solution was poured to remove non-adhered molecules. Then, the LbL process was reproduced by alternating MH and PAH solutions to obtain eight-bilayers, following the same procedure described before.

Morphological analysis of the samples before and after LbL dip assembly was performed by SEM (Philips XL30-ESEM). Specimens were priory sputtered with a thin layer of gold (∼10 nm, sputter time of 40 s at 40 mA). All the images were taken at 20 kV and working distance of 10 mm.

Atomic force microscopy (AFM) characterization was performed with a Bruker Icon AFM with TESPA-V2 probes in tapping mode at 320 kHz frequency. The fibers were bonded to a metal stub using two part-epoxy, and the loose fibers above the surface were manually removed to allow probe access to the well-bonded fibers beneath.

X-ray photoelectron spectroscopy (XPS) was performed with Theta Probe (Thermo Scientific, UK) equipped with a microfocused AlKa X-ray source (1,486.6 eV), operated with a 400-μm spot size (100 W power). Process parameters were 200 eV pass energy, 1 eV step size, and 50 ms dwell time in not angle-resolved lens mode. Moreover, high-resolution spectra were acquired with 40 eV pass energy, 0.1 eV step size, and 200 ms as dwell time. Fourier transform infrared spectra were acquired in a wavenumber range of 4,000–550 cm^{-1} using Spectrum Two PE instrument equipped with a horizontal attenuated total reflectance crystal (ZnSe) (PerkinElmer Inc., USA; 4 cm^{-1} resolution and 32 scans).

The amount of MH released from the membranes was analyzed by *in vitro* tests after immersion of 1 × 1 cm membranes in 1 ml of phosphate-buffered saline (PBS, Sigma-Aldrich, UK) solution at 37°C for different time points (up to 4 weeks). The released solution of the soaked membranes was assayed for glucose (Glucose Assay Kit, Sigma-Aldrich, UK) as proposed by Hixon (Hixon et al., 2017).

Cell Tests

Membranes with a dimeter of 15 cm were treated with Sudan Black (SB, Sigma-Aldrich, UK) to avoid the autofluorescence of the electrospun membranes: 0.3% (*w*/*v*) SB solution was prepared in 70% ethanol, and the membranes were immersed in this solution for 15 min and then rinsed three times in PBS solution and sterilized under ultraviolet light for 30 min (Dai et al., 2016).

Different cell lines were used to test the membranes' cytocompatibility. Human telomerase reverse transcriptase immortalized fibroblasts from non-malignant myoma (T-HESCs, ATCC, CRL-4003™) were cultured from frozen stock in a 1:1 mixture of Dulbecco's modified Eagle's medium and Ham's F-12 medium with 3.1 g/L glucose and 1 mM sodium pyruvate and without phenol red (Sigma-Aldrich, UK) supplemented with 1.5 g/L sodium bicarbonate, 1% ITS+ Premix (Corning, UK), 500 ng/ml puromycin, and 10% charcoal/dextran treated fetal

bovine serum (HyClone, US). Healthy skin human fibroblasts, kindly donated by Ana Tiganescu at Saint James's Teaching Hospital in Leeds (isolated from skin biopsies samples obtained from the Tissue Bank repository), were cultured in 1:1 mixture of Dulbecco's modified Eagle's medium with high glucose, Glutamax, and 10% fetal bovine serum. Finally, primary human umbilical vein endothelial cells were isolated from umbilical cord obtained from deidentified term placenta collected from patients who underwent elective Cesarean section between 37 and 39 weeks of gestation. After isolation, 95% purity of endothelial cells was observed, validated morphologically and by immunofluorescent staining for CD31 (DAKO, USA) before seeding on the membranes. Cells were cultured in EBM-2 medium supplemented with EGM-2 Single Quot growth factors (Lonza, USA). All the cell lines were maintained at 37°C in a saturated humidity atmosphere containing 5% CO_2, and they were subcultured before reaching 60–70% confluence (approximately every 2 days) up to passage 5. All the cells were passaged and seeded on the different meshes at density of 5,000 cells/cm^2 (∼20,000 cells/well in a 12-well plate).

LIVE/DEAD staining (ReadyProbes® Cell Viability Imaging Kit, Molecular probes) was used following manufacturer protocols to determine the viability of cells and to check proliferation of cells exposed for 8 days to medium conditioned with MH (1.3 and 8.3% *v*/*v*) and on the different substrates after 8 days in culture.

Bacterial Tests

The minimum inhibitory concentration (MIC) of MH to Gram-positive *Staphylococcus aureus* (ATCC 25923) and *Staphylococcus epidermidis* (ATCC 12228) and Gram-negative *Escherichia coli* (ATCC 25922) and *Pseudomonas aeruginosa* (ATCC 10145) was determined according to Wiegand et al. (Wiegand et al., 2008). MH was tested at concentrations ranging from 3.125 to 500 mg/ml. Bacterial suspensions at the concentration of 5×10^5 colony forming units (CFUs)/ml were inoculated into Mueller–Hinton broth in the absence (control) or presence of the different concentrations of honey and the multiwell plates incubated at 37°C for 16–20 h. MIC was identified as the lowest concentration of honey that prevents visible growth of the tested strains as observed with the unaided eye. Assays were conducted in triplicate and repeated twice.

The antimicrobial effectiveness of LbL-functionalized electrospun membranes was assessed using 3-[4,5-dimethylthiazol-2-yl]-2,5-diphenyltetrazolium bromide (MTT)-based colorimetric assay (Tonda-Turo et al., 2018a). Bacterial suspensions at a concentration of 5×10^5 CFU/ml were prepared in Tryptic soy broth. Afterwards, 1 ml of each of these suspensions was used to dip all the membranes, previously sterilized by 30 min ultraviolet treatment, in 5-ml tubes. Samples were incubated at 37°C for 24 h at 120 rpm. At the end of the incubation time, bacteria were harvested by centrifugation at 12,000 rpm for 10 min and incubated for 30 min in 1 ml of MTT working solution containing 0.03 g MTT (Sigma-Aldrich, Italy) in 9.85 ml PBS supplemented with 50 μl of a 20% glucose solution and 100 μl of a 1 mM menadione solution. Bacteria were then harvested by centrifugation at 12,000 rpm for 10 min and resuspended in 1 ml of DMSO/glycine 0.1 M pH 10.2 (7:1) buffer. Finally, absorbance of each sample was measured by spectrophotometric reading at 570 nm wavelength. The percentage of inhibition of functionalized fibers, compared to PCL fibers (controls), was determined as [1 – (Abstreat/Absctrl)] × 100, where Abstreat indicates optical density of functionalized samples and Absctrl corresponds to the optical density of controls.

Statistical Analysis

All the experiments were performed at least in triplicate. Results were expressed as a mean ± standard deviation, and statistical significance was calculated using analysis of variance (ANOVA). The comparison between two means was analyzed using Tukey's test with statistical significance level set at $^*p < 0.05$, $^{**}p < 0.01$, and $^{***}p < 0.001$.

RESULTS

Electrophoresis measurements were performed, showing that MH-based solutions ranging from 1.5 to 12% *w*/*v* were negatively charged with ζ-potentials from −12.6 to −22.4 mV, while PAH solution was positively charged with a ζ-potential of +14.5 mV. As a control, negatively charge PSS solution was selected to favor complexation due to its strong interaction with PAH. This had a ζ-potential of −18.8 mV. Furthermore, the evaluation of the electrostatic interaction between MH in different concentrations and PAH was investigated by QCM-D measurements, to confirm the formation of the multilayered structures (Tonda-Turo et al., 2018b).

As shown in **Figure 1**, the presence of ED solution caused a shift in both frequency and dissipation when NH_2 groups interacted with the Au surface of the sensor. The subsequent cleaning step partially removed the layer as confirmed by the increase in Δf values (Δf value after cleaning step ≈ −300 Hz) at ∼620 s. Then, MH and PAH PE solutions were alternatively flowed across the positively charged functionalized Au crystal for 15 min to simulate the LbL dipping conditions of electrospun membranes. The addition of PEs molecules on the crystal surface was confirmed by a cumulative stepwise response of Δf and ΔD, where the black stars indicated the shift caused by the MH-based solutions. The subsequent cleaning step removed the majority of both PEs in the first bilayers. Starting from the third bilayer, the deposition of MH was more evident, particularly for MH_6 and MH_12, while for MH_3, a significant Δf was observed with the formation of the fourth bilayer. Furthermore, the ΔD trend confirmed the formation of a thicker layer on the top of the Au crystal as the dissipation factor increased with time.

The surface morphology of the multilayered coating after LbL assembly was analyzed by scanning electron microscopy (SEM) (**Figure 2A**). The electrospun membranes presented an average fiber diameter of 0.75 ± 0.22 μm and an intrinsic microporosity. After LbL functionalization, the membranes coated with MH and PAH appeared smooth and uniform, leading to an increase in the fiber diameter, which in turn resulted proportional to the number of bilayers used. The control PSS/PAH-coated membranes showed a formation of irregularly shaped protuberances and

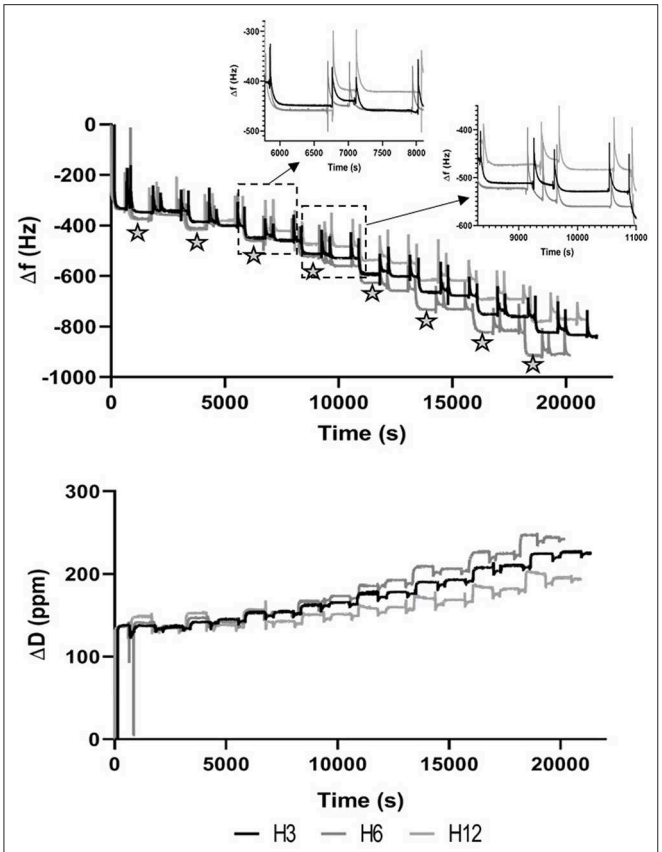

FIGURE 1 | Plot of the fifth overtone of Δf **(A)** and ΔD **(B)** vs. time. Stars indicate events associated to the dipping step in Manuka Honey solution.

a consequently higher surface roughness and fiber diameter in comparison to the bare substrate. Furthermore, AFM analysis (**Figure 2B**) confirmed the successful functionalization of the membranes, and in addition, it was possible to visualize the extent of the MH coating in detail using the tapping mode phase contrast signal. The clean PCL fibers were smooth to a subnanometer level but, in phase contrast, showed striations of 13.5 nm periodicity around the circumference of the fiber (alternative dark and light stripes of ∼7 nm width) (**Figure 3**).

As with SEM, the PSS/PAH showed a thick, irregular, and continuous coating. MH 1.5–12% *w*/*v* revealed a clear progression of MH coverage. At 1.5% *w*/*v* MH, the coating (bright gold vs. the darker brown PCL in **Figures 2B**, **3**) forms a quite sparse network across the fiber surface. At 3% MH, the strands of this network have thickened and begin to enclose regions of clean PCL. At 6% MH, the network has fused into an almost continuous coating with a small number of patches of PCL fiber visible. These remaining patches were almost entirely gone at 12% MH, and a continuous coating has formed.

The surface coverage of MH visible in the high-resolution AFM phase images (**Figure 4A**) was analyzed by thresholding to discriminate the coating (**Figure 3**) and analyzing in ImageJ (NIH) using the histogram function. The resultant concentration vs. coverage response (**Figure 4B**) is reminiscent of an absorption isotherm, and a Langmuir–Freundlich isotherm (Ratkowsky and Giles, 1990) (allowing for heterogeneous and multilayer films) was used to fit the film growth, giving an absorption rate constant $k = 6.35 \times 10^{-3}$ L/g.

Fourier transform infrared spectroscopy–attenuated total reflectance and X-ray photoelectron (XPS) were performed to analyze the surface membranes composition before and after LbL assembly. Particularly, the infrared spectra (**Figure 5**) revealed the presence of the characteristic chemical bands of the PEs used for coating the PCL electrospun membranes. For the poly(allylamine hydrochloride), the following chemical bands were observed: νN–H stretching (3,360 cm^{-1}), alkyl νC–H stretching (2,920 cm^{-1}), N–H symmetric and asymmetric scissoring vibrations (1,490 and 1,580 cm^{-1}, respectively), and νN–H asymmetric stretching (1,330 cm^{-1}) (Gentile et al., 2015b), while the presence of the honey was characterized by different absorption zones dominated by two water bands at 3,300–3,400 cm^{-1} (OH stretch) and 1,641 cm^{-1} (OH deformation). The band from about 1,500–750 cm^{-1} was related to the most sensitive absorption region of the honey's major components, particularly the most suitable region to quantify honey sugar (59–75%) and organic acids. The small peak at 1,110 cm^{-1} corresponded to stretching of the C–O band of the C–O–C linkage, and the peak at ∼1,690 cm^{-1} corresponded to C=O stretching (Anjos et al., 2015). However, all the other honey distinctive peaks were overlapped with the other components of PCL and PAH.

Figure 6 shows the XPS survey spectra before and after LbL assembly functionalization. The surveys showed N1s peak at 399.5 eV, demonstrating PAH was successfully introduced, while C1s at 285 eV and O1s at 630 eV peaks were characteristics of both PAH and MH. Moreover, the presence of Na1s at 1,070 eV and Cl2p at 200 eV was due to the addition of NaCl in the PE solution for maintaining a stable charge (Rojas et al., 1998). The high-resolution spectra for C1s along with the curve fit showed three peaks attributed to the different carbon oxidation states: (1) 284.7–285.0 eV, (2) 286.8–287.0 eV, and (3) 288.5–289 eV, corresponding to –C–H or –C–C– bonds, to –C–O– bond, and to –C=O groups, respectively. It was observed that these components content varied significantly with the formation of the layers. The concentration of C=O decreased with the formation of the nanocoating because it was characteristic of PCL chemical structure. On the other hand, the component corresponding to C–N bonds increased suggesting the PEs coating. Finally, the high-resolution spectra for N1s revealed the presence of PAH layers in all the coated electrospun membranes (no signal present in bare PCL membrane).

The release of glucose was measured over 14 days (**Figure 7**). The LbL-functionalized membranes showed three different stages in the release profile as shown for all the samples, where, as expected, the membrane functionalized with the higher MH content showed the highest glucose released. A burst release was observed with approximately the 10–12% of MH delivered during the initial 24 h of incubation (392.6 ± 47.5 μg/ml for MH_12), followed by a controlled and linear MH release up to 14 days (1.9 ± 0.2 mg/ml for MH_12). At 28 days, no

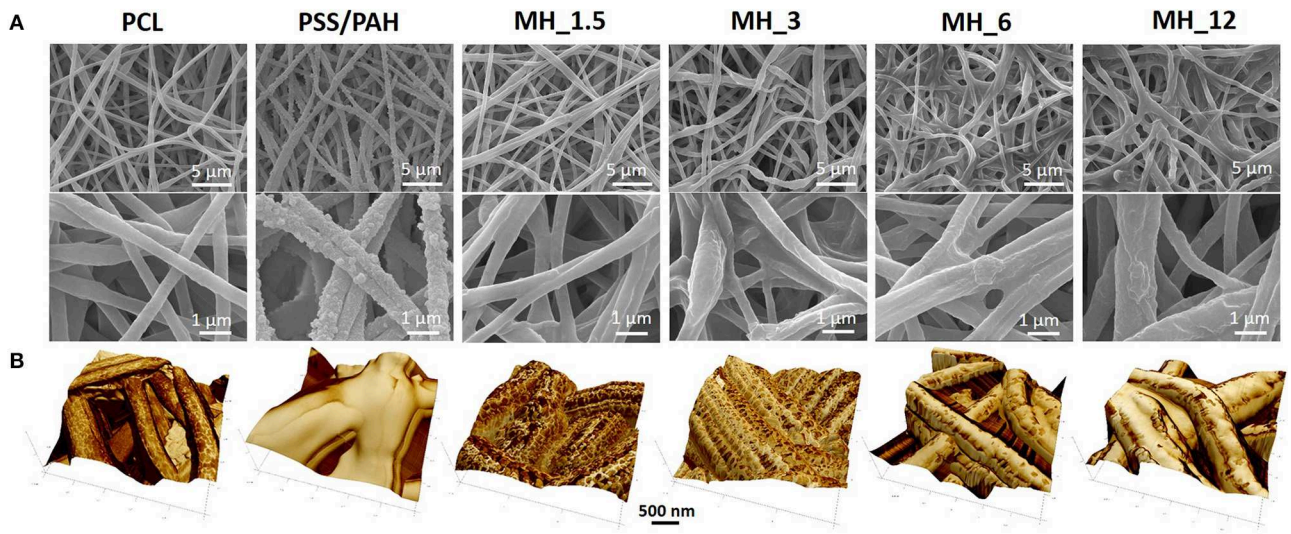

FIGURE 2 | (A) Scanning electron microscopy (SEM) and **(B)** atomic force microscopy (AFM) images of the electrospun membranes before and after LbL assembly functionalization.

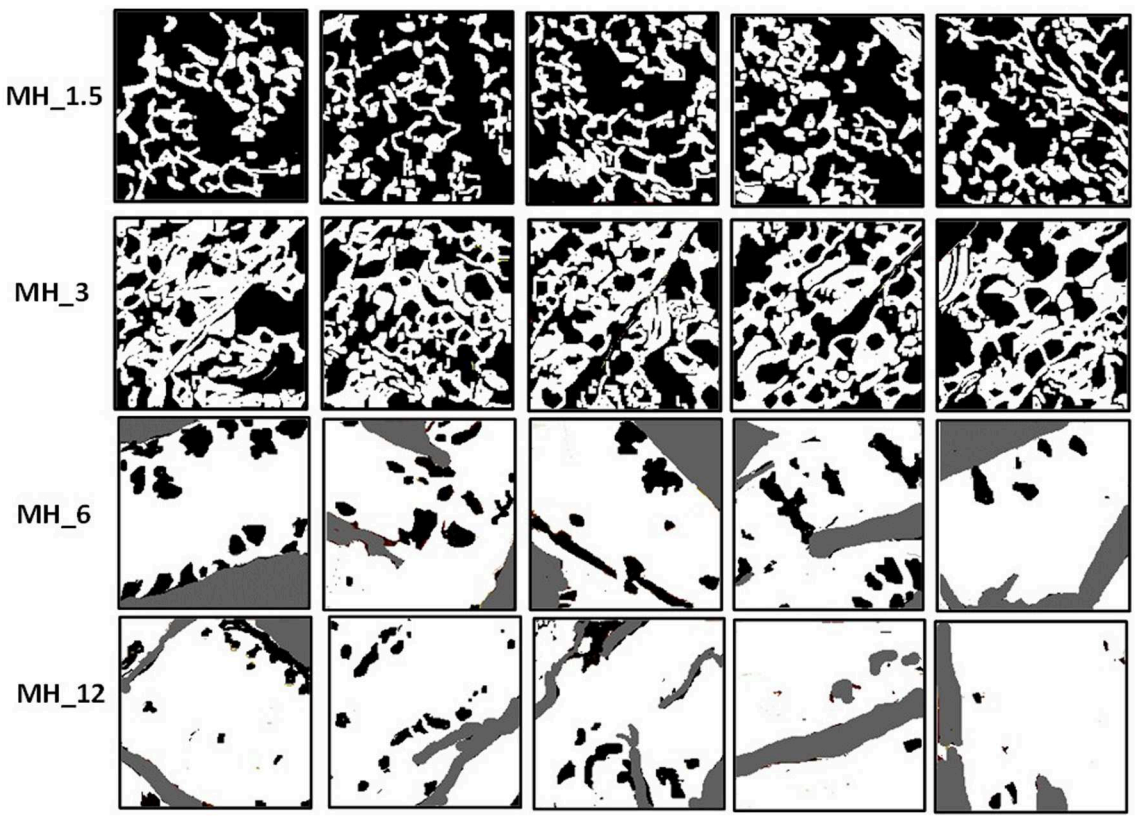

FIGURE 3 | MH adsorption analysis—conversion to thresholded images before image analysis in ImageJ.

significant change in MH release was noticed for all the samples, probably due to the nanocoating degradation that implied a zero-order release.

When the effect of medium supplemented with MH was evaluated in respect to MH-free medium, the LIVE/DEAD staining showed 100% viable healthy fibroblasts in all the sample:

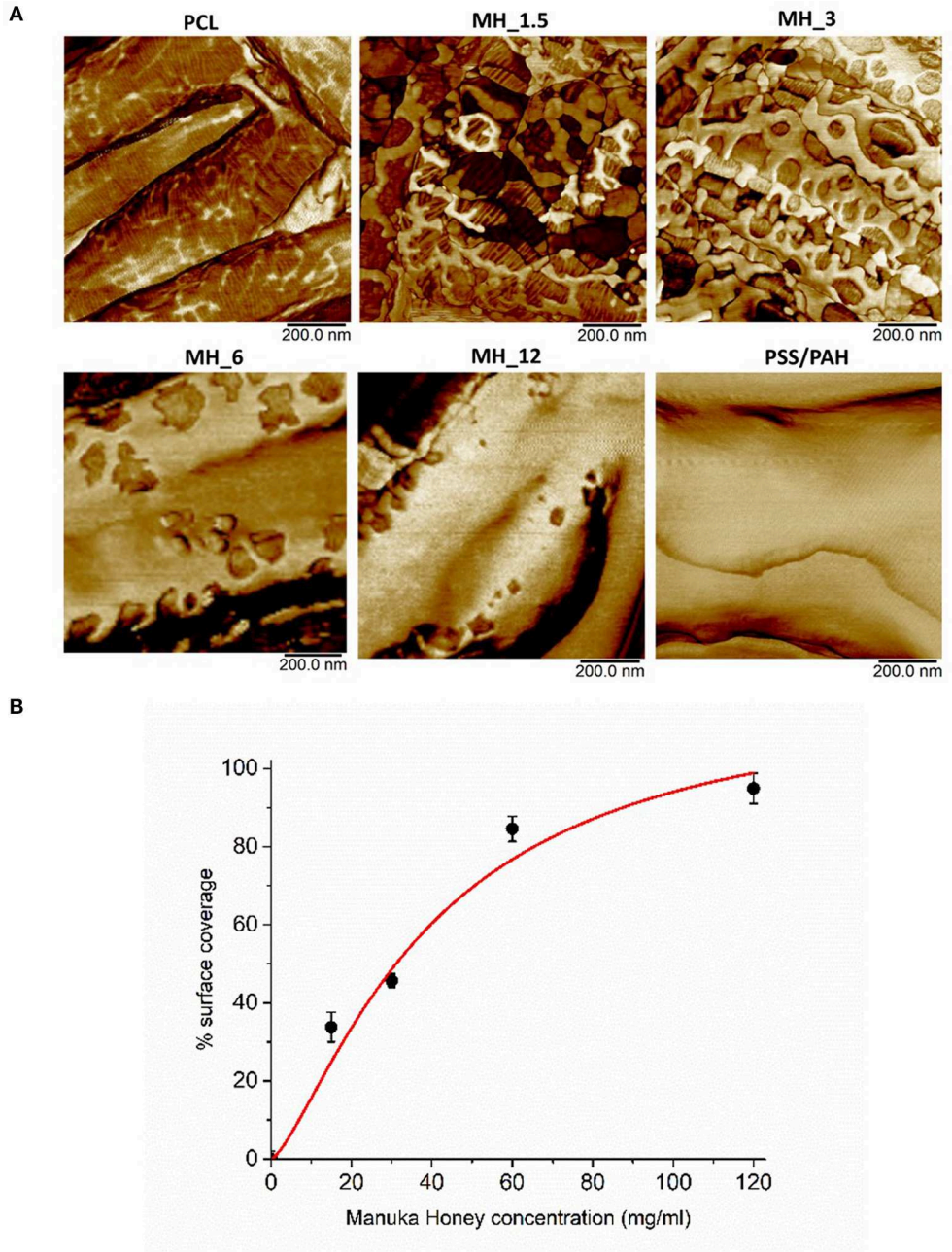

FIGURE 4 | (A) High-resolution atomic force microscopy (AFM) phase contrast images. **(B)** Analysis of MH coating coverage from high-resolution AFM images.

after staining with propidium iodide solution, no signal was detected using a standard tetramethylrhodamine/red fluorescent protein (orange) filter set, meaning that all the cells had an intact plasma membrane (**Figure 8**). A slower proliferation, however, was observed in high concentrated samples, but not significant in comparison to the control condition.

Then, three different cell types were seeded on all the functionalized electrospun meshes for 8 days. Before seeding the cells, all the substrates were treated with SB. This is a quenching compound commonly used in lipid histochemistry to better visualize biological structure. Using a concentration of 0.3% (*w*/*v*) SB in ethanol that was previously proven to be not toxic and to successfully cancel background fluorescence of polymeric scaffolds (Qi et al., 2017), it was possible to image the live and dead cells after 10 days in culture on most of the samples.

Significant differences ($p < 0.05$) were observed only between proliferation on PSS/PAH and MH_6 and MH_12 coated fibers (as shown in **Figure 9A**). The proliferation of

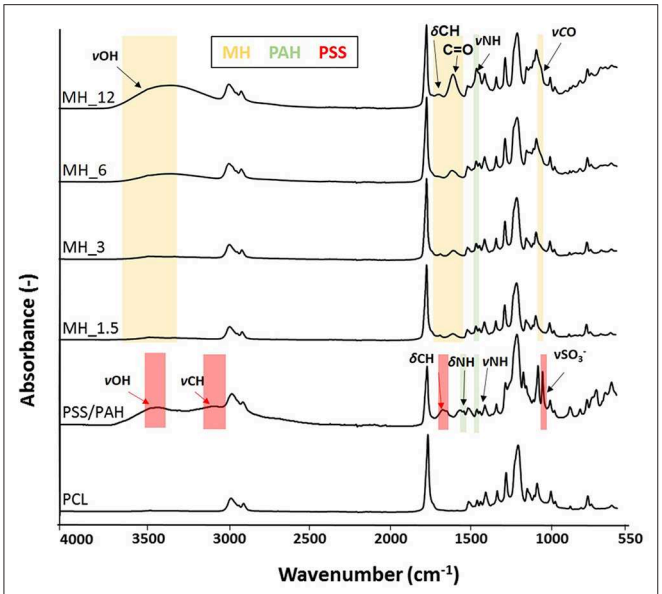

FIGURE 5 | Fourier transform infrared spectroscopy–attenuated total reflectance (FTIR-ATR) spectra of the electrospun membranes before and after layer-by-layer (LbL) assembly functionalization.

fibroblasts on PSS/PAH sample was lower and statistically different compared to all the other samples. For immortalized T-HESC, the proliferation was significantly decreased on PCL samples, while the concentration of MH did not significantly affect the viability. Significant higher proliferation was observed on PSS/PAH fibers compared to MH_6-coated substrates. Honey-coated fibers supported proliferation of primary endothelial cells with no significant differences depending on the concentration of honey. Proliferation was significantly lower on PSS/PAH and bare PCL samples compared to the maximum value obtained on MH_1.5- and MH_3-coated fibers ($p < 0.05$).

Finally, the antibacterial activity of MH against both Gram-positive and Gram-negative species was evaluated by the broth microdilution method. The assay showed an MIC at 200 mg/ml (13.6% *v*/*v*) for *S. aureus* and *S. epidermidis*, at 300 mg/ml (20.4% *v*/*v*) for *E. coli* and at 500 mg/ml (34% *v*/*v*) for *P. aeruginosa*. The antibacterial activity of 2 mg of each LbL-functionalized electrospun membrane was quantified by means of the MTT assay. **Figure 9B** shows the differences in the metabolic activity of cells coincubated for 24 h with the different types of membranes. In comparison with neat PCL membranes, PSS/PAH samples showed no antibacterial activity. On the other hand, the efficacy of honey-LbL-functionalized electrospun membranes depended on the content of MH and on the tested strain. Honey-functionalized membranes had no significant efficacy against the Gram-negative species *E. coli* and *P. aeruginosa* (averagely from 1.1 to 11.1% inhibition). Increasing but negligible inhibitions were observed against *S. aureus* for MH_1.5, MH_3, and MH_6 samples, whereas a significant reduction of 27.2% was detected for MH_12 ($p < 0.001$). For *S. epidermidis*, significant inhibitory activities of 13.5% for MH_3, of 23.4% for MH_6, and of 34.3% for MH_12 were found ($p < 0.001$).

DISCUSSION

Bacterial resistance to antimicrobial agents is an increasing health and economic problem (Frieri et al., 2017). As an alternative to antimicrobial drugs, the therapeutic use of ancient remedies has been revaluated in recent years. Honey is known for its therapeutic potential, including wound healing properties and antimicrobial activity. Since ancient times, honey has been a traditional remedy of several human diseases (Eteraf-Oskouei and Najafi, 2013). The antibacterial properties of honey are strongly influenced by its high osmolarity, acidity, content of hydrogen peroxide, and, in the specific case of MH, also by phytochemical components like methylglyoxal and leptosperin (Jenkins et al., 2015). However, toxic cellular effects of the honey-derived agents could potentially limit its clinical use. To date, only a few papers have shown the cytocompatibility of MH-based structures for tissue engineering applications, reporting the correlation of MH concentration with its toxicity to human cells. In this work, we proposed the following: (1) LbL assembly as an effective surface functionalization technology and (2) for the first time, MH as a PE within the LbL assembly strategy to confer antibacterial properties and preserve the cytocompatibility of PCL electrospun membranes. Among others, electrospinning technology offers the unique opportunity to develop ECM-like substrates, with biomimetic features, able to enhance soft tissue regeneration. In addition to this, as demonstrated recently by Gentile et al. (2015b), LbL technology allows the incorporation of a relatively small amount of loaded drug/biomolecules needed to achieve effective concentrations for a localized and controlled delivery system without affecting the physicochemical properties of the substrate.

Therefore, to consider MH as a novel PE, electrophoresis measurements were performed, and they showed that MH-based solutions were negatively charged and the MH trend was in accordance with previous studies, where the ζ-potential was significantly influenced by the concentration of different studied polysaccharides. Particularly, sodium alginate and k-carrageenan solutions, considered as weak PEs, showed that the increase in the polysaccharide concentrations lead to more negative ζ-potential values (Carneiro-da-Cunha et al., 2011). On the other hand, it was reported in the literature that strong PEs, such as polyethyleneimine, were characterized by an opposite trend, where an increase in the polymer concentration lead to lower ζ-potential values (Lindquist and Stratton, 1976). This indicates that MH acts as a partially weak PE as the natural-based PEs.

A confirmation of the MH potential within LbL functionalization was provided by QCM-D measurements, where MH and PAH demonstrated a stable electrostatic complexation with the tendency of PAH to form a more rigid layer in comparison to MH, as the dissipation factor underwent a more pronounced shift when MH layer was recorded (Deligöz and Tieke, 2014).

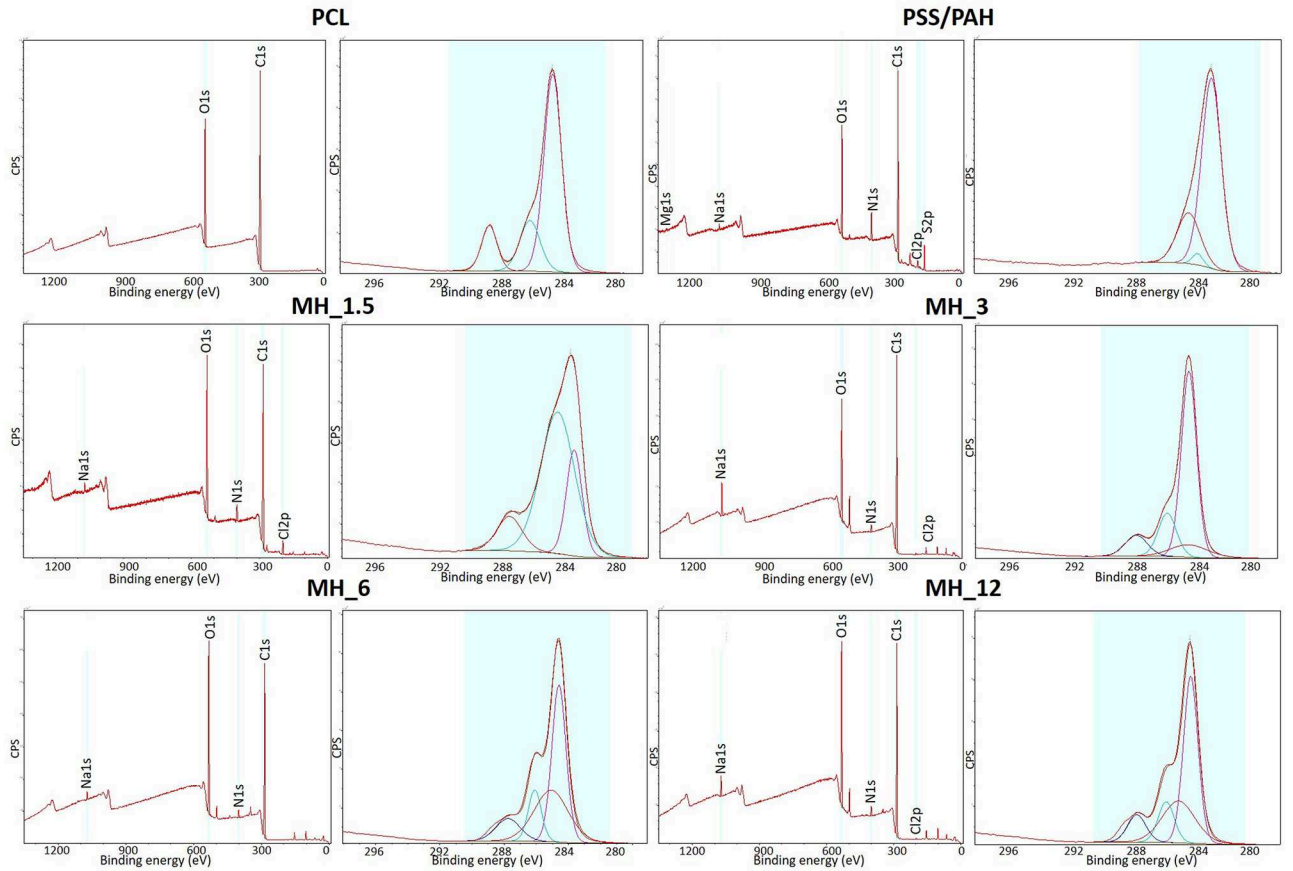

FIGURE 6 | X-ray photoelectron spectroscopy (XPS) survey spectra and high-resolution C1s spectra of the electrospun membranes before and after LbL assembly functionalization.

Biomimetic fiber-based membranes were produced through electrospinning to mimic the nanofibrous structure of the native ECM (Wang et al., 2013). Among other polymers, PCL was selected as former material, thanks to its well-known biocompatibility and its stability during LbL processing without compromising bulk material properties and structure morphology (Malikmammadov et al., 2018). For the optimal functionalization conditions of PCL-based electrospun membranes via LbL assembly, the process parameters were set as follows: a total number of 16 nanolayers, dipping time into the PE solutions of 15 min, PAH molar concentration of 0.5 M, in accordance to a previous work reported by the authors (Gentile et al., 2017). To favor the absorption of the first PE, aminolysis treatment was performed before the LbL assembly functionalization to incorporate primary and secondary NH_2 groups onto the substrate (Ferreira et al., 2016). The surface functionalization did not influence the intrinsic microporosity of the electrospun membranes, which is fundamental for cell penetration, nutrient transport, and waste removal (Sell et al., 2008), and to make them available biocues of the native ECM (Wang et al., 2013). Particularly, SEM showed for the control PSS/PAH-coated membranes a formation of irregularly shaped protuberances and a consequently higher surface roughness and fiber diameter in comparison to the bare substrate. This is typical of strong complexation between these two PEs and becomes more evident with an increasing number of bilayers, as demonstrated by several studies (Park et al., 2008; Gribova et al., 2011). On the other hand, similarly to other natural PEs, MH coating appeared smooth and uniform, leading to an increase in the fiber diameter, which in turn resulted proportional to the number of bilayers used (Park et al., 2009; Gomes et al., 2015).

Although not quantitative, AFM tapping mode phase contrast signal can very clearly differentiate different material properties, and in our work, the coating substance showed a reduced phase lag (lighter in the images) compared with the PCL fiber (darker phase contrast). In phase contrast, PCL fibers showed typical striations (13.5 nm periodicity around the fiber circumference), which are the polymer crystalline lamellae of the PCL layered between amorphous regions, as observed previously in 100% PCL fibers with a spacing of 14.8 $\pm$ 2.9 nm (Goonoo et al., 2015), a value which increased upon addition of another polymer to the fiber composition. In most partially crystalline polymers, these lamellae typically lie in the range of 10–20 nm. They are more visible in the high-resolution AFM phase contrast

images of the fibers (for PCL and MH_1.5). Furthermore, AFM indicated that the resultant concentration vs. coverage response was indicative of an absorption isotherm, where the progressive coverage with concentration indicates that absorption of the partially strong PE to this heterogeneous and porous surface follows a typical surface absorption mechanism, as well as being subject to LbL growth once the initial absorption site have taken hold. During the LbL process at a given concentration, these sites will gradually thicken and spread out filling in the remaining uncoated regions (for a cartoon schematic of this mechanism, see **Figure 10**).

In this work, we reported a lower MH-loaded content, comparing with other papers reported in the literature, with a more controlled release in the longer period. Hixon et al. reported a release of 0.5 mg/ml of MH for the first 24 h, followed by a slight decrease at 4 days and a sustained break down after 7 days (Hixon et al., 2017). In our work, we demonstrated that LbL assembly can be an effective methodology for having a controlled release of the natural antibacterial agent within 2 weeks, which represent the period in which most implant-associated infections are initiated (Birlutiu et al., 2017).

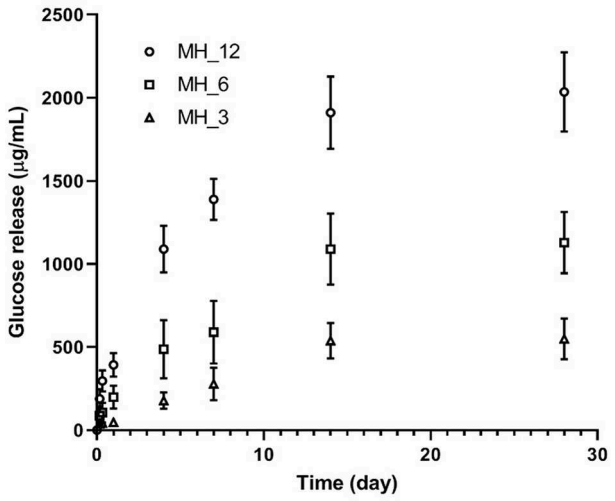

FIGURE 7 | Glucose assay for honey detection.

Finally, biological tests demonstrated that MH coating supported proliferation of different cell types (fibroblasts and endothelial cells) without compromising the biocompatibility of the meshes, while the antibacterial ones showed that the antimicrobial MH activity was dependent on the concentration used and the bacteria strain tested. In accordance with our observation, Bucekova et al. (2018) demonstrated that medical-grade MH was more effective against Gram-positive than Gram-negative bacteria. Similar results were shown by Tan et al. (2009) with MIC_{95} values of 12.5% (*v*/*v*) and 20% (*v*/*v*) for *S. aureus* and *E. coli*, respectively.

Furthermore, *E. coli* inhibition was demonstrated by means of the agar diffusion assay for PCL scaffolds containing 10 and 20% of MH by Guthrie et al. (2012). Yang et al. reported bacterial inhibition rates of different MH/silk fibroin fibrous matrices (Yang et al., 2017). In particular, for MH (10%)/silk fibroin, an inhibitory effect ranging from 5 to 10% was detected against *S. aureus*, *E. coli*, *P. aeruginosa*, and methicillin-resistant *S. aureus* strains. The observed dependence to the bacterial strain might be identified, at first, in the structural differences of their cell walls. In comparison to Gram-negative strains, in fact, Gram-positive strains do not have an outer membrane that offers protection to the peptidoglycan layer from lysozyme and other antimicrobial agents, making them easier to penetrate and damage (Johnston et al., 2018). Second, the different grade of susceptibility of bacterial strains might be also due to the different mechanisms of action involved in MH's antibacterial activity (Henriques et al., 2010). For example, for *S. aureus*, it was observed that MH interferes with the regular cell division process (Gomes et al., 2015). Conversely, for *P. aeruginosa*, it was observed that inhibitory concentrations cause the loss of cellular integrity, extensive cell lysis, and death (Henriques et al., 2011).

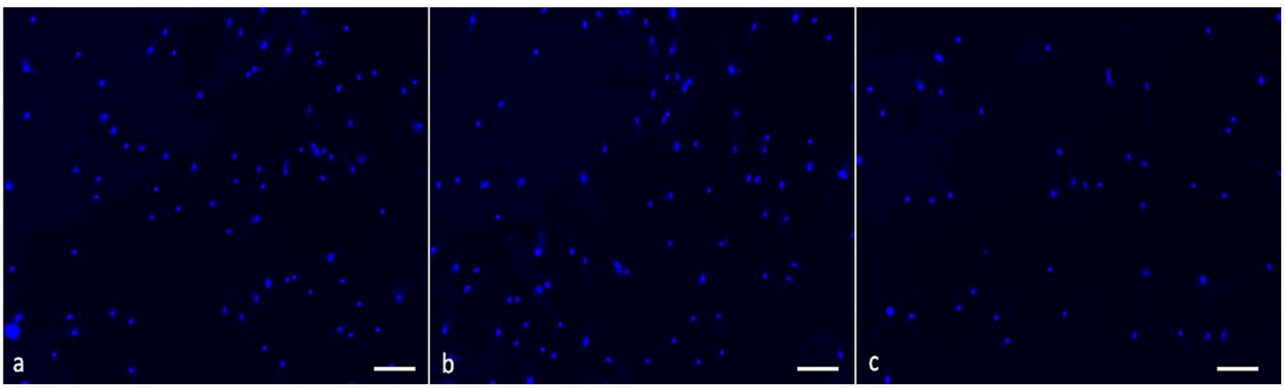

FIGURE 8 | Proliferation of fibroblasts in medium supplemented with Manuka honey at different concentrations. Blue nuclei staining (NucBlue Live reagent) of cells cultured in **(a)** Dulbecco's modified Eagle's medium (DMEM) (control), **(b)** DMEM supplemented with honey 1.3% *v*/*v*, **(c)** DMEM supplemented with honey 8.3 % *v*/*v* was detected using a standard DAPI filter. All the pictures are recorded with magnification 4×, scale bar 100 mm.

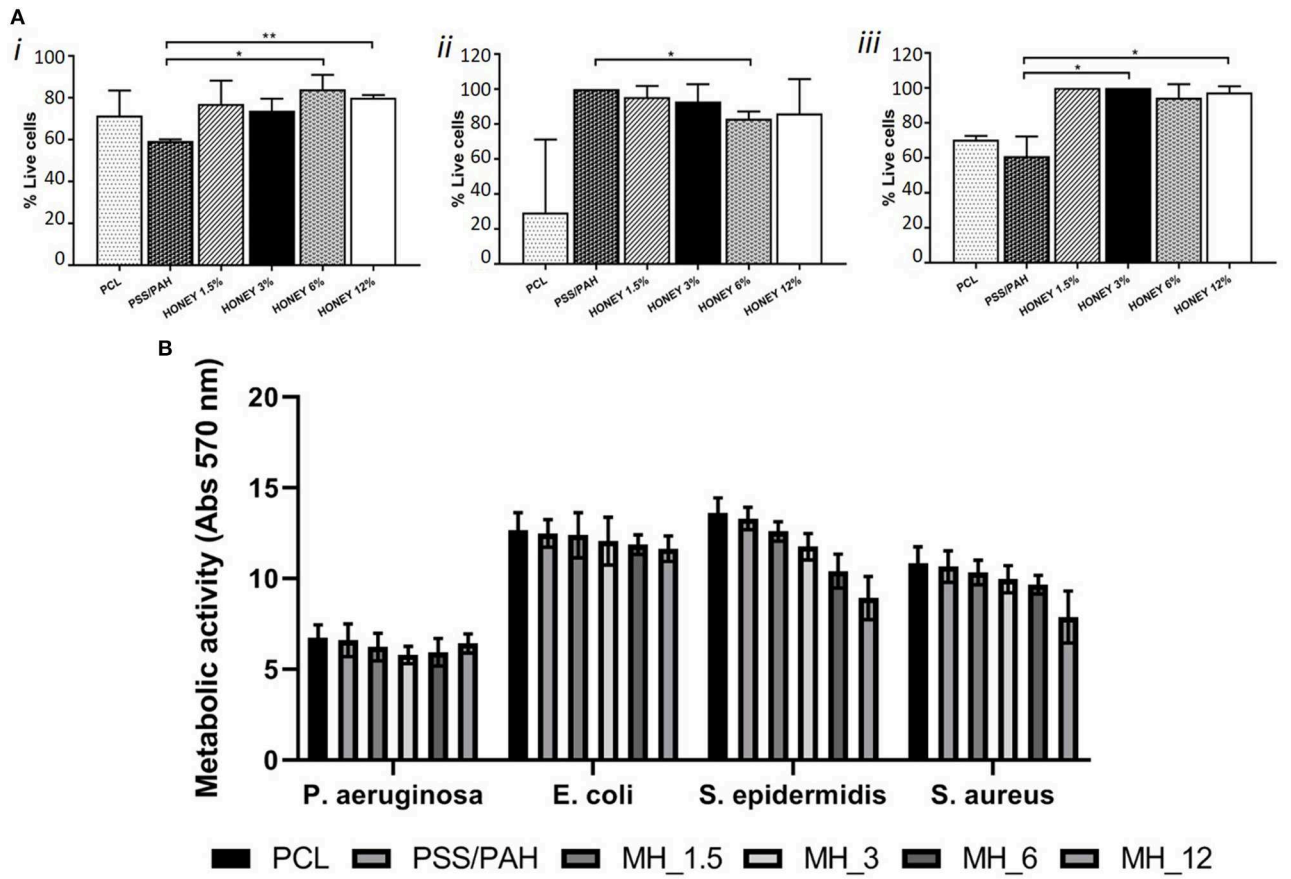

FIGURE 9 | (A) Cell viability of dermal fibroblasts (i), immortalized T-HESC (ii) and human umbilical vein endothelial cells (HUVECs) (iii) on PCL, PSS/PAH, Honey1.5, 3, 6, 12%. *Mark significantly different samples. **(B)** Metabolic activity measured by 3-[4,5-dimethylthiazol-2-yl]-2,5-diphenyltetrazolium bromide (MTT) assay of four different strains incubated for 24 h with nanofunctionalized membranes.

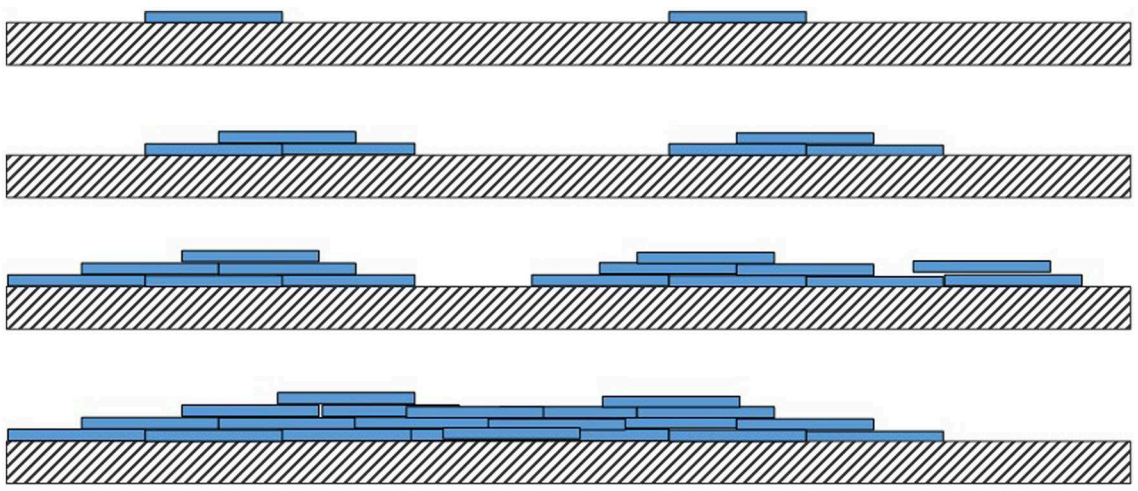

FIGURE 10 | Schematic cartoon of the layer-by-layer (LbL) mechanism.

Overall, the advantages of the nanofunctionalization strategy described here are marked: (1) to allow the manufacturing of biomimetic systems with expectable functional properties without compromising the physicochemical properties of the electrospun membranes; (2) *in vitro* release demonstrated that the MH-loaded meshes were capable of effectively delivering MH in a controlled way within 2–3 weeks of incubation; and (3) *in vitro* tests confirmed the cytocompatibility of all the proposed MH-based systems while the antibacterial ones showed that the antimicrobial MH activity was dependent on the concentration used and the bacteria strain tested. This study has therefore demonstrated that the combination of naturally derived antibacterial agent with LbL technique may be applied to the manufacture of medical devices with advanced functionality.

DATA AVAILABILITY STATEMENT

The raw data supporting the conclusions of this manuscript will be made available by the authors, without undue reservation, to any qualified researcher.

AUTHOR CONTRIBUTIONS

EM and PG conceived the study. EM, LF, SC, and PG designed the experiments. EM and PG performed the LbL functionalization. CT-T produced the membranes and performed the QCM. SC performed the AFM. EM performed the SEM. VP performed the *in vitro* cell tests. CC and LF performed the bacterial tests. All authors analyzed and interpreted the data and prepared the manuscript.

FUNDING

This research was supported by the UK NIHR-EPSRC IMPRESS Network (EP/M000109/1 and EP/N027345/1) and by PROM project (748903), funded by H2020-MSCA-IF-2016. Microbiological assays are supported by the Università del Piemonte Orientale (local research project 2016-ex60%).

REFERENCES

Anjos, O., Campos, M. G., Ruiz, P. C., and Antunes, P. (2015). Application of FTIR-ATR spectroscopy to the quantification of sugar in honey. *Food Chem.* 169, 218–223. doi: 10.1016/j.foodchem.2014.07.138

Armstrong, D. G. (2009). Manuka honey improved wound healing in patients with sloughy venous leg ulcers. *Evid. Based Med.* 14:148. doi: 10.1136/ebm.14.5.148

Birlutiu, R. M., Birlutiu, V., Mihalache, M., Mihalache, C., and Cismasiu, R. S. (2017). Diagnosis and management of orthopedic implant-associated infection: a comprehensive review of the literature. *Biomed. Res.* 28, 5063–5073.

Bonifacio, M. A., Cometa, S., Cochis, A., Gentile, P., Ferreira, A. M., Azzimonti, B., et al. (2018). Antibacterial effectiveness meets improved mechanical properties: Manuka honey/gellan gum composite hydrogels for cartilage repair. *Carbohyd. Polymers* 198, 462–472. doi: 10.1016/j.carbpol.2018.06.115

Bucekova, M., Buriova, M., Pekarik, L., Majtan, V., and Majtan, J. (2018). Phytochemicals-mediated production of hydrogen peroxide is crucial for high antibacterial activity of honeydew honey. *Sci. Rep.* 8:9061. doi: 10.1038/s41598-018-27449-3

Carneiro-da-Cunha, M. G., Cerqueira, M. A., Souza, B. W. S., Teixeira, J. A., and Vicente, A. A. (2011). Influence of concentration, ionic strength and pH on zeta potential and mean hydrodynamic diameter of edible polysaccharide solutions envisaged for multinanolayered films production. *Carbohyd. Polymers* 85, 522–528. doi: 10.1016/j.carbpol.2011.03.001

Cokcetin, N. N., Pappalardo, M., Campbell, L. T., Brooks, P., Carter, D. A., Blair, S. E., et al. (2016). The antibacterial activity of Australian Leptospermum honey correlates with methylglyoxal levels. *PLoS ONE* 11:e0167780. doi: 10.1371/journal.pone.0167780

Dai, Z., Ronholm, J., Tian, Y., Sethi, B., and Cao, X. (2016). Sterilization techniques for biodegradable scaffolds in tissue engineering applications. *J. Tissue Eng.* 7:2041731416648810. doi: 10.1177/2041731416648810

Deligöz, H., and Tieke, B. (2014). QCM-D study of layer-by-layer assembly of polyelectrolyte blend films and their drug loading-release behavior. *Col. Surf. A Physicochem. Eng. Aspects* 441, 725–736. doi: 10.1016/j.colsurfa.2013.10.033

Du Toit, D. F., and Page, B. J. (2009). An *in vitro* evaluation of the cell toxicity of honey and silver dressings. *J. Wound Care* 18, 383–389. doi: 10.12968/jowc.2009.18.9.44307

Esposito, S., Bassetti, M., Concia, E., De Simone, G., De Rosa, F. G., Grossi, P., et al. (2017). Diagnosis and management of skin and soft-tissue infections (SSTI). A literature review and consensus statement: an update. *J. Chemother.* 29, 197–214. doi: 10.1080/1120009X.2017.1311398

Eteraf-Oskouei, T., and Najafi, M. (2013). Traditional and modern uses of natural honey in human diseases: a review. *Iran. J. Basic Med. Sci.* 16, 731–742.

Ferreira, A. M., Gentile, P., Toumpaniari, S., Ciardelli, G., and Birch, M. A. (2016). Impact of collagen/heparin multilayers for regulating bone cellular functions. *ACS Appl. Mater. Interfaces* 8, 29923–29932. doi: 10.1021/acsami.6b09241

Ferreira, A. M., Tonda-Turo, C., Mancuso, E., and Gentile, P. (2019). Multilayer nanoscale functionalisation to treat disorders and enhance regeneration of bone tissue. *Nanomedicine* 19:22–38. doi: 10.1016/j.nano.2019.03.009

Frieri, M., Kumar, K., and Boutin, A. (2017). Antibiotic resistance. *J. Infect. Public Health* 10, 369–378. doi: 10.1016/j.jiph.2016.08.007

Gentile, P., Carmagnola, I., Nardo, T., and Chiono, V. (2015a). Layer-by-layer assembly for biomedical applications in the last decade. *Nanotechnology* 26:422001. doi: 10.1088/0957-4484/26/42/422001

Gentile, P., Ferreira, A. M., Callaghan, J. T., Miller, C. A., Atkinson, J., Freeman, C., et al. (2017). Multilayer nanoscale encapsulation of biofunctional peptides to enhance bone tissue regeneration *in vivo*. *Adv. Healthcare Mater.* 6:1601182. doi: 10.1002/adhm.201601182

Gentile, P., Frongia, M. E., Cardellach, M., Miller, C. A., Stafford, G. P., Leggett, G. J., et al. (2015b). Functionalised nanoscale coatings using layer-by-layer assembly for imparting antibacterial properties to polylactide-co-glycolide surfaces. *Acta Biomater.* 21, 35–43. doi: 10.1016/j.actbio.2015.04.009

Gomes, A. P., Mano, J. F., Queiroz, J. A., and Gouveia, I. C. (2015). "Layer-by-layer assembly for biofunctionalization of cellulosic fibers with emergent antimicrobial agents," in *Cellulose Chemistry and Properties: Fibers, Nanocelluloses and Advanced Materials* ed O. J. Rojas (Raleigh, NC: Springer), 225–240. doi: 10.1007/12_2015_318

Goonoo, N., Bhaw-Luximon, A., Rodriguez, I. A., Wesner, D., Schönherr, H., Bowlin, G. L., et al. (2015). Poly (ester-ether) s: III. assessment of cell behaviour on nanofibrous scaffolds of PCL, PLLA and PDX blended with amorphous PMeDX. *J. Mater. Chem. B*, 3, 673–687. doi: 10.1039/C4TB01350F

Gribova, V., Auzely-Velty, R., and Picart, C. (2011). Polyelectrolyte multilayer assemblies on materials surfaces: from cell adhesion to tissue engineering. *Chem. Mater.* 24, 854–869. doi: 10.1021/cm2032459

Guthrie, K. M., Agarwal, A., Tackes, D. S., Johnson, K. W., Abbott, N. L., Murphy, C. J., et al. (2012). Antibacterial efficacy of silver-impregnated polyelectrolyte multilayers immobilized on a biological dressing in a murine wound infection model. *Ann. Surg.* 256, 371–377. doi: 10.1097/SLA.0b013e318256ff99

Henriques, A. F., Jenkins, R. E., Burton, N. F., and Cooper, R. A. (2010). The intracellular effects of manuka honey on *Staphylococcus aureus*. *Eur. J. Clin. Microbiol. Infect. Dis.* 29, 45–50. doi: 10.1007/s10096-009-0817-2

Henriques, A. F., Jenkins, R. E., Burton, N. F., and Cooper, R. A. (2011). The effect of manuka honey on the structure of *Pseudomonas aeruginosa*. *Eur. J. Clin. Microbiol. Infect. Dis.* 30, 167–171. doi: 10.1007/s10096-010-1065-1

Hixon, K. R., Lu, T., McBride-Gagyi, S. H., Janowiak, B. E., and Sell, S. A. (2017). A comparison of tissue engineering scaffolds incorporated with Manuka honey of varying UMF. *BioMed Res. Int.* 2017:4843065. doi: 10.1155/2017/4843065

Jenkins R., Roberts A., Brown H. L. (2015). On the antibacterial effects of manuka honey: mechanistic insights. *Res. Rep. Biol.* 6, 215–224. doi: 10.2147/RRB.S75754

Johnston, M., McBride, M., Dahiya, D., Owusu-Apenten, R., and Nigam, P. S. (2018). Antibacterial activity of Manuka honey and its components: an overview. *AIMS Microbiol.* 4:655. doi: 10.3934/microbiol.2018.4.655

Kruk, T., Szczepanowicz, K., Kregiel, D., Szyk-Warszynska, L., and P. (2016). Warszynski: Nanostructured multilayer polyelectrolyte films with silver nanoparticles as antibacterial coatings. *Coll. Surf. B Biointerfaces* 137, 158–166. doi: 10.1016/j.colsurfb.2015.06.016

Kumar, V. R. M. N. (2000). A review of chitin and chitosan applications. *Reactive Funct. Polymers* 46, 1–27. doi: 10.1016/S1381-5148(00)00038-9

Li, B., and Webster, T. J. (2018). Bacteria antibiotic resistance: new challenges and opportunities for implant-associated orthopedic infections. *J. Orthopaed. Res.* 36, 22–32. doi: 10.1002/jor.23656

Lindquist, G. M., and Stratton, R. A. (1976). The role of polyelectrolyte charge density and molecular weight on the adsorption and flocculation of colloidal silica with polyethylenimine. *J. Colloid Interface Sci.* 55, 45–59. doi: 10.1016/0021-9797(76)90007-2

Malikmammadov, E., Tanir, T. E., Kiziltay, A., Hasirci, V., and Hasirci, N. (2018). PCL and PCL-based materials in biomedical applications. *J. Biomater. Sci. Polymer Ed.* 29, 863–893. doi: 10.1080/09205063.2017.1394711

Maxson, T., and Mitchell, D. A. (2016). Targeted treatment for bacterial infections: prospects for pathogen-specific antibiotics coupled with rapid diagnostics. *Tetrahedron* 72:3609. doi: 10.1016/j.tet.2015.09.069

Miller, L. G., Eisenberg, D. F., Liu, H., Chang, C.-L., Wang, Y., Luthra, R., et al. (2015). A. Incidence of skin and soft tissue infections in ambulatory and inpatient settings, 2005–2010. *BMC Infect. Dis.* 15:362. doi: 10.1186/s12879-015-1071-0

Minden-Birkenmaier, B., and Bowlin, G. (2018). Honey-based templates in wound healing and tissue engineering. *Bioengineering* 5:46. doi: 10.3390/bioengineering5020046

Molan, P. C. (2001). Honey as a topical antibacterial agent for treatment of infected wounds. *World Wide Wounds* 10.

Park, J. H., Kim, B. S., Tae, H. J., Kim, I. S., Kim, H. Y., and Khi, M. S. (2009). Polyelectrolyte multilayer coated nanofibrous mats: Controlled surface morphology and cell culture. *Fibers Polymers* 10, 419–424. doi: 10.1007/s12221-009-0419-8

Park, J. H., Kim, B. S., Yoo, Y. C., Khil, M. S., and Kim, H. Y. (2008). Enhanced mechanical properties of multilayer nano-coated electrospun nylon 6 fibers via a layer-by-layer self-assembly. *J. Appl. Polymer Sci.* 107, 2211–2216. doi: 10.1002/app.27322

Park, S., Han, U., Choi, D., and Hong, J. (2018). Layer-by-layer assembled polymeric thin films as prospective drug delivery carriers: design and applications. *Biomater. Res.* 22:29. doi: 10.1186/s40824-018-0139-5

Pfalzgraff, A., Brandenburg, K., and Weindl, G. (2018). Antimicrobial peptides and their therapeutic potential for bacterial skin infections and wounds. *Front. Pharmacol.* 9:281. doi: 10.3389/fphar.2018.00281

Qi, L., Knapton, E. K., Zhang, X., Zhang, T., Gu, C., and Zhao, Y. (2017). Pre-culture Sudan Black B treatment suppresses autofluorescence signals emitted from polymer tissue scaffolds. *Sci. Rep.* 7:8361. doi: 10.1038/s41598-017-08723-2

Ratkowsky, D. A., and Giles, D. E. (1990). *A Handbook of Nonlinear Regression Models.* Ann Arbor, MI: University of Michigan; Marcel Dekker Inc.

Richardson, J. J., Björnmalm, M., and Caruso, F. (2015). Technology-driven layer-by-layer assembly of nanofilms. *Science* 348:aaa2491. doi: 10.1126/science.aaa2491

Rojas, O. J., Claesson, P. M., Muller, D., and Neuman, R. D. (1998). The effect of salt concentration on adsorption of low-charge-density polyelectrolytes and interactions between polyelectrolyte-coated surfaces. *J. Coll. Interface Sci.* 205, 77–88. doi: 10.1006/jcis.1998.5596

Roy, R., Tiwari, M., Donelli, G., and Tiwari, V. (2018). Strategies for combating bacterial biofilms: a focus on anti-biofilm agents and their mechanisms of action. *Virulence* 9, 522–554. doi: 10.1080/21505594.2017.s1313372

Sadeghi-Aliabadi, H., Hamzeh, J., and Mirian, M. (2015). Investigation of Astragalus honey and propolis extract's cytotoxic effect on two human cancer cell lines and their oncogen and proapoptotic gene expression profiles. *Adv. Biomed. Res.* 4:42. doi: 10.4103/2277-9175.151251

Sell, S., Barnes, C., Simpson, D., and Bowlin, G. (2008). Scaffold permeability as a means to determine fiber diameter and pore size of electrospun fibrinogen. *J. Biomed. Mater. Res. A* 85, 115–126. doi: 10.1002/jbm.a.31556

Séon, L., Lavalle, P., Schaaf, P., and Boulmedais, F. (2015). Polyelectrolyte multilayers: a versatile tool for preparing antimicrobial coatings. *Langmuir* 31, 12856–12872. doi: 10.1021/acs.langmuir.5b02768

Tan, H. T., Rahman, R. A., Gan, S. H., Halim, A. S., Asma'Hassan, S., Sulaiman, S. A., and B. S. (2009). Kirnpal-Kaur: the antibacterial properties of Malaysian tualang honey against wound and enteric microorganisms in comparison to manuka honey. *BMC Complement. Altern. Med.* 9:34. doi: 10.1186/1472-6882-9-34

Tonda-Turo, C., Carmagnola, I., and Ciardelli, G. (2018b). Quartz crystal microbalance with dissipation monitoring: a powerful method to predict the *in vivo* behavior of bioengineered surfaces. *Front. Bioeng. Biotechnol.* 6:158. doi: 10.3389/fbioe.2018.00158

Tonda-Turo, C., Ruini, F., Ceresa, C., Gentile, P., Varela, P., Ferreira, A. M., et al. (2018a). Nanostructured scaffold with biomimetic and antibacterial properties for wound healing produced by 'green electrospinning'. *Coll. Surf. B Biointerface*, 172, 233–243. doi: 10.1016/j.colsurfb.2018.08.039

Tun, K., Shurko, J. F., Ryan, L., and Lee, G. C. (2018). Age-based health and economic burden of skin and soft tissue infections in the United States, 2000 and 2012. *PLoS ONE* 13:e0206893. doi: 10.1371/journal.pone.0206893

Wang, X., Ding, B., and Li, B. (2013). Biomimetic electrospun nanofibrous structures for tissue engineering. *Mater. Tdy* 16, 229–241. doi: 10.1016/j.mattod.2013.06.005

Wiegand, I., Hilpert, K., and Hancock, R. E. (2008). W. Agar and broth dilution methods to determine the minimal inhibitory concentration (MIC) of antimicrobial substances. *Nat. Protoc.* 3:163. doi: 10.1038/nprot.2007.521

Yang, X., Fan, L., Ma, L., Wang, Y., Lin, S., Yu, F., et al. (2017). Green electrospun Manuka honey/silk fibroin fibrous matrices as potential wound dressing. *Mater. Design*, 119, 76–84. doi: 10.1016/j.matdes.2017.01.023

Zahin, N., Anwar, R., Tewari, D., Kabir, M. T., Sajid, A., Mathew, B., et al. (2019). Nanoparticles and its biomedical applications in health and diseases: special focus on drug delivery. *Environ. Sci. Pollut. Res.* 26, 1–18. doi: 10.1007/s11356-019-05211-0

Zhang, L., Huang, Y., Zhou, Y., Buckley, T., and Wang, H. H. (2013). Antibiotic administration routes significantly influence the levels of antibiotic resistance in gut microbiota. *Antimicrob. Agents Chemother.* 57, 3659–3666. doi: 10.1128/AAC.00670-13

Zhu, T., Sha, Y., Yan, J., Pageni, P., Rahman, M. A., Yan, Y., et al. (2018). Metallo-polyelectrolytes as a class of ionic macromolecules for functional materials. *Nat. Commun.* 9:4329. doi: 10.1038/s41467-018-06475-9

Zimlichman, E., Henderson, D., Tamir, O., Franz, C., Song, P., Yamin, C. K., et al. (2013). Health care–associated infections: a meta-analysis of costs and financial impact on the US health care system. *JAMA Internal Med.* 173, 2039–2046. doi: 10.1001/jamainternmed.2013.9763

Zinoviadou, K. G., Koutsoumanis, K. P., and Biliaderis, C. G. (2009). Physico-chemical properties of whey protein isolate films containing oregano oil and their antimicrobial action against spoilage flora of fresh beef. *Meat Sci.* 82, 338–345. doi: 10.1016/j.meatsci.2009.02.004

Conflict of Interest: The authors declare that the research was conducted in the absence of any commercial or financial relationships that could be construed as a potential conflict of interest.

frontiers in Bioengineering and Biotechnology

ORIGINAL RESEARCH
published: 14 February 2020
doi: 10.3389/fbioe.2020.00055

Amphiphilic Cationic Macromolecules Highly Effective Against Multi-Drug Resistant Gram-Positive Bacteria and Fungi With No Detectable Resistance

*Sudip Mukherjee, Swagatam Barman, Riya Mukherjee and Jayanta Haldar**

Antimicrobial Research Laboratory, New Chemistry Unit and School of Advanced Materials, Jawaharlal Nehru Centre for Advanced Scientific Research, Bengaluru, India

The ever increasing threats of Gram-positive superbugs such as methicillin-resistant *Staphylococcus aureus* (MRSA), vancomycin-resistant *Staphylococcus aureus* (VRSA), and vancomycin-resistant *Enterococccus faecium* (VRE) are serious matter of concern worldwide toward public health. Such pathogens cause repeated recurrence of infections through the formation of biofilms which consist of metabolically inactive or slow growing dormant bacterial population in vast majority. Concurrently, dispersal of biofilms originates even more virulent dispersed cells responsible for pathogenesis. Along with this, fungal infections most commonly associated with *Candida albicans* also created a major complicacy in human healthcare. Moreover, concomitant survival of *C. albicans* and MRSA in a multispecies biofilms created extremely complicated polymicrobial infections. Surprisingly, infections associated with single species biofilm as well as multiple species biofilm (co-existence of MRSA and *C. albicans*) are almost untreatable with conventional antibiotics. Therefore, the situation demands an urgent development of antimicrobial agent which would tackle persistent infections associated with bacteria, fungi and their biofilms. Toward this goal, herein we developed a new class of branched polyethyleneimine based amphiphilic cationic macromolecules (ACMs) bearing normal alkyl, alkyl ester and alkyl amide moieties. An optimized compound with dual activity against drug-resistant bacteria (MIC = 2–4 μg/mL) and fungi (MIC = 4–8 μg/mL) was identified with minimal toxicity toward human erythrocytes (HC_{50} = 270 μg/mL). The lead compound, ACM-A_{Hex} (**12**) displayed rapid bactericidal and fungicidal kinetics (> 5 log CFU/mL reduction within 1–4 h). It also killed metabolically dormant stationary (MRSA and VRE) and persister (*S. aureus*) cells. Moreover, this compound was able to disrupt the preformed biofilm of MRSA and reduced the bacterial burden related to the dispersed cells. It showed significant proficiencies to eliminate polymicrobial biofilms of MRSA and *C. albicans*. Bacteria also could not develop any resistant against this class of membrane active molecules even after 15 days of successive passages. Taken together this class of macromolecule can be developed further as a dual therapeutic agent to combat infections associated with bacterial and fungal co-existence.

Keywords: antimicrobial resistance, AMP mimics, macromolecular antimicrobial agent, polymicrobial biofilm, metabolically inactive bacteria

OPEN ACCESS

Edited by:
Gianluca Ciardelli, Politecnico di Torino, Italy

Reviewed by:
Georgia Papavasiliou, Illinois Institute of Technology, United States
Letizia Fracchia, University of Eastern Piedmont, Italy

***Correspondence:**
Jayanta Haldar
jayanta@jncasr.ac.in

Specialty section:
This article was submitted to Biomaterials, a section of the journal Frontiers in Bioengineering and Biotechnology

Received: *29 September 2019*
Accepted: *22 January 2020*
Published: *14 February 2020*

Citation:
Mukherjee S, Barman S, Mukherjee R and Haldar J (2020) Amphiphilic Cationic Macromolecules Highly Effective Against Multi-Drug Resistant Gram-Positive Bacteria and Fungi With No Detectable Resistance. Front. Bioeng. Biotechnol. 8:55. doi: 10.3389/fbioe.2020.00055

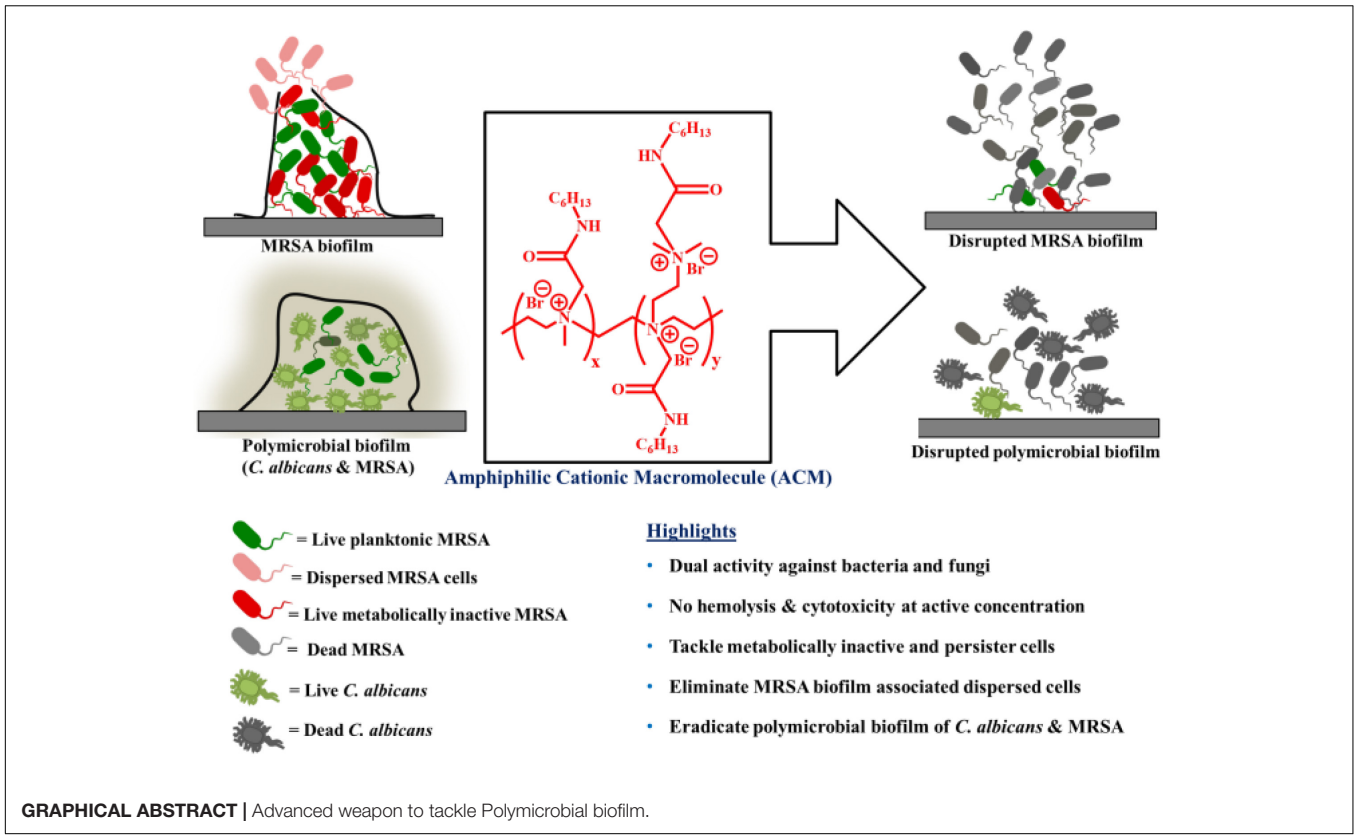

GRAPHICAL ABSTRACT | Advanced weapon to tackle Polymicrobial biofilm.

INTRODUCTION

The overgrowing population of multidrug-resistant (MDR) pathogens has created a serious clinical ultimatum which leads the public health toward a pre-antibiotic era (Bush et al., 2011). In addition to the emergence of Gram-negative bacteria, infections caused by MDR Gram-positive bacteria have also become one of the major hurdles to tackle with conventional antibiotic therapy (Davies and Davies, 2010). In a recent report, the World Health Organization (WHO) identified a list of Gram-positive bacteria of high priority which included MRSA, VRSA, and VRE which are responsible for majority of infections in clinical settings (Willyard, 2017). The root cause of such deadly infections is the formation of bacterial biofilms, a rigid and multilayer bacterial assembly (Hall-Stoodley et al., 2004; Campoccia et al., 2013). Typically, this assembly is composed of extracellular matrix (a hurdle for antibiotics penetration) and lion's share of it contains metabolically inactive dormant bacterial populations (Stewart and Costerton, 2001). Owing to these facts, antibiotics are inefficient to tackle chronic infections related to biofilm formation (Davies, 2003). Additionally, dispersal process in biofilms sparks more virulent dispersed cells which create a new infection foci within the host (Chua et al., 2014). Such dispersed cells are also difficult to kill with the conventional antibiotic therapy as they are distinct from the planktonic bacterial cells.

Contemporarily, fungal infection is another major problem to the human healthcare (Wilson et al., 2002). Particularly, *Candida albicans* is one of the common fungi which cause invasive infections (Brown et al., 2012). In addition to this, *C. albicans* is known to co-exist with MRSA resulting the formation of polymicrobial biofilms (Harriott and Noverr, 2009, 2011; Lohse et al., 2018). At the current situation there are limited treatment options for infection associated with such multi-species assemblies. Therefore, the situation demands an urgent need for the development of new class of antimicrobial agents with dual potency to counter bacterial as well as fungal infections associated with single and multispecies biofilm formation.

In past few decades, naturally occurring antimicrobial peptides (AMPs: a short cationic peptide) have emerged as potent, broad spectrum antimicrobials, which act as a frontline defense against a wide range of microbes (Zasloff, 2002). AMPs selectively target the negatively charged microbial membrane over zwitterionic mammalian membrane primarily through electrostatic and hydrophobic interaction (Hancock and Sahl, 2006). Owing to their membrane acting nature, microbial species find difficulties to develop resistance propensity against AMPs. However, the translation of AMPs to the clinical settings is limited majorly due to synthetic complexities, high manufacture cost and lack of *in vivo* stability. In order to address these limitations associated with AMPs, efforts have already been taken to develop several AMP-mimicking synthetic antimicrobial polymers in addition to the small molecular peptidomimetics (Ghosh et al., 2014; Konai et al., 2014). They include polynorbornene (Ilker et al., 2004), polymethacrylates (Kuroda and DeGrado, 2005), polycarbonates (Nederberg et al., 2011; Chin et al., 2018), poly-β-lactam (Porter et al., 2000; Liu et al., 2014), polymalemide

(Uppu et al., 2013; Barman et al., 2019), polyamide (Yavvari et al., 2017) and many other polymeric amphiphiles (Krumm et al., 2014; Zhang et al., 2014; Konai et al., 2018; Palermo et al., 2019). The antibacterial activity is well documented for different polymeric designs, however, antifungal activity is reported for very few cases (Li et al., 2012; Liu et al., 2015; Qian et al., 2018). Typically, developing a selective antifungal agent is challenging as both the fungal and mammalian cells resemble many similarities. Hence, identifying less cytotoxic antimicrobial polymers with significant antibacterial and antifungal activity is highly desirable. Beside these hurdles, one of the major challenges is to achieve an antimicrobial polymer with ability to retain activity in complex medium such as blood plasma.

Toward this goal, herein, we report a new class of water soluble AMP-mimicking macromolecules consisting of small molecular weight (Mn ∼ 600 Da) of branched polyethyleneimine (PEI) backbone through a two-step post-functionalization strategy. It has been reported that polyethyleneimine (PEI) derivatives of higher molecular weight are potent antimicrobial agents (Hoque et al., 2015, 2019), but toxicity limits their scope for further development. Therefore, we have used small molecular weight branched PEI as a backbone polymer, aiming to obtain a lead antimicrobial agent with minimum toxicity toward mammalian cells. The molecular weight (M_n) of the final macromolecules was bound to be in the range of 3.5–6 kDa which is much below the threshold for renal clearance (<50 kDa). In order to achieve an optimum balance of amphiphilicity (hydrophilic/hydrophobic balance), hydrophobicity was varied using various alkyl chain lengths with and without ester and amide groups. A permanent cationic charge (contributed by quaternary ammonium moiety) has been introduced through quaternization of tertiary nitrogen centers with different alkyl chain. This cationic charge is introduced for a selective interaction with the negatively charged microbial membrane over mammalian membrane. Antimicrobial activity against various drug-sensitive, drug-resistant Gram-positive bacteria and fungi was tested. Additionally, toxicity against both human red blood cell (hRBC) and HEK-293 cell were evaluated. Time kill kinetics of the optimized macromolecule was investigated against both Gram-positive bacteria and fungi. Furthermore, efficacy of the lead macromolecule was investigated against difficult-to-treat metabolically inactive different Gram-positive bacteria. The membrane active mechanism of action was also investigated against these metabolically distinct cells of bacteria and fungi. Next, biofilm disruption ability and killing efficiency against biofilm associated dispersed cells were studied. Additionally, potency of the lead molecule to eradicate polymicrobial biofilm of MRSA and *C. albicans* was investigated. To the end propensity of resistance development was also studied against MRSA superbugs.

MATERIALS AND METHODS

Reagents and Microbial Strains

1-Butanol, 1-Hexanol, 1-Octanol, 1-Aminobutane 1-Aminohexane, 1-Aminooctane, Bromoacetyl bromide, Branched polyethyleneimine M_n ∼600 Da, were purchased from Sigma-Aldrich and used as received. 1-Bromobutane, 1-Bromohexane, 1-Bromooctane and 1-Bromodecane, Phosphorous pentaoxide (P_2O_5), potassium carbonate (K_2CO_3), anhydrous sodium sulfate (Na_2SO_4), potassium hydroxide (KOH), dichloromethane (DCM), chloroform and anhydrous diethyl ether were purchased from Spectrochem, India and were of analytical grade. DCM and chloroform were dried over P_2O_5 and stored over molecular sieves (4 Å). An attenuated total reflectance Fourier transform infrared (ATR FT-IR) spectrometer was used to record IR spectra using diamond as ATR crystal. Bruker (AMX-400) (400 MHz for ^{1}H-NMR) spectrometer was used to record nuclear magnetic resonance (NMR) spectra in deuterated solvents. Tecan infinite pro series M200 microplate reader was used to record optical density (OD) and fluorescence intensity. *Staphylococcus aureus* and *Escherichia coli* (MTCC737 and 443) were purchased from MTCC (Chandigarh, India). Methicillin-resistant *Staphylococcus aureus* MRSA (ATCC33591), *E. faecium* (ATCC19634) and *C. albicans* (ATCC10231) were obtained from ATCC (Rockville, MD, United States). Growth media and agar for bacteria and fungal culture were provided by HIMEDIA, India. MRSA R3545, MRSA R3889, MRSA R3890 were obtained from National Institute of Mental Health and Neurosciences, Bangalore, India. VRSA-1, VRSA-4, VRE903, and VRE909 were obtained from Dr. Siddharth Chopra, CSIR-Central Drug Research Institute, Lucknow, India. Fungal strains (*C. albicans* AB226 and *C. albicans* AB399) were obtained from Anthem Biosciences, Bangalore, India.

Synthesis

Synthesis of *N*-Methylated PEI (1)

Briefly, branch polyethyleneimine (PEI, 600Da) (5 g, 116 mmol) was dissolved with 20 mL of water. Then, Formic acid (17.5 mL, 464 mmol) and formaldehyde (28 mL, 348 mmol) was added to the aqueous solution of PEI (Hoque et al., 2019, p. 57). Afterward, the entire reaction mixture was refluxed at 90°C for 60 h with constant stirring. Next, the mixture was cooled down to room temperature and the pH of the solution was adjusted to 11 using aqueous solution of 8M KOH. Finally, the deprotonated *N*-methylated PEI was extracted 5 times using chloroform. To the end, the extracted organic layer was removed using Rota-evaporator to yield a brown viscous product with quantitative yield (**Scheme 1**). The product was characterized by FT-IR and ^{1}H NMR spectroscopy (data provided in **Supplementary Material**).

General Synthetic Procedure for the Intermediates (2a–2c) and (3a–3c)

1-alkanols (5 g) or 1-aminoalkanes (5 g) were dissolved in DCM (50 mL) and 50 mL aqueous solution of K_2CO_3 (12.2 g, 88.3 mmol) was added to it. The binary mixture was then cooled to 4-5°C. Next, bromoacetyl bromide (7.7 mL, 88.3 mmol) was dissolved in DCM (50 mL) and was added to the mixture drop wise for 30 min. The entire biphasic reaction mixture was then stirred vigorously at room temperature for 4 and 12 h for alcohol and amines respectively. Afterward, DCM layer was separated using a separating funnel and was passed through anhydrous Na_2SO_4. Then the DCM solution was evaporated

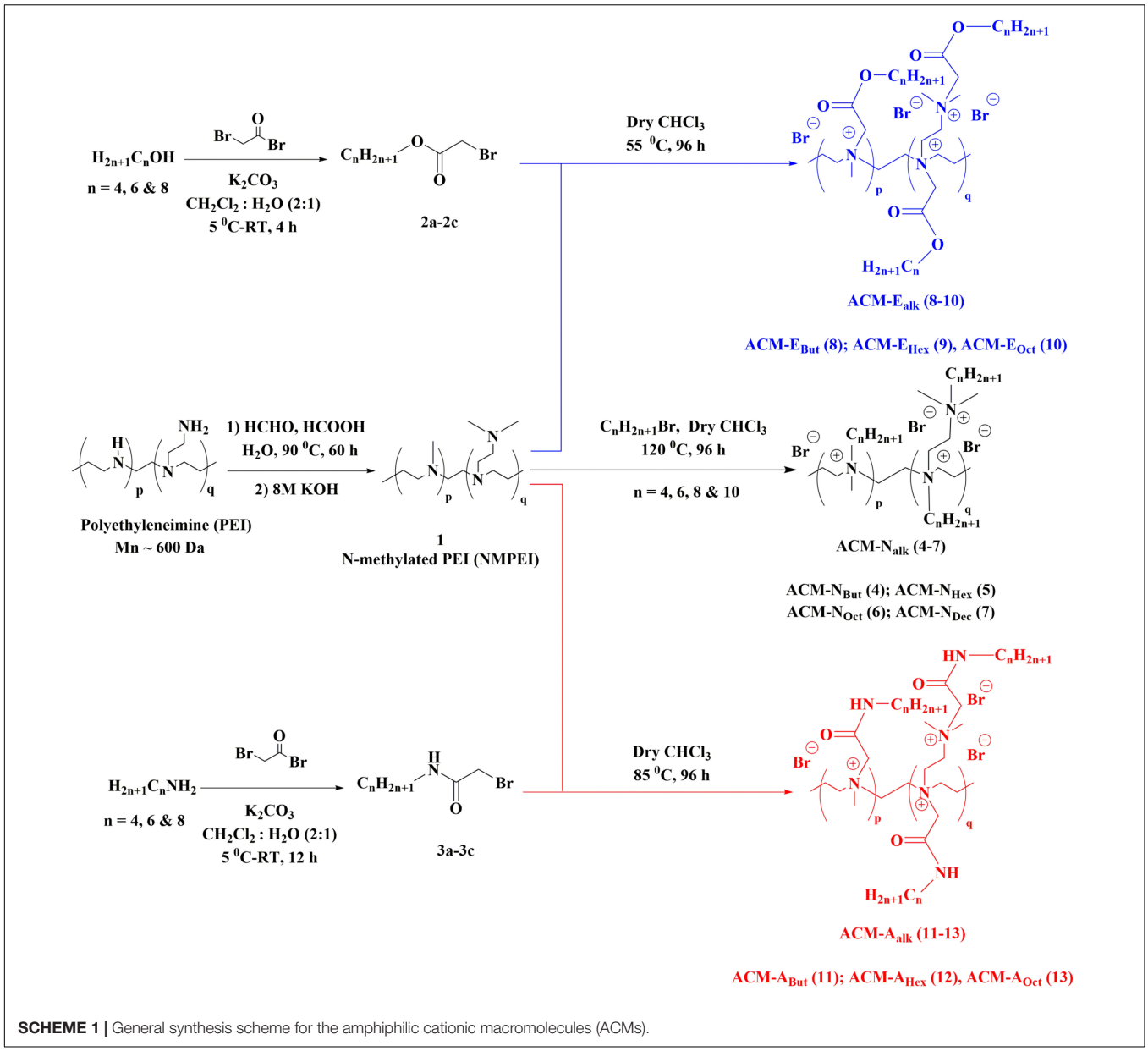

SCHEME 1 | General synthesis scheme for the amphiphilic cationic macromolecules (ACMs).

using rota-evaporator to obtain colorless liquids with 95–100% yield (**Scheme 1**). These activated alky ester or amide bromide derivatives were characterized by ^{1}H-NMR and data are provided in **Supplementary Material**.

General Synthetic Procedure for ACM-N$_{alk}$ (4–7)

To a solution of *N*-methylated PEI (**1**) (17.8 mmol) in dry chloroform, 1-bromoalkanes (71.4 mmol) were added and stirred at 120°C for 96 h in a screw-top pressure tube. At the end, the excess solvent was evaporated to reduce the volume of reaction mixture. Finally, the product was precipitated by using excess anhydrous diethyl ether and the residue was washed repeatedly with the same to obtain the cationic macromolecules with 80–85% yield (**Scheme 1**). The final compounds were characterized by ^{1}H-NMR spectroscopy (**Supplementary Material**).

General Synthetic Procedure for ACM-E$_{alk}$ (8–10) and ACM-A$_{alk}$ (11–13)

The synthesized activated esters and amides (**2a-2c** and **3a-3c**) (3 equivalent) were individually reacted with *N*-methylated PEI (**1**) in dry $CHCl_3$ at 55–85°C in a screw-top pressure tube. At the end of 96 h, the reaction mixture was evaporated to reduce the volume. Finally, the product was precipitated by using anhydrous diethyl ether and the residue was washed repeatedly with the same to obtain the cationic macromolecules with 75–80% yield (**Scheme 1**). All the final compounds were characterized by ^{1}H-NMR spectroscopy (**Supplementary Material**).

Antibacterial Activity

Antibacterial assay was performed by our following previously reported protocol (Konai and Haldar, 2017). Three microliter

of the bacterial solution from frozen stock (–80°C) in glycerol was grown for 24 h by incubating at 37°C on NB agar plate and MacConkey agar plate for Gram-positive and Gram-negative bacteria respectively. A single bacterial colony was then allowed to grow in 3 mL nutrient broth medium for 6 h to grow mid-log phase bacteria at 37°C before starting the experiments. The mid-log phase culture was titered to give $\sim 10^8$ CFU/mL by the drop plating method. This culture was then diluted to $\sim 10^5$ CFU/mL in Muller Hinton Broth (MHB) medium. As the compounds (**4–6**, **8–9**, **11–12**) were highly soluble in water and the stock solutions were prepared in Millipore water. Whereas stock solutions of the compounds **7**, **10,** and **13** were prepared in 50% DMSO in water as they were partially water soluble. Then, all compounds were serially diluted by twofold in 96 well plates in Millipore water. After that, 180 μL of diluted bacterial suspension was added to the 96 well plate containing 20 μL of compound solution. The plates were then allowed to incubate for 24 h at 37°C. The OD was recorded at 600 nm using TECAN (Infinite series, M200 pro) plate reader. Each concentration was maintained to have triplicate values and the entire experiment was performed twice. The final minimum inhibitory concentration (MIC) value was determined by visual turbidity.

Antifungal Activity

Following our standard lab protocol (Ghosh et al., 2017) fungal strains were grown on YPD agar plates streaked from frozen stock (–80°C) supplemented with glycerol and incubated for 28°C for 24 h (Ghosh et al., 2014). A single fungal colony was then allowed to grow in 3 mL YPD medium for 10 h at 28°C to grow mid-log phase fungi which was titered and fungal concentration was $\sim 10^8$ CFU/mL. This mid-log phase culture was then diluted to $\sim 10^5$ CFU/mL in RPMI medium. Further procedure was similar to antibacterial assay. The O.D. was recorded after 48 h of incubation at 30°C at 600 nm using TECAN (Infinite series, M200 pro) plate reader. Each concentration of the compound was tested in triplicate and the entire experiment was performed twice. The final minimum inhibitory concentration (MIC) value was determined by visual turbidity.

Hemolytic Activity

According to our published protocol (Ghosh et al., 2014), briefly the macromolecules (**4–13**) were serially diluted in Millipore water in 96-well plates. Fifty microliter of 1 × PBS and 50 μL of 0.1% Triton X-100 solution were taken as negative and positive control respectively. Then human blood was collected from a healthy donor in a 10 mL heparinized tube. Then the freshly collected erythrocytes were centrifuged down and suspended in 1 × PBS (pH = 7.4). Next, 150 μL of this suspension (5 vol%) was added to the plates containing serially diluted macromolecules. These plates were then incubated at 37°C for 1 h. After that, they were centrifuged at 3500 rpm for 5 min, and 100 μL of the supernatant was then transferred to another 96-well plate to measure the absorbance at 540 nm. To calculate the hemolysis percentage, the following formula was used: $(A_{tret} - A_{nontret})/(A_{TX-tret} - A_{nontret}) \times 100$, where A_{tret} is the absorbance of the compound-treated well, $A_{nontret}$ the absorbance of the negative controls (without compound), and $A_{TX-tret}$ the absorbance of the Triton X-100-containing well. Each concentration had triplicate values and the entire experiment was performed twice. The HC_{50} value was determined by taking the average of triplicate O.D. values and error bars represent the standard deviation.

Cytotoxicity

Alamar Blue Assay: Cytotoxicity of the macromolecules ACM-N_{Dec} (**7**) and ACM-A_{Hex} (**12**) was examined against HEK-293 cell line by Alamer Blue assay. Briefly, cells ($\sim 10^4$ cells/well) were seeded onto the wells of a 96-well plate in DMEM media supplemented with 10% fetal bovine serum and 5% penicillin-streptomycin. Then 100 μL of serially diluted compound solution in DMEM media was added to the each well of the plates containing the cells. Same volume of media (untreated cells) and the cells treated with 0.1% (v/v) Triton-X solution was taken as positive and negative control respectively. The plates were then kept for incubation at 37°C for 24 h maintaining 5% CO_2 atmosphere. Afterward, 10 μL of 10× Alamar Blue solution was added to each well followed by 4 h of further incubation at the same condition. Then, the absorbance was recorded at 570 nm wavelength and 600 nm wavelength was used as the reference. The percentage of cell viability was calculated using the following equation: cell viability (%) = $(A_c - A_t)/(A_0 - A_t) \times 100$, where A_c indicates the absorbance for cells treated with compound, A_t is the absorbance for the cells treated with 0.1% (v/v) Triton-X and A_0 is the absorbance of the untreated cells, all at 570 nm. Each concentration had triplicate values and the entire experiment was performed twice. The average of triplicate absorbance values was plotted against concentration followed by fitting with a sigmoidal plot and the standard deviation was represented by error bars. From the curve the values were determined corresponding to 50% cell viability.

Fluorescence microscopy: Briefly, HEK-293 cells were seeded into the wells of 96 well tissue culture plates ($\sim 10^4$ cells/well). Afterward, the cells were treated with ACM-A_{Hex} (**12**) at a concentration of 16 μg/mL. 0.1 vol% of Triton-X and untreated cells were taken as positive and negative control. The cells were then washed with 1× PBS for a single time and the treated and untreated cells were stained with calcein-AM (2 μM) and propidium iodide (4.5 μM) by incubating for 15 min. at 37°C under 5% CO_2 atmosphere. After that, the cells were washed with 1× PBS to remove the excess dye and images were captured by Leica DM2500 microscope at 40× objective. To capture the images, for calcein-AM band pass filter of 500–550 nm wavelength and for propidium iodide long-pass filter of 590–800 nm wavelength was used.

Antibacterial Activity in Physiological Fluids

The antibacterial activity of ACM-A_{Hex} (**12**) against MRSA ATCC33591 was examined after incubating it with 50% plasma and 50% mice liver homogenate. Briefly, the compound was mixed with human blood plasma and mice liver homogenate in 1:1 ratio then incubated for different time interval (3, 6, 12, and 24 h) at 37°C. Then, these mixtures were serially twofold diluted

in 1 × PBS. After that, 180 μL of diluted bacterial suspension was added to the 96 well plate containing serially diluted 20 μL of compound and plasma or liver homogenate mixture solution and incubated at 37°C for 24 h. Next, the MIC was determined similarly like the previous protocol. Each concentration had triplicate values and the experiment was performed twice. The average data was reported.

Bactericidal Kinetics Against Planktonic Bacteria

Time kill kinetics was performed to evaluate the bactericidal nature of the lead molecule ACM-A_{Hex} (**12**) by our standard lab protocol (Barman et al., 2019). The 6 h grown (mid-log phase) bacterial culture was diluted to ∼10^5 CFU/mL in MHB. One hundred and eighty microliter of diluted bacterial suspensions were then incubated with 20 μL of compound solution at different concentration (8, 16, and 32 μg/mL) of the optimized compound at 37°C. Twenty microliter of Millipore water without any compound was used as negative control. Twenty microliter aliquot was taken after different time interval of 0, 1, 2, 4, and 6 h and serially 10-fold diluted in 0.9% saline. From these diluted solutions 20 μL was drop casted on nutrient agar plates and was allowed to incubate for 18 h at 37°C. The viable bacterial colonies were counted and the result plotted as Log CFU/mL vs. time (hours). The experiment was performed twice and the average data was reported. Error bars indicate standard deviation.

Bactericidal Kinetics Against Metabolically Inactive Bacteria

Time kill against stationary phase bacteria was determined according to our standard lab protocol (Konai et al., 2015; Konai and Haldar, 2017). To grow the stationary phase bacteria, 5 μL of mid-log phase planktonic bacteria was inoculated in 5 mL of nutrient broth (BHI for *E. faecium* and VRE) and incubated for 16 h at 37°C. Next, the stationary phase bacteria were diluted in 1 × PBS. One hundred and eighty microliter of diluted bacterial suspensions were then incubated with 20 μL of compound ACM-A_{Hex} (**12**) solution, vancomycin and linezolid at different concentration and allowed to incubate at 37°C for different time intervals. Twenty microliter of Millipore water without any compound was used as negative control. Afterward, similar procedure was performed like planktonic phase and the result was plotted as Log CFU/mL vs. time (hours). The experiment was performed twice and the average data was reported. Error bars indicate standard deviation.

Kinetics of Fungal Killing

Time-kill kinetics against fungi was similar to the bactericidal killing kinetics. Briefly, the 10 h grown mid-log phase culture was diluted to ∼10^5 CFU/mL in RPMI media. Then 180 μL these diluted fungal suspensions were added to the wells of 96 well plates containing 20 μL of the compound ACM-A_{Hex} (**12**) solutions at different concentrations and incubated at 30°C for different time intervals. Similarly, then 20 μL aliquot was taken and serially 10-fold diluted in 0.9% saline. From these diluted solutions 20 μL was drop casted on YPD agar plates and was allowed to incubate for 48 h at 30°C. The viable fungal colonies were counted and the result plotted as Log CFU/mL vs. time (hours). The experiment was performed twice and the average data was reported. Error bars indicate standard deviation.

Anti-biofilm Activity: Biofilm Disruption, Inactivation of Dispersed Cells From Biofilm and Elimination of Metabolically Inactive Cells Within Biofilm

Biofilms were grown on sterile glass coverslips by following our earlier published protocol (Konai and Haldar, 2017). MRSA ATCC33591 and MRSA R3545 were grown in nutrient broth for 6 h to obtain mid-log phase bacteria (∼10^8 CFU/mL). Then they were diluted in nutrient broth, supplemented with 1% glucose and 1% NaCl, to 10^5 CFU/mL. Then 2 mL of this bacterial suspension was added to the each wells of 6 well plate containing 18 mm sterile glass coverslip. The plates were incubated at static condition for 24 h at 37°C. Biofilm containing coverslips were carefully washed with 0.9% saline and transferred to the wells of 2 mL of biofilm media containing compound ACM-A_{Hex} (**12**) at different concentration in a new 6 well plate and incubated at static condition for 24 h at 37°C. Two milliliter of the same medium was used as a untreated control and vancomycin (32 μg/mL) was taken as an antibiotic control. Afterward, these coverslips were carefully washed with 0.9% saline and kept in a new 6 well plate and the anti-biofilm activity of the compound was performed by following methods:

CV staining: For the biofilm biomass quantification, preformed biofilm containing coverslips were carefully washed with 0.9% saline and dried for 10–15 min. After that, they were stained with 2 mL of 0.1% crystal violet solution and incubated for 10 min. These stained biofilms were again washed with 0.9% saline and then cautiously scratched with 2 mL of 95% aqueous ethanol solution and the O.D. was recorded at 522 nm by using plate reader. The experiment was performed twice and the average data was reported. Error bars indicate standard deviation.

Biofilm cell viability: The biofilms were trypsinized using 2 mL of trypsin-EDTA solution in saline (1:4) and incubated for 15 min. Then the coverslips were carefully scratched and the cell suspension was then serially 10-fold diluted in saline and 20 μL of the diluted solutions was spot plated on nutrient agar plate and allowed to incubate for 18 h at 37°C. Finally, viable bacterial colonies were counted. The experiment was performed twice and the average data was reported. Error bars indicate standard deviation.

Dispersed cell viability: To quantify the viability of dispersed bacterial cells, 20 μl of dispersed cell suspension present in the biofilm growing media was serially 10-fold diluted in 0.9% saline and 20 μL of the diluted solutions was spot plated on nutrient agar plate and allowed to incubate for 18 h at 37°C. Afterward the viable bacterial colonies were counted. The experiment was performed twice and the average data was reported. Error bars indicate standard deviation.

Fluorescence Microscopy: The untreated and treated [with ACM-A_{Hex} (**12**) and vancomycin] preformed biofilm containing coverslips were washed in saline and kept in a glass slide. Next the biofilms were stained by adding 5 μL of SYTO-9 (60 μM) and PI (15 μM) mixture. Then the images were captured by Leica DM2500 microscope at 40× objective.

Activity Against Polymicrobial Biofilm

Activity against polymicrobial biofilm (Harriott and Noverr, 2009) was performed against *C. albicans* and MRSA. Briefly, the individual culture of mid-log phase fungi (*C. albicans* AB226) and bacteria (MRSA ATCC33591) was diluted to $\sim 10^6$ CFU/mL and $\sim 10^7$ CFU/mL in BHI media. Then 2 mL of fungal solution and 200 μL of bacterial solution were added to the wells of a 6 well plate containing sterilized glass coverslip and they were incubated at 37°C for 24 h. Afterward, coverslips were washed in saline and treated with the same volume of compound ACM-A_{Hex} (**12**) solution at different concentrations and allowed to incubate at 37°C for 24 h. The biofilms were then trypsinized using 2 mL of trypsin-EDTA solution in saline (1:10) and incubated for 15 min. Next these coverslips were carefully scratched and the cell suspension was then serially 10-fold diluted in saline and 20 μL of the diluted solutions was spot plated on amphotericin B (100 μg/mL) containing nutrient agar plate for MRSA and vancomycin (150 μg/mL) containing YPD agar plates for *C. albicans*. These plates were then incubated for 24 h at 37°C for bacteria and 48 h at 30°C for fungi. The experiment was performed twice and the average data was reported. Error bars indicate the standard deviation.

Membrane Active Mechanism of Action

Briefly, the planktonic and stationary phase bacterial cells of MRSA ATCC33591 ($\sim 10^8$ CFU/mL) and *C. albicans* ($\sim 10^8$ CFU/mL) cells were pelleted down by centrifuging at 3500 rpm for 5 min. The media was discarded and washed with 5 mM HEPES buffer (pH = 7.4) followed by resuspension in 1:1:1 ratio of 5 mM HEPES buffer, 5 mM glucose and 100 mM KCl solution. Next, 2 μM $DiSC_3$ (**5**) (3,3′-Dipropylthiadicarbocyanine iodide) dye was added in the bacterial suspension and was incubated in dark for 30 min. Then 190 μL of this bacterial suspension was then transferred into the wells of black and clear bottom 96-well plate and the fluorescence intensity was recorded. Then, 10 μL of compound ACM-A_{Hex} (**12**) solution (8, 16, and 32 μg/mL) was added and the fluorescence intensity was recorded for 26 min. Same volume of Millipore water without any compound was taken as negative control.

Live Dead Assay Against Bacteria

In brief 1 mL of planktonic bacterial cells (MRSA ATCC33591) was pelleted down by centrifuging at 3500 RPM for 5 min. The media was discarded and the cells were washed with 0.9% saline followed by resuspension in 1 mL saline. Then ACM-A_{Hex} (**12**) was added to this suspension to obtain a final concentration of 16 μg/mL. Then it was allowed to incubate for 2 h at 37°C. Afterward, the solution was centrifuged and the cells were re-suspended in saline followed by the addition of SYTO-9 and PI to obtain a final concentration of 3 and 15 μM respectively. This dye containing solution was incubated in dark for 15 min. The solution was centrifuged and washed with saline to remove the excess dye. Next 5 μL of this solution was subjected to fluorescence microscopy and the images were captured by Leica DM2500 microscope at 100× objective. For SYTO-9 band pass filter of 450–490 nm wavelength and for propidium iodide filter of 515–560 nm wavelength was used.

Live Dead Assay Against Fungi

This experiment was performed similar as Live Dead Assay against Bacteria. In brief 1 mL of fungal cells (*C. albicans* ATCC10231) was pelleted down by centrifuging at 3500 RPM for 5 min. The media was discarded and the cells were washed with 0.9% saline followed by resuspension in 1 mL saline. Then ACM-A_{Hex} (**12**) was added to this suspension to obtain a final concentration of 32 μg/mL. Then it was allowed to incubate for 4 h at 30°C. Afterward, the solution was centrifuged and the cells were re-suspended in saline followed by the addition of SYTO-9 and PI to obtain a final concentration of 3 and 15 μM respectively. This dye containing solution was incubated in dark for 30 min. The solution was centrifuged and washed with saline to remove the excess dye. Next 5 μL of this solution was subjected to fluorescence microscopy and the images were captured by Leica DM2500 microscope at 40× objective. For SYTO-9 band pass filter of 450–490 nm wavelength and for propidium iodide filter of 515–560 nm wavelength was used.

Development of Resistance Propensity

Resistance development study was performed by our previously published protocol (Barman et al., 2019). In brief, the MIC of ACM-A_{Hex} (**12**) and norfloxacin was evaluated by the protocol mentioned for antibacterial assay. In the subsequent days bacterial solution from the sub-MIC concentration was diluted to $\sim 10^5$ CFU/mL and was used for another MIC determination. After 15 days of serial passages the increment in MIC was plotted vs. the number of days. Here each concentration was tested in triplicate and fold of increase in MIC was obtained by dividing first MIC value from MIC value of every subsequent day.

Statistical Analysis

Statistical analysis was performed by using Graph Pad Prism version 8.3.0 software. The reported values were expressed as average ± standard deviation. The $p < 0.05$ was considered to be statistically significant.

RESULTS

Design and Synthesis

The synthesis of amphiphilic cationic macromolecules (ACMs) was carried out through simple three synthetic steps involving post-functionalization strategy as shown in **Scheme 1**. At first *N*-methylated polyethleneimine (NMPEI) (**1**) was synthesized by Eschweiler-Clarke methylation of the precursor branched polyethyleneimine (PEI). This process led to the conversion of all primary and secondary amines moieties of PEI to tertiary amines. One new peak at 2.2 ppm (corresponding to the –N(CH_3)– group) and another broad peak in the region of 2.3–2.5 ppm (correspond to –N(CH_2CH_2)– groups) have appeared in ^{1}H-NMR spectrum of *N*-methyl polyethyleneimine (NMPEI) (**1**). Further, in FT-IR spectrum, peaks at 3280 and 1600 cm^{-1} corresponding to the N–H stretching and bending of parent PEI

respectively was completely disappeared. The appearance of new peaks and disappearance of existing peaks in ^{1}H-NMR and FT-IR spectrum respectively therefore confirmed the full conversion of primary and secondary amines to tertiary amines in NMPEI (**1**) intermediate. Afterward, NMPEI (**1**) was reacted with different normal alkyl bromides (1-Butyl bromide, 1-Hexyl bromide, 1-Octyl bromide and 1-Decyl bromide) at 120°C for 96 h in order to produce first set of amphiphilic cationic macromolecules, ACM-N_{alk} (**4–7**). Herein, alkyl long chains were varied from butyl to decyl in order to establish the effect of hydrophobicity on antimicrobial activity and toxicity.

Next, to find out the effect of ester and amide moiety in the pendant alkyl chain toward their antimicrobial activity and toxicity we also have synthesized another two sets of amphiphilic cationic macromolecules consisting ester moieties, ACM-E_{alk} (**8–10**) and the amide moieties, ACM-A_{alk} (**11–13**). Initially, different alcohols (1-Butanol, 1-Hexanol, and 1-Octanol) and amines (1-Butanamine, 1-Hexanamine and 1-Octanamine) were reacted with bromoacetyl bromide to synthesize the activated esters (**2a–2c**) and activated amides (**3a–3c**). Subsequently, these activated esters and amides were reacted with NMPEI (**1**) to synthesize other sets of cationic amphiphilic macromolecules ACM-E_{alk} (**8–10)** and ACM-A_{alk} (**11–13**). In this case also similar long chain variation from butyl to octyl was executed. All the final compounds were characterized through ^{1}H-NMR and FI-IR spectroscopy. The disappearance of peak in the region of 2.3–2.5 ppm corresponding to –N(CH_2CH_2)– group of the NMPEI confirmed the complete quaternization in all final macromolecules. This result therefore suggested the 100% degree of quaternization (DQ) of all the final macromolecules (**4–13**). The molecular weight (M_n) of the macromolecules was determined through ^{1}H-NMR spectroscopy and was found to be in the range of 3.5–6 kDa (**Supplementary Table S1** and **Supplementary Material**). Most of the amphiphilic cationic macromolecules (**4–6**, **8–9,** and **11–12**) were water soluble (>10 mg/mL) however the macromolecules **7**, **10,** and **13** were partially soluble in water.

Antimicrobial Activity

Initially, antimicrobial activity of the cationic amphiphilic macromolecules, ACMs (**4–13**) was evaluated against ATCC and MTCC strains of Gram-positive bacterium (MRSA), Gram-negative bacterium (*E. coli*) and fungi (*C. albicans*) as depicted in **Table 1**. The antimicrobial activity was performed through broth dilution assay and was expressed in terms of minimum inhibitory concentration (MIC), the minimum concentration of the compounds required for microbial growth inhibition. Mostly all the macromolecules displayed appreciable antimicrobial activity against MRSA (MIC = 2–32 μg/mL), *E. coli* (MIC = 4–128 μg/mL) and *C. albicans* (MIC = 1–32 μg/mL). In case of first set of amphiphilic cationic macromolecules, where normal aliphatic alkyl chains with varying hydrophobicity (ACM-N_{alk}: **4–7**) were introduced into the *N*-methyl PEI backbone in order to investigate the effect of hydrophobicity on antimicrobial activity. The compound consisting of shorter alkyl chain (butyl), ACM-N_{But} (**4**) did not display any antimicrobial activity even at 1024 μg/mL against MRSA, *E. coli* and *C. albicans*. While a moderate activity was observed for the compound consisting hexyl chain with the MIC values of 16 μg/mL against MRSA, 128 μg/mL against *E. coli* and 32 μg/mL against *C. albicans*. Further increment of hydrophobicity by incorporating octyl long chain in case of ACM-N_{Oct} (**6**), did not increase the activity much against MRSA (MIC = 8–16 μg/mL) and *C. albicans* (MIC = 32 μg/mL) whereas increase in activity was observed against *E. coli* (MIC = 32 μg/mL). The macromolecule, ACM-N_{Dec} (**7**) bearing higher hydrophobic decyl chain displayed good activity with the MIC value of 2 μg/mL against MRSA, 4–8 μg/mL against *E. coli* and 1 μg/mL against *C. albicans*.

Next, to investigate the effect of ester and amide moieties on the antimicrobial activity, we synthesized other two sets of macromolecules consisting ester (ACM-E_{alk}: **8–10**) and amide (ACM-A_{alk}: **11–13**) functionalities in the pendant side chain of *N*-methyl PEI. In this case, the variation of alkyl chain hydrophobicity of ester and amide group also resulted the similar observation, i.e., in general, antimicrobial activity improves with increasing hydrophobicity of alkyl chain. The macromolecule ACM-E_{But} (**8**) bearing shorter alkyl chain (butyl ester) exhibited moderate to no activity against MRSA, *E. coli* and *C. albicans*. However, further increment of hydrophobicity by introducing hexyl ester moiety in case of ACM-E_{Hex} (**9**) 16–32-fold improved activity was observed with MIC values of 8–16, 32, and 16 μg/mL against MRSA, *E. coli* and *C. albicans* respectively. Likewise the previous analog, ACM-E_{Oct} (**10**) (consisting octyl ester functionality) showed enhanced antimicrobial activity (MIC = 4 μg/mL for MRSA, 8 μg/mL for *E. coli,* and 4 μg/mL for *C. albicans*) against all the tested pathogens. Moving from ester to amide bearing macromolecules, ACM-A_{But} (**11**) consisting of butyl amide residue displayed better antimicrobial activity against MRSA (MIC = 16–32 μg/mL) and *E. coli* (MIC = 256 μg/mL) compared to its butyl ester bearing analog ACM-E_{But} (**8**) while similar activity was observed against *C. albicans* (MIC > 1024 μg/mL). In the same way, ACM-A_{Hex} (**12**) (consisting higher hydrophobic hexyl amide moiety) displayed improved MIC values of 2–4 μg/mL against MRSA, 8 μg/mL against *E. coli* and 4 μg/mL against *C. albicans* compared to its previous butyl amide analog (ACM-A_{But}). Interestingly, hexyl amide containing macromolecule (ACM-A_{Hex}**: 12**) also displayed better antimicrobial efficacy compared to its same ester analog bearing macromolecule (ACM-E_{Hex}). However, increase of further hydrophobicity in case of octyl amide bearing macromolecule ACM-A_{Oct} (**13**) resulted not much improvement of activity (MIC in the range of 4–16 μg/mL) against the tested pathogens. Herein, the approved antibiotics showed good activity such as vancomycin against MRSA with MIC = 0.5–1 μg/mL, colistin against *E. coli* with MIC = 1 μg/mL and amphotericin B against *C. albicans* with MIC < 0.25 μg/mL.

Hemolytic Activity and Selectivity

Potent antimicrobial activity with minimal toxicity is one of the important criterions for the development of any antimicrobial agents. Initially, toxicity of this class of macromolecules was evaluated against human red blood cells (hRBCs) and was expressed in terms of HC_{50}, the concentration of the compound corresponding to lysis of 50% hRBCs (**Table 1** and **Figure 1A**).

TABLE 1 | Antimicrobial and hemolytic activity of the amphiphilic cationic macromolecules (ACMs).

Compounds	Minimum inhibitory concentration, MIC (μg/mL)			HC_{50} (μg/mL)	Selectivity Index	
	MRSA	*E. coli*	*C. albicans*		HC_{50}/MIC_{MRSA}	$HC_{50}/MIC_{C.\ albicans}$
ACM-N_{But} **(4)**	>1024	>1024	>1024	>2048	–	–
ACM-N_{Hex} **(5)**	16	128	32	>2048	>128	>64
ACM-N_{Oct} **(6)**	8–16	32	32	>2048	>128–256	32
ACM-N_{Dec} **(7)**	2	4–8	1	260	130	260
ACM-E_{But} **(8)**	128	>1024	>1024	>2048	>16	–
ACM-E_{Hex} **(9)**	8–16	32	16	750	47–93	93
ACM-E_{Oct} **(10)**	4	8	4	25	~6	~6
ACM-A_{But} **(11)**	16–32	256	>1024	>2048	>64–128	–
ACM-A_{Hex} **(12)**	2–4	8	4	270	67–135	67
ACM-A_{Oct} **(13)**	4	16	4	45	~10	2.5
Vancomycin	0.5–1	[a]N.D.	N.D.	N.D.	N.D.	N.D.
Colistin	N.D.	1	N.D.	N.D.	N.D.	N.D.
Amphotericin B	N.D.	N.D.	<0.25	N.D.	N.D.	N.D.

[a]*N.D. stands for not determined.*

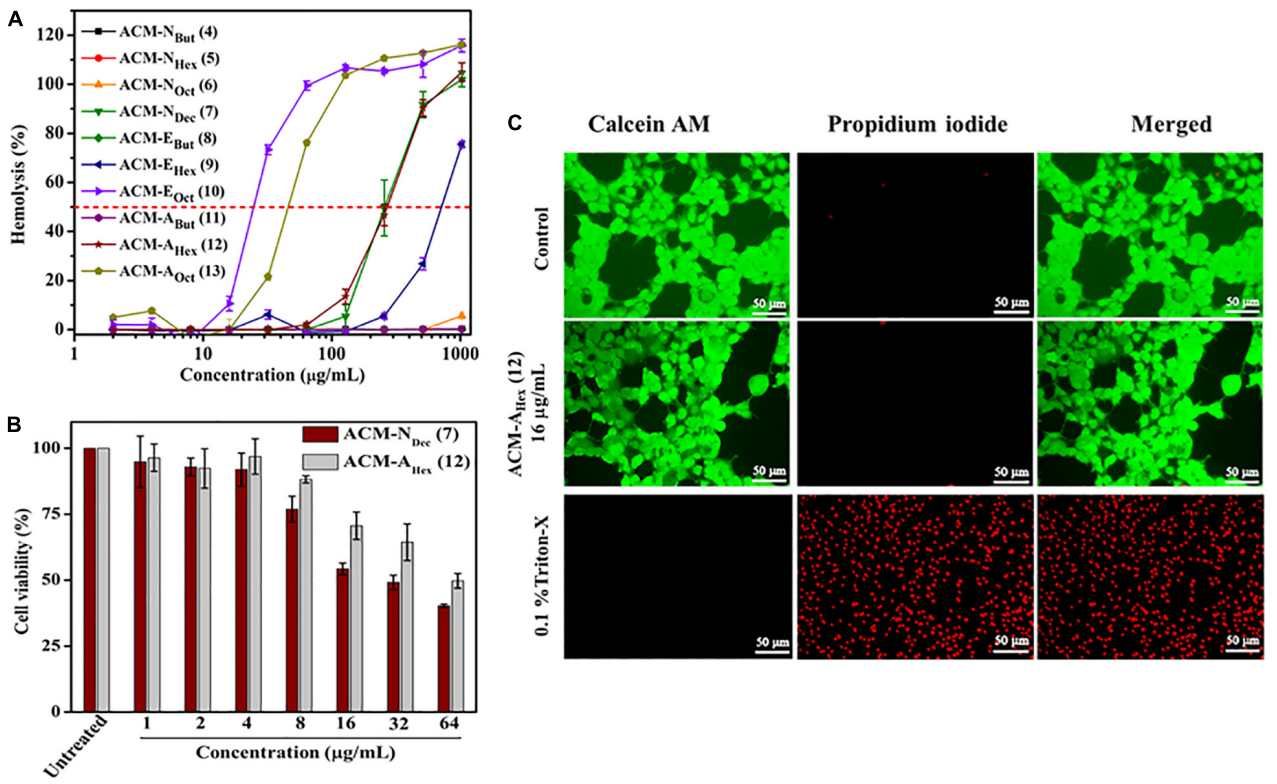

FIGURE 1 | *In vitro* toxicity of amphiphilic cationic macromolecules (ACMs): **(A)** toward human erythrocytes ($p < 0.0001$, two-way ANOVA); **(B)** toward HEK-293 cells ($p = 0.0232$, two-way ANOVA). Here each value represents average of three different experimental values and error bar indicates standard deviation. **(C)** Fluorescence microscopy images of HEK-293 cells upon compound treatment. Scale bar is 50 μm.

This class of macromolecules (ACMs: **4–13**) displayed overall HC_{50} values in the range of 25 to > 2048 μg/mL. In detail, most of the compounds bearing normal aliphatic alkyl moieties ACM-N_{alk} (**4–6**) displayed almost no toxicity (<5% hemolysis) even at the highest tested concentration (2048 μg/mL). Interestingly in this case, enhancement of hydrophobicity (moving from butyl to hexyl and octyl long chain consisting macromolecules) did not display significant impact toward hRBC lysis, although the antimicrobial activity was improved drastically. The compound bearing decyl chain, ACM-N_{Dec} (**7**) did not display any toxicity at 64 μg/mL and showed a minimal hRBC lysis (~5%) at 128 μg/mL. While the HC_{50} value was found to be 260

μg/mL despite exhibiting a broad spectrum antimicrobial activity (MIC) at much lower concentration of 1–8 μg/mL. In case of macromolecules bearing alkyl ester group ACM-E_{But} (**8**), ACM-E_{Hex} (**9**), ACM-E_{Oct} (**10**) displayed HC_{50} values of >2048, 750, and 25 μg/mL respectively. However, only 5% hemolysis was observed at 256 μg/mL for the macromolecule bearing hexyl ester moiety (**9**) which displayed a considerable antimicrobial activity. Simultaneously, the molecule consisted of butyl amide functionality ACM-A_{But} (**11**) exhibited no toxicity toward hRBCs like the butyl ester containing macromolecule. The hexyl (ACM-A_{Hex}; **12**) and octyl (ACM-A_{Oct}; **13**) amide bearing molecules displayed HC_{50} values of 270 and 45 μg/mL respectively. Particularly, ACM-A_{Hex} (**12**) showed very minimal hemolysis (<2%) at 64 μg/mL whereas it exhibited a good antimicrobial activity at much lower concentration in the range of 2–8 μg/mL.

In order to select the lead macromolecules for further investigation of antibacterial and antifungal efficacy in detail, selectivity index (SI) (ratio of HC_{50} and MIC) was calculated considering the MIC values of macromolecules against both MRSA and *C. albicans*. Most of the normal alkyl chain bearing macromolecules (ACM-N_{Alk}: **5–7**) showed moderate to good selectivity index in the range of >128–256 and 32–260 against MRSA and *C. albicans* respectively. ACM-N_{Oct} (**6**) and ACM-N_{Dec} (**7**) displayed appreciable selectivity against MRSA with a selectivity index of >128–256 and 130 respectively. Simultaneously, they also exhibited good selectivity index (SI of ACM-N_{Oct} = 32 and ACM-N_{Dec} = 260) against *C. albicans*. In general ester bearing molecules (**8–10**) showed relatively low selectivity index compared to normal alkyl chain bearing macromolecules. However, hexyl ester containing ACM-E_{Hex} (**9**) revealed relatively moderate selectivity (SI = 47–93) against both MRSA and *C. albicans*. On the contrary, amide bearing macromolecules exhibited better selectivity in comparison to the molecules consisting ester analog. Besides the butyl amide containing macromolecule (ACM-A_{But}: **11,** selectivity index = 64–128), a good selectivity was observed for ACM-A_{Hex} (**12**) bearing hexyl amide with a selectivity index of 67–135 against MRSA and 67 against *C. albicans*. Therefore, based on the selectivity index, we have selected two molecules (ACM-N_{Oct}; **6** and ACM-N_{Dec}; **7**) from ACM-N_{Alk} series, one molecule (ACM-E_{Hex}; **9**) from the ACM-E_{Alk} series and one molecule (ACM-A_{Hex}; **12**) from the ACM-A_{Alk} series for the further studies.

Antimicrobial Activity Against Clinical Isolates of Drug-Resistant Gram-Positive Bacteria and Fungi

Considering the emergence and severity of MRSA, VRSA, VRE, and C. *albicans* associated infections, we therefore investigated the antimicrobial activity against their different clinical isolates for the aforementioned four selective macromolecules ACM-N_{Oct} (**6**), ACM-N_{Dec} (**7**), ACM-E_{Hex} (**9**), and ACM-A_{Hex} (**12**) (**Table 2**). In detail, ACM-N_{Oct} (**6**) and ACM-E_{Hex} (**9**) displayed antimicrobial activity against different clinical isolates of MRSA (MIC = 8–16 μg/mL), VRSA (MIC = 8 μg/mL), VRE (MIC = 16–64 μg/mL) and *C. albicans* (16–64 μg/mL). On the other hand, ACM-N_{Dec} (**7**) and ACM-A_{Hex} (**12**) showed better activity with MIC values of 2–4, 4–8, and 1–8 μg/mL against all the tested clinical isolates of MRSA, VRSA, VRE, and *C. albicans* respectively. In order to compare the efficacy of the macromolecules, methicillin, vancomycin, amphotericin B and fluconazole were included in our studies as a positive control. Overall these result suggested that compound consisting aliphatic decyl long chain ACM-N_{Dec} (**7**) and hexyl amide conjugated macromolecule ACM-A_{Hex} (**12**) have potent efficacy against drug-resistant Gram-positive bacteria and fungi among the four best selective compounds. Hence these two compounds ACM-N_{Dec} (**7**) and ACM-A_{Hex} (**12**) were selected for further detailed investigations.

Cytotoxicity

In order to have a clear idea on the toxicity profile, further cytotoxicity of two best lead macromolecules, ACM-N_{Dec} (**7**) and ACM-A_{Hex} (**12**) were examined against human embryonic kidney (HEK-293) cell line by Alamar blue assay. As a measure of toxicity, EC_{50} (concentration corresponds to 50% cell viability) values of these compounds were determined (**Figure 1B**). The compound with normal decyl long chain, ACM-N_{Dec} (**7**) displayed EC_{50} value of 30 μg/mL. Whereas, hexyl amide bearing macromolecule, ACM-A_{Hex} (**12**) exhibited relatively reduced cytotoxicity toward HEK-293 cells with an EC_{50} value of 60 μg/mL. Therefore, we consider the compound ACM-A_{Hex} (**12**) as the optimized lead molecule among all the amphiphilic cationic macromolecules (ACMs: **4–13**).

The toxicity of the optimum compound, ACM-A_{Hex} (**12**) was further studied through fluorescence microscopy by simultaneous staining of HEK-293 cells with calcein-AM and propidium iodide (PI). It can be clearly visualized from **Figure 1C** that most of the cells were alive even after compound treatment at 16 μg/mL which was 2-8 times higher than its MIC value. No cells can be seen which are labeled with red fluorescence corresponds to dead cells which suggested the minimal toxic nature of this macromolecule toward mammalian cells.

Antibacterial Activity in Physiological Fluids

One of the major limitations of antimicrobial peptides (AMPs) is the loss of antibacterial activity in physiological fluids owing to protease degradation. The compound which sustains its antibacterial potency in such conditions would be highly desirable. Toward this goal, antibacterial activity (MIC) of the lead compound ACM-A_{Hex} (**12**) was evaluated against MRSA ATCC33591 after incubating the compound with 50% human plasma and mice liver homogenate at different time interval (3, 6, 12, and 24 h). Pre-incubation of compound in 50% plasma resulted in slight increase of MIC (two-fold) within 3–24 h time duration (**Supplementary Figure S1** and **Supplementary Material**). When the compound was incubated in 50% liver homogenate no change in MIC was noticed upto 6 h of pre-incubation while only twofold increment of MIC was found after 12–24 h incubation. This result therefore indicated that unlike AMPs this

TABLE 2 | Antimicrobial activity of amphiphilic cationic macromolecules (ACMs) against clinical isolates of drug-resistant Gram-positive bacteria and fungi.

Microbes	Minimum inhibitory concentration, MIC (μg/mL)							
	ACM-N_{Oct} (6)	ACM-N_{Dec} (7)	ACM-E_{Oct} (9)	ACM-A_{Hex} (12)	Methicillin	Vancomycin	Amphotericin B	Fluconazole
MRSA R3545	8	2	8	4	16–32	1	[a]N.D.	N.D.
MRSA 3889	8	2	8	4	16–32	1	N.D.	N.D.
MRSA R3890	16	4	16	4	>32	1	N.D.	N.D.
VRSA 1	8	2	8	4	N.D.	512	N.D.	N.D.
VRSA 4	8	2	8	4	N.D.	512	N.D.	N.D.
VRE903	64	8	16	4	N.D.	> 1024	N.D.	N.D.
VRE909	64	8	16	4	N.D.	512	N.D.	N.D.
C. albicans AB226	32	4	32	8	N.D.	N.D.	0.25	>256
C. albicans AB399	64	4	64	8	N.D.	N.D.	0.25	>256

N.D., stands for not determined.

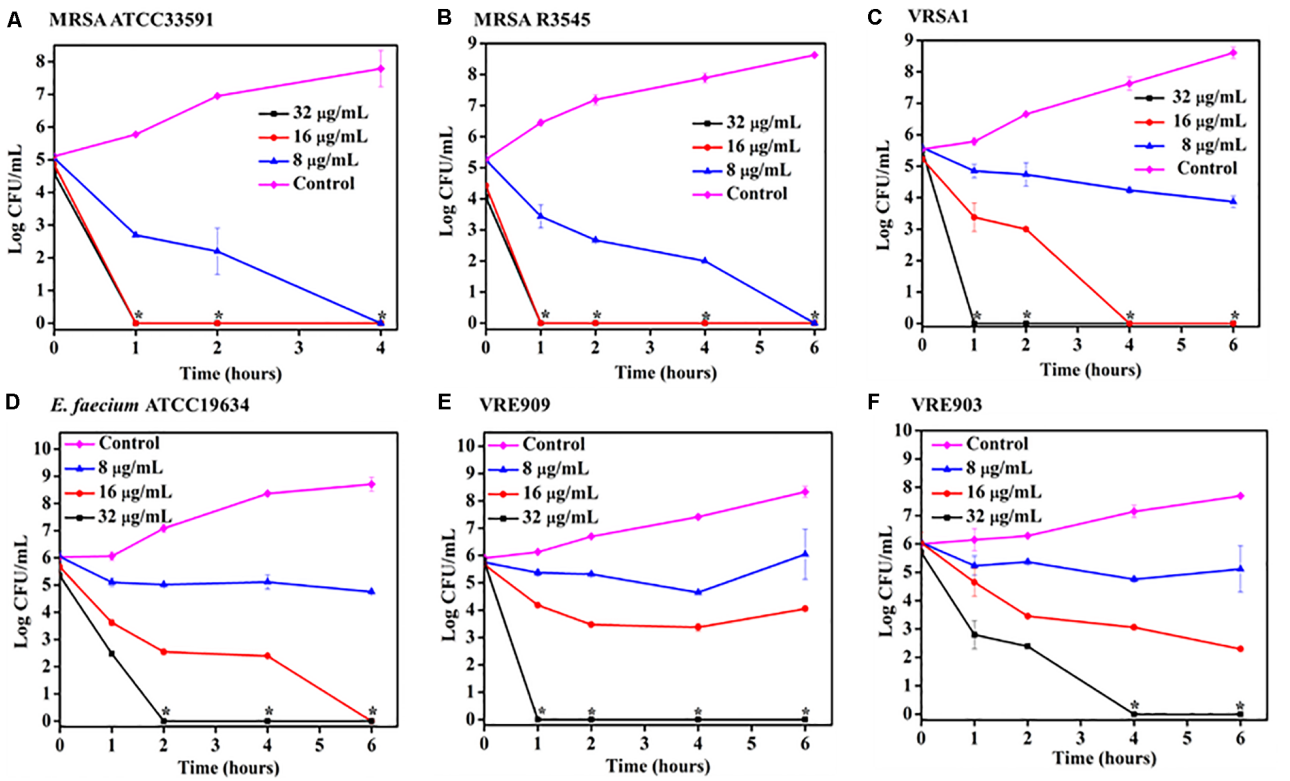

FIGURE 2 | Time kill kinetics of ACM-A_{Hex} **(12)** against planktonic cells **(A)** MRSA ATCC33591; **(B)** MRSA R3545; **(C)** VRSA1; **(D)** *E. faecium* ATCC19634; **(E)** VRE909; **(F)** VRE903. (Asterisks corresponds to <50 CFU/mL). Each point represents average of four different values and error bar indicates standard deviation ($p < 0.0001$, two-way ANOVA).

macromolecule can be used in *in vivo* settings in order to tackle systemic infections.

Bactericidal Kinetics Against Planktonic Bacteria

Time kill kinetics of ACM-A_{Hex} (**12**) was performed against different MRSA, VRSA, and *E. faecium* (both vancomycin susceptible and resistant) strains including the clinical isolates (**Figure 2**). In general, the compound was rapidly bactericidal in nature. The complete killing (>5 Log CFU/mL reduction) of MRSA ATCC33591 was observed within 4 h at 8 μg/mL (2 × MIC) (**Figure 2A**). At the same concentration, more than 5 Log CFU/mL reduction (complete killing) was observed in case of MRSA R3545 clinical isolate within 6 h (**Figure 2B**). However, at 16 (4 × MIC) and 32 μg/mL (8 × MIC), the macromolecule displayed even faster bactericidal kinetics with complete killing of both the MRSA strains within 1 h. In case of, VRSA at 16 μg/mL ACM-A_{Hex} (**12**) was able to kill the bacteria completely (∼5.5 Log CFU/mL reduction) within 4 h (**Figure 2C**). A complete

killing was observed within 1 h at a higher concentration of 32 μg/mL. At 32 μg/mL *E. faecium* was completely killed within 2 h (**Figure 2D**). Simultaneously, the compound was able to kill both VRE909 and VRE903 within 1 and 4 h at 32 μg/mL respectively (**Figures 2E,F**). Overall, these results demonstrated rapidly bactericidal nature of the lead macromolecule against multi-drug resistant Gram-positive bacteria.

Bactericidal Kinetics Against Metabolically Inactive Bacteria

The emergence of metabolically inactive or dormant bacteria has created a huge complicacy in clinical settings. One such metabolically inactive species is stationary phase bacteria which slow down all biological processes. Therefore, conventional antibiotics which target various cellular processes (such as cell wall biosynthesis, protein synthesis, DNA replication etc.) become ineffective to kill such stationary cells. On the other hand, persister, another type of metabolically inactive species is a sub-population of planktonic bacteria survivors after antibiotic treatment. Hence, the situation demands an urgent development of antibacterial agents effective to kill such dormant bacteria. Toward this aim, we inspected the efficacy of our lead compound, ACM-A_{Hex} (**12**) against stationary phase MRSA, *E. faecium*, VRE, and *S. aureus* persister by performing bactericidal killing kinetics. The efficacy of the lead compound was compared with vancomycin and linezolid, last resort of Gram-positive antibiotics (**Figure 3**). Vancomycin even at very high concentration 64 μg/mL (64 × MIC) was completely ineffective to kill stationary and persister cells of MRSA and *S. aureus* respectively whereas it was highly active against their planktonic cells. On the contrary, ACM-A_{Hex} (**12**) at 16 μg/mL (4 × MIC) fully eradicated (∼6 Log reduction) stationary phase cells of MRSA ATCC33591 and MRSA R3545 within 1–2 h (**Figures 3A,B**). This also eliminated difficult-to-kill persister cells of *S. aureus* within 2 h at 16 μg/mL (4 × MIC) (**Figure 3C**). Similarly, stationary phase *E. faecium* ATCC19634 and VRE909 was also killed entirely at 16 μg/mL (4 × MIC) concentration of the compound (**Figures 3A,B**). In case of VRE909 stationary cells, linezolid was inefficient even at 64 μg/mL. Taken together, these results suggested that the macromolecule is highly efficient to tackle stationary as well as persister phase bacteria.

Time-Kill Kinetics Against Fungi

To evaluate the fungicidal nature of the lead compound, ACM-A_{Hex} (**12**) time-kill kinetics was performed against *C. albicans*. Likewise the rapid bactericidal nature, it also exhibited a rapid fungicidal nature. ACM-A_{Hex} (**12**) was able to kill (∼5 Log reduction) fungi completely at 32 μg/mL (8 × MIC) within 1 h against both the strains of *C. albicans* (ATCC10231 and AB226) (**Figures 4A,B**). In contrast, amphotericin B did not display any reduction of fungal cell viability at 2.5 μg/mL which was 10 times higher than its MIC. This result therefore demonstrated that the lead molecule may be a promising candidate to tackle both bacterial and fungal infections.

Anti-biofilm Activity: Biofilm Disruption, Inactivation of Dispersed Cells From Biofilm and Elimination of Metabolically Inactive Cells Within Biofilm

Bacterial biofilm formation is one of the emerging issues in clinical settings which mostly accounts for complicated and chronic infections. Biofilm is a multicellular microbial assembly composed of self-produced extracellular matrix with diffusion barriers for antimicrobial agents and predominance of metabolically inactive or dormant bacterial cells. In addition to this, dispersed cells originated upon the mature biofilm dispersal were found to be distinct in nature in comparison to the planktonic and biofilm embedded bacterial cells. Such dispersed cells are highly virulent compared to the planktonic cells (Chua et al., 2014). Due to the, aforesaid facts, biofilm associated infections are almost untreatable by conventional antibiotics. Hence, this scenario necessitates the development of anti-bacterial agents with potent anti-biofilm efficacy. Therefore, we evaluated anti-biofilm properties of the optimized macromolecule ACM-A_{Hex} (**12**) against MRSA including clinical isolates through crystal violet straining as well as by counting bacterial cell viability within the biofilm and in dispersed cells (**Figure 5**). The compound was found to eradicate ∼80% of biofilm biomass at 32 μg/mL for both the preformed the biofilm of MRSA ATCC33591 and MRSA R3545 strains. On the contrary, vancomycin displayed hardly any biofilm biomass reduction at the same concentration (**Figures 5A,B**).

Furthermore, this macromolecule was highly efficient to kill the bacteria embedded within the biofilm matrix. It displayed 2.5 Log and 3 Log reduction of bacterial burden of MRSA R3545 and MRSA ATCC33591 respectively within the biofilm (**Figure 5C**). More importantly, the compound was also able to eliminate virulent dispersed cells of MRSA ATCC33591 (∼3 Log reduction) while vancomycin was almost incompetent to kill them (**Figure 5D**).

Next the extent of biofilm disruption was visualized by fluorescence microscopy studies with simultaneous staining of SYTO-9 (green fluorescence) and PI (red fluorescence) (**Figure 5E**). In the untreated and the vancomycin (32 μg/mL) treated cases the biofilm showed green fluorescence, displaying the presence of live bacterial cells. In contrast, for compound treated case, a strong red fluorescence was observed, indicating the presence of dead bacterial cell associated with biofilm matrix. Collectively, these results demonstrated that the lead compound showed significant promises to be developed as future anti-biofilm therapeutics.

Activity Against Polymicrobial Biofilm

Dual existence of MRSA and *C. albicans* give rise to the formation of polymicrobial biofilms which is not fully curable even with multiple antibiotics treatment. Thus, antimicrobial agent with efficiency to tackle such multispecies infections is of high demand. Dual efficacy of our lead macromolecule ACM-A_{Hex} (**12**) against both bacteria and fungi therefore motivated us to evaluate its efficacy against polymicrobial biofilms. Upon the treatment with this compound, we could observe a significant

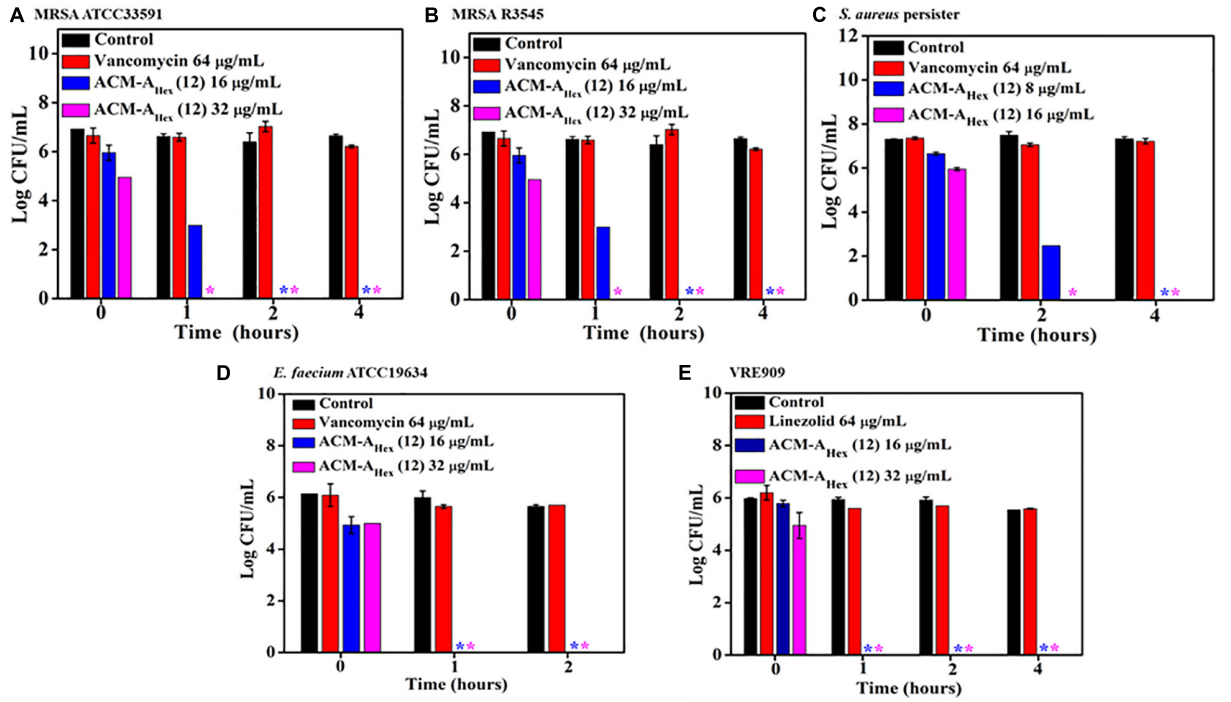

FIGURE 3 | Time kill kinetics of ACM-A$_{Hex}$ (**12**) against **(A)** stationary phase MRSA ATCC33591; **(B)** stationary phase MRSA R3545; **(C)** persisters of *S. aureus* MTCC737; **(D)** stationary phase *E. faecium* ATCC19634; **(E)** stationary phase VRE909. (Asterisks corresponds to <50 CFU/mL). Each value represents average of four different values and error bar indicates standard deviation ($p < 0.0001$, two-way ANOVA).

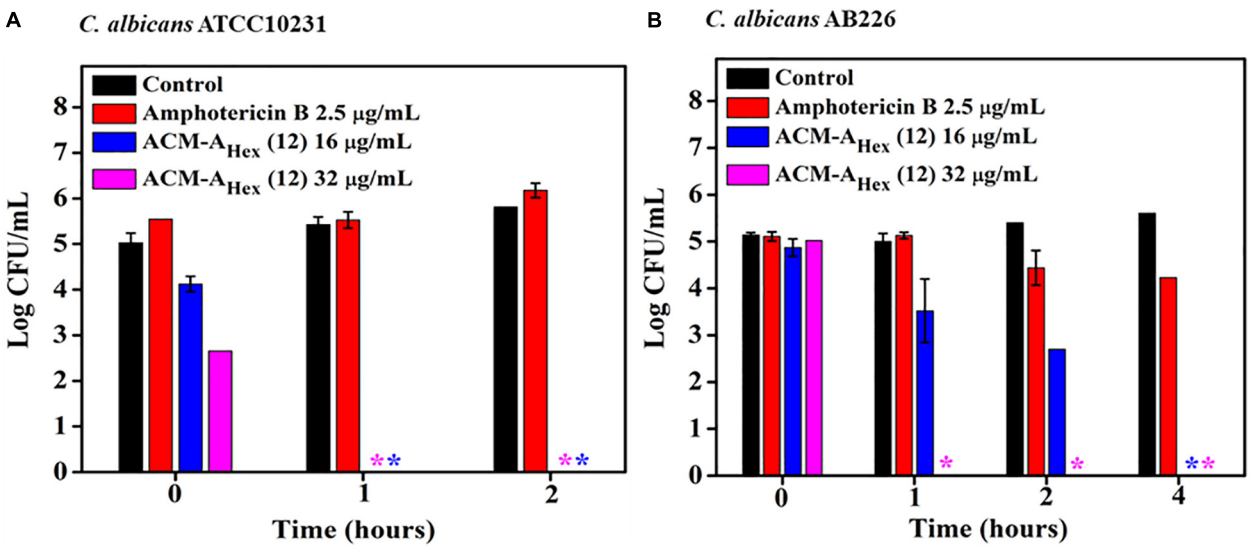

FIGURE 4 | Time kill kinetics of ACM-A$_{Hex}$ (**12**) against **(A)** *C. albicans* ATCC10231 and **(B)** *C. albicans* AB226. (Asterisks corresponds to <50 CFU/mL). Each point represents average of four different values and error bar indicates standard deviation ($p < 0.0001$, two-way ANOVA).

reduction of both fungal and bacterial burden (**Figure 6**). In case of fungi, around 2.5 log reduction was found at 64 μg/mL of the compound whereas amphotericin B displayed comparatively less reduction (2 log) even at its high therapeutic concentration (>16 × MIC). On the other hand, the compound displayed 2 log reduction of MRSA at 32 μg/mL and completely killed MRSA (∼8 log reduction) at 64 μg/mL. Whereas vancomycin was totally inefficient even at 32 μg/mL. None of the antibiotics used in this study were able to kill simultaneously both the organisms. Interestingly, our lead molecule ACM-A$_{Hex}$ (**12**)

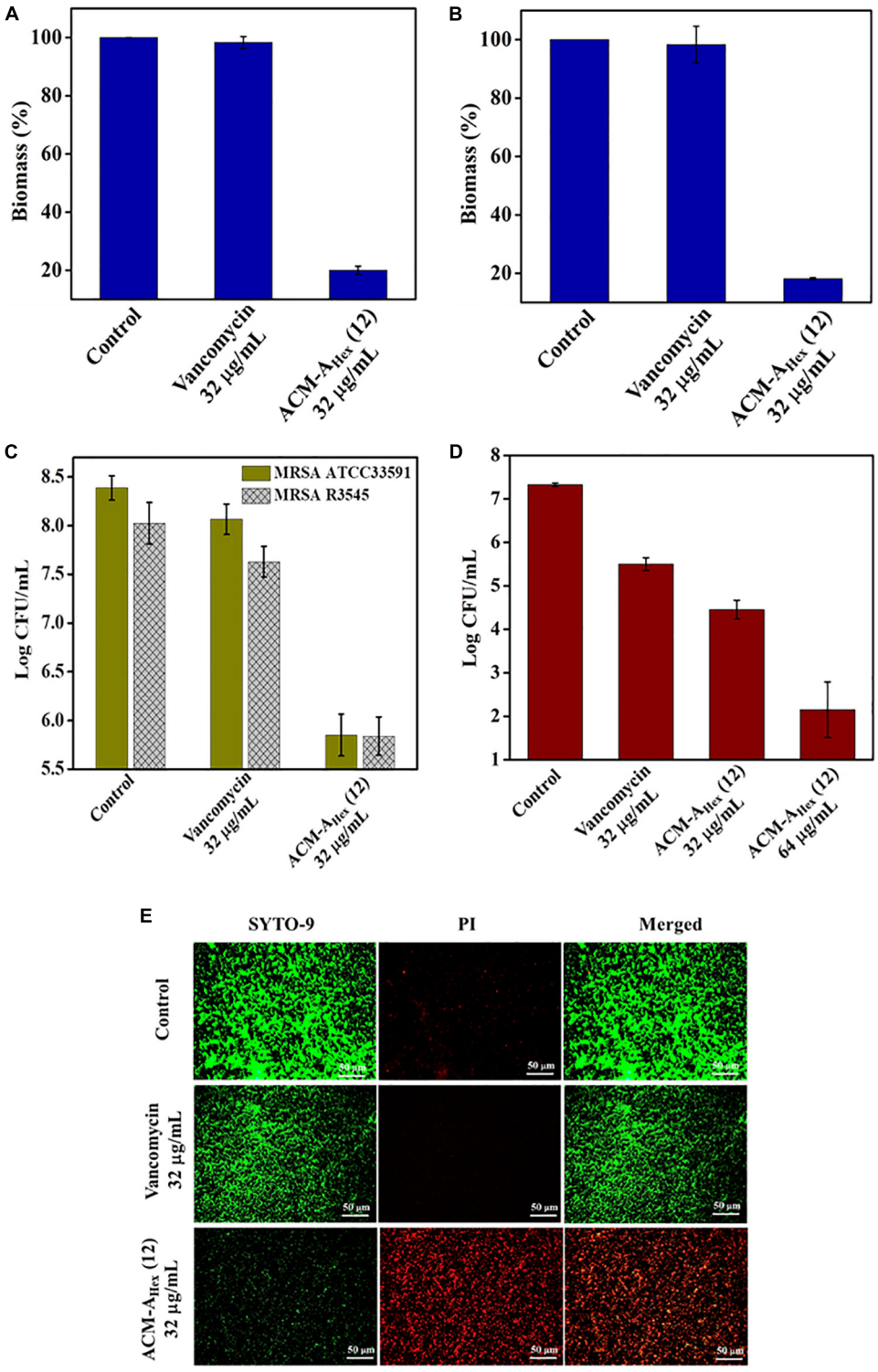

FIGURE 5 | Anti-biofilm activity of ACM-A$_{Hex}$ (**12**). Quantification of biofilm biomass after crystal violet straining for **(A)** MRSA ATCC33591 ($p = 0.0046$, one-way ANOVA) and **(B)** MRSA R3545 ($p = 0.0007$, one-way ANOVA). Quantification of bacterial cells after treatment for **(C)** MRSA ATCC33591 ($p = 0.014$, one-way ANOVA) and MRSA R3545 ($p = 0.0198$, one way ANOVA). **(D)** Activity against dispersed cells originated from MRSA ATCC33591 biofilm ($p = 0.0114$, one-way ANOVA). Herein, each value represents average of three different experimental values and error bar indicates standard deviation. **(E)** Fluorescence microscopy images of MRSA ATCC33591 biofilm by SYTO-9 and PI staining. Scale bar is 50 μm.

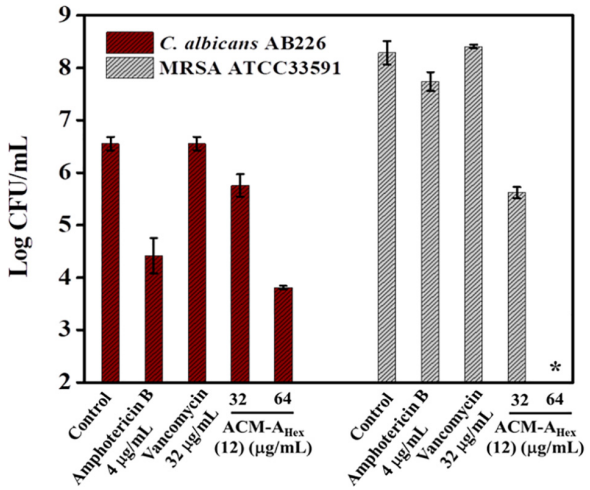

FIGURE 6 | Quantification of microbial cells embedded within Polymicrobial biofilm of *C. albicans* AB226 and MRSA ATCC33591. (Asterisks corresponds to <50 CFU/mL). Each value represents average of two different experimental values and error bar indicates standard deviation ($p < 0.0001$, two-way ANOVA).

successfully brought down the microbial burden associated with both *C. albicans* and MRSA. This result demonstrated the unique properties of this class of macromolecule.

Membrane Active Mechanism of Action

As a preliminary mechanism of action, membrane depolarizing ability of the lead molecule was investigated against both bacteria (MRSA) and fungi (*C. albicans*) (**Figure 7**). In addition to the MRSA planktonic cells, membrane activity of the compound was also studied against metabolically inactive stationary phase cells. This study was performed using membrane-potential sensitive dye 3,3′-dipropylthiadicarbocyanine iodide [$DiSC_3$ (**5**)]. This dye distributes both inside and outside microbial cell under normal potential across the membrane. Thus, the fluorescence intensity decreases owing to its self-quenching inside the microbial cells. Membrane active agent which can perturb the membrane potential leads to the release of such dye from interior to the exterior part of bacterial cells. This results in the enhancement of the fluorescence intensity gradually with time. Herein, addition of various concentrations of the lead compound ACM-A_{Hex} (**12**) (8, 16, and 32 μg/mL) resulted an increment in fluorescence intensity of $DiSC_3$ (**5**) for bacteria (both planktonic and stationary phase cells) (**Figures 7A,B**) as well as for fungi (**Figures 7C,D**). The extent of fluorescence enhancement followed a concentration dependency (greater effect at higher concentration of the compound). These results establish that the macromolecule primarily target the microbial membrane for killing through perturbing the membrane polarization.

Live/Dead Assay Against Bacteria and Fungi

In order to visualize the extent of bacterial and fungal killing qualitatively, we performed fluorescence microscopy using SYTO-9 and PI. These results exhibited the presence of dead microbial cells corresponding to red fluorescence upon treatment with lead compound ACM-A_{Hex} (**12**) at 16 and 32 μg/mL against bacteria and fungi respectively (**Figures 7E,F**). In case of the untreated control bright green fluorescence was observed indicating almost all the cells were alive.

Development of Resistance Propensity

Resistance development in bacteria against the conventional antibiotics has become a serious concern worldwide. Hence, antibacterial agent with sustained activity is highly desirable in clinical settings. Toward this goal, propensity of resistance development in bacteria (MRSA ATCC33591) was studied against the lead compound, ACM-A_{Hex} (**12**) with respect to norfloxacin for 15 days. It was observed that bacteria could not develop any detectable resistance against the compound after continuous exposure for 15 days whereas the known antibiotic to treat MRSA infection norfloxacin displayed a 32-fold increment in MIC from 1 μg/mL after 8 days (**Figure 8**). After 15 days of serial passages bacteria developed a high level of resistance against norfloxacin with 128-fold increase in MIC. This result suggested that the compound is suitable for prolonged use in clinical settings.

DISCUSSION

Pathogenesis caused by drug-resistant Gram-positive bacteria such as MRSA, VRSA and VRE and their biofilm forming capability have created an alarming situation in the current scenario (Cantas et al., 2013; Brown and Wright, 2016; Cheng et al., 2016). Alongside, fungal infections majorly caused by *C. albicans* are also prevalent in terms of their severity to cause huge mortality and morbidity. In addition to these, polymicrobial infections owing to the co-existence of MRSA and *C. albicans* are another major threat in the face of global public health (Harriott and Noverr, 2009, 2011; Lohse et al., 2018). The situation has further been deteriorated by the evolutionary pressure of microbial resistance to the last resort antibiotics and anti-fungal drugs.

In this direction, numerous AMP mimicking membrane active agents has been developed by various groups all over the world. Most of the cases, the potency of such membrane active molecules was investigated against a broad spectra of pathogenic bacteria (Dhanda et al., 2019; Ghosh et al., 2019; Gupta V. K. et al., 2019). Antifungal efficacy was documented for very few amphiphilic polymers such as poly β-lactam and peptidopolysaccharides (Li et al., 2012; Liu et al., 2015). However, antimicrobial agent with dual efficacy to combat polymicrobial infections caused by MRSA and *C. albicans* has rarely been reported (Gupta S. et al., 2019). In this regard, we have designed a new class of amphiphilic cationic macromolecules (ACMs) based on branched polyethyleneimine (PEI) through a simple two-step post-functionalization strategy. In the molecular design, small molecular weight PEI (∼600 Da) has been used in order to obtain a less cytotoxic antimicrobial agent. Another rationale behind choosing such backbone with

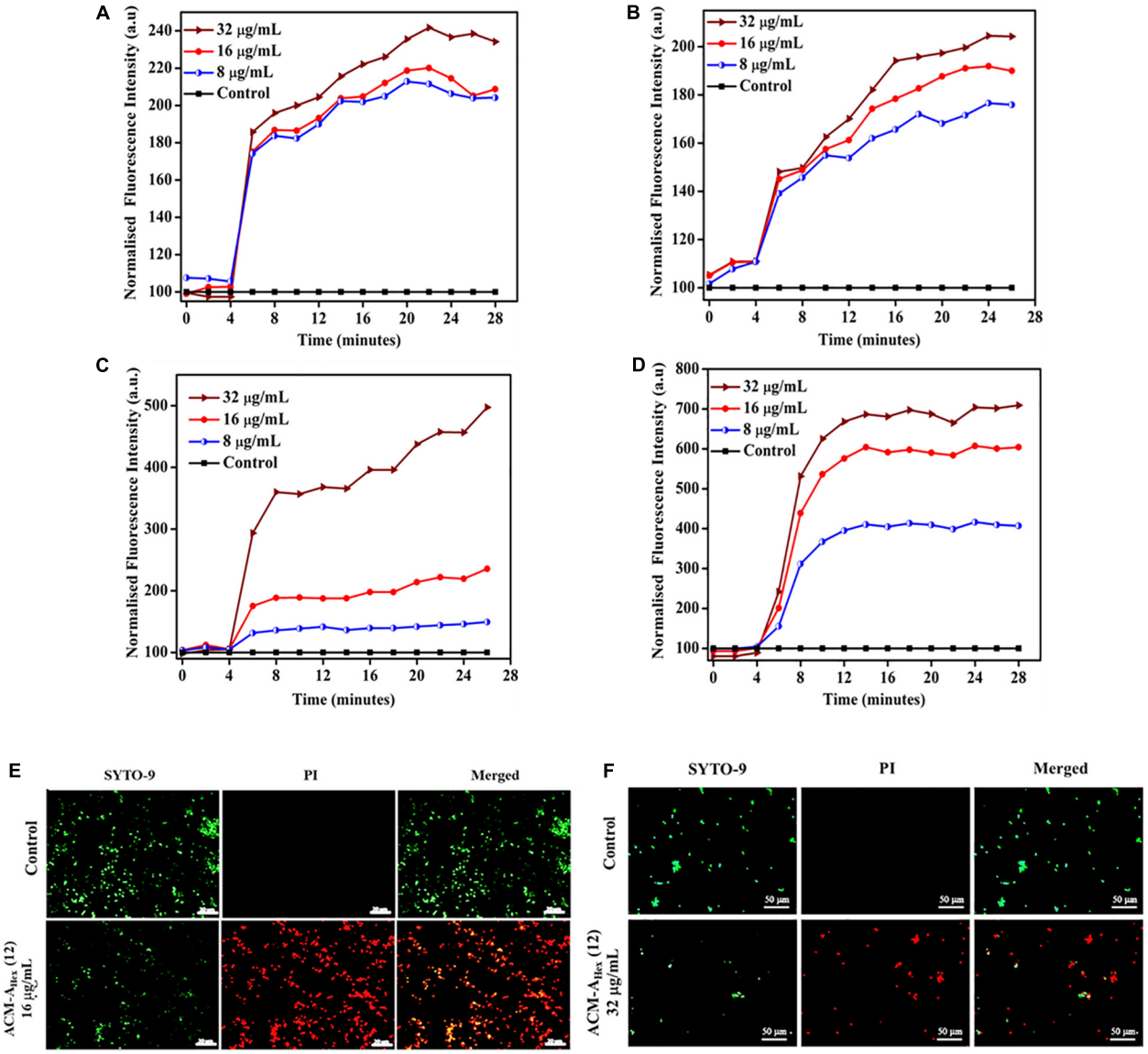

FIGURE 7 | Membrane active mechanism of action by ACM-A_{Hex} (**12**)**:** membrane depolarization against **(A)** growing planktonic MRSA ATCC33591; **(B)** stationary phase MRSA ATCC33591; Membrane depolarization against **(C)** *C. albicans* ATCC10231 and **(D)** *C. albicans* AB226. **(E)** Life-Dead assay against MRSA ATCC33591. Scale bar is 20 μm. **(F)** Life-Dead assay against *C. albicans* ATCC10231. Scale bar is 50 μm.

small molecular weight was to achieve final macromolecules (3.5–6 kDa) with molecular weight less than 50 kDa, a maximum threshold for renal clearance.

An optimum amphiphilic balance (hydrophobicity/hydrophilicity) is a crucial parameter for an antimicrobial agent with superior selectivity toward microbes over mammalian cells. In order to do that, various normal alkyl, alkyl esters, and alkyl amides functionalities has been incorporated in the molecular design. A thorough structure-activity relationship (SAR) was accomplished which suggested an increase of antibacterial activity with increasing hydrophobicity. In case of macromolecules bearing normal alkyl chain, moving from shorter hydrophobic butyl (ACM-N_{But}; **4**) to hexyl (ACM-N_{Hex}; **5**) to octyl (ACM-N_{Oct}; **6**) chain antimicrobial activity was found to be increased gradually. Interestingly, the increment of hydrophobicity did not result any increment in the hemolytic activity (HC_{50}) for these macromolecules. Although, the molecule consisting decyl chain, ACM-N_{Dec} (**7**) was moderately toxic toward hRBCs despite displaying a broad spectrum antimicrobial activity. In case of macromolecule bearing alkyl ester (ACM-E_{Alk}; **8–10**) and amide (ACM-A_{Alk}; **11–13**) functionalities, we also observed a similar trend of increasing antimicrobial activity and toxicity with increasing hydrophobicity. However, macromolecule with alkyl amide analogs showed improved activity-toxicity profile in comparison to the molecules with same alkyl ester moiety. This observation

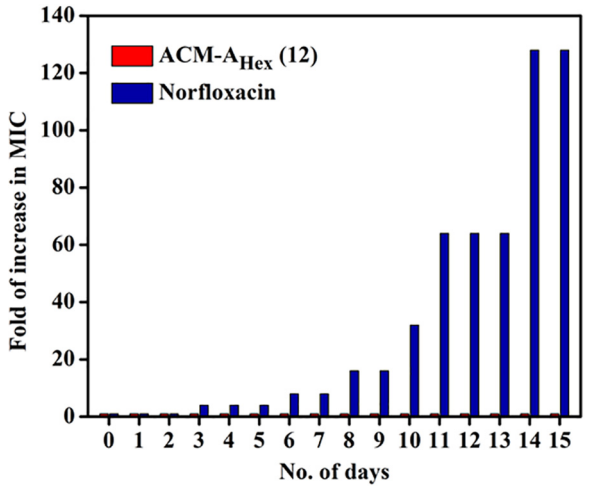

FIGURE 8 | Propensity of resistance development of MRSA ATCC33591 against ACM-A_{Hex} (**12**) and Norfloxacin. In each passage, MIC was performed in triplicate and reproducible experimental results were obtained (p = 0.0147, Student's t-test with Welch's correction).

is possibly due to the additional hydrogen bonding interaction with the microbial membrane lipids which is originated from the amide functionality present in the macromolecular pendant chain (Uppu et al., 2016).

Afterward, suitability for wide range of application of this class of macromolecules motivated us to find out their therapeutic indices (SI = HC_{50}/MIC) against pathogenic microbes over mammalian cells. Herein, antimicrobial activity of ACM-N_{Oct} (**6**), ACM-N_{Dec} (**7**), ACM-E_{Hex} (**9**) and ACM-A_{Hex} (**12**) can be considered as a good reflection of potentiality against MRSA and *C. albicans* in comparison to their toxic effect toward mammalian cells. Thus, a high therapeutic index was observed for these four compounds.

In a recent report, the world health organization (WHO) identified MRSA, VRSA, and VRE as a top high priority pathogen considering their severity to cause difficult-to-treat infections. Furthermore, drug-resistant *C. albicans* are also responsible for complicated invasive infections. Hence, drug-resistant clinical isolates of both Gram-positive bacteria and fungi were challenged with the aforementioned four best selective compounds. In this context, molecule consisting aliphatic decyl long chain ACM-N_{Dec} (**7**) and hexyl amide conjugated macromolecule ACM-A_{Hex} (**12**) displayed superior activity. In following studies, we found that hexyl amide bearing molecule, ACM-A_{Hex} exhibited relatively better cell viability of HEK-293 cells compared to the molecule devoid of amide functionality (ACM-N_{Dec}). This result indicated that the incorporation of amide moieties in the macromolecular design increased the biocompatibility further. Hence, ACM-A_{Hex} was selected as the optimized lead molecule for further studies in detail.

The molecular structure of the lead compound revealed the presence of amide linkages which connects the *N*-methylated PEI backbone with the pendant alkyl chain. Thereby, we assumed that this molecule may not retain its activity due to non-specific interactions with the proteins and degradation by amidases present in complex physiological fluids such as human plasma and mice liver homogenate. Interestingly, pre-incubation for shorter time period with these complex fluids resulted almost no change in MIC. We believe that retention of MIC may be due to the presence of non-peptidic amide linkage in the molecular architecture, possibly not recognizable by the proteases present in the aforementioned fluids. Even pre-incubation for longer time period (24 h) exhibited marginally twofold increase of MIC. This may be resulted due to non-specific interactions with the various complex components (proteins, enzymes etc.) present in the physiological fluids.

It was also found that, the compound was rapidly bactericidal and fungicidal in nature at different therapeutic concentrations. This rapid killing indicated that the molecule possibly has membrane targeting mode of action. Noticeably, most challenging stationary cells (MRSA and VRE) and persister cells (*S. aureus*) were completely eliminated very fast by this compound at similar concentrations. The compound exhibited potent activity against both planktonic cells and metabolically inactive (stationary cells) and antibiotic tolerant cells (persister) due to the membrane active mode of actions caused by non-specific interactions of cationic lipophilic macromolecules with negatively charged bacterial cell envelope.

Additionally, this class of compound was also able to eradicate preformed rigid biofilm of MRSA. This indicated that the compound has enough membrane active nature so that it disrupts the extracellular matrix of biofilm which contains various negatively charged polysaccharides, lipids, nucleic acid components, peptides etc. It is well established that biofilm consists of different metabolically inactive bacterial population. As the compound can kill metabolically inactive bacteria therefore along with biofilm disruption, it was efficient enough to kill different bacterial population embedded within the biofilm. It was interesting to observe that this class of macromolecule not only kill planktonic and metabolically inactive cells embedded within biofilm but also killed dispersed cells originated from biofilm. Whereas, vancomycin could only inactivate planktonic bacteria and was incompetent in killing dispersed cells and bacteria within biofilm.

Over the emergence of individual Gram-positive bacterial and fungal burden, co-existence of MRSA and *C. albicans* is prevalent in majority of nosocomial infections associated with *C. albicans* (Harriott and Noverr, 2009, 2011; Lohse et al., 2018) This co-existence resulted the formation of polymicrobial biofilms for which treatment options are limited. A broad spectrum antimicrobial activity of the lead compound against a wide range of Gram-positive bacteria and fungi motivated us to evaluate its efficacy to eradicate such polymicrobial biofilm. The compound indeed exhibited a significant reduction of both MRSA and *C. albicans* embedded in the polymicrobial biofilm. Needless to mention that efficacy against multi-species biofilm is a significant contribution in the field.

The studies to investigate the membrane active modes of action revealed that our compound perturbed the membrane potential of both bacteria and fungi. PI straining of bacterial cells in presence of our compound further proved its membrane

permeablizing ability. It was also able to permeablize the fungal cells, proved by substantial PI staining upon compound treatment. More importantly, bacteria did not develop any detectable resistance against these class amphiphilic cationic molecules possibly due to non-specific membrane active mode of action. Whereas, bacteria developed a high level of resistance toward known antibiotic norfloxacin within 2 weeks.

CONCLUSION

In conclusion, we have developed a new class of water soluble polyetheleneimine based ACMs by involving minimal simple synthetic steps through post-functionalization strategy. In general, this new class of macromolecules displayed selective antimicrobial activity against both drug-resistant Gram-positive bacteria and fungi over the mammalian cells. The lead macromolecule (ACM-A_{Hex}: **12**) displayed a broad spectrum antimicrobial activity while exhibiting no hemolysis at the active concentration. Noticeably, unlike the AMPs, it retained the antibacterial activity even after incubation with complex physiological fluids. Particularly, it was capable of killing most challenging metabolically inactive stationary phase cells and persisters of MRSA. It also demonstrated the ability to eradicate preformed rigid biofilms of MRSA along with their dispersed cells. In addition to these, one of the important highlights of this molecule is its potential to eliminate polymicrobial biofilms formed by a mixed population of *C. albicans* and MRSA. Interestingly, bacteria were not able to develop resistance against the lead molecule possibly due to its membrane targeting mode of action. As per the best of our knowledge, dual efficacy of this class of compound to tackle bacteria and fungi, proficiency to kill metabolically inactive bacteria, disruption of single and multi-species biofilm and elimination of distinct dispersed bacterial cell is a significant contribution in the field of antimicrobial research. Altogether, the overall results suggested that this class of membrane targeting macromolecules bears an immense potential to be developed as a promising future therapeutic to tackle infections associated with the co-existence of bacteria and fungi.

DATA AVAILABILITY STATEMENT

All datasets generated for this study are included in the article/**Supplementary Material**.

ETHICS STATEMENT

All the animal studies were performed in agreement with the Guidelines for Care and Use of Laboratory Animals of Jawaharlal Neheru Center for Advanced Scientific Research (JNCASR) and permitted by the Animal Ethics Committee of JNCASR.

AUTHOR CONTRIBUTIONS

SM and JH designed the project. SM, SB, and RM performed the experiments and analyzed the data. SM, SB, and JH wrote the manuscript.

ACKNOWLEDGMENTS

We acknowledge Prof. C. N. R. Rao for being the constant source of inspiration. JH acknowledges Sheikh Saqr Career Award Fellowship. SM acknowledges JNCASR for research fellowship. SB acknowledges CSIR for fellowship. RM thanks DBT-RA program for postdoctoral fellowship.

SUPPLEMENTARY MATERIAL

The Supplementary Material for this article can be found online at: https://www.frontiersin.org/articles/10.3389/fbioe.2020.00055/full#supplementary-material

REFERENCES

Barman, S., Konai, M. M., Samaddar, S., and Haldar, J. (2019). Amino acid conjugated polymers: antibacterial agents effective against drug-resistant *Acinetobacter baumannii* with no detectable resistance. *ACS Appl. Mater. Interfaces* 11, 33559–33572. doi: 10.1021/acsami.9b09016

Brown, E. D., and Wright, G. D. (2016). Antibacterial drug discovery in the resistance era. *Nature* 529, 336–343. doi: 10.1038/nature17042

Brown, G. D., Denning, D. W., Gow, N. A., Levitz, S. M., Netea, M. G., and White, T. C. (2012). Hidden killers: human fungal infections. *Sci. Transl. Med.* 4:165rv113. doi: 10.1126/scitranslmed.3004404

Bush, K., Courvalin, P., Dantas, G., Davies, J., Eisenstein, B., Huovinen, P., et al. (2011). Tackling antibiotic resistance. *Nat. Rev. Microbiol.* 9, 894–896. doi: 10.1038/nrmicro2693

Campoccia, D., Montanaro, L., and Arciola, C. R. (2013). A review of the clinical implications of anti-infective biomaterials and infection-resistant surfaces. *Biomaterials* 34, 8018–8029. doi: 10.1016/j.biomaterials.2013.07.048

Cantas, L., Shah, S. Q., Cavaco, L. M., Manaia, C. M., Walsh, F., Popowska, M., et al. (2013). A brief multi-disciplinary review on antimicrobial resistance in medicine and its linkage to the global environmental microbiota. *Front. Microbiol.* 4:96. doi: 10.3389/fmicb.2013.00096

Cheng, G., Dai, M., Ahmed, S., Hao, H., Wang, X., and Yuan, Z. (2016). Antimicrobial drugs in fighting against antimicrobial resistance. *Front. Microbiol.* 7:470. doi: 10.3389/fmicb.2016.00470

Chin, W., Zhong, G., Pu, Q., Yang, C., Lou, W., De Sessions, P. F., et al. (2018). A macromolecular approach to eradicate multidrug resistant bacterial infections while mitigating drug resistance onset. *Nat. Commun.* 9:917. doi: 10.1038/s41467-018-03325-6

Chua, S. L., Liu, Y., Yam, J. K., Chen, Y., Vejborg, R. M., Tan, B. G., et al. (2014). Dispersed cells represent a distinct stage in the transition from bacterial biofilm to planktonic lifestyles. *Nat. Commun.* 5:4462. doi: 10.1038/ncomms5462

Davies, D. (2003). Understanding biofilm resistance to antibacterial agents. *Nat. Rev. Drug Discov.* 2, 114–122. doi: 10.1038/nrd1008

Davies, J., and Davies, D. (2010). Origins and evolution of antibiotic resistance. *Microbiol. Mol. Biol. Rev.* 74, 417–433. doi: 10.1128/MMBR.00016-10

Dhanda, G., Sarkar, P., Samaddar, S., and Haldar, J. (2019). Battle against vancomycin-resistant bacteria: recent developments in chemical strategies. *J. Med. Chem.* 62, 3184–3205. doi: 10.1021/acs.jmedchem.8b01093

Ghosh, C., Manjunath, G. B., Akkapeddi, P., Yarlagadda, V., Hoque, J., Uppu, D. S., et al. (2014). Small molecular antibacterial peptoid mimics: the simpler the better! *J. Med. Chem.* 57, 1428–1436. doi: 10.1021/jm401680a

Ghosh, C., Sarkar, P., Issa, R., and Haldar, J. (2019). Alternatives to conventional antibiotics in the era of antimicrobial resistance. *Trends Microbiol.* 27, 323–338. doi: 10.1016/j.tim.2018.12.010

Ghosh, C., Yadav, V., Younis, W., Mohammad, H., Hegazy, Y. A., Seleem, M. N., et al. (2017). Aryl-alkyl-lysines: membrane-active fungicides that act against biofilms of *Candida albicans*. *ACS Infect. Dis.* 3, 293–301. doi: 10.1021/acsinfecdis.6b00192

Gupta, S., Thakur, J., Pal, S., Gupta, R., Mishra, D., Kumar, S., et al. (2019). Cholic acid-peptide conjugates (CAPs) as potent antimicrobials against interkingdom polymicrobial biofilms. *Antimicrob. Agents Chemother.* 63: e00520-19. doi: 10.1128/AAC.00520-19

Gupta, V. K., Gaur, R., Sharma, A., Akther, J., Saini, M., Bhakuni, R. S., et al. (2019). A novel bi-functional chalcone inhibits multi-drug resistant *Staphylococcus aureus* and potentiates the activity of fluoroquinolones. *Bioorg. Chem.* 83, 214–225. doi: 10.1016/j.bioorg.2018.10.024

Hall-Stoodley, L., Costerton, J. W., and Stoodley, P. (2004). Bacterial biofilms: from the natural environment to infectious diseases. *Nat. Rev Microbiol* 2, 95–108. doi: 10.1038/nrmicro821

Hancock, R. E., and Sahl, H. G. (2006). Antimicrobial and host-defense peptides as new anti-infective therapeutic strategies. *Nat. Biotechnol.* 24, 1551–1557. doi: 10.1038/nbt1267

Harriott, M. M., and Noverr, M. C. (2009). *Candida albicans* and *Staphylococcus aureus* form polymicrobial biofilms: effects on antimicrobial resistance. *Antimicrob. Agents Chemother.* 53, 3914–3922. doi: 10.1128/AAC.00657-09

Harriott, M. M., and Noverr, M. C. (2011). Importance of Candida-bacterial polymicrobial biofilms in disease. *Trends Microbiol.* 19, 557–563. doi: 10.1016/j.tim.2011.07.004

Hoque, J., Akkapeddi, P., Yadav, V., Manjunath, G. B., Uppu, D. S., Konai, M. M., et al. (2015). Broad spectrum antibacterial and antifungal polymeric paint materials: synthesis, structure-activity relationship, and membrane-active mode of action. *ACS Appl. Mater. Interfaces* 7, 1804–1815. doi: 10.1021/am507482y

Hoque, J., Ghosh, S., Paramanandham, K., and Haldar, J. (2019). Charge-switchable polymeric coating kills bacteria and prevents biofilm formation in vivo. *ACS Appl. Mater. Interfaces*. 11, 39150–39162. doi: 10.1021/acsami.9b11453

Ilker, M. F., Nusslein, K., Tew, G. N., and Coughlin, E. B. (2004). Tuning the hemolytic and antibacterial activities of amphiphilic polynorbornene derivatives. *J. Am. Chem. Soc.* 126, 15870–15875. doi: 10.1021/ja045664d

Konai, M. M., Adhikary, U., Samaddar, S., Ghosh, C., and Haldar, J. (2015). Structure-activity relationship of amino acid tunable lipidated norspermidine conjugates: disrupting biofilms with potent activity against bacterial persisters. *Bioconjug Chem.* 26, 2442–2453. doi: 10.1021/acs.bioconjchem.5b00494

Konai, M. M., Bhattacharjee, B., Ghosh, S., and Haldar, J. (2018). Recent progress in polymer research to tackle infections and antimicrobial resistance. *Biomacromolecules* 19, 1888–1917. doi: 10.1021/acs.biomac.8b00458

Konai, M. M., Ghosh, C., Yarlagadda, V., Samaddar, S., and Haldar, J. (2014). Membrane active phenylalanine conjugated lipophilic norspermidine derivatives with selective antibacterial activity. *J. Med. Chem.* 57, 9409–9423. doi: 10.1021/jm5013566

Konai, M. M., and Haldar, J. (2017). Fatty acid comprising lysine conjugates: anti-MRSA agents that display in vivo efficacy by disrupting biofilms with no resistance development. *Bioconjug Chem.* 28, 1194–1204. doi: 10.1021/acs.bioconjchem.7b00055

Krumm, C., Harmuth, S., Hijazi, M., Neugebauer, B., Kampmann, A. L., Geltenpoth, H., et al. (2014). Antimicrobial poly(2-methyloxazoline)s with bioswitchable activity through satellite group modification. *Angew. Chem. Int. Ed. Engl.* 53, 3830–3834. doi: 10.1002/anie.201311150

Kuroda, K., and DeGrado, W. F. (2005). Amphiphilic polymethacrylate derivatives as antimicrobial agents. *J. Am. Chem. Soc.* 127, 4128–4129. doi: 10.1021/ja044205

Li, P., Zhou, C., Rayatpisheh, S., Ye, K., Poon, Y. F., Hammond, P. T., et al. (2012). Cationic peptidopolysaccharides show excellent broad-spectrum antimicrobial activities and high selectivity. *Adv. Mater.* 24, 4130–4137. doi: 10.1002/adma.201104186

Liu, R., Chen, X., Chakraborty, S., Lemke, J. J., Hayouka, Z., Chow, C., et al. (2014). Tuning the biological activity profile of antibacterial polymers via subunit substitution pattern. *J. Am. Chem. Soc.* 136, 4410–4418. doi: 10.1021/ja500367u

Liu, R., Chen, X., Falk, S. P., Masters, K. S., Weisblum, B., and Gellman, S. H. (2015). Nylon-3 polymers active against drug-resistant *Candida albicans* biofilms. *J. Am. Chem. Soc.* 137, 2183–2186. doi: 10.1021/ja512567y

Lohse, M. B., Gulati, M., Johnson, A. D., and Nobile, C. J. (2018). Development and regulation of single- and multi-species *Candida albicans* biofilms. *Nat. Rev. Microbiol.* 16, 19–31. doi: 10.1038/nrmicro.2017.107

Nederberg, F., Zhang, Y., Tan, J. P., Xu, K., Wang, H., Yang, C., et al. (2011). Biodegradable nanostructures with selective lysis of microbial membranes. *Nat. Chem.* 3, 409–414. doi: 10.1038/nchem.1012

Palermo, E. F., Lienkamp, K., Gillies, E. R., and Ragogna, P. J. (2019). Antibacterial activity of polymers: discussions on the nature of amphiphilic balance. *Angew. Chem. Int. Ed. Engl.* 58, 3690–3693. doi: 10.1002/anie.201813810

Porter, E. A., Wang, X., Lee, H. S., Weisblum, B., and Gellman, S. H. (2000). Non-haemolytic beta-amino-acid oligomers. *Nature* 404:565. doi: 10.1038/35007145

Qian, Y., Qi, F., Chen, Q., Zhang, Q., Qiao, Z., Zhang, S., et al. (2018). Surface modified with a host defense peptide-mimicking beta-peptide polymer kills bacteria on contact with high efficacy. *ACS Appl. Mater. Interfaces* 10, 15395–15400. doi: 10.1021/acsami.8b01117

Stewart, P. S., and Costerton, J. W. (2001). Antibiotic resistance of bacteria in biofilms. *Lancet* 358, 135–138. doi: 10.1016/s0140-6736(01)05321-1

Uppu, D., Konai, M. M., Baul, U., Singh, P., Siersma, T. K., Samaddar, S., et al. (2016). Isosteric substitution in cationic-amphiphilic polymers reveals an important role for hydrogen bonding in bacterial membrane interactions. *Chem. Sci.* 7, 4613–4623. doi: 10.1039/c6sc00615a

Uppu, D. S., Akkapeddi, P., Manjunath, G. B., Yarlagadda, V., Hoque, J., and Haldar, J. (2013). Polymers with tunable side-chain amphiphilicity as non-hemolytic antibacterial agents. *Chem. Commun.* 49, 9389–9391. doi: 10.1039/c3cc43751e

Willyard, C. (2017). The drug-resistant bacteria that pose the greatest health threats. *Nature* 543:15. doi: 10.1038/nature.2017.21550

Wilson, L. S., Reyes, C. M., Stolpman, M., Speckman, J., Allen, K., and Beney, J. (2002). The direct cost and incidence of systemic fungal infections. *Value Health* 5, 26–34. doi: 10.1046/j.1524-4733.2002.51108.x

Yavvari, P. S., Gupta, S., Arora, D., Nandicoori, V. K., Srivastava, A., and Bajaj, A. (2017). Clathrin-independent killing of intracellular mycobacteria and biofilm disruptions using synthetic antimicrobial polymers. *Biomacromolecules* 18, 2024–2033. doi: 10.1021/acs.biomac.7b00106

Zasloff, M. (2002). Antimicrobial peptides of multicellular organisms. *Nature* 415, 389–395. doi: 10.1038/415389a

Zhang, J., Chen, Y. P., Miller, K. P., Ganewatta, M. S., Bam, M., Yan, Y., et al. (2014). Antimicrobial metallopolymers and their bioconjugates with conventional antibiotics against multidrug-resistant bacteria. *J. Am. Chem. Soc.* 136, 4873–4876. doi: 10.1021/ja5011338

Conflict of Interest: The authors declare that the research was conducted in the absence of any commercial or financial relationships that could be construed as a potential conflict of interest.

frontiers in Bioengineering and Biotechnology

ORIGINAL RESEARCH
published: 25 February 2020
doi: 10.3389/fbioe.2020.00124

Response of Human Macrophages to Clinically Applied Wound Dressings Loaded With Silver

Patrícia Varela[1,2], Lennart Marlinghaus[3], Susanna Sartori[1], Richard Viebahn[2], Jochen Salber[2†] and Gianluca Ciardelli[1†]*

[1] Department of Mechanical and Aerospace Engineering, Politecnico di Torino, Turin, Italy, [2] Department of Experimental Surgery, Universitätsklinikum Knappschaftskrankenhaus Bochum, Ruhr-University Bochum, Bochum, Germany, [3] Department of Medical Microbiology, Ruhr-University Bochum, Bochum, Germany

OPEN ACCESS

Edited by:
Francesca Boccafoschi, Università degli Studi del Piemonte Orientale, Italy

Reviewed by:
Subhamoy Das, Stanford University, United States
Lia Rimondini, University of Eastern Piedmont, Italy

***Correspondence:**
Patrícia Varela
patricia.varela@polito.it;
patricia.varela.martins@gmail.com

† These authors have contributed equally to this work and share senior authorship

Specialty section:
This article was submitted to Biomaterials, a section of the journal Frontiers in Bioengineering and Biotechnology

Received: *30 September 2019*
Accepted: *10 February 2020*
Published: *25 February 2020*

Citation:
Varela P, Marlinghaus L, Sartori S, Viebahn R, Salber J and Ciardelli G (2020) Response of Human Macrophages to Clinically Applied Wound Dressings Loaded With Silver. Front. Bioeng. Biotechnol. 8:124. doi: 10.3389/fbioe.2020.00124

Wound infections constitute an increasing clinical problem worldwide. To reverse this trend, several wound dressings with antimicrobial properties have been developed. Considering the increasing presence of antibiotic-resistant microorganisms, product developers have been focusing their efforts in introducing antibiotic-free antibacterial wound dressings to the market, with silver being the most commonly incorporated antimicrobial agent. In this scenario, gaining information about the microbial and eukaryotic cells' response to these dressings is needed for a proper selection of antimicrobial dressings for the different cases of infected wounds. In particular, one insufficiently explored parameter is the effect of the dressings on the immunomodulation of macrophages, the main immune cell population participating in the repair process, because of their pivotal role in the transition of the inflammation to the proliferation phase of wound healing. In this work, three different clinically applied antimicrobial, silver impregnated wound dressings were selected: Atrauman® Ag, Biatain® Alginate Ag and PolyMem WIC Silver® Non-adhesive. Antimicrobial susceptibility tests (disk diffusion and broth dilution), cell viability evaluation (CellTiter-Blue®) and experiments to determine macrophage polarization (e.g., flow cytometry, ELISA and glucose uptake) were performed after 24 h of incubation. Among all products tested, Biatain® Alginate Ag induced the most evident bactericidal effect on Gram-positive and Gram-negative bacteria, followed by PolyMem WIC Silver® Non-adhesive, but did not show good cytocompatibility *in vitro*. On the other hand, Atrauman® Ag showed excellent cytocompatibility on L929 fibroblasts, HaCaT keratinocytes and THP-1 derived macrophages, but no significant antimicrobial activity was observed. Overall, it was confirmed that macrophages initiate, in fact, an alteration of their metabolism and phenotype in response to wound dressings of different composition in a short period of contact (24 h). M0 resting state macrophages common response to all silver-containing dressings used in this study was to increase the production of the anti-inflammatory cytokine TGF-β, which indicates an acquisition of M2-like macrophages characteristics.

Keywords: wound infections, wound dressings, silver, immunomodulation, macrophages

INTRODUCTION

Clinicians are daily faced with the extremely difficult challenge of selecting the most appropriate dressing among those available in the market (Dhivya et al., 2015). The selection must be done for each specific case, by doing a comprehensive assessment of the wound status and collecting clinical data of the patient's physical features (Baranoski and Ayello, 2012). The market has been introducing dressings with antimicrobial properties in accordance with the prevalent high number of skin and soft tissue infection cases (also known as acute bacterial skin structure infections) of inpatient and outpatient health care (Burnham et al., 2016; Simões et al., 2018). In particular, antibiotic-free antibacterial wound dressings are on the rise, in accordance with the constantly increasing number of bacterial species isolated from non-healing wounds that are resistant to commonly used antibiotics in the hospital setting (Piddock, 2017). Among the available products, silver-based wound dressings definitely dominate the market, due to silver's broad antimicrobial activity against more than 600 clinically isolated strains of non- and more importantly drug-resistant bacteria (Nam et al., 2015; Zewde et al., 2016; Simões et al., 2018). Generally, the antimicrobial principle of these silver dressings relies on the release of silver ions (Ag^+) that induce the antimicrobial activity. Silver ions are antibacterial through various mechanisms of action, such as interacting with the bacterial membrane leading to the destabilization of the phospholipidic layer or provoking a decrease of adenosine triphosphate (ATP) levels. Silver ions are also known for causing the induction of an increased production of reactive oxygen species (ROS) and interaction with cytosolic components as enzymes and nucleic acids (Sütterlin et al., 2012). However, these dressings are not sufficiently investigated, especially concerning the effects on immunomodulation of macrophages (Krzyszczyk et al., 2018). Acquisition of data on macrophage-biomaterial interactions is decisive to gain a more complete assessment of the characteristics of each wound product and could lead to the selection of the most appropriate material to prevent or reduce local infection. Wound healing is a highly complex, finely regulated process. Based on our current knowledge, the optimal wound healing stages in chronological order go through haemostasis, inflammation, proliferation and remodeling phases (Velnar et al., 2009; Krzyszczyk et al., 2018). During this process, macrophages are deeply involved, by shifting from a predominant M1 pro-inflammatory population to an anti-inflammatory/tissue-remodeling M2 phenotype, while some populations might share characteristics of both M1 and M2 macrophages (Ferrante and Leibovich, 2012). A very important function of macrophages is their role in the transition from the inflammatory to the proliferation phase in wound healing (Landén et al., 2016). After an injury, during the early stages of repair in cutaneous healing, M1 macrophages are more frequently found (Sindrilaru and Scharffetter-Kochanek, 2013). They are specialized in phagocytosing dead cells and their components, besides attracting other macrophages to the damage location (Hesketh et al., 2017). M1 macrophages are known for being antigen presenting cells and for producing the antibacterial oxidative metabolite nitric oxide (NO). Their metabolism is activated toward the production of high levels of pro-inflammatory cytokines such as IFN-γ, IL-1, IL-6, and TNF-α (Schairer et al., 2012; Novak and Koh, 2013). Typically, M1 macrophages present augmented levels of major histocompatibility complex (MHC) cell surface receptors, known as HLA-DR, and the chemokine receptors CD197 that bind CCL19 and CCL21 (Yamane and Leung, 2016).

In contrast, M2-like macrophages appear in higher quantity during proliferation and remodeling phases of the wound healing process. Different from M1 macrophages, M2-like macrophages express high levels of galactose receptors, mannose receptors (CD206) and hemoglobin scavenger receptors (CD163) (Ferrante and Leibovich, 2012; Novak and Koh, 2013). Moreover, these cells constantly produce anti-inflammatory cytokines such as IL-4 and IL-10, and the growth factor TGF-β that has the important function of inducing proliferation of fibroblasts, leading to remodeling of new extracellular matrix for an optimal wound closure (Berg et al., 2003; Ogle et al., 2016).

Unfortunately, in infected wounds a transition from inflammatory to proliferation/remodeling phases is not achieved and a persistent inflammation environment is evident (Hesketh et al., 2017). In such cases, it is needed to avoid external factors, such as biomaterials composition which would prompt this unfavorable environment. Hence it is of paramount importance to evaluate the immunomodulatory effect that different types of commercially available products induce.

Therefore, this work explores the antimicrobial efficacy of silver containing biomaterials that are clinically used on colonized or infected wounds, with a major focus on the response of macrophages to different wound products. A comparative test of the matrix without and with the antimicrobial agent (silver) is also included, in order to obtain information about different cytocompatibility and macrophage immunomodulation responses to the presence of silver.

MATERIALS AND METHODS

Wound Dressing Materials

The commercially available wound dressings for this research work were selected according to the most applied products in clinical set-ups at the University Medical Centre (UMC) of Bochum in Germany. The selected dressings have the same active component – silver ions – being released in different concentrations/time and from diverse systems: metallic silver, patented ion silver complex salt (patent EP1654013B1, registered by Coloplast) or nanocrystalline silver particles. The characteristics of the chosen untreated wound dressings and their correspondent dressings incorporated with a specific type of silver are described in **Table 1**. Before starting the biological experiments, disks were cut out of the wound dressings in a non-sterile environment and afterward were sterilized under ultra-violet light for 20 min at a wavelength of 253.7 nm, since it is a simple and non-expensive technique extensively used in the area of medical research, and has a strong antimicrobial activity (Valente et al., 2016). All samples were maintained in sealed

TABLE 1 | Selected commercially available wound dressing products (adapted from the informative documents provided by the suppliers).

Name of product	Base constitution	Quantity and type of silver	Other characteristics
Atrauman®	Polyester Mesh	Not present	Porous structure (1 mm pore size) and impregnated with neutral ointment that contains fatty acids to promote wound closure
Atrauman® Ag	Polyamide Mesh	300–500 $\mu g/cm^2$ of unreactive metallic silver Ag(0) that in aqueous or moist environment is rapidly ionized to silver ions Ag^+	Impregnated with ointment made of ester mixture of natural and vegetable fatty acids (Macrogol 2000)
Biatain® Alginate	Dressing consisting of 85% alginate and 15% carboxymethyl Cellulose	Not present	High dressing integrity and calcium ions are released from the dressing inducing a haemostatic effect
Biatain® Alginate Ag		950 $\mu g/cm^2$ of inorganic salt that releases ionic silver Ag^+ in the presence of wound exudate	Highly absorbent, and provides a haemostatic effect
PolyMem® WIC Non-adhesive	Polyurethane foam	Not present	
PolyMem WIC Silver® Non-adhesive		124 $\mu g/cm^2$ of nanocrystalline silver particles that release clusters of extremely small and highly reactive silver particles, and silver ions, in wound fluid taken up by the dressing	Contains a humectant (glycerol) that avoids the dressing to dry and to adhere to the wound bed, a non-ionic surfactant (poloxamer 188) that facilitates wound cleansing, and a starch copolymer to enhance the fluid handling properties of the foam

sterile petri dishes at 4°C for a maximum of one-week before further use in biological experiments.

Culture Conditions of Bacterial and Eukaryotic Cell Lines

Four bacterial strains known to infect open wounds were selected for this work. All strains were obtained from the American Type Culture Collection (ATCC). Two of them are Gram-positive – *Staphylococcus aureus subsp. aureus* Rosenbach (ATCC® 29213™) and *Staphylococcus epidermidis* (Winslow and Winslow) Evans (ATCC® 12228™) – and the others are Gram-negative bacteria – *Escherichia coli* (Migula) Castellani and Chalmers (ATCC® 25922™) and *Pseudomonas aeruginosa* (Schroeter) Migula (ATCC® 27853™). For all experiments, bacterial cells were grown at 37°C for 18h on blood agar plates (mixture of nutrient agar with 5% sheep blood pH ∼7.4).

Fibroblasts, keratinocytes and monocyte-derived macrophages, which are cell populations that constitute skin, were used to evaluate the effects of the dressings on 2D cell culture layers of mammalian cells. For all cell lines, the cell number was determined on a Neubauer counting chamber in the presence of 0.4% trypan blue (Gibco) to exclude non-viable cells.

Murine fibroblasts L929 cell line (German Collection of Microorganisms and Cell Cultures – DSMZ) was cultured in RPMI 1640 medium with stable glutamine (PAN Biotech), supplemented with 10% heat-inactivated Fetal bovine serum - FBS (PAN Biotech), and 100 U/mL penicillin - 0.1 mg/mL streptomycin (PAN Biotech). Cells were maintained in T75 vented cap culture flasks (ThermoFisher Scientific) at 37°C in an atmosphere containing 5% CO_2, by sub-passage with 0.25% Trypsin 1 mM EDTA (PAN Biotech) at each 2–3 days.

The keratinocyte immortalized cell line HaCaT (Deutsches Krebsforschungszentrum - DKFZ, Heidelberg) was expanded in 4.5 g/L glucose Dulbecco's Modified Eagle Medium – high glucose DMEM (ThermoFisher Scientific) supplemented with 10% heat-inactivated Fetal bovine serum (FBS) (PAN Biotech), and 100 U/mL penicillin - 0.1 mg/mL streptomycin (PAN Biotech) in T75 vented cap culture flasks (ThermoFisher Scientific) at 37°C and 5% CO_2. The detachment of adhered cells was performed with TrypLE Express (ThermoFisher Scientific). The splitting ratio was from 1:5 to 1:10.

Human monocytic cell line THP-1 (ATCC) was grown at 37°C and 5% CO_2 in vertically positioned T75 vented cap culture flasks (ThermoFisher Scientific) in the exact same complete RPMI 1640 medium as previously described for L929 cells. Additional medium was added or renewed every 2–3 days when the maximum cell concentration was reached – 8×10^5 cells/mL.

To induce THP-1 monocyte differentiation to M0 macrophages, monocytes were first seeded on cell culture treated 24-well plates (density of 10^6 cells/mL) in the presence of 200 ng/mL of phorbol 12-myristate-13-acetate (PMA) (Sigma Aldrich) for 24 h (37°C, 5% CO_2). Afterward the medium was replaced to complete RPMI and cells were again incubated for 48 h before any further experiment.

Antibacterial Susceptibility Tests

Disk Diffusion

The European Committee on Antimicrobial Susceptibility Testing (EUCAST) guidelines were followed for this experiment (Matuschek et al., 2014). Briefly, well-isolated colonies were selected and immersed in 2 mL of 0.9% NaCl. Density was adjusted to MacFarland 0.5 turbidity standard (corresponds to ∼1-2 $\times$ 10^8 colony forming units per milliliter - CFU/mL). With a sterile swab the inoculum was spread evenly on Mueller-Hinton agar plates.

Afterward, the disks obtained from the antimicrobial dressing materials with 1 cm diameter size were carefully placed on the agar plates. As a first control, disks of untreated materials were placed on the agar to observe if there is not a bacterial growth inhibition without the antibacterial agent. A second control was included in the tests with specific antibiotics known to inhibit the strains growth in order to validate the assay: 1 μg oxacillin for *S. aureus* and *S. epidermidis*, and 300 μg streptomycin for *E. coli* and *P. aeruginosa*. Plates were incubated at 37°C for 16–20 h (in duplicates). Photographs were acquired with a Panasonic Lumix DMC-FZ100 digital camera.

Colonies Count to Determine Bacterial Reduction in Broth Medium

In order to determine the bacterial reduction in the presence of the material, the broth microdilution method was performed following the EUCAST recommendation to use the ISO 20776-1:2006 standard, with some modifications. The dressing material was cut to circles of 6.5 mm diameter that were placed in duplicates on the bottom of 96-well plates. Colonies selected from an overnight culture grown on blood agar plates were inserted in a tube with 2 mL 0.9% saline solution NaCl. Turbidity was adjusted to MacFarland 0.5 and the inoculum was diluted 400-fold in Mueller-Hinton broth ($\sim 3.75 \times 10^5$ CFU/ml). 100 μL of the bacteria suspension was added on the material on each well. The plate was incubated for 24 h at 37°C. After this period, the turbidity of the well was visualized to determine if the material had sufficient concentration of antibacterial agent to inhibit the growth (minimal inhibitory concentration – MIC) of each bacteria strain. Following to the broth MIC test, the entire volume of the well was spread evenly on blood agar plates. These plates were incubated from 16 to 20 h at 37°C and the colony forming units (CFU) were counted and compared to the initial CFU/mL.

Cytocompatibility Test on Different Cell Populations of Skin

In a sterile flat bottom 24-well plate, 5×10^4 cells per well for L929 fibroblasts and 5×10^5 cells per well for HaCaT keratinocytes were cultured and incubated at 37°C and 5% CO_2 for 24 h to allow cell adherence. In the case of THP-1 monocytes, the period of incubation was longer due to the induced stimulation for its differentiation into M0 macrophages as previously described in the section *Culture conditions of bacterial and eukaryotic cell lines*. After this time, the medium of the wells was renewed, and the sterilized materials (6.5 mm diameter) were quickly soaked in cell culture medium and added in triplicates on top of the cells layer on each well. The plate was kept in a humidified incubator (37°C and 5% CO_2) for 24 h. Afterward, CellTiter-Blue® viability assay was performed following the provider instructions. Briefly, the CellTiter-Blue® is based on the conversion of resazurin (a redox dye) to resorufin (a fluorescent end-product) by living cells. After 2 h of incubation with CellTiter-Blue reagent, the fluorescence intensity was quantified on a black 96 well-plate by measuring the fluorescence at 590 nm, after excitation at 560 nm in a Tecan microplate reader Infinite® 200 PRO. As positive control a lysis solution of 9% Triton® X-100 (Promega) was added to the cells, and as negative control, cells were plated on the Tissue Culture Polystyrene (TCPS). This procedure was adapted from the ISO norm 10993-5:2009 (International Organization for Standardization, 2009).

Evaluation of the Effects of the Materials on Macrophages

Morphological Evaluation

Bright field images were acquired on an Olympus IX51 microscope with a magnification of 20× to observe the morphological characteristics of monocyte-derived macrophages after being exposed to the material for 24 h.

Flow Cytometry Analysis

Analysis of the phenotypical characteristics of macrophages in the presence of wound dressings for 24 h was performed by flow cytometry (Partec, Münster, Germany).

For direct labeling of cells, all fluorescein-isothiocyanate (FITC)- or phycoerythrin (PE)- conjugated anti-human monoclonal antibodies (Biolegend UK Ltd) were diluted 1:25 and incubated for 30 min at 4°C. The following antibodies were added to cells suspended in 1.5% paraformaldehyde (PFA): FITC-labeled mouse anti-human CD197 (clone G043H7), PE-labeled mouse anti-human HLA-DR (clone L243), PE-labeled mouse anti-human CD163 (clone GHI/61) and FITC-labeled mouse anti-human CD206 (clone 15-2). As autofluorescence control, unstained M0 macrophages were used. Data was analyzed with FloMax software version 2.3 (Partec).

Quantification of Cytokine Production (ELISA)

Legend Max™ ELISA kits with pre-coated plates (BioLegend UK Ltd) were used to measure the pro-inflammatory cytokine IL-1β and anti-inflammatory cytokines, IL-10 and TGF-β, present in the cell culture supernatant of the different conditions tested following the manufacturer's procedure.

Nitric Oxide Detection

Nitrate/Nitrite Colometric assay kit (Cayman Chemical, Biomol GmbH, Germany) was used to quantify the concentration of total NO products (nitrate NO_3^- + nitrite NO_2^-) in the supernatant that was produced by macrophages in the presence of six different materials for 24 h. The method was according to manufacturer's instructions.

Glucose Uptake

After 24 h in the presence of the unloaded and antibacterial loaded dressing materials, the glucose uptake by macrophages was evaluated. After washing the wells of the 24-well plates with PBS, RPMI 1640 medium without glucose (Gibco™) supplemented with 100 μM of fluorescent D-glucose analog 2-[*N*-(7-nitrobenz-2-oxa-1,3-diazol-4-yl) amino]-2-deoxy-D-glucose (2-NBDG) (Cayman Chemical, Biomol GmbH, Germany) was added. The plates were incubated at 37°C for 60 min in the dark. The supernatant was removed and the wells were washed once with PBS. Accutase (PAN Biotech) was added to induce the detachment of the cells and the content of the wells was transferred to a black 96-well plate to read fluorescence

(excitation 465/emission 540 nm) in a Tecan microplate reader Infinite® 200 PRO.

Statistical Analysis

All data was first expressed as mean ± standard deviation of three independent assays in triplicate. The statistical analysis was performed with the GraphPad Prism 5.00.288 software by one-way analysis of variance (ANOVA) followed by Bonferroni's multiple comparison test. Statistically significant values are represented as $^{*}p < 0.05$, $^{**}p < 0.01$, and $^{***}p < 0.001$.

RESULTS

Antibacterial Susceptibility to the Clinically Used Antimicrobial Wound Dressings

The antibacterial efficacy of the selected wound dressings was evaluated on four bacterial strains typically found in wound infections (*S. aureus*, *S. epidermidis*, *E. coli*, and *P. aeruginosa*) (Gjødsbøl et al., 2006; Ibberson et al., 2017). Disk diffusion was first performed to assess the antibacterial capacity of the materials in a warmed and humidified condition. No bacterial inhibition was observed with the untreated materials (**Figures 1A,C,E**). In our evaluation, it was observed that only Biatain Alginate Ag was able to inhibit the growth of the four strains tested (**Figure 1** and **Table 2**). Atrauman Ag and PolyMem WIC Silver induced an inhibition zone against *S. epidermidis* only (**Figure 1** and **Table 2**).

TABLE 2 | Diameter of the Halo of bacterial growth inhibition induced by the placed antibacterial commercial wound dressings ($n = 3$).

Dressing material	Diameter of the inhibition zone (mm)			
	S. aureus	*S. epidermidis*	*E. coli*	*P. aeruginosa*
Atrauman® Ag	–	13.5 ± 0.5	–	–
Biatain® Alginate Ag	12.5 ± 0.5	16.5 ± 0.5	13.0 ± 0	15.5 ± 0.5
PolyMem WIC Silver®	–	12.5 ± 0.5	–	–

Average ± Standard deviation.

Another antibacterial method was performed as complement to the disk diffusion results. In this method, the dressings were completely submersed in Mueller-Hinton broth providing a more liquid environment than disk diffusion and differences on the antibacterial properties were clearly observed. Moreover, with the colony forming units (CFU) counted after 24 h, it was possible to determine the exact reduction of CFU/mL provoked by each antimicrobial dressing. Atrauman Ag seems to prevent the continuous growth of *S. epidermidis* and *E. coli* (**Figure 2**). In case of *E. coli* this effect was not observed on the disk diffusion test (**Figure 1**). Biatain Alginate Ag was able to induce 80 to 99% reduction of CFU/mL on all strains tested, showing significantly different values of CFU in the presence of this material versus the initial bacterial concentration (**Figure 2**). This result in combination with the disk diffusion suggests that Biatain Alginate Ag allows a more rapid dissociation of the inorganic salt in contact with a moist or aqueous environment leading to the release of Ag^{+} in the first 24 h than the other dressings. PolyMem WIC Silver showed efficient antibacterial properties

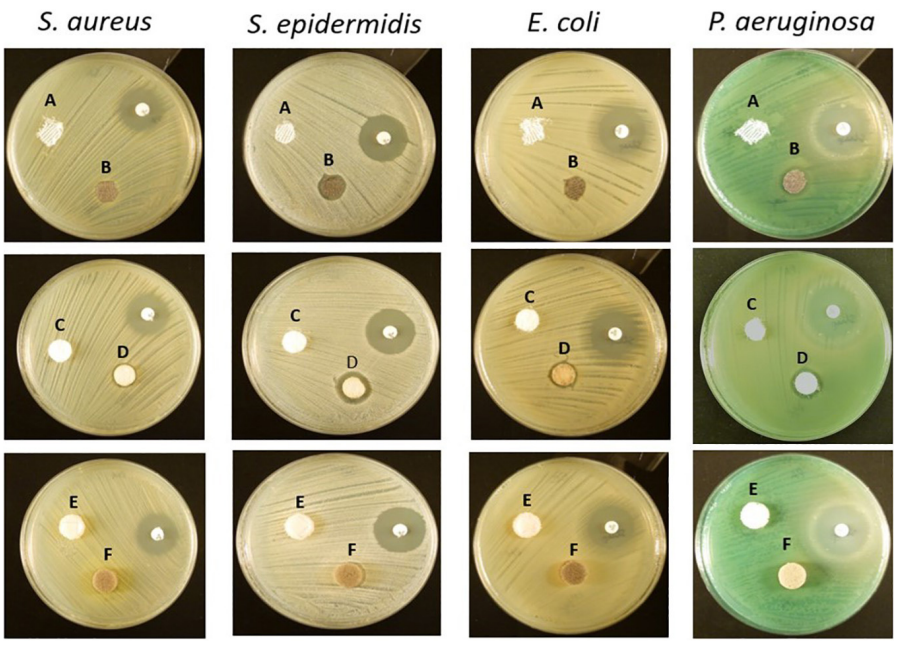

FIGURE 1 | Representative images of the antibacterial susceptibility to the wound dressings by the disk diffusion method. A – Atrauman; B – Atrauman Ag; C – Biatain Alginate; D – Biatain Alginate Ag; E – PolyMem WIC; F – PolyMem WIC Silver. The used non-labeled antibiotic disks on the images were oxacillin (on *S. aureus* and *S. epidermidis* plates) and streptomycin (on *E. coli* and *P. aeruginosa* petri dishes).

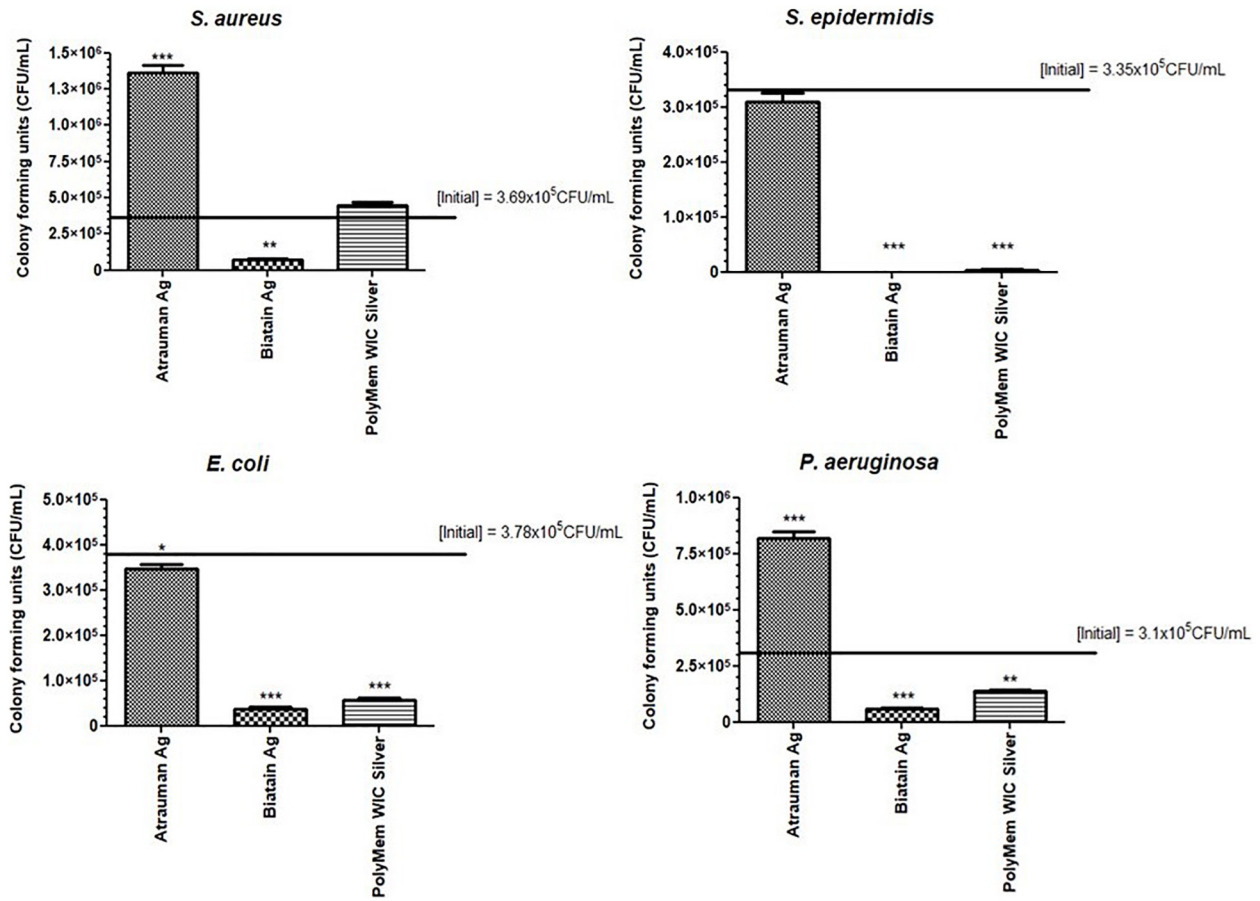

FIGURE 2 | Bacterial growth or reduction (in reference to the initial inoculum) in the presence of the antibacterial materials for 24 h assessed by counting the colony forming units/mL. *p* values were determined for all groups versus initial CFU/mL. Statistical significance was performed with data from three independent experiments and is presented as following $^{*}p \leq 0.05$, $^{**}p \leq 0.01$, and $^{***}p \leq 0.001$. Error bars represent standard deviation.

in a liquid medium, in comparison with the disk agar diffusion method. Here a significant reduction of bacterial CFU against *S. epidermidis* and both Gram-negative strains was determined. For *S. aureus* this dressing seems to induce a bacteriostatic effect (**Figure 2**).

Bioevaluation of the Cytocompatibility of the Wound Dressings

Three cell populations that are involved in wound regeneration (fibroblasts, keratinocytes and monocyte-derived macrophages) were selected to perform a preliminary direct contact assessment of the biomaterial compatibility *in vitro* on 2D-cell cultures (Shaw and Martin, 2009).

Among the 6 types of materials, Atrauman and Atrauman Ag showed an excellent cytocompatibility to the three different cell lines (**Figure 3**). Biatain Alginate Ag leads to the release of the active component's (Ag^{+}), that turned out to be cytotoxic to the populations tested (**Figure 3**). The lower cell viability can be ascribed to the incorporated Ag^{+} ions due to the statistical difference observed in comparison with silver-free Biatain Alginate, which showed an optimal cell viability (≥70%). Moreover, PolyMem WIC induced a reduction of cell viability by more than 30%. In combination with nanocrystalline silver, a higher reduction of cell viability was observed, showing significant values of $^{***}p \leq 0.001$ for L929 fibroblasts and $^{*}p \leq 0.05$ for HaCaT keratinocytes (**Figure 3**).

Response of Monocyte-Derived Macrophages to Wound Dressings: Phenotypical and Metabolic Characterization of Macrophages After Being Exposed to the Materials for One Day Period of Contact

After incubating M0 macrophages with the 6 different wound dressings, tests were conducted in order to gain insight in the metabolic mechanisms, that lead to the activation of macrophages in the first 24 h. Therefore, the phenotypical and metabolic profile of the monocyte-derived macrophages were analyzed after an incubation with the material on top of the cell layer for 24 h. For phenotypical characterization, besides obtaining bright field images, macrophages were stained with cell surface

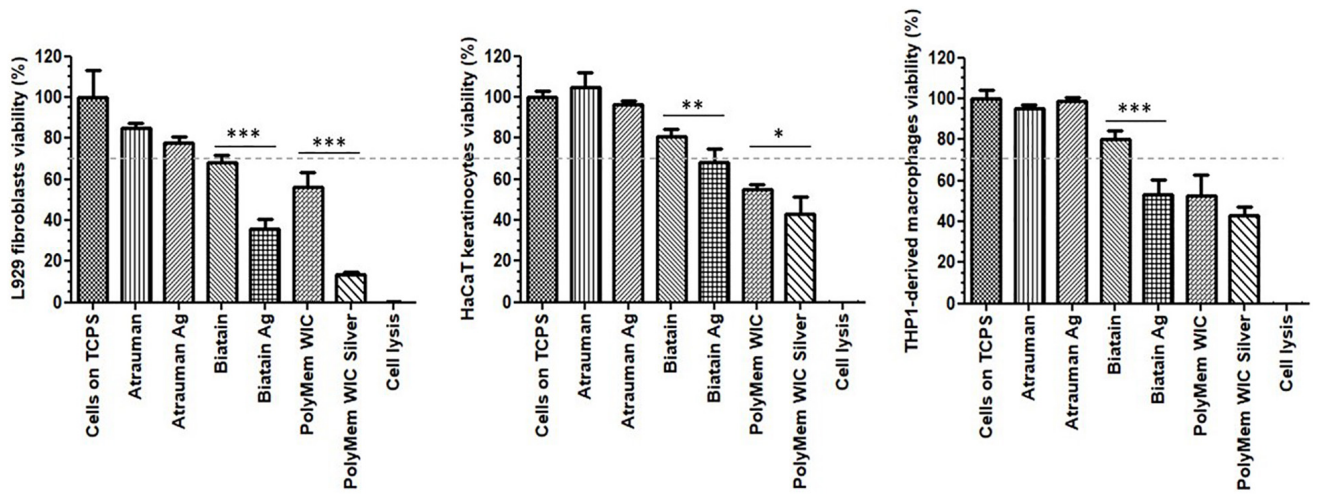

FIGURE 3 | Cell viability in the presence of unloaded and silver loaded dressing materials for 24 h. The dashed line represents 70% viability. The negative control are the cells seeded directly on tissue culture polystyrene (Cells on TCPS) and the positive control are dead cells that were lysed with 9% Triton® X-100 at the endpoint of the assay (Cell lysis). Error bars represent standard deviation. *p* statistical significance values (*$p \leq 0.05$, **$p \leq 0.01$, and ***$p \leq 0.001$) were determined for unloaded vs. respective silver containing material ($n = 3$).

markers CD197/HLA-DR and CD163/CD206 that are typically expressed by M1 and M2, respectively, and were analyzed by flow cytometry. For further characterization, metabolic changes were analyzed in terms of cytokine production (IL-1β, IL-10, and TGF-β), nitric oxide (NO) release and glucose uptake.

In the presence of silver-free Atrauman, cell morphology was very similar to the M0 macrophages (**Figures 4A–C**). However, after exposure to Atrauman Ag, the cell morphology was altered in comparison with the control condition (**Figures 4A,B,D**). The bright field microscopic images show generally a more elongated cell morphology in comparison with the M0 macrophages for the Biatain Alginate dressings (**Figures 4A,B,E,F**). In the presence of PolyMem alone two different shapes of cell morphology are observed in **Figure 4G** that shows more rounded cells than stretched ones. Moreover, from the microscopic images, the presence of some stretched shape macrophages is visible in the presence of PolyMem WIC silver (**Figure 4H**).

No noticeable impact on macrophage immunomodulation was observed for macrophages in the presence of Silver-free Atrauman since the markers expressed on the membrane and levels of signals production were very similar to the M0 macrophages (**Figures 5C,D**, **6**). After contact with silver-containing Atrauman, the THP-1 derived macrophages decreased slightly NO production and increased significantly the secretion of the anti-inflammatory TGF-β cytokine (**Figures 6B,D**). Both silver-free Biatain Alginate and Biatain Alginate Ag raised the levels of TGF-β (**Figure 6D**). An augmented expression of HLA-DR which is a M1-associated marker was detected in macrophages previously exposed to Biatain Alginate alone (**Figure 5C**). Interestingly, Biatain Alginate alone also induced the production of pro-inflammatory molecules: slightly higher IL-1β concentration and significantly more nitric oxide concentration in the supernatant (**Figures 6A,B**). However, macrophages in the presence of Biatain Alginate Ag produced reduced NO levels and a significant increase of single positive $CD206^+$ cells and double positive $CD163^+/CD206^+$ on the membrane of macrophages was determined (**Figures 5D**, **6B**). It is well observed on **Figure 5B**, that the previously mentioned markers are less detected in the correspondent quadrants of the plot for a representative sample of M0 macrophages population. The PolyMem dressing induced a slight increase of populations that express HLA-DR and double CD197/HLA-DR markers, that are considered pro-inflammatory receptors (**Figures 5A,D**). A significant increase in the production of IL-1β, IL-10, and TGF- β was observed additionally (**Figures 6A,C,D**). In comparison to the respective silver-free foam, the macrophages in contact with PolyMem WIC Silver maintain the induction of high TGF-β production but typical cell surface markers of M1 and pro-inflammatory cytokines are not detected anymore (**Figures 5C**, **6D**).

The glucose uptake by macrophages exposed to unloaded versus silver containing dressings increased significantly in all conditions compared to M0 resting state macrophages, with exception of Atrauman Ag. Still it is clear that macrophages consume slightly less glucose in the presence of the silver containing materials (**Figure 7**). The most significant increase of glucose consumption occurred to macrophages that were previously exposed to PolyMem WIC (**Figure 7**).

DISCUSSION

Microbial contamination of wounds is a significant contributor for the delay of wound healing (Leaper et al., 2015). The usage of antimicrobial wound dressings has been increased in hospitals as a common practice for the prevention of infections or the reduction of bacterial burden in the wound environment. Incorporation of silver as an antimicrobial agent

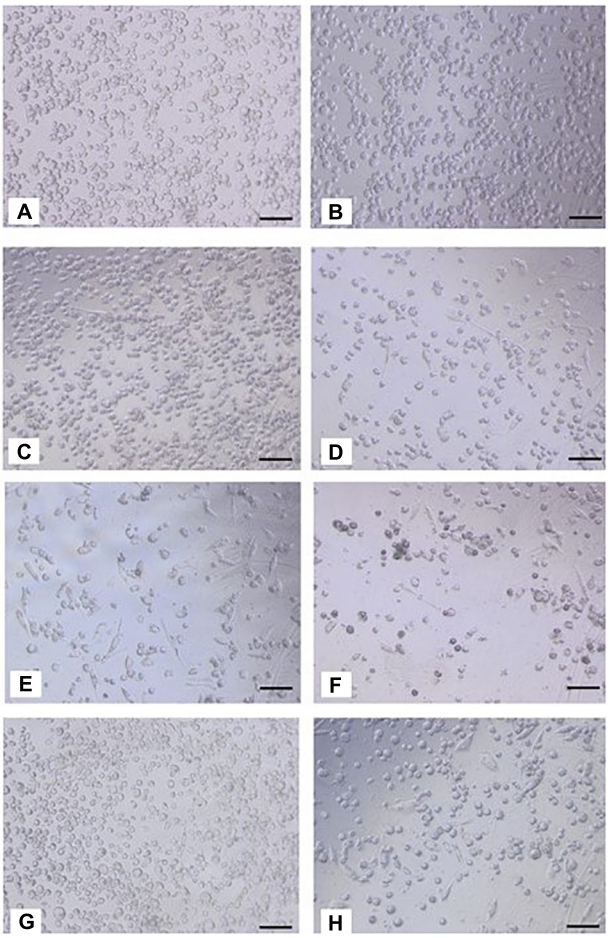

FIGURE 4 | Bright field images of macrophages after 24 h of exposure to silver-free and silver-containing wound dressings. **(A,B)** M0 macrophages on TCPS; **(C)** Atrauman; **(D)** Atrauman Ag; **(E)**, Biatain Alginate; **(F)** Biatain Alginate Ag; **(G)** PolyMem WIC; **(H)** PolyMem WIC Silver. Bar represents 100 μm.

that is not a conventional systemic antibiotic treatment in such matrixes is one of the most common strategies. In the last years many clinical cases were reported, in which currently-used antibiotics failed in their bactericidal or bacteriostatic effect, due to the evolution and propagation of multidrug-resistant species (Blair et al., 2015).

Out of the three antimicrobial wound dressings selected for this study, Biatain Alginate Ag decreased the number of Gram-positive (*S. aureus* and *S. epidermidis*) and Gram-negative (*E. coli* and *P. aeruginosa*) bacteria significantly in the first 24 h. All materials tested achieve the antibacterial inhibition by releasing silver ions, that occurs optimally in contact with a moist or liquid environment, such as the exudate of wounds. However, these ions have a different origin for each material, and the polymeric component and the amount of silver is also different. In a short period of time, the Ag^+ generated from the inorganic salt used in Biatain Alginate Ag, diffuses quicker than the one originated by the metallic silver incorporated into Atrauman Ag and the silver ions and particles that are formed from the nanocrystalline silver of PolyMem WIC Silver. This is probably because among all dressings Biatain Alginate Ag is the material with the highest silver amount per cm^2 (0.95 mg/cm^2) (Coloplast, 2015). However, in a direct contact test, it also provoked a cytotoxic outcome on fibroblasts and monocyte-derived macrophages, reducing the viability of about 50%. Nevertheless, this material is clearly stimulating the polarization of M0 macrophages to the M2-state since an increase of expression of membrane M2 markers $CD163^+/CD206^+$ and production of TGF-β was verified and a decrease of anti-inflammatory molecules induced by Biatain Alginate alone was also confirmed. Biatain Alginate consists of 85% alginate and 15% carboxymethylcellulose. Although, the information about the origin of the alginate is not openly available, it was previously reported that alginate isolated from *Sargassum vulgare* has pro-inflammatory activity (Lins et al., 2013). Hence, the M1 characteristics observed on macrophages in the presence of Biatain might be a consequence of the contact with alginate. The combination of the matrix properties with the ionic silver complex salt has a clear action in initiating the immunomodulation of macrophages toward the M2-state, possibly to M2a or M2c which are both pro-angiogenic subtypes that show similar characteristics (Novak and Koh, 2013; Hesketh et al., 2017). Therefore, with a rapid killing of microorganisms and shifting macrophages to a tissue-healing population, Biatain Alginate Ag seems promising for regressing the inflammatory perpetual state on chronic wounds which would impulse a proper cutaneous closure.

Atrauman and Atrauman Ag showed excellent cytocompatibility features on the cell lines used in this work. One specific observation was that Atrauman itself seems to be ineffective in inducing any alteration to the macrophage's phenotype for a period of 24 h. This can be an advantage in clinical situations that no interference with the natural wound healing is demanded, such as acute wounds that eventually recover naturally and a dressing is just necessary to protect the wound from external factors. The presence of metallic silver influenced the production of TGF-β to a significant extent, which shows that silver is in fact stimulating the macrophages to secrete this anti-inflammatory signal. In this case, it seems that the effect comes from the Ag^+ ions released by the matrix that have been reported to have anti-inflammatory properties (Hermans, 2006; Leaper, 2006; Wilkinson et al., 2011; Lansdown, 2014; Rosique et al., 2015). As observed in disk diffusion, no antibacterial effect was detected against *S. aureus* and *P. aeruginosa* (**Figure 1**). These results are not in accordance with previous studies performed by the material developers, that observed bacterial reductions of all strains within 24 h. However, their antibacterial evaluation method was entirely different from the ones applied in the present study. The EUCAST guidelines followed here were performed to have uniformity in all tests with the different wound dressings, whereas in the other company's study the standard method 2180 of the American Society for Testing Materials was used, in which the melted agar was inoculated with the different bacterial strains and then dispersed onto the dressing to be examined (Ziegler et al., 2006). In the latter

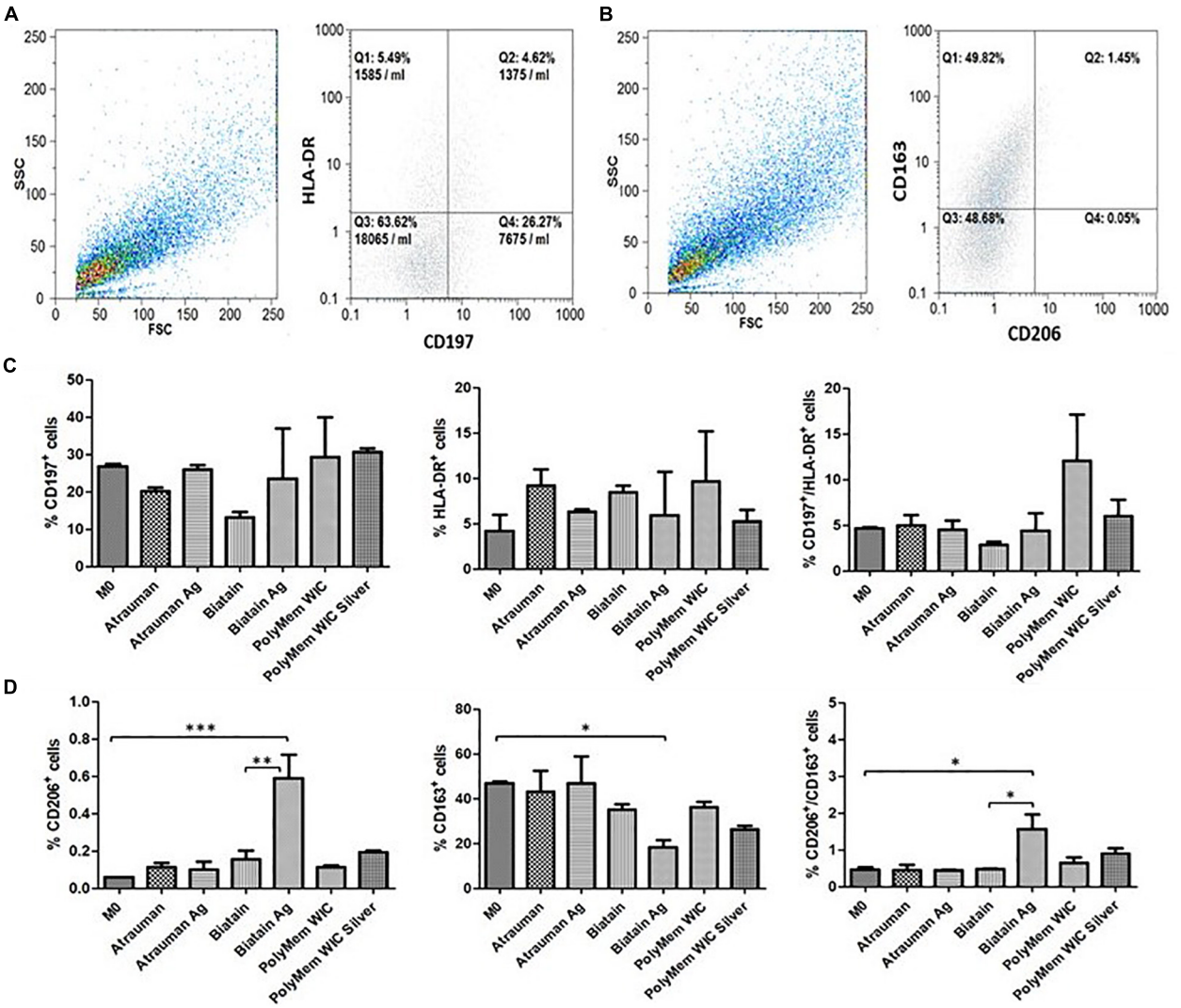

FIGURE 5 | Surface markers for phenotypical characterization of macrophage populations. **(A,B)** Representative dot plots from Flow cytometry of M0 macrophages; **(C)** Percentage of single positive CD197 cells, single positive HLA-DR and double positive $CD197^{+}$/HLA-DR. **(D)** Percentage of single positive CD206 cells, single positive CD163 and double positive $CD206^{+}/CD163^{+}$. p values ($^{*}p \leq 0.05$, $^{**}p \leq 0.01$, and $^{***}p \leq 0.001$) were determined for M0 vs. all materials and unloaded vs respective silver containing material of three independent experiments. Error bars represent standard deviation.

method, bacteria are "forced" to grow on the silver dressing creating an enclosed environment in which the thin agar inoculated layer is in closer contact with the wound dressing. This might be an explanation for the different results, because in both methods applied in our study bacteria are still growing on an optimal surface (MHB agar) or in a nutritious medium (MHB broth), probably avoiding the antibacterial effect from the Atrauman Ag dressing *in vitro*. It is also important to notice that metallic silver is relatively inert and releases biocidal Ag^{+} ions when interacting with moisture and wound fluid on skin, which have different constituents than the ones existing on MHB (Qin, 2009). This can be a factor that influenced the release of silver ions.

The polarization of macrophages involves plasticity in a continuous spectrum. Hence, in the case of PolyMem alone, macrophages might be shifting from a M1- to M2-state or be part of a mixed activation of M1/M2 phenotypes population (Bosurgi et al., 2011; Dalmas et al., 2011). This observation is not in accordance with the product description on the company website, in which it is strongly defined that PolyMem WIC (that contains glycerol and poloxamer 188) is an anti-inflammatory dressing. As published by Szél et al. (2015) glycerol is a simple polyol with anti-inflammatory properties Additionally, the anti-inflammatory effect induced by the non-ionic block copolymer surfactant Poloxamer 188 has also been confirmed (Harting et al., 2008). Hence it becomes clear that the increase on the production of the anti-inflammatory cytokines IL-10 and TGF-β is due to stimulation by glycerol and poloxamer 188, both present in this product. The reason concerning the increase on IL-1β secretion and expression of typical pro-inflammatory

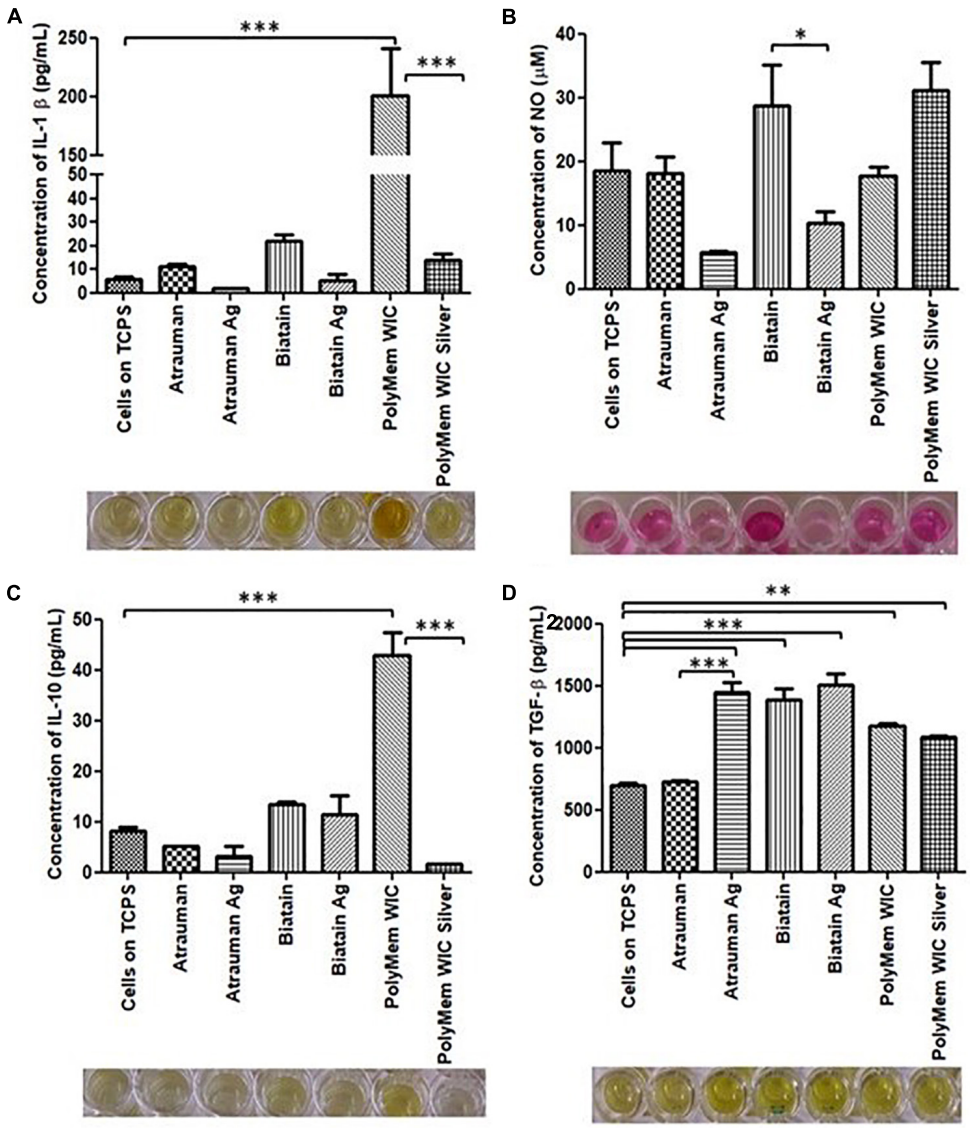

FIGURE 6 | Concentration of produced pro-inflammatory and anti-inflammatory signals by macrophages in the presence of different commercially available materials for 24 h. **(A)** concentration of IL-1β; **(B)** concentration of nitric oxide (NO); **(C)** concentration of IL-10; **(D)** concentration of TGF-β. p values (*$p \leq 0.05$, **$p \leq 0.01$, and ***$p \leq 0.001$) were determined for cells on TCPS (M0 macrophages) vs. all materials and untreated vs. respective silver containing dressing ($n = 3$). Error bars represent standard deviation.

membrane markers is not yet fully understood and it needs to be further investigated. It cannot be ruled out to be an artifact of the experimental design. Nonetheless, a significant drop on IL-1β production was observed when the macrophages were in the presence of PolyMem WIC with the nanocrystalline silver particles, proving once again the anti-inflammatory impact induced by silver ions and particles. This antimicrobial dressing showed a great antibacterial effect against the most common strains found in infected wounds exclusively in liquid medium. PolyMem WIC Silver was studied previously against *S. aureus* and *P. aeruginosa* and the same lack of antibacterial effect was observed on the agar disk diffusion test (Yunoki et al., 2015). Thus, the release of clusters of reactive small particles and silver ions from the nanocrystalline silver seems to be very reduced on agar. Moreover, Boonkaew et al. (2014) observed a zone of inhibition against *Staphylococcus aureus* if the material is pre-activated in 0.85% saline solution by inducing its swelling, before it is placed on the agar plate. Hence, it becomes clear that the fluid taken up by this polyurethane foam plays a major role in unleashing the antimicrobial power of nanocrystalline silver. Among all the dressings tested, it was noted that PolyMem and PolyMem WIC Silver were highly absorbent, entrapping a part of the liquid medium in the foam material. This was also observed by Burd et al. (2007) in which this absorbency capacity was associated with the very low release of silver ions measurement still in the presence of a significant antibacterial

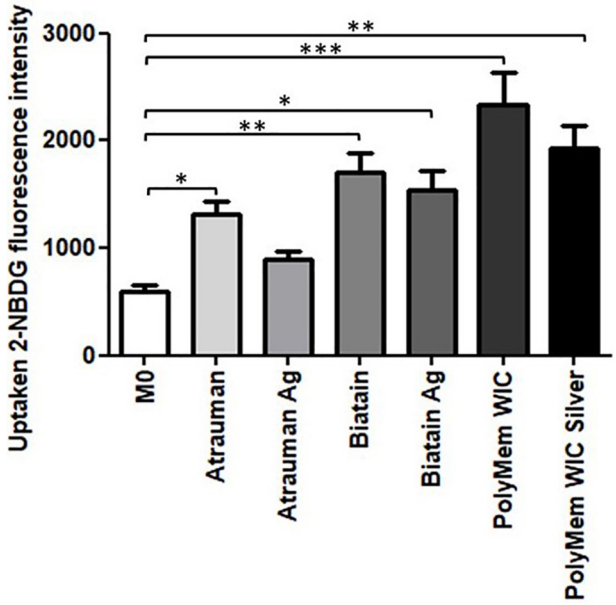

FIGURE 7 | Glucose consumption by monocyte-derived macrophages after exposure to the materials during 24 h. 2-NBDG, fluorescent D-glucose analog. Error bars represent standard deviation. Statistical significance determination is represented as $*p \leq 0.05$, $**p \leq 0.01$, and $***p \leq 0.001$ for cells on TCPS (M0 macrophages) vs. all materials, and untreated vs. respective silver containing dressing of three independent experiments.

effect. This result lead the authors to conclude that PolyMem WIC silver dressing induces its antibacterial effect mainly by "soaking" the pathogenic bacteria and its contaminants into the foam structure and induce its "killing" internally. In addition, the same authors stated that this could be a benefit, because it will decrease the possibility for toxicity on the healthy wound cells (Burd et al., 2007). However, this dressing brought a toxic effect to the 2D cell culture of fibroblasts, keratinocytes and monocyte-derived macrophages.

All silver-containing dressings tested induced a significant increase of TGF-β secretion, which has profibrotic activities and is associated to M2a and M2c subsets of M2 macrophages (Lu et al., 2013). Profibrotic action means that it promotes fibrosis which involves the overgrowth of an organ or tissue during a reparative process, by deposition of ECM components such as collagen (Wynn, 2008). Also, it was detected that macrophages consume slightly less glucose in the presence of the silver containing materials, demonstrating that these macrophages are polarizing on a continuous spectrum toward M2-macrophages (**Figure 7**) since an increased expression of glucose transporters (mainly GLUT1) on the membrane and higher rates of consumption of glucose has been associated to pro-inflammatory M1 macrophages. This is due to their metabolic adaptation in which they perform fermentation of glucose to obtain a rapid production of energy (Freemerman et al., 2014).

Although this study gives significant indications about the response of macrophages to different clinically applied biomaterials, the macrophages used were in a resting state (M0 macrophages), hence in future studies it is necessary to investigate the immunomodulatory effects of these same dressings on macrophages polarized to the M1 pro-inflammatory state due to the fact that in the wound environment this macrophage phenotype is predominant. It would be interesting to explore the same features with monocytes isolated from donors' blood, to have an *in vitro* set closer to human conditions. However, the main advantage of using a cell line such as THP-1 human monocytes is that the origin of cells is consistent in every assay, meaning less variability in the results obtained. Hence, these cells are anyway an effective tool to give insights of immunomodulation owed by biomaterial-macrophages interactions.

In addition, there was a decrease of viability of monocyte-derived macrophages in the presence of Biatain Alginate Ag, PolyMem WIC and PolyMem WIC Silver after 24 h. Toxicity of PolyMem Silver and Biatain Alginate Ag has been reported before, on *in vitro* indirect contact studies on diabetic fibroblasts, in which the authors registered a decrease in cell viability of more than 50% (Zou et al., 2013). Moreover, cytotoxicity of PolyMem Ag has been described in Yunoki et al. (2015) research article, in which the authors attribute the negative effect on mammalian cells to the uptake of silver clusters of large size by endocytosis. This may have influenced the results of the measured concentrations of pro-inflammatory and anti-inflammatory molecules, and the uptake of glucose. Nevertheless, in comparison with M0 macrophages, secretion of IL-1β, IL-10, and TGF-β increased significantly in macrophages in contact with PolyMem WIC. Also, for Biatain Alginate Ag and PolyMem WIC Silver the production of TGF-β was significantly higher than the M0 state, and the glucose uptake was increased in cells at the presence of the three wound dressings. Hence, although a smaller number of cells were attached to the bottom of the wells by the endpoint of the assay, higher concentrations of secreted cytokines in the supernatant and more glucose uptake were still detected.

CONCLUSION

One main finding of this work is that macrophages start to change their metabolism and phenotype in response to wound dressings of different composition in a short 1-day period. Moreover, silver has shown to possess anti-inflammatory properties. The other major final remark from this research work is, that it is clear that even with commercially available and clinically applied products the balance between antibacterial activity versus cytotoxicity *in vitro*, and stimulation of an optimal wound environment toward cutaneous-healing remains a significant challenge.

DATA AVAILABILITY STATEMENT

All datasets generated for this study are included in the article/supplementary material.

AUTHOR CONTRIBUTIONS

PV planned and performed all the experiments, conducted the treatment and interpretation of data, and contributed substantially to the writing of this article. LM helped in experimental work related to microbiological assays. SS and RV contributed to the revision of the manuscript. GC and JS contributed to the planning of experiments, interpretation of data, and manuscript writing and revision.

FUNDING

This work was supported by the "Drug-Free Antibacterial Hybrid Biopolymers for Medical Applications" HyMedPoly project and the European Union's Horizon 2020 Research and Innovation Programme under the Marie Skłodowska-Curie Action MSCAITN-2014-EID: Marie Skłodowska-Curie Innovative Training Networks (Grant number 643050).

ACKNOWLEDGMENTS

The authors would like to acknowledge Dr. Marcus Peters and Prof. Dr. med. Albrecht Bufe from Experimental Pneumology Group, Department of the Medical Faculty, Ruhr-Universität Bochum for the support in Flow Cytometry experiments. Moreover, the authors express their gratitude to Prof. Dr. med. Sören Gatermann from the Institute of Hygiene and Microbiology, Department of Medical Microbiology, Ruhr-Universität Bochum for the partnership established in the microbiology laboratory facilities.

REFERENCES

Baranoski, S., and Ayello, E. A. (2012). Wound dressings: an evolving art and science. *Adv. Ski. Wound Care* 25, 87–92. doi: 10.1097/01.ASW.0000411409.05554.c8

Berg, C., Trofast, C., and Bengtsson, T. (2003). Platelets induce reactive oxygen species-dependent growth of human skin fibroblasts. *Eur. J. Cell Biol.* 82, 565–571. doi: 10.1078/0171-9335-00344

Blair, J. M. A., Webber, M. A., Baylay, A. J., Ogbolu, D. O., and Piddock, L. J. V. (2015). Molecular mechanisms of antibiotic resistance. *Nat. Rev. Microbiol.* 13, 42–51.

Boonkaew, B., Kempf, M., Kimble, R., Supaphol, P., and Cuttle, L. (2014). Antimicrobial efficacy of a novel silver hydrogel dressing compared to two common silver burn wound dressings: ActicoatTM and PolyMem Silver®. *Burns* 40, 89–96. doi: 10.1016/j.burns.2013.05.011

Bosurgi, L., Manfredi, A. A., and Rovere-Querini, P. (2011). Macrophages in injured skeletal muscle: a perpetuum mobile causing and limiting fibrosis, prompting or restricting resolution and regeneration. *Front. Immunol.* 2:62. doi: 10.3389/fimmu.2011.00062

Burd, A., Kwok, C. H., Hung, S. C., Chan, H. S., Gu, H., Lam, W. K., et al. (2007). A comparative study of the cytotoxicity of silver-based dressings in monolayer cell, tissue explant, and animal models. *Wound Repair Regen.* 15, 94–104. doi: 10.1111/j.1524-475x.2006.00190.x

Burnham, J. P., Kirby, J. P., and Kollef, M. H. (2016). Diagnosis and management of skin and soft tissue infections in the intensive care unit: a review. *Intens. Care Med.* 42, 1899–1911. doi: 10.1007/s00134-016-4576-0

Coloplast (2015). *Biatain Ag Non-Adhesive*. Humlebaek: Coloplast.

Dalmas, E., Clément, K., and Guerre-Millo, M. (2011). Defining macrophage phenotype and function in adipose tissue. *Trends Immunol.* 32, 307–314. doi: 10.1016/j.it.2011.04.008

Dhivya, S., Padma, V. V., and Santhini, E. (2015). Wound dressings - a review. *Biomedicine* 5, 24–28.

Ferrante, C. J., and Leibovich, S. J. (2012). Regulation of macrophage polarization and wound healing. *Adv. Wound Care* 1, 10–16. doi: 10.1089/wound.2011.0307

Freemerman, A. J., Johnson, A. R., Sacks, G. N., Milner, J. J., Kirk, E. L., Troester, M. A., et al. (2014). Metabolic reprogramming of macrophages: glucose transporter 1 (GLUT1)-mediated glucose metabolism drives a proinflammatory phenotype. *J. Biol. Chem.* 289, 7884–7896. doi: 10.1074/jbc.M113.522037

Gjødsbøl, K., Christensen, J. J., Karlsmark, T., Jørgensen, B., Klein, B. M., and Krogfelt, K. A. (2006). Multiple bacterial species reside in chronic wounds: a longitudinal study. *Int. Wound J.* 3, 225–231. doi: 10.1111/j.1742-481x.2006.00159.x

Harting, M. T., Jimenez, F., Kozar, R. A., Moore, F. A., Mercer, D. W., Hunter, R. L., et al. (2008). Effects of poloxamer 188 on human PMN cells. *Surgery* 144, 198–203. doi: 10.1016/j.surg.2008.05.001

Hermans, M. H. (2006). Silver-containing dressings and the need for evidence. *Am. J. Nurs.* 106, 60–68. doi: 10.1097/00000446-200612000-00025

Hesketh, M., Sahin, K. B., West, Z. E., and Murray, R. Z. (2017). Macrophage phenotypes regulate scar formation and chronic wound healing. *Int. J. Mol. Sci.* 18, 1–10.

Ibberson, C. B., Stacy, A., Fleming, D., Dees, J. L., Rumbaugh, K., Gilmore, M. S., et al. (2017). Co-infecting microorganisms dramatically alter pathogen gene essentiality during polymicrobial infection. *Nat. Microbiol.* 2, 1–6. doi: 10.1038/nmicrobiol.2017.79

International Organization for Standardization (2009). *ISO 10993-5 Biological Evaluation Of Medical Devices - Part 5: Tests for in Vitro Cytotoxicity*. Geneva: International Organization for Standardization.

Krzyszczyk, P., Schloss, R., Palmer, A., and Berthiaume, F. (2018). The role of macrophages in acute and chronic wound healing and interventions to promote pro-wound healing phenotypes. *Front. Physiol.* 9:419. doi: 10.3389/fphys.2018.00419

Landén, N. X., Li, D., and Ståhle, M. (2016). Transition from inflammation to proliferation: a critical step during wound healing. *Cell. Mol. Life Sci.* 73, 3861–3885. doi: 10.1007/s00018-016-2268-0

Lansdown, A. B. G. (2014). Silver I: its antibacterial properties and mechanism of action. *J. Wound Care* 11, 125–130. doi: 10.12968/jowc.2002.11.4.26389

Leaper, D., Assadian, O., and Edmiston, C. E. (2015). Approach to chronic wound infections. *Br. J. Dermatol.* 173, 351–358. doi: 10.1111/bjd.13677

Leaper, D. J. (2006). Silver dressings: their role in wound management. *Int. Wound J.* 3, 282–311.

Lins, K. O. A. L., Vale, M. L., Ribeiro, R. A., and Costa-Lotufo, L. V. (2013). Proinflammatory activity of an alginate isolated from *Sargassum vulgare*. *Carbohydr. Polym.* 92, 414–420. doi: 10.1016/j.carbpol.2012.08.101

Lu, J., Cao, Q., Zheng, D., Sun, Y., Wang, C., Yu, X., et al. (2013). Discrete functions of M 2a and M 2c macrophage subsets determine their relative efficacy in treating chronic kidney disease. *Kidney Int.* 84, 745–755. doi: 10.1038/ki.2013.135

Matuschek, E., Brown, D. F. J., and Kahlmeter, G. (2014). Development of the EUCAST disk diffusion antimicrobial susceptibility testing method and its implementation in routine microbiology laboratories. *Clin. Microbiol. Infect.* 20, 255–266. doi: 10.1111/1469-0691.12373

Nam, G., Rangasamy, S., Purushothaman, B., and Song, J. M. (2015). The application of bactericidal silver nanoparticles in wound treatment. *Nanomater. Nanotechnol.* 5:23. doi: 10.5772/60918

Novak, M. L., and Koh, T. J. (2013). Macrophage phenotypes during tissue repair. *J. Leukoc. Biol.* 93, 875–881. doi: 10.1189/jlb.1012512

Ogle, M. E., Segar, C. E., Sridhar, S., and Botchwey, E. A. (2016). Monocytes and macrophages in tissue repair: implications for immunoregenerative biomaterial design. *Exp. Biol. Med.* 241, 1084–1097. doi: 10.1177/1535370216650293

Piddock, L. J. V. (2017). Understanding drug resistance will improve the treatment of bacterial infections. *Nat. Rev. Microbiol.* 15, 639–640. doi: 10.1038/nrmicro.2017.121

Qin, Y. (2009). Antimicrobial textile dressings in managing wound infection. *Adv. Text. Wound Care* 2009, 179–197. doi: 10.1533/9781845696306.1.179

Rosique, R. G., Rosique, M. J., and Farina Junior, J. A. (2015). Curbing inflammation in skin wound healing: a review. *Int. J. Inflam.* 2015:316235. doi: 10.1155/2015/316235

Schairer, D. O., Chouake, J. S., Nosanchuk, J. D., and Friedman, A. J. (2012). The potential of nitric oxide releasing therapies as antimicrobial agents. *Virulence* 3, 271–279. doi: 10.4161/viru.20328

Shaw, T. J., and Martin, P. (2009). Wound repair at a glance. *J. Cell Sci.* 122(Pt 18), 3209–3213. doi: 10.1242/jcs.031187

Simões, D., Miguel, S. P., Ribeiro, M. P., Coutinho, P., Mendonça, A. G., and Correia, I. J. (2018). Recent advances on antimicrobial wound dressing: a review. *Eur. J. Pharm. Biopharm.* 127, 130–141. doi: 10.1016/j.ejpb.2018.02.022

Sindrilaru, A., and Scharffetter-Kochanek, K. (2013). Disclosure of the culprits: macrophages—versatile regulators of wound healing. *Adv. Wound Care* 2, 357–368. doi: 10.1089/wound.2012.0407

Sütterlin, S., Tano, E., Bergsten, A., Tallberg, A. B., and Melhus, A. (2012). Effects of silver-based wound dressings on the bacterial flora in chronic leg ulcers and its susceptibility in vitro to silver. *Acta Derm. Venereol.* 92, 34–39. doi: 10.2340/00015555-1170

Szél, E., Polyánka, H., Szabõ, K., Hartmann, P., Degovics, D., Balázs, B., et al. (2015). Anti-irritant and anti-inflammatory effects of glycerol and xylitol in sodium lauryl sulphate-induced acute irritation. *J. Eur. Acad. Dermatol. Venereol.* 29, 2333–2341. doi: 10.1111/jdv.13225

Valente, T. A. M., Silva, D. M., Gomes, P. S., Fernandes, M. H., Santos, J. D., and Sencadas, V. (2016). Effect of sterilization methods on electrospun poly(lactic acid) (PLA) fiber alignment for biomedical applications. *ACS Appl. Mater. Interf.* 8, 3241–3249. doi: 10.1021/acsami.5b10869

Velnar, T., Bailey, T., and Smrkolj, V. (2009). The wound healing process: an overview of the cellular and molecular mechanisms. *J. Int. Med. Res.* 37, 1528–1542. doi: 10.1177/147323000903700531

Wilkinson, L. J., White, R. J., and Chipman, J. K. (2011). Silver and nanoparticles of silver in wound dressings: a review of efficacy and safety. *J. Wound Care* 20, 543–549. doi: 10.12968/jowc.2011.20.11.543

Wynn, T. A. (2008). Cellular and molecular mechanisms of fibrosis. *J. Pathol.* 214, 199–210.

Yamane, K., and Leung, K. P. (2016). Rabbit M1 and M2 macrophages can be induced by human recombinant GM-CSF and M-CSF. *FEBS Open Bio.* 6, 945–953. doi: 10.1002/2211-5463.12101

Yunoki, S., Kohta, M., Ohyabu, Y., and Iwasaki, T. (2015). In vitro parallel evaluation of antibacterial activity and cytotoxicity of commercially available silver-containing wound dressings. *Plast. Surg. Nurs.* 35, 203–211. doi: 10.1097/PSN.0000000000000096

Zewde, B., Ambaye, A., Stubbs Iii, J., and Raghavan, D. (2016). A review of stabilized silver nanoparticles – Synthesis, biological properties, characterization, and potential areas of applications. *JSM Nanotechnol. Nanomed.* 4:1043.

Ziegler, K., Görl, R., Effing, J., Ellermann, J., Mappes, M., Otten, S., et al. (2006). Reduced cellular toxicity of a new silver-containing antimicrobial dressing and clinical performance in non-healing wounds. *Skin Pharmacol. Physiol.* 19, 140–146. doi: 10.1159/000092594

Zou, S. B., Yoon, W. Y., Han, S. K., Jeong, S. H., Cui, Z. J., and Kim, W. K. (2013). Cytotoxicity of silver dressings on diabetic fibroblasts. *Int. Wound J.* 10, 306–312. doi: 10.1111/j.1742-481X.2012.00977.x

Conflict of Interest: The authors declare that the research was conducted in the absence of any commercial or financial relationships that could be construed as a potential conflict of interest.

frontiers in Bioengineering and Biotechnology

ORIGINAL RESEARCH
published: 15 May 2020
doi: 10.3389/fbioe.2020.00442

Activated Polyhydroxyalkanoate Meshes Prevent Bacterial Adhesion and Biofilm Development in Regenerative Medicine Applications

Sheila Piarali[1,2], Lennart Marlinghaus[3], Richard Viebahn[1], Helen Lewis[4], Maxim G. Ryadnov[4], Jürgen Groll[5], Jochen Salber[1†] and Ipsita Roy[6*†]*

[1] Department of Surgery, Universitätsklinikum Knappschaftskrankenhaus Bochum, Ruhr-University, Bochum, Germany, [2] Applied Biotechnology Research Group, School of Life Sciences, College of Liberal Arts and Sciences, University of Westminster, London, United Kingdom, [3] Department of Medical Microbiology, Ruhr-University Bochum, Bochum, Germany, [4] National Physical Laboratory, Teddington, United Kingdom, [5] Department for Functional Materials in Medicine and Dentistry and Bavarian Polymer Institute, University of Würzburg, Würzburg, Germany, [6] Department of Material Science and Engineering, Faculty of Engineering, University of Sheffield, Sheffield, United Kingdom

OPEN ACCESS

Edited by:
Francesca Boccafoschi,
Università degli Studi del Piemonte Orientale, Italy

Reviewed by:
Livia Visai,
University of Pavia, Italy
Joanna Mystkowska,
Białystok Technical University, Poland

***Correspondence:**
Jochen Salber
jochen.salber@hotmail.com
Ipsita Roy
I.Roy@sheffield.ac.uk

† These authors have contributed equally to this work and share senior authorship

Specialty section:
This article was submitted to Biomaterials, a section of the journal Frontiers in Bioengineering and Biotechnology

Received: 29 February 2020
Accepted: 17 April 2020
Published: 15 May 2020

Citation:
Piarali S, Marlinghaus L, Viebahn R, Lewis H, Ryadnov MG, Groll J, Salber J and Roy I (2020) Activated Polyhydroxyalkanoate Meshes Prevent Bacterial Adhesion and Biofilm Development in Regenerative Medicine Applications. Front. Bioeng. Biotechnol. 8:442. doi: 10.3389/fbioe.2020.00442

Regenerative medicine has become an extremely valuable tool offering an alternative to conventional therapies for the repair and regeneration of tissues. The re-establishment of tissue and organ functions can be carried out by tissue engineering strategies or by using medical devices such as implants. However, with any material being implanted inside the human body, one of the conundrums that remains is the ease with which these materials can get contaminated by bacteria. Bacterial adhesion leads to the formation of mature, alive and complex three-dimensional biofilm structures, further infection of surrounding tissues and consequent development of complicated chronic infections. Hence, novel tissue engineering strategies delivering biofilm-targeted therapies, while at the same time allowing tissue formation are highly relevant. In this study our aim was to develop surface modified polyhydroxyalkanoate-based fiber meshes with enhanced bacterial anti-adhesive and juvenile biofilm disrupting properties for tissue regeneration purposes. Using reactive and amphiphilic star-shaped macromolecules as an additive to a polyhydroxyalkanoate spinning solution, a synthetic antimicrobial peptide, Amhelin, with strong bactericidal and anti-biofilm properties, and Dispersin B, an enzyme promoting the disruption of exopolysaccharides found in the biofilm matrix, were covalently conjugated to the fibers by addition to the solution before the spinning process. *Staphylococcus epidermidis* is one of the most problematic pathogens responsible for tissue-related infections. The initial antibacterial screening showed that Amhelin proved to be strongly bactericidal at 12 μg/ml and caused >50% reductions of biofilm formation at 6 μg/ml, while Dispersin B was found to disperse >70% of pre-formed biofilms at 3 μg/ml. Regarding the cytotoxicity of the agents toward L929 murine fibroblasts, a CC_{50} of 140 and 115 μg/ml was measured for Amhelin and Dispersin B, respectively. Optimization of the electrospinning process resulted in aligned fibers. Surface activated fibers with Amhelin and Dispersin B resulted in 83% reduction of adhered bacteria on the surface of the fibers. Additionally, the materials developed

were found to be cytocompatible toward L929 murine fibroblasts. The strategy reported in this preliminary study suggests an alternative approach to prevent bacterial adhesion and, in turn biofilm formation, in materials used in regenerative medicine applications such as tissue engineering.

Keywords: polyhydroxyalkanoates, Amhelin, Dispersin B, biofilm, electrospinning

INTRODUCTION

Within regenerative medicine applications, the failure of implantable *in situ* tissue engineering scaffolds, that should replace missing or damaged tissue and recruit cells from the surrounding tissues of the host, bears generally the probability of bacterial adhesion to its external and internal surface and subsequent biofilm formation at the time point of implantation or even later by hematogenous spread. Finally, this leads to a chronically colonized biomaterial scaffold with the intrinsic capability to induce an infection at any later time (Brancatisano et al., 2014; Segev-Zarko et al., 2015; Batoni et al., 2016).

Biofilms can tolerate various types of physicochemical treatments including UV light, heavy metals, acidity, changes in hydration or salinity, and phagocytosis. Additionally, biofilms typically resist antibiotics even at high concentrations (Lebeaux et al., 2014). The complexity of the biofilm structure, decreased growth rates, secretion of enzymes capable of degrading antibiotics, horizontal gene transfer and communication via quorum sensing systems are just few of the main factors involved in the resistance of biofilms against antibiotics (Donlan and Costerton, 2002; Wi and Patel, 2018). Clearly this leads to many therapeutic difficulties and most of the times the solution involves surgical removal of all foreign material (e.g., medical device, implant or scaffold) and comprehensive debridement of the infected tissue (Zimmerli and Moser, 2012). This, along with the lack of treatment options against biofilms, emphasizes the need to develop new locally acting antibacterial, anti-adhesive and anti-biofilm materials in the regenerative medicine field.

Tissue formation can be prompted by using polymeric scaffolds with specific characteristics. For instance, fibrous polymeric scaffolds are extremely attractive for tissue engineering applications due to their topographical similarities with the fibrillae of the extracellular matrix (ECM) and can be produced using a simple, cost-effective, and versatile approach such as electrospinning (Repanas et al., 2016).

In terms of the choice of the polymeric material, there are a variety of natural and synthetic polymers suitable for the development of tissue engineering scaffolds, development of medical implants and antimicrobial surfaces. Polyhydroxyalkanoates (PHAs) are highly biocompatible and naturally occurring bacteria-derived polyesters and are produced by bacterial fermentation (Lebeaux et al., 2014; Li et al., 2016). A variety of PHAs with different properties and degradation rates can be obtained by changing the conditions of the fermentation process. Furthermore, PHAs can be processed using several techniques such as solvent casting, dip molding, 3D printing and electrospinning, making them attractive candidates for a variety of medical applications (Reis et al., 2008; Roy and Visakh, 2014).

Regarding the fiber activation against bacteria, it can be done by covalent attachment of antibacterial agents such as enzymes and antimicrobial peptides.

Dispersin B (DB) is a 42 kDa glycoside hydrolase produced by a Gram-negative bacteria *Aggregatibacter actinomycetemcomitans*, a human periodontal pathogen. DB is capable of degrading polysaccharides present in the biofilm matrix of many bacterial strains, resulting in the detachment of the bacterial cells (swarming phenotypes) and their release into the environment. More specifically, it degrades cationic extracellular polysaccharides, namely β-1,6-poly-N-acetylglucosamine (PNAG), that work as adhesins and mediate the attachment of bacteria to abiotic surfaces (Kaplan, 2009, 2010).

Antimicrobial peptides (AMPs), on the other hand, have been extensively explored as an alternative to conventional antibiotics due to their exceptionally broad spectrum of activity against bacteria, bactericidal efficacy at low concentrations as well as their multiple modes of action (Onaizi and Leong, 2011). AMPs vary by size, comprising 10–50 amino-acid residues, net charge, primary and secondary structures. However, these peptides also share common characteristics. Most of them are cationic and fold upon binding to anionic microbial membranes into amphipathic structures by clustering cationic and hydrophobic residues in two distinct faces (Ebbensgaard et al., 2015). Because their action is folding mediated, it can be controlled in a dose dependent and reversible manner (Ryan et al., 2013). Once in the membranes, the peptides arrange into membrane-disrupting pores or channels that destabilize microbial cells, resulting in cell lysis and death (Powers and Hancock, 2003; Brogden, 2005; Hancock and Sahl, 2006). One of the reasons for conventional antibiotics to fail against biofilms is their inability to target cells with low metabolic activity. Membrane integrity is essential to bacteria regardless of their metabolic state, whilst AMPs do not differentiate between dormant, dividing or mature bacterial cells, killing all. Therefore, the use of AMPs against cells that are resistant to antibiotics presents an effective strategy to prevent biofilm formation or treat established biofilms. However, despite their activity, naturally occurring AMPs pose some limitations regarding their toxicity against eukaryotic cells and therefore synthetic AMPs are now gaining more attention as they can show reduced cytotoxicity (Steinstraesser et al., 2002). Antimicrobial helix insert (here termed as Amhelin) is a novel *de novo* sequence designed as an archetypal antimicrobial peptide. The peptide folds into an amphipathic α helix in microbial lipid bilayers where it forms progressively expanding pores (Rakowska et al., 2013).

Unlike many AMPs, Amhelin does not cause hemolytic effects either, with median lethal concentrations (LC_{50}) against human erythrocytes significantly exceeding the measured CC_{50} (Ryadnov et al., 2009; Li et al., 2017).

Antimicrobial peptides or enzymes are normally attached to fiber surfaces post-processing by covalent attachment, which usually involves several activation steps and includes the use of chemical cross-linkers. An alternative approach was reported by Grafahrend et al., where they used an amphiphilic six-armed star-shaped poly(ethylene oxide-stat-propylene oxide) containing reactive isocyanate groups at the distal ends of the polymer chains, NCO-sP(EO-stat-PO), as an additive to the PLGA spinning solution. The presence of the isocyanate groups facilitated the covalent coupling of cell adhesion peptides by addition of these peptides to the spinning solution, thus resulting in the production of surface-activated fibers in a single step (Grafahrend et al., 2011). This approach has recently been used to produce artificial basement-membranes as a component for the generation of *in vitro* skin tissue and expanded for multi-functionalization with peptides and antibodies for immunomodulatory properties (Wistlich et al., 2015; Rossi et al., 2016).

In this study, we transferred this strategy to PHAs and developed PHA-[NCO-sP(EO-stat-PO)] based blend fibers which we functionalized with membrane targeting Amhelin and with the biofilm-disrupting enzyme DB. These substrates allowed us to study the effect of fiber functionalization against bacterial adhesion and the establishment of predominantly polysaccharide-based biofilms, such as staphylococcal biofilms, whilst still allowing for eukaryotic cell attachment. Our experiments demonstrate that the resulting material combines anti-adhesive and anti-biofilm properties, and hence holds huge promise for medical applications.

MATERIALS AND METHODS

Materials

Chemicals, reagents and materials were obtained from Sigma-Aldrich Company Ltd., (United Kingdom and Germany), Thermo Fisher Scientific (United Kingdom and Germany), VWR International (United Kingdom), and Carl Roth GmbH + Co., KG (Germany).

Polymers and Antibacterial Agents

Polyhydroxyalkanoates were produced by bacterial fermentation under nitrogen limiting conditions and with glucose as the carbon source using *Pseudomonas mendocina* CH50 at the Department of Life Sciences in the University of Westminster, London, United Kingdom.

Amphiphilic six-armed star-shaped poly(ethylene oxide-stat-propylene oxide) containing reactive isocyanate groups at the distal ends of the polymer chains, NCO-sP(EO-stat-PO), was provided by Prof. Jürgen Groll, Department for Functional Materials in Medicine and Dentistry and Bavarian Polymer Institute, University of Würzburg, Würzburg, Germany.

Dispersin B was provided by Kane Biotech Inc., (Canada) in vials containing a buffer solution consisting of 50 mM phosphate buffer (pH 5.8) with 100 mM sodium chloride and 50% glycerol at a concentration of 475 μg/mL per vial. Amhelin was synthesized by the National Physical Laboratory (United Kingdom) and was provided in the form of a lyophilized powder. The peptide was kept in the freezer, at −20°C for routine usage.

Bacterial Strains

All antibacterial tests were conducted using the biofilm forming strain *Staphylococcus epidermidis* (ATCC® 35984™), purchased from the American Type Culture Collection (ATCC). The bacterial culture was stored as glycerol stocks in the freezer, at −20°C, for routine usage or at −80°C for longer storage duration.

The preparation of the inoculum for all antibacterial tests was done by culturing bacteria overnight on blood agar plates at 37°C for 16 h. Using a sterile loop, a single colony was re-suspended in a glass tube containing 2 mL of 0.9% NaCl and using a densitometer, the bacterial suspension was adjusted to McFarland 0.5 (10^8 CFU/mL). According to each experiment, the bacterial suspension was further diluted in Mueller-Hinton-Broth (MHB) to the desired concentration.

Cell Lines and Cell Culture Materials

L929 murine fibroblasts were obtained from DSMZ (German Collection of Microorganisms and Cell Cultures GmbH). Roswell Park Memorial Institute (RPMI) medium, L-glutamine, 10% fetal bovine serum and 1% Penicillin-Streptomycin (10.000 U/mL Penicillin, 10 mg/mL Streptomycin) were obtained from PAN Biotech (Germany), as well as trypsin 0.25%/1 mM EDTA and Dulbecco's Phosphate-Buffered Saline (DPBS) without calcium and magnesium. Triton® X-100 lysis solution and CellTiter-Blue® Cell Viability Assay Kit were purchased from Promega. Live/dead Cell Staining Kit II was purchased from PromoKine.

L929 murine fibroblasts were cultivated in complete Roswell Park Memorial Institute medium, containing L-glutamine, 10% fetal bovine serum and 1% Penicillin-Streptomycin (10.000 U/mL Penicillin, 10 mg/mL Streptomycin) (cRPMI) and maintained in a humidified atmosphere at 5% CO_2 in air at 37°C. When cells reached 70–80% confluency, they were detached using a trypsin/EDTA solution, collected, and the number of cells was adjusted in a cell suspension according to each experiment. In order to avoid variations in cell viability tests, cells were used until passage 10.

Minimum Inhibitory and Minimum Bactericidal Concentrations of Amhelin Against Bacteria

The minimum inhibitory concentration (MIC) and the minimum bactericidal concentration (MBC) of Amhelin was determined against *S. epidermidis* (ATCC® 35984™) according to the ISO 20776-1:International Organization for Standardization [ISO], 2006 guidelines in 96 tissue-culture polystyrene (TCPS) microplates (ISO 20776-1:International Organization for Standardization [ISO], 2006(E)).

Briefly, Amhelin was prepared by making a stock solution of 1 mg/mL in sterile Milli Q water. The stock solution was further diluted in MHB to a final concentration of 200 μg/mL. A fresh bacterial suspension of 5×10^5 CFU/mL was prepared in MHB and serial 2-fold dilutions were prepared by incubating 50 μL of the bacterial suspension with 50 μL of the Amhelin solution. The plates were incubated at 37°C for 24 h and the MIC was determined as the lowest concentration of Amhelin that completely inhibited bacterial growth by observing the turbidity of the wells by naked eye. Wells containing 100 μL of MHB without bacteria were considered as negative controls and wells containing 100 μL of MHB with bacteria were considered as the growth controls. The experiments were performed in three independent experiments, in triplicates ($N = 3$, $n = 3$). The MBC was determined directly after identifying the MIC. For that, the supernatant of the wells corresponding to the MIC and of three concentrations above were removed and spread homogeneously onto blood agar plates with the help of a sterile loop. The plates were incubated at 37°C for 24 h. After the incubation period, the number of colonies were counted and compared to the number of colonies obtained in the growth controls at the beginning of the experiment. The MBC was determined as the lowest concentration of the compound that killed 99.9% or more of the bacteria, relative to that in the initial inoculum. The experiments were performed in three independent experiments, in duplicates ($N = 3$, $n = 2$).

Inhibition of Biofilm Formation by Amhelin

The ability of Amhelin to inhibit biofilm formation was evaluated by quantifying the amount of biofilm formed after a 24-hour incubation of bacteria with increasing concentrations of Amhelin, by adapting the protocol described by Kiran et al. (2008). Similar to the previous method, serial dilutions of Amhelin were incubated with a fresh bacterial suspension of 5×10^5 CFU/mL. After a 24-hour incubation period, the supernatant was entirely removed from the wells and the wells were carefully washed twice with 100 μL of DPBS and dried at room temperature. To fix the biofilms, 100 μL of 100% ethanol were added to each well and the plate was incubated for 15 minutes at room temperature. The ethanol was removed, and the biofilms were stained with 100 μL of a 0.1% safranin-O solution and incubated for 5 min at room temperature followed by a washing step with 100 μL of DPBS. Finally, the stained biofilms were re-suspended in 100 μL of 1% sodium dodecyl sulfate (SDS) and the amount of biofilm was quantified by measuring the optical density of the dissolved safranin-O at 495 nm (OD_{495}). The experiments were performed in three independent experiments, in triplicates ($N = 3$, $n = 3$).

Dispersion of Pre-established Biofilms by Dispersin B

The ability of DB to disperse 24-hour pre-formed biofilms was tested against *S. epidermidis* (ATCC® 35984™) in a 96 well TCPS microplate according to Marcano et al. (2015).

Each well was loaded with 100 μL of a bacterial suspension of 5×10^5 CFU/mL and incubated at 37°C for 24 h. After this period, the supernatant was carefully removed and filled with 100 μL of serially diluted concentrations of DB in MHB and incubated at 37°C for 24 h. After the incubation period, the supernatant was removed, and the quantification of the biofilm biomass was performed as described in section "Inhibition of Biofilm Formation by Amhelin." The experiments were performed in three independent experiments, in triplicates ($N = 3$, $n = 3$).

In vitro Direct Cytotoxicity Evaluation of Amhelin and Dispersin B

The cytotoxicity of Amhelin and DB were evaluated by performing a direct cytotoxicity study and by calculating the cell viability using the CellTiter-Blue® Cell Viability Assay. The experiment was performed following the ISO 10993-5 guidelines [ISO 10993- 5:International Organization for Standardization [ISO], 2009(E)] in 96 well TCPS microplates.

The CellTiter-Blue® Cell Viability Assay was used to estimate the number of viable cells after their exposure to increasing concentrations of Amhelin and DB for a period of 24 h. The assay is based on the capability of metabolically active cells, that is, living cells to convert the redox dye resazurin into a fluorescent resorufin which is analyzed using a plate-reading fluorometer. Briefly, on a 96 well TCPS microplate, 100 μL of a cell suspension containing 10^4 cells was seeded per well and incubated in a humidified atmosphere at 5% CO_2 in air, at 37°C, for 24 h, to promote cell attachment. On the next day, the cell media was discarded from each well and 100 μL of increasing concentrations of each agent, in cRPMI, were added to each well. The cells were incubated in a humidified atmosphere at 5% CO_2, in air, at 37°C, for another 24 h. TCPS was used as negative control and the positive control was composed of lysed cells after being treated with 2 μL of 9% Triton® X-100 (Promega) for 5 min after the 24-hour incubation period. After the incubation period, the cell supernatant was removed from the wells and 120 μL of the assay reagent (CellTiter-Blue diluted with cRMPI) was added to each well and incubated in a humidified atmosphere at 5% CO_2 in air at 37°C, for 2 h. After the incubation period, the supernatant was transferred to a black 96 well TCPS microplate and the fluorescence was read at 560 nm. The experiments were performed in two independent experiments, in quadruplicate ($N = 2$, $n = 4$).

Fabrication of Aligned and Bead-Less PHA Fibers by Electrospinning

The production of PHA fibers was carried out using a custom-built electrospinning setting composed of a high voltage power supply, a syringe pump and a rotating steel cylindrical collector. A 2 mL polypropylene syringe (BD Discardit™ II) equipped with a 23-gauge steel needle with a blunt tip was used to fabricate the fibers. The polymer solutions were fed free of air bubbles to the 2 mL syringe and the fibers were electrospun at a flow rate of 5 mL/h, with a 14 kV voltage, a needle-to-collector distance of 14 cm and a rotator speed of 1000 rpm. All fibers were electrospun to 1 cm diameter glass coverslips. After the electrospinning process, a drying period of at least 24 h was used to allow the complete evaporation of any remaining solvent

from the fibers inside a biological safety cabinet, in ambient conditions. Subsequently, the fibers were sterilized under the UV light – UVGI at short-wavelength ultraviolet light (UV-C, mercury-based lamp emitting UV light of 253.7 nm) for 30 min. PHAs were dissolved in a 60:40 chloroform/acetone solution at 20 w/v% and the fibers were electrospun directly from this solution.

The surface morphology of the fibers was analyzed by scanning electron microscopy (SEM). The images were taken with an acceleration voltage of 5 kV at a 10 mm working distance. The analysis was carried out at the Analytical Chemistry – Center for Electrochemical Sciences (CES) at the Ruhr-University Bochum, Germany.

Surface Activation of PHA Fibers

The activation of the PHA fibers was carried out using NCO-sP(EO-stat-PO), in order to promote the covalent coupling of active agents. For that, PHA was dissolved in a 60:40 chloroform/acetone solution at 20 w/v% and NCO-sP(EO-stat-PO) was dissolved in acetone at 5 w/v%. Once each solution was homogeneous, both solutions were mixed and vortexed vigorously. PHA-NCO-sP(EO-stat-PO) fibers were electrospun directly from this solution.

Bioactivated fibers were produced by coupling Amhelin and DB to PHA-NCO-sP(EOstat-PO) fibers. Briefly, using a ratio of 1:10, Amhelin:NCO-sP(EO-stat-PO), the required amount of peptide in the form of lyophilized powder was dissolved in a solution containing 50 μg/mL of DB. The solution was mixed and vortexed vigorously and fibers were electrospun directly from this solution.

Using the same conditions described in section "Fabrication of Aligned and Bead-Less PHA Fibers by Electrospinning," fibers were electrospun onto 1 cm diameter glass coverslips. After the electrospinning process, a drying period of at least 24 h was used to allow the complete evaporation of any remaining solvent from the fibers, inside a biological safety cabinet, in ambient conditions. Subsequently, the fibers were sterilized under the UV light - UVGI at short-wavelength ultraviolet (UV-C, mercury-based lamp emitting UV light at the 253.7 nm line) for 30 min.

The set of fibers produced in this study were PHA fibers, PHA-NCO-sP(EO-stat-PO) fibers and PHA-NCO-sP(EO-stat-PO) + Amhelin + DB fibers.

Water Contact Angle of Activated Fibers

The wettability of the modified fibers was evaluated by the static sessile drop method using a custom-built contact angle goniometer. On an average, 30 μL of deionized water was dropped onto the surface of the fibers with the help of a syringe. The contact angle was measured using a custom-built software. Analysis was carried out by the Analytical Chemistry – Biointerfaces group located at the Ruhr-University Bochum, Germany. The measurements were performed in triplicates ($n = 3$).

Further experiments were carried out with PHA and PHA-NCO-sP(EO-stat-PO) fibers on glass coverslips using different pre-conditioning procedures to verify the WCAs measured on the dried fiber mesh surfaces. The substrates were incubated in a deionized water-saturated atmosphere at 37°C for 4 h. Afterward, WCA measurements were carried out as previously described but this time as two independent experiments, in 10-fold ($N = 2$, $n = 10$).

Anti-adhesive Properties of Activated Fibers

To evaluate the anti-adhesion properties of the modified fibers, glass coverslips containing the fibers were placed in a sterile 24-well polystyrene microtiter plate and each well was inoculated with 1 ml of a bacterial suspension containing 5×10^5 CFU/mL. The plate was incubated at 37°C for 24 h in under static conditions. After the incubation period, the liquid content from the wells was removed and each fiber coated glass coverslip was washed twice with PBS to remove loosely adhered bacterial cells. Each sample was placed in sterile tubes containing 10 mL of 0.9% sodium chloride and sonicated in a sonication bath for 5 min followed by vortex mixing for 10 s to detach the bacterial cells. The procedure was repeated three times. The sonicates were serially diluted in 0.9% sodium chloride and 100 μL of each dilution were plated onto blood agar plates. After an 18-hour incubation at 37°C, the colonies were counted and expressed as CFU/ml. To complement the test, after the sonication procedure, the glass coverslips were immersed in an 100% ethanol solution for 15 min, then stained with a 0.1% safranin-O solution and incubated for 5 min at room temperature, followed by two-washing steps with DPBS. The stained-glass coverslips were dried overnight and imaged using a Panasonic DMC-FZ100. The experiments were performed in three independent experiments, in triplicates ($N = 3$, $n = 3$).

In vitro Direct Cytotoxicity Evaluation of Activated Fibers

To evaluate the fiber cytocompatibility, the CellTiter-Blue® Cell Viability Assay was performed. Briefly, sterile glass coverslips containing the modified fibers were placed in a 24-well polystyrene microtiter plate. A L929 cell suspension containing 5×10^4 cells was seeded per well on top of each glass coverslip and incubated in a humidified atmosphere of 5% CO_2 in air at 37°C for 24 h. Following the incubation period, the cell supernatant was removed and 250 μL of assay reagent (CellTiter-Blue diluted with cRMPI) was added to each well and incubated in a humidified atmosphere of 5% CO_2 in air at 37°C, for 2 h. After the incubation period, 120 μL of each well were transferred to a black 96-well polystyrene microtiter plate and the fluorescence was read at 560 nm. Tissue Culture Plastic (TCP) and non-modified fibers were used as the positive controls and the negative control was a lysis solution composed of Triton® X-100 used to cause cell lysis.

Live-Dead Staining of L929 Murine Fibroblasts on Activated Fibers

In order to correlate the data obtained via the CellTiter-Blue® Cell Viability Assay, a fluorescent cell staining was performed using a two-color fluorescent staining. Calcein-AM was used to stain live cells in green and Ethidium homodimer-III (EthD-III) was used to stain dead cells in red. Living cells are characterized by

the presence of intracellular esterase activity which can convert non-fluorescent Calcein-AM to green fluorescent Calcein. On the other hand, EthD-III can enter the cells that have a damaged membrane and upon binding to nucleic acids can produce red fluorescence. After growing the cells on top of the modified fibers, the culture medium was removed, and each well was washed with DPBS. A staining solution of 2 μM Calcein-AM/4 μM EthD-III was prepared in PBS and 480 μL of the staining solution were added directly to each well. The cells were imaged using an inverted fluorescence microscope (Olympus IX51).

Statistical Analysis

Experiments were performed on freshly prepared samples and the results were reported as averages and standard deviations of these measurements. The statistical analysis was done using GraphPad Prism 5 version 5.00. Data were compared using unpaired *t*-test or a one-way analysis of variance (ANOVA) Tukey and Dunnett's test. Differences were considered significant for *p*-values lower than 0.05 ($p < 0.05$).

RESULTS

Antibacterial Characterization of Amhelin Against *Staphylococcus epidermidis* (ATCC® 35984™)

As a starting point, the antibacterial properties of Amhelin were tested against *S. epidermidis* (ATCC® 35984™) by determining the MIC and MBC, respectively. The bacterial strain was cultured in the presence of increasing concentrations of Amhelin for a period of 24 h. The peptide concentration that completely inhibited visible bacterial growth was determined as the MIC, while the peptide concentration that resulted in a reduction of 99.9% of CFUs relative to that in the initial inoculum was determined as the MBC. The MIC and the MBC of Amhelin against *S. epidermidis* (ATCC® 35984™) were found to be 6 and 12 μg/mL, respectively (**Table 1**).

Furthermore, the anti-biofilm properties of Amhelin were evaluated by quantifying the biofilm biomass that was produced after a 24-hour bacterial exposure to increasing concentrations of Amhelin. The biofilm biomass was quantified using a safranin staining method and the results were expressed as a percentage of biofilm inhibition compared to a typical biofilm growth control. With the lowest peptide concentration, that is 1 μg/mL, biofilm formation was inhibited by only 3%. A more significant effect was observed with a peptide concentration of 3 μg/mL, where 50% of biofilm formation was inhibited. With concentrations equal or higher to the MIC, that is 6 μg/mL, biofilm formation was inhibited by more than 90% (**Figure 1**).

TABLE 1 | MIC and MBC of Amhelin against *S. epidermidis* (ATCC® 35984™).

Amhelin	MIC	MBC
S. epidermidis (ATCC® 35984™)	6 μg/mL	12 μg/mL

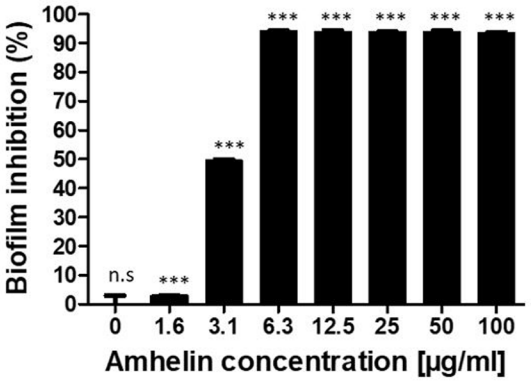

FIGURE 1 | Percentage of inhibition of biofilm formation of *S. epidermidis* (ATCC® 35984™) by Amhelin when exposed to increasing concentrations of Amhelin for a period of 24 h. The biofilm growth control is represented by the column in which no Amhelin was added. The experiments were performed in three independent experiments, in triplicates ($N = 3$, $n = 3$). ***$p < 0.0001$ and n.s indicates no statistical difference when compared with biofilm growth control.

Dispersin B Is Capable of Detaching Pre-formed Biofilms

The ability of DB to disperse pre-formed biofilms was tested against *S. epidermidis* (ATCC® 35984™) by incubating 24-hour pre-formed biofilms with increasing concentrations of DB for a period of 24-hours and by quantifying the biofilm biomass that remained intact after the incubation period, using a safranin staining method. The results were expressed as a percentage of biofilm dispersal compared to a typical biofilm growth control.

A similar dispersal activity was observed for all the testing DB concentrations. With concentrations up until 50 μg/mL, 70% of pre-established biofilms were dispersed. By increasing the DB concentrations to 100, 200, and 400 μg/mL, pre-established biofilms were dispersed by 76, 73, and 78%, respectively (**Figure 2**).

L929 Murine Fibroblasts Can Grow in the Presence of Amhelin and Dispersin B

In order to evaluate the cytotoxicity of each of the active agents, cytocompatibility studies were performed by incubating pre-adhered L929 murine fibroblasts with increasing concentrations of either Amhelin or DB for a period of 24 h and by evaluating the percentage of cell viability after the incubation period. Each graph shows the percentage of viable L929 murine fibroblasts after being exposed to increasing concentrations of Amhelin and DB for 24 h in comparison to a cell growth control.

With the results obtained, it was possible to determine the 50% cytotoxicity concentration (CC_{50}), that is, the concentration resulting in a 50% viability of L929 murine fibroblasts of each agent as well as to compare the concentrations of the agents at which high antibacterial performance was obtained with the L929

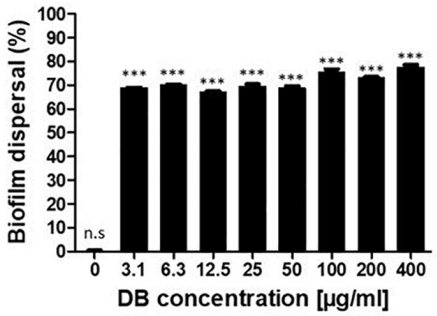

FIGURE 2 | Percentage of biofilm dispersal as a result of the incubation of 24-hour pre-established biofilms of *S. epidermidis* (ATCC® 35984™) with increasing concentrations of DB for 24 h. The biofilm growth control is represented by the column in which no DB was added. The experiments were performed in three independent experiments, in triplicates ($N = 3$, $n = 3$). ***$p < 0.0001$ and n.s indicates no statistical difference when compared with biofilm growth control.

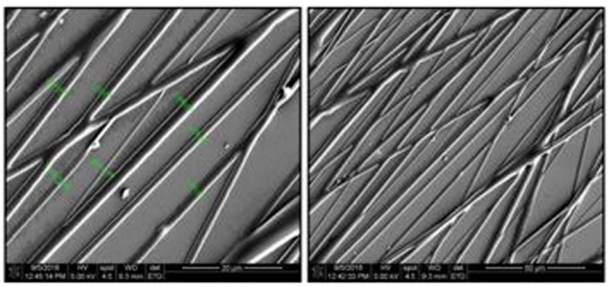

FIGURE 4 | SEM micrographs of PHA fibers using a 20 w/v% polymer concentration in a 60/40, chloroform/acetone solution, 14 kV, 5 mL/h flow rate, needle-to-collector distance of 14 cm and target's rotation speed of 1000 rpm. Magnification of micrographs on the left-side of 1500× and scale bar of 20 μm. Magnification of micrographs on the right-side of 500× and scale bar of 50 μm. Low fiber density samples were used for imaging purposes only.

cell viability. Amhelin showed a CC_{50} of 143 μg/mL while DB showed a CC_{50} of 134 μg/mL.

The concentrations at which Amhelin showed strong bactericidal and anti-biofilm properties, that is, 12 and 3 μg/mL resulted in a L929 cell viability higher than 90%. In the case of DB, with concentrations up until 50 μg/mL, a cell viability higher than 70% was obtained (**Figure 3**).

Fabrication of Polyhydroxyalkanoate-Based Fibers

The electrospinning process resulted in well aligned and bead-less fibers with diameters ranging from 500 nm to 2.5 microns (**Figure 4**).

Water Contact Angle of Activated Fibers

To evaluate the wettability changes after the functionalization process, wettability studies were conducted by measuring the water contact angle of PHA-NCO-sP(EO-stat-PO) fibers, PHA-NCO-sP(EO-stat-PO) + Amhelin + DB fibers and compared to the water contact angle of PHA disks obtained by a solvent casting method and PHA fibers. PHA disks, PHA fibers, PHA-NCO-sP(EO-stat-PO) fibers were also pre-incubated in a deionized water-saturated atmosphere at 37°C for 4 h to assess the changes in wettability.

Polyhydroxyalkanoates disks exhibited a water contact angle of 88^o confirming the hydrophobic nature of the material. After fiber formation, PHA fibers showed a significant increase in hydrophobicity, with a water contact angle of 124°. A further increase in hydrophobicity was observed for PHA-NCO-sP(EO-stat-PO) fibers which showed a water contact angle of 132°. On the other hand, PHA-NCO-sP(EO-stat-PO) + Amhelin + DB

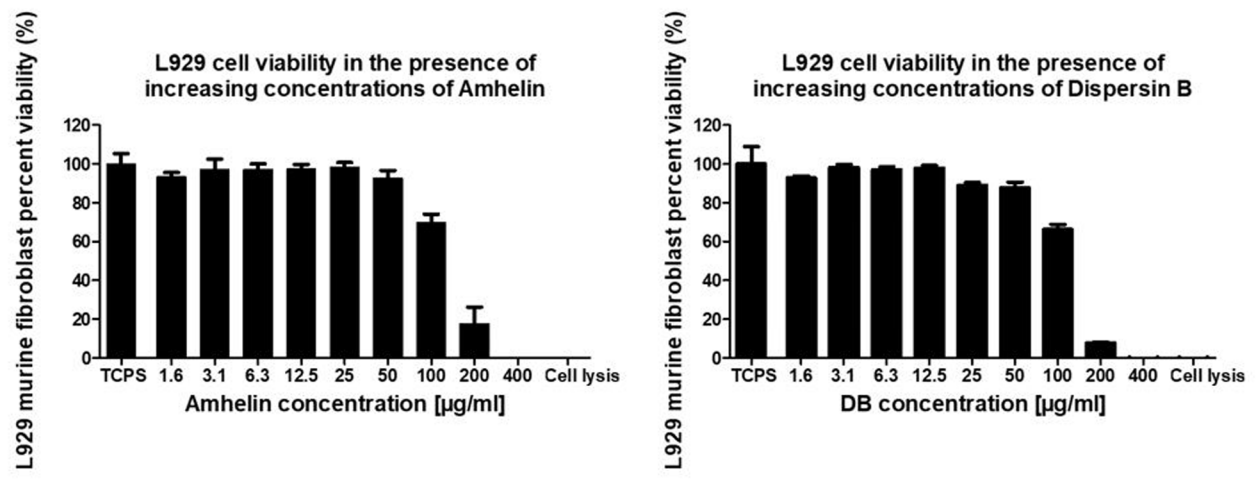

FIGURE 3 | Percentage of cell viability of L929 murine fibroblasts, after growing in the presence of increasing concentrations of Amhelin and DB, for a period of 24 h. A typical cell growth control and a positive control were considered and are represented as TCPS and cell lysis, respectively.

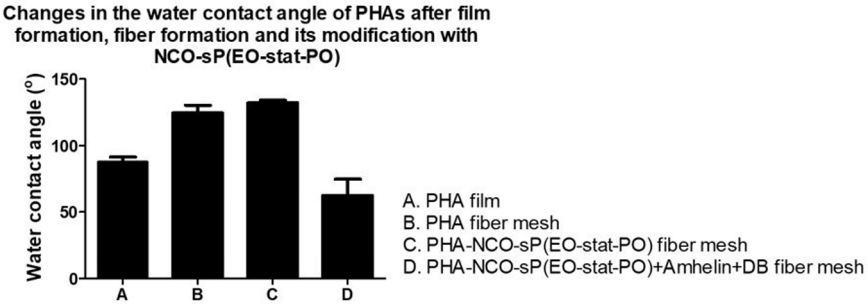

FIGURE 5 | Water contact angle of PHA disks, PHA fibers, PHA-NCO-sP(EO-stat-PO) fibers and PHA-NCO-sP(EO-stat-PO) + Amhelin + DB fibers.

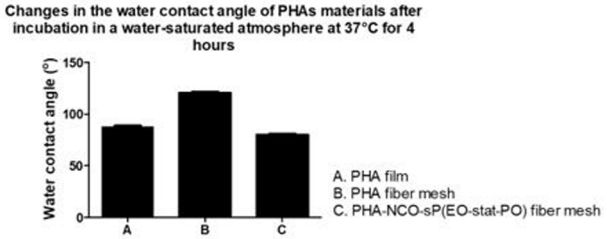

FIGURE 6 | Water contact angle of PHA disks, PHA fibers, PHA-NCO-sP (EO-stat-PO) fibers after incubation in a deionized water-saturated atmosphere at 37°C for 4 h.

fibers showed a water contact angle of 62° (**Figure 5**). The pre-incubation in a deionized water-saturated atmosphere, at 37°C, for 4 h, showed that the PHA disks and PHA fibers maintained their wettability properties, showing water contact angles of 88 and 120°, respectively. On the other hand, PHA-NCO-sP(EO-stat-PO) fibers showed a decrease in the water contact angle, to a value of 80° (**Figure 6**).

In vitro Direct Cytotoxicity Studies on Activated Fibers

In order to evaluate the cytotoxicity of the functionalized fibers against mammalian cells, L929 murine fibroblasts were seeded on the surface of PHA fibers, and on modified PHA fibers for a period of 24 h. The cytotoxicity of each material was evaluated by calculating the percentage cell viability after the incubation period in comparison to the growth control. Additionally, a fluorescent cell staining was carried out to observe the presence of live and dead cells on the fibers.

The graph shows the percentage of viable L929 murine fibroblasts that grew in the presence of the different fibers in comparison to the cell growth control, TCPS, after an incubation period of 24 h. A cell viability of 76 and 84% was observed for PHA and PHA-NCO-sP(EO-stat-PO) fibers, respectively. PHA-NCO-sP(EO-stat-PO) + Amhelin + DB fibers exhibited a cell viability of 80% (**Figure 7**).

The fluorescent micrographs showed the presence of live cells (green) on the three different types of fibers. Furthermore, the morphology of the cells grown on the fibers was similar to the morphology of cells grown on TCPS. PHA fibers and PHA-NCO-sP(EO-stat-PO) fibers showed a slightly lower cell density as compared to the remaining types of fibers (**Figure 8**).

Prevention of Bacterial Cell Adhesion on Activated Fibers

The anti-adhesive properties of the materials against bacteria was evaluated by incubating the different fibers with *S. epidermidis* (ATCC® 35984™) for a period of 24 h. The bacteria that adhered to the surface of the fibers was removed by sonication and quantified by plating on blood agar plates. The ability of the functionalized fibers to prevent bacterial adhesion was expressed as a percentage by comparing the number of bacteria that adhered to the surface of unmodified fibers with the number of bacteria that adhered to the surface of functionalized fibers. Additionally, after the incubation period, the biofilm biomass that was formed on the surface of the fibers was stained using the safranin method.

The results showed that PHA-NCO-sP(EO-stat-PO) + Amhelin + DB fibers were able to prevent the bacterial adhesion by 88% when compared to unmodified PHA fibers. The fibers containing NCO-sP(EO-stat-PO) only showed similar bacterial adhesion to that of the PHA fibers (**Figure 9**).

The staining method showed that PHA fibers and PHA-NCO-sP(EO-stat-PO) fibers were completely covered by a biofilm biomass layer while the fibers functionalized with Amhelin + DB showed the absence of *S. epidermidis* (ATCC® 35984™) biofilms on their surface (**Figure 10**).

DISCUSSION

Despite the success of many regenerative medicine strategies, such as tissue engineering, the problem of contamination of implantable biomaterials by bacteria persists. Bacteria can rapidly recognize a foreign material and start its adhesion process. As the implants get more and more colonized by bacteria, they start forming a protective layer which becomes much harder to treat than common planktonic bacteria. Thus, there is a strong need to mitigate bacterial adhesion on implants with features such as surface activated properties that are unfavorable for bacterial

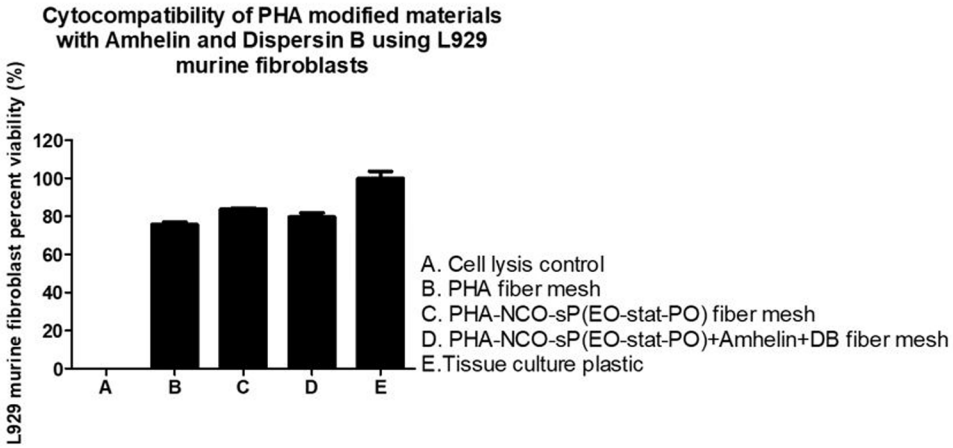

FIGURE 7 | Percentage of cell viability of L929 murine fibroblasts after its seeding on the surface of PHA fibers, PHA-NCO-sP(EO-stat-PO) fibers and PHA-NCO-sP(EO-stat-PO) + Amhelin + DB fibers for a period of 24 h. A typical cell growth control and a positive control were considered and are represented by TCPS and cell lysis, respectively.

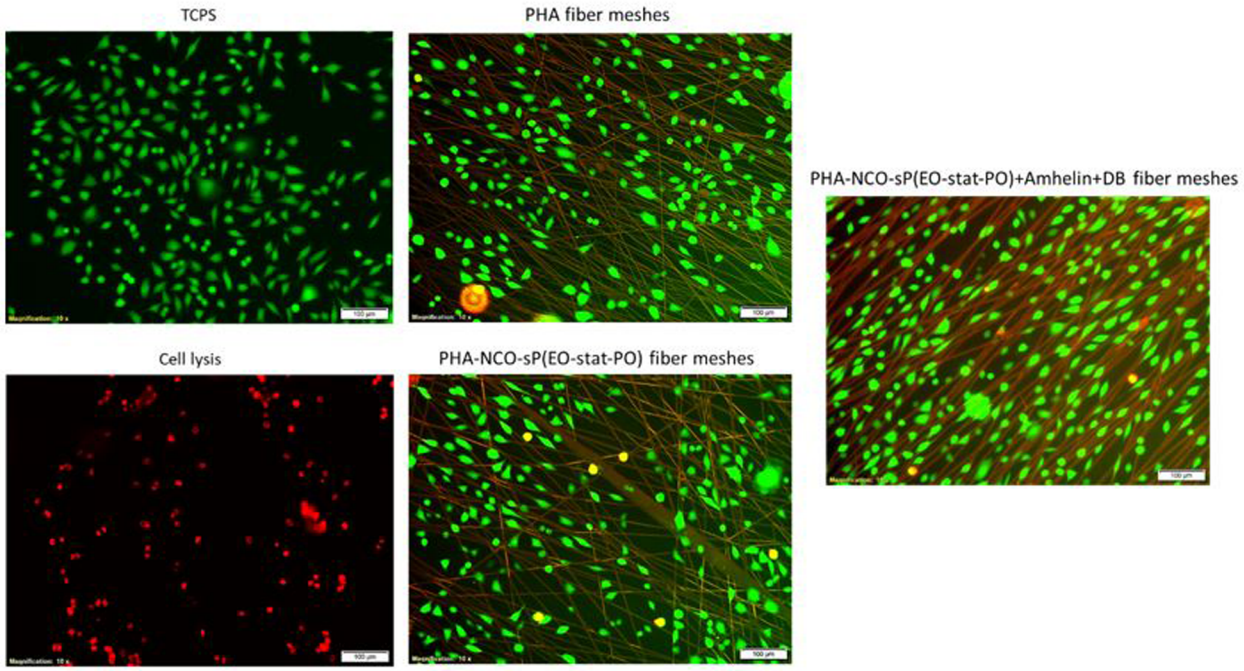

FIGURE 8 | Fluorescence micrographs of L929 murine fibroblasts grown on top of PHA fibers, PHA-NCO-sP(EO-stat-PO) fibers and PHA-NCO-sP(EO-stat-PO) + Amhelin + DB fibers. The dead cells are represented in red and live cells are represented in green. Magnification of micrographs of 10x and scale bar of 100 μm. Negative and positive controls are represented by TCPS and cell lysis, respectively.

adhesion but favorable for eukaryotic cell adhesion. The development of non-cytotoxic and anti-adhesive fiber meshes was achieved by surface modifying PHA fibers with bacterial membrane targeting Amhelin and the biofilm disrupting enzyme DB.

The antibacterial screening of Amhelin showed the bacteriostatic and bactericidal nature of this AMP. According to the European Committee on Antimicrobial Susceptibility Testing (EUCAST) MIC Breakpoints, the most commonly used antibiotics such as vancomycin, gentamycin and rifampicin

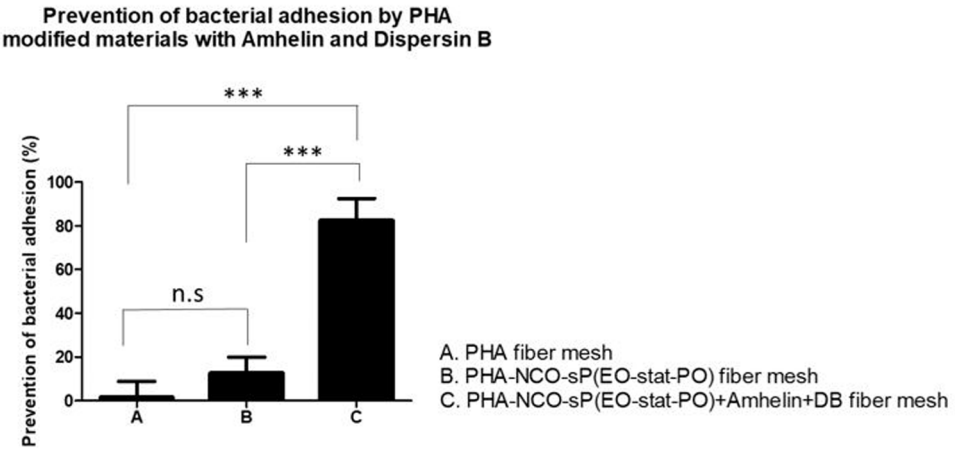

FIGURE 9 | Percentage of prevention of bacterial adhesion of PHA fibers, PHA-NCO-sP(EO-stat-PO) fibers and PHA-NCO-sP(EO-stat-PO) + Amhelin + DB fibers after their incubation with *S. epidermidis* (ATCC® 35984™) for a period of 24 h. The experiments were performed in two independent experiments, in triplicates ($N = 2$, $n = 3$). All columns were compared with each other. ***$p < 0.0001$ and n.s indicates no statistical difference.

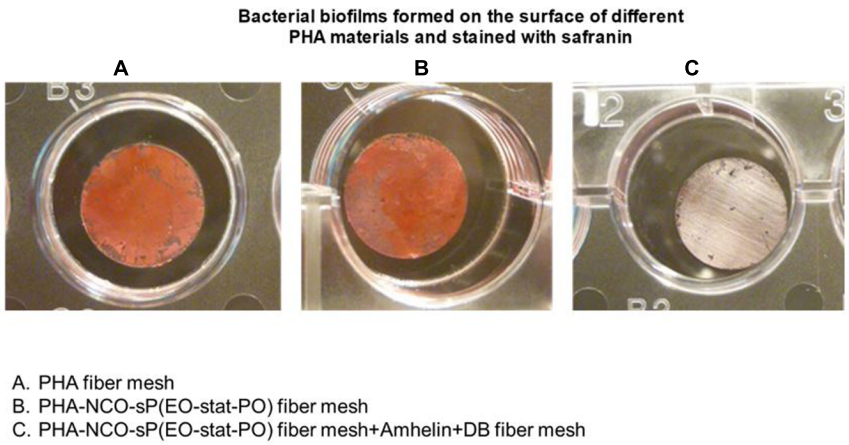

FIGURE 10 | Safranin staining of bacterial biofilms formed on top of PHA fibers **(A)**, PHA-NCO-sP(EO-stat-PO) fibers **(B)** and PHA-NCO-sP(EO-stat-PO) + Amhelin + DB fibers **(C)** after a 24-hour bacterial incubation.

have a MIC of 4 mg/mL, 1 mg/mL and 60 μg/mL, respectively, against some of the most relevant pathogenic bacteria (The European Committee on Antimicrobial Susceptibility Testing, 2019). Herein, the obtained MIC and MBC values showed concentrations ranging from 6 to 12 μg/mL, suggesting an extremely good efficacy at low concentrations. Also, in previous experiments performed in our lab we observed inhibitory growth effects against a methicillin-resistant *S. epidermidis* strain, showing a potential effect against antibiotic-resistant strains.

Besides the indication of the bacteriostatic and bactericidal nature of the peptide, promising results were obtained regarding the anti-biofilm action of Amhelin as in this work, we showed for the first time that Amhelin had the ability to inhibit biofilm formation at just 3 μg/mL. The antibacterial screening showed that with concentrations equivalent to the MIC, biofilm formation was inhibited between 80 to 90% compared to the biofilm growth control.

Although the mechanism of action by which AMPs act against biofilms is not entirely understood, literature suggests that they interfere with cell communication systems such as quorum sensing, bind to polysaccharides present in the biofilm matrix, downregulate genes responsible for biofilm formation or disrupt and depolarize the membrane potential of biofilm embedded cells (Yasir et al., 2018). Since Amhelin predominantly functions by creating pores in bacterial phospholipid bilayers, it is likely that the anti-biofilm action of the peptide takes place at a membrane level.

The initial evidence that DB could promote biofilm dispersal came from studies which showed that the DB mutant (mutant strain not producing the enzyme) lacked the biofilm dispersal ability since the cells resulting from the mutant produced biofilm colonies that were not released to the medium as opposed to the wild-type strain (Kaplan et al., 2003). Other studies provided further proof that DB was indeed causing biofilm dispersal as the

purified enzyme was shown to disperse cells from pre-formed biofilm colonies of bacteria. The MALDI-TOF mass spectra of the extracellular polysaccharide, after being digested with DB showed a high degree of depolymerization (Itoh et al., 2005; Izano et al., 2007). In addition, it was shown that DB could act against Staphylococci strains including *S. epidermidis* and *Staphylococcus aureus* (Kaplan et al., 2004; Izano et al., 2008). The present study confirmed the anti-biofilm activity of DB against *S. epidermidis* (ATCC® 35984™).

The cytocompatibility evaluation of the different agents demonstrated a higher selectivity for bacteria over mammalian cells, as the estimated MICs and MBCs were considerably lower than the CC_{50} calculated for L929 murine fibroblasts. The fact of having such a safe therapeutic window in which the agents could be used was extremely convenient if the aim was to prevent bacterial adherence to the maximum without interfering with the adherence of eukaryotic tissue cells.

Bead formation is a common problem in the electrospinning process and can affect the quality of the fibers. On the other hand, non-aligned fibers can affect the process of eukaryotic tissue cell adhesion due to differences in morphology as aligned fiber structures resemble the ECM pattern (Bourget et al., 2013). Beadless and slightly aligned fibers were obtained using the appropriate spinning conditions and parameters resulting in fibers with a suitable morphology for cell attachment, spreading and proliferation.

The surface properties of the materials such as wettability are known to play a critical role in the process of eukaryotic tissue cell adhesion, proliferation and differentiation as well as bacterial adhesion, therefore the wettability of the materials produced in this study were evaluated and its effect considered in the process of eukaryotic tissue cell adhesion and bacterial adhesion. In this study, it was shown that when PHA was processed to form electrospun fiber meshes, the WCA increased drastically to values of 120° and further increased when processed to form electrospun fiber meshes along with NCO-sP(EO-stat-PO), to a WCA of 132°, granting the materials almost superhydrophobic properties. It is known that roughness has a great influence on the water contact angle of a material, and that hydrophobic materials, when fabricated into highly rough and porous substrates, such as electrospun fiber meshes, become even more hydrophobic (Wilson et al., 2005; Yuan and Lee, 2013; Law, 2014). The fact that similar contact angles for fiber meshes with and without NCO-sP(EO-stat-PO) were obtained indicates that there was not a strong tendency for surface segregation, possibly due to a good miscibility of the additive with the polymer. On the other hand, and as expected when covalently coupling the active agents to the fibers, a much lower WCA was obtained. This evidenced the introduction of hydrophilic groups on the surface of the fibers, derived from Amhelin and DB, causing the fibers to have a significantly lower contact angle. Additionally, the results suggested that these molecules contained enough polar groups to interact with the charges during the spinning process and to promote surface segregation. Additionally, when PHA fibers with and without NCO-sP(EO-stat-PO) were incubated in a humidified atmosphere for 4 h, the water contact angle remained the same for the PHA fibers, while it decreased significantly in the case of the PHA-NCO-sP(EO-stat-PO) fibers. Isocyanate groups, NCO, are highly moisture-sensitive (Rolph et al., 2016). The samples containing NCO-sP(EO-stat-PO) when incubated in a deionized water-saturated atmosphere could have resulted in the deactivation of the NCO groups causing changes in its wettability properties caused primarily by water uptake in the polymer matrix. Further experiments assessing the stability of PHA-NCO-sP(EO-stat-PO) + Amhelin + DB fibers should also be considered to evaluate the long-term effect of the materials.

Quantitative cytocompatibility assays revealed cell viability values higher than 70% for all the electrospun fibers prepared in this study when compared to the TCPS control, showing in general, a good cytocompatibility toward L929 murine fibroblasts. Relatively hydrophilic surfaces are generally preferred by eukaryotic tissue cells as they tend to promote the attraction of proteins from the media, such as adhesion of growth factors, onto their surfaces, hence facilitating the process of cell adhesion and growth (Lampin et al., 1997; Wilson et al., 2005). For this reason, when observing the qualitative fluorescent micrographs it was seen that, the material with the lowest contact angle, that is PHA-NCOsP(EOstat PO) + Amhelin + DB fibers, 62°, not only exhibited a higher cell density, but also showed that the cells were able to attach and elongate better along the fibers, indicating that the relatively more hydrophilic properties of the fibers may have promoted the process of cell adhesion.

The colonization on bioactive fibers by *S. epidermidis* (ATCC® 35984™) was significantly lower than that on the unmodified PHA fibers and PHA-NCO-sP(EO-statPO) fibers, serving as an indicator that the covalent coupling of the agents had successfully conferred anti-adhesive properties to the electrospun meshes. More specifically, it prevented bacterial adhesion by more than 80% as compared to the unmodified PHA fibers and PHA-NCO-sP(EO-statPO) fibers. The safranin staining also gave an indication as to whether the bacteria that adhered to the fibers was capable of forming biofilms in a 24-hour bacterial incubation period and the results showed the absence of biofilm biomass on the bioactivated fibers, suggesting that the materials could prevent biofilm formation because as a rule of thumb, if bacteria are unable to adhere to a surface, they are unable to colonize it and form a biofilm.

As mentioned before, PNAG is responsible for the process of bacterial adhesion and although the biofilm matrix and chemical composition of biofilms can vary among bacterial strains, PNAG has been identified as the main exopolysaccharide present in Staphylococcal biofilms and other bacterial strains including *E. coli* (Wang et al., 2004; Arciola et al., 2015). Given the results obtained and given that this polysaccharide is present in the composition of biofilms of major pathogens reiterates the importance of exploring DB to tackle biofilm formation of other relevant pathogens.

Another important aspect of this study is that although still in preliminary stages, it complements the portfolio of medical materials with antibacterial properties. The chemical modification of natural and synthetic polymers with either AMPs or DB has progressively become a strategy to enhance the performance of implantable materials. For instance, Piras et al. (2015) performed the encapsulation of frog-skin derived

AMP, temporin B (TB) into chitosan nanoparticles (CS-NPs) in which antibacterial action was seen against various strains of *S. epidermidis*. In a study conducted by Pavlukhina et al. (2012) the surface of poly(allylamine hydrochloride) (PAH) was modified with DB showing anti-biofilm properties against *S. epidermidis*. And, in a study conducted by Marcano et al. (2017) PHA asymmetric membranes containing DB were developed for wound healing applications showing activity against *S. epidermidis* biofilms. DB has also been combined with other agents such as antibiotic cefamandole nafate and triclosan that were physically adsorbed to the surface of polyurethanes resulting in active materials against Staphylococcal biofilms (Donelli et al., 2007; Darouiche et al., 2009). Despite encouraging results, the medical community still strives to develop alternative strategies to prevent biofilm formation on implantable materials and our study adds a newly developed 3D polymeric structure with unprecedented anti-adhesive and antibiofilm properties.

Plus, these materials could be used in a range of medical applications in the form of wound dressings, patches, tissue engineering scaffolds or medical device coatings. For instance, osteomyelitis is a condition where bones get infected and it is one of the most challenging chronic infections found in patients with open fractures and in patients requiring orthopedic procedures. Usually, its treatment includes high doses of antibiotics for long periods of time, surgery and debridement. As an example, when bacteria infect a bone, the blood flow of the infected area decreases and necrotic bone or dead bone is formed, called the sequestrum. In cases where a sequestrum is formed, surgical debridement is carried out to remove the sequestrum but often other tissues are affected and can get damaged such as the periosteum. The periosteum is a membrane covering the bone structure which provides nutrients and also serves as a reservoir of mesenchymal stem cells. If the periosteum is not repaired after surgery, there is a delay in the healing process accompanied with lack of nutrients and a much slower and compromised regeneration process. Therefore, one of the applications of such fiber meshes could be as a periosteum patch which would aid in the regenerative process and at the same time prevents further bacterial contaminations. Additionally, it sometimes happens that after the removal of the sequestrum, a large bone defect is present which is usually compensated by the introduction of intermedullary titanium nails. However, the prevention of infections is compromised as because of the absence of vascularization, the antibiotics cannot reach this area (Berebichez-Fridman et al., 2017). Therefore, one of the applications of the materials developed here could be as a coating of such nails.

To achieve this, further in-depth studies are required. For instance, further characterization steps are needed and are here suggested as future work. Chemical analysis such as X-ray photoelectron spectroscopy, atomic force microscopy or Attenuated total reflectance-Fourier transform infrared spectrometry should be employed to detect the presence of the agents on the fibers as well as its spatial topographical distribution and to quantify the amount of agent present in the fibers. *In vitro* screening of the biodegradation profile would also be very important to evaluate the stability of the materials and finally an *in vitro* release profile of the antimicrobials should also be investigated. Nonetheless, our proof of principle study showed a straightforward, one-step procedure to engineer bioactive fiber meshes based on PHAs and demonstrated that the idea of combining different novel and innovative antibacterial agents with different mechanisms of action against bacteria could be a promising approach toward the development of effective and efficient anti-biofilm therapies.

DATA AVAILABILITY STATEMENT

All datasets generated for this study are included in the article/supplementary material.

AUTHOR CONTRIBUTIONS

SP: original draft preparation. SP, JS, and IR: design of the study, investigation. LM: support and revision of experiments. RV: critical proofreading. HL, MR, and JG: supply of antimicrobial agents. MR, JG, JS, and IR: revision of the manuscript and provision of intellectual contributions to the manuscript. JS, IR: funding acquisition.

FUNDING

This work was financially supported by the European Union's Horizon 2020 Research and Innovation Program, Marie Sklodowska-Curie Grant Agreement No. 643050 (HyMedPoly Project).

ACKNOWLEDGMENTS

We thank Prof. Dr. Axel Rosenhahn and Ph.D. student Wenfa Yu for their support with the water contact angle measurements. We also thank Dr. Sabine Seisel for her support with the SEM surface characterization of the fibers.

REFERENCES

Arciola, C. R., Campoccia, D., Ravaioli, S., and Montanaro, L. (2015). Polysaccharide intercellular adhesin in biofilm: structural and regulatory aspects. *Front. Cell. Infect. Microbiol.* 5:7. doi: 10.3389/fcimb.2015.00007

Batoni, G., Maisetta, G., and Esin, S. (2016). Antimicrobial peptides and their interaction with biofilms of medically relevant bacteria. *Biochim. Biophys. Acta (BBA)-Biomembr.* 1858, 1044–1060. doi: 10.1016/j.bbamem.2015.10.013

Berebichez-Fridman, R., Montero-Olvera, P., Gómez-García, R., and Berebichez-Fastlicht, E. (2017). An intramedullary nail coated with antibiotic and growth factor nanoparticles: an individualized state-of-the-art treatment for chronic

osteomyelitis with bone defects. *Med. Hypoth.* 105, 63–68. doi: 10.1016/j.mehy.2017.06.023

Bourget, J. M., Guillemette, M., Veres, T., Auger, F. A., and Germain, L. (2013). "Alignment of cells and extracellular matrix within tissue-engineered substitutes," in *Advances in Biomaterials Science and Biomedical Applications*, ed. R. Pignatello (London: IntechOpen), 365–390.

Brancatisano, F. L., Maisetta, G., Di Luca, M., Esin, S., Bottai, D., Bizzarri, R., et al. (2014). Inhibitory effect of the human liver-derived antimicrobial peptide hepcidin 20 on biofilms of polysaccharide intercellular adhesin (PIA)-positive and PIA-negative strains of *Staphylococcus epidermidis*. *Biofouling* 30, 435–446. doi: 10.1080/08927014.2014.888062

Brogden, K. A. (2005). Antimicrobial peptides: pore formers or metabolic inhibitors in bacteria? *Nat. Rev. Microbiol.* 3, 238–250. doi: 10.1038/nrmicro1098

Darouiche, R. O., Mansouri, M. D., Gawande, P. V., and Madhyastha, S. (2009). Antimicrobial and antibiofilm efficacy of triclosan and DispersinB® combination. *J. Antimicrob. Chemother.* 64, 88–93. doi: 10.1093/jac/dkp158

Donelli, G., Francolini, I., Romoli, D., Guaglianone, E., Piozzi, A., Ragunath, C., et al. (2007). Synergistic activity of dispersin B and cefamandole nafate in inhibition of staphylococcal biofilm growth on polyurethanes. *Antimicrob. Agents Chemother.* 51, 2733–2740. doi: 10.1128/AAC.01249-06

Donlan, R. M., and Costerton, J. W. (2002). Biofilms: survival mechanisms of clinically relevant microorganisms. *Clin. Microbiol. Rev.* 15, 167–193. doi: 10.1128/cmr.15.2.167-193.2002

Ebbensgaard, A., Mordhorst, H., Overgaard, M. T., Nielsen, C. G., Aarestrup, F. M., and Hansen, E. B. (2015). Comparative evaluation of the antimicrobial activity of different antimicrobial peptides against a range of pathogenic bacteria. *PLoS ONE* 10:e0144611. doi: 10.1371/journal.pone.0144611

European Committee on Antimicrobial Susceptibility Testing (2019). *Breakpoint Tables for Interpretation of MICs and Zone Diameters*. Växjö: European Committee on Antimicrobial Susceptibility Testing.

Grafahrend, D., Heffels, K. H., Beer, M. V., Gasteier, P., Möller, M., Boehm, G., et al. (2011). Degradable polyester scaffolds with controlled surface chemistry combining minimal protein adsorption with specific bioactivation. *Nat. Mater.* 10, 67–73. doi: 10.1038/nmat2904

Hancock, R. E., and Sahl, H. G. (2006). Antimicrobial and host-defense peptides as new anti-infective therapeutic strategies. *Nat. Biotechnol.* 24, 1551–1557. doi: 10.1038/nbt1267

International Organization for Standardization [ISO] (2006). *ISO 20776-1: 2006: Clinical Laboratory Testing and in Vitro Diagnostic Test Systems-Susceptibility Testing of Infectious Agents and Evaluation of Performance of Antimicrobial Susceptibility Test Devices: Reference Method for Testing the in Vitro Activity of Antimicrobial Agents Against Rapidly Growing Aerobic Bacteria Involved in Infectious Diseases*. Geneva: International Organization for Standardization [ISO].

International Organization for Standardization [ISO] (2009). *ISO 10993-5: Biological Evaluation of Medical Devices-Part 5: Tests for In Vitro Cytotoxicity*. Geneva: International Organization for Standardization [ISO].

Itoh, Y., Wang, X., Hinnebusch, B. J., Preston, J. F., and Romeo, T. (2005). Depolymerization of β-1, 6-N-acetyl-d-glucosamine disrupts the integrity of diverse bacterial biofilms. *J. Bacteriol.* 187, 382–387. doi: 10.1128/JB.187.1.382-387.2005

Izano, E. A., Amarante, M. A., Kher, W. B., and Kaplan, J. B. (2008). Differential roles of poly-N-acetylglucosamine surface polysaccharide and extracellular DNA in *Staphylococcus aureus* and *Staphylococcus epidermidis* biofilms. *Appl. Environ. Microbiol.* 74, 470–476. doi: 10.1128/AEM.02073-07

Izano, E. A., Wang, H., Ragunath, C., Ramasubbu, N., and Kaplan, J. B. (2007). Detachment and killing of *Aggregatibacter actinomycetemcomitans* biofilms by dispersin B and SDS. *J. Dent. Res.* 86, 618–622. doi: 10.1177/154405910708600707

Kaplan, J. B. (2009). Therapeutic potential of biofilm-dispersing enzymes. *Int. J. Artif. Organs* 32, 545–554.

Kaplan, J. B. (2010). Biofilm dispersal: mechanisms, clinical implications, and potential therapeutic uses. *J. Dent. Res.* 89, 205–218. doi: 10.1177/0022034509359403

Kaplan, J. B., Ragunath, C., Ramasubbu, N., and Fine, D. H. (2003). Detachment of Actinobacillus actinomycetemcomitans biofilm cells by an endogenous β-hexosaminidase activity. *J. Bacteriol.* 185, 4693–4698. doi: 10.1128/jb.185.16.4693-4698.2003

Kaplan, J. B., Ragunath, C., Velliyagounder, K., Fine, D. H., and Ramasubbu, N. (2004). Enzymatic detachment of Staphylococcus epidermidis biofilms. *Antimicrob. Agents Chemother.* 48, 2633–2636. doi: 10.1128/AAC.48.7.2633-2636.2004

Kiran, M. D., Adikesavan, N. V., Cirioni, O., Giacometti, A., Silvestri, C., Scalise, G., et al. (2008). Discovery of a quorum-sensing inhibitor of drug-resistant staphylococcal infections by structure-based virtual screening. *Mol. Pharmacol.* 73, 1578–1586. doi: 10.1124/mol.107.044164

Lampin, M., Warocquier-Clérout, R., Legris, C., Degrange, M., and Sigot-Luizard, M. F. (1997). Correlation between substratum roughness and wettability, cell adhesion, and cell migration. *J. Biomed. Mater. Res.* 36, 99–108. doi: 10.1002/(sici)1097-4636(19981205)42:3<473::aid-jbm18>3.0.co;2-h

Law, K. Y. (2014). Definitions for hydrophilicity, hydrophobicity, and superhydrophobicity: getting the basics right. *J. Phys. Chem. Lett.* 686–688. doi: 10.1021/jz402762h

Lebeaux, D., Ghigo, J. M., and Beloin, C. (2014). Biofilm-related infections: bridging the gap between clinical management and fundamental aspects of recalcitrance toward antibiotics. *Microbiol. Mol. Biol. Rev.* 78, 510–543. doi: 10.1128/MMBR.00013-14

Li, J., Koh, J. J., Liu, S., Lakshminarayanan, R., Verma, C. S., and Beuerman, R. W. (2017). Membrane active antimicrobial peptides: translating mechanistic insights to design. *Front. Neurosci.* 11:73. doi: 10.3389/fnins.2017.00073

Li, Z., Yang, J., and Loh, X. J. (2016). Polyhydroxyalkanoates: opening doors for a sustainable future. *NPG Asia Mater.* 8:e265.

Marcano, A., Ba, O., Thebault, P., Crétois, R., Marais, S., and Duncan, A. C. (2015). Elucidation of innovative antibiofilm materials. *Colloids Surf. B Biointerf.* 136, 56–63. doi: 10.1016/j.colsurfb.2015.08.007

Marcano, A., Bou Haidar, N., Marais, S., Valleton, J. M., and Duncan, A. C. (2017). Designing biodegradable PHA-based 3D scaffolds with antibiofilm properties for wound dressings: optimization of the microstructure/nanostructure. *ACS Biomater. Sci. Eng.* 3, 3654–3661.

Onaizi, S. A., and Leong, S. S. (2011). Tethering antimicrobial peptides: current status and potential challenges. *Biotechnol. Adv.* 29, 67–74. doi: 10.1016/j.biotechadv.2010.08.012

Pavlukhina, S. V., Kaplan, J. B., Xu, L., Chang, W., Yu, X., Madhyastha, S., et al. (2012). Noneluting enzymatic antibiofilm coatings. *ACS Appl. Mater. Interf.* 4, 4708–4716.

Piras, A. M., Maisetta, G., Sandreschi, S., Gazzarri, M., Bartoli, C., Grassi, L., et al. (2015). Chitosan nanoparticles loaded with the antimicrobial peptide temporin B exert a long-term antibacterial activity in vitro against clinical isolates of Staphylococcus epidermidis. *Front. Microbiol.* 6:372. doi: 10.3389/fmicb.2015.00372

Powers, J. P. S., and Hancock, R. E. (2003). The relationship between peptide structure and antibacterial activity. *Peptides* 24, 1681–1691. doi: 10.1016/j.peptides.2003.08.023

Rakowska, P. D., Jiang, H., Ray, S., Pyne, A., Lamarre, B., Carr, M., et al. (2013). Nanoscale imaging reveals laterally expanding antimicrobial pores in lipid bilayers. *Proc. Natl. Acad. Sci. U.S.A.* 110, 8918–8923. doi: 10.1073/pnas.1222824110

Reis, R. L., Neves, N. M., Mano, J. F., Gomes, M. E., Marques, A. P., and Azevedo, H. S. (2008). *Natural-Based Polymers for Biomedical Applications*. Amsterdam: Elsevier.

Repanas, A., Andriopoulou, S., and Glasmacher, B. (2016). The significance of electrospinning as a method to create fibrous scaffolds for biomedical engineering and drug delivery applications. *J. Drug Deliv. Sci. Technol.* 31, 137–146.

Rolph, M. S., Markowska, A. L., Warriner, C. N., and O'Reilly, R. K. (2016). Blocked isocyanates: from analytical and experimental considerations to non-polyurethane applications. *Polym. Chem.* 7, 7351–7364.

Rossi, A., Wistlich, L., Heffels, K. H., Walles, H., and Groll, J. (2016). Isotropic versus bipolar functionalized biomimetic artificial basement membranes and their evaluation in long-term human cell co-culture. *Adv. Healthc. Mater.* 5, 1939–1948. doi: 10.1002/adhm.201600224

Roy, I., and Visakh, P. M. (eds) (2014). *Polyhydroxyalkanoate (PHA) Based Blends, Composites and Nanocomposites*, Vol. 30. London: Royal Society of Chemistry.

Ryadnov, M. G., Mukamolova, G. V., Hawrani, A. S., Spencer, J., and Platt, R. (2009). RE coil: an antimicrobial peptide regulator. *Angew. Chem. Int. Ed.* 48, 9676–9679. doi: 10.1002/anie.200904780

Ryan, L., Lamarre, B., Diu, T., Ravi, J., Judge, P. J., Temple, A., et al. (2013). Anti-antimicrobial peptides folding-mediated host defense antagonists. *J. Biol. Chem.* 288, 20162–20172. doi: 10.1074/jbc.M113.459560

Segev-Zarko, L. A., Saar-Dover, R., Brumfeld, V., Mangoni, M. L., and Shai, Y. (2015). Mechanisms of biofilm inhibition and degradation by antimicrobial peptides. *Biochem. J.* 468, 259–270. doi: 10.1042/BJ20141251

Steinstraesser, L., Tack, B. F., Waring, A. J., Hong, T., Boo, L. M., Fan, M. H., et al. (2002). Activity of novispirin G10 against *Pseudomonas aeruginosa* in vitro and in infected burns. *Antimicrob. Agents Chemother.* 46, 1837–1844. doi: 10.1128/aac.46.6.1837-1844.2002

Wang, X., Preston, J. F., and Romeo, T. (2004). The pgaABCD locus of *Escherichia coli* promotes the synthesis of a polysaccharide adhesin required for biofilm formation. *J. Bacteriol.* 186, 2724–2734. doi: 10.1128/jb.186.9.2724-2734.2004

Wi, Y. M., and Patel, R. (2018). Understanding Biofilms and novel approaches to the diagnosis, prevention, and treatment of medical device-associated infections. *Infect. Dis. Clin.* 32, 915–929. doi: 10.1016/j.idc.2018.06.009

Wilson, C. J., Clegg, R. E., Leavesley, D. I., and Pearcy, M. J. (2005). Mediation of biomaterial–cell interactions by adsorbed proteins: a review. *Tissue Eng.* 11, 1–18. doi: 10.1089/ten.2005.11.1

Wistlich, L., Kums, J., Heffels, K., Wajant, H., and Groll, J. (2015). A one-step approach for multimodal functionalization of electrospun nanofibers and their application for immune-regulatory surfaces. *Tissue Eng. Part A* 21, S50–S50.

Yasir, M., Willcox, M. D. P., and Dutta, D. (2018). Action of antimicrobial peptides against bacterial biofilms. *Materials* 11:2468. doi: 10.3390/ma11122468

Yuan, Y., and Lee, T. R. (2013). "Contact angle and wetting properties," in *Surface Science Techniques*, eds G. Bracco and B. Holst (Berlin: Springer), 3–34.

Zimmerli, W., and Moser, C. (2012). Pathogenesis and treatment concepts of orthopaedic biofilm infections. *FEMS Immunol. Med. Microbiol.* 65, 158–168. doi: 10.1111/j.1574-695X.2012.00938.x

Conflict of Interest: The authors declare that the research was conducted in the absence of any commercial or financial relationships that could be construed as a potential conflict of interest.

frontiers in Bioengineering and Biotechnology

ORIGINAL RESEARCH
published: 12 June 2020
doi: 10.3389/fbioe.2020.00561

Evaluation of Nisin and LL-37 Antimicrobial Peptides as Tool to Preserve Articular Cartilage Healing in a Septic Environment

Ziba Najmi[1,2†], Ajay Kumar[1,2†], Alessandro C. Scalia[1,2], Andrea Cochis[1,2], Bojana Obradovic[3], Federico A. Grassi[1], Massimiliano Leigheb[1], Meriem Lamghari[4,5], Iraida Loinaz[6], Raquel Gracia[6] and Lia Rimondini[1,2]*

[1] Department of Health Sciences, University of Piemonte Orientale UPO, Novara, Italy, [2] Center for Translational Research on Autoimmune and Allergic Diseases–CAAD, Novara, Italy, [3] Faculty of Technology and Metallurgy, University of Belgrade, Belgrade, Serbia, [4] Instituto de Engenharia Biomédica (INEB), Universidade do Porto, Porto, Portugal, [5] Instituto de Investigação e Inovação em Saúde (i3S), Universidade do Porto, Porto, Portugal, [6] CIDETEC Basque Research and Technology Alliance (BRTA), Donostia-San Sebastian, Spain

OPEN ACCESS

Edited by:
Gianluca Ciardelli,
Politecnico di Torino, Italy

Reviewed by:
Livia Visai,
University of Pavia, Italy
Arianna Barbara Lovati,
Istituto Ortopedico Galeazzi (IRCCS), Italy

***Correspondence:**
Lia Rimondini
lia.rimondini@med.uniupo.it

[†] These authors have contributed equally to this work

Specialty section:
This article was submitted to Biomaterials, a section of the journal Frontiers in Bioengineering and Biotechnology

Received: 29 February 2020
Accepted: 11 May 2020
Published: 12 June 2020

Citation:
Najmi Z, Kumar A, Scalia AC, Cochis A, Obradovic B, Grassi FA, Leigheb M, Lamghari M, Loinaz I, Gracia R and Rimondini L (2020) Evaluation of Nisin and LL-37 Antimicrobial Peptides as Tool to Preserve Articular Cartilage Healing in a Septic Environment. Front. Bioeng. Biotechnol. 8:561. doi: 10.3389/fbioe.2020.00561

Cartilage repair still represents a challenge for clinicians and only few effective therapies are nowadays available. In fact, surgery is limited by the tissue poor self-healing capacity while the autologous transplantation is often forsaken due to the poor *in vitro* expansion capacity of chondrocytes. Biomaterials science offers a unique alternative based on the replacement of the injured tissue with an artificial tissue-mimicking scaffold. However, the implantation surgical practices and the scaffold itself can be a source of bacterial infection that currently represents the first reason of implants failure due to the increasing antibiotics resistance of pathogens. So, alternative antibacterial tools to prevent infections and consequent device removal are urgently required. In this work, the role of Nisin and LL-37 peptides has been investigated as alternative to antibiotics to their antimicrobial performances for direct application at the surgical site or as doping chemicals for devices aimed at articular cartilage repair. First, peptides cytocompatibility was investigated toward human mesenchymal stem cells to determine safe concentrations; then, the broad-range antibacterial activity was verified toward the Gram-positive *Staphylococcus aureus* and *Staphylococcus epidermidis* as well as the Gram-negative *Escherichia coli* and *Aggregatibacter actinomycetemcomitans* pathogens. The peptides selective antibacterial activity was verified by a cells-bacteria co-culture assay, while chondrogenesis was assayed to exclude any interference within the differentiation route to simulate the tissue repair. In the next phase, the experiments were repeated by moving from the cell monolayer model to 3D cartilage-like spheroids to revisit the peptides activity in a more physiologically relevant environment model. Finally, the spheroid model was applied in a perfusion bioreactor to simulate an infection in the presence of circulating peptides within a physiological environment. Results suggested that 75 μg/ml Nisin can be considered as a very promising candidate since it was shown to be more cytocompatible and potent against the investigated bacteria than LL-37 in all the tested models.

Keywords: antimicrobial peptides, pro-chondrogenic agents, co-cultures, bioreactor, human mesenchymal stem cells, antibacterial study

INTRODUCTION

Articular cartilage (AC) represents a unique tissue in human body due to the lack of vascularization and innervation; it is composed of 80% water and populated by only one cell type represented by chondrocytes (Cohen et al., 1998). Despite its fundamental role in body support, AC exhibits a very low capacity for spontaneous repair mainly due to its avascular nature and a decreased mitotic capability of resident mature chondrocytes. These evidences represent a serious problem for clinicians as cartilage defects are not uncommon due to trauma (Aigner and Fan, 2003; Stone and Schaal, 2012; Makris et al., 2015), time deterioration and excessive body mass index (BMI) in both young and old population. As a further complication, AC defects are often associated with bone lesions and type II collagen breakdown (Widuchowski et al., 2007), thus causing pain and severe movement difficulties in affected patients.

Nowadays, treatment of focal chondral defects is mainly based on surgery and autologous chondrocyte transplantation. Surgery is performed onto the subchondral bone in order to create small microfractures and force stem cell migration from the neighboring bone to the cartilage injured site (Camp et al., 2014). Autologous chondrocyte transplantation includes collection and *in vitro* expansion of patient's own chondrocytes that are subsequently injected to repopulate the injured site (Camp et al., 2014). However, both treatment solutions are affected by severe limitations. In fact, autologous chondrocyte transplantation can result in terminal differentiation of the newly implanted cells into hypertrophy. Similarly, the microfracture surgery approach may lead to the formation of fibrocartilage, which is far less effective at bearing loads due to its poorer mechanical properties and weaker resistance to impact as compared to the native AC tissue. Moreover, the graft size and availability of cells for transplantation can be limiting factors despite good predicted outcomes of the selected therapy in certain cases. In addition, the surgical procedure can lead to bone damage (Chalmers et al., 2013). The problem of failures in cartilage repair procedures is probably underestimated: literature dealing with this surgery is not conclusive in identifying the causes of failure, and in many studies there is not even a clear definition of failure (clinical, radiological, or both).

Biomaterials science recently offered an alternative approach for articular cartilage repair based on the possibility to replace the injured tissue by an artificial scaffold substitute resembling the naïve tissue, thus allowing for temporary replacement and a progressive guided self-repair. Some promising examples include the use of hydrogels (Cochis et al., 2017; Cipriani et al., 2019; Bonifacio et al., 2020; Meng et al., 2020), polymers (Pourbashir et al., 2020; Xuan et al., 2020), and composites (Gao et al., 2019; Sun et al., 2019). However, the scaffold synthesis and surgical procedures aimed at the scaffold implantation open the possibility of bacterial infection. This is a rare eventuality (0.04–0.86%), but the clinical consequences can be particularly severe in case of septic arthritis (Stutz et al., 2000; Bauer et al., 2015; Wyatt et al., 2017). The improvements in biomaterials design for articular cartilage repair prefigure a larger use in implantology for the close future, with a potential increase in the number of septic complications.This evidence was recently reviewed by Bauer et al. which reported that the introduction of implants and transplants was probably the main reason of a 3-fold increase of infections (0.14–2.25%) in comparison with the data published previously (Bauer et al., 2015). Moreover, recent findings suggested also that low-grade infections might play a role, as it came to light recently for *Cutibacterium acnes* infection in shoulder surgery (Pruijn et al., 2020).

Articular cartilage infections have been commonly caused by *Staphylococcus aureus* and *Staphylococcus epidermidis* (Gram-positive), but other pathogens such as *Escherichia coli* (Gram-negative) can be responsible for septic arthritis, too (Balato et al., 2017). Once bacteria colonize the injured site, the infection evolves till a biofilm is formed, a 3D dense structure composed of proteins, lipids, DNA, and polysaccharides. In this scenario, the orthopedic surgeons' approach is based on the surgical removal of these biofilm communities; even in the case of a device implant, this represents a necessary pre-condition for eradication of the device-related infection. However, if the device infection proceeds to an advanced phase, the above-mentioned strategy is not sufficient. In fact, direct observation of the bacterial biofilm growth associated with orthopedic devices is very important for surgeons to determine the rational approach to the treatment; accordingly, when the bacterial biofilm is inherently resistant to the host defense and antibiotic therapy, both the device and the adherent biofilm have to be completely removed by a fastidious surgery in order to prevent the tissue infection. In fact, in the severe septic arthritis scenario, device removal and thorough debridement represent the only strategy to preserve surrounding tissues from the biofilm contamination. Accordingly, there is the urgent need for effective strategies to prevent septic arthritis by validating the use of new molecules effective in directly counteracting bacteria or suitable to be coupled with implantable biomaterials.

An interesting alternative to antibiotics is represented by antimicrobial peptides (AMPs). AMPs, or host defense peptides, were firstly discovered in the 1980's demonstrating effectiveness toward pathogenic bacteria, fungi and viruses (Sierra et al., 2017). They hold a double, direct and indirect activity toward bacteria. AMPs can directly bind to the negatively charged membrane phospholipids causing bacteria death due to pore formation, as well as by inhibitions of the ATPase actions of DnaK thus preventing chaperone-assisted protein folding (Rahnamaeian, 2011). In parallel, the presence of AMPs activates recruitment of neutrophils at the infection site, thus activating the immunological reaction cascade and indirectly counteracting the infection (Koziel and Potempa, 2013). Among the large class of AMPs, Nisin and LL-37 were considered of interest due to their proven antibacterial activity. Nisin is a lantibiotic widely used for preservation of food and beverages; it has been shown to be effective in counteracting mastitis (Fernández et al., 2008), dermatitis (Valenta et al., 1996) and gingivitis (Howell et al., 1993). LL-37 is the active cathelicidin peptide released by proteases from the pro-peptide hCAP18 transcribed from the human cathelicidin gene (Xhindoli et al., 2016). It has been shown to be beneficial for wound healing and skin protection

by inhibiting proliferation of *Staphylococcus epidermidis* (Cogen et al., 2008).

So, considering the Nisin and LL-37 antibacterial activity, in this work their effectiveness in preserving articular cartilage healing in the presence of an infected environment was tested. Accordingly, AMPs *in vitro* ctytocompatibility was verified toward stem cell metabolism and chondrogenic differentiation in order to identify a range of safe concentrations. AMPs cytocompatible amounts were then investigated regarding antibacterial efficacy that is the ability in directly counteracting Gram-positive articular cartilage infection pathogens *S. aureus* and *S. epidermidis*; then, the AMPs broad range activity was further confirmed by using Gram-negative strains *E. coli* and *A. actinomycetemcomitans,* too. To test the AMPs selective antibacterial activity, a cells-bacteria co-culture assay was established. Next, a 3D cartilage-like spheroids model was applied to confirm the obtained results in a more physiologically relevant environment model; finally, a perfusion bioreactor was applied to simulate infection in the presence of circulating peptides within a physiological system.

MATERIALS AND METHODS

Antimicrobial Peptides (AMPs)

Antimicrobial peptides (AMPs) were purchased from Merck (Merck, Milan, Italy). Sterile Nisin (liquid, ready-to-use solution, 1.02 g/ml in 0.02N HCl, SBR00021) and LL-37 (powder, human trifluoroacetate salt, 94261) were stored protected from light at 4°C and −20°C, respectively.

LL-37 mother solution was prepared by dissolving the powder into a 0.02N HCl solution (in sterile ultrapure water, from Millipore) until a final concentration of 1 mg/ml by vortexing (1 min, room temperature); all the procedures were performed under laminar air flow cabinet to preserve sterile conditions. AMPs solutions were prepared fresh prior to each experiment by diluting the AMPs' mother solutions directly in the appropriate cell or bacteria culture medium. AMPs were tested at the concentrations detailed in **Table 1**, based on previously reported MIC values in literature for LL-37 (Overhage et al., 2008; Leszczynska et al., 2013; Luo et al., 2017; Saporito et al., 2018; Kamysz et al., 2020) and Nisin (Brumfitt et al., 2002; Piper et al., 2009; Dosler and Gerceker, 2011; Iancu et al., 2012; Shin et al., 2015).

TABLE 1 | AMPs tested concentrations (diluted in the appropriate medium).

AMP	Tested Concentration (μg/ml)	Reported MIC range (μg/ml)	References
Nisin	12.5, 25, 50, 75, 100	0.5–50	(Brumfitt et al., 2002; Piper et al., 2009; Dosler and Gerceker, 2011; Iancu et al., 2012; Shin et al., 2015)
LL-37	5, 7.5, 10, 25, 50, 75	1–50	(Overhage et al., 2008; Leszczynska et al., 2013; Luo et al., 2017; Saporito et al., 2018; Kamysz et al., 2020)

Cytocompatibility

Cell Cultivation

Human bone marrow—derived stem cells (hMSC) were obtained from Merck (PromoCell C-12974) and cultivated in low-glucose Dulbecco's modified Eagle Medium (DMEM, Merck) supplemented with 15% fetal bovine serum (FBS, Merck) and 1% antibiotics (penicillin/streptomycin, Merck) at 37°C, 5% CO_2 atmosphere. Cells were cultivated until 80–90% confluence, detached by a trypsin-EDTA solution (0.25% in PBS, from Merck), harvested and used for experiments.

Metabolic Activity Evaluation

Cells were directly seeded onto the wells of a 96 multiwell plate at a defined density ($5x10^3$ cells/well) and cultivated for 24 h to allow adhesion and spread. Next, Nisin or LL-37 peptides were added to each well according to the concentration stated in **Table 1** by directly diluting mother solutions into the medium and incubated for 24 h in direct contact with cells. Then, the cells viability was evaluated by means of metabolic activity by using the metabolic colorimetric Alamar blue assay (alamarBlue™, ready-to-use solution from Life Technologies, Milan, Italy) following the Manufacturer's instructions. Briefly, supernatants were removed from each well-containing cells and replaced with the Alamar blue solution (0.015% in fresh medium). Plates were incubated in the dark for 4 h at 37°C and then 100 μl aliquots were removed, placed into a new black 96 well plate and fluorescence signals were evaluated by a spectrophotometer (Spark, Tecan Trading AG, Basel, CH) using the following set-up: fluorescence excitation wavelength of 570 nm, fluorescence emission reading at 590 nm. Cells cultivated in the AMPs-free medium were considered as a control. The experiment was performed using six replicates for each application.

Antibacterial Activity Evaluation

Strains Growth Conditions

Bacteria were purchased from the American Type Culture Collection (ATCC, Manassas, USA). To test the AMPs antibacterial activity, two Gram-positive *Staphylococcus aureus* (ATCC 43300) and *Staphylococcus epidermidis* (ATCC 14990), and two Gram-negative *Escherichia coli* (ATCC 25922) and *Aggregatibacter actinomycetemcomitans* (ATCC 33384) strains were used. Bacteria were cultivated on Trypticase Soy Agar (TSA, Merck) and incubated at 37°C until round single colonies were formed; then, 2–3 colonies were collected and spotted into 30 ml of Luria Bertani broth (LB, Merck, Milan, Italy). Broth cultures were incubated overnight at 37°C under agitation (120 rpm in an orbital shaker). A fresh culture was prepared prior to each experiment; bacteria concentration was adjusted to 1×10^5 cells/ml by diluting in the fresh media until optical density of 0.001 at 600 nm was reached as determined by a spectrophotometer (Spark, Tecan, Mannedorf, Switzerland). Pure LB medium was used as a blank.

Biofilm Metabolic Activity Evaluation

Biofilms were formed under static conditions at the bottom of 96 well plates as previously described (Cochis et al., 2016). Briefly, 100 μl/well suspension containing 1×10^5 bacteria prepared as described in the chapter Strains Growth Conditions

was incubated for 90 min under agitation (120 rpm) at 37°C to force separation of the adherent biofilm cells and not-adherent floating planktonic cells (separation phase). Next, supernatants containing planktonic cells were removed and replaced with 200 µl of fresh media to cultivate surface-adhered biofilm cells (growth phase). Biofilms were grown at 37°C for 24 h. Afterwards, Nisin and LL-37 peptides were added to each well in direct contact with bacteria at the concentrations stated in **Table 1** and incubated for 24 h at 37°C. The biofilm cells viability was assessed by means of metabolic activity by the Alamar blue assay as described above in the chapter Metabolic Activity Evaluation. Bacteria cultivated in the AMPs-free medium were considered as controls. The experiment was performed using six replicates for each application.

Co-cultures

After cytocompatibility and antibacterial assays, the following optimal (intended as safe for cells and effective toward bacteria) AMPs concentrations were selected and used in further experiments: Nisin 75 µg/ml and LL-37 10 µg/ml. To verify the antibacterial activity of the targeted AMPs a cells-bacteria co-culture assay was performed as in our previous studies (Jekabsone et al., 2019; Cochis et al., 2020).

The co-culture method was designed to monitor the viability of both cells and bacteria that are challenging in the same environment for the same surface colonization, thus allowing for the validation of the AMPs' targeted activity toward bacteria (Cochis et al., 2020).

Briefly, cells (5×10^3 cells/well) were seeded onto 96 well plates and allowed to adhere and spread for 24 h using the complete DMEM growth medium. The day after, medium was removed and replaced by a bacteria suspension prepared by using the antibiotic-free DMEM as described above for 24 h (DMEM was here used as blank for the optical density evaluation). Nisin (75 µg/ml) and LL-37 (10 µg/ml) peptides were added to test wells by diluting mother solutions directly in the medium while AMPs-free wells were used as controls. Results were collected after 24 h by means of viable cells counting by using trypan blue and bacteria number determination by the Colony forming unit (CFU) count. Briefly, after washing 3 times with PBS, cells and adherent bacteria were detached by 1 ml of trypsin-EDTA (0.25% in PBS) and collected into 1.5 ml tubes. Cells were immediately stained with trypan blue and counted using a Burker chamber. Viable bacteria numbers were obtained by the CFU count. Briefly, 100 µl of the bacteria/cell suspension were collected and transferred to a new 96 wells plate; here, 6 serials 1:10 dilutions were performed by mixing progressively 20 µl of the bacterial suspension with 180 µl of PBS as previously detailed in literature (Harrison et al., 2010). Then, 20 µl of each serial dilutions were spotted into a LB agar plate and incubated for 24 h until round colonies were visually checked; the final number of CFU was calculated by using the following formula (Harrison et al., 2010):

$$CFU = [(number\ of\ colonies) \times (dilution\ factor)^{(serial\ dilution)}]$$

The presence of cells in the control and infected wells were visually checked by light microscopy (Invitrogen EVOSfloid, Thermo Fisher Scientific, USA) prior to undergo cell and bacteria counts in order to provide a visual confirmation of the AMPs target activity. The experiment was performed using 3 different replicates for each application.

Chondrogenesis

To exclude any interference due to the AMPs presence during cartilage repair, hMSC chondrogenesis was studied in an additional experimental series. Stem cells were seeded in 24 well plates at a density of $1x10^4$ cells/well for 24 h to allow adhesion and spreading. Then, 1 ml of the chondrogenic medium (DMEM High Glucose (4.5 g/L) supplemented with 10% ITS+1 Premix Tissue Culture Supplement, 10^{-7} M dexamethasone, 1 µM ascorbate-2-phosphate, 1% sodium pyruvate and 10 ng/mL transforming growth factor-beta 1 (TGF-β1), all from Merck, Milan, Italy) (Bonifacio et al., 2018, 2020) was added supplemented with 75 µg/ml of Nisin or 10 µg/ml of LL-37. The AMPs-free medium was considered as a control. Cells were cultivated for 21 days with the fresh medium change every 3 days. Finally, chondrogenesis was investigated by means of real-time PCR. Briefly, cells were digested for 5 min by Trizol (Merck, Milan, Italy) while RNA was reverse transcribed using the TaqMan reverse transcription kit. For real-time PCR, TaqMan Gene Expression Assay was used in a GeneAmp7500Real-Time PCR System (Applied Biosystems, USA). Data were normalized toward the housekeeping gene18S and compared to day 0 (=seeding day) by the $^{\Delta\Delta}$CT method (Cochis et al., 2017). Chondrogenic collagen-II (COLII), aggrecan (ACAN) and collagen-I (COLI) (all from Applied Biosystems, USA) expressions were evaluated. Finally, to confirm the gene expression results, cells were stained with specific chondrogenic markers Safranin-O and Alcian blue to confirm the presence of a cartilage-like matrix. Briefly, Safranin-O solution (1%) was prepared by diluting the commercial ready-to-use solution (Merck, Milan, Italy) in ultrapure water (MilliQ from Millipore), while Alcian Blue solution was prepared by dissolving 0,5 g in 50 ml of 3% acetic acid to a final pH of 2,5. Following the cell fixation in 4% paraformaldehyde (5 min, room temperature), dyes solutions were applied to cells for 15 and 30 min (room temperature) for Safranin-O and alcian blue, respectively. Finally, cells were washed three times with PBS to remove unbounded dyes and images were collected by light microscopy (Invitrogen EVOSfloid, Thermo Fisher Scientific, USA). Chondrogenesis experiments were performed using three replicates for each application.

3D Spheroids Studies

Spheroid Cultivation

To confirm the results obtained in monolayer cultures, a 3D cartilage-like spheroid model was realized according to the literature (De Hoogt et al., 2017; Langhans, 2018). Briefly, after detachment hMSC were counted and suspended in 15 ml tubes at a final concentration of $4x10^5$/ml using 1 ml of medium. The tubes were centrifuged (130 g, 5 min) to obtain a pellet; the hMSC pellet was maintained at the bottom of the tubes and cultivated

in 1 ml of fresh medium. By this method, the pellet resembled a cartilage-like spheroid morphology after 48 h.

Spheroid Metabolic Activity Evaluation

To exclude any interference of the investigated AMPs with the 3D cartilage-like formation, spheroids were cultivated as detailed in the chapter Spheroid Cultivation and allowed to equilibrate for 48 h. Next, 1 ml of chondrogenic medium supplemented with 75 μg/ml of Nisin or 10 μg/ml LL-37 was added to the spheroids and cultivated in direct contact under static conditions for 48 h. Finally, the cell metabolic activity was verified by the Alamar blue assay; spheroids cultivated in the AMPs-free medium were considered as a control. Cell density in spheroids was visually inspected by confocal microscopy (Leica SP8 confocal platform, Leica Microsystems, Wetzlar, Germany): samples were fixed in formaldehyde (20 min, room temperature), permeabilized with Triton-X100 for 5 min at room temperature (0.1% in PBS, from ThermoFisher Scientific) and stained for 20 min with 4,6-diamidino-2-phenylindole (DAPI, Merck). After staining, the spheroids were gently laid down onto glass coverslips and immediately analyzed by the confocal microscope. The experiment was performed using 3 different samples for each application.

Spheroids-Bacteria Static Co-cultures

The AMPs targeted antimicrobial activity was investigated in co-cultures by using 3D spheroids and *S. aureus* as a reference strain for articular cartilage infections as we have previously shown (Bonifacio et al., 2018, 2020). Briefly, spheroids were allowed to equilibrate for 48 h in the complete medium; then, the medium was replaced by 1 ml of the antibiotic-free DMEM containing 1×10^5 bacteria. Spheroids and bacteria were cultivated in direct contact for 48 h and then the numbers of viable cells and bacteria were determined. Specimens were collected into 15 ml tubes and enzymatically disaggregated by 1 ml of a collagenase/trypsin solution (1 mg/ml collagenase, 0.25% trypsin in PBS, all from Sigma-Aldrich) for 10 min at 37°C. Then, the tubes were vortexed for 3 times 30 s to favor cells separation and the trypan blue assay and the CFU count were used to evaluate the number of viable cells and bacteria, respectively. The experiment was carried using three different samples.

Chondrogenesis in Spheroids

As a further confirmation of the AMPs cytocompatibility, 3D spheroids were induced toward chondrogenesis as described above for cells in monolayers in the chapter Chondrogenesis. Accordingly, spheroids were allowed to equilibrate for 48 h in the basal medium (DMEM low glucose, 15% FBS) and then cultivated for 21 days in 1 ml/spheroid of the chondrogenic medium. AMPs (75 μg/ml Nisin or 10 μg/ml LL-37) were applied directly in the chondrogenic medium while AMPs-free spheroids were used as a control. Gene expression was determined after 21 days. Histology of spheroids was analyzed by means of the specific anti-collagen type II antibody (LS-C121638 from AbCam, UK); briefly, after fixing in formaldehyde (20 min, room temperature) the primary antibody (1:500 in a PBS 5% goat serum solution) was applied to the specimens and incubated overnight at 4°C. Then, the specimens were washed 3 times with PBS and collagen was unmasked by an appropriate secondary antibody (1:500, Alexa Fluor 568, ThermoFisher, USA); then, the cells were co-stained with 1:200 phalloidin (ab235137, AbCam, UK) and 1:1000 4,6-diamidino-2-phenylindole (DAPI, Merck, Milan, Italy) to visualize cytoskeleton f-actin filaments and nuclei, respectively. Fluorescence images were collected by a confocal microscope (Leica SP8 confocal platform, Leica Microsystems). The experiment was performed using 3 different samples for each application.

Bioreactor Studies

After experiments under static conditions, a commercial 3D perfusion bioreactor (3D Perfuse, from the Innovation Center of the Faculty of Technology and Metallurgy, Belgrade, Serbia) was used to simulate 3D spheroids infection in a physiological environment. The bioreactor was equipped with a Shenchen LabN1 peristaltic pump (Baoding Shenchen Precision Pump Co. Ltd, China) and located in the incubator. Experiments were performed using the following conditions: 37°C, 5% CO_2, 95% humidity, 300 μl/min flow rate (Freyria et al., 2005; Piola et al., 2013), 10 ml/bioreactor medium (DMEM low glucose, 15% FBS). The system was operated 24 h/day and the experiment was performed using three bioreactor cartridges with spheroids-bacteria co-cultures and Nisin and 3 bioreactor cartridges spheroids-bacteria co-cultures as controls.

Spheroids-Bacteria Perfusion Bioreactor Co-cultures

After 48 h of cultivation in plates, spheroids were moved into the bioreactor chambers (1 spheroid/chamber); bioreactor was operated for 24 h to equilibrate the system at the conditions detailed in Bioreactor Studies. Then, medium was removed and replaced with an antibiotic-free DMEM supplemented with 1×10^5 *S. aureus* from the inlet n.1 of the bioreactor (**Figure 9B**); immediately after, 75 μg/ml of Nisin was introduced in the system using the bioreactor inlet n.2 (**Figure 9B**) using 1 ml of DMEM medium. The AMPs-free medium containing bacteria was used as a control. The bioreactor was operated for 48 h to allow the complete interaction between the spheroids located in the chamber, the floating bacteria and Nisin. After this time, medium and spheroids were collected, enzymatically digested and analyzed for viable cell and bacteria counts by means of trypan blue and CFU, respectively, as described above in the chapter Co-cultures.

Statistical Analysis of Data

Statistical analysis of data was performed using the Statistical Package for Social Sciences (SPSSv.20.0, IBM, US). Data normal distribution and homogeneity of variance was checked by Shapiro-Wilk's and the Levene's test respectively and then data were compared by ANOVA, followed by the Tukey's test. The significance level was set at $p < 0.05$.

RESULTS AND DISCUSSION

AMPs Cytocompatibility

The increase in septic arthritis cases due to the growing use of implants and transplants as well as due to the rise of pathogens antibiotic resistance urgently requires finding new candidates to counteract such infections as prior debated in the Introduction section. Antimicrobial peptides (AMPs) represent an interesting class of candidates due to their broad-range activity toward both Gram-positive and Gram-negative bacteria. This non-specific interaction between AMPs and bacteria is due to the AMPs structure: in general, they are short sequences of amino acids (ranging from 15 to 600) characteristic by the amphiphilic configuration, due to cationic residues on one side of the peptide, and hydrophobic residues on the other side (Hancock and Sahl, 2006). AMPs can be found in different districts of the human body such as skin, gut and saliva; they are mostly associated with inflammatory processes as they can be expressed by neutrophils and act as a natural killer after epithelium inflammation due to bacteria colonization as a defensive tool (Tjabringa et al., 2005). Accordingly, AMPs can be associated with toxic events and therefore their cytocompatibility has been assayed in this work first in order to determine Nisin and LL-37 safety concentrations prior to undergo with antibacterial properties evaluation. Human mesenchymal stem cells (hMSC) have been selected as model cells due to their pivotal role in tissue repair, while Nisin and LL-37 were assayed in a range of concentrations that were selected in accordance with their MICs in association with different strains previously reported in literature as detailed in **Table 1**. Therefore, our aim was to test whether these suggested amounts were compatible with stem cells in order to be applied as antimicrobial compounds in the context of a pathological state of articular cartilage undergoing healing.

Results are summarized in **Figure 1**. Nisin demonstrated high compatibility *in vitro*: negligible differences were detected in terms of hMSC metabolic activity between Nisin-doped and untreated control cells after 24 h of direct contact (**Figure 1A**, $p > 0.05$). These findings are in line with most of previous literature reports showing that Nisin is cytocompatible toward keratinocytes, fibroblasts and osteoblasts at concentrations $<100\,\mu g/ml$ (Shin et al., 2015). Still the use of Nisin in combination with stem cells with the aim of tissue repair was not studied yet. Here 100% metabolic activity was observed up to the Nisin concentration of 75 μg/ml, so that this concentration was selected as optimal for this AMP for further investigations.

Differently, LL-37 is known to be toxic at high concentrations due to its interactions with zwitterionic mammalian lipids (Lozeau et al., 2018); accordingly, concentrations $<75\,\mu g/ml$ were reported here (**Figure 1B**). Results confirmed previous findings, showing high LL-37 toxicity at concentrations above 25 μg/ml. In fact, cytotoxicity of LL-37 at the concentrations of 25 and 50 μg/ml was significant in comparison with the untreated control causing death of >70% cells (**Figure 1B**, $p < 0.05$ indicated by *). Unlike for Nisin, some literature reports can be found regarding direct effects of LL-37 toward stem cells showing that the peptide was effective in promoting stem cell proliferation and differentiation: dental pulp stem cells (at 5–10 μg/ml LL-37 concentration, Milhan et al., 2017), adipose derived stem cells (at 2.5–20 μg/ml LL-37 concentration, Yang et al., 2016), and bone marrow derived stem cells (at 10 μg/ml LL-37 concentration, Yu et al., 2018). Still, in these works the applied LL-37 concentrations ranged between 5–20 μg/ml, thus confirming the possible use of this peptide only at low concentrations. So, in the present study the concentration of 10 μg/ml was considered as optimal for LL-37 for further investigations.

AMPs Antibacterial Activity

After investigating the AMPs cytocompatibility *in vitro*, the same concentrations (with the exception of LL-37 at 75 μg/ml that was avoided due to the high toxicity) were applied toward 2 Gram-positive strains, *S. aureus* and *S. epidermidis*, as well as toward 2 Gram-negative bacteria that is *E. coli* and *A. actinomycetemcomitans*. Despite the evidence that *S. aureus* and *S. epidermidis* are mostly related with septic arthritis, the decision to extend the study toward two Gram-negative strains was made in order to evaluate any difference in efficacy of the selected AMPs. The main aim was to correlate these results with cytocompatibility results in order to determine Nisin and/or LL-37 concentrations that will ensure both safety and antimicrobial properties in potential applications.

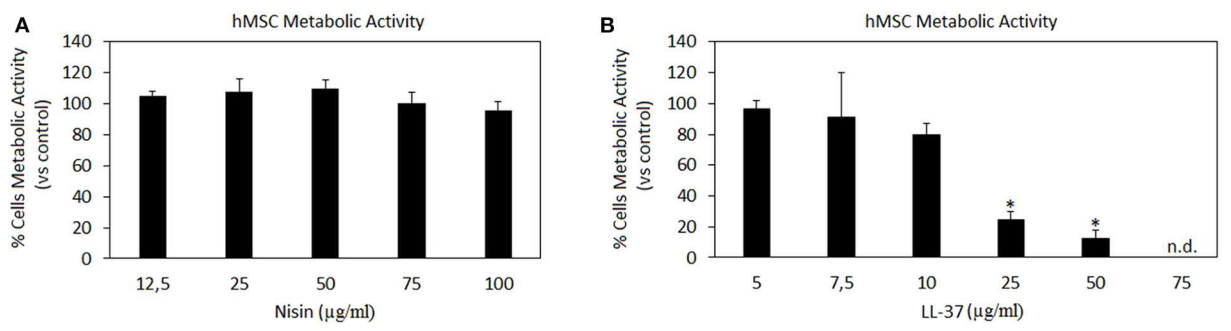

FIGURE 1 | AMPs cytocompatibility. Nisin **(A)** was shown as *in vitro* cytocompatible at all the tested concentrations ($p > 0.005$ *vs.* the untreated control), while LL-37 **(B)** demonstrated high toxicity starting from the concentration of 25 μg/ml ($p < 0.005$ *vs.* the untreated control, indicated by the *). Bars represent means and standard deviations. n.d., not detected.

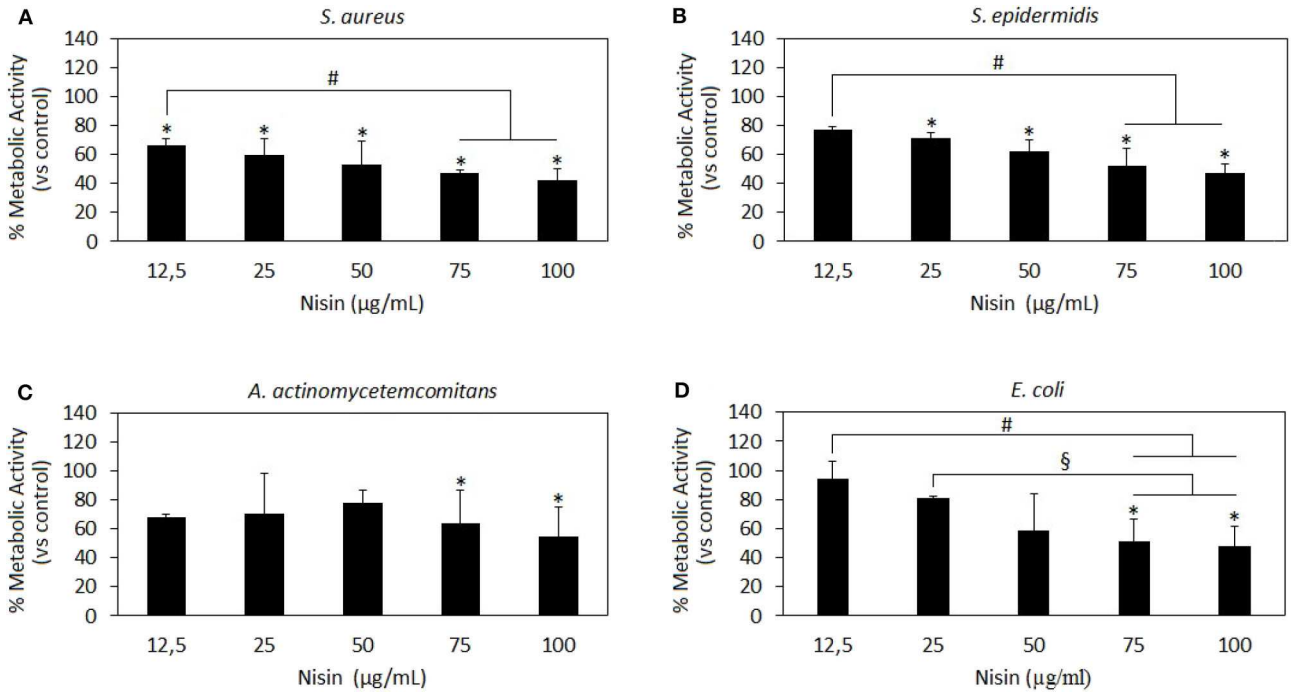

FIGURE 2 | Nisin antibacterial activity. Nisin was shown as very effective toward the Gram-positive strains *S. aureus* **(A)** and *S. epidermidis* **(B)** wherein results at all concentrations >12.5 μg/ml are significant as compared to the untreated control (**A,B**, $p < 0.05$ indicated by the *). Moreover, the results at 75 and 100 μg/ml concentrations were significant as compared to those at the lowest 12.5 μg/ml concentration (**A,B** $p < 0.05$ indicated by the #), thus indicating a dose-dependent effect. Nisin 75 and 100 mg/ml showed also a high efficacy toward the Gram-negative *A. actinomycetemcomitans* **(C)** and *E. coli* **(D)** in comparison to untreated controls ($p < 0.05$ indicated by the *) and lower concentrations (**D**, $p < 0.05$, indicated by the # and §). Bars represent means and standard deviations.

Results are reported in **Figures 2** and **3** for Nisin and LL-37, respectively.

Nisin has shown to be more effective toward Gram-positive strains *S. aureus* and *S. epidermidis* (**Figures 2A,B**, respectively) as compared to Gram-negative strains (**Figures 2C,D**). In fact, all the concentrations >12.5 μg/ml resulted in significant reduction of the bacteria metabolism in comparison to untreated controls (**Figures 2A,B**, $p < 0.05$ indicated by the *). Moreover, the increase in Nisin concentration up to 75 and 100 μg/ml induced a more evident metabolism reduction that was significant in comparison to the effects of the lowest concentration used of 12.5 μg/ml. Differently, only 75 and 100 μg/ml were effective to significantly reduce Gram-negative *A. actinomycetemcomitans* (**Figure 2C**, $p < 0.05$ indicated by *) and *E. coli* metabolism (**Figure 2D**, $p < 0.05$ indicated by *). Keeping in mind the primary goal to couple safety and antimicrobial properties, Nisin concentrations of 75 and 100 μg/ml look as promising candidates as they demonstrated high cytocompatibility and confirmed significant reduction in the viability of both Gram-positive and Gram-negative strains. These findings are in line with previous literature reports suggesting Nisin as an active agent toward Gram-positive bacteria. In fact, Nisin is classified as a Type A (I) lantibiotic (Asaduzzaman and Sonomoto, 2009), a class of molecules holding amphipathic and cationic properties known to affect Gram-positive bacteria (Smith and Hillman, 2008). The Nisin activity is targeted toward the integrity of the cellular membrane that is perturbed by forming small pores by binding the cell-wall precursor lipid II with high affinity (Wiedemann et al., 2001). This binding acts also as a precursor to inhibit other vital mechanisms such as cell wall biosynthesis, spore outgrowth, and activation of autolytic enzymes (Peschel and Sahl, 2006). This complex ensemble of different mechanisms is probably the reason why bacteria have difficulties in developing anti-Nisin strategies.

LL-37 results are reported in **Figure 3**. In general, only the 50 μg/ml concentration induced significantly different results as compared to those in the untreated controls for all the assayed strains (**Figures 3A–D**, $p < 0.05$ indicated by *). In particular, LL-37 was found to be less effective toward the Gram-positive strains *S. aureus* (**Figure 3A**) and *S. epidermidis* (**Figure 3B**). However, this was not an encouraging finding as the 50 μg/ml concentration was shown as toxic toward hMSC in the cytocompatibility evaluation thus not displaying the required coupling of safety and antimicrobial properties. Moving to the Gram-negative strains, LL-37 was shown to be more effective; in fact, a statistically significant difference in comparison with the untreated controls was observed starting from the concentration of 10 μg/ml for both *A. actinomycetemcomitans* (**Figure 3C**, $p < 0.05$ indicated by *) and *E. coli* (**Figure 3D**, $p < 0.05$ indicated by *) where the same concentrations (10–25–50 μg/ml) induced significant different results also as compared to those obtained at the lowest concentration of 5 μg/ml ($p < 0.05$ indicated

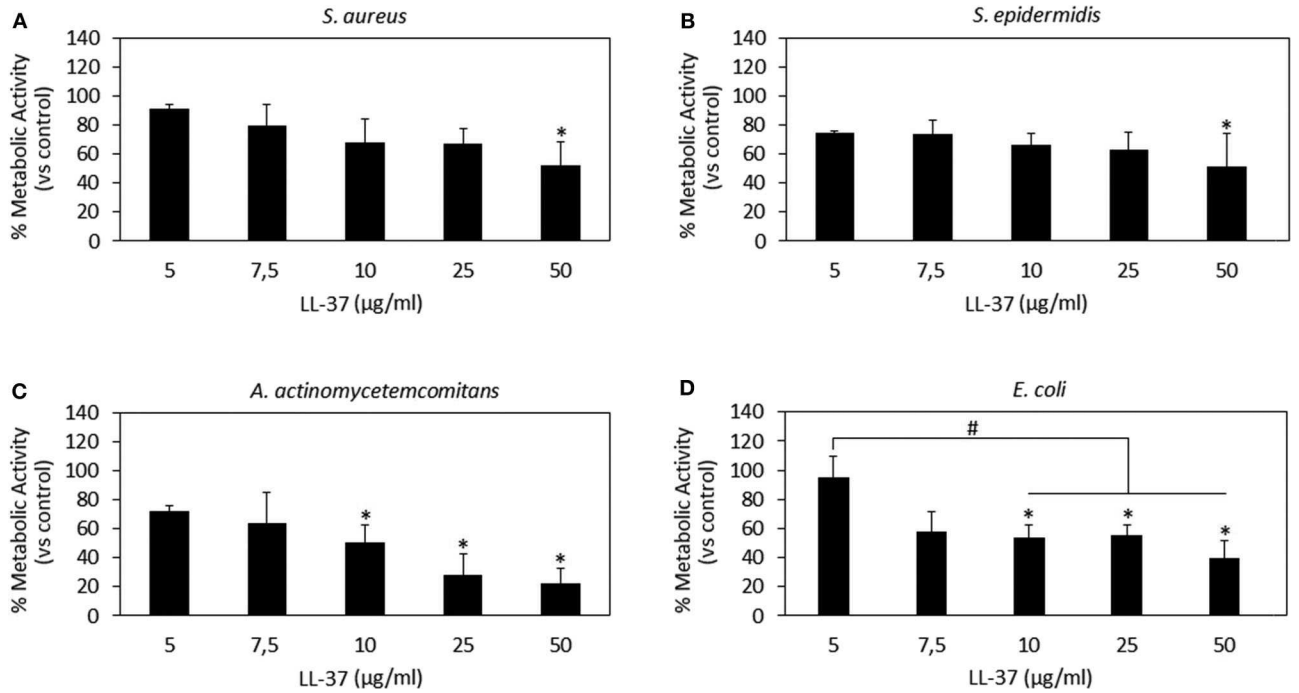

FIGURE 3 | LL-37 antibacterial activity. LL-37 was shown as very effective toward the Gram-negative strains *A. actinomycetemcomitans* **(C)** and *E. coli* **(D)** at concentrations starting from 10 μg/ml inducing significantly different results as compared to the untreated controls (**C,D**, $p < 0.05$ indicated by the *) and lower concentrations (**D**, $p < 0.05$ indicated by the #). A less effective activity was noted toward the Gram-positive *S. aureus* **(A)** and *S. epidermidis* **(B)** where only the use of 50 μg/ml induced a significant reduction in the bacteria metabolism ($p < 0.05$ indicated by the *). Bars represent means and standard deviations.

by #). Our results seem to be in line with those presented in literature where LL-37 was shown to exhibit a strong killing capacity toward Gram-negative strains such as *E. coli* whereas to only antagonize Gram-positive bacteria such as *S. aureus* (Wang et al., 2014). Similarly to Nisin, the difference can be ascribed to the non-targeted activity against the cell membrane: due to its cationic and amphipathic features, LL-37 can accumulate within bacteria cell walls leading to the disruption of the curved anionic membrane surfaces by development of pores (Wang, 2014). The latter are probably due to the ion channels that derive from the formation of long helix-bundle structures linking the AMP with the bacterial membrane that cause modification of the membrane permeability (Wang, 2014).

Finally, as a general consideration it should be mentioned that in this work the effect of AMPs was tested in a direct manner by using a metabolic assay to rank the peptides effects toward bacteria. So, further studies in the future should be addressed to verify other important aspects such as biofilm thickness that is a key step for drug resistance acquisition as well as the bacterial ability to develop intrinsic resistance toward the peptides. Moreover, the use of AMPs directly in the medium is probably not the best choice and it is open to some limitations related to leakage and targeting: ideally, surface modification and the use of nanocarriers will be considered in the future to minimize AMPs leaking and ensure it maintenance in the joint to avoid occurrence of septic arthritis. As an example, He et al. (2019) reported that LL-37 loaded onto silk fibroin nanoparticles enhanced recruitment and differentiation of stem cells toward bone-like phenotype onto titanium as well as macrophages activation. Similarly, Ron-Doitch et al. (2016) demonstrated how the toxicity of free LL-37 peptide was lowered by encapsulation within liposomes, thus confirming the importance of development of functional delivery systems to improve AMPs properties.

Co-cultures

After the evaluation of AMPs cytocompatibility and antibacterial activity, the following concentrations were selected as the most promising in reducing the pathogen metabolism while preserving the cell viability that was considered as the key factor in this study: 75 μg/ml Nisin and 10 μg/ml LL-37. However, those results were obtained by keeping separated cells and bacteria in different environments; so, to check whether the AMPs activity was really targeting only (or at least mainly) bacteria, a co-culture assay was performed as we have previously described (Jekabsone et al., 2019; Cochis et al., 2020) to evaluate the AMPs performance in the same environment containing both cells and bacteria. Therefore, it should be clarified that only the number of adherent bacteria was evaluated as suggestive for those able to colonize the same surface as cells when cultivated in the same environment. This choice can represent the limitation of this technique as the lack of data related to floating viable bacteria can probably lead to an underestimation of the infection rate; however, this evaluation allows to focus on those bacteria that are able to adhere and

proliferate onto a surface designed for cell population such as that of an implantable device thus representing the major risk for the healing success.

Results are reported in **Figure 4**. In general, Nisin demonstrated superior performances in comparison to LL-37. Looking at the viable cell count (**Figure 4A**), it was noticed that after 48 h cultivation (24 h seeding + 24 h in contact with the bacteria and AMPs) the presence of Nisin allowed the cell growth in the case of infection with *S. aureus* (SA) and *S. epidermidis* (SE). Conversely, the cell number was similar to the starting number (=seeding time) for the infection with *A. actinomycetemcomitans* (AA) whereas it was decreased when *E. coli* (EC) was used for the infection. These results were justified by the count of viable bacteria coming from the same environment as the cells (**Figure 4C**); in fact, the number of viable colonies was decreased in comparison to the starting number for SA, SE, and AA, while an increase of about 1 log was observed for EC. Coming back to the antibacterial assay results (**Figure 2**), a similar trend was here observed, thus confirming the Nisin strong activity toward Gram-positive strains. When

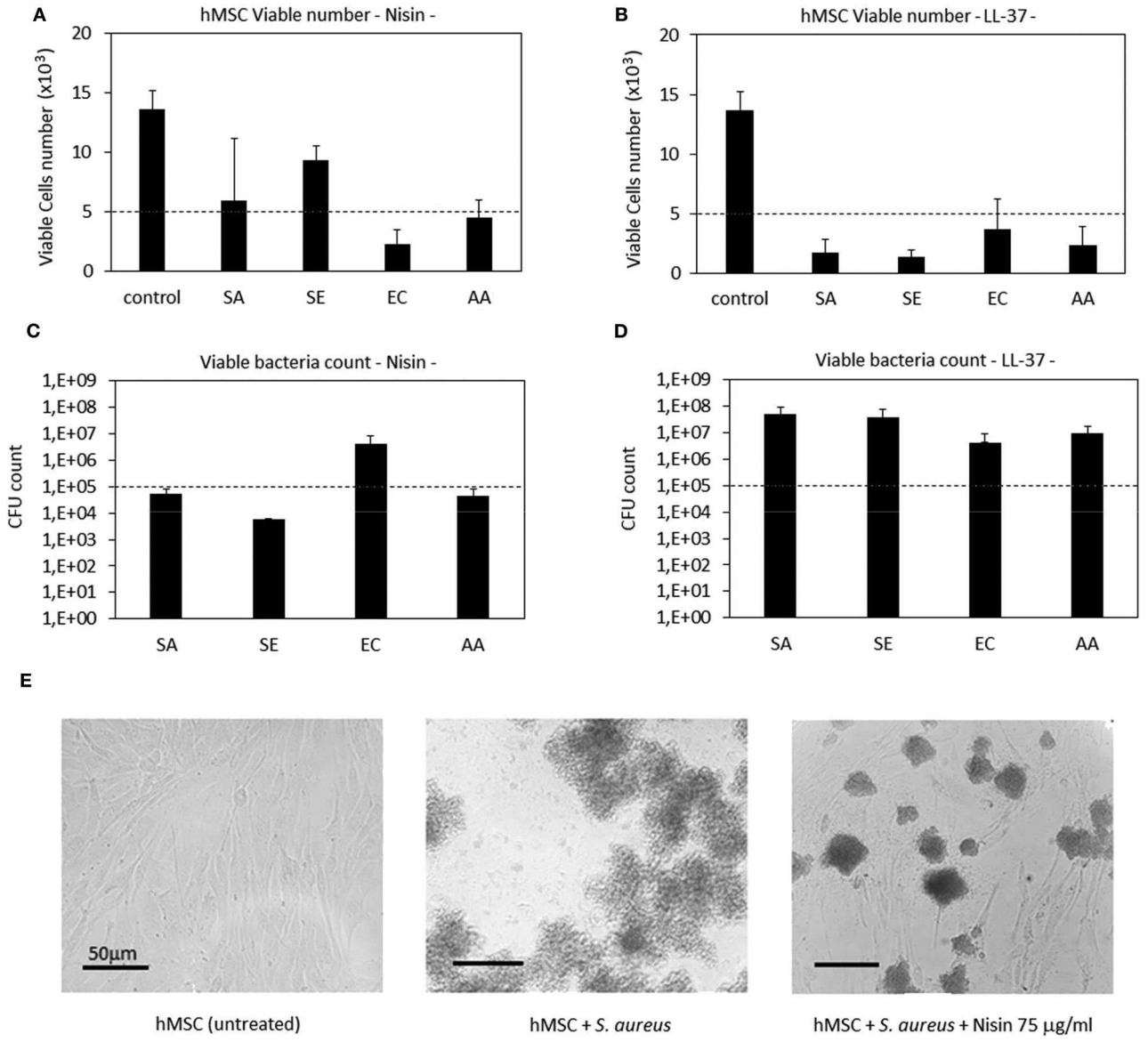

FIGURE 4 | Cells-bacteria co-culture. Nisin showed a targeted activity in decreasing the viable bacteria number **(C)** and at the same time preserving cells **(A)**. Differently, the use of LL-37 was not effective in protecting cells from infection; in fact, they decreased from the starting number **(B)** while the bacteria were able to proliferate **(D)**. Finally, representative optical micrographs of *S. aureus* and hMSC cultures are shown **(E)** to demonstrate the difference between the control cells (left), cells and bacteria co-culture without Nisin (middle) and cells and bacteria co-culture with the addition of Nisin (right). Bars represent means and standard deviations; dashed lines indicate starting cell and bacteria numbers. SA, *S. aureus*; SE, *S. epidermidis*; EC, *E. coli*; AA, *A. actinomycetemcomitans*.

cells were cultivated in the presence of bacteria without the AMPs addition, viable cells were not detected (data not shown). As a confirmation, representative images of cells infected with *S. aureus* in the presence of Nisin are shown (**Figure 4E**): while the infection induced the death of all cells (middle panel), the presence of 75 μg/ml of Nisin preserved most of the cells (right panel) that had a comparable morphology as the untreated controls (left panel). So, the targeted activity was verified for Nisin as it was able to counteract surface-adhered bacteria proliferation while preserving at the same time the ability of cells to grow.

LL-37 exhibited a lower antibacterial activity in comparison with Nisin when applied in the co-culture. In fact, all the strains applied in the assay induced a reduction in the cell number in comparison to the starting one (**Figure 4B**). As a consequence, the bacteria number was found to be increased in comparison to the starting infection (**Figure 4D**). So, the use of LL-37 for the co-culture did not satisfy the requirement to inhibit the bacterial proliferation for the benefit of cells as it was the case for Nisin. This difference can be probably ascribed to the different concentrations of applied AMPs (75 μg/ml Nisin vs. 10 μg/ml LL-37); in fact, it can be supposed that a part of the peptides aggregates with the medium proteins and precipitates thus losing its activity toward bacteria (Zozu et al., 2018). As debated above, direct use of AMPs in the medium is probably not the best solution for their administration due to leakage; surface modification and the use of nanocarriers can probably ameliorate AMPs effectiveness thus permitting reduction of the effective amount and allowing the use of more cytocompatible concentration ranges. However, according to the presented findings, the use of a low concentration of LL-37 was necessary due to its toxic effect toward stem cells as it was shown in the cytotoxicity assay (**Figure 1**).

Chondrogenesis in Cell Monolayers

After confirming the AMPs cytocompatibility with mesenchymal stem cells, their role was investigated toward chondrogenesis. Stem cell commitment toward cartilage-like tissue in the presence of AMPs was assayed to exclude any possible interference of the peptides during the healing process. Accordingly, the selected AMPs concentrations (75 μg/ml Nisin and 10 μg/ml LL-37) were introduced into the chondrogenic medium to evaluate any differences in comparison to the AMPs-free controls. Results are reported in **Figure 5**.

In general, chondrogenic collagen type II (COL 2, **Figure 5A**) and aggrecan (ACAN, **Figure 5B**) expressions revealed that the presence of AMPs did not induce a down-regulation of these genes, thus suggesting that stem cell differentiation toward cartilage-like phenotype occurred in a similar manner as in the untreated controls. As a consequence, low expression of the

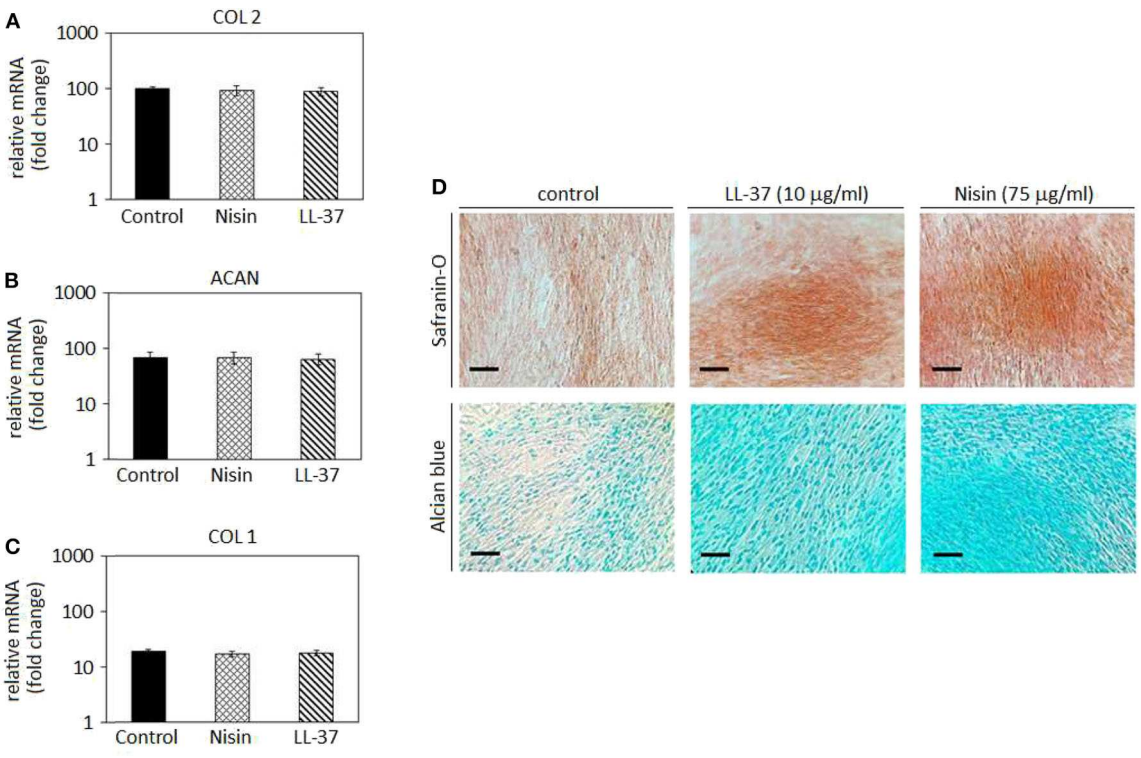

FIGURE 5 | Chondrogenesis in cell monolayers. The use of 75 μg/ml Nisin or 10 μg/ml LL-37 did not affect the hMSC chondrogenesis as chondrogenic genes collagen type II (**A**, COL 2) and aggrecan (**B**, ACAN) were expressed in a similar manner as in the untreated control. As a confirmation, the osteogenic collagen type I (COL 1) gene was not up-regulated **(C)**. Histology **(D)** confirmed the presence of a cartilage-like matrix by specific Safranin-O and Alcian blue staining. Scale bar = 100 μm.

bone-related collagen type I gene (COL 1, **Figure 5C**) confirmed that the cell differentiation moved toward the chondrogenic phenotype and not toward the osteogenic one. Such findings were predictable: as previously discussed in section AMPs Cytocompatibility, LL-37 was shown to be effective in promoting stem cells differentiation and adverse effects were not observed at the same concentrations (5–20 μg/ml) (Yang et al., 2016; Milhan et al., 2017; Yu et al., 2018). Conversely, at the best of our knowledge, Nisin was not assayed for effects on the stem cell commitment; however, the lack of toxic effects noticed in the cytocompatibility assay allowed for the speculation that Nisin could be also regarded as inert, not inducing any impairments to the stem cell commitment.

Gene expression results were visually confirmed by histology analysis (**Figure 5D**): in fact, cells cultivated with AMPs-doped medium were shown as positive for Safranin-O (upper panel) and Alcian blue (lower panel). These specific markers suggested the presence of glycosaminoglycans (GAGs) and proteoglycans in the cell matrix thus resembling a cartilage-like tissue. The lack of precipitates or a specific background suggests that AMPs did not interfere with the staining that can be therefore ascribed to the presence of GAGs and proteoglycans synthesized by the cells during cartilage commitment.

To the best of our knowledge, this is the first time that Nisin and LL-37 were investigated in relation to hMSC maturation toward cartilage. Considering the proved antibacterial and safety properties at the selected concentrations, our results suggest that the use of 75 μg/ml Nisin or 10 μg/ml LL-37 does not affect or interfere with hMSC maturation toward cartilage-like phenotype and represents a promising tool to preserve articular cartilage healing and protect from bacterial infection. However, a study from Baranska-Rybak et al. (2006) reported a decrease in the LL-37 antibacterial activity in biological fluids rich in GAGs; considering that the expression of GAGs represents the most indicative evidence of the cartilage-like commitment this evidence can represent a drawback for the use of LL-37 for cartilage healing thus pointing toward the use of Nisin.

3D Spheroid Studies

AMPs Cytocompatibility

After studies using cells in monolayers, a more physiological cartilage-like 3D spheroid model (Scalzone et al., 2019) was applied for further studies. This model is commonly applied for chondrogenic studies and is based on the use of mesenchymal stem cells that substitute chondrocytes for *in vitro* studies in order to overcome the poor expansion capacity of the latter cells. However, the key of this model is the cell-to-cell interaction that allows the formation of strong interconnections that are of a pivotal importance for chondrogenesis. Of course, the extracellular matrix is of fundamental importance to ensure tight connections of cells and the biochemical crosstalk. As previously debated, AMPs are able to link to the outer cell membrane thus representing a possible hitch for the spheroid integrity. Accordingly, after cell aggregation upon centrifugation, spheroids were cultivated for 24 and 48 h in a direct contact with AMPs; then the cell metabolic activity was evaluated and compared to that of the untreated spheroids that were considered as a control. Results are reported in **Figure 6**.

In general, the use of AMPs did not perturb the cell viability (**Figure 6A**, $p > 0.05$ *vs.* the untreated control) and the spheroid cells density, which was confirmed for all the specimens. These results were somehow expected as the applied AMPs concentrations (75 μg/ml Nisin and 10 μg/ml LL-37) were chosen according to their cytocompatibility. Cell density was not decreased as determined by observation of spheroids by using confocal microscopy and DAPI signals number evaluation (**Figure 6B**, representative for cell density recovered into the spheroids' core). By comparing results of 3D spheroids and cell monolayers, a similar tolerance toward AMPs was noticed. This is a promising result as the possible use of AMPs to preserve articular cartilage healing when infection occurs requires experimental investigations under physiological-like conditions to which are those in 3D spheroids much more similar than in the cell monolayers, especially for the matrix development (Scalzone et al., 2019).

It is again not straightforward to compare the obtained findings with literature reports as very few examples of the use of AMPs with 3D tissues (none dealing with cartilage-like tissues) can be found and none for Nisin. Lombardo Bedran et al. (2015) showed that LL-37 alone or in combination with other polyphenols was effective in reducing the inflammatory response in a three-dimensional co-culture model of gingival epithelial cells and fibroblasts. Accordingly, the present results encourage further investigations of the use of AMPs in 3D cell and tissue culture models.

Co-cultures

After confirming the AMPs compatibility with 3D spheroids, the co-culture experiment was repeated to further confirm their targeted activity toward bacteria. Accordingly, as performed with cells in monolayers, the spheroids were allowed to equilibrate for 48 h in the complete medium and then they were infected with the antibiotics-free medium containing 1×10^5 *S. aureus* and the peptides. After 48 h, the spheroids were enzymatically disaggregated and viable cells and adhered bacteria were counted by the trypan blue staining and CFU counts, respectively. Results are reported in **Figure 7**.

In general, we observed a lower decrease in the viable cell number for both AMPs after infection in comparison to the previous experiment performed with cells in monolayers (**Figure 4**). First explanation of these findings can be related to the hMSC intrinsic antibacterial properties (Mezey and Nemeth, 2015). In fact, while for the monolayer experiments 5×10^3 cells were used, here each spheroid was composed of 4×10^5 cells, thus holding ≈80× more cells. Furthermore, the cells were arranged in a 3D structure resembling the physiological environment, enhancing cell differentiation, and protecting the cells in the interior from the external factors. So, the number of cells in the spheroids was similar in all cultures and not significantly different from the initial number (**Figure 7A**). On the other hand, differences were noticed between the numbers of colonies adhered to the spheroids and the floating ones (**Figure 7B**). In fact, only few colonies were able to adhere to the spheroid while

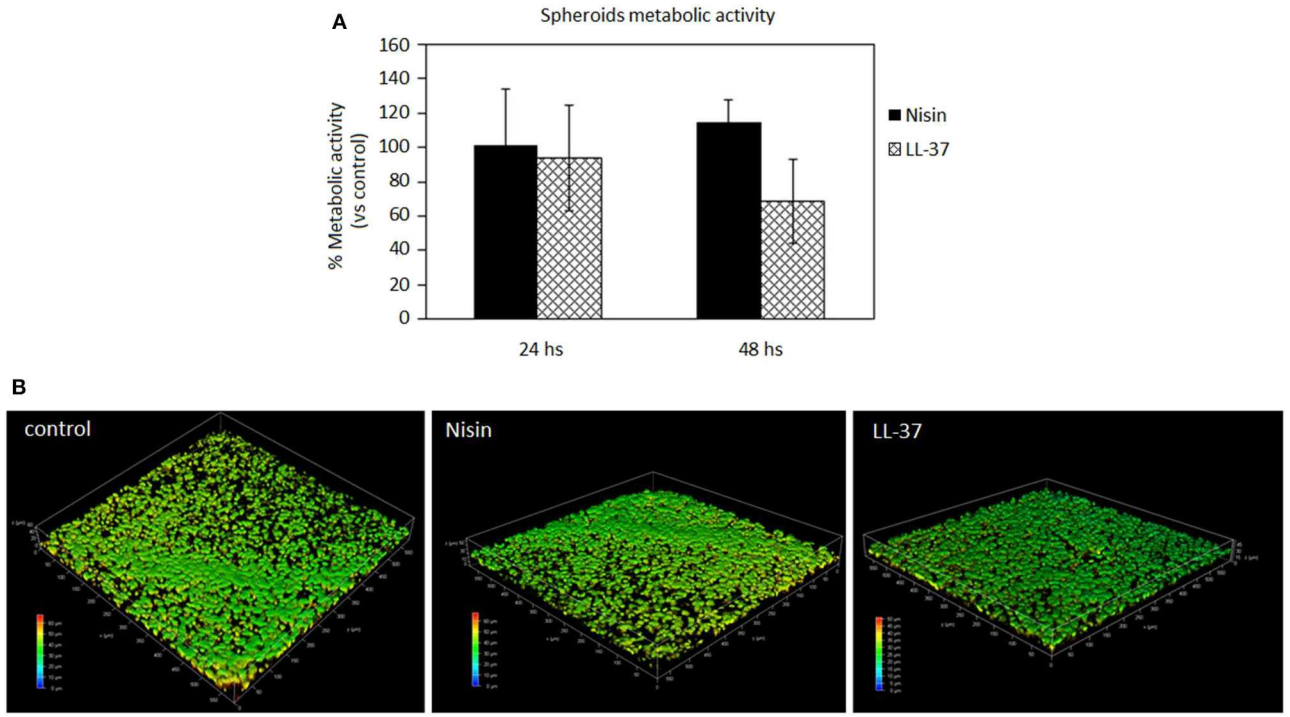

FIGURE 6 | AMPs cytocompatibility in the spheroid 3D model. The use of both Nisin (75 μg/ml) or LL-37 (10 μg/ml) did not affect the cell metabolic activity (**A**, $p > 0.05$ *vs.* untreated controls) as well as the cell density **(B)**. Bars represent means and standard deviations.

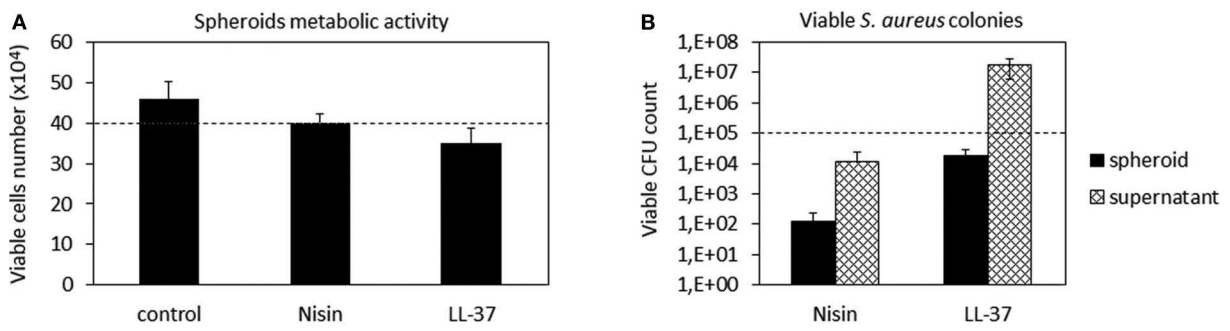

FIGURE 7 | 3D Spheroids-bacteria co-culture. The cell number **(A)** was preserved by both Nisin and LL-37 as values were comparable to the untreated control. Differently, Nisin confirmed a superior antibacterial activity in comparison to LL-37 as the number of viable bacteria in the supernatant was reduced for about 1 log **(B)**. Bars represent means and standard deviations; dashed lines indicate the starting cell and bacteria numbers.

most of bacteria remained in the supernatant; here, the activity of Nisin was confirmed to be superior in comparison to LL-37 as it reduced the bacterial count for about 1 log in comparison to the starting number (**Figure 7B**). Accordingly, the message of the results obtained in the monolayer experiments were here confirmed, suggesting Nisin as the most promising candidate.

As a general consideration, in our opinion these findings also suggest the importance to perform analyses by using physiologically relevant models such as 3D cell and tissue cultures even for *in vitro* studies. This consideration seems to be of particular importance when cartilage is under consideration: in fact, as previously demonstrated for example by Kim et al. (2003) there is an evident difference in terms of the cell biological response in 2D monolayer and 3D tissue-like cultivation. Therefore, it can be supposed that a different cell response to the environmental changes (such as infection or injury) is also conditioned by the cultivation method applied for *in vitro* studies; in fact, in this study the performance of LL-37 was improved in 3D spheroid cultures in comparison with cell monolayers. Therefore, we believe that an important confirmation coming from this work is related to the appropriate choice of the study design as it

is also evidenced in the fluidic studies described in chapter Bioreactor Studies.

Chondrogenesis in Spheroids

The 3D spheroid model was further applied to study the hMSC chondrogenesis in the presence of AMPs. The use of high-density cell spheroids as a study model was indicated to resemble better the physiological conditions required for autologous cartilage repair in comparison to typical monolayer cultivation (De Hoogt et al., 2017; Langhans, 2018). Results are reported in **Figure 8**.

In general, chondrogenic genes collagen type II (COL 2) and aggrecan (ACAN) up-regulation revealed that the presence of AMPs did not interfere with stem cell commitment toward the cartilage-like phenotype as also observed for the cells in monolayers (**Figure 5**). Accordingly, low expression of the bone-related collagen type I gene (COL 1) provided a further proof that cells differentiated toward the chondrogenic phenotype and not toward the osteogenic one. However, by applying the 3D model a general more evident upregulation was observed for chondrogenic genes in comparison to the 2D model; in fact, COL2 as well as ACAN were much more upregulated in 3D culture (**Figure 8**) than in cells in monolayers (**Figure 5**). This was a further confirmation of the importance to apply 3D models also for *in vitro* studies to better mimic physiological conditions that influence cell responses.

The gene expression results were confirmed by fluorescent staining (**Figure 8B**, representative for Nisin): in fact, spheroids cultivated with AMPs-doped medium preserved their high cellular density (nuclei stained in blue by DAPI) as well as high cells-to-cell tight junctions were maintained as shown by the interconnected cytoskeletons (marked in green with phalloidin). Moreover, the strong red signal representative for chondrogenic collagen type II showed that the ECM formed within the spheroids is highly cartilage-like.

As discussed above, to the best of our knowledge this is the first manuscript hypothesizing the use of Nisin and LL-37 for articular cartilage healing preservation in a septic environment; accordingly, other works are not useful to compare with our findings. However, due to the lack of toxicity of the selected concentrations toward 3D spheroids and the expression of chondrogenic genes after the stem cell commitment in the presence of AMPs, we consider these findings as very promising

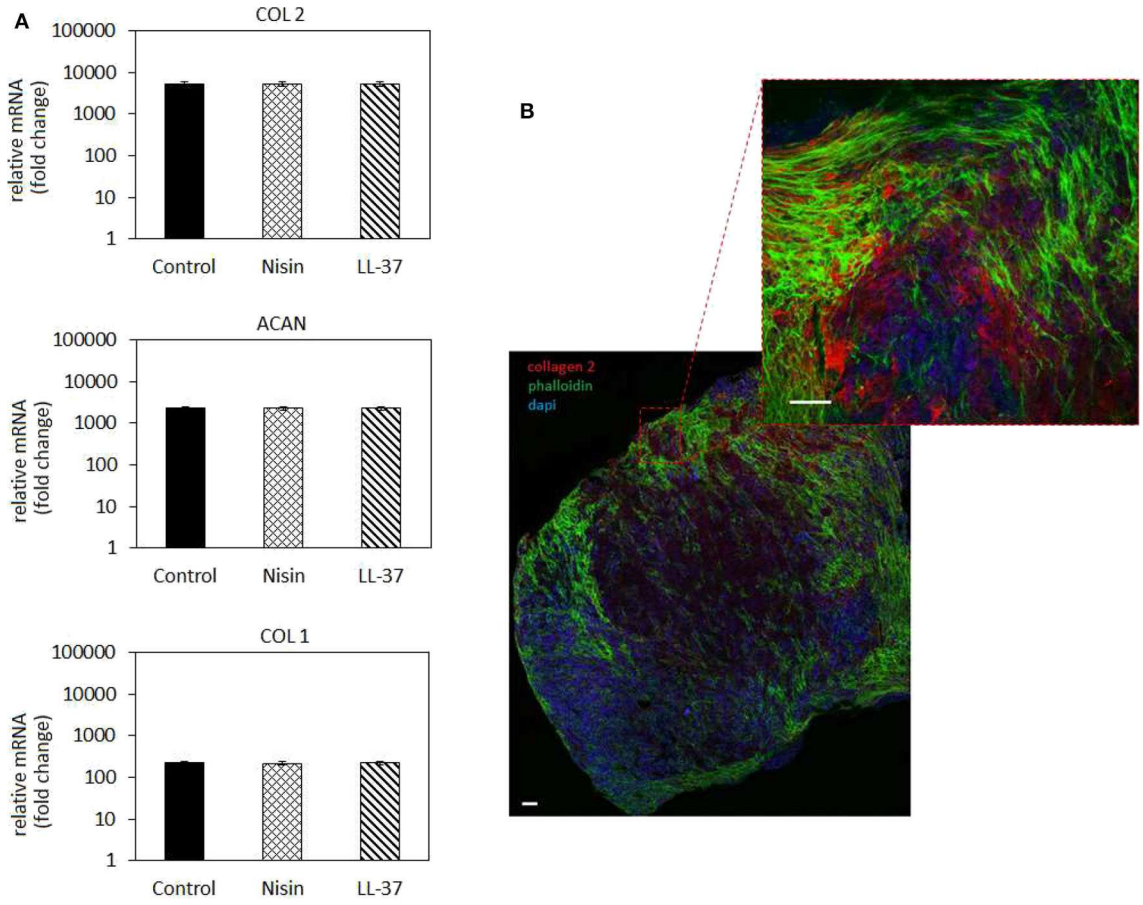

FIGURE 8 | Chondrogenesis in 3D spheroids. **(A)** The use of 75 μg/ml Nisin or 10 μg/ml LL-37 did not affect the hMSC chondrogenesis: chondrogenic genes for collagen type II (COL 2) and aggrecan (ACAN) were up-regulated at the same levels as in the untreated control. Fluorescent images **(B)** confirmed the presence of a cartilage-like matrix by the presence of the specific collagen type II staining (in red). Scale bar = 100 μm.

to explore the possible use of Nisin and LL-37 for applications aimed at cartilage healing.

Bioreactor Studies

Taking into account cytocompatibility and antibacterial results obtained from both monolayer and 3D experiments, Nisin was considered as the more promising peptide for further evaluations. Accordingly, we moved from static to hydrodynamic conditions to better mimic the physiological environment. Articular cartilage is normally subjected to dynamic compression and shear deformations as the main mechanical stimuli, while inducing, in the same time, interstitial fluid flow. It has been recognized that fluid flow and corresponding shear stresses affect cell metabolism, differentiation, morphoregulation and ECM synthesis (Rutkowski and Swartz, 2006) although exact mechanisms are not yet precisely defined. Perfusion was shown to stimulate chondrocyte proliferation and ECM synthesis (Pazzano et al., 2000; Freyria et al., 2005; Chen et al., 2012) as well as chondrogenic differentiation of hMSCs (Alves da Silva et al., 2011) while the effects may be donor-dependent (Kock et al., 2014). In the case of *in vitro* cultivation of 3D cell and tissue cultures, such as spheroids ∼2 mm in size in the present work, application of fluid flow is necessary to ensure efficient mass transport in the liquid phase and adequate delivery of both, bacteria and AMPs to the spheroids. Thus, we have used a perfusion bioreactor: the spheroids were hosted in the chamber while bacteria (*S. aureus*) and AMPs (Nisin 75 μg/ml) were separately introduced into the circulating medium by the upper and lower inlets using syringes (schematized in **Figures 9A,B**). Then, the system was recirculated to allow a simultaneous introduction of bacteria and Nisin to the spheroids chamber. After 48 h of continuous flow, spheroids and medium were collected and analyzed regarding the cell viability and bacterial count (both spheroid-adhered and floating) by the trypan blue and CFU count, respectively. Spheroids cultivated in the normal medium were considered as a control. Results are reported in **Figure 9**.

In general, results were very promising. In fact, the number of viable cells was comparable between the untreated control and infected spheroids when Nisin was added (**Figure 9C**). So, the cell protective while, at the same time, targeted antibacterial activity of Nisin was fully confirmed also under flow conditions. However, a slight decrease in the cell number from the starting number (4×10^5) was noticed in both control (∼3.4×10^5)

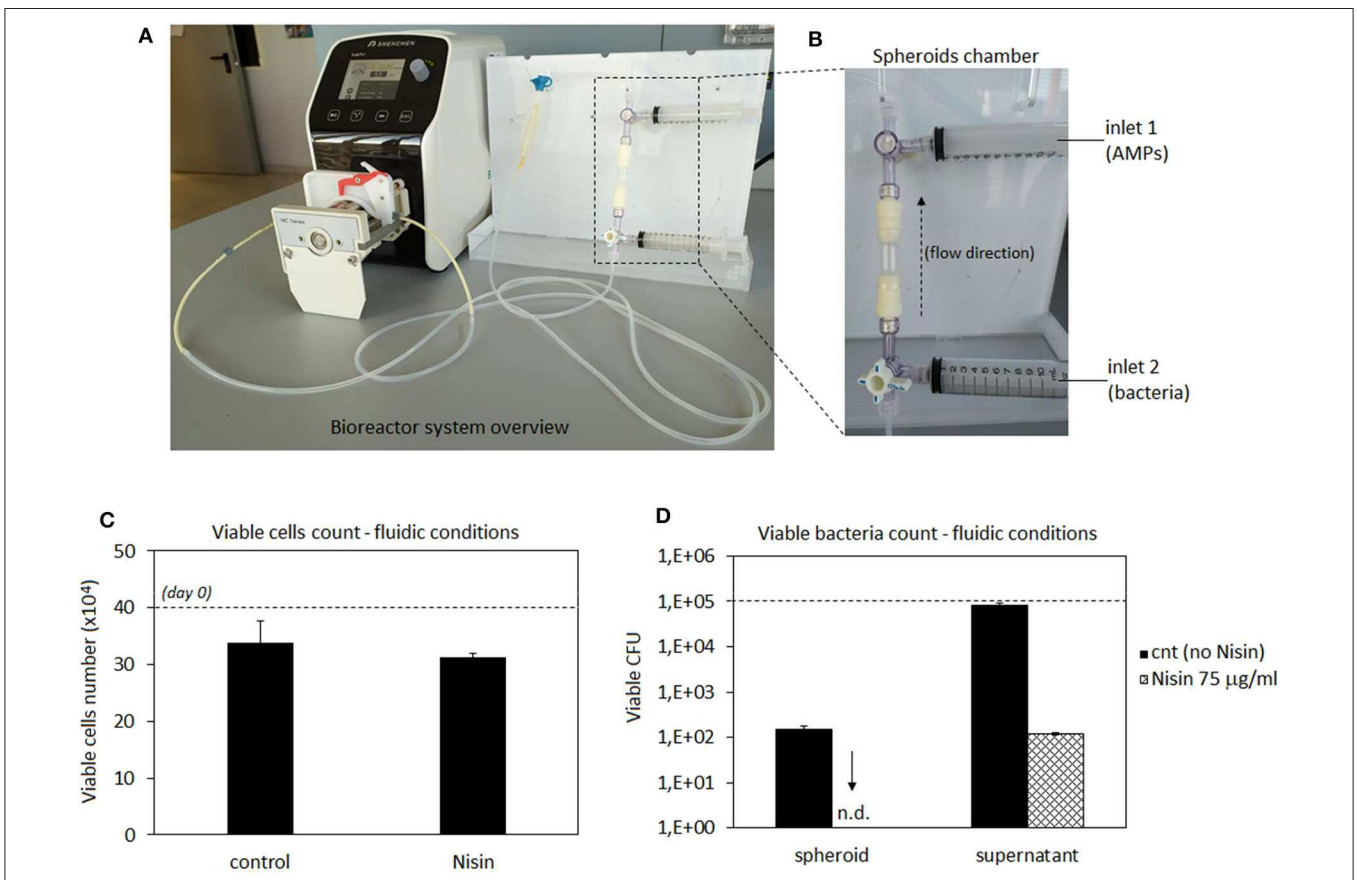

FIGURE 9 | Bioreactor studies. A general overview of the perfusion bioreactor **(A)** and its chamber with 2 external inlets **(B)**. Nisin was very effective to counteract the *S. aureus* infection as the number of viable cells was preserved and comparable to that in the untreated control **(C)** while adherent bacteria were not detected on the spheroid surfaces and the number of floating bacteria was significantly reduced **(D)** by the presence of Nisin in comparison with the untreated controls. Bars represent means and standard deviations. n.d, not detected; dashed lines represent seeding number of cells and bacteria.

and test spheroids ($\sim 3.1 \times 10^5$), which could be probably ascribed to the shear stress induced by the medium flow. In fact, undifferentiated hMSC have been demonstrated to be sensitive to mechanical stresses caused by hydrostatic pressure (Tower, 2012). However, the comparable values reported by control and Nisin treated cells suggest that Nisin did not introduce any toxic effect besides the shear stress due to the medium flow.

More importantly, the CFU count revealed that bacteria were not able to adhere to the spheroids when Nisin was introduced into the flow (**Figure 9D**). On the contrary, when the system was operated in the absence of Nisin, bacteria were able to adhere and colonize the spheroid. This is a crucial difference in comparison to static conditions (**Figure 7B**). Some explanations can be hypothesized. First of all, bacterial adhesion under static conditions is eased by the lack of shear stresses that affect, deform and remove bacterial cells from the surfaces. This was demonstrated for example by Garny et al. who showed how the shear stress applied by rotating conditions significantly reduced the biofilm adhesion, biomass and thickness in comparison to the same static conditions (Garny et al., 2008). So, hydrodynamic conditions are more difficult for biofilm development in comparison to the static cultivations. We also observed a similar trend as some bacteria colonizing the spheroid were detected in the absence of Nisin ($\sim 1.2 \times 10^2$) but this number was lower than of that of the initial inoculum as well as the number of floating bacteria that was comparable to day 0. Second, the presence of AMPs can strongly affect the bacterial adhesion due to the membrane damaging, which could be further promoted by the shear stress. In fact, the initial bacteria adhesion is mediated by a number of cell wall proteins such as adhesins that provide anchorage to the host surface (Otto, 2013). AMPs cause severe wall damages such as pore formation due to the interaction with the membrane; this damaged wall condition leads to the failure in adhesins expression thus preventing the bacterial adhesion. Moreover, the number of floating viable bacteria was reduced in comparison to the starting number of bacteria (1×10^5) thus in general confirming the Nisin antibacterial activity also under hydrodynamic conditions.

In conclusion, it can be speculated that the dynamic conditions involving the use of 3D spheroids provided better understanding of the Nisin efficacy thanks to the simultaneous combination of hMSC-shear stress-AMP effects exploited under physiologically relevant conditions. So, taking into account a possible use of a delivery system to ameliorate the AMPs performances in future studies, the complexity of the study design applied here provided the selection of the most promising peptide and the possible working concentration range.

CONCLUSIONS

Biomaterials science offers a promising solution to solve articular cartilage repair. However, surgical implantation and the scaffold preparation accompanied with the increased bacteria resistance to antibiotics open possibilities for development of septic arthritis at increased rates. Accordingly, the use of Nisin and LL-37 antimicrobial peptides was here investigated by a novel biomimetic approach of using co-cultures of hMSC and bacteria in the presence of the antimicrobial agents. Furthermore, comparative studies in cell monolayers and in spheroid cultures indicated similar trends but also revealed the effects of the cell microenvironment, the 3D structure being more protective and inductive of cell differentiation. In addition, static and hydrodynamic culture conditions affected differently both the cells in spheroids and bacteria survival and adhesion. The hydrodynamic shear stresses were indicated as the key feature that also promoted the antibacterial activity of Nisin. These results demonstrated the importance of establishing the appropriate culture conditions in studies of novel devices and therapies that should closely resemble the physiological environment and biomimetic bioreactors may be considered as useful tools in this respect. Overall, the present work suggested that 75 μg/ml Nisin can be considered as safe and effective toward both Gram-positive and Gram-negative strains. Moreover, Nisin did not interfere with chondrogenesis thus suggesting a targeted activity toward bacteria while preserving articular cartilage healing.

DATA AVAILABILITY STATEMENT

The datasets generated for this study are available on request to the corresponding author.

AUTHOR CONTRIBUTIONS

ZN, AK, AS, and AC performed experiments. BO was responsible for bioreactor set-up. FG and MLe critically revised the manuscript. MLa, IL, RG, and LR designed and supervised the work. All authors agree to be accountable for the content of the work.

FUNDING

The authors acknowledge received funding from European Union's Horizon 2020 research and innovation program under grant agreement number 814558 project RESTORE.

REFERENCES

Aigner, T., and Fan, Z. (2003). "Anatomy and biochemistry of articular cartilage," in *Cartilage Surgery and Future Perspectives*, eds C. Hendrich, U. Nöth, and J. Eulert (Berlin; Heidelberg: Springer), 3–7. doi: 10.1007/978-3-642-19008-7_1

Alves da Silva, M. L., Martins, A., Costa-Pinto, A. R., Correlo, V. M., Sol, P., Bhattacharya, M., et al. (2011). Chondrogenic differentiation of human bone marrow mesenchymal stem cells in chitosan-based scaffolds using a flow-perfusion bioreactor. *J. Tissue Eng. Regen. Med.* 5, 722–732. doi: 10.1002/term.372

Asaduzzaman, S. M., and Sonomoto, K. (2009). Lantibiotics: diverse activities and unique modes of action. *J. Biosci. Bioeng.* 107, 475–487. doi: 10.1016/j.jbiosc.2009.01.003

Balato, G., Di Donato, S., Ascione, T., D'Addona, A., Smeraglia, F., Di Vico, G., et al. (2017). Knee septic arthritis after arthroscopy: incidence, risk factors, functional outcome, and infection eradication rate. *Joints* 5, 107–113. doi: 10.1055/s-0037-1603901

Baranska-Rybak, W., Sonesson, A., Nowicki, R., and Schmidtchen, A. (2006). Glycosaminoglycans inhibit the antibacterial activity of LL-37 in biological fluids. *J. Antimicrob. Chemother.* 57, 260–265. doi: 10.1093/jac/dki460

Bauer, T., Boisrenoult, P., and Jenny, J. Y. (2015). Post-arthroscopy septic arthritis: current data and practical recommendations. *Orthop. Traumatol. Surg. Res.* 101, S347–S350. doi: 10.1016/j.otsr.2015.09.004

Bonifacio, M. A., Cochis, A., Cometa, S., Scalzone, A., Gentile, P., Procino, G., et al. (2020). Advances in cartilage repair: the influence of inorganic clays to improve mechanical and healing properties of antibacterial gellan gum-manuka honey hydrogels. *Mater. Sci. Eng. C Mater. Biol. Appl.* 108:110444. doi: 10.1016/j.msec.2019.110444

Bonifacio, M. A., Cometa, S., Cochis, A., Gentile, P., Ferreira, A. M., Azzimonti, B., et al. (2018). Antibacterial effectiveness meets improved mechanical properties: manuka honey/gellan gum composite hydrogels for cartilage repair. *Carbohydr. Polym.* 198, 462–472. doi: 10.1016/j.carbpol.2018.06.115

Brumfitt, W., Salton, M. R., and Hamilton-Miller, J. M. (2002). Nisin, alone and combined with peptidoglycan-modulating antibiotics: activity against methicillin-resistant *Staphylococcus* aureus and vancomycin-resistant enterococci. *J. Antimicrob. Chemother.* 50, 731–734. doi: 10.1093/jac/dkf190

Camp, C. L., Stuart, M. J., and Krych, A. J. (2014). Current concepts of articular cartilage restoration techniques in the knee. *Sports Health* 6, 265–273. doi: 10.1177/1941738113508917

Chalmers, P. N., Vigneswaran, H., Harris, J. D., and Cole, B. J. (2013). Activity-related outcomes of articular cartilage surgery: a systematic review. *Cartilage* 4, 193–203. doi: 10.1177/1947603513481603

Chen, T., Buckley, M., Cohen, I., Bonassar, L., and Awad, H. A. (2012). Insights into interstitial flow, shear stress, and mass transport effects on ECM heterogeneity in bioreactor-cultivated engineered cartilage hydrogels. *Biomech. Model. Mechanobiol.* 11, 689–702. doi: 10.1007/s10237-011-0343-x

Cipriani, F., Ariño Palao, B., Gonzalez de Torre, I., Vega Castrillo, A., Aguado Hernández, H. J., Alonso Rodrigo, M., et al. (2019). An elastin-like recombinamer-based bioactive hydrogel embedded with mesenchymal stromal cells as an injectable scaffold for osteochondral repair. *Regen. Biomater.* 6, 335–347. doi: 10.1093/rb/rbz023

Cochis, A., Azzimonti, B., Della Valle, C., De Giglio, E., Bloise, N., Visai, L., et al. (2016). The effect of silver or gallium doped titanium against the multidrug resistant acinetobacter baumannii. *Biomaterials* 80, 80–95. doi: 10.1016/j.biomaterials.2015.11.042

Cochis, A., Barberi, J., Ferraris, S., Miola, M., Rimondini, L., Vernè, E., et al. (2020). Competitive surface colonization of antibacterial and bioactive materials doped with strontium and/or silver ions. *Nanomaterials (Basel).* 10:120. doi: 10.3390/nano10010120

Cochis, A., Grad, S., Stoddart, M., Fare, S., Altomare, L., Azzimonti, B., et al. (2017). Bioreactor mechanically guided 3D mesenchymal stem cell chondrogenesis using a biocompatible novel thermo-reversible methylcellulose-based hydrogel. *Sci. Rep.* 7:45018. doi: 10.1038/srep45018

Cogen, A., Nizet, V., and Gallo, R. (2008). Skin microbiota: a source of disease or defence? *Br. J. Dermatol.* 158, 442–455. doi: 10.1111/j.1365-2133.2008.08437.x

Cohen, N. P., Foster, R. J., and Mow, V. C. (1998). Composition and dynamics of articular cartilage: structure, function, and maintaining healthy state. *J. Orthop. Sports Phys. Ther.* 28, 203–215. doi: 10.2519/jospt.1998.28.4.203

De Hoogt, R., Estrada, M. F., Vidic, S., Davies, E. J., Osswald, A., Barbier, M., et al. (2017). Protocols and characterization data for 2D, 3D, and slice-based tumor models from the PREDECT project. *Sci. Data.* 4:170170. doi: 10.1038/sdata.2017.170

Dosler, S., and Gerceker, A. A. (2011). *In vitro* activities of nisin alone or in combination with vancomycin and ciprofloxacin against methicillin-resistant and methicillin-susceptible Staphylococcus aureus strains. *Chemother* 57, 511–516. doi: 10.1159/000335598

Fernández, L., Delgado, S., Herrero, H., Maldonado, A., and Rodriguez, J. M. (2008). The bacteriocin nisin, an effective agent for the treatment of *Staphylococcal* mastitis during lactation. *J. Hum. Lact.* 24, 311–316. doi: 10.1177/0890334408317435

Freyria, A. M., Yang, Y., Chajra, H., Rousseau, C., Ronziere, M. C., Herbage, D., et al. (2005). Optimization of dynamic culture conditions: effects on biosynthetic activities of chondrocytes grown in collagen sponges. *Tissue Eng. A* 11, 674–684. doi: 10.1089/ten.2005.11.674

Gao, F., Xu, Z., Liang, Q., Li, H., Peng, L., Wu, M., et al. (2019). Osteochondral regeneration with 3D-printed biodegradable high-strength supramolecular polymer reinforced-gelatin hydrogel scaffolds. *Adv. Sci. (Weinh).* 6:1900867. doi: 10.1002/advs.201900867

Garny, K., Horn, H., and Neu, T. R. (2008). Interaction between biofilm development, structure and detachment in rotating annular reactors. *Bioprocess. Biosyst. Eng.* 31, 619–629. doi: 10.1007/s00449-008-0212-x

Hancock, R. E., and Sahl, H. G. (2006). Antimicrobial and host-defense peptides as new anti-infective therapeutic strategies. *Nat. Biotechnol.* 24, 1551–1557. doi: 10.1038/nbt1267

Harrison, J. J., Stremick, C. A., Turner, R. J., Allan, N. D., Olson, M. E., and Ceri, H. (2010). Microtiter susceptibility testing of microbes growing on peg lids: a miniaturized biofilm model for high-throughput screening. *Nat. Protoc.* 5, 1236–1254. doi: 10.1038/nprot.2010.71

He, Y., Yang, X., Yuan, Z., Shen, X., Xu, K., Lin, C., et al. (2019). Regulation of MSC and macrophage functions in bone healing by peptide LL-37-loaded silk fibroin nanoparticles on a titanium surface. *Biomater. Sci.* 7, 5492–5505. doi: 10.1039/C9BM01158G

Howell, T., Fiorellini, J., Blackburn, P., Projan, S., De la Harpe, J., and Williams, R. (1993). The effect of a mouthrinse based on nisin, a bacteriocin, on developing plaque and gingivitis in beagle dogs. *J. Clin. Periodontol.* 20, 335–339. doi: 10.1111/j.1600-051X.1993.tb00369.x

Iancu, C., Grainger, A., Field, D., Cotter, P. D., Hill, C., and Ross, R. P. (2012). Comparison of the potency of the lipid II targeting antimicrobials nisin, lacticin 3147 and vancomycin against gram-positive bacteria. *Probiotics Antimicrob Proteins* 4, 108–115. doi: 10.1007/s12602-012-9095-x

Jekabsone, A., Sile, I., Cochis, A., Makrecka-Kuka, M., Laucaityte, G., Makarova, E., et al. (2019). Investigation of antibacterial and antiinflammatory activities of proanthocyanidins from pelargonium sidoides DC root extract. *Nutrients* 11:2829. doi: 10.3390/nu11112829

Kamysz, E., Sikorska, E., Jaśkiewicz, M., Bauer, M., Neubauer, D., Bartoszewska, S., et al. (2020). Lipidated analogs of the LL-37-derived peptide fragment KR12-structural analysis, surface-active properties and antimicrobial activity. *Int. J. Mol. Sci.* 21:887. doi: 10.3390/ijms21030887

Kim, T. K., Sharma, B., Williams, C. G., Ruffner, M. A., Malik, A., McFarland, E. G., et al. (2003). Experimental model for cartilage tissue engineering to regenerate the zonal organization of articular cartilage. *Osteoarthr. Cartilage* 11, 653–664. doi: 10.1016/S1063-4584(03)00120-1

Kock, L. M., Malda, J., Dhert, W. J., Ito, K., and Gawlitta, D. (2014). Flow-perfusion interferes with chondrogenic and hypertrophic matrix production by mesenchymal stem cells. *J. Biomech.* 47, 2122–2129. doi: 10.1016/j.jbiomech.2013.11.006

Koziel, J., and Potempa, J. (2013). Protease-armed bacteria in the skin. *Cell. Tissue Res.* 351, 325–337. doi: 10.1007/s00441-012-1355-2

Langhans, S. A. (2018). Three-dimensional *in vitro* cell culture models in drug discovery and drug repositioning. *Front. Pharmacol.* 9:6. doi: 10.3389/fphar.2018.00006

Leszczynska, K., Namiot, D., Byfield, F. J., Cruz, K., Zendzian-Piotrowska, M., Fein, D. E., et al. (2013). Antibacterial activity of the human host defence peptide LL-37 and selected synthetic cationic lipids against bacteria associated with oral and upper respiratory tract infections. *J. Antimicrob. Chemother.* 68, 610–618. doi: 10.1093/jac/dks434

Lombardo Bedran, T. B., Palomari, S. D., and Grenier, D. (2015). Green tea polyphenol epigallocatechin-3-gallate and cranberry proanthocyanidins act in synergy with cathelicidin (LL-37) to reduce the LPS-induced inflammatory response in a three-dimensional co-culture model of gingival epithelial cells and fibroblasts. *Arch. Oral. Biol.* 60, 845–53. doi: 10.1016/j.archoralbio.2015.02.021

Lozeau, L. D., Rolle, M. W., and Camesano, T. A. (2018). A QCM-D study of the concentrateion-and time-dependent interactions of human LL37 with model mammalian lipid bilayers. *Colloids Surf. B Biointerfaces* 167, 229–238. doi: 10.1016/j.colsurfb.2018.04.016

Luo, Y., McLean, D. T., Linden, G. J., McAuley, D. F., McMullan, R., and Lundy, F. T. (2017). The naturally occurring host defense peptide, LL-37, and its truncated mimetics KE-18 and KR-12 have selected biocidal and antibiofilm activities against candida albicans, *Staphylococcus* aureus, and *Escherichia coli in vitro*. *Front. Microbiol.* 8:544. doi: 10.3389/fmicb.2017.00544

Makris, E. A., Gomoll, A. H., Malizos, K. N., Hu, J. C., and Athanasiou, K. A. (2015). Repair and tissue engineering techniques for articular cartilage. *Nat. Rev. Rheumatol.* 11, 21–34. doi.org/10.1038/nrrheum.2014.157

Meng, Y., Cao, J., Chen, Y., Yu, Y., and Ye, L. (2020). 3D printing of a poly (vinyl alcohol)-based nano-composite hydrogel as an artificial cartilage replacement and the improvement mechanism of printing accuracy. *J. Mater. Chem. B*. 8, 677–690. doi: 10.1039/C9TB02278C

Mezey, É., and Nemeth, K. (2015). Mesenchymal stem cells and infectious diseases: smarter than drugs. *Immunol. Lett*. 168, 208–214. doi: 10.1016/j.imlet.2015.05.020

Milhan, N. V. M., de Barros, P. P., de Lima Zutin, E. A., de Oliveira, F. E., Camargo, C. H. R., and Camargo, S. E. A. (2017). The antimicrobial peptide LL-37 as a possible adjunct for the proliferation and differentiation of dental pulp stem cells. *J. Endod*. 43, 2048–2053. doi: 10.1016/j.joen.2017.08.010

Otto, M. (2013). *Staphylococcal* infections: mechanisms of biofilm maturation and detachment as critical determinants of pathogenicity. *Annu. Rev. Med*. 64, 175–188. doi: 10.1146/annurev-med-042711-140023

Overhage, J., Campisano, A., Bains, M., Torfs, E. C., Rehm, B. H., and Hancock, R. E. (2008). Human host defense peptide LL-37 prevents bacterial biofilm formation. *Infect. Immun*. 76, 4176–4182. doi: 10.1128/IAI.00318-08

Pazzano, D., Mercier, K. A., Moran, J. M., Fong,S. S., Di Biasio, D. D., Rulfs, J. X., et al. (2000). Comparison of chondrogenesis in static and perfused bioreactor culture. *Biotechnol. Prog*. 16, 893–896. doi: 10.1021/bp000082v

Peschel, A., and Sahl, H.-G. (2006). The co-evolution of host cationic antimicrobial peptides and microbial resistance. *Nat. Rev. Microbiol*. 4, 529–536. doi: 10.1038/nrmicro1441

Piola, M., Soncini, M., Cantini, M., Sadr, N., Ferrario, G., and Fiore, G. B. (2013). Design and functional testing of a multichamber perfusion platform for three-dimensional scaffolds. *Sci. World J*. 2013:123974. doi: 10.1155/2013/123974

Piper, C., Draper, L. A., Cotter, P. D., Ross, R. P., and Hill, C. (2009). A comparison of the activities of lacticin 3147 and nisin against drug-resistant Staphylococcus aureus and Enterococcus species. *J. Antimicrob. Chemother*. 64, 546–551. doi: 10.1093/jac/dkp221

Pourbashir, S., Shahrousvand, M., and Ghaffari, M. (2020). Preparation and characterization of semi-IPNs of polycaprolactone/poly (acrylic acid)/cellulosic nanowhisker as artificial articular cartilage. *Int. J. Biol. Macromol*. 142, 298–310. doi: 10.1016/j.ijbiomac.2019.09.101

Pruijn, N., van Diek, F. M., Meis, J. F., Kosse, N. M., and Dorrestijn, O. (2020). Cutibacterium acnes infections in revision surgery for persistent shoulder complaints: a retrospective cohort study. *Arch. Orthop. Trauma Surg*. doi: 10.1007/s00402-020-03415-5. [Epub ahead of print].

Rahnamaeian, M. (2011). Antimicrobial peptides: modes of mechanism, modulation of defense responses. *Plant. Signal. Behav*. 6, 1325–1332. doi: 10.4161/psb.6.9.16319

Ron-Doitch, S., Sawodny, B., Kühbacher, A., David, M. M. N., Samanta, A., Phopase, J., et al. (2016). Reduced cytotoxicity and enhanced bioactivity of cationic antimicrobial peptides liposomes in cell cultures and 3D epidermis model against HSV. *J. Control. Release* 229, 163–171. doi: 10.1016/j.jconrel.2016.03.025

Rutkowski, J. M., and Swartz, M. A. (2006). A driving force for change: interstitial flow as a morphoregulator. *Trends Cell. Biol.* 17, 44–50. doi: 10.1016/j.tcb.2006.11.007

Saporito, P., Vang Mouritzen, M., Løbner-Olesen, A., and Jenssen, H. (2018). LL-37 fragments have antimicrobial activity against *Staphylococcus* epidermidis biofilms and wound healing potential in HaCaT cell line. *J. Pept. Sci*. 24:e3080. doi: 10.1002/psc.3080

Scalzone, A., Ferreira, A. M., Tonda-Turo, C., Ciardelli, G., Dalgarno, K., and Gentile, P. (2019). The interplay between chondrocyte spheroids and mesenchymal stem cells boosts cartilage regeneration within a 3D natural-based hydrogel. *Sci. Rep*. 9:14630. doi: 10.1038/s41598-019-51070-7

Shin, J. M., Ateia, I., Paulus, J. R., Liu, H., Fenno, J. C., Rickard, A. H., et al. (2015). Antimicrobial nisin acts against saliva derived multi-species biofilms without cytotoxicity to human oral cells. *Front. Microbiol*. 6:617. doi: 10.3389/fmicb.2015.00617

Sierra, J., Fusté E., Rabanal, F., Vinuesa, T., and Viñas, M. (2017). An overview of antimicrobial peptides and the latest advances in their development. *Expert. Opin. Biol. Ther*. 17, 663–676. doi: 10.1080/14712598.2017.1315402

Smith, L., and Hillman, J. (2008). Therapeutic potential of type A (I) lantibiotics, a group of cationic peptide antibiotics. *Curr. Opin. Microbiol*. 11, 401–408. doi: 10.1016/j.mib.2008.09.008

Stone, J. Y., and Schaal, R. (2012). Postoperative management of patients with articular cartilage repair. *J. Knee Surg*. 25, 207–212. doi: 10.1055/s-0032-1322603

Stutz, G., Kuster, M. S., Kleinstück, F., and Gächter, A. (2000). Arthroscopic management of septic arthritis: stages of infection and results. *Knee Surg. Sports Traumatol. Arthrosc*. 8, 270–274. doi: 10.1007/s001670000129

Sun, Y., You, Y., Jiang, W., Zhai, Z., and Dai, K. (2019). 3D-bioprinting a genetically inspired cartilage scaffold with GDF5-conjugated BMSC-laden hydrogel and polymer for cartilage repair. *Theranostics* 9, 6949–6961. doi: 10.7150/thno.38061

Tjabringa, G. S., Rabe, K. F., and Hiemstra, P. S. (2005). The human cathelicidin LL-37: a multifunctional peptide involved in infection and inflammation in the lung. *Pulm. Pharmacol. Ther*. 18, 321–327. doi: 10.1016/j.pupt.2005.01.001

Tower, J. (2012). Stress and stem cells. *Wiley Interdiscip. Rev. Dev. Biol*. 1, 789–802. doi: 10.1002/wdev.56

Valenta, C., Bernkop-SchnüRch, A., and Rigler, H. P. (1996). The antistaphylococcal effect of nisin in a suitable vehicle: a potential therapy for atopic dermatitis in man. *J. Pharm. Pharmacol*. 48, 988–991. doi: 10.1111/j.2042-7158.1996.tb06019.x

Wang, G. (2014). Human antimicrobial peptides and proteins. *Pharma* 7, 545–594. doi: 10.3390/ph7050545

Wang, G., Hanke, M. L., Mishra, B., Lushnikova, T., Heim, C. E., Chittezham Thomas, V., et al. (2014). Transformation of human cathelicidin LL-37 into selective, stable, and potent antimicrobial compounds. *ACS Chem. Biol*. 9, 1997–2002. doi: 10.1021/cb500475y

Widuchowski, W., Widuchowski, J., and Trzaska, T. (2007). Articular cartilage defects: study of 25,124 knee arthroscopies. *Knee* 14, 177–182. doi: 10.1016/j.knee.2007.02.001

Wiedemann, I., Breukink, E., van Kraaij, C., Kuipers, O. P., Bierbaum, G., de Kruijff, B., et al. (2001). Specific binding of nisin to the peptidoglycan precursor lipid II combines pore formation and inhibition of cell wall biosynthesis for potent antibiotic activity. *J. Biol. Chem*. 276, 1772–1779. doi: 10.1074/jbc.M006770200

Wyatt, R. W., Maletis, G. B., Lyon, L. L., Schwalbe, J., and Avins, A. L. (2017). Efficacy of prophylactic antibiotics in simple knee arthroscopy. *Arthroscopy* 33, 157–162. doi: 10.1016/j.arthro.2016.05.020

Xhindoli, D., Pacor, S., Benincasa, M., Scocchi, M., Gennaro, R., and Tossi, A. (2016). The human cathelicidin LL-37-A pore-forming antibacterial peptide and host-cell modulator. *Biochim. Biophys. Acta* 1858, 546–566. doi: 10.1016/j.bbamem.2015.11.003

Xuan, H., Hu, H., Geng, C., Song, J., Shen, Y., Lei, D., et al. (2020). Biofunctionalized chondrogenic shape-memory ternary scaffolds for efficient cell-free cartilage regeneration. *Acta Biomater*. 105, 97–110. doi: 10.1016/j.actbio.2020.01.015

Yang, Y., Choi, H., Seon, M., Cho, D., and Bang, S. I. (2016). LL-37 stimulates the functions of adipose-derived stromal/stem cells via early growth response 1 and the MAPK pathway. *Stem Cell Res. Ther*. 7:58. doi: 10.1186/s13287-016-0313-4

Yu, X., Quan, J., Long, W., Chen, H., Wang, R., Guo, J., et al. (2018). LL-37 inhibits LPS-induced inflammation and stimulates the osteogenic differentiation of BMSCs via P2X7 receptor and MAPK signaling pathway. *Exp. Cell. Res*. 372, 178–187. doi: 10.1016/j.yexcr.2018.09.024

Zozu, R., Zhu, X., Tu, Y., Wu, J., and Landry, M. P. (2018). Activity of antimicrobial peptide aggregates decreases with increased cell membrane embedding free energy cost. *Biochemistry* 57, 2606–2610. doi: 10.1021/acs.biochem.8b00052

Conflict of Interest: The authors declare that the research was conducted in the absence of any commercial or financial relationships that could be construed as a potential conflict of interest.

frontiers in Bioengineering and Biotechnology

ORIGINAL RESEARCH
published: 26 June 2020
doi: 10.3389/fbioe.2020.00634

Assessment of Growth Reduction of Five Clinical Pathogens by Injectable S53P4 Bioactive Glass Material Formulations

Eline G. J. Thijssen[1], Nicole A. P. van Gestel[2,3], Raymond Bevers[1], Sandra Hofmann[2,3], Jan Geurts[1], Inge H. M. van Loo[4] and J. J. Arts[1,2]*

[1] Laboratory for Experimental Orthopedics, Department of Orthopedic Surgery, Research School CAPHRI, Maastricht University Medical Centre, Maastricht, Netherlands, [2] Orthopaedic Biomechanics, Department of Biomedical Engineering, Eindhoven University of Technology, Eindhoven, Netherlands, [3] Institute for Complex Molecular Systems, Eindhoven University of Technology, Eindhoven, Netherlands, [4] Department of Medical Microbiology, Research School CAPHRI, Maastricht University Medical Centre, Maastricht, Netherlands

OPEN ACCESS

Edited by:
Gianluca Ciardelli,
Politecnico di Torino, Italy

Reviewed by:
Diego Mantovani,
Laval University, Canada
Lina Altomare,
Politecnico di Milano, Italy

***Correspondence:**
Eline G. J. Thijssen
egj.thijssen@gmail.com

Specialty section:
This article was submitted to Biomaterials, a section of the journal Frontiers in Bioengineering and Biotechnology

Received: 31 January 2020
Accepted: 22 May 2020
Published: 26 June 2020

Citation:
Thijssen EGJ, van Gestel NAP, Bevers R, Hofmann S, Geurts J, van Loo IHM and Arts JJ (2020) Assessment of Growth Reduction of Five Clinical Pathogens by Injectable S53P4 Bioactive Glass Material Formulations. Front. Bioeng. Biotechnol. 8:634. doi: 10.3389/fbioe.2020.00634

The one-stage treatment of chronic osteomyelitis with S53P4 bioactive glass (BAG) granules has shown excellent results. However, these granules possess suboptimal handling properties. Therefore, new injectable S53P4 putty materials have been developed by the incorporation of a synthetic binder to contain glass granules. The goal of the current study was to assess their potential to eradicate five clinically relevant pathogens: *methicillin sensitive Staphylococcus aureus* (MSSA), *methicillin resistant Staphylococcus aureus* (MRSA), *Enterococcus coli* (*E. coli*), *Enterococcus faecalis* (*E. faecalis*), and *Pseudomonas aeruginosa* (*P. aeruginosa*). As a control, S53P4 granules (500–800 μm) and S66 glass (< 45 μm) were used. To evaluate the antimicrobial properties, the materials were cultured with the pathogens in a Müller-Hinton II broth for a week with daily colony forming unit (CFU) counting. One of the tested putty formulations was observed to reduce the number of CFU/mL compared to a negative control (no material, only pathogen in broth) for *E. coli, E. faecalis* and *P. aeruginosa*. However, none of the tested putty formulations was able to completely eradicate the pathogens in the broths, which would be needed for safe infection treatment. The results obtained for the control materials were unexpected. S66 glass showed full eradication of *P. aeruginosa* and reduced the number of CFUs of other pathogens, while the S53P4 granules did not show eradication. The observations on the loose S53P4 granules in this study contradict available literature, which needs further investigation. The results obtained in this study also stretch the importance for a better understanding of the underlying antimicrobial mechanism of S53P4 BAG and how this is related to the dosage. In addition, it should be elucidated how these antimicrobial properties are affected by changes in the material formulation, for example by addition of binders to improve the handling properties or by changing the surface area.

Keywords: biomaterials, S53P4, bioglass, eradication, S53P4 formulations, bacteria

INTRODUCTION

Chronic bone infections, or chronic osteomyelitis, are a major problem in the field of orthopedic surgery. Invasive treatment is needed to prevent the loss of the affected limb, sepsis or even death (Parsons and Strauss, 2004). For years the gold standard treatment consisted of a two-stage surgical treatment. During the first surgery, an excessive debridement of the infected tissues is performed, followed by the implantation of a local antibiotic carrier (e.g., poly- (methyl methacrylate) (PMMA) beads loaded with gentamycin). When the infection is completely eradicated, the antibiotic carrier is removed, and the bone defect is grafted with either autograft or allograft bone for reconstruction in a second surgery. In addition to the surgical treatment, systemic antibiotics, specific for the cultured strains, are administered for at least 6 weeks (2 weeks intravenously and 4 weeks orally) (Walenkamp et al., 1998; Geurts et al., 2016; Lindfors et al., 2016).

Osteomyelitis causes vasoconstriction of local vessels, diminished vessel quality and poor penetration of systemic antibiotics into the bone (Calhoun et al., 2009). Therefore, systemic antibiotics alone may not achieve sufficiently high doses at the site of infection and a localized administration of antibiotics is needed in order to treat the osteomyelitis. Another challenging factor in the treatment of chronic osteomyelitis is the worldwide increase of antibiotic-resistant bacteria (Geurts et al., 2016; Vugt et al., 2016). Therefore, it is important to develop biomaterials that have a different mechanism to eradicate bacteria, compared to current antibiotics (Drago et al., 2015). S53P4 bioactive glass (Bonalive® Biomaterials Ltd., Turku, Finland) has shown to be clinically effective in the treatment of chronic osteomyelitis (McAndrew et al., 2013; Geurts et al., 2016; Lindfors et al., 2016). The S53P4 bioactive glass is believed to increase the local pH and osmotic pressure through an exchange of ions with the environmental fluid, which is believed to result in bacterial death. In addition, the use of this biomaterial has been reported to be (cost) effective in the treatment of osteomyelitis, in a one-stage surgical procedure when accompanied by systemic antibiotic administration (Lindfors et al., 2016).

Currently, the major drawback of loose S53P4 BAG granules is the handling. Surgeons prefer an injectable and moldable biomaterial. To accommodate this, novel S53P4 bioactive glass putty formulations have been developed (van Gestel et al., 2017). These formulations consist of S53P4 bioactive glass granules surrounded by a synthetic binder of poly(ethylene) glycol (PEG) and glycerol. Currently, the putty formulations are used as a filler of bone defects. However, it remains unclear whether and how the incorporation of the binder would affect the antibacterial properties of the S53P4 granules. Therefore, the goal of the current study was to assess the antimicrobial properties of the newly developed injectable putty formulations against 5 clinically relevant bacteria strains. It was investigated whether these biomaterials could reduce the number of colonies over time compared to S53P4 granules and a S66 glass control group.

TABLE 1 | Experimental groups and corresponding concentrations of the tested biomaterials in the MH-II broth.

Biomaterial	Glass compositions and biomaterial formulations [wt%]	Concentration [mg biomaterial/mL]
S53P4 granules (500–800 μm)	53% SiO, 2.4% P_2O_5, 23% Na_2O, 20% CaO	400
Putty A	37% binder, 63% S53P4*	645.8
Putty B	22% binder, 78% S53P4*	670.9
S66 powder (<45 μm)	66.4% SiO_2, 9.5% Na_2O, 3.3% CaO, 6.1% Ba, 6.3% K_2O, 2.2% Cr, 4.6% Pb	400.3

**The binder consists of polyethylene glycols (PEGs), glycerol, S53P4 granules of 500–800 μm, and S53P4 <45 μm powder. The specific compositions are confidential (Bonalive® Biomaterials Ltd.).*

MATERIALS AND METHODS

Pathogens

This study was performed to determine the antimicrobial activity of four biomaterials on five different bacterial strains: *methicillin sensitive Staphylococcus aureus (MSSA; ATCC 29213)*, *methicillin resistant Staphylococcus aureus (MRSA; ATCC 12493)*, *Enterococcus coli (ATCC 25922)*, *Enterococcus faecalis (ATCC 29212)*, and *Pseudomonas aeruginosa (ATCC 27853)*. Per strain, a clean colony was entered in 5 mL sterile Müller-Hinton II broth (MH-II broth, Merck KGaA, Darmstadt, Germany) and cultured overnight at 37°C and 5% CO_2 (Balouiri et al., 2016). The bacterial cultures were diluted with sterile MH-II broth until 0.5 McFarland (1.5×10^8 CFU/mL) using a McFarland measure (Grant Bio Densitometer DEN-1, Grant Instruments™, Cambridge, Great Britain). These solutions were then further diluted to approximately 1.5×10^7 CFU/mL (experimental pathogen solution).

Biomaterials

The biomaterials included S53P4 bioactive glass (500–800 μm granules), Putty A, Putty B (Bonalive® Biomaterials Ltd.) and loose S66 powder (**Table 1**). The biomaterials were added to 2 mL fresh MH-II broth (without pathogens) and incubated overnight (16–18 h) on a rolling plate (IKA® roller 6 digital, IKA®-Werke GmbH & Co. KG, Staufen, Germany) at room temperature. This overnight incubation was performed to precondition the broths by the ions released from the different biomaterials. Per tested biomaterial, 11 test tubes were preconditioned of which 10 were used to for the pathogen cultures ($n = 2$ per bacterial strain) and 1 was used as a negative control to evaluate the pH of the broth with biomaterial, over time. The pH was measured with a Litmus red paper and a pH meter (FiveEasy F20, Mettler Toledo®, Tiel, The Netherlands); no bacteria were added to this specific test tube.

Pathogen Cultures With Biomaterials

After the overnight incubation (T0), the broths with biomaterials were tested for their capacity to reduce the number of colony forming units (CFUs). 2 mL of the experimental pathogen

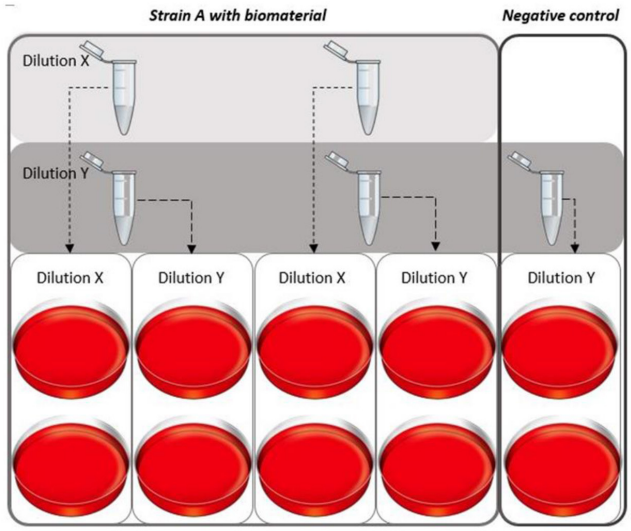

FIGURE 1 | Plating dilution series of the different pathogens. For every strain a dilution series was created for each time point. Two different dilutions for the solutions with biomaterial were plated [dilution to 10^3 CFU/mL (X) and 10^2 CFU/mL (Y)] in duplicates. Per experiment, a growth control was cultured simultaneously, for this culture only dilution Y was plated in duplicates.

solution was added per tube ($n = 4$ per bacterial strain for every biomaterial). Per culture, one growth or positive control was added, which was a test tube with fresh MH-II broth, without biomaterials, but with pathogens ($n = 4$). All test tubes were then cultured for 7 days at 37°C and 5% CO_2. During this 7-day culture, the colonies were counted daily.

Colony Counting

Briefly, after vortexing the complete cultured test tube, serial dilutions were prepared by mixing 100 μL from the broth with 900 μL 0.9% sodium chloride (NaCl) in water. Dilutions of 10^3 CFU/mL ("dilution X") and 10^2 CFU/mL ("dilution Y") were prepared and plated (100 μL per plate) on agar plates with 5% sheep blood (BD™ Columbia Agar with 5% Sheep Blood, Becton Dickinson GmbH, Heidelberg, Germany) in duplicates (**Figure 1**). For the growth control (no biomaterial, only pathogen) only dilution Y (10^2 dilution) was plated in duplicate (**Figure 1**). The plates were placed on a shaking plate (IKA® KS4000 IC, IKA®-Werke GmbH & Co. KG Staufen, Germany) at 37°C and were cultured for 16–18 h before colonies were counted. The loss of broth for plating per time point (100 μL per test tube), was not replenished, since the loss of bacteria was expected to be negligible.

After 16–18 h, the agar plates were photographed and CFUs were counted using OpenCFU 3.9.0 for *MSSA*, *MRSA*, *E. coli* and *E. faecalis* (Geissmann, 2013). The CFU for *P. aeruginosa* were counted manually, since these colonies could not be detected by OpenCFU software due to low contrast of the colonies on the blood agar plate.

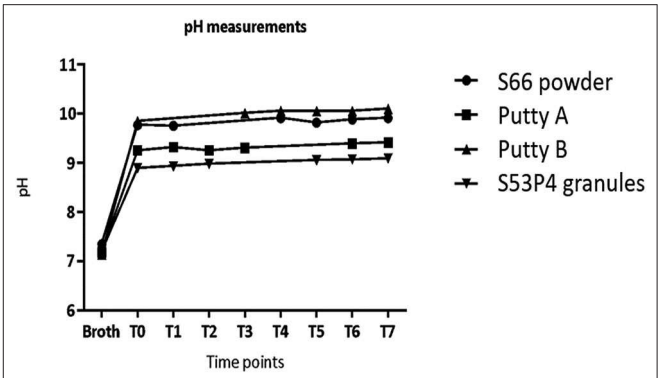

FIGURE 2 | The pH values in the test tubes without the presence of pathogens increase directly after addition of material at T0 and level off in values around 9 and higher after 1 day of incubation.

RESULTS

pH Measurements

The initial pH of the broths was between 7.14 and 7.35 (**Figure 2**). After the addition of the biomaterials, the pH increased to values of 9 and higher. The largest pH increase was observed for Putty B to 10.10 at T7 (**Figure 2**). The lowest pH at T7 was 9.22, observed for the S53P4 granules. After a fast increase within the first day of incubation (measured at T0), the measured pH values only slightly increased further until T7.

Reduced CFU by the Biomaterials per Bacterial Strain

MSSA

The number of colonies of MSSA was slightly reduced by all biomaterials (**Figure 3**). With a 2 $\log_{10}$ reduction of CFUs measured compared to the number measured in the growth controls, the S66 powder showed the highest reduction. S53P4 granules reduced the number of CFUs by 1 $\log_{10}$, compared to the growth control.

MRSA

A slight reduction of CFUs compared to the growth control was initially observed for al biomaterials (**Figure 4**). Fluctuations of counted CFUs are observed for the S66 powder and the S53P4 granules. For the S66 powder, at T2 no CFUs were counted but that value of CFUs increased again. At T7, S66 powder showed a 5 $\log_{10}$ reduction in CFUs compared to the number counted in the growth control. In the S53P4 granules group, a 2 $\log_{10}$ reduction was observed compared to the growth control at T3. However, after this time point the number of counted CFUs for the S53P4 granule group increased again and at T7 this reduction was undone.

E. coli

The amount of *E. coli* CFUs counted compared to the growth control were only decreased in the Putty A group with a final 2 $\log_{10}$ reduction at T7 (**Figure 5**). For Putty B and S66 powder a slight reduction in CFUs compared to the growth

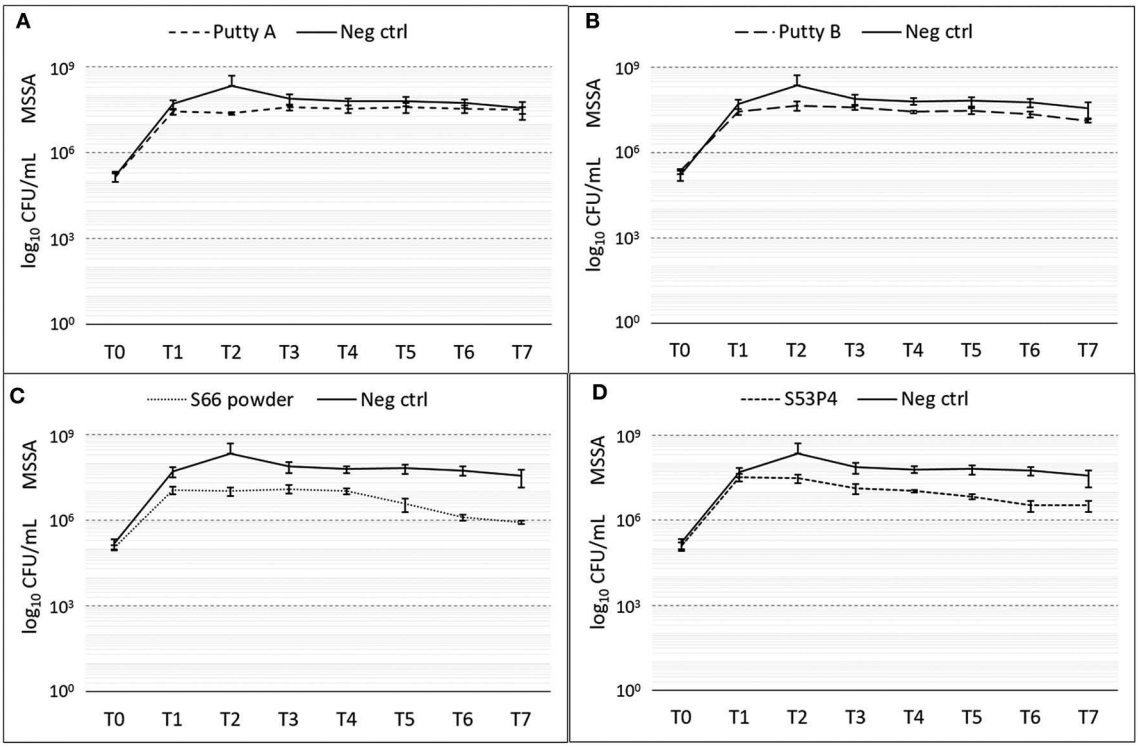

FIGURE 3 | Growth of MSSA in the presence of the different biomaterials in CFU/ml compared to the growth control (continuous line in all graphs) over 7 days (T_0 until T_7). **(A)** shows Putty A (dashed line) compared to the growth control (continuous line), **(B)** Putty B, **(C)** S66 powder, and **(D)** SS3P4 powder. The results are presented as mean ± standard deviation on a logarithmic scale.

control was observed at T2 until T5, but at T7 this reduction was disappeared for both these groups. The S53P4 granules did not show any reduced counted CFUs compared to the growth control.

E. faecalis

Putty A was most effective in eradicating *E. faecalis* showing a 2 $\log_{10}$ reduction at T_7 (**Figure 6**), while the S53P4 granules and S66 powder showed almost no change in CFU compared to the growth control over time. Putty B reduced the number of counted CFUs with 1 $\log_{10}$ compared to the growth control. At T2 the data for the S66 powder are missing due to contamination on the agar plate.

P. aeruginosa

Of the four biomaterials tested, the S66 powder was the most effective in the eradication of *P. aeruginosa* as it fully eradicated the pathogen (**Figure 7**). Already at T1 a 3 $\log_{10}$ reduction was observed with this biomaterial, compared to the growth control. From T2 onwards, no CFUs could be detected anymore. Both putty formulations showed a reduction in the number of CFUs compared to the growth control samples. Putty A reduced the number of counted CFUs by 1 $\log_{10}$ and the Putty B 2 $\log_{10}$, at T7. The S53P4 granules did not reduce the number of CFUs compared to the growth control.

DISCUSSION

The goal of the current study was to screen two newly developed injectable S53P4 putty formulations on their antibacterial properties against 5 clinically relevant bacterial strains, *in vitro*. These putty formulations, consisting of S53P4 bioactive glass granules surrounded by a synthetic binder of poly(ethylene) glycol (PEG) and glycerol, were developed to improve the handling of S53P4 BAG granules. The specific composition of the synthetic binder is confidential. The study by Stoor and Frantzen (2017) observed no clear antibacterial effect for the PEG-glycerol polymer, which insinuates the antimicrobial properties of S53P4 are not enhanced by the binder (Stoor and Frantzen, 2017). The mechanical behavior of five different putty formulations is described by van Gestel et al. (2017), which showed a higher content of synthetic binder is related to increased residual strains and decreased impactability, and limited load bearing due to dissolving of the matrix (van Gestel et al., 2017).

The effective antibacterial properties of the loose S53P4 BAG granules by increasing pH and osmotic pressure have been reported previously, but it remains unclear if the incorporation of a synthetic binder, to create the putty, affect this antibacterial behavior (Leppäranta et al., 2008; Munukka et al., 2008; Zhang et al., 2010). The results obtained in this study stretch the importance that a better understanding of the underlying antimicrobial mechanism of S53P4 BAG is needed and in

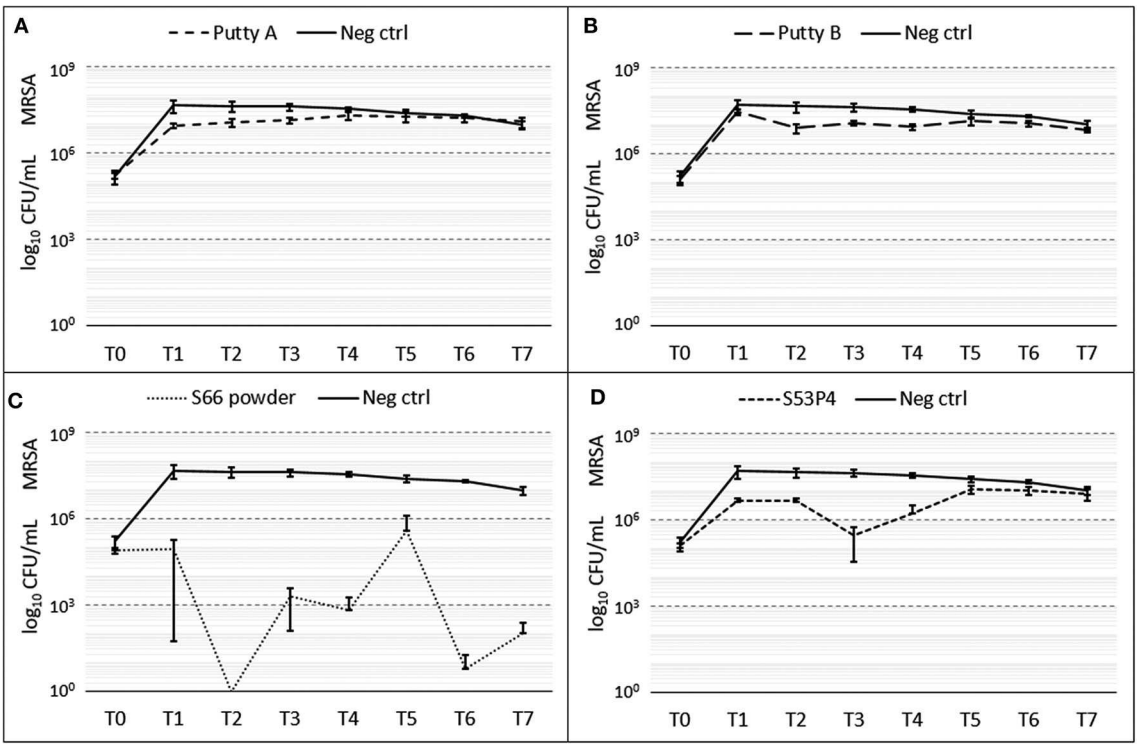

FIGURE 4 | Growth of MRSA in the presence of the different biomaterials in CFU/ml compared to the growth control (continuous line in all graphs) over 7 days (T_0 until T_7). **(A)** shows Putty A (dashed line) compared to the growth control (continuous line), **(B)** Putty B, **(C)** S66 powder, and **(D)** SS3P4 powder. The results are presented as mean ± standard deviation on a logarithmic scale.

particular how this is related to the dosage, changes in biomaterial formulation and by changes in surface area.

Differences in capacity to reduce the number of CFUs were observed between all biomaterials and between all pathogens tested. But only in one case a full eradication of the pathogen was observed. Surprisingly, it was the S66 powder that managed to fully eradicate *P. aeruginosa*, all other biomaterials failed to completely eradicate the pathogens. Some log10 reductions in CFU/mL have been observed, but they were dependent on the biomaterial and the tested pathogen. The *in vitro* growth reduction is defined as bacteriostatic or bactericidal (Pankey and Sabath, 2004). When a material is bacteriostatic it prevents the growth of bacteria. When a material is bactericidal it means it kills the bacterial (full eradication) (Pankey and Sabath, 2004). A bacteriostatic material often shows a small growth reduction in the first 18–24 h in *in vitro* tests, while a bactericidal material reduces more than 3 log10 CFU/mL (Pankey and Sabath, 2004). Therefore, all tested biomaterials in this study showed some bacteriostatic effects. Only the S66 showed some bactericidal effects. It has been shown that S53P4 glass eradicates bacteria by a local increase in pH and osmotic pressure, created by the ions that are released upon fluid contact (Stoor et al., 1998; Munukka et al., 2008; Drago et al., 2015; van Gestel et al., 2015). As expected, the pH of the MH-II broth increased in all groups containing bioactive glass and the increase in pH was not hindered by the addition of the binder. However, the supposedly negative control, the S66 powder, even showed the highest pH increase, while the S53P4 granules showed the lowest pH increase. The relatively low pH for the S53P4 granules may be due to the used particle size of 500–80 μm, compared to the other tested biomaterials which contained particles with a size of < 45 μm. It has been reported that in *in situ* measurements, the pH may differ for different particle sizes for S53P4 BAG granules in simulated body fluid (Zhang et al., 2008). The particle sizes are directly affecting the available surface area per weight of biomaterial from which ions are being released. Smaller particles have a larger surface area, which results in more ions that can be released (Stoor et al., 1998). This might also explain the high pH observed for the S66 powder, which had a much smaller particle size (< 45 μm) than the S53P4 granules. A particle size of 500 μm has been related to a surface area that is 8x smaller compared to particles < 45 μm (Zhang et al., 2008). Unfortunately, particle size and therefore surface area has not been homogenized in the current study and also the osmotic pressure has not been evaluated. It remains unclear from our results what caused the differences in pH for different formulations.

Two putty formulations based on the S543P4 bioactive glass were tested in this study to screen for their potential to be used in infection treatment. Our screening against five clinically relevant bacterial strains showed no complete eradication of pathogens by the new biomaterials, but neither for the one that has showed eradication of over 40 bacteria in previous tests (Leppäranta

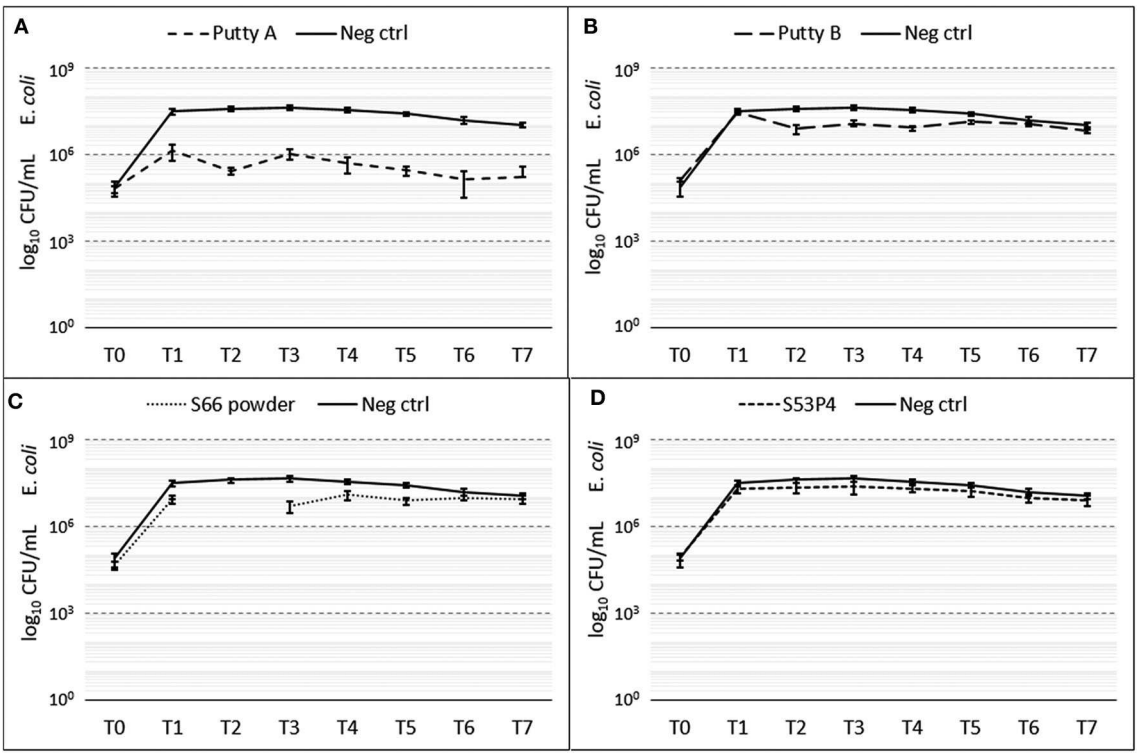

FIGURE 5 | Growth of *E. coli* in the presence of the different biomaterials in CFU/ml compared to the growth control (continuous line in all graphs) over 7 days (T_0 until T_7). **(A)** shows Putty A (dashed line) compared to the growth control (continuous line), **(B)** Putty B, **(C)** S66 powder, and **(D)** SS3P4 powder. The results are presented as mean ± standard deviation on a logarithmic scale.

et al., 2008; Munukka et al., 2008; Zhang et al., 2010). The tests showed different effects per strain. This could be explained on a microbiological perspective since cell wall components and mucus layer are variable per species and may also may per strain. By this, the formulation and dimension of bioglass particles van vary in the antimicrobial activity in different strains and species. The difference in eradication between the two putty formulations may be based on the difference in concentration S53P4 bioactive glass. However, the putty with higher concentration S53P4 bioactive glass (Putty B) did not result in a higher eradication rate compared to Putty A, while Putty B resulted in a higher increase in pH compared to Putty A.

The supposedly negative control biomaterial, the S66 powder, showed a reduction of CFUs for several of the tested pathogens. *P. aeruginosa* was completely eradicated by this biomaterial and MSSA and MRSA showed a 2 $\log_{10}$ reduction and 5 $\log_{10}$ reduction, respectively, compared to the growth control without biomaterials. These results were unexpected and should be further investigated and understood for the assessment of new antimicrobial biomaterials in the future.

The results obtained for the control group with S53P4 granules contradict findings reported in literature, as these granules have been observed to effectively eradicate these tested pathogens (Munukka et al., 2008; Zhang et al., 2010; Drago et al., 2013). However, two of these studies did not report the antibacterial properties as a CFU reduction, but in a rather quantitatively manner. Zhang et al. (2010), reported the antimicrobial properties of S53P4 (granules with diameters smaller than 45 μm) in a classification system, with good, moderate, weak, very weak or no growth of bacteria as classifiers. No growth of *E. coli*, *E. faecalis*, and *P. aeruginosa* with the S53P4 powder was reported (Zhang et al., 2010). Munukka et al. (2008) reported at least a reduced growth of *S. aureus* and complete eradication of a clinical MRSA isolate and *E. coli* by S53P4 powder (granules with diameter smaller than 45 μm), based on a live-dead assay (Munukka et al., 2008). In addition, they reported a bactericidal effect on *P. aeruginosa*, which means that the growth of this pathogen was inhibited by the S53P4 powder. Whether this led to full eradication of the pathogen was not reported (Munukka et al., 2008). Not only different approaches in the quantitative vs. qualitative description of the results compared to our study could be identified. An important difference in particle size which is related to a big difference in surface area could explain the differences in results (Zhang et al., 2008). Drago et al. (2013) tested the same size of S53P4 granules as used in the current study and observed a complete eradication of *S. aureus* and *P. aeruginosa* after 72 h *in vitro* for both 400 mg glass/mL and 800 mg glass/mL broth (Drago et al., 2013). Another study used both sizes of S53P4 biomaterials (500–800 μ m granules and < 45 μm powder, both 1,000 mg glass/mL MH broth) to test whether biofilms of *S. aureus*, formed on titanium discs could be effectively treated by addition of these

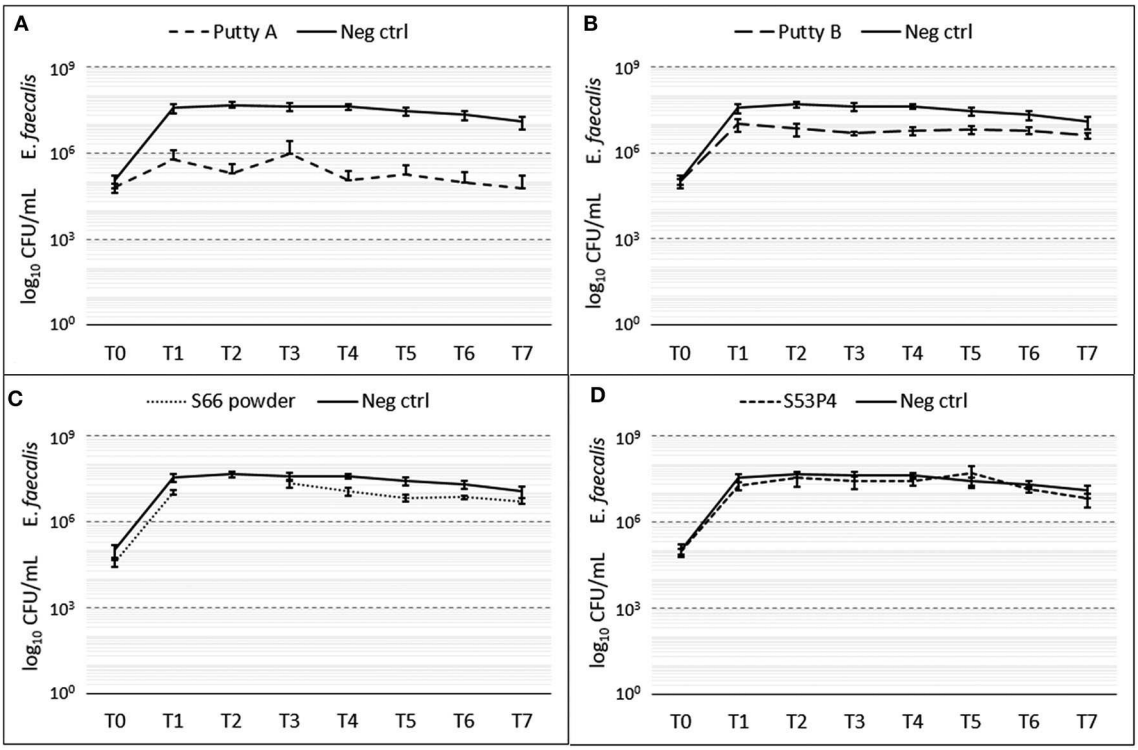

FIGURE 6 | Growth of *E. faecalis* in the presence of the different biomaterials in CFU/ml compared to the growth control (continuous line in all graphs) over 7 days (T_0 until T_7). **(A)** shows Putty A (dashed line) compared to the growth control (continuous line), **(B)** Putty B, **(C)** S66 powder, and **(D)** SS3P4 powder. The results are presented as mean ± standard deviation on a logarithmic scale and at T2 data for the S66 powder is missing due to a contamination on the agar plate.

biomaterials to the biofilm culture (Coraca-Huber et al., 2014). In their study, differences between particle sizes were observed. Both particle sizes could reduce the number of counted CFU/mL, but the powder reduced the number of colonies significantly more than the granules (Coraca-Huber et al., 2014). These results were confirmed in another recent study (Stoor and Frantzen, 2017). It needs to be determined if indeed the particle size of the S53P4 was the reason for the contradictive results, compared to literature. Additional tests with an S53P4 powder ($< 45\ \mu m$) should be used to validate the used approach and the currently obtained results. Full eradication of MRSA, *E. coli*, *E. faecalis*, and *P. aeruginosa* is expected when using the powder form (Munukka et al., 2008; Zhang et al., 2010). The surface area of the biomaterial should be standardized and the concentration of the released ions should be measured, to control the environment created by the biomaterials and define the dosage dependence. In addition, the concentration of bacteria should be taken into account. In clinical practice, the biomaterials are administered after thorough debridement of the infected area. This may result in a lower concentration of bacteria at the infection site compared to the number of bacteria used in this study. Additional research is needed to assess the influence of the mentioned variables on the antimicrobial effect.

From a clinical point of view, the larger S53P4 granules are more relevant than powder. For example in the treatment of osteomyelitis, usually bigger sized granules are used (Hulsen et al., 2017). Good clinical results have been obtained in the treatment of infections with the S53P4 granules (McAndrew et al., 2013; Geurts et al., 2016; Lindfors et al., 2016; Al Malat et al., 2018). During the treatment of osteomyelitis extensive debridement and cleaning is performed, the defect is fully packed with BAG granules, and additional systemic antibiotics are administered (Geurts et al., 2016; Lindfors et al., 2016). These aspects may contribute to the good clinical results, as potentially a much lower number of bacteria is left in the treated area after debridement compared to the used number of bacteria in the setup of this study. Furthermore, changes in osmotic pressure due to the release of ions was not measured. These aspects were not considered in our *in vitro* tests and these are therefore worst-case scenarios. A fully packed defect may result in a different concentration of ions and a locally higher pH than what was simulated in our experiments.

The current increase of antimicrobial resistance stresses the need for representative and reproducible *in vitro* tests that are predictive of the *in vivo* situation and even more the need to develop new antimicrobial biomaterials (Alanis, 2005; Kohanski et al., 2010; O'Neill, 2016; WHO, 2018). Unfortunately, the current setup did not confirm the antimicrobial activity of S53P4 BAG granules observed in patients. We could therefore not quantify to what extend the addition of a binder would affect antimicrobial properties. In addition, an inert biomaterial did show unexpected antibacterial effects, which highlights a lack of understanding of the underlying mechanisms. It has

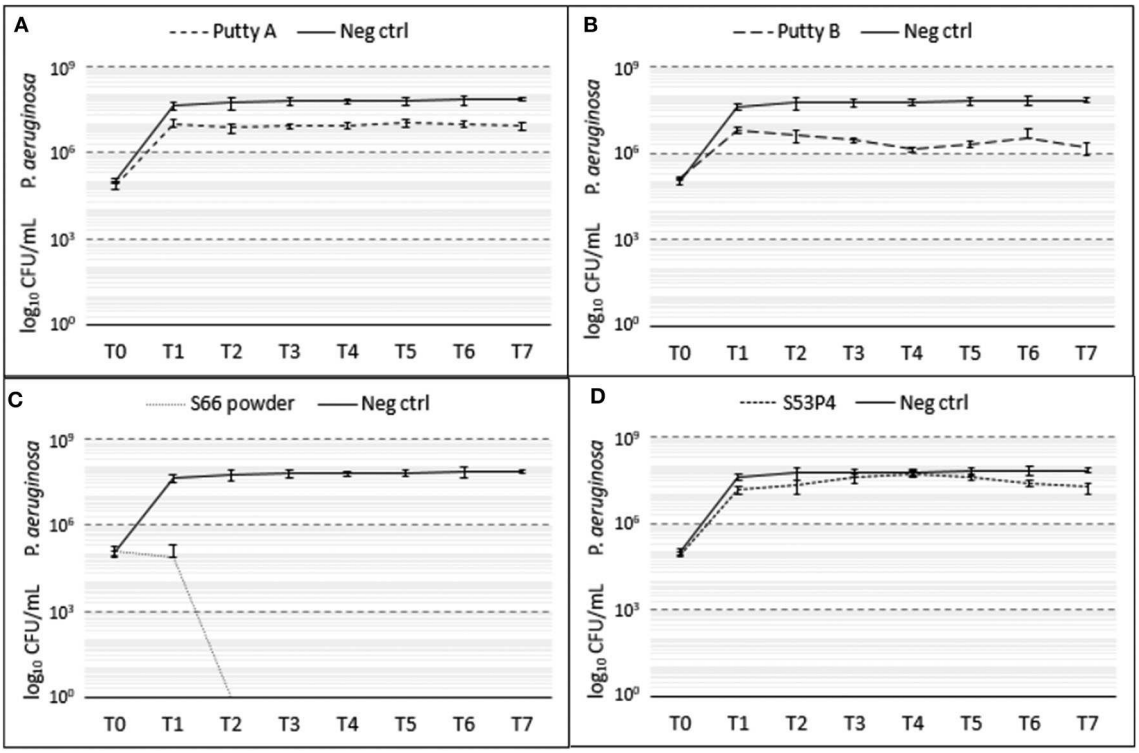

FIGURE 7 | Growth of *P. aeruginosa* in the presence of the different biomaterials in CFU/ml compared to the growth control (continuous line in all graphs) over 7 days (T_0 until T_7). **(A)** shows Putty A (dashed line) compared to the growth control (continuous line), **(B)** Putty B, **(C)** S66 powder, and **(D)** SS3P4 powder. The results are presented as mean ± standard deviation on a logarithmic scale.

been proposed that the local increase in pH and osmotic pressure changes the morphology of bacteria and damages the cell wall (Drago et al., 2015). This mechanism would be completely different than the mechanisms reported common for antibiotics against which pathogens can develop resistance (Alanis, 2005; Kohanski et al., 2010; O'Neill, 2016; WHO, 2018). This antimicrobial resistance is a major treat for future public health and one of our biggest current challenges according the world health organization (Alanis, 2005; Kohanski et al., 2010; O'Neill, 2016; WHO, 2018). Further research is needed to evaluate the exact mechanism of S53P4 BAG and whether bacteria could develop resistance against this mechanism.

CONCLUSION

This study stresses the importance of a better understanding the antimicrobial mechanism by S53P4 biomaterials and how these properties can be affected by changing the biomaterial, in size or by addition of binders to improve the handling properties. In addition, this study stresses the need to develop an *in vitro* system that is more representative of the *in vivo* situation during treatment.

DATA AVAILABILITY STATEMENT

The datasets generated for this study are available on request to the corresponding author.

AUTHOR CONTRIBUTIONS

ET carried out the experiments. ET and NG analyzed the data and wrote the manuscript with support from SH, JG, IL, and JA. IL, RB, and JA helped supervise the project. All authors provided critical feedback, helped shape the research, analysis, and manuscript.

FUNDING

This study, including the biomaterials tested in this study were funded by Bonalive® Biomaterials Ltd.

ACKNOWLEDGMENTS

The authors acknowledge biomaterials in kind (biomaterials) by Bonalive® Biomaterials Ltd.

REFERENCES

Al Malat, T., Glombitza, M., Dahmen, J., Hax, P., and Steinhausen, E. (2018). The use of bioactive glass S53P4 as bone graft substitute in the treatment of chronic osteomyelitis and infected non-unions – a retrospective study of 50 patients. *Z. Orthop. Unfall* 152–159. doi: 10.1055/s-0043-124377

Alanis, A. J. (2005). Resistance to antibiotics: are we in the post-antibiotic era? *Arch. Med. Res.* 36, 697–705. doi: 10.1016/j.arcmed.2005.06.009

Balouiri, M., Sadiki, M., and Ibnsouda, S. K. (2016). Methods for *in vitro* evaluating antimicrobial activity: a review. *J. Pharm. Anal.* 6, 71–79. doi: 10.1016/j.jpha.2015.11.005

Calhoun, J. H., Manring, M. M., and Shirtliff, M. (2009). Osteomyelitis of the long bones. *Semin. Plast. Surg.* 23, 59–72. doi: 10.1055/s-0029-1214158

Coraca-Huber, D. C., Fille, M., Hausdorfer, J., Putzer, D., and Nogler, M. (2014). Efficacy of antibacterial bioactive glass S53P4 against *S. aureus* biofilms grown on titanium discs *in vitro*. *J. Orthop. Res.* 32, 175–177. doi: 10.1002/jor.22463

Drago, L., Romanò, D., De Vecchi, E., Vassena, C., Logoluso, N., Mattina, R., et al. (2013). Bioactive glass BAG-S53P4 for the adjunctive treatment of chronic osteomyelitis of the long bones: an *in vitro* and prospective clinical study. *BMC Infect. Dis.* 13, 584–592. doi: 10.1186/1471-2334-13-584

Drago, L., Vecchi, E. D., Bortolin, M., Toscano, M., Mattina, R., and Romanò, C. L. (2015). Antimicrobial activity and resistance selection of different bioglass S53P4 formulations against multidrug resistant strains. *Future Microbiol.* 10, 1293–1299. doi: 10.2217/FMB.15.57

Geissmann, Q. (2013). OpenCFU, a new free and open-source software to count cell colonies and other circular objects. *PLoS ONE* 8:e54072. doi: 10.1371/journal.pone.0054072

Geurts, J., Vranken, T., and Arts, J. J. C. (2016). Treatment of osteomyelitis by means of bioactive glass - initial experience in the Netherlands. *Ned. Tijdschr. voor Orthop.* 23, 37–41.

Hulsen, D. J., van Gestel, N. A., Geurts, J. A. P., and Arts, J. J. (2017). "S53P4 bioactive glass," in *Management of Periprosthetic Joint Infections (PJIs)* (Elsevier), 69–80. doi: 10.1016/B978-0-08-100205-6.00004-5

Kohanski, M. A., Dwyer, D. J., and Collins, J. J. (2010). How antibiotics kill bacteria: from targets to networks. *Nat. Rev. Microbiol.* 8, 423–435. doi: 10.1038/nrmicro2333

Leppäranta, O., Vaahtio, M., Peltola, T., Zhang, D., Hupa, L., Hupa, M., et al. (2008). Antibacterial effect of bioactive glasses on clinically important anaerobic bacteria *in vitro*. *J. Mater. Sci. Mater. Med.* 19, 547–551. doi: 10.1007/s10856-007-3018-5

Lindfors, N. C., Geurts, J., Drago, L., Arts, J. J., Juutilainen, V., Hyvönen, P., et al. (2016). Antibacterial bioactive glass, S53P4, for chronic bone infection - a multinational study. *Adv. Exp. Med. Biol. Respir.* 6, 57–66. doi: 10.1007/5584_2016_156

McAndrew, J., Efrimescu, C., Sheehan, E., and Niall, D. (2013). Through the looking glass; bioactive glass S53P4 (BonAlive®) in the treatment of chronic osteomyelitis. *Ir J Med Sci.* 182, 509–511. doi: 10.1007/s11845-012-0895-5

Munukka, E., Leppäranta, O., Korkeamäki, M., Vaahtio, M., Peltola, T., Zhang, D., et al. (2008). Bactericidal effects of bioactive glasses on clinically important aerobic bacteria. *J. Mater. Sci. Mater. Med.* 19, 27–32. doi: 10.1007/s10856-007-3143-1

O'Neill, J. (2016). Tackling drug-resistant infections globally: final report and recommendations. *Rev. Antimicrob. Resist.* 84. Available online at: https://amr-review.org/sites/default/files/160518_Final%20paper_with%20cover.pdf

Pankey, G. A., and Sabath, L. D. (2004). Clinical relevance of bacteriostatic versus bactericidal mechanisms of action in the treatment of gram-positive bacterial infections. *Clin. Infect. Dis.* 38, 864–870. doi: 10.1086/381972

Parsons, B., and Strauss, E. (2004). Surgical management of chronic osteomyelitis. *Am. J. Surg.* 188, 57–66. doi: 10.1016/S0002-9610(03)00292-7

Stoor, P., and Frantzen, J. (2017). Influence of bioactive glass S53P4 granules and putty on osteomyelitis associated bacteria *in vitro*. *Biomed. Glas.* 3, 79–85. doi: 10.1515/bglass-2017-0007

Stoor, P., Söderling, E., and Salonen, J. I. (1998). Antibacterial effects of a bioactive glass paste on oral microorganisms. *Acta Odontol. Scand.* 56, 161–165. doi: 10.1080/000163598422901

van Gestel, N. A. P., Geurts, J., Hulsen, D. J. W., van Rietbergen, B., Hofmann, S., and Arts, J. J. (2015). Clinical applications of S53P4 bioactive glass in bone healing and osteomyelitic treatment: a literature review. *Biomed Res. Int.* 2015:684826. doi: 10.1155/2015/684826

van Gestel, N. A. P., Hulsen, D. J. W., Geurts, J., Hofmann, S., Ito, K., Arts, J. J., et al. (2017). Composition dependent mechanical behaviour of S53P4 bioactive glass putty for bone defect grafting. *J. Mech. Behav. Biomed. Mater.* 69, 301–306. doi: 10.1016/j.jmbbm.2017.01.024

Vugt, T. A. G., Geurts, J., and Arts, J. J. (2016). Clinical application of antimicrobial bone graft substitute in osteomyelitis treatment : a systematic review of different bone graft substitutes available in clinical treatment of osteomyelitis. *Biomed Int. Res.* 2016:6984656. doi: 10.1155/2016/6984656

Walenkamp, G. H. I. M., Kleijn, L. L. A., and de Leeuw, M. (1998). Osteomyelitis treated with gentamicin-PMMA beads. *Acta Orthop. Scand.* 69, 518–522. doi: 10.3109/17453679808997790

WHO. (2018). *World Health Organization Antibiotic Resistance.* Available online at: https://www.who.int/news-room/fact-sheets/detail/antibiotic-resistance (accessed June 9, 2019).

Zhang, D., Hupa, M., and Hupa, L. (2008). In situ pH within particle beds of bioactive glasses. *Acta Biomater.* 4, 1498–1505. doi: 10.1016/j.actbio.2008.04.007

Zhang, D., Leppäranta, O., Munukka, E., Ylänen, H., Viljanen, M. K., Eerola, E., et al. (2010). Antibacterial effects and dissolution behavior of six bioactive glasses. *J. Biomed. Mater. Res. Part A* 93, 475–483. doi: 10.1002/jbm.a.32564

Conflict of Interest: JG and JA are clinical advisors and NG is a scientific advisor for Bonalive® Biomaterials Ltd. Neither this nor the funding by Bonalive® played a role in the collection, analyses, or interpretation of data; in the writing of the manuscript, or in the decision to publish the results.

The remaining authors declare that the research was conducted in the absence of any commercial or financial relationships that could be construed as a potential conflict of interest.

frontiers in Bioengineering and Biotechnology

ORIGINAL RESEARCH
published: 23 July 2020
doi: 10.3389/fbioe.2020.00865

Bioactive Dental Adhesive System With *tt*-Farnesol: Effects on Dental Biofilm and Bonding Properties

Diana Leyva del Rio[1], Neimar Sartori[1], Nichole Barton Tomblin[2], Jin-Ho Phark[1], Vanessa Pardi[3], Ramiro M. Murata[3]* and Sillas Duarte Jr.[1]*

[1] Advanced Program in Operative and Adhesive Dentistry, Division of Restorative Sciences, Herman Ostrow School of Dentistry, University of Southern California, Los Angeles, CA, United States, [2] Division of Periodontology Diagnostic Sciences, Dental Hygiene & Biomedical Science, Herman Ostrow School of Dentistry, University of Southern California, Los Angeles, CA, United States, [3] Department of Foundational Sciences, School of Dental Medicine, East Carolina University, Greenville, NC, United States

OPEN ACCESS

Edited by:
Aldo R. Boccaccini, University of Erlangen-Nuremberg, Germany

Reviewed by:
Joanna Mystkowska, Bialystok University of Technology, Poland
Rossana Mara Da Silva Moreira Thiré, Federal University of Rio de Janeiro, Brazil

***Correspondence:**
Neimar Sartori
nsartori@dental.ufl.edu
Ramiro M. Murata
muratar16@ecu.edu

Specialty section:
This article was submitted to Biomaterials, a section of the journal Frontiers in Bioengineering and Biotechnology

Received: *05 February 2020*
Accepted: *06 July 2020*
Published: *23 July 2020*

Citation:
Leyva del Rio D, Sartori N, Tomblin NB, Phark J-H, Pardi V, Murata RM and Duarte S Jr (2020) Bioactive Dental Adhesive System With tt-Farnesol: Effects on Dental Biofilm and Bonding Properties. Front. Bioeng. Biotechnol. 8:865. doi: 10.3389/fbioe.2020.00865

Background: Composite dental restorations are commonly used to restore cavitated carious lesions. Unfortunately, the main reason for failure is the development of secondary caries adjacent to the restoration. To improve the long-term survival of restorations, antibacterial agents have been added into dental materials. In this study, we assessed the antibacterial and bonding capacity of a commercial universal dental adhesive incorporated with the antibacterial agent *tt*-farnesol creating 3 experimental adhesives: 0.38% (v/v), 1.90% (v/v), and 3.80% (v/v), plus a control (no incorporation of *tt*-farnesol).

Methods: The antibacterial activity was evaluated by assessing colony-forming units (CFU), biofilm dry weight (DW) and production of extracellular insoluble polysaccharides (EIP) at day 2, 3, and 5 of biofilm growth post surface treatment on the surface of composite disks. The effect of *tt*-farnesol on the chemical and bonding capacity of the adhesive system was assessed via pH analysis, degree of conversion (DC), and microtensile bond strengths to human dentin in both self-etch and etch-and-rinse application modes. A qualitative analysis of the effects of *tt*-farnesol on biofilm formation was evaluated using scanning electron microscopy (SEM). The sealing capacity of all adhesive systems tested was evaluated using confocal laser scanning microscopy (CLSM).

Results: The 3.80% (v/v) experimental adhesive exhibited the lowest CFU count and lowest production of EIP at day 5. DW and pH values did no exhibit statistical differences among all tested groups. Bond strengths and DC decreased with the incorporation of the antibacterial agent into the adhesive system regardless of the concentration of *tt*-farnesol.

Conclusion: The incorporation of *tt*-farnesol into the adhesive system significantly reduced bacterial viability and production of EIP; however, the bonding properties of the experimental dental adhesives were altered.

Keywords: dental adhesive systems, *tt*-farnesol, universal adhesive, antibacterial activity, antibacterial adhesive system, hybrid layer, bond strength

INTRODUCTION

Cavitated dental caries lesions are usually treated by removing the infected tooth tissue and restoring the missing portion of the tooth with restorative materials such as adhesive composite restorations. The use of composite resin restorations has been increasing due to its high esthetics when compared to amalgam, however, in the long-term one of the main reasons for failure of these restorations is due to the occurrence of secondary caries adjacent to the restoration (Beck et al., 2015). Cariogenic biofilm plays an important role in the establishment and progression of secondary caries. In the oral microenvironment, biofilm forms due to complex interactions between microorganisms, sugar-rich diet, and the host that result in the production of acids that demineralize the dental substrate (Kidd and Fejerskov, 2004). Biofilms are microbial communities that are immersed in a three-dimensional extracellular matrix (EM) that have the capability of attaching to surfaces. From the wide range of microorganisms that are involved in the carious process, *Streptococcus mutans* is still considered the principal producer of EM in dental biofilms (Bowen and Koo, 2011). *S. mutans* is a highly aciduric and acidogenic microorganism that encodes glucosyltransferases (Gtfs) which produce extracellular polysaccharides in the presence of sucrose. Extracellular polysaccharides (insoluble and soluble) are the main constituent of the EM and have the capability of providing a supportive framework for biofilm development while promoting microbial adhesion to surfaces as well serving as a barrier to diffusion (Koo et al., 2013).

The formation of oral biofilms does not only occur on the surface of dental hard tissues, but also on the surface of restorative materials. Resin composites are in particular susceptibility to the initiation and development of biofilms because of its surface properties (Cazzaniga et al., 2015) affecting the longevity of the restoration in the oral cavity. A potential alternative for reducing the incidence of secondary caries is the incorporation of antibacterial agents into restorative materials (Chen et al., 2018). Amongst dental restorative materials, dental adhesive systems are the ideal material to have antibacterial properties due to their intimate contact with dental hard tissues. Although some highly acidic adhesives have been shown to produce some antibacterial effects against *S. mutans* (Imazato et al., 1998; Herrera et al., 2000), the low pH of these adhesive agents may cause bond degradation at the interface due the activation of matrix metalloproteinases (MMPs; Pashley et al., 2011) that ultimately reduces the life of the restoration. Therefore, to increase the long-term outcome of dental restorations, some antibacterial agents have been incorporated into commercial adhesive systems such as 0.12% chlorhexidine that is found in Peak Universal Bond and 5% of 12-methacryloyloxydodecypyridinium bromide (MDPB) that has been incorporated into Clearfil SE Protect. The limited number of adhesive systems with antibacterial properties currently in the market yields the need to investigate compounds that could potentially be added into dental adhesives.

Trans,*trans*-farnesol (*tt*-farnesol, 3, 7, 11 – trymethyl-2,6,10-dodecatrien-1-ol), is a natural sesquiterpene alcohol found in propolis which has demonstrated a reduction in the incidence and severity of dental caries with negligible effects on the oral microflora in a study *in vivo* (Koo et al., 2002a), demonstrating its potential as an antibacterial agent against cariogenic bacteria. The mechanism of action of *tt*-farnesol focuses on the disruption of the proton permeability of the *S. mutans* membrane, which alters the acid production, acid tolerance, and polysaccharide synthesis (Koo et al., 2002b, 2003; Jeon et al., 2011). Thus, the introduction of *tt*-farnesol into restorative materials is justified due its demonstrated antibacterial properties against cariogenic pathogens. In recent literature, *tt*-farnesol was incorporated into dental restorative materials such as a glass ionomer (de Castilho et al., 2019) and into a self-etch (5th generation) and etch-and-rinse (7th generation) dental adhesives (André et al., 2017). Although the addition of agents such as epigallocatechin-3-gallate have been recently introduced (Silva et al., 2020) into universal adhesive systems (8th generation) demonstrating an antimicrobial potential against *S. mutans*, the incorporation of *tt*-farnesol into universal adhesive systems has not yet been described in the literature. Universal adhesives are the latest addition to dental adhesive systems that have the advantage of a simplified less technique sensitive one-step bonding system that provides a stable bonded interphase to the dental substrate (Cuevas-Suárez et al., 2019) making it potentially beneficial to the integration of an antibacterial agent into this novel adhesive system.

The aim of this study was to investigate the antibacterial properties of experimental adhesives by incorporating different concentrations of *tt*-farnesol into a commercially available universal adhesive system and analyze its effect on *S. mutans* biofilm viability, quantified by colony forming units (CFU), biofilm dry weight (DW), and extracellular insoluble polysaccharide production (EIP). Furthermore, the physical and bonding properties of the experimental adhesives were assessed by pH of the solution, degree of conversion (DC), and microtensile bond strength (μTBS).

MATERIALS AND METHODS

Antibacterial Properties of an Antibacterial-Incorporated Adhesive

Antimicrobial Activity

In order to measure the antimicrobial activity, *S. mutans* UA159 bacterial strain (ATCC# 700610) was used. An initial bacterial inoculum at 1×10^5 was prepared with different concentrations of the *tt*-farnesol (3, 7, 11-trimethyl-2, 6, 10-dodecatrien-1ol; Sigma-Aldrich Co, St Louis, MO, United States) against *S. mutans* UA159, ranging from 10 to 500 μM of the antibacterial agent. The solutions were incubated at 37°C and 5% CO_2 for 24 h. The minimum inhibitory concentration (MIC) of *tt*-farnesol was obtained by observing bacterial growth inhibition at 150 μM of the antibacterial agent and determined by triplicates.

Antibacterial-Incorporated Adhesive

A commercially available universal dental adhesive (Adper Scotchbond Universal, 3 M ESPE, St. Paul, MN, United States) was combined with the antibacterial agent *tt*-farnesol. Due to the liquid nature of the antibacterial agent, this was directly

incorporated into the adhesive by pipetting for 90 s and then placed the mix in a centrifuge for 1 min at 1000 rpm to remove any air from the mix. Experimental adhesive systems at 3 different concentrations were fabricated based on the MIC: 100xMIC = 0.38% (v/v), 500xMIC = 1.90% (v/v), and 1000xMIC = 3.80% (v/v). The adhesive with no addition of *tt*-farnesol or any other solvent served as a control: 0xMIC.

Biofilm Preparation and Analysis

Composite disks of 13 mm in diameter and 1 mm thickness were fabricated with a microhybrid resin composite (Filtek Z250, 3 M ESPE, St. Paul, MN, United States) using a circular stainless steel mold to obtain smooth and uniform surfaces. The composite disks were sterilized with ethylene oxide and later degasified for 48 h. To evaluate the *S. mutans* UA159 strain biofilm growth on the composite disks, 20 μL (one drop) of the experimental adhesives was applied to one surface of the composite disks. The adhesive system was agitated on the surface of the disk for 20 s with a microbrush, air-dried, and light-cured for 10 s with a halogen unit (Elipar 2500, 3 M ESPE) with 600 mW/cm^2 light output. The disks were then immediately placed in 24-well plates fully covered in 1 mL of BHI + sucrose + *S. mutans* (1×10^5) inoculum medium for biofilm growth (**Figure 1**). The media was changed daily without disrupting the biofilm on top of the disks. Biofilm was collected at days 2, 3, and 5 after surface treatment and later sonicated in 5 mL of phosphate-buffered saline (PBS) solution to obtain a homogenized solution (Murata et al., 2008; Salles Branco-De-Almeida et al., 2011; Zancopé et al., 2016).

Colony Forming Units

Colony forming units' assay was performed as followed: 1 mL of the homogenized solution was subjected to serial dilution (1×10^{-1}–1×10^{-4}), in which 20 μL of each dilution was inoculated in a tryptic soy agar plate with 5% sheep's blood (TSA 5% SB) and placed in an incubator for 24–48 h at 37°C and 5% CO_2 to allow colony growth. After this period, the colonies were counted and recorded. The numbers of colonies were normalized and converted into Log_{10} values for data interpretation. The CFU assay was performed in triplicate in at least three different experiments (Murata et al., 2008; Salles Branco-De-Almeida et al., 2011; Zancopé et al., 2016).

Biofilm Dry Weight

Two milliliters of the original homogenized suspension was completely dried in a SpeedVac concentrator (Thermo Scientific, Rockford, IL, United States) to obtain a dry pellet. The dry pellet was first weighted to obtain the biofilm biomass DW and later processed for EIP assay (Murata et al., 2008; Salles Branco-De-Almeida et al., 2011; Zancopé et al., 2016).

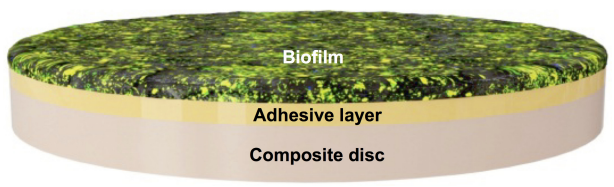

FIGURE 1 | Representative illustration of *S. mutans* biofilm growing on top of a composite disk.

Production of Extracellular Insoluble Polysaccharides

After obtaining and weighting the pellet for the biofilm DW analysis, the pellet was resuspended and washed in 1 ml of water; this procedure was repeated twice to remove the soluble polysaccharides. The pellet was dried in a SpeedVac concentrator and the extracellular insoluble (alkali soluble) polysaccharides were extracted using 0.05 mL of 1 M NaOH per 1 mg of biofilm biomass DW. The samples were homogenized for 1 min, maintained under agitation for 3 h at room temperature and the concentration of insoluble carbohydrate was determined in the supernatant by a phenol–sulfuric acid method (Dubois et al., 1956); determination of polysaccharides by colorimetric assays has been widely used to estimate the polysaccharide content in dental plaque and *S. mutans* biofilms (Almeida et al., 2008; Murata et al., 2008, 2010; Zancopé et al., 2016).

Scanning Electron Microscopy Analysis

Disks with 5-day grown biofilms were processed for scanning electron microscopy (SEM) analysis. The specimens were immersed in 2.5% glutaraldehyde in 0.1 M sodium cacodylate buffer (Electron Microscopy Sciences, Hatfield, PA, United States) at pH 7.4 for 12 h at 4°C, rinsed with 0.2 M sodium cacodylate buffer (Electron Microscopy Sciences, Hatfield) at pH 7.4 for 1 h for three periods, followed by a distilled water rinse for 1 min. The specimens were then dehydrated in ascending concentrations of ethanol (25% for 20 min, 50% for 20 min, 75% for 20 min, 95% for 30 min, and 100% for 60 min). Subsequently, the specimens were immersed in hexamethyldisilazane (Electron Microscope Sciences, Fort Washington, PN, United States) for 10 min and then placed on a filter paper inside a covered glass vial and air-dried at room temperature inside a fume hood for 12 h (Dekker et al., 1991). The dried specimens were mounted on aluminum stubs and sputter-coated with gold/palladium. Images of specimens were obtained using a field-emission scanning electron microscope (JSM-7001F, JEOL, Tokyo, Japan) at an accelerating voltage of 5–0 kV with up to 10,000 times of magnification.

Chemical Properties of an Antibacterial-Incorporated Adhesive

pH Measurement

The pH values of the control and each of the experimental groups were measured with a pH meter (Mettler Toledo, Columbus, OH, United States). The meter probe was calibrated with a buffer standard solution then submerged in 2 mL of the experimental solution for 2 min. For each measurement, pH values were recorded and the tip of the probe was rinsed with ethyl alcohol and distilled water to remove any remnants of previous solution. Measurements were performed under minimum light to avoid polymerization of the adhesive systems. Five different readings for each individual adhesive were performed, and the mean pH value was calculated.

Degree of Conversion

The DC was evaluated using micro-Raman spectroscopy (InVia, Spectrometer, Renishaw, New Mills, United Kingdom) with a laser wavelength of 532 nm, power output at 750 mW, microscope objective of 50X, and with a pin-hole aperture of 370 μm. The spectra range obtained was from 400 to 2000 cm^{-1}, with an integration time of 20 s using a RenCam CCD detector with a 1024 × 256 pixel resolution. Data was processed using Origin2015 software (OriginLab Corporation, Northampton, MA, United States).

Three different samples were fabricated for the control and each of the experimental adhesives. After spectrometer calibration with a silicon sample, one drop (20 μL) of *tt*-farnesol-adhesive mixture was placed on top of a glass slide and spectra of the uncured adhesive was obtained and recorded. The adhesive drop was agitated in top of the sample for 20 s with a microbrush and then gently air thinned for 5 s to promote solvent evaporation. A thin glass slide was placed on top of the drop to both create a uniform layer and prevent oxygen inhibition layer formation. The surface was light-cured for 10 s. The thin glass slide was removed and additional spectra of the cured sample was taken and recorded. At least 5 spectra per sample were recorded. The DC was calculated using the formula, $DC\% = \left[1 - \frac{Rcured}{Runcured} \times 100\right]$ in which R is the ratio of areas under the aliphatic 1639 cm^{-1} peak and aromatic 1609 cm^{-1} peak in cured and uncured material.

Bonding and Sealing Properties of an Antibacterial-Incorporated Adhesive

Microtensile Bond Strength

Caries-free human third molars where collected in accordance of the University of Southern California's IRB (IRB #APP-13-05027). The external surface of the teeth was cleaned of any remaining organic debris and stored in 0.5% chloramine-T solution for no more than 2 months prior to μTBS testing and hybrid layer permeability analysis. 24 teeth were sectioned perpendicular to the longitudinal axis of the tooth, 2.5 mm above the cement-enamel junction (CEJ), and 3 mm bellow the CEJ using a low speed diamond saw (Isomet 1000, Buehler Ltd., Lake Bluff, IL, United States) and water-cooling to remove the coronal enamel and root. The occlusal surfaces of the crown segments were polished using a waterproof 600-grit silicon carbide paper under running water for 60 s to create a standard smear layer (Pashley, 1984). The crown segments were sorted into eight experimental groups using two bonding approaches, etch-and-rinse mode and self-etch mode for each of the experimental groups. The adhesive system was applied following the manufacturers' instructions (**Table 1**) and light-cured for 10 s. Microhybrid composite resin (Filtek Z250, 3 M ESPE) was built up on top of the bonded surfaces with 3 successive increments of 2 mm, each light-cured for 20 s.

After 24 h of storage in distilled water at 37°C, the samples were cut under water-cooling in both X/Y axis parallel of the long axis of the tooth to obtain untrimmed sticks with a cross-sectional surface area of 0.8 ± 0.2 mm^2.

TABLE 1 | Adhesive system composition and its application, according to the manufacturer recommendations.

Adhesive	Composition	Application modes
Adper Scotchbond Universal (3 M ESPE)	10-MDP Phosphate monomer Dimethacrylate resins HEMA Methacrylate-modified polyalkenoic acid copolymer Fillers Ethanol Water Initiators Silane	*A. Two-step etch-and-rinse* Apply etchant for 15 s Rinse Blot dry Apply adhesive for 20 s rubbing it against the tooth surface Air dry for 5 s until the adhesive doesn't move Light-cure for 10 s *B. One-step self-etch* Apply adhesive for 20 s rubbing it against the surface Air dry for 5 s until the adhesive doesn't move Light-cure for 10 s

Specimens were measured with a digital caliper (Mitutoyo digital caliper, Mitutoyo Corp., Tokyo, Japan) to obtain the bonded surface area of the interface and these values were recorded. Later, specimens were fixed to a testing jig with cyanoacrylate glue (Zapit, Dental Ventures of America, Corona, CA, United States), placed in a universal testing machine (Instron Model 4400, Instron Corp., Canton, MA, United States), and loaded in tensile force at a cross-head speed of 1 mm/min until fracture. The load (Newtons) and the bonding surface area (mm^2) of the specimens were registered using the software TestWorks 4 (MTS Nano Instruments, Eden Prairie, MN, United States). μTBS were calculated by dividing the maximum load (N) applied in tension before failure by the bonding surface area (mm^2) to obtain Mega Pascals (MPa) values. The failure modes were evaluated at 32× of magnification in a stereoscopic microscope and classified as cohesive (failure entirely within dentin substrate or resin composite), mixed (failure at dentin/resin interface including cohesive failure of one of the substrates), or adhesive (failure at the dentin/resin interface).

Hybrid Layer Permeability

Two additional teeth from each group were prepared for confocal laser scanning microscopy (CLSM) to observe the interaction between the adhesive system and internal dentinal fluids at the dentin-resin layer. Three drops of each adhesive system were mixed with one grain of tetramethylrhodamine B isothiocyanate (Sigma-Aldrich) to form a homogeneous solution. Tooth samples were restored using the methodology described above for each of the groups. After 24 h of storage in water, the pulpal chambers were filled with a solution of 0.1% fluorescein sodium (Sigma-Aldrich) for 4 h. The restored tooth segments were cut perpendicular to the adhesive interface using a slow-speed precision saw to obtain 2–3 slabs with 1.0 mm thickness from the center of the tooth. The samples were evaluated under a CLSM (LSM 5 Pascal, Zeiss, Jena, Germany) and images of the adhesive interface with 63 times of magnification at 1024 × 1024 pixels and 2.0 μs/pixel speed were obtained.

Statistical Analysis

To detect differences between all the groups, data from at least 3 separate experiments were analyzed for the CFU, DW, and EIP assays. The three time points of evaluation were independently analyzed in each of the assays. This data was checked for normality with Shapiro–Wilk test. When normal distribution was detected, data was analyzed with one-way ANOVA followed by Tukey HSD *post-hoc* test ($\alpha = 0.05$). When no normal distribution was detected, nonparametric multiple comparisons test with Dunn *post hoc*-test was used ($\alpha = 0.05$). For μTBS tests, pH, and DC evaluation, data was checked for normality with Kolmogorov–Smirnov test. μTBS data was analyzed using two-way ANOVA followed by Tukey HSD post-hoc test ($\alpha = 0.05$) to detect differences between both application modes in all the groups, meanwhile DC and pH values were analyzed using one-way ANOVA followed by Tukey HSD post-hoc test ($\alpha = 0.05$).

RESULTS

Antibacterial Properties of an Antibacterial-Incorporated Adhesive

Colony Forming Units

The effects of the different concentrations of *tt*-farnesol on the CFU activity are shown in **Figure 2**. No statistical differences ($P > 0.05$) were found between groups at day 2. At day 3, results show statistical differences ($P < 0.05$) between control and 3.80% (v/v) groups and 0.38% (v/v) with 3.80% (v/v) groups. At day 5, differences between groups was highly evident showing a significant reduction in CFU values between control vs. 1.90% (v/v) and 3.80% (v/v) groups and it was also observed a significant difference between 0.38% (v/v) group and 3.80% (v/v) group.

Biofilm Dry Weight

There was no statistical difference ($P > 0.05$) in biofilm biomass among all tested groups at any time point evaluated (**Figure 3**).

Production of Extracellular Insoluble Polysaccharides

At days 2 and 3, no statistical differences were observed amongst the groups (**Figure 4**). At day 5, it can be observed a 3-fold increase in the production of extracellular polysaccharides in both control and 0.38% (v/v) groups when compared to the previous time points evaluated. A significant difference ($P < 0.05$) in the amount of EIP production was observed for 3.80% (v/v) group and the rest of the groups.

Scanning Electron Microscopy

Scanning Electron Microscopy images exhibited bacterial colonies coating the surface of the composite disks. At 100× magnification (**Figure 5A**), it can be observed a thick and uniform biofilm formation covering the surface of the disk on both control and 0.38% (v/v) groups. On the other hand, for group 3.80% (v/v), it can be observed a disruption and reduction in biofilm formation showing individual bacterial colonies that spread throughout the surface of the disk. Higher magnification reveals chain-like cell arrangements of the *S. mutans* surrounded by fibrous hair-like structures of extracellular polysaccharides

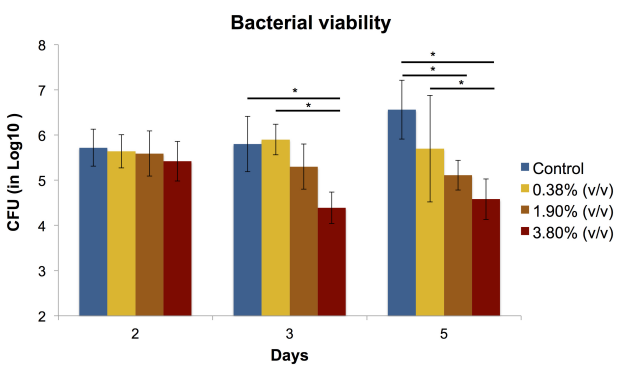

FIGURE 2 | Means (±SD) of CFU (in Log10) count in *S. mutans* biofilms according to the experimental adhesives used at 2, 3, and 5 days after surface treatment. Groups connected by bars with an asterisk are statistically significant ($P < 0.05$).

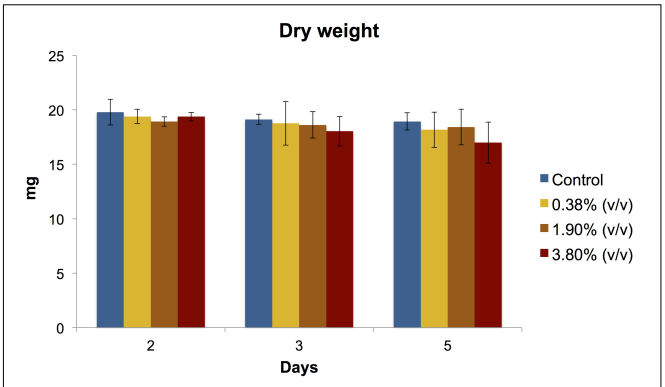

FIGURE 3 | Means (±SD) of dry biomass weight (in mg) production of *S. mutans* biofilms according to the experimental adhesives used at 2, 3, and 5 days after surface treatment. There was no statistical difference ($P > 0.05$) between the experimental groups evaluated at any day.

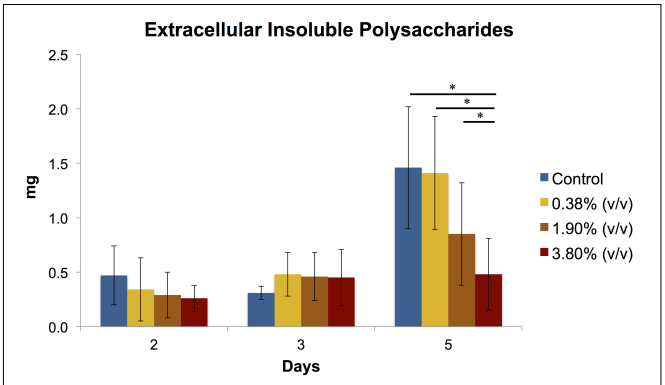

FIGURE 4 | Means (±SD) of extracellular insoluble polysaccharides (in mg) production of *S. mutans* biofilms according to the experimental adhesives used at 2, 3, and 5 days after surface treatment. Groups connected by bars with an asterisk are statistically significant ($P < 0.05$).

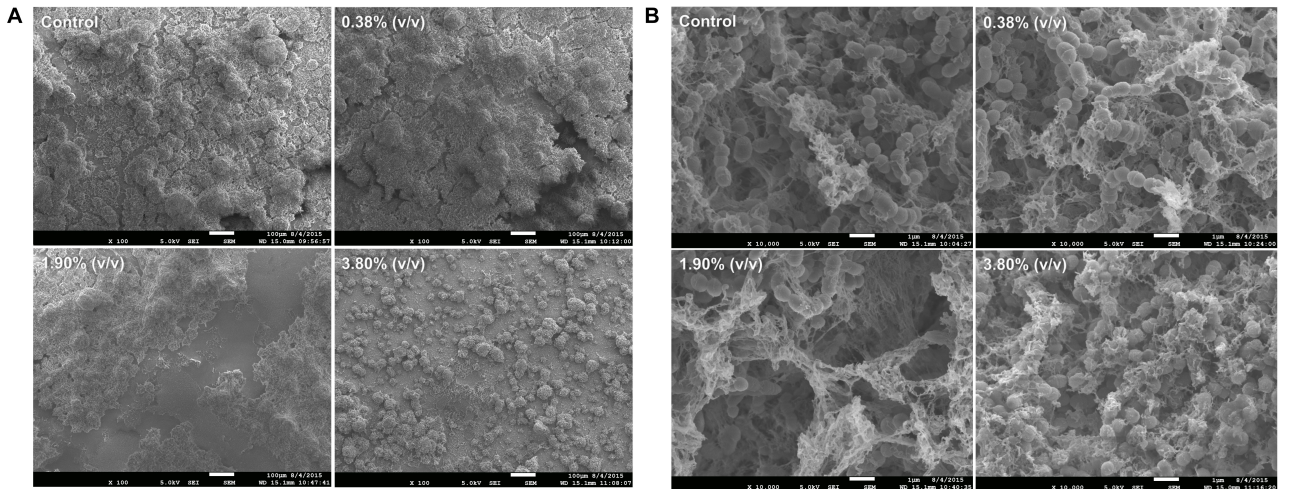

FIGURE 5 | Representative SEM images revealing the biofilm growth on the top to the adhesive layer at 100× magnification **(A)** and at 10,000× magnification **(B)**. Control: 0.0% of *tt*-farnesol; 100×MIC: 0.38% (v/v) of *tt*-farnesol; 500×MIC: 1.90% (v/v) of *tt*-farnesol; and 1000×MIC: 3.80% (v/v) of *tt*-farnesol.

that are present in all groups (**Figure 5B**), on the other hand, on group 3.80% (v/v) it can be observed disorganized bacterial chain formation surrounded by a decreased and irregular EIP production.

Chemical Properties of an Antibacterial-Incorporated Adhesive

pH Measurement

The pH mean values varied from 2.98 to 3.01 and there was no statistical difference ($P > 0.05$) amongst the experimental groups or the control group (**Table 2**). The addition of *tt*-farnesol did not alter the pH of the universal adhesive system Adper Scotchbond Universal.

Degree of Conversion

The incorporation of the antibacterial agent decreased the DC of all experimental groups, regardless of its concentration of *tt*-farnesol. The control group obtained the highest mean with a 73.11% monomer-to-monomer conversion, showing a statistical difference ($P < 0.05$) from all the experimental groups. The mean DC values of the experimental groups ranged between 45.48 and 49.23% and no statistical differences were observed amongst the experimental groups ($P > 0.05$; **Table 2**).

Bonding and Sealing Properties of an Antibacterial-Incorporated Adhesive

Microtensile Bond Strength

A reduction of μTBS was observed in all experimental groups ($P < 0.05$) when compared to the control group regardless of the application mode (**Table 2**). The control groups in both bonding modes yielded the highest bond strength means, 74.34 ± 26.1 MPa for the etch-and-rinse mode and 66.90 ± 16.4 MPa for the self-etch mode. When comparing etch-and-rinse and self-etch bonding modes, there were no statistical differences ($P > 0.05$) between the two in the control, 1.90% (v/v), and 3.80% (v/v) groups. Pre-testing failure occurred only in the experimental adhesives applied in the self-etch mode (**Table 3**). The percentage of adhesive failure increased when *tt*-farnesol was incorporated within the adhesive system, regardless of the application mode, indicating that *tt*-farnesol alters adhesive and dentin interaction.

Permeability of the Hybrid Layer

Representative CLSM images illustrate the resin-dentin interface created by Adper Scotchbond Universal and the experimental adhesives when it was applied in both etch-and-rinse (**Figure 6A**) and self-etch (**Figure 6B**) modes. The adhesive resin is shown dyed in red, water dyed in green, whereas yellow areas represent the mixture between unpolymerized resin and water. For the etch-and-rinse groups, the hybrid layer formed in the control and 0.38% (v/v) groups adequately sealed the adhesive interface. The intradentinal hybrid layer around the resin tags obstructed water ingress from the pulp into the hybrid layer, thus preventing the hydrolytic degradation of the adhesive interface. However, when higher concentrations of *tt*-farnesol were incorporated into the adhesive system, monomers dissolved from the basal portion of the resin tags (shown as red globules inside dentin tubules). The resin tags formed on 1.90% (v/v) and 3.80% (v/v) groups were shorter than the control group, which did not allow for proper sealing the resin-dentin interface. For the self-etch approach, resin tags were shorter than those created by the etch-and-rinse approach. Water accumulation could be observed at the resin-adhesive interface in all experimental groups showing a different sealing capability of the experimental adhesive systems.

DISCUSSION

Dental caries is considered the most prevalent disease affecting populations worldwide which results in billions of individuals suffering from pain, loss of function, compromised esthetics,

TABLE 2 | pH, degree of conversion (DC) in % and microtensile bond strength (μTBS) in MPa results.

Group	pH	DC (%)	μTBS	
			Etch-and-rinse mode	Self-etch mode
Control	2.978 ± 0.037^{a}	73.11 ± 8.54^{a}	74.34 ± 26.1^{aA}	66.90 ± 16.4^{aA}
0.38% (v/v)	3.010 ± 0.031^{a}	49.23 ± 6.06^{b}	64.29 ± 17.8^{bA}	54.35 ± 20.9^{bB}
1.90% (v/v)	2.990 ± 0.041^{a}	48.78 ± 18.38^{b}	59.80 ± 13.5^{bA}	55.71 ± 19.9^{bA}
3.80% (v/v)	2.994 ± 0.029^{a}	45.48 ± 10.04^{b}	55.69 ± 16.0^{bA}	57.69 ± 19.1^{bA}

Means, standard deviation and statistical results of control and experimental adhesive systems bonded to human dentin in etch-and-rinse and self-etch modes. Within the same vertical column, means with same superscript lower-case letters (comparing different concentrations of tt-farnesol) are not statistically different ($P > 0.05$). Within the same horizontal row, means with the same superscript upper-case letters (comparing application mode) are not statistically different ($P > 0.05$).

TABLE 3 | Failure mode distribution (%).

Application mode and Experimental adhesives	Failure mode				
	PTF	A	CD	CC	M
Etch-and-rinse mode					
Control	0	56.1	43.9	0	0
0.38% (v/v)	0	44.8	50	5.2	0
1.90% (v/v)	0	54.0	44.4	2.6	0
3.80% (v/v)	0	70.0	30.0	0	0
Self-etch mode					
Control	0	43.6	52.6	3.8	0
0.38% (v/v)	5.3	69.2	26.9	0	0
1.90% (v/v)	7	84.7	9.4	1.2	0
3.80% (v/v)	7	68.2	25.0	2.3	0

Classification of failure modes: (PTF) Pre-testing failures: Specimens that failed before testing. (A) Adhesive: adhesive failure along bonded interface. (CD) Cohesive failure within dentin. (CC) Cohesive failure within composite. (M) Mixed failure: adhesive failure along bonded interface associated with a cohesive failure within dentin or composite.

and speech (Kassebaum et al., 2015). Dependent on size and severity, carious lesions are generally treated by removing all demineralized and contaminated dental tissue and replacing it with a composite restoration. Ideally, these restorations would last a lifetime, reducing costs and discomfort to the patient. Unfortunately, a significant amount of restorations fail due to the initiation and progression of secondary caries adjacent to the restorative material. In order to prolong the longevity of composite restorations, antibacterial agents have been added into both experimental and commercial dental materials in an effort to counteract the activity of cariogenic bacteria and consequently reduce the incidence of secondary caries (Chen et al., 2018). Some antibacterial agents recommended for caries control such as chlorhexidine, and triclosan are based on their ability to reduce *S. mutans* viability, unfortunately, they exert a wide spectrum of antimicrobial activity also suppressing benign oral microflora. Thus, natural alternatives that specifically target important virulence factors like microbial adherence and polysaccharide synthesis (Seleem et al., 2016a,b) without altering normal microflora is an attractive therapeutic alternative (Philip et al., 2019).

In biofilms, microorganisms generally account for less than 10% of the dry mass, meanwhile the EM accounts for the remaining 90%. This matrix mostly consists of extracellular polysaccharides formed by the microorganisms themselves and in which they are embedded. These multifunctional extracellular polysaccharides will form a three-dimensional scaffold that is also responsible for the adhesion of the biofilm to surfaces, the aggregation of additional bacterial cells, providing mechanical stability of the biofilm and providing a protective barrier to specific host defenses (Flemming and Wingender, 2010). Therefore, it is crucial that novel antibacterial therapies target these important virulence factors of cariogenic bacteria to prevent the initiation and/or progression of dental caries. In this study, novel experimental dental adhesives effectively reduced virulence factors such as EIPs and viable cells of *S. mutans* biofilm demonstrating the potential for the delivery of an anticariogenic agent at the bonded interfaces.

We incorporated for the first time different concentrations of the natural antibacterial agent *tt*-farnesol into a commercially available universal adhesive forming experimental adhesives, which some significantly reduced both production of extracellular polysaccharides and cell viability of *S. mutans* biofilm. At day 2 and 3 after treatment, the effect of *tt*-farnesol on EP production had not yet manifested; however, at day 5 the experimental adhesive at 3.80% (v/v) concentration showed a significant reduction ($P < 0.05$) when compared to its control and was closely followed by the 1.90% (v/v) experimental adhesive. A similar trend could be observed for the *S. mutans* viability of the biofilms where a significant reduction ($P < 0.05$) of recoverable viable cells at day 3 was observed in the 3.80% (v/v) experimental adhesive when compared with the control. At day 5 this trend becomes more evident where this group shows a $\approx$2 $\log_{10}$ difference with the control group. Additionally, the 1.90% (v/v) experimental adhesive shows a $\approx$1.5 $\log_{10}$ difference when compared also to the control group. Mean biomass DW values obtained from all experimental adhesives were lower than its control group at the three time points evaluated, however, these values were not statistically significant ($P > 0.05$). This study is consistent in demonstrating the antibacterial activity of the propolis-derived agent *tt*-farnesol on cariogenic bacteria, which it has been studied for nearly 2 decades. So far the literature has been consistent in demonstrating the effect of *tt-farnesol* on the reduced production of EIP by Gtfs of *S. mutans* biofilms in both *in vitro* and *in vivo*, which is significantly important since it is well established the critical role of EIP in the adherence and colonization of this specific cariogenic

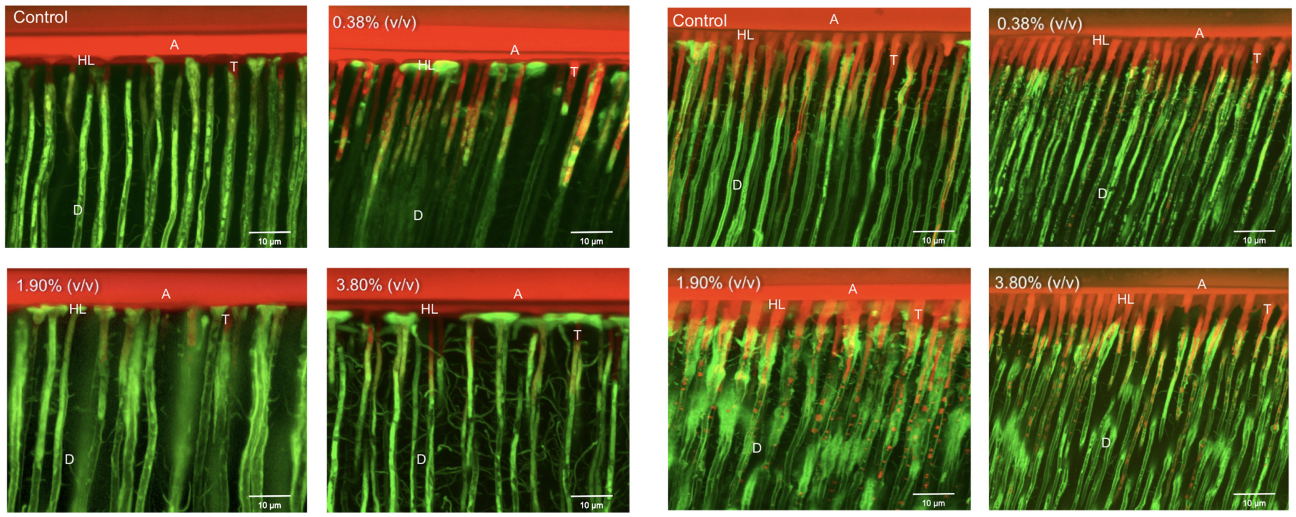

FIGURE 6 | Representative CLSM images of the adhesive interfaces of the different experimental groups bonded using the etch-and-rinse **(A)** and self-etch **(B)** modes. Control: 0.0% of *tt*-farnesol; 100×MIC: 0.38% (v/v) of *tt*-farnesol; 500×MIC: 1.90% (v/v) of *tt*-farnesol; and 1000×MIC: 3.80% (v/v) of *tt*-farnesol. A: Adhesive layer; D: Dentin; T: Resin tags; HL: Hybrid layer.

microorganism on tooth surfaces (Schilling and Bowen, 1992; Yamashita et al., 1993) showing a direct impact on the initiation and progression of a carious lesion. The action of *tt*-farnesol on important virulence factors such as EIP production and amount of viable cells at later stages (3 and 5 days) of biofilm formation could be because the antibacterial agent got trapped within the polymeric chain and was being slowly released onto the medium, thus not having immediate contact with the cariogenic biofilm. This mechanism of action has been previously reported in the literature; for example, the commercial product Gluma 2 Bond that contains glutaraldehyde has been demonstrated that requires at least 24 h. to produce any antibacterial effect against *S. mutans* (André et al., 2015). In the same study, chlorhexidine-containing adhesive Peak Universal Bond killed only strict anaerobic microorganisms also after 24 h. It was previously demonstrated the effect of the antibacterial properties and dentin bond strength of experimental adhesives formed with the addition of *tt*-farnesol into 2 commercial products, Clearfil S3 Bond Plus which is a 7th generation (single step self-etch) and OptiBond S, a 5th generation (two-step etch-and-rinse) adhesive systems (André et al., 2017). In the mentioned study, there was no reduction of bacterial viability measured in CFU for any of the experimental adhesives tested. Also, the experimental adhesive formed with OptiBond S + *tt*-farnesol showed significant reduction in EIPs production that is in agreement with our results. Meanwhile in the mentioned study there was not a significant reduction in dentin bond strength for the experimental composites formed with the 2 commercial composites and *tt*-farnesol, in our study we found a significant reduction in dentin bond strength that seems to be associated with the reduction DC values. Recently, it was reported a universal adhesive incorporated with epigallocatechin-3-gallate, which is a polyphenol present in green tea and is known to have antioxidant, antimicrobial, anti-diabetic, and anti-inflammatory properties (Silva et al., 2020). Here it was demonstrated the antimicrobial potential of an experimental adhesive at 0.5% concentration of epigallocatechin-3-gallate against *S. mutans* biofilm, however, it showed significantly higher water sorption and solubility.

Dental adhesives are used to bond dental restorations to the tooth and have a direct contact with the dental substrate, which makes it relevant to investigate in whether the incorporation of an antibacterial agent (such as *tt*-farnesol) would help reduce the development of secondary caries. Nevertheless, it is essential to also evaluate if the incorporation of *tt*-farnesol has any effect on the intrinsic chemical properties as well as the bonding and sealing capabilities of the adhesive system. In this study the pH, DC, μTBS, and hybrid layer permeability were evaluated. The adhesive system used in this study is the so called "Universal" or "multi-mode" and represents the latest generation of dentin bonding system launched in the market. Is designed to be used in either one-step self-etch or in a two-step etch-and-rinse mode (Hanabusa et al., 2012; Wagner et al., 2014) without compromising the material's bonding effectiveness (Muñoz et al., 2013). Additionally, universal adhesives also include in their formulation certain components that allow to chemically bond to zirconia or silica-based glass ceramics without the application of accessory priming agents (Özcan and Bernasconi, 2015; Siqueira et al., 2016). The pH or "acidity" of the adhesive system is strongly correlated to the material's ability to demineralize dentin and enamel that result in varying etching depths (Van Meerbeek et al., 2011). Therefore, it important that added compounds such as *tt*-farnesol do not modify the material's pH and its ability to etch the dental substrate. The pH evaluation revealed that all experimental adhesives with different concentrations of *tt*-farnesol yielded similar pH values ($P > 0.05$) to that of the control

(pH ≈ 3) demonstrating that the intrinsic acidity of the material remained unaltered.

Degree of conversion is a quantitative evaluation of the monomer conversion after polymerization of light-cured dental materials, which may predict the bonding and mechanical capabilities of the system (Dickens and Cho, 2005; Kanehira et al., 2006). Results of this study reveal that the addition of *tt*-farnesol in different concentrations resulted in a significant reduction ($P < 0.05$) ranging from 32 to 37% decrease of reacted monomers of the experimental adhesives, which could compromise the adhesive bonding and sealing ability of the material. It is known that the incomplete polymerization of dental adhesive systems can leave a fraction of residual monomers that can diffuse through the dentinal tubules reaching the pulp tissue or leach into the neighboring soft tissues resulting in adverse reactions. Nonetheless, the result of a recent systematic review demonstrates that there is still a lack of agreement amongst the literature regarding the relationship between cytotoxicity and DC of dental adhesive systems (Caldas et al., 2019). Further analysis of the cytotoxic effects of leached monomers of experimental composites containing *tt*-farnesol is needed to ensure the safe use of this adhesive system in the oral environment. The bonding capability of the experimental adhesives to human dentin in both application modes: one-step self-etch and two-step etch-and-rinse was then evaluated. μTBS test to dentin produced values that ranged between 64.29 and 55.59 MPa in the etch-and-rinse mode, and values in the self-etch mode that ranged between 66.90 and 57.69 MPa of the experimental adhesives used in this study. There was a significant reduction ($P < 0.05$) in the bond strength in the experimental adhesive systems irrespective of the application mode when compared to its control. These results appear to be similar to the DC results, suggesting a relationship between decreased DC values and reduced bonding effectiveness of the experimental composites. When comparing both application modes, the observed bonding properties of the experimental composites evaluated in this study go somewhat in accordance with results observed in the current literature, that dictates that the adhesive performance of universal adhesives such as Adper Scothbond Universal is not dependent on the application mode used, suggesting that they can be used in both etch-and-rinse or self-etch mode. The use of previous step of phosphoric acid before the adhesive application has shown to remove the smear layer and smear plugs facilitating the penetration of the adhesive and the generation of longer resin tags (Langer and Ilie, 2013). On the other hand, in self-etch mode, the success of the bonding capability relies on partial demineralization of dentin and chemical bonding to hydroxyapatite (HAp) produced by the action of functional monomers such as 10-MDP present in the adhesive system (Wagner et al., 2014).

Confocal Laser Scanning Microscopy images illustrate the integration of the adhesive system and the dentinal fluids, allowing a better understanding of the permeability of the experimental adhesives into dentin. In the etch-and-rinse application mode, similar hybrid layer and resin tag formation was observed in all tested groups (**Figure 6A**). It can be noted that groups 1.90% (v/v) and 3.80% (v/v) displayed small droplets of unpolymerized monomers that leached out from the resin tags within the dentinal tubules, indicative of a reduced monomer conversion. These droplets are formed due to a phase separation of inadequate polymerization monomers of the experimental adhesive systems (Sartori et al., 2015). When the adhesive system was applied in the self-etch mode (**Figure 6B**) all adhesive systems (control and experimental) partially dissolved the smear layer and chemically bonded to dentin substrate to create a thin hybrid layer. However, the hybrid layer created by both the control and experimental groups demonstrated its inadequacy in properly sealing dentinal tubules from water permeation. In other words, all tested groups applied in the self-etch mode produced a semipermeable hybrid layer after polymerization (Sartori et al., 2016). The presence of pre-testing failures for the experimental adhesives used the in self-etch mode could be the result of neutralization of its etching capability to dentin; whereas, there were no pre-testing failures in the experimental adhesives when used in the etch-and-rinse mode. It was observed an evident increase in adhesive failures in both application modes at the highest concentration of *tt*-farnesol when compared to its control group. This can be explained because of the reduction in the mechanical properties as shown in the reduced monomer conversion that hindered the adhesion to the dental substrate of the adhesive systems.

In this study we observed the antibacterial effect of experimental adhesives containing *tt*-farnesol at concentrations that started at 0.38% (v/v), future work could be focused in evaluating lower concentrations of the antibacterial agent to possibly overcome the detrimental effects on the degree of monomer conversion and the resulting bonding effectiveness of the material without much compromise to the antibacterial properties. We evaluated the antibacterial effect on biofilms up to 5 days after surface treatment; this observation period could be extended to observe any differences between short-term and long-term effects also possibly including other important microorganisms that are present in mixed-species oral biofilms. Great effort is placed in the discovery and incorporation of antibacterial agents into dental materials; therefore, it would be relevant to introduce other natural agents that have shown important antibacterial properties against cariogenic microorganisms. For example, apigenin is another compound found in propolis that has shown to be an efficient inhibitor of Gtfs produced by *S. mutans* (Koo et al., 2002b). Another natural agent is 7-epiclusianone, a prenylated benzophenone isolated from the plant Rheedia gardneriana, has shown to greatly reduce DW, EIP, and the acidogenicity of *S. mutans* biofilms (Murata et al., 2008).

Although many factors are to account in the overall clinical performance and longevity of a restoration (Manhart et al., 2002), one of the main reasons for restoration failure is the development of secondary caries that demands the improvement of the current materials that are used for dental restorations. The creation of a dental adhesive system with antibacterial properties is a promising milestone in the advancement of preventive and adhesive dentistry; however, the complexity in developing an

effective antibacterial adhesive is great. A better understanding of the antibacterial, chemical and bonding properties of experimental adhesives will guide the development of new bonding agents with antibacterial properties that overcome some limitations of current adhesive systems.

CONCLUSION

The incorporation of *tt*-farnesol into a universal adhesive system reduced both the production of EIPs and the bacterial viability of *S. mutans* biofilm. However, the complex adhesive chemical composition created by the incorporation of antibacterial agent altered the original DC and bonding effectiveness of the adhesive system.

DATA AVAILABILITY STATEMENT

The datasets generated for this study are available on request to the corresponding author.

AUTHOR CONTRIBUTIONS

NS and RM contributed to the conception and design of the study. DL and NT carried sample preparation and experimentation. VP and NS contributed to the statistical analysis. J-HP, NS, RM, and SD contributed to the interpretation of the results. DL wrote the manuscript. All authors contributed to manuscript revision and approve the submitted version.

FUNDING

Research reported in this publication was supported by: National Center for Complementary and Integrative Health of the National Institutes of Health under award number R00AT006507 and Herman Ostrow School of Dentistry of USC Seed Grant. The funders had no role in study design, data collection and analysis, decision to publish, or preparation of the manuscript. The authors report no conflict of interest with respect to the authorship and/or publication of this article.

ACKNOWLEDGMENTS

This manuscript is part of the requirements for the degree of Advanced Operative Dentistry and Master of Science in Craniofacial Biology of University of Southern California for DL. We thank Dr. Stephen B. Cronin, from the USC Viterbi School of Engineering, for facilitating the InVia Spectrometer and Ph.D. candidate Bingya Hou for the support in the spectra analysis. Additionally, we thank Karen Denisse Guillen for the editorial assistance as well as Shweta Bansal and Meng Lin for their support to obtain data of this manuscript.

CLINICAL RELEVANCE

Adhesive systems with antibacterial properties might reduce the incidence of secondary caries adjoining to bonded interface and increase the lifespan of bonded restorations.

REFERENCES

Almeida, L. S. B., Murata, R. M., Yatsuda, R., Dos Santos, M. H., Nagem, T. J., Alencar, S. M., et al. (2008). Antimicrobial activity of Rheedia brasiliensis and 7-epiclusianone against Streptococcus mutans. *Phytomedicine* 15, 886–891.

André, C. B., Gomes, B. P. F. A., Duque, T. M., Stipp, R. N., Chan, D. C. N., Ambrosano, G. M. B., et al. (2015). Dentine bond strength and antimicrobial activity evaluation of adhesive systems. *J. Dent.* 43, 466–475.

André, C. B., Rosalen, P. L., Galvão, L. C., de, C., Fronza, B. M., Ambrosano, G. M. B., et al. (2017). Modulation of *Streptococcus mutans* virulence by dental adhesives containing anti-caries agents. *Dent. Mater.* 33, 1084–1092.

Beck, F., Lettner, S., Graf, A., Bitriol, B., Dumitrescu, N., Bauer, P., et al. (2015). Survival of direct resin restorations in posterior teeth within a 19-year period (1996-2015): a meta-analysis of prospective studies. *Dent. Mater.* 31, 958–985.

Bowen, W. H., and Koo, H. (2011). Biology of *Streptococcus mutans*-derived glucosyltransferases: role in extracellular matrix formation of cariogenic biofilms. *Caries Res.* 45, 69–86.

Caldas, I. P., Alves, G. G., Barbosa, I. B., Scelza, P., de Noronha, F., and Scelza, M. Z. (2019). In vitro cytotoxicity of dental adhesives: a systematic review. *Dent. Mater.* 35, 195–205.

de Castilho, A. R. F., Rosalen, P. L., de Souza Araujo, I. J., Kitagawa, I. L., Costa, C., Janal, M. N., et al. (2019). Trans,trans-farnesol, an antimicrobial natural compound, improves glass ionomer cement properties. *PLoS One* 14:e0220718. doi: 10.1371/journal.pone.0220718

Cazzaniga, G., Ottobelli, M., Ionescu, A., Garcia-Godoy, F., and Brambilla, E. (2015). Surface properties of resin-based composite materials and biofilm formation: a review of the current literature. *Am. J. Dent.* 28, 311–320.

Chen, L., Suh, B. I., and Yang, J. (2018). Antibacterial dental restorative materials: a review. *Am. J. Dent.* 31, 6B–12B.

Cuevas-Suárez, C. E., da Rosa, W. L., de, O., Lund, R. G., da Silva, A. F., and Piva, E. (2019). Bonding performance of universal adhesives: an updated systematic review and meta-analysis. *J. Adhes. Dent.* 21, 7–26.

Dekker, N. P., Lammel, C. J., and Brooks, G. F. (1991). Scanning electron microscopy of piliated *Neisseria gonorrhoeae* processed with hexamethyldisilazane. *J. Electron. Microsc. Tech.* 19, 461–467.

Dickens, S. H., and Cho, B. H. (2005). Interpretation of bond failure through conversion and residual solvent measurements and Weibull analyses of flexural and microtensile bond strengths of bonding agents. *Dent. Mater.* 21, 354–364.

Dubois, M., Gilles, K. A., Hamilton, J. K., Rebers, P. A., and Smith, F. (1956). Colorimetric method for determination of sugars and related substances. *Anal. Chem.* 28, 350–356.

Flemming, H.-C., and Wingender, J. (2010). The biofilm matrix. *Nat. Rev. Microbiol.* 8, 623–633.

Hanabusa, M., Mine, A., Kuboki, T., Momoi, Y., Van Ende, A., Van Meerbeek, B., et al. (2012). Bonding effectiveness of a new 'multi-mode' adhesive to enamel and dentine. *J. Dent.* 40, 475–484.

Herrera, M., Carrión, P., Bravo, M., and Castillo, A. (2000). Antibacterial activity of four dentin bonding systems. *Int. J. Antimicrob. Agents* 15, 305–309.

Imazato, S., Imai, T., and Ebisu, S. (1998). Antibacterial activity of proprietary self-etching primers. *Am. J. Dent.* 11, 106–108.

Jeon, J.-G., Pandit, S., Xiao, J., Gregoire, S., Falsetta, M. L., Klein, M. I., et al. (2011). Influences of trans-trans farnesol, a membrane-targeting sesquiterpenoid, on *Streptococcus mutans* physiology and survival within mixed-species oral biofilms. *Int. J. Oral Sci.* 3, 98–106.

Kanehira, M., Finger, W. J., Hoffmann, M., Endo, T., and Komatsu, M. (2006). Relationship between degree of polymerization and enamel bonding strength with self-etching adhesives. *J. Adhes. Dent.* 8, 211–216.

Kassebaum, N. J., Bernabé, E., Dahiya, M., Bhandari, B., Murray, C. J. L., and Marcenes, W. (2015). Global burden of untreated caries: a systematic review and metaregression. *J. Dent. Res.* 94, 650–658.

Kidd, E. A. M., and Fejerskov, O. (2004). What constitutes dental caries? Histopathology of carious enamel and dentin related to the action of cariogenic biofilms. *J. Dent. Res.* 83, 35–38.

Koo, H., Falsetta, M. L., and Klein, M. I. (2013). The exopolysaccharide matrix. *J. Dent. Res.* 92, 1065–1073.

Koo, H., Hayacibara, M. F., Schobel, B. D., Cury, J. A., Rosalen, P. L., Park, Y. K., et al. (2003). Inhibition of *Streptococcus mutans* biofilm accumulation and polysaccharide production by apigenin and tt-farnesol. *J. Antimicrob. Chemother.* 52, 782–789.

Koo, H., Pearson, S. K., Scott-Anne, K., Abranches, J., Cury, J. A., Rosalen, P. L., et al. (2002a). Effects of apigenin and tt-farnesol on glucosyltransferase activity, biofilm viability and caries development in rats. *Oral Microbiol. Immunol.* 17, 337–343.

Koo, H., Rosalen, P. L., Cury, J. A., Park, Y. K., and Bowen, W. H. (2002b). Effects of compounds found in propolis on *Streptococcus mutans* growth and on glucosyltransferase activity. *Antimicrob. Agents Chemother.* 46, 1302–1309.

Langer, A., and Ilie, N. (2013). Dentin infiltration ability of different classes of adhesive systems. *Clin. Oral Investig.* 17, 205–216.

Manhart, J., Garcıìa-Godoy, F., and Hickel, R. (2002). Direct posterior restorations: clinical results and new developments. *Dent. Clin. North Am.* 46, 303–339.

Van Meerbeek, B., Yoshihara, K., Yoshida, Y., Mine, A., De Munck, J., and Van Landuyt, K. L. (2011). State of the art of self-etch adhesives. *Dent. Mater.* 27, 17–28.

Muñoz, M. A., Luque, I., Hass, V., Reis, A., Loguercio, A. D., and Bombarda, N. H. C. (2013). Immediate bonding properties of universal adhesives to dentine. *J. Dent.* 41, 404–411.

Murata, R. M., Branco-de-Almeida, L. S., Franco, E. M., Yatsuda, R., dos Santos, M. H., de Alencar, S. M., et al. (2010). Inhibition of *Streptococcus mutans* biofilm accumulation and development of dental caries in vivo by 7-epiclusianone and fluoride. *Biofouling* 26, 865–872.

Murata, R. M., Branco de Almeida, L. S., Yatsuda, R., Dos Santos, M. H., Nagem, T. J., Rosalen, P. L., et al. (2008). Inhibitory effects of 7-epiclusianone on glucan synthesis, acidogenicity and biofilm formation by *Streptococcus mutans*. *FEMS Microbiol. Lett.* 282, 174–181.

Özcan, M., and Bernasconi, M. (2015). Adhesion to zirconia used for dental restorations: a systematic review and meta-analysis. *J. Adhes. Dent.* 17, 7–26.

Pashley, D. H. (1984). Smear layer: physiological considerations. *Oper. Dent. Suppl.* 3, 13–29.

Pashley, D. H., Tay, F. R., and Imazato, S. (2011). How to increase the durability of resin-dentin bonds. *Compend. Contin. Educ. Dent.* 32, 60–64, 66.

Philip, N., Leishman, S., and Walsh, L. (2019). Potential role for natural products in dental caries control. *Oral Health Prev. Dent.* 17, 479–485.

Salles Branco-De-Almeida, L., Murata, R. M., Franco, E. M., Dos Santos, M. H., De Alencar, S. M., Koo, H., et al. (2011). Effects of 7-epiclusianone on *Streptococcus mutans* and caries development in rats. *Planta Med.* 77, 40–45.

Sartori, N., Peruchi, L. D., Phark, J.-H., and Duarte, S. (2016). The influence of intrinsic water permeation on different dentin bonded interfaces formation. *J. Dent.* 48, 46–54.

Sartori, N., Peruchi, L. D., Phark, J. H., Lopes, M. M., Araujo, E., Vieira, L. C., et al. (2015). Permeation of intrinsic water into ethanol- and water-saturated, monomer-infiltrated dentin bond interfaces. *Dent. Mater.* 31, 1385–1395.

Schilling, K. M., and Bowen, W. H. (1992). Glucans synthesized in situ in experimental salivary pellicle function as specific binding sites for *Streptococcus mutans*. *Infect. Immun.* 60, 284–295.

Seleem, D., Benso, B., Noguti, J., Pardi, V., and Murata, R. M. (2016a). In vitro and in vivo antifungal activity of lichochalcone-A against *Candida albicans* biofilms. *PLoS One* 11:e0157188. doi: 10.1371/journal.pone.0157188

Seleem, D., Chen, E., Benso, B., Pardi, V., and Murata, R. M. (2016b). In vitro evaluation of antifungal activity of monolaurin against *Candida albicans* biofilms. *PeerJ* 4:e2148.

Silva, P., Terto, C., Andrade, R., Fernandes, A., Rolim, J., and Neri, J. (2020). Antimicrobial evaluation, degree of solubility, and water sorption of universal dental adhesive incorporated with epigallocatechin-3-gallate: an in-vitro study. *Eur. J. Gen. Dent.* 9:79.

Siqueira, F., Cardenas, A. M., Gutierrez, M. F., Malaquias, P., Hass, V., Reis, A., et al. (2016). Laboratory performance of universal adhesive systems for luting CAD/CAM restorative materials. *J. Adhes. Dent.* 18, 331–340.

Wagner, A., Wendler, M., Petschelt, A., Belli, R., and Lohbauer, U. (2014). Bonding performance of universal adhesives in different etching modes. *J. Dent.* 42, 800–807.

Yamashita, Y., Bowen, W. H., Burne, R. A., and Kuramitsu, H. K. (1993). Role of the *Streptococcus mutans* gtf genes in caries induction in the specific-pathogen-free rat model. *Infect. Immun.* 61, 3811–3817.

Zancopé, B. R., Dainezi, V. B., Nobre-dos-Santos, M., Duarte, S. Jr., Pardi, V., and Murata, R. M. (2016). Effects of CO2 laser irradiation on matrix-rich biofilm development formation-an in vitro study. *PeerJ* 4:e2458. doi: 10.7717/peerj.2458

Conflict of Interest: The authors declare that the research was conducted in the absence of any commercial or financial relationships that could be construed as a potential conflict of interest.

frontiers in Bioengineering and Biotechnology

ORIGINAL RESEARCH
published: 01 September 2020
doi: 10.3389/fbioe.2020.01039

Toward a Closed Loop, Integrated Biocompatible Biopolymer Wound Dressing Patch for Detection and Prevention of Chronic Wound Infections

*Andrew C. Ward[1], Prachi Dubey[2], Pooja Basnett[2], Granit Lika[2], Gwenyth Newman[1], Damion K. Corrigan[1], Christopher Russell[3], Jongrae Kim[4], Samit Chakrabarty[5], Patricia Connolly[1] and Ipsita Roy[6]**

[1] Department of Biomedical Engineering, Faculty of Engineering, University of Strathclyde, Glasgow, United Kingdom, [2] School of Life Sciences, College of Liberal Arts and Sciences, University of Westminster, London, United Kingdom, [3] Vivisco Pvt Ltd, London, United Kingdom, [4] School of Mechanical Engineering, Faculty of Engineering, University of Leeds, Leeds, United Kingdom, [5] School of Biomedical Sciences, Faculty of Biological Sciences, University of Leeds, Leeds, United Kingdom, [6] Department of Materials Science and Engineering, Faculty of Engineering, The University of Sheffield, Sheffield, United Kingdom

OPEN ACCESS

Edited by:
Elisa Mele, Loughborough University, United Kingdom

Reviewed by:
Rosalia Bertorelli, Italian Institute of Technology (IIT), Italy
Giulia Suarato, Italian Institute of Technology (IIT), Italy

***Correspondence:**
Ipsita Roy
I.Roy@sheffield.ac.uk

Specialty section:
This article was submitted to Nanobiotechnology, a section of the journal Frontiers in Bioengineering and Biotechnology

Received: *29 April 2020*
Accepted: *11 August 2020*
Published: *01 September 2020*

Citation:
Ward AC, Dubey P, Basnett P, Lika G, Newman G, Corrigan DK, Russell C, Kim J, Chakrabarty S, Connolly P and Roy I (2020) Toward a Closed Loop, Integrated Biocompatible Biopolymer Wound Dressing Patch for Detection and Prevention of Chronic Wound Infections. Front. Bioeng. Biotechnol. 8:1039. doi: 10.3389/fbioe.2020.01039

Chronic wound infections represent a significant burden to healthcare providers globally. Often, chronic wound healing is impeded by the presence of infection within the wound or wound bed. This can result in an increased healing time, healthcare cost and poor patient outcomes. Thus, there is a need for dressings that help the wound heal, in combination with early detection of wound infections to support prompt treatment. In this study, we demonstrate a novel, biocompatible wound dressing material, based on Polyhydroxyalkanoates, doped with graphene platelets, which can be used as an electrochemical sensing substrate for the detection of a common wound pathogen, *Pseudomonas aeruginosa*. Through the detection of the redox active secondary metabolite, pyocyanin, we demonstrate that a dressing can be produced that will detect the presence of pyocyanin across clinically relevant concentrations. Furthermore, we show that this sensor can be used to identify the presence of pyocyanin in a culture of *P. aeruginosa*. Overall, the sensor substrate presented in this paper represents the first step toward a new dressing with the capacity to promote wound healing, detect the presence of infection and release antimicrobial drugs, on demand, to optimized healing.

Keywords: wound dressing, biopolymer, pyocyanin, *Pseudomonas aeruginosa*, graphene, Polyhydroxyalkanoates, artificial intelligence, electrochemical

INTRODUCTION

Chronic wound infections can have life changing consequences to patients and represent a significant burden to healthcare providers such as the NHS. Infections delay wound healing and can result in a worsening of the patient's condition. A wound is considered to be chronic if it does not show evidence of progression through the normal healing stages within a timely manner, usually considered to be 30 days (Frykberg and Banks, 2015). The most common chronic wounds

are diabetic ulcers, vascular ulcers and pressure ulcers. A number of strategies have been explored to improve chronic wound outcomes. Tissue engineering approaches, such as the use of stem cells, modulating the immune response, and the use of scaffolds, cell therapies or growth factors are widely reported (Rezaie et al., 2019). Evidence based decision systems have also been developed to progress from decision based support systems (Schaarup et al., 2018) and a large field of research is devoted to the point of care monitoring and analysis of chronic wounds (Sheets et al., 2016).

Chronic wounds are at a great risk of infection due to the prolonged loss of the protective skin barrier providing an attractive climate for bacterial colonization. *Pseudomonas aeruginosa* is one of the most common bacteria that infect chronic wounds (Serra et al., 2015). For example, in one study, *P. aeruginosa* was isolated in 52.2% of chronic leg ulcers and ulcers infected by *P. aeruginosa* were shown to cover a significantly larger area than those in which the bacteria was not present (Gjødsbøl et al., 2006). Furthermore, *P. aeruginosa* has been shown to infect deeper regions of the wound bed, often forming resistant biofilms (Kirketerp-Møller et al., 2008; Serra et al., 2015). In this way *P. aeruginosa* can develop a serious and persistent infection within chronic wounds, greatly contributing to the likelihood of resorting to more severe treatments, such as amputation. Additionally, *P. aeruginosa* is widely associated with burn wounds, where it is responsible for high rates of morbidity and mortality (Bodey et al., 1983; McManus et al., 1985; Sharma et al., 2006; Öncül et al., 2014).

Due to the persistent nature of *P. aeruginosa* infections, the ability to detect the presence of the bacteria would allow for early diagnosis and application of an appropriate treatment plan before the infection becomes too widespread. Wound pH is widely recognized as a key factor in wound healing and has been used as a basis for the development biosensors to detect infection and a number of previous investigators have used this as a basis for infection detection (Songkakul et al., 2019; Kuo et al., 2020). Some have also included closed loop release of antimicrobials in the device design (Mostafalu et al., 2018; Rivero et al., 2020). Humidity and analysis of the microenvironment within the wound have also been used as sensor strategies to assess the progress of wound healing and potentially predict the onset of infection (McColl et al., 2007, 2009). Recent reviews of the state-of-the-art in smart wound dressings can be found in Scalamandré and Bogie (2020), and McLister et al. (2017).

Phenazines are redox-active, highly diffusible and soluble compounds that are produced by a range of bacteria as secondary metabolites during the stationary phase of growth (Mavrodi et al., 2006). In particular, the phenazine, pyocyanin is produced by 96–98% of *P. aeruginosa* strains (Reyes et al., 1981). Pyocyanin production is density-dependent; regulated through QS signals, with a variety of roles in the pathogenicity (Lau et al., 2004) and phenotypic characteristics of the bacteria (Dietrich et al., 2008). The redox-active properties of pyocyanin are widely reported to enhance bacterial pathogenicity, but it also provides an opportunity for electrochemical detection of *P. aeruginosa* (Wang and Newman, 2008; Sharp et al., 2010; Bellin et al., 2014; Ward et al., 2014; Alatraktchi et al., 2016; Sismaet et al., 2016).

The biopolymer used in this study is a medium chain length Polyhydroxyalkanoate (MCL-PHA) which belongs to a family of natural biopolyesters of 3-, 4-, 5-, and 6-hydroxyalkanoic acids. PHAs are synthesized by a wide range of bacteria such as *Bacillus cereus*, *Pseudomonas putida*, *Pseudomonas oleovorans* and act as energy reserves under nutrient limiting conditions. These limiting conditions hinder cell growth and division and switch on the biosynthetic pathway of the PHAs (Valappil et al., 2007, 2008; Hyakutake et al., 2011). Hence, bacteria including *Cupriavidus necator*, *Alcaligenes latus*, *Pseudomonas mendocina* accumulate these polyesters as insoluble inclusions in the cytoplasm. These water insoluble polymers are biodegradable, thermoplastic and exhibit high molecular weight (Byrom, 1994). PHAs can be divided into two main classes: Short chain length PHAs (SCL-PHAs), that have monomers consisting of 3–5 carbons such as poly(3-hydroxybutyrate), P(3HB); poly-4-hydroxybutyrate, P(4HB); and poly(3-hydroxybutyrate-co-3-hydroxyvalerate), P(3HB-co-3HV), are partially crystalline, and thermoplastic in nature. They generally lack toughness, except for P(4HB) and hence are brittle polymers and have high melting points. MCL-PHAs have monomers consisting of 6–14 carbons such as polyhydroxyundecenoate, PHU and Poly(3-hydroxyoctanoate), P(3HO) (Dufresne and Vincendon, 2000; Rai et al., 2011) and these polymers are elastomeric in nature with low crystallinity, low tensile strength, low melting point and high elongation at break (Nomura and Taguchi, 2007). The degradation products of PHAs (hydroxyl acids) have almost no cytotoxicity as compared to the degradation products of synthetic polymers (lactic acid in case of PLA) which leads to low immunogenicity (Rai et al., 2011; Basnett et al., 2018; Constantinides et al., 2018). This is because the hydroxyl acids such as hydroxybutyric acid, hydroxyoctanoic acid are natural metabolites. In addition, they degrade via surface degradation as opposed to the bulk degradation observed in the case of PLA, resulting in a controlled degradation of the construct. Hence PHAs are advantageous over synthetic polymers in the context of biomedical applications (Volova, 2004; Rai et al., 2011). The absence of any non-toxic compound produced during polymer degradation along with it being non-immunogenic enhances the acceptance of the scaffold by the body and hence promotes biocompatibility (Zhao et al., 2003; Zheng et al., 2005). PHAs have a diverse monomeric composition resulting in versatile physical properties making them applicable in a wide range of applications. Compared to the other natural polymers such as collagen, PHAs can be produced on a large scale, in a sustainable manner. Based on life cycle analysis, PHAs have been considered to be the safest options amongst the bioplastics that are currently available (Lakshmanan et al., 2013; Basnett et al., 2017). There are various *in vitro* and *in vivo* cytocompatibility studies conducted on PHA scaffolds which conclude that the scaffolds promoted angiogenesis, cell growth, and enabled cell attachment (Williams et al., 1999; Shishatskaya et al., 2002; Sevastianov et al., 2003; Qu et al., 2006; Shijun et al., 2016). The effect of PHA degradation products was established by Sun et al. (2007) where cellular responses of the mouse fibroblast cell line L929 were studied in the presence of PHA degradation products. It was observed that MCL-PHAs are even more biocompatible than the SCL-PHAs

(Sun et al., 2007). Hence, Polyhydroxyalkanoates exhibit excellent biocompatibility and bioresorbability which make them highly suitable for their application in wound healing and other medical applications. The biodegradability rate of the PHAs depends on various factors such as the local environment, PHA composition, pH, moisture, surface area, microbial and enzymatic activity. PHA can be degraded by eukaryotic lipases and esterases in addition to environmental degradation (Ojumu et al., 2004). Volova et al. (2014) investigated the *in vivo* degradation of various PHA blends. They concluded that the biodegradability rate was higher in PHA copolymers with low crystallinity.

Artificial Intelligence (AI) algorithms represented by Deep Learning Neural Networks (Goodfellow et al., 2016) have shown huge impacts already in computer sciences and are expanding their applications to almost all human activities such as economy, science, engineering, psychology, linguistics, and more. In recent decades, these sudden jumps in advancements are realized through the exponential increases of computing power, the realization of massive parallel processing through Graphical Processing Units (GPU), and several important theoretical achievements. The theoretical achievements include finding Rectified Linear Unit (ReLU) (Lu et al., 2017) for feeding the gradient information more efficiently into the deeper layers of the neural network during the training of the algorithm and finding various important network structures such as Recurrent Neural Network (RNN), Long and Short Term Memory (LSTM), and Convolutional Neural Network (CNN). A thorough history of the AI developments can be found in Schmidhuber (2015). However, the robustness and the explainability (i.e., the ability for the mechanics of machine learning to be explained in human terms) of the decisions made by the AI algorithms are yet to be fully addressed (Szegedy et al., 2014; Holzinger et al., 2017). Also, it is observed that the algorithms would frequently show poor performance for unseen data (Mc Loone and Irwin, 2001), while requiring a huge amount of training data sets. Given these limitations of the current AI algorithms, there is still tremendous potential in the current AI algorithms to be applied to diverse areas to improve the performances of the overall outputs. This potential has started to gain impetus through the study of closed loop control systems in point of care devices (see Tan et al., 2019 for a recent review).

In this study we explore the use of a novel biopolymer material, an MCL-PHA, functionalized with graphene nanoplatelets (GnP) for the detection of the wound pathogen *P. aeruginosa*. Through the addition of graphene during the processing of the biopolymer into a wound dressing patch, we show that it is possible to detect the presence of pyocyanin. Pyocyanin is produced by almost all strains of *P. aeruginosa* during colonization of a wound and is hence a suitable diagnostic biomarker for infection. To the best of our knowledge, this is the first time that a Polyhydroxyalkanoate-based patch has been developed for the detection of pyocyanin. This study provides the potential for the development of a smart biocompatible wound dressing patch that could be used to detect the presence of an infection, followed by its reactive simultaneous treatment using a trained neural network to correct the errors in a prediction model. This will allow determination of the optimal release timing and concentration of the antimicrobial drug to be delivered in the wound bed, a truly revolutionary concept. Future work will build upon this *in vitro* study, focusing on the performance of the sensor in a real wound, *in vivo,* in order to determine and optimize the performance of the material as a sensor in this scenario.

MATERIALS AND METHODS

Reagents and Media

Biopolymer Reagents

The MCL-PHA was produced using a Gram-negative bacterium *P. mendocina* CH50 which was obtained from the National Collection of Industrial and Marine Bacteria (NCIMB 10541), Aberdeen, United Kingdom. The chemicals for the production of MCL-PHA were purchased from Sigma-Aldrich or BDH Ltd. (Dorset, United Kingdom), VWR (Leicestershire, United Kingdom) unless otherwise stated. GnP were bought from Strem Chemicals with the dimensions of 6–8 nm thickness and 5 microns width.

Electrochemical Reagents

Pseudomonas aeruginosa reference strain PA14 (Mikkelsen et al., 2011) was used for all growth experiments. Luria Bertani (LB) media was used for all electrochemical measurements and growth experiments with *P. aeruginosa* PA14. LB was produced by mixing 10 g of tryptone (Fisher Scientific), 5 g NaCl (Sigma Aldrich), and 5 g yeast extract (Fluka) with 1000 mL of w/v dH_2O. The media was then autoclaved at 121°C for 20 min. Iron (III) chloride (Sigma Aldrich) was mixed with dH_2O to a concentration of 200 mM. Purified pyocyanin (Sigma Aldrich) was dissolved in EtOH to produce a stock concentration of 23.8 mM and was subsequently diluted in LB media to achieve the required working concentrations.

Production and Characterization of MCL-PHA

Sterilized nutrient broth was inoculated using a single colony of *P. mendocina* CH50 and was incubated for 16 h at 30°C at 200 rpm. This was then used to inoculate the second stage media which was incubated at 30°C at 150 rpm until the optical density reached 1.6 without dilution. The second stage media comprised of minimal salt media (MSM) which included ammonium sulfate; 0.45 g/L, sodium hydrogen phosphate; 3.42 g/L and potassium dihydrogen phosphate; 2.38 g/L. Glucose at 20 g/L concentration was used as the carbon source. Magnesium sulfate heptahydrate and trace element were also added to the media at a concentration of 0.8 g/L and 1 mL/L, respectively. The inoculated second stage media was used to further inoculate the production media (10% of culture volume) for 48 h at 30°C at 150 rpm which comprised of MSM, glucose, magnesium sulfate heptahydrate and trace elements. The MSM comprised of ammonium sulfate; 0.50 g/L, sodium hydrogen phosphate; 3.80 g/L, potassium dihydrogen phosphate; 2.65 g/L.

After the incubation, the cells were harvested at 48 h by centrifugation at 4600 rpm for 30 min. The centrifuged cells

were washed with distilled water followed by 10% ethanol and finally with distilled water. The obtained cells were homogenized for 15 min using a homogenizer. They were then kept at −20°C overnight and were finally placed in the freeze dryer for lyophilization.

The dried cells were used to extract polymer using the soxhlet extraction method. The cells were washed with methanol under reflux conditions for 24 h to remove impurities. Then the methanol was replaced with chloroform and the cells were incubated for 24 h under reflux conditions. This chloroform solution was used to extract polymer by concentrating it in a rotary evaporator. The polymer was then precipitated using ice-cold methanol solution. Although chloroform and methanol were used in this study, it should be noted that several non-chlorinated solvents such as cyclohexane, gamma-butyrolactone, butyl acetate and ethyl acetate have been used to extract PHAs (Aramvash et al., 2015; Jiang et al., 2018). Another environmentally sustainable method used in the extraction of PHAs include the use of supercritical fluid (Kunasundari and Sudesh, 2011).

Fourier Transform Infrared Spectroscopy (FTIR)

Chemical characterization of the polymer was carried out using by Attenuated Total Reflectance Fourier Transform Infrared (ATR-FTIR) spectroscopy. The analyses were performed in a spectral range of 4000–400 cm^{-1} with a resolution 4 cm^{-1} using PerkinElmer FTIR spectrometer Spectrum Two (PerkinElmer Inc., United States).

Molecular Weight Analysis

The number average molecular weight (M_n), and the weight average molecular weight (M_w) of the polymer were determined using gel permeation chromatography (GPC, Model 1260 Infinity GPC, Agilent Technologies) as described in Constantinides et al. (2018).

Graphene-Biopolymer Composite Production

The composite film was prepared using solvent casting by weighing 0.5 g of MCL-PHA and adding to 10 mL of chloroform. This solution was left stirring overnight until completely dissolved resulting in a 5 wt% solution of the polymer. Once the MCL-PHA was dissolved, different concentrations (15, 20, and 30%) of GnP were added. This was then vortexed for a minute and left to sonicate in a water bath sonicator for 7 h (**Figure 1A**). After sonication, the contents were immediately poured into a petri dish covered to allow slow and even evaporation and left to air dry in a fume cupboard. Upon drying, water was added in the petri dish and subsequently the composite films were peeled and air dried. The water is required because MCL-PHA is elastomeric in nature and tends to stick to the glass petri dish. Adding water to the petri dish helps in the removal of the film without causing a tear in the film.

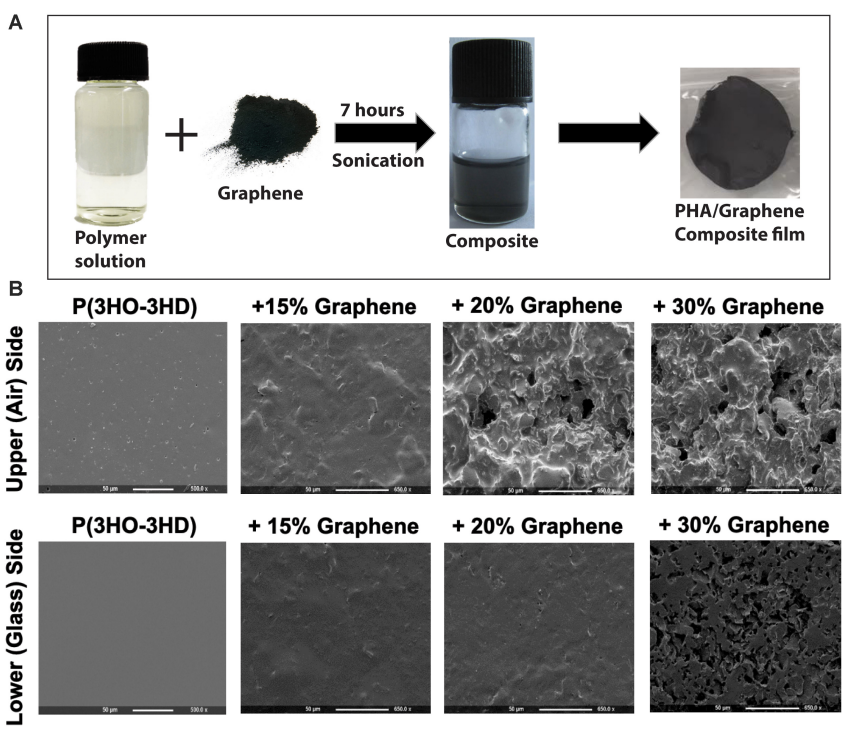

FIGURE 1 | (A) The production of P(3HO-co-3HD)/graphene films, consisting of mixing the polymer solution with the graphene followed by casting in a glass petri dish. **(B)** Scanning electron microscopy of the film showing the change in the surface topography of the films with varying amounts of graphene content (both the upper side and the lower side of the films are shown).

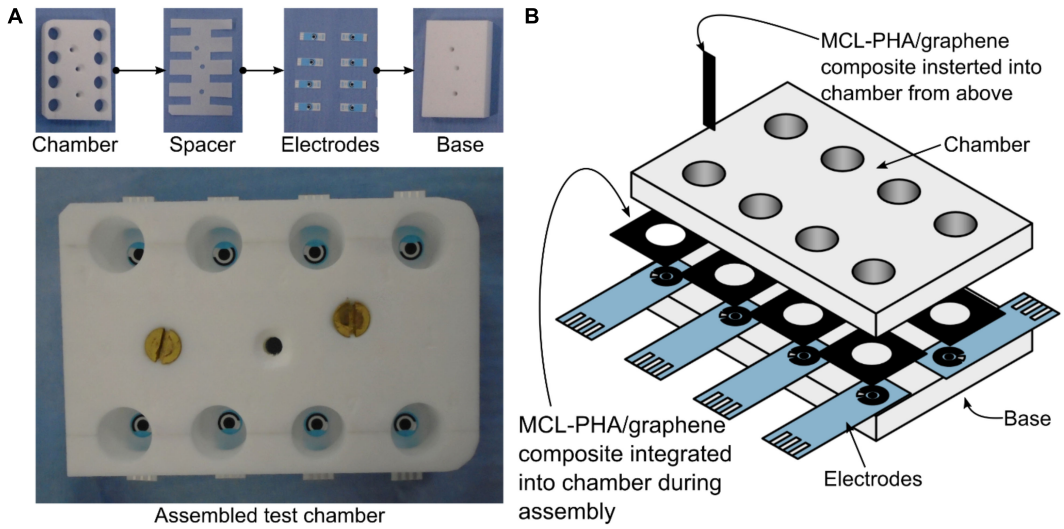

FIGURE 2 | Bespoke electrode chambers used for measurements with commercial electrodes and MCL-PHA/graphene composite. The chambers were cut from a 15-mm-thick sheet of PTFE and assembled using silicon adhesive sealant. 1 mL of solution was used in each chamber. **(A)** Photographs of the layers of the assembly. **(B)** A detailed view of the assembly, showing the two locations where the PHA/graphene composite was inserted.

Cell Proliferation Study

A cell proliferation study was carried out to test the cytocompatibility of the composite films with the mammalian cells. It was carried out using HaCaT cells (keratinocyte). Cells at a seeding density of 10,000 cells/mL were added directly on to the sterile graphene composite film samples. They were cultured for 24 h. Cell viability was measured using Alamar Blue assay. TCP was used as a positive control. Neat MCL-PHA was tested for comparative study.

Graphene-Polymer Surface Characterization

Scanning electron microscopy analysis was performed to evaluate the surface topography of the MCL-PHA/graphene composite films. The SEM images were taken using a beam of 5 keV at 10 cm working distance (JEOL 5610LV-SEM). For the analysis, all the samples were coated with gold for 2 min using a EMITECH-K550 gold spluttering device. This analysis was carried out at the Eastman Dental Hospital, University College London.

Electrode Preparation and Chamber Design

Commercially available screen-printed carbon electrodes were purchased from DropSens. Standard carbon electrodes (DRP110), standard carbon modified with carbon nanotubes (DRP110-CNT), and standard carbon modified with graphene (DRP110-GPH) were used. Where the MCL-PHA was used as the sensing substrate, the counter electrode and reference electrode on a standard carbon electrode (DRP110) completed the electrochemical cell. In order to provide a stable reference, the silver reference electrode was modified by incubating the electrode surface for 10 min in a 200 mM solution of Iron(III) chloride in dH_2O. It was found that 3 μl of Iron(III) chloride was sufficient to cover the reference electrode without touching the working or counter electrodes. Following the addition of the chloride, the electrodes were thoroughly rinsed in distilled water.

Electrode chambers were produced through the use of a custom-made PTFE plate (**Figure 2A**). The 15-mm-thick plate consisted of eight 16-mm-diameter chambers, a base layer of PTFE and a leveling layer to accommodate the thickness of the electrodes. The top plate was mounted on top of the electrodes and the bottom plate using silicon adhesive sealant and allowed to cure for 24 h prior to use. The MCL-PHA/graphene composite was cut into 5 mm strips with a sharp scalpel and held in the prepared chamber with a pair of metal forceps, so that approximately 5 mm of the MCL-PHA/graphene composite was submerged in the media (taking care that the forceps were not in contact with the media). Alternatively, the MCL-PHA/composite was integrated into the bottom of the electrode chamber by cutting a 10-mm-diameter hole through the center. This allowed the biopolymer patch to be integrated over the top of the commercial electrode (**Figure 2B**). 1 mL of LB was used in the electrode chambers during the experiments.

MCL-PHA/Graphene Composite Patch Conductivity Measurements

The complex impedance of the polymers was measured using a PalmSens3 potentiostat (PalmSens) in a two-electrode configuration (Working – Counter/Reference). Two gold electrodes with 1 mm separation were brought into contact with the MCL-PHA/graphene composite patch, where a 0.5 V_{DC} with a 0.25 V_{AC} signal amplitude was applied across the frequency range from 0.1 to 10 kHz. In total, 51 frequency points were measured on a logarithmic scale. The reference

measurement was performed by measuring the impedance between the two gold electrodes in free space. Both the smooth and rough surfaces (bottom- and top-side) of the MCL-PHA/graphene composite patches were measured, with three randomly positioned measurements, from which an average value was recorded.

Electrochemical Measurements

Square wave voltammetry (SWV) was used to perform all electrochemical measurements, based upon previously published parameters for the detection of pyocyanin (Sharp et al., 2010). A potential window from −600 to 400 mV (vs. Ag/AgCl) was used, with a step potential of 2 mV and an amplitude of 50 mV. The measurement frequency used was 25 Hz. Electrochemical sweep data was either recorded in PSTrace, or directly in Matlab, by controlling the potentiostat through the PalmSens software development kit[1].

Standard Curve Measurements

Pyocyanin was diluted in sterile LB media to produce a working stock with a starting concentration of 2.5 mM. 1 mL of sterile LB was added to each electrode chamber and an initial SWV measurement was performed. Following this, 2 µl of pyocyanin working stock was added to the chamber and mixed by aspiration using the pipette, to achieve a final pyocyanin concentration of 5 µM. An SWV measurement was then performed and a further 2 µl of pyocyanin working stock was added in order to increase the concentration to 10 µM pyocyanin, followed by a further SWV measurement. This was repeated until a final calculated concentration of 97 µM pyocyanin existed in the measurement chamber.

P. aeruginosa Measurements

Pseudomonas aeruginosa PA14 was used to produce cultures by inoculating 2 mL of sterile LB in a 30 mL universal bottle with a single colony of PA14 from a LB solid agar plate. This was then incubated at 37°C in a shaking incubator for 24 h. The overnight culture was then added to the electrode chamber and SWV measurements were performed with the biopolymer or commercial electrodes as described above.

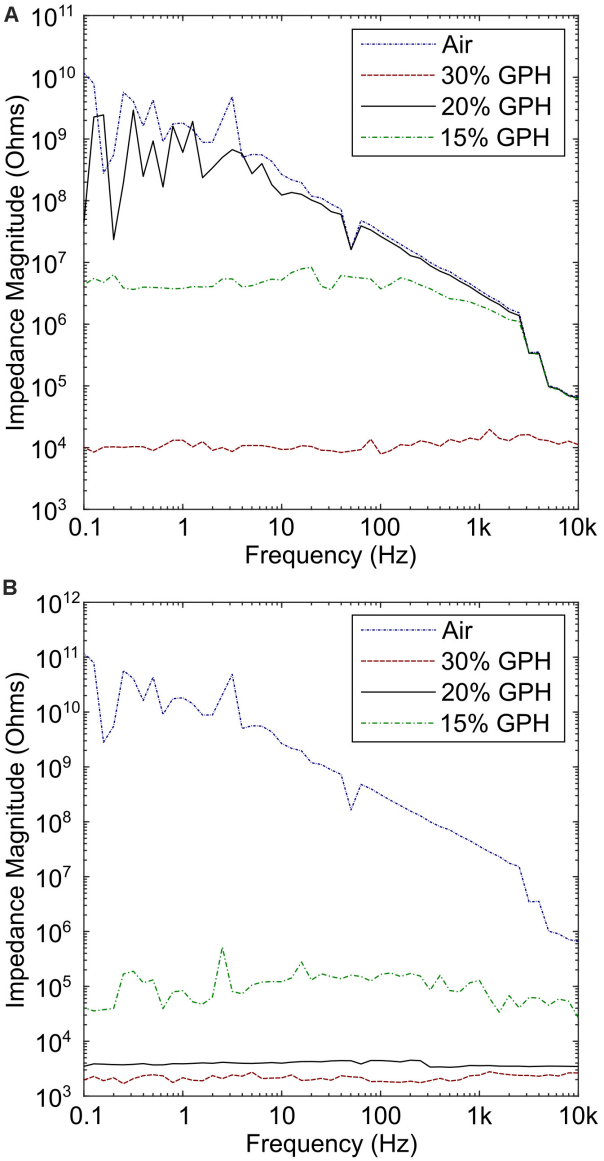

FIGURE 3 | Conductivity measurements of the upper (air) side and lower (glass) side of the composite film. **(A)** High impedance was observed across all concentrations of graphene, with the lowest observed in the 30% graphene polymer. **(B)** Measurements performed on the lower side of the polymer indicate that the resistance is several times lower, particularly for the 30% graphene polymer.

RESULTS AND DISCUSSION

Biopolymer Production With Integration of Graphene Platelets and Cell Proliferation Study

Medium chain length Polyhydroxyalkanoate was produced by *P. mendocina* CH50 using glucose as the carbon source. ATR-FTIR was used to identify the purified polymer as an MCL-PHA. Characteristic peaks (1727.4 cm^{-1}, corresponded to the ester carbonyl bond and 1161 cm^{-1} corresponded to the C-O stretching) of MCL-PHA were present in the FTIR spectrum (see **Supplementary Data Sheet S1** – supplementary information). Molecular weight, M_w, of the MCL-PHA was measured to be 542 kDa with a polydispersity index (PDI) of 3. The percentage cell viability on the neat biopolymer film at 24 h was 85%. On the composite films with 15, 20, and 30% graphene content, %cell viability were 55, 53, and 49% respectively at 24 h. There was no significant difference between the films. There was a decrease in the cell viability in comparison to the neat biopolymer film.

[1]www.palmsens.com

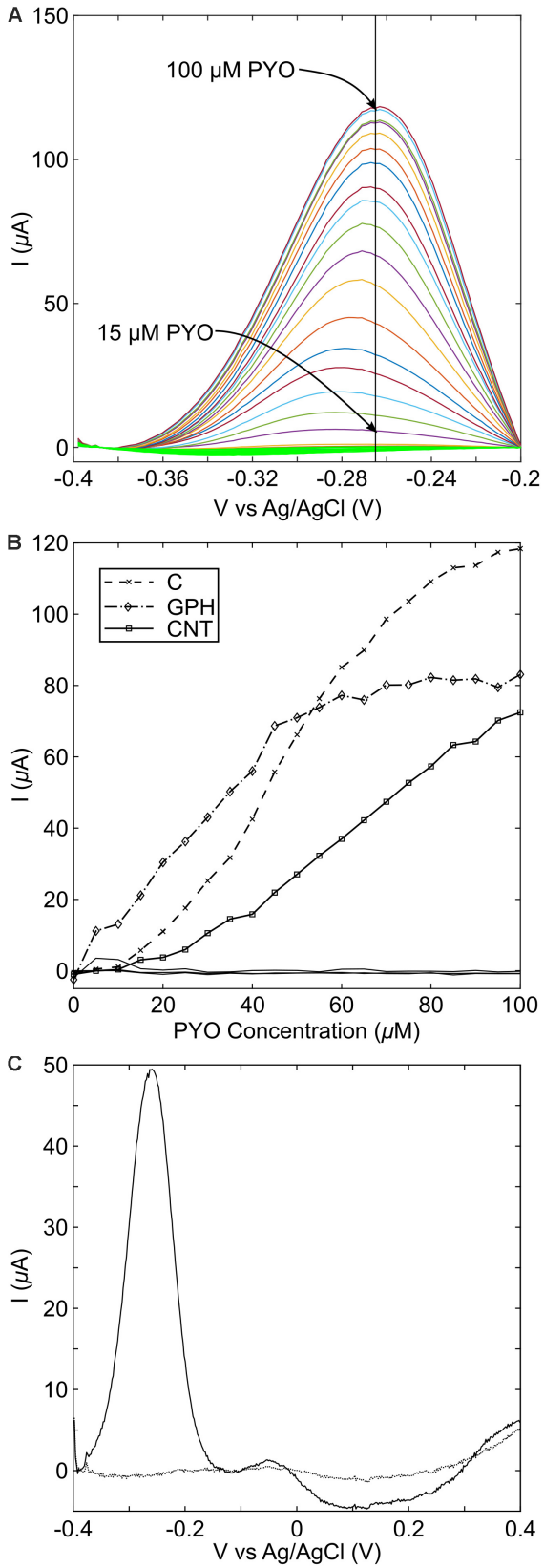

FIGURE 4 | Continued

FIGURE 4 | Pyocyanin standard curve measurements with different carbon electrode materials. **(A)** Peaks are easily identifiable following the addition of pyocyanin from 15 µM. On standard carbon screen printed electrodes, the peak was found to occur at –265 mV vs. Ag/AgCl; **(B)** Standard curve measurements at the peak potential for each measurement. C, standard carbon; GPH, graphene; CNT, carbon nanotubes; **(C)** overnight growth of PA14 shows that pyocyanin production can readily be detected on standard screen-printed carbon electrodes.

Biopolymer Composite Surface Properties and Resistance Measurements on MCL-PHA/Graphene Composites

SEM analysis of the two sides of the polymer film indicated different morphologies, which were influenced by the concentration of graphene added to the MCL-PHA and the side of the polymer (exposed to air or glass while casting in a glass petri dish) was being considered. As the concentration of graphene increased, both the upper and lower surfaces of the biopolymer increased in roughness (**Figure 1B**). Furthermore, initial electrochemical measurements with the MCL-PHA/graphene composites indicated that the response was dependent upon which side of the composite was used as a sensing surface. To understand the difference between the upper and lower surfaces, conductivity measurements were performed from 0.1 to 10 kHz. The measurements show that the rough, upper (air) side of the composite had a high resistance, regardless of the concentration of graphene present in the sample (**Figure 3A**). In contrast, it was found that the resistance of the lower (glass) side of the composite was several orders of magnitude less (**Figure 3B**). Furthermore, the resistance of the smooth lower side of the composite was found to be concentration dependent. As the concentration of graphene increased, the impedance of the layer decreased from a mean 111.8 kOhms (SD 79.4 kOhms) across the frequency range measured with the MCL-PHA/15 wt% graphene composite to 2.18 kOhms (SD 276 Ohms) for the MCL-PHA/30 wt% graphene composite. This suggests that during the curing phase of the MCL-PHA/graphene composite, the graphene settles toward the bottom of the polymer in a concentration dependent manner. Interestingly, the upper, rough surface of the 30 wt% MCL-PHA/graphene composite had a higher resistance than the rough surface with other concentrations of graphene. This is probably caused by the high graphene concentration in the 30 wt% composite, which settled down better toward the lower glass face. As this study is focused on the electrochemical properties and not the mechanical properties, the lower (glass) biopolymer side was used for subsequent electrochemical experiments as this side had the lowest resistance.

Detection of Pyocyanin on Carbon-Based Substrates

The use of graphene as a basis for the detection of pyocyanin relies on a redox reaction, which is linear across the range of interest. A series of standard curve experiments were performed to explore this, using screen printed carbon, graphene and carbon

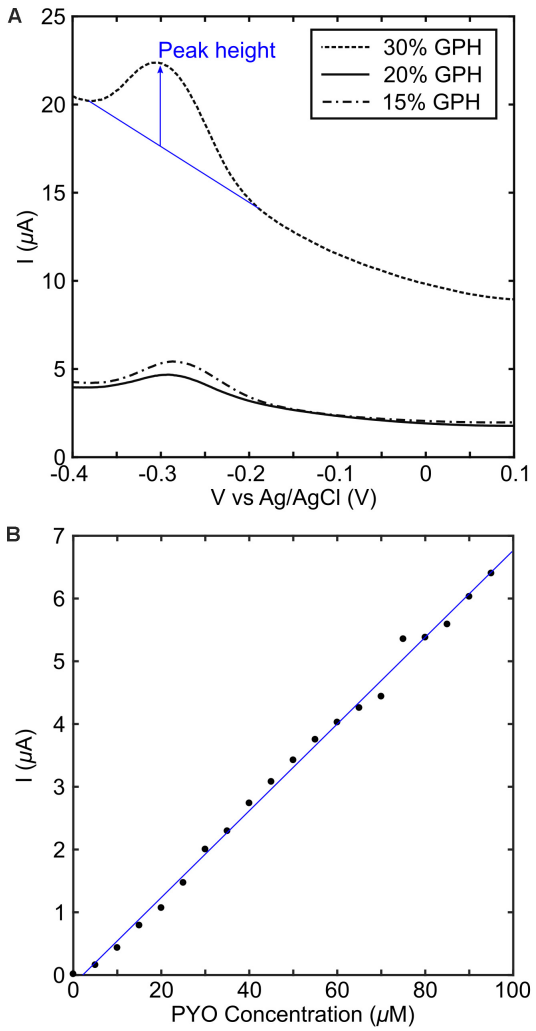

FIGURE 5 | Electrochemical performance of MCL-PHA/graphene composites. **(A)** The composites with different concentrations of graphene were measured in a buffer of LB media containing 100 μM pyocyanin. The peak height (indicated in blue) was obtained using the approach described in SI1. **(B)** A standard curve was produced using the 30 wt/v% the PHA/graphene composite, with pyocyanin added in 5 μM steps up to 95 μM. The blue line represents a linear fit and was used to calculate pyocyanin concentration in the PA14 experiments.

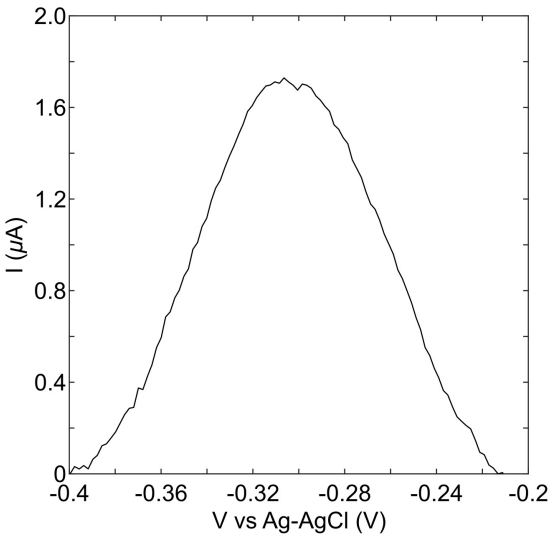

FIGURE 6 | Detection of pyocyanin in an overnight culture of PA14. An aliquot of overnight culture was placed onto the graphene doped biopolymer and DPV measurements were performed. These show that a peak is observed in the same location as that seen in experiments with purified pyocyanin, suggesting that it is possible to detect the presence of pyocyanin in an overnight culture of PA14 using the biopolymer as a sensor.

nanotube (CNT) electrodes, across a range of concentrations from 0 to 100 μM pyocyanin. A large background current was observed upon DPV measurements will all electrode types, therefore, a computer script was written in order to remove the background current, so that the peak could easily be resolved (**Supplementary Data Sheet S2**). In our study, across all types of carbon electrodes, a peak was observed between −265 and −292 mV vs. Ag-AgCl (**Figure 4A**), which is similar to SWV peaks previously reported for pyocyanin (Sharp et al., 2010; Bellin et al., 2014; Sismaet et al., 2016). For the graphene modified electrodes, the pyocyanin-current curve was linear up to 45 μM pyocyanin, at which point the rate of current increase changed (**Figure 4B**). In order to assess the implications of this for our sensor, we measured an overnight culture of *P. aeruginosa* PA14 after growth in conditions that promoted high concentrations of pyocyanin (**Figure 4C**). These measurements demonstrate that a redox peak relating to pyocyanin can be observed with a peak height of 49.36 μA, corresponding to approximately 42 μM pyocyanin, on the basis of the standard curve when a spline interpolation was used. In other studies (Wilson et al., 1988; Muller et al., 2009), clinically relevant concentrations of pyocyanin have been found to be less than 50 μM, highlighting that further development would be required to use these commercial screen printed electrodes as a sensor substrate for the linear detection of pyocyanin.

Detection of Pyocyanin on the MCL-PHA/Graphene Composites With Different Concentrations of Graphene

The MCL-PHA/graphene composites with different concentrations of graphene were tested in conjunction with pyocyanin in order to determine the electrochemical performance, in contrast to the commercially available electrodes measured above. This was achieved by placing a strip of the MCL-PHA/graphene composite film, connected using forceps, into a well with a commercial screen-printed carbon electrode in the bottom. The screen-printed carbon electrode was used as the counter electrode and Ag-AgCl reference electrode, whereas the MCL-PHA/graphene composite formed the working electrode. The results indicate that a peak can be resolved in the SWV plot at −287 mV (**Figure 5A**), which is close to the location of the peak observed on graphene and CNT modified electrodes. This suggested that a similar electron transfer mechanism to

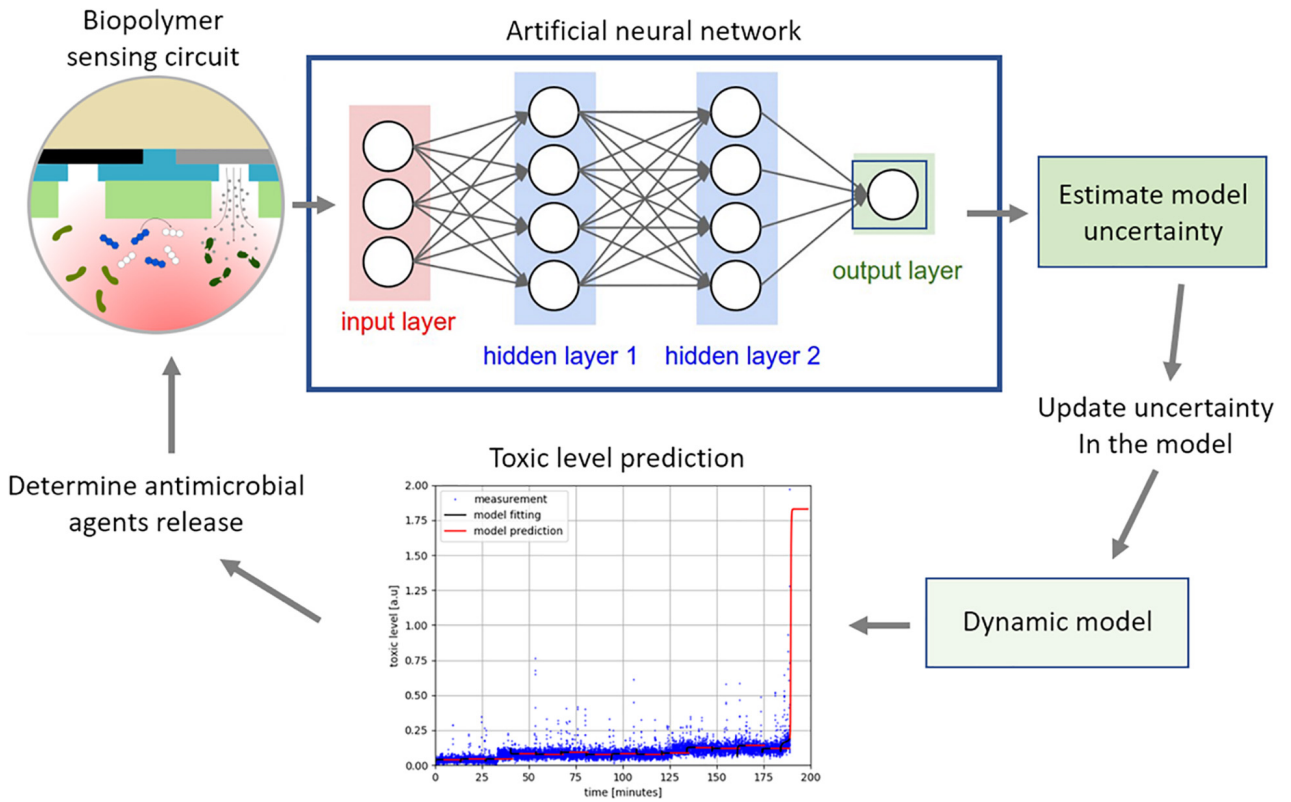

FIGURE 7 | The measurement from the electrochemical biopolymer sensor are used as the input to the neural network, *a priori* trained, to estimate the model uncertainty. The uncertainty in the dynamic model is updated to improve the prediction accuracy of the model. The model predicts changes in the pyocyanin concentration as shown in the graph, where the blue is measured data and the red is the prediction. When the pyocyanin increases above a threshold level, another algorithm would determine optimal time and concentration of the antimicrobial silver required to kill *P. aeruginosa*.

that observed with the DRP110-GPH commercial electrodes was occurring. The 30% MCL-PHA/graphene composite showed the largest peak response to pyocyanin and was therefore explored further through the production of a standard curve (**Figure 5B**). This showed that the MCL-PHA/graphene composite has a lower current response to pyocyanin than the commercially modified electrodes. However, the response to increasing concentrations of pyocyanin is linear and peaks can be resolved from a low concentration of approximately 5 μM pyocyanin.

Measurement of Pyocyanin With the MCL-PHA/Graphene Composite Electrodes

The stationary phase culture of *P. aeruginosa* PA14 was strongly pigmented with a blue-green color, indicating the production of pyocyanin. Measurement of the overnight culture with a strip of the MCL-PHA/graphene composite indicated that a clear peak can be observed when PA14 is present (**Figure 6**). Much like the measurements performed using the commercial electrodes, these results confirmed that it is possible to identify the presence of *P. aeruginosa* PA14, once high concentrations of pyocyanin have been produced. Although the pyocyanin peak for the MCL-PHA/graphene composite was much lower than that observed with the commercial screen-printed electrodes, the results demonstrate the potential of the composite for the indirect identification of *P. aeruginosa* PA14.

In contrast to an overnight culture of *P. aeruginosa*, wound exudate is a complex matrix consisting of potential interferents including, glucose, pH, proteins, human cells, and other microorganisms. A previous study has demonstrated the ability to detect pyocyanin electrochemically in wound exudate with a carbon based electrode (Sismaet et al., 2016). In terms of polymicrobial infections, we have shown previously that it is possible to detect pyocyanin in a polymicrobial competition model in conjunction with *Staphylococcus aureus* (Ward et al., 2014). The production rate of pyocyanin in the presence of other common clinical isolates has also been investigated. In this study it was found that there was no statistical difference in pyocyanin concentration when *P. aeruginosa* was co-cultured alongside *Enterococcus faecalis*, *S. aureus*, or *Staphylococcus epidermidis* (Santiveri et al., 2018). Hence, literature suggests that it will be possible to electrochemically identify the presence of pyocyanin in wound exudate. In future studies, we will explore if this is also possible with our MCL/PHA graphene composite.

Electrochemical detection of pyocyanin has been explored in other studies with a view to producing low cost diagnostic tests. Sharp et al. (2010) demonstrate the ability to detect

the presence of pyocyanin in concentration ranges between 1 and 100 μM using a carbon fiber tow in buffer. Alatraktchi et al. (2016) used commercially available screen printed gold electrodes to detect pyocyanin in a concentration range between 2 and 100 μM with cyclic voltammetry in buffer. This shows that the results reported in our study with the biocompatible polymer are comparable to other work. Interestingly, Ciui et al. (2018) produced a "swipeable" sensor, capable of detecting pyocyanin between 10 and 100 nM with a carbon electrode screen printed onto a disposable glove. This demonstrates that much higher sensitivities can be achieved with low cost, carbon-based substrates.

Closed Loop Feedback and Control System Concept and Design

The MCL-PHA described in this paper has previously been demonstrated to be non-cytotoxic toward HaCaT cells (keratinocytes) *in vitro*. This study potentially adds additional benefits to the MCL-PHA by allowing it to be used as a sensing substrate to detect the presence of one potentially pathogenic microorganism. In order to fully exploit the benefits of MCL-PHA based graphene composites as a novel sensing circuit, we explored a feedback and control system that could be used to release antimicrobial agents into the wound bed when an infection is identified. Heavy metal ions, such as silver (Jung et al., 2008; Fromm, 2013; Sharma et al., 2015) have antimicrobial properties and could be electrochemically dissolved by applying a potential between two silver electrodes. This would cause silver ions to be dissolved into the wound bed and exert a toxic effect on the invading pathogen. Integration of a printed sliver substrate within the wound dressing could therefore provide a mechanism through which an antimicrobial metal ion could be electrochemically released on demand, as soon as pyocyanin is detected. The approach is conceptually attractive as the same electrochemical instrumentation used for the measurement could also be used to release silver ions from the silver substrate.

To achieve this, we designed an overall structure of the feedback control system for regulating the concentration of silver to a toxic level while maintaining the concentration at a minimum used as shown in **Figure 7**. The neural network is trained off-line using simulated data, generated using the dynamic model represented in a set of ordinary differential equations (Dockery and Keener, 2001), to estimate the uncertainties. Training the network using simulated data is common practice when there is limited real measurement data available to train the network. The trained network determines the model uncertainty using the measurement from the sensing circuit. The dynamic model predicts the future toxic level after correcting the model error to identify whether the toxic level was achieved or not. The graph in **Figure 7** demonstrates the prediction capability of the algorithm where the blue lines are the true toxic level and the red is the predicted one. This could be used to determine when and how much of the antimicrobial agents should be released to exert a toxic effect. Note that the true toxic level is generated using a stochastic molecular interaction model in Barbuti et al. (2008). It is our aim to build and verify this model further in the future through the production of in-depth experimental data.

CONCLUSION

This paper describes, for the first time, a novel MCL-PHA/graphene composite wound dressing patch that can be used to detect the presence of an infection by *P. aeruginosa* PA14, a major wound pathogen in real time. The study demonstrated that clinically relevant concentrations of pyocyanin can be reliably detected using the composite. Furthermore, an outline closed loop algorithm was outlined and will be developed further to create a system which could be used to dynamically control silver concentrations within a wound bed to actively kill *P. aeruginosa* in response to an infection. In future work, we will explore the use of the developed composite to detect the presence of *P. aeruginosa* PA14 in complex clinical samples along with the optimization of the biopolymer composite properties for an efficient and effective smart wound dressing.

DATA AVAILABILITY STATEMENT

All datasets presented in this study are included in the article/**Supplementary Material**. Data used to create key tables is provided in **Supplementary Table S1**.

AUTHOR CONTRIBUTIONS

All authors contributed to the design and conception of the study, manuscript revision, read and approved the submitted version. AW, DC, and GN carried out electrochemical measurements. PB, PD, and IR produced the MCL-PHA using bacterial fermentation and the MCL-PHA/graphene composite. CR and SC performed the conductivity measurements. JK produced the control and feedback model.

FUNDING

This work was funded through the Cyclops Healthcare Network funded by the EPSRC, grant number: EP/N026985/1. IR and PB were also funded by the BBI/JU H2020 projects POLYBIOSKIN (Grant Agreement Number 745839) and ECOAT (Grant Agreement Number 837863).

ACKNOWLEDGMENTS

We would like to thank Prof. Jonathan Knowles for access to the SEM at Eastman Dental Institute, UCL, London.

SUPPLEMENTARY MATERIAL

The Supplementary Material for this article can be found online at: https://www.frontiersin.org/articles/10.3389/fbioe.2020.01039/full#supplementary-material

REFERENCES

Alatraktchi, F. A., Breum Andersen, S., Krogh Johansen, H., Molin, S., and Svendsen, W. E. (2016). Fast selective detection of pyocyanin using cyclic voltammetry. *Sensors* 16:408. doi: 10.3390/s16030408

Aramvash, A., Gholami-Banadkuki, N., Moazzeni-Zavareh, F., and Hajizadeh-Turchi, S. (2015). An environmentally friendly and efficient method for extraction of PHB biopolymer with non-halogenated solvents. *J. Microbiol. Biotechnol.* 25, 1936–1943. doi: 10.4014/jmb.1505.05053

Barbuti, R., Caravagna, G., Maggiolo-Schettini, A., Milazzo, P., and Pardini, G. (2008). "The calculus of looping sequences," in *Formal Methods for Computational Systems Biology*, eds M. Bernardo, P. Degano, and G. Zavattaro (Berlin: Springer), 387–423. doi: 10.1007/978-3-540-68894-5_11

Basnett, P., Lukasiewicz, B., Marcello, E., Gura, H. K., Knowles, J. C., and Roy, I. (2017). Production of a novel medium chain length poly(3-hydroxyalkanoate) using unprocessed biodiesel waste and its evaluation as a tissue engineering scaffold. *Microb. Biotechnol.* 10, 1384–1399. doi: 10.1111/1751-7915.12782

Basnett, P., Marcello, E., Lukasiewicz, B., Panchal, B., Nigmatullin, R., Knowles, J. C., et al. (2018). Biosynthesis and characterization of a novel, biocompatible medium chain length polyhydroxyalkanoate by *Pseudomonas* mendocina CH50 using coconut oil as the carbon source. *J. Mater. Sci. Mater. Med.* 29:179. doi: 10.1007/s10856-018-6183-9

Bellin, D. L., Sakhtah, H., Rosenstein, J. K., Levine, P. M., Thimot, J., Emmett, K., et al. (2014). Integrated circuit-based electrochemical sensor for spatially resolved detection of redox-active metabolites in biofilms. *Nat. Commun.* 5:3256. doi: 10.1038/ncomms4256

Bodey, G. P., Bolivar, R., Fainstein, V., and Jadeja, L. (1983). Infections caused by *Pseudomonas aeruginosa*. *Rev. Infect. Dis.* 5, 279–313. doi: 10.1093/clinids/5.2.279

Byrom, D. (1994). *Plastics From Microbes: Microbial Synthesis of Polymers and Polymer Precursors*. Munich: Hanser, 5–33.

Ciui, B., Tertiş, M., Cernat, A., Săndulescu, R., Wang, J., and Cristea, C. (2018). Finger-based printed sensors integrated on a glove for on-site screening of *Pseudomonas aeruginosa* virulence factors. *Anal. Chem.* 90, 7761–7768. doi: 10.1021/acs.analchem.8b01915

Constantinides, C., Basnett, P., Lukasiewicz, B., Carnicer, R., Swider, E., Majid, Q. A., et al. (2018). In vivo tracking and 1H/19F magnetic resonance imaging of biodegradable Polyhydroxyalkanoate/Polycaprolactone blend scaffolds seeded with labeled cardiac stem cells. *ACS Appl. Mater. Interf.* 10, 25056–25068. doi: 10.1021/acsami.8b06096

Dietrich, L. E. P., Teal, T. K., Price-Whelan, A., and Newman, D. K. (2008). Redox-active antibiotics control gene expression and community behavior in divergent bacteria. *Science* 321, 1203–1206. doi: 10.1126/science.1160619

Dockery, J. D., and Keener, J. P. (2001). A mathematical model for quorum sensing in *Pseudomonas aeruginosa*. *Bull. Math. Biol.* 63:95. doi: 10.1006/bulm.2000.0205

Dufresne, A., and Vincendon, M. (2000). Poly (3-hydroxybutyrate) and poly (3-hydroxyoctanoate) blends: morphology and mechanical behavior. *Macromolecules* 33, 2998–3008. doi: 10.1021/ma991854a

Fromm, K. M. (2013). Silver coordination compounds with antimicrobial properties. *Appl. Organometal. Chem.* 27, 683–687. doi: 10.1002/aoc.3047

Frykberg, R. G., and Banks, J. (2015). Challenges in the treatment of chronic wounds. *Adv. Wound Care* 4, 560–582. doi: 10.1089/wound.2015.0635

Gjødsbøl, K., Christensen, J. J., Karlsmark, T., Jørgensen, B., Klein, B. M., and Krogfelt, K. A. (2006). Multiple bacterial species reside in chronic wounds: a longitudinal study. *Intern. Wound J.* 3, 225–231. doi: 10.1111/j.1742-481X.2006.00159.x

Goodfellow, I., Bengio, Y., and Courville, A. (2016). *Deep Learning*. Cambridge, MA: The MIT Press.

Holzinger, A., Biemann, C., Pattichis, C. S., and Kell, D. B. (2017). What do we need to build explainable AI systems for the medical domain?. *arXiv* [Preprint], Available online at: http://arxiv.org/abs/1712.09923 (accessed June 18, 2020).

Hyakutake, M., Saito, Y., Tomizawa, S., Mizuno, K., and Tsuge, T. (2011). Polyhydroxyalkanoate (PHA) synthesis by class IV PHA synthases employing Ralstonia eutropha PHB- 4 as host strain. *Biosci. Biotechnol. Biochem.* 75, 1615–1617. doi: 10.1271/bbb.110229

Jiang, G., Johnston, B., Townrow, D. E., Radecka, I., Koller, M., Chaber, P., et al. (2018). Biomass extraction using non-chlorinated solvents for biocompatibility improvement of polyhydroxyalkanoates. *Polymers* 10:e070731. doi: 10.3390/polym10070731

Jung, W. K., Koo, H. C., Kim, K. W., Shin, S., Kim, S. H., and Park, Y. H. (2008). Antibacterial activity and mechanism of action of the silver ion in *Staphylococcus aureus* and *Escherichia coli*. *Appl. Environ. Microbiol.* 74, 2171–2178. doi: 10.1128/AEM.02001-07

Kirketerp-Møller, K., Jensen, P. Ø, Fazli, M., Madsen, K. G., Pedersen, J., Moser, C., et al. (2008). Distribution, organization, and ecology of bacteria in chronic wounds. *J. Clin. Microbiol.* 46, 2717–2722. doi: 10.1128/JCM.00501-08

Kunasundari, B., and Sudesh, K. (2011). Isolation and recovery of microbial polyhydroxyalkanoates. *Express Polym. Lett.* 5, 620–634. doi: 10.3144/expresspolymlett.2011.60

Kuo, S.-H., Shen, C.-J., Shen, C.-F., and Cheng, C.-M. (2020). Role of pH value in clinically relevant diagnosis. *Diagnostics* 10:107. doi: 10.3390/diagnostics10020107

Lakshmanan, R., Krishnan, U. M., and Sethuraman, S. (2013). Polymeric scaffold aided stem cell therapeutics for cardiac muscle repair and regeneration. *Macromol. Biosci.* 13, 1119–1134. doi: 10.1002/mabi.201300223

Lau, G. W., Hassett, D. J., Ran, H., and Kong, F. (2004). The role of pyocyanin in *Pseudomonas aeruginosa* infection. *Trends Mol. Med.* 10, 599–606. doi: 10.1016/j.molmed.2004.10.002

Lu, Z., Pu, H., Wang, F., Hu, Z., and Wang, L. (2017). "The expressive power of neural networks: a view from the width," in *Proceedings of the 31st International Conference on Neural Information Processing Systems NIPS'17*, Long Beach, CA.

Mavrodi, D. V., Blankenfeldt, W., and Thomashow, L. S. (2006). Phenazine compounds in fluorescent *Pseudomonas* Spp. biosynthesis and regulation. *Annu. Rev. Phytopathol.* 44, 417–445. doi: 10.1146/annurev.phyto.44.013106.145710

Mc Loone, S., and Irwin, G. (2001). Improving neural network training solutions using regularisation. *Neurocomputing* 37, 71–90. doi: 10.1016/S0925-2312(00)00314-3

McColl, D., Cartlidge, B., and Connolly, P. (2007). Real-time monitoring of moisture levels in wound dressings in vitro: an experimental study. *Intern. J. Surg.* 5, 316–322. doi: 10.1016/j.ijsu.2007.02.008

McColl, D., MacDougall, M., Watret, L., and Connolly, P. (2009). Monitoring moisture without disturbing the wound dressing. *Wounds* 5, 94–99.

McLister, A., Mathur, A., and Davis, J. (2017). Wound diagnostics: deploying electroanalytical strategies for point of care sensors and smart dressings. *Curr. Opin. Electrochem.* 3, 40–45. doi: 10.1016/j.coelec.2017.05.002

McManus, A. T., Mason, A. D., McManus, W. F., and Pruitt, B. A. (1985). Twenty-five year review of*Pseudomonas aeruginosa* bacteremia in a burn center. *Eur. J Clin. Microbiol.* 4, 219–223. doi: 10.1007/BF02013601

Mikkelsen, H., McMullan, R., and Filloux, A. (2011). The *Pseudomonas aeruginosa* reference strain PA14 displays increased virulence due to a mutation in ladS. *PLoS One* 6:e29113. doi: 10.1371/journal.pone.0029113

Mostafalu, P., Tamayol, A., Rahimi, R., Ochoa, M., Khalilpour, A., Kiaee, G., et al. (2018). Smart bandage for monitoring and treatment of chronic wounds. *Small* 14:1703509. doi: 10.1002/smll.201703509

Muller, M., Li, Z., and Maitz, P. K. M. (2009). *Pseudomonas* pyocyanin inhibits wound repair by inducing premature cellular senescence: role for p38 mitogen-activated protein kinase. *Burns* 35, 500–508. doi: 10.1016/j.burns.2008.11.010

Nomura, C. T., and Taguchi, S. (2007). PHA synthase engineering toward superbiocatalysts for custom-made biopolymers. *Appl. Microbiol. Biotechnol.* 73, 969–979. doi: 10.1007/s00253-006-0566-4

Ojumu, T. V., Yu, J., and Solomon, B. O. (2004). Production of Polyhydroxyalkanoates, a bacterial biodegradable polymers. *Afr. J. Biotechnol.* 3, 18–24. doi: 10.4314/ajb.v3i1.14910

Öncül, O., Öksüz, S., Acar, A., Ülkür, E., Turhan, V., Uygur, F., et al. (2014). Nosocomial infection characteristics in a burn intensive care unit: analysis of an eleven-year active surveillance. *Burns* 40, 835–841. doi: 10.1016/j.burns.2013.11.003

Qu, X. H., Wu, Q., Liang, J., Zou, B., and Chen, G. Q. (2006). Effect of 3-hydroxyhexanoate content in poly (3-hydroxybutyrate-co-3-hydroxyhexanoate) on in vitro growth and differentiation of smooth muscle cells. *Biomaterials* 27, 2944–2950. doi: 10.1016/j.biomaterials.2006.01.013

Rai, R., Keshavarz, T., Roether, J. A., Boccaccini, A. R., and Roy, I. (2011). Medium chain length polyhydroxyalkanoates, promising new biomedical materials

for the future. *Mater. Sci. Eng. R Rep.* 72, 29–47. doi: 10.1016/j.mser.2010.11.002

Reyes, E. A., Bale, M. J., Cannon, W. H., and Matsen, J. M. (1981). Identification of *Pseudomonas aeruginosa* by pyocyanin production on Tech agar. *J. Clin. Microbiol.* 13, 456–458. doi: 10.1128/jcm.13.3.456-458.1981

Rezaie, F., Momeni-Moghaddam, M., and Naderi-Meshkin, H. (2019). Regeneration and repair of skin wounds: various strategies for treatment. *Intern. J. Lower Extrem. Wounds* 18, 247–261. doi: 10.1177/1534734619859214

Rivero, G., Meuter, M., Pepe, A., Guevara, M. G., Boccaccini, A. R., and Abraham, G. A. (2020). Nanofibrous membranes as smart wound dressings that release antibiotics when an injury is infected. *Coll. Surf. A* 587:124313. doi: 10.1016/j.colsurfa.2019.124313

Santiveri, C. R., Sismaet, H. J., Kimani, M., and Goluch, E. D. (2018). Electrochemical detection of *Pseudomonas aeruginosa* in polymicrobial environments. *Chem. Select* 3, 2926–2930. doi: 10.1002/slct.201800569

Scalamandré, A., and Bogie, K. M. (2020). "Chapter 13 - smart technologies in wound prevention and care," in *Innovations and Emerging Technologies in Wound Care*, ed. A. Gefen (Cambridge, MA: Academic Press), 225–244. doi: 10.1016/B978-0-12-815028-3.00013-4

Schaarup, C., Pape-Haugaard, L. B., and Hejlesen, O. K. (2018). Models used in clinical decision support systems supporting healthcare professionals treating chronic wounds: systematic literature review. *JMIR Diabetes* 3, e11. doi: 10.2196/diabetes.8316

Schmidhuber, J. (2015). Deep learning in neural networks: an overview. *Neural Netw.* 61, 85–117. doi: 10.1016/j.neunet.2014.09.003

Serra, R., Grande, R., Butrico, L., Rossi, A., Settimio, U. F., Caroleo, B., et al. (2015). Chronic wound infections: the role of *Pseudomonas aeruginosa* and *Staphylococcus aureus*. *Expert Rev. Anti Infect. Ther.* 13, 605–613. doi: 10.1586/14787210.2015.1023291

Sevastianov, V. I., Perova, N. V., Shishatskaya, E. I., Kalacheva, G. S., and Volova, T. G. (2003). Production of purified polyhydroxyalkanoates (PHAs) for applications in contact with blood. *J. Biomater. Sci. Polym. Ed.* 14, 1029–1042. doi: 10.1163/156856203769231547

Sharma, B. K., Saha, A., Rahaman, L., Bhattacharjee, S., and Tribedi, P. (2015). Silver inhibits the biofilm formation of *Pseudomonas aeruginosa*. *Adv. Microbiol.* 05, 677–685. doi: 10.4236/aim.2015.510070

Sharma, B. R., Harish, D., Singh, V. P., and Bangar, S. (2006). Septicemia as a cause of death in burns: an autopsy study. *Burns* 32, 545–549. doi: 10.1016/j.burns.2006.02.008

Sharp, D., Gladstone, P., Smith, R. B., Forsythe, S., and Davis, J. (2010). Approaching intelligent infection diagnostics: carbon fibre sensor for electrochemical pyocyanin detection. *Bioelectrochemistry* 77, 114–119. doi: 10.1016/j.bioelechem.2009.07.008

Sheets, A. R., Hwang, C. K., and Herman, I. M. (2016). *Developing "Smart" Point-of-Care Diagnostic Tools for "Next-Generation" Wound Care*, Chap. 17. ed. J. Laurence (Translating Regenerative Medicine to the Clinic: Academic Press), 251–264. Available online at: https://doi.org/10.1016/B978-0-12-800548-4.00017-6

Shijun, X., Junsheng, M., Jianqun, Z., and Ping, B. (2016). *In vitro* three-dimensional coculturing poly3-hydroxybutyrate-co-3-hydroxyhexanoate with mouse-induced pluripotent stem cells for myocardial patch application. *J. Biomater. Appl.* 30, 1273–1282. doi: 10.1177/0885328215612115

Shishatskaya, E. I., Volova, T. G., and Gitelson, I. I. (2002). In vivo toxicological evaluation of polyhydroxyalkanoates. *Doklady Biol. Sci.* 383, 109–111. doi: 10.1023/a:1015325504494

Sismaet, H. J., Banerjee, A., McNish, S., Choi, Y., Torralba, M., Lucas, S., et al. (2016). Electrochemical detection of *Pseudomonas* in wound exudate samples from patients with chronic wounds. *Wound Repair. Regen.* 24, 366–372. doi: 10.1111/wrr.12414

Songkakul, T., Bhushan, P., Umasankar, Y., Yokus, M., Daniele, M. A., Bhansali, S., et al. (2019). "Towards a long-term multi-site electrochemical wound monitoring system," in *Proceedings of the 2019 IEEE SENSORS*, Montreal, QC.

Sun, J., Dai, Z., Zhao, Y., and Chen, G. Q. (2007). *In vitro* effect of oligo-hydroxyalkanoates on the growth of mouse fibroblast cell line L929. *Biomaterials* 28, 3896–3903. doi: 10.1016/j.biomaterials.2007.05.011

Szegedy, C., Zaremba, W., Sutskever, I., Bruna, J., Erhan, D., Goodfellow, I., et al. (2014). Intriguing properties of neural networks. *arXiv* [Preprint], Available online at: http://arxiv.org/abs/1312.6199 (accessed June 18, 2020).

Tan, E. K. W., Au, Y. Z., Moghaddam, G. K., Occhipinti, L. G., and Lowe, C. R. (2019). Towards closed-loop integration of point-of-care technologies. *Trends Biotechnol.* 37, 775–788. doi: 10.1016/j.tibtech.2018.12.004

Valappil, S. P., Boccaccini, A. R., Bucke, C., and Roy, I. (2007). Polyhydroxyalkanoates in Gram-positive bacteria: insights from the genera *Bacillus* and *Streptomyces*. *Antonie Van Leeuwenhoek* 91, 1–17. doi: 10.1007/s10482-006-9095-5

Valappil, S. P., Rai, R., Bucke, C., and Roy, I. (2008). Polyhydroxyalkanoate biosynthesis in *Bacillus cereus* SPV under varied limiting conditions and an insight into the biosynthetic genes involved. *J. Appl. Microbiol.* 104, 1624–1635. doi: 10.1111/j.1365-2672.2007.03678.x

Volova, T. (2004). *Polyhydroxyalkanoates-Plastic Materials of the 21st Century: Production, Properties, Applications*. Hauppauge, NY: Nova Science Publishers.

Volova, T. G., Shishatskaya, E. I., Nikolaeva, E. D., and Sinskey, A. J. (2014). In vivo study of 2D PHA matrices of different chemical compositions: tissue reactions and biodegradations. *Mater. Sci. Technol.* 30, 549–557. doi: 10.1179/1743284713Y.0000000470

Wang, Y., and Newman, D. K. (2008). Redox reactions of phenazine antibiotics with ferric (Hydr)oxides and molecular oxygen. *Environ. Sci. Technol.* 42, 2380–2386. doi: 10.1021/es702290a

Ward, A. C., Connolly, P., and Tucker, N. P. (2014). *Pseudomonas aeruginosa* can be detected in a polymicrobial competition model using impedance spectroscopy with a novel biosensor. *PLoS One* 9:e91732. doi: 10.1371/journal.pone.0091732

Williams, S., Martin, D., Horowitz, D., and Peoples, O. (1999). PHA applications: addressing the price performance issue. I. Tissue engineering. *Int. J. Biol. Macromol.* 25, 111–121. doi: 10.1016/s0141-8130(99)00022-7

Wilson, R., Sykes, D. A., Watson, D., Rutman, A., Taylor, G. W., and Cole, P. J. (1988). Measurement of *Pseudomonas aeruginosa* phenazine pigments in sputum and assessment of their contribution to sputum sol toxicity for respiratory epithelium. *Infect. Immun.* 56, 2515–2517. doi: 10.1128/iai.56.9.2515-2517.1988

Zhao, K., Deng, Y., Chen, J. C., and Chen, G. Q. (2003). Polyhydroxyalkanoate (PHA) scaffolds with good mechanical properties and biocompatibility. *Biomaterials* 24, 1041–1045. doi: 10.1016/s0142-9612(02)00426-x

Zheng, Z., Bei, F. F., Tian, H. L., and Chen, G. Q. (2005). Effects of crystallization of polyhydroxyalkanoate blend on surface physicochemical properties and interactions with rabbit articular cartilage chondrocytes. *Biomaterials* 26, 3537–3548. doi: 10.1016/j.biomaterials.2004.09.041

Conflict of Interest: The authors declare that the research was conducted in the absence of any commercial or financial relationships that could be construed as a potential conflict of interest.

frontiers in Bioengineering and Biotechnology

ORIGINAL RESEARCH
published: 24 September 2020
doi: 10.3389/fbioe.2020.557885

Chemical Modification of Bacterial Cellulose for the Development of an Antibacterial Wound Dressing

*Isabel Orlando[1,2,3], Pooja Basnett[1], Rinat Nigmatullin[4], Wenxin Wang[2], Jonathan C. Knowles[5,6,7] and Ipsita Roy[8]**

[1] School of Biosciences, College of Liberal Arts and Sciences, University of Westminster, London, United Kingdom, [2] School of Medicine and Medical Sciences, Charles Institute of Dermatology, University College Dublin, Dublin, Ireland, [3] Université Clermont Auvergne, Centre Nationale de la Recherche Scientifique (CNRS), SIGMA Clermont, Institut de Chimie de Clermont-Ferrand (ICCF), Clermont–Ferrand, France, [4] Advanced Composites Collaboration for Science and Innovation, University of Bristol, Bristol, United Kingdom, [5] Division of Biomaterials and Tissue Engineering, University College London (UCL) Eastman Dental Institute, London, United Kingdom, [6] Department of Nanobiomedical Science and BK21 Plus NBM, Global Research Center for Regenerative Medicine, Dankook University, Cheonan, South Korea, [7] The Discoveries Centre for Regenerative and Precision Medicine, University College London, London, United Kingdom, [8] Department of Materials Science and Engineering, Faculty of Engineering, University of Sheffield, Sheffield, United Kingdom

OPEN ACCESS

Edited by:
Francesco Cellesi, Politecnico di Milano, Italy

Reviewed by:
Xin Zhao, Hong Kong Polytechnic University, Hong Kong
Guang Yang, Huazhong University of Science and Technology, China

***Correspondence:**
Ipsita Roy
I.Roy@sheffield.ac.uk

Specialty section:
This article was submitted to Nanobiotechnology, a section of the journal Frontiers in Bioengineering and Biotechnology

Received: *30 April 2020*
Accepted: *20 August 2020*
Published: *24 September 2020*

Citation:
Orlando I, Basnett P, Nigmatullin R, Wang W, Knowles JC and Roy I (2020) Chemical Modification of Bacterial Cellulose for the Development of an Antibacterial Wound Dressing. Front. Bioeng. Biotechnol. 8:557885. doi: 10.3389/fbioe.2020.557885

Bacterial cellulose is a bacterially derived polymer with great potential for application in wound healing due to its innate properties such as high biocompatibility and biodegradability. In addition to this, it is naturally biosynthesized by bacteria as a hydrogel, which makes it an optimal substrate for the treatment of dry wounds, where additional moisture is required to facilitate the healing process. However, this polymer lacks antibacterial properties. As bacterial infections are becoming increasingly common and difficult to treat due to antimicrobial resistance, it is of crucial importance to develop strategies for the modification of cellulose to ensure protection against bacterial contamination. In this study, a green-chemistry approach was proposed for the functionalization of cellulose to introduce antibacterial functional groups. Two different active agents, namely glycidyl trimethylammonium chloride and glycidyl hexadecyl ether, were used for the covalent derivatization of the hydroxyl groups of glucose through a heterogeneous reaction in basic aqueous conditions. The modified material was chemically and mechanically characterized by solid-state techniques and rheological measurements. A biological assessment was then carried out both using bacterial cells and human keratinocytes. It was observed that the functionalization performed induced a reduction of approximately half of the bacterial population within 24 h of direct contact with *Staphylococcus aureus* subsp. aureus Rosenbach 6538P^{TM} and *Escherichia coli* (Migula) Castellani and Chalmers ATCC® 8739^{TM} (respectively, a reduction of 53% and 43% in the cell number was registered for the two strains). In parallel, cytotoxicity studies performed on keratinocytes (HaCaT cell line) showed cell viability in the range of 90 to 100% for up to 6 days of direct contact with both unmodified and modified samples. The morphology of the cells was also visually evaluated, and no significant difference was noted as compared to the control. Finally, the *in vitro* scratch assay evidenced good wound closure rates in the presence of the samples, with complete coverage of

the scratched area after 5 days for both the modified cellulose and the positive control (i.e., keratinocytes growth medium). Overall, the modified hydrogel showed promising features, confirming its potential as an alternative substrate to develop a sustainable, antibacterial and biocompatible wound dressing.

Keywords: bacterial cellulose, antibacterial, wound dressing, green chemistry, biodegradable polymers

INTRODUCTION

Over the last decades, the exceptional intensification of antimicrobial resistance (AMR) has led the scientific community to allocate time and money to researching alternative strategies to fight the spreading of infections. Resistance mechanisms started to arise soon after antibiotic discovery, but only with their worldwide distribution and availability at low prices they have come to pose a real threat to human health (Walsh, 2000; Tenover, 2006). It is in fact generally acknowledged that the overuse of antibiotics, both in developed and developing countries (where they can be purchased over the counter), has triggered bacteria to develop resistance, not only because of the over-exposure but also as a result of their consumption in wrong dosages (Reardon, 2014). In addition to this, the void in the discovery of new classes of antibiotics for the last 30 years has contributed to an increase in the mortality rate (The PEW charitable trust, 2016). It has been estimated that 700,000 people die every year as a result of infections and malaria, and the number is likely to increase over the next years (O'Neill, 2018). One major medical area affected by AMR is wound healing. Wounds can in fact provide an access for bacteria to the inner tissues and organs, thus posing a high risk of bloodstream infections that can lead to morbidity. An example of wound-related infections is represented by surgical site infections (SSIs), i.e., infections contracted within the first 30 days of surgery. SSIs account for about 20% of all the healthcare associated infections and increase the risk of death in post-operative patients by 2–11 times. SSIs also prolong the hospitalization time, resulting in higher costs for health-care institutions (Anderson et al., 2014).

In this context, the need for alternative materials that can effectively inhibit bacterial growth without triggering resistance has become urgent. One of the most important classes of biomedical materials is represented by polymers. In particular, the use of natural polymers has recently increased thanks to their specific features. These polymers are in fact characterized by a high degree of biocompatibility, mostly due to their chemical structures that resemble that of the extracellular matrix components. Furthermore, such structures are often difficult if not impossible to replicate through synthetic pathways, making these polymers a precious resource for various biomedical applications (Aravamudhan et al., 2014; Olatunji, 2016). Bacterial cellulose (BC) is one of the most studied natural polymers thanks to its unusual characteristics. This polymer is naturally produced by fermentation of various bacteria, although there are examples in the literature of self-assembly of BC through cell-free methodologies based on the use of *in vitro* enzymatic systems (Ullah et al., 2015; Kim et al., 2019). Among the different BC-producing strains, *Gluconacetobacter xylinus* (formerly *Acetobacter xylinum*) is the most commonly used due to its high polymer production yield and the wide range of carbon and nitrogen sources that it can utilize (Chawla et al., 2009). The average degree of polymerization for this strain has been found to be in the range between 2190 and 3470 with peaks of 6000 after 5 days, although it has been reported that the molecular weight shows a linear increase with the generation change of bacteria (Legge, 1990; Okajima et al., 1991; Iguchi et al., 2000). The biosynthesis of BC involves the incorporation of huge quantities of water in the macromolecular structure, resulting in the formation of a natural hydrogel with over 90% of its total mass consisting of water. This is a crucial parameter for wound healing, as dry wounds require additional moisture to ensure the regeneration of new tissues and to avoid necrosis. These wounds are in fact characterized by the presence of devitalized necrotic tissue, which gives them a black color. Such a feature is a consequence of dehydration and cell death, and it has been observed that the removal of necrotic tissue (for instance through excision) is necessary to promote wound healing (Abdelrahman and Newton, 2011; Kavitha, 2014). However, when surgery is not possible due to the patient's conditions or if the amount of necrotic tissue is too low, alternative solutions can be adopted such as the use of hydrogels as wound dressings, which can facilitate the autolytic debridement of necrotic tissue (Abdelrahman and Newton, 2011; Dhivya et al., 2015). BC is also characterized by higher purity as compared to plant-derived cellulose, for which harsh chemical treatments are necessary to remove other wood-pulp components such as hemicellulose and lignin (Helenius et al., 2006). Additionally, its nanofibrillar structure gives this biopolymer high porosity and surface area, resulting in improved water-holding capacity as compared to plant cellulose. BC is also characterized by higher crystallinity and higher mechanical properties than the plant-derived one, such as better tensile strength and Young's modulus (Picheth et al., 2017; Ul-Islam et al., 2019a). For these reasons, BC is particularly suitable for applications in the biomedical field and, more specifically, for skin tissue engineering and wound healing. However, due to its lack of antibacterial activity, chemical or physical modifications are needed to ensure protection against bacterial contamination.

In the field of wound healing, several approaches have been investigated, often involving the absorption of external agents that are released from the polymer matrix over time. A very common example of active compounds is represented by metal ions. In this context, silver is probably the most common metal, and it has been incorporated into BC in different forms such as salts (Chen et al., 2019), bound to zeolites (Gupta et al., 2016) or montmorillonite (Horue et al., 2020), silver-based fluorescent complex (namely, $[Ag(ImD)_2]ClO_4$) (DeBoer et al., 2015) and

silver sulfadiazine (Faisul Aris et al., 2019). Other metals have also been explored for this purpose, in particular, the introduction of zinc and zinc oxide has been investigated (Janpetch et al., 2016; Shahmohammadi Jebel and Almasi, 2016; Khalid et al., 2017; Wahid et al., 2019a; Dharmalingam and Anandalakshmi, 2020; Dincă et al., 2020) as well as titanium oxide (Khan et al., 2015; Ullah et al., 2016). In addition to this, organic compounds have been used, including natural extracts (Siddhan et al., 2016) and antibiotics (Shao et al., 2016). Although this methodology often allows to develop efficient biomaterials through easy processes, there are a few drawbacks related to the use of leachable agents, such as the maximum amount that can be loaded into the matrix, the stability of low molecular weight compounds, which are often characterized by higher reactivity and volatility (for instance, in the case of antibacterial natural compounds) and the short-term activity, which is dependent on the release profile of such agents (Giano et al., 2014; Deka et al., 2015). Another strategy for the development of BC-based antibacterial materials involves the combination of BC with antibacterial polymers such as chitosan (Lin et al., 2013; Kingkaew et al., 2014; Wahid et al., 2019b; Yin et al., 2020) and ε-polylysine (Gao et al., 2014). In this case, however, it is fundamental to ensure good compatibility between the two components to avoid phase separation. To overcome these issues, a chemical modification can be performed to impart long-term and structural-related activity to the system.

In this study, BC was chemically functionalized following a green-chemistry approach to introduce antibacterial functionalities. In particular, its surface hydroxyl groups were derivatized under heterogeneous conditions in water. For this purpose, two epoxides containing, respectively, a quaternary ammonium group and an alkyl chain were subjected to base-catalyzed ring-opening reaction. Quaternary ammonium groups are widely used substrates for the development of biocides utilized in various fields, including water disinfection (Abid et al., 2010; Farah et al., 2015), textiles (Nayak and Padhye, 2015) and biomedical applications such as dental (Antonucci et al., 2012; Cheng et al., 2012), orthopedic (Tan et al., 2013), and wound healing (Fan et al., 2015; Liu et al., 2018). Their structure presents a cationic nitrogen that allows the adsorption of the compound onto the negatively charged portions of the bacterial membrane. The mechanism of action of quaternary ammonium groups is believed to involve membrane damage, with consequent alteration of the bacterial equilibrium and leakage of intracellular constituents. After a first attraction, the hydrophobic tails of the compound are in fact able to penetrate through the lipid regions of the membrane, causing its disruption and, ultimately, cell death (Ioannou et al., 2007). Along with cationic ammonium groups, alkyl chains (C_{14}) were attached to the polymer backbone. Similarly to the mechanism described for quaternary ammonium groups, these structures can also interact hydrophobically with the bacterial cell wall and induce cell death (Denis et al., 2010; Wiener and Horanyi, 2011; Zheng et al., 2016). A fundamental parameter to be considered, however, is the length of the chain. It has been found that the optimum can vary for Gram-positive and Gram-negative strains, although generally higher activity is achieved for lengths higher than C_{12}, whereas no antibacterial effect has been observed below C_4, probably due to the inability of crossing the hydrophobic region of the membrane (Devínsky et al., 1990; Zhao and Sun, 2008). After the reaction, the material obtained was chemically and mechanically characterized, and its features were compared to unmodified BC. A biological assessment was then conducted toward both bacterial and human cells to determine the antibacterial activity and the cytotoxicity of the hydrogels as well as their suitability as wound healing platforms.

MATERIALS AND METHODS

Materials

Dulbecco's modified Eagle medium (DMEM), fetal bovine serum (FBS), sodium pyruvate, penicillin/streptomycin, 0.25% trypsin/ethylenediaminetetraacetic acid (EDTA), trypan blue, Alamar Blue, rhodamine phalloidin and 4',6-diamino-2-phenylindole, dilactate (DAPI) were purchased from Thermo Fischer Scientific Inc. Sodium hydroxide was purchased from VWR International. All the other chemicals and reagents used in this work were purchased from Sigma-Aldrich (now Merck kGaA). Gram-negative bacterium *Gluconacetobacter xylinus* JCM10150 used to produce bacterial cellulose was obtained from the culture collection of the University of Westminster, London, United Kingdom. The antibacterial assays described were performed using Gram-positive *Staphylococcus aureus* subsp. aureus Rosenbach 6538P^{TM} and Gram-negative *Escherichia coli* (Migula) Castellani and Chalmers ATCC® 8739^{TM}, both purchased from ATCC®. The cytotoxicity studies were carried out using *in vitro* spontaneously transformed keratinocytes (HaCaT) from histologically normal skin (catalog number: T0020001), bought from AddexBio.

Bacterial Cellulose Production and Purification

Bacterial cellulose was produced by *Gluconacetobacter xylinus* using glucose as the main carbon source. In particular, a modified Hestrin and Schramm medium was used as the production medium, which contained glucose (50 g/L), yeast extract (5 g/L), and $CaCO_3$ (12 g/L). The final pH was adjusted to 5.5 using 1 M HCl and 1 M NaOH. The medium constituents were sterilized in an autoclave at different temperatures depending on their nature to avoid thermal degradation of the sugar. Pre-inoculation was then carried out using frozen bacterial glycerol stocks and 10 mL of production medium into 20 mL glass vials. The vials were kept slightly open to ensure sufficient air flow, although filters or cotton caps might also be used to minimize the risk of cross-contamination. After formation of the pellicle, 3 mL of inoculum were transferred into 500 mL Erlenmeyer flasks containing 300 mL of sterile production medium. Static fermentation was performed at 30°C for 5–7 days or until pellicles with a thickness of 1–1.5 cm were obtained. The membranes were then harvested and washed several times using distilled water. In order to remove residual biomass, cellulose pellicles were treated with 1 M NaOH for 2 h at 80°C under continuous agitation and washed with distilled water until neutral pH was achieved. The process was

repeated twice. Prior to their use, the pellicles were sterilized in the autoclave at 110°C for 10 min.

Evaluation of Water Content

The water content of the cellulose pellicles was determined through evaluation of their weight before and after a drying period of 24 h under a fume-hood. 9 samples from three different pellicles were used. The percent of water was calculated using the following formula:

$$\text{Water content } \% = \frac{A - B}{A} \times 100$$

A = Weight of the wet sample.
B = Weight of the dry sample.

Chemical Functionalization

The surface of bacterial cellulose membranes was functionalized using two different epoxides containing quaternary ammonium groups and hydrophobic tails. The reaction was carried out in aqueous system. First, 5% w/w NaOH with respect to cellulose (dry) was used for the deprotonation of the hydroxyl groups of glucose. After 15 min of basic pre-treatment of the samples at room temperature, glycidyl trimethylammonium chloride (GTMAC) and glycidyl hexadecyl ether (GHDE) were added in excess to the stoichiometric ratio. The stoichiometric ratio was calculated considering that each monomeric unit of cellulose (i.e., glucose) presents three hydroxyl groups. The reaction was performed at 65°C in a water bath for 4 h under continuous stirred conditions. The samples were then washed with distilled water for several hours until neutral pH was reached.

Morphological Analysis

The morphology of the pellicles was studied through Scanning Electron Microscopy on dry samples after evaporation for 24–48 h (depending on the thickness) under a fume-hood. Non-modified and modified cellulose structures were observed using a JOEL 5610LV scanning electron microscope. The samples were placed on the 8 mm diameter aluminum stubs and gold-coated for 2 min using the gold sputtering device (EMITECH-K550). Operating pressure of 7×10^{-2} bar and deposition current of 20 mA (for 2 min) were used. The analysis was carried out at the Eastman Dental Institute, Department of Biomaterials and Tissue Engineering, University College London, United Kingdom.

Chemical Characterization

The chemical structure of the pellicles before and after modification was also investigated. Prior to each analysis, the samples were dried for 24–48 h under a fume-hood. The same equipment described in section "Morphological Analysis" was used to carry out an elemental analysis through Energy-dispersive X-ray spectroscopy (EDX). Chemical characterization of the polymer was also performed by X-ray photoelectron spectroscopy (XPS) using a Thermo Escalab 220iXL system. The analysis was conducted with an Al K_α mono-chromated X-ray source and data were elaborated using CASAXPS (Casa Software Ltd, Teignmouth, United Kingdom). For all the samples, both survey and high-resolution spectra were recorded. The measurement was carried out at the School of Chemistry, Cardiff University, United Kingdom.

Rheological Studies

The viscoelastic behavior of the cellulose membranes was determined through rheological measurements using a Discovery HR-2 Rheometer (TA Instruments). The test was performed on 1 cm^2 samples of non-modified cellulose and cellulose after modification. A parallel plate geometry with a diameter of 8 mm was used and the gap was set at 3.85 mm for all the measurements. First, the linear viscoelastic region (LVR) was determined through oscillation sweep test by applying increasing amplitude stress (0.01–100 Pa) and constant frequency (1.0 Hz). All the other assays were conducted using a stress within the LVR. Frequency sweep analysis was carried out to measure the variations of storage modulus and loss modulus for each cellulose type. Stress of 6 Pa, temperature of 32°C and increasing frequency from 0.1 to 50 Hz were applied. The influence of temperature on the storage modulus and loss modulus was also evaluated through temperature ramp assay in the range between 10 and 60°C with an increasing rate of 5°C/min. The test was performed using a stress of 6 Pa and a frequency of 1 Hz.

Stability of Bacterial Cellulose

The stability of the cellulose pellicles in aqueous media was studied for 7 days. Three samples of 1 cm^2 were used for both unmodified and modified cellulose in order to investigate the effect of the reaction performed. The weight variation was registered both in phosphate buffer solution (PBS) and keratinocytes growth medium through evaluation of the initial hydrated weight and the hydrated weight of each sample after 1, 3, 5, and 7 days. The specimens were placed in 24-well plates with 2 mL of medium in each well and incubated in static conditions at 32°C. The percent weight variation (ΔW) for each time point was calculated using the formula below:

$$\Delta W\% = \frac{W_x}{W_0} \times 100$$

W_x = Weight of the sample at time x.
W_0 = Weight of the sample at time 0.

Antibacterial Activity Evaluation

Bacterial Culture Methods

The antibacterial tests were carried out using two strains, i.e., *Staphylococcus aureus* subsp. aureus Rosenbach 6538^{TM} and *Escherichia coli* (Migula) Castellani and Chalmers ATCC® 8739^{TM} (from here onwards referred to as, respectively, *S. aureus* and *E. coli*). Selective mannitol agar was used as the solid culture medium for *S. aureus*, while MacConkey agar was used for *E. coli*. The plates were prepared by streaking a loopful of inoculum from the glycerol stocks and kept in the incubator at 37°C under static conditions overnight. The culture was prepared through inoculation of 150 mL of nutrient broth No. 2 in a 500 mL Erlenmeyer flask using a single colony. The inoculum was incubated at 37°C in shaking conditions at 120 rpm until

log phase (approximately 16 h). The optical density (OD) was then measured at 600 nm and the culture was diluted to 0.5 MacFarland concentration (i.e., 1.5×10^8 CFU/mL), which corresponds to $OD_{600} = 0.132$. The assay was performed through dilution of such inoculum using nutrient broth diluted 1:500 until the appropriate cell concentration was reached.

Direct Contact Test (DCT)

The antibacterial properties of modified cellulose were studied by adapting an ISO 22196 procedure for the quantitative evaluation of the activity upon direct contact. As indicated in the protocol, untreated cellulose was used as the control. Three 2.5 cm^2 samples of functionalized cellulose as well as six 2.5 cm^2 samples of non-functionalized cellulose were sterilized in an autoclave and placed onto agar plates. 100 μL of *S. aureus* or *E. coli* inoculum at cell concentration of 1.2×10^6 CFU/mL were pipetted directly on the surface of each sample. Three of the unmodified pellicles as well as three of the modified ones were incubated under static conditions at 37°C for 24 h, while the remaining three samples of unmodified cellulose were washed to quantify the number of bacterial cells recovered at time 0. For the recovery of bacteria, the samples were transferred to a sterile glass vial containing a known amount of phosphate buffer saline (PBS) solution and the bacteria were detached through vortexing of the mixture for 3 min. Several 10-fold dilutions were prepared using PBS. 10 μL of each dilution were then plated on nutrient agar plates through drop plate technique. When the drops were completely dry, the plates were placed upside down in the incubator at 37°C under static conditions for 20 h. The same method was used for the recovery of bacteria at 0 and 24 h. The number of viable cells was evaluated by colony counting. The antibacterial activity was then calculated using the following formula:

$$R\% = \frac{(a)\ [unmodified] - (a)\ [modified]}{(a)\ [unmodified]} * 100$$

where a is the average of the viable bacterial cells recovered after 24 h expressed as CFU/(mL*cm^2).

Biocompatibility Assessment

Cell Culture Methods

Keratinocyte (HaCaT cell line) cells were cultured in T75 flasks using Dulbecco's modified Eagle medium (DMEM) supplemented with 10% v/v fetal bovine serum (FBS), 1% v/v sodium pyruvate and 1% v/v penicillin/streptomycin and incubated at 37°C in 5% CO_2 atmosphere. Upon reaching a confluency of 80–90%, cells were sub-cultured with a 1:5 ratio through incubation for 3 min with 3 mL of 0.25% trypsin/ethylenediaminetetraacetic acid (EDTA). The reagent was then inactivated by addition of 12 mL of serum-supplemented medium. The cells were centrifuged at 120 x g for 5 min, and the pellet obtained was resuspended using a known volume of medium. The count of the cells was carried out using a Neubauer counting chamber by trypan blue exclusion method.

Indirect Cytotoxicity Assay

For the evaluation of the indirect cytotoxicity, 1 cm^2 samples of non-functionalized and functionalized cellulose in triplicate were sterilized in autoclave and incubated in a 24-well plate with 1 mL of growth medium for 24 h at 37°C in 5% CO_2 atmosphere. On the same day, 5×10^4 cells per well were seeded in a 24-well plate and incubated with 1 mL of growth medium in the same conditions. After 24 h, the medium was removed and replaced with conditioned medium. Non-conditioned medium was used as the positive control, whereas pure dimethyl sulfoxide (DMSO) was used as the negative control. The cells were incubated with the eluates for 24 h at 37°C in 5% CO_2 atmosphere. On the following day, the medium was removed and 1 mL of fresh medium containing 10% v/v of Alamar Blue was added to each well. The plate was then incubated in the same conditions for 4 h. After this time, 200 μL of the solution from each well were transferred into a 96-well plate. The absorbance was measured at 570 nm and normalized to the absorbance at 600 nm using a FluoStar Optima plate reader (SMG Labtech). The cell viability was then calculated through comparison of each value to the positive control using the formula below:

$$\text{Cell viability} = \frac{Ax}{Ap} \times 100$$

A_x = absorbance of the solution – absorbance of TCP/10% Alamar Blue.

A_p = absorbance of the positive control – absorbance of TCP/10% Alamar Blue.

Direct Cytotoxicity Assay

The cell viability after direct contact with functionalized cellulose was evaluated following the ISO 10993-5 procedure for the biological characterization of medical devices. 1 cm^2 samples of non-functionalized and functionalized cellulose in triplicate were sterilized in an autoclave and pre-conditioned with 1 mL of growth medium for 24 h at 37°C in 5% CO_2 atmosphere. On the same day, 5×10^4 cells per well were seeded in a 24-well plate and incubated with 1 mL of growth medium under the same conditions. After 24 h, the medium was removed from the cells and the samples were placed directly onto the cell layer. 1 mL of fresh medium was added into each well. Growth medium was used as the positive control and pure DMSO was used as the negative control. The cells were incubated with the samples at 37°C in a 5% CO_2 atmosphere. Cell viability was determined after 1, 3, and 6 days through Alamar Blue assay following the procedure described in section "Indirect Cytotoxicity Assay." After 6 days of contact with the samples, the cells were stained and their morphology was visually evaluated. Two stains were used, i.e., rhodamine phalloidin and 4',6-diamino-2-phenylindole, dilactate (DAPI). First, the cells were fixed with a 4% formaldehyde-based fixation buffer and incubated for 30 min at room temperature. After this, the excess buffer was removed by washing with PBS solution. 0.1% Triton X-100 in PBS was then added to increase the permeability, incubated for 3–5 min and washed with PBS three times. Finally, the staining solution containing 8 μL/mL rhodamine phalloidin and 1 μL/mL DAPI was

added to the cells. The images were acquired with a confocal microscope, Leica TCS SP2.

In vitro Scratch Assay

The migratory and proliferative ability of keratinocytes in the presence of the cellulose samples were evaluated through *in vitro* scratch assay. 1 cm^2 samples in triplicate of non-functionalized and functionalized cellulose were sterilized in an autoclave and pre-conditioned with 1 mL of growth medium for 24 h at 37°C in 5% CO_2 atmosphere. On the same day, 1×10^5 cells per well were seeded in a 24-well plate and incubated with 1 mL of growth medium in the same conditions. After 24 h, the medium was removed from the cells and a scratch was made in the cell monolayer using the tip of a P200 pipette. The cells were then washed with 1 mL of PBS solution to remove the cell debris and a reference mark was made next to the scratch with an ultrafine tip marker. The cellulose samples were then placed directly onto the cell layer together with 1 mL of fresh medium. Growth medium was used as the positive control, whereas pure DMSO was used as the negative control. At time 0, the width of the scratch was set as 100% and the scratch coverage by cells at 0%. The progressive coverage of the scratched area by cells was observed using an Olympus CKX41 microscope, bright field, magnification 40× and 100×. The images were acquired with a QIClick^{TM} CCD Camera from QImaging. The pictures were adjusted using GIMP, an open source software: the contrast was minimized and the brightness was increased in order to have a clear distinction between the cells (white pixels) and the scratch (black pixels). The analysis of the image was carried out with ImageJ (National Institutes of Health, United States). The percentage of coverage of the scratch was considered as the ratio between white pixels and black pixels in that area and was monitored over time through quantification of the black pixels in the image.

RESULTS

Bacterial Cellulose Production

Bacterial cellulose is secreted extracellularly by bacteria in the form of glucan chains that self-assemble into microfibrils immediately outside the cell membrane (Chawla et al., 2009; McCarthy et al., 2019). As a result, *Gluconacetobacter xylinus* cells remain trapped within the highly porous structure in the interstices between the fibrils. In light of this, a high-temperature basic treatment was carried out to ensure the complete removal of the biomass (**Figure 1**).

The SEM analysis of the pellicles before purification showed the presence of cells in the network, whereas after the treatment bacteria appeared to be successfully removed without significant degradation or alteration of the arrangement of the chains and the supramolecular structure of cellulose.

The water content of the pellicles produced was also evaluated. The difference in the weight of cellulose samples was evaluated before and after drying under a hood for 24 h. As expected, the pellicles presented an average 97% w/w of water, confirming the hydrogel nature of the biomaterial. The moisture incorporated during the synthesis was in fact retained and stabilized by the highly porous network, which turns BC into an optimal substrate for applications on dry wounds. Moreover, the drying time was found to be much longer when exposed to air, with a total of 4–5 days required for dehydration, which is beyond the range of the average dressing change period for hydrogels, i.e., 1–3 days (Purser, 2010; Sood et al., 2014).

Chemical Functionalization

As cellulose lacks antibacterial features, the pellicles produced were subjected to chemical treatment in order to incorporate active functional groups through covalent attachment to the polymer backbone. More specifically, two different epoxides were used for this purpose, namely glycidyl trimethylammonium chloride (GTMAC) and glycidyl hexadecyl ether (GHDE) (**Figure 2**).

A ring-opening reaction was carried out under heterogeneous conditions by basic pre-treatment to achieve the deprotonation of the surface hydroxyl groups of cellulose followed by simultaneous addition of the epoxides. First, the hydroxyl groups were deprotonated through basic pre-treatment using 5% w/w NaOH. The active reagents were then added to the reaction mix simultaneously (**Figure 3**). No macroscopic modifications were observed after the reaction, with the hydrogel retaining the same color and appearance.

Chemical Characterization

As cellulose does not present inherent antibacterial properties, the membranes produced were chemically modified in order to achieve this functionality through reaction with two epoxides, namely GTMAC and GHDE. To investigate the degree of substitution, the material was characterized using solid-state techniques due to the insolubility of cellulose in common solvents. First, EDX spectroscopy was performed to confirm the presence of the elements belonging to the functional groups introduced (**Figure 4**). As carbon and oxygen were already present in the structure of unmodified cellulose, the analysis did not allow to confirm the incorporation of GHDE. However, it was observed that nitrogen and chlorine were successfully introduced as a result of the reaction with GTMAC.

A quantitative indication of the surface elemental composition of the functionalized material was then obtained through XPS spectroscopy (**Table 1**). The analysis evidenced a significant increase in the nitrogen content (from 0.29 to 2.63 of atomic percent) as a result of the reaction performed. The presence of nitrogen in plain cellulose could be attributed to residual traces of the culture medium or environmental impurities. As regards the amount of carbon and oxygen, their abundance remained almost constant due to their predominance in the material; however, the relative oxygen content in the modified cellulose showed a decrease (from 38.35 to 35.83%), while the amount of carbon remained constant. This result could indicate the successful incorporation of GHDE. The reagent presents in fact long alkyl chains with a carbon to oxygen ratio of 9:1, whereas the ratio in glucose is 1.2:1, which is closer to the C/O ratio obtained for the unmodified sample as compared to the modified one.

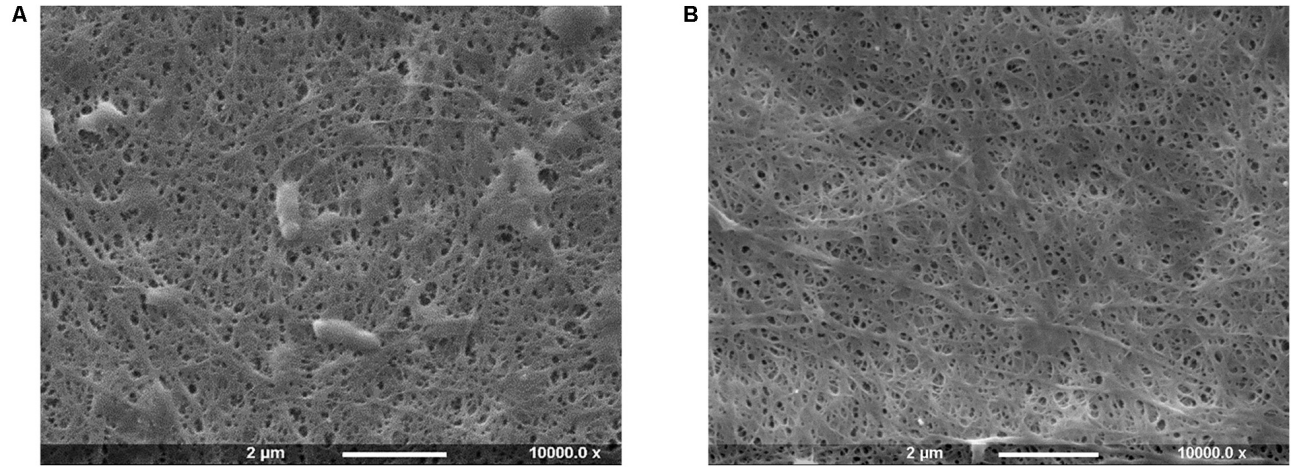

FIGURE 1 | SEM images of bacterial cellulose pellicles before **(A)** and after **(B)** purification treatment.

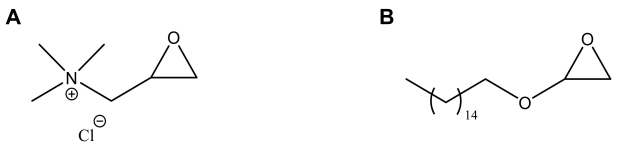

FIGURE 2 | Chemical structure of **(A)** GTMAC and **(B)** GHDE.

Rheological Measurements

The viscoelastic properties of the material upon chemical modification were investigated through rheological studies. The storage and loss moduli (respectively, G' and G'') for frequency sweep and temperature ramp assays were determined and compared. Both tests were performed in the linear viscoelastic region (LVR).

The frequency sweep analysis (also called small amplitude oscillatory shear, SOAS) showed that both materials behaved as self-standing hydrogels, with the storage modulus (G') higher than the loss modulus (G'') at all the frequencies tested (**Figure 5**). The two materials exhibited similar behavior, with same trend for both dynamic moduli. In particular, G' increased proportionally with the frequency, while G'' presented relatively lower degree of variation throughout the test. This result indicated that the elastic component of the mechanical properties of the material was more affected by the increase in the shear rate, which is typical for hydrogels. Although both samples showed a more elastic-like response to the stimuli, the reaction performed caused a significant decrease of the storage modulus from 2000 Pa for the unmodified sample to almost 900 Pa for the modified one at 0.1 Hz. The same tendency was noted at higher frequencies, where the maximum storage modulus value for the unmodified was about 11,700 Pa vs. ≈9000 Pa for the modified specimen. As regards the viscous component (expressed by the loss modulus), for both hydrogels a linear increase of circa 1000 Pa was observed from 0.1 Hz up to about 35–40 Hz. At higher shear rate, i.e., in the 40–50 Hz region, a higher increase was registered especially in the case of the modified cellulose, with a final G'' value of about 1570 Pa and 1700 Pa, respectively, for plain cellulose and functionalized cellulose.

The effect of the temperature variation on the viscoelastic behavior of the hydrogels was then analyzed by performing a temperature ramp assay in the range between 10 and 60°C (**Figure 6**). For this test, the two materials showed overlapping values for both storage and loss moduli at all temperatures. As in the case of the frequency sweep assay, the hydrogels presented a solid-like response ($G' > G''$) in the range considered. The storage modulus values at 10°C showed minimal decrease for the functionalized sample (1230 Pa) as compared to the non-functionalized one (1260 Pa). The same trend was observed at higher temperatures, with G' of about 1030 Pa and 1020 Pa, respectively, for the unmodified and modified pellicles at 60°C. For both samples, a decrease of ≈17–18% in the storage modulus was detected with the increase of temperature, which indicated a more viscous behavior at higher temperatures, as expected in the case of a solid material. However, the presence of a high amount of water (i.e., 97%) did not appear to massively affect the mechanical properties, with the hydrogels retaining a solid-like behavior with good degree of stiffness up to 60°C. The loss modulus values for the two hydrogels showed once again very similar behavior, with only a slight decrease at higher temperatures (about 236–200 Pa for the unmodified and about 237–190 Pa for the modified cellulose), thus indicating that there was no significant effect of the temperature on the viscous component. Overall, the assay confirmed that the functionalization process did not have an adverse impact on the structure and the viscoelastic properties of the material, which maintained a self-standing network in the range of temperatures tested.

Stability Studies

The stability of the pellicles in liquid media before and after the reaction was also investigated. The test was conducted

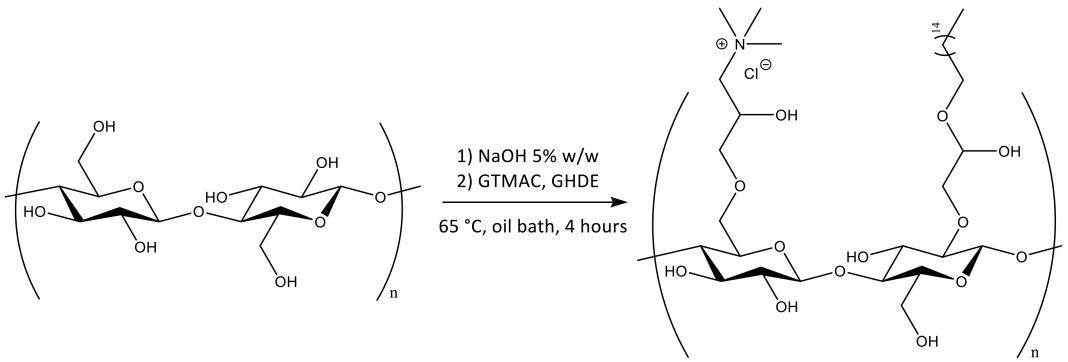

FIGURE 3 | Chemical functionalization of the surface hydroxyl groups of BC by reaction with GTMAC and GHDE.

FIGURE 4 | EDX spectrum of modified cellulose.

in PBS solution and keratinocytes growth medium (KGM) at 32°C, which has been reported as the average temperature of an acute wound-bed (Fierheller and Sibbald, 2010; Power et al., 2017). The weight variation (ΔW) over 7 days of static incubation in both media was calculated for the two samples and compared (**Figure 7**).

Both tests indicated that no significant degradation of the material took place in the timeframe considered as a result of the functionalization. As regards the stability in PBS solution, the weight of modified cellulose reached a plateau after about 3 days, with a value of 85% of the initial wet weight that remained constant for up to 7 days upon incubation in the medium. The weight of the unmodified hydrogel, on the other hand, presented a higher degree of variation over time. After 3 days, the sample lost about 10% of the initial weight, and the weight remained almost constant until day 7, with total weight loss of about 5–10%. Overall, the two materials did not show any statistically significant difference at any time point ($p > 0.05$). In the case of incubation in keratinocytes growth medium, the behavior appeared to be reversed, with the non-functionalized sample reaching a plateau in the weight after 3 days (final value: 85% of the initial weight). The weight of the functionalized cellulose decreased by 10% after one day, with a final weight of 90–93% as compared to the initial one. Once again, the two sets of data did not differ significantly for the time points considered, except for day 3 ($p = 0.01$).

TABLE 1 | XPS quantitative elemental analysis of unmodified and modified cellulose.

	Element	Area	Atomic %
Non-functionalized cellulose	O 1s	2386607.93	38.35
	C 1s	1303162.96	61.36
	N 1s	11008.54	0.29
Functionalized cellulose	O 1s	2072893.74	35.83
	C 1s	1215029.43	61.54
	N 1s	93556.40	2.63

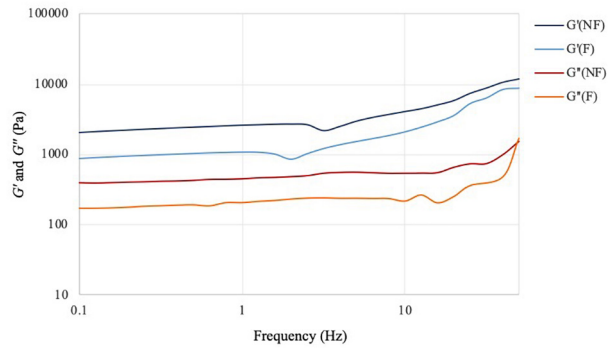

FIGURE 5 | Frequency sweep test of bacterial cellulose before (NF) and after (F) functionalization. T = 32°C; preload = 6 Pa.

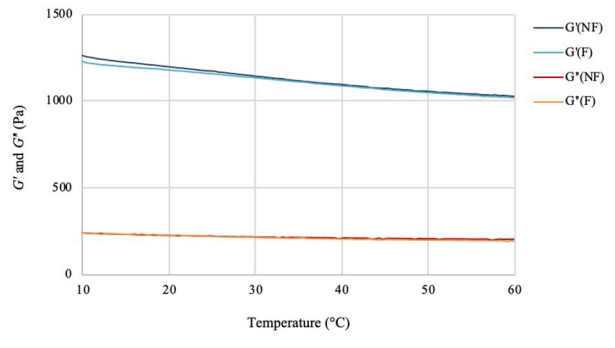

FIGURE 6 | Temperature ramp test of bacterial cellulose before (NF) and after (F) functionalization. f = 1 Hz; preload = 6 Pa, rate = 5°C/min.

Biological Characterization

Antibacterial Assessment

The functionalization of the hydroxyl groups of cellulose led to the development of an inherently antibacterial hydrogel with covalently bonded agents, as confirmed by the characterizations carried out after thorough washing of the pellicles to remove any unreacted species. In light of this, the antibacterial properties assessment was conducted through evaluation of the activity upon direct contact with bacteria. The study was carried out following an adapted protocol based on the standard procedure ISO 22196, which involves the quantification of the antibacterial activity with respect to the untreated material (i.e., non-functionalized BC). As indicated in the standard,

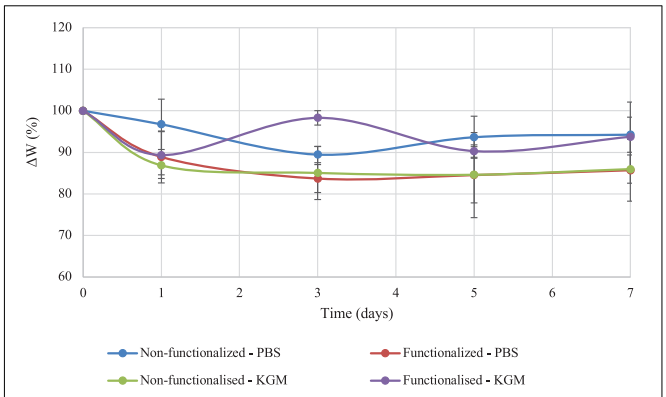

FIGURE 7 | Stability of unmodified and modified bacterial cellulose in PBS solution and keratinocytes growth medium (KGM) at 32°C.

two strains were used, namely Gram-positive *Staphylococcus aureus* subsp. aureus Rosenbach 6538^{TM} and Gram-negative *Escherichia coli* (Migula) Castellani and Chalmers ATCC® 8739^{TM}. The test was first conducted against *S. aureus*. The percent antibacterial activity (*R%*) obtained was calculated as the difference between the number of residual cells on the modified sample and the control divided by the number of residual cells on the control (**Figure 8**). The value obtained indicated that the bacterial cells growing on the surface of the modified pellicle were reduced by more than half as compared to the unmodified one (i.e., 53%), with a statistically significant reduction of about one order of magnitude in the population in the first 24 h.

The assay was then performed using *E. coli* to investigate the effect of the material against Gram-negative strains. The same ISO 22196 procedure was followed to obtain comparable results and the *R%* value was calculated using the same formula (**Figure 9**). Once again, the number of viable cells

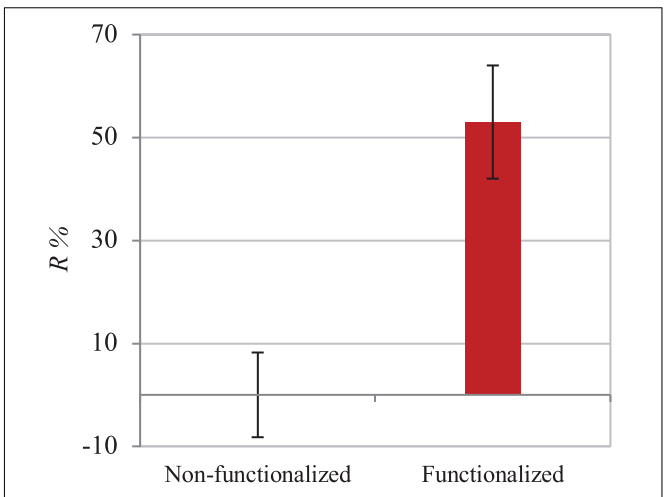

FIGURE 8 | Antibacterial activity of non-functionalized and functionalized BC against *S. aureus*.

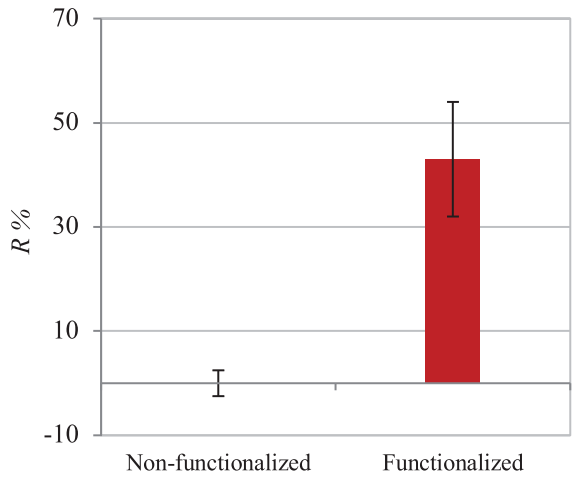

FIGURE 9 | Antibacterial activity of non-functionalized and functionalized BC against *E. coli*.

decreased by almost half in 24 h as compared to the untreated hydrogel (43%). A statistically significant difference ($p < 0.05$) between the samples before and after functionalization was in fact observed, confirming the effect of the reaction in the successful inhibition of bacterial proliferation.

Biocompatibility Studies

Cytotoxicity evaluation

The direct and indirect cytotoxicity of the cellulose hydrogels was assessed using keratinocyte human epidermal cells (HaCaT cell line). First, the indirect cytotoxicity was studied to evaluate the presence of leachable products released from the membranes that could cause an adverse effect on the cellular growth (**Figure 10**). Both samples presented a high degree of biocompatibility, with over 90% cell viability. Furthermore, it was possible to observe that the reaction carried out did not introduce any leachable compound that could have a cytotoxic effect on keratinocytes, as no statistically significant difference was observed between the unmodified and the modified pellicle.

The direct cytotoxicity of the materials was then evaluated following the standard ISO 10993-5 for the biological characterization of medical devices. The cell viability was evaluated after 1, 3, and 6 days of direct contact with the samples (**Figure 11**). Once again, cell viability values of at least 90% as compared to the positive control were registered for the hydrogels at all timepoints. After 1 day, both samples presented ≈100% cell viability, with no statistically significant difference with the positive control ($p > 0.05$), whereas on day 3 the viability was found to be in the range of 90–95% (94 and 92% for the unmodified and modified pellicles, respectively). After 6 days of incubation with the samples, the cell viability was almost 90% for the neat cellulose and about 93% for the functionalized one. Overall, although the average values of cell viability in the presence of functionalized and, especially, non-functionalized BC seem to decrease over time, no statistically significant difference was observed between the two materials and the positive control for up to 6 days of direct contact with the cells ($p >> 0.05$ for non-functionalized and functionalized BC as compared to the positive control at all time points).

In addition to this, the morphology of the cells after 6 days of contact with the hydrogels was evaluated through fluorescent staining of the nuclei and the actin filaments using, respectively, DAPI and phalloidin, and was compared to the control group (**Figure 12**).

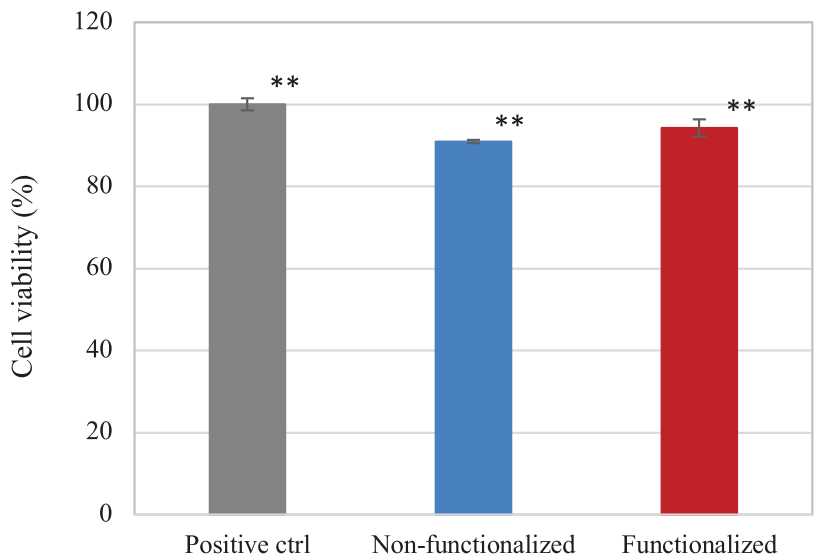

FIGURE 10 | Viability of HaCaT cells upon contact with undiluted eluates from the BC samples. Non-functionalized and functionalized cellulose were found to be significantly different as compared to the positive control, i.e., keratinocytes growth medium (**$p < 0.01$), whereas no significant difference was observed between the two samples ($p = 0.06$).

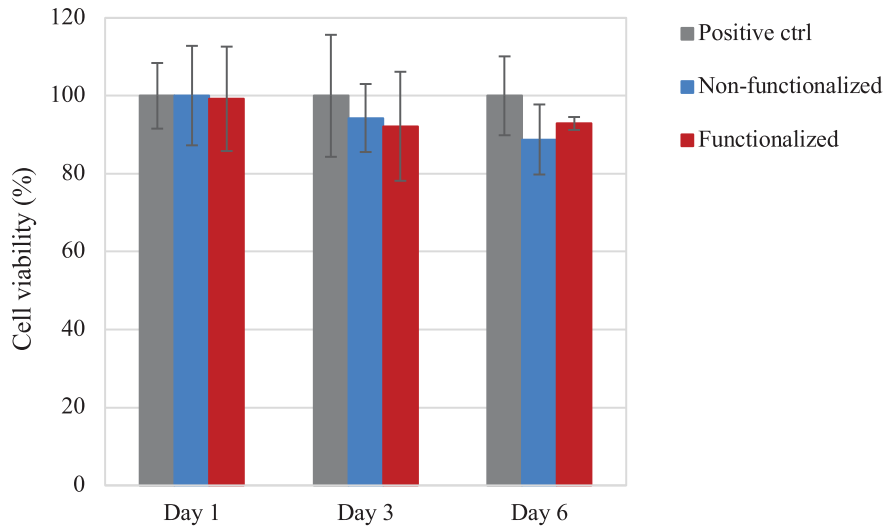

FIGURE 11 | Viability of HaCaT cells upon direct contact with the BC samples. No statistically significant difference was observed between both cellulose samples and the positive control (i.e., tissue culture plastic, TCP) at any time point ($p > 0.05$).

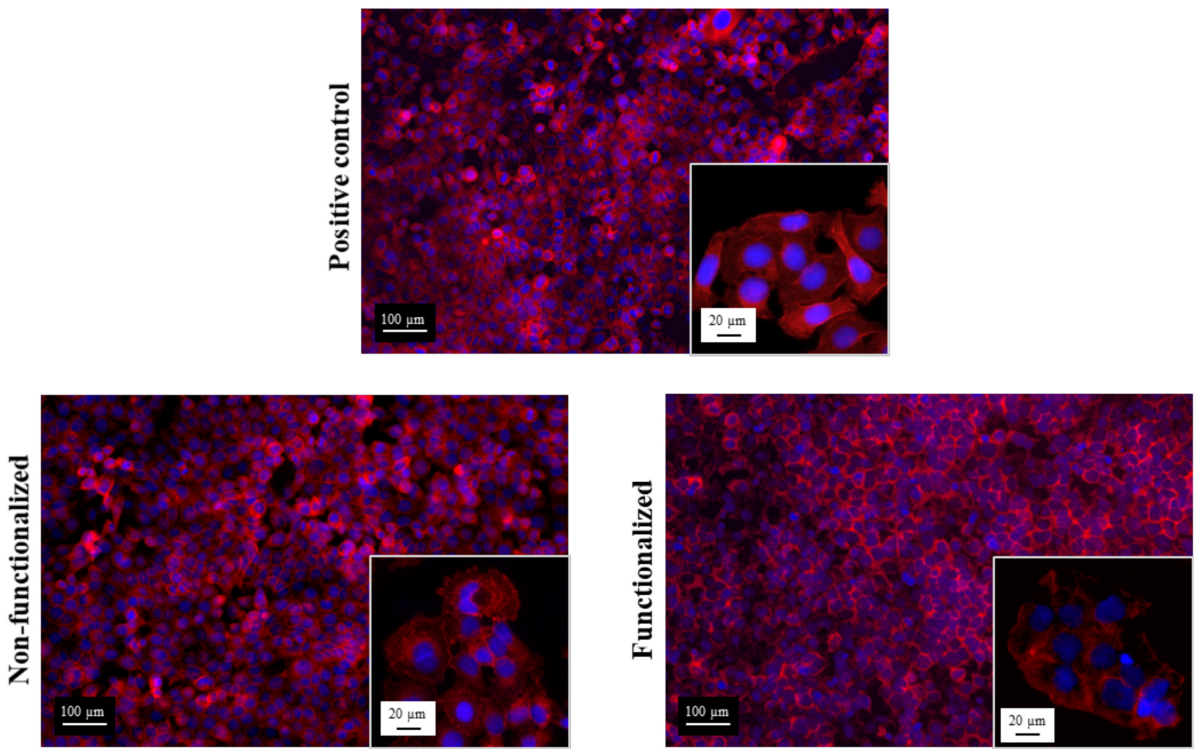

FIGURE 12 | Confocal microscopies of keratinocytes after 6 days of incubation on the bacterial cellulose stained using phalloidin (red) and DAPI (blue).

All the images confirmed the formation of a homogeneous monolayer of adherent keratinocytes. No qualitative difference in the morphology was observed between the three groups, confirming that the cellulose hydrogels supported the growth and proliferation of the cells. In particular, a polygonal morphology typical of keratinocytes was observed, with the cells arranged in a "cobblestone" pattern. The nuclei appeared to be spherical, surrounded by a homogeneous cytoplasmic region. The size and structure of the cells was found to be the same for the ones in contact with the samples and the positive control, with an average diameter of about 15–20 µm.

In vitro scratch assay

An *in vitro* scratch assay was carried out using immortalized keratinocyte cells obtained from histologically normal skin in order to investigate the wound healing process in the presence of the hydrogels. This test allows in fact to assess the cell mobility without and in the presence of cellulose samples through creation of a scratch in the cell monolayer. The migration and proliferation of the cells over time was then evaluated until wound closure. In this study, the wound margins were observed over 7 days until complete coverage of the scratch (**Figures 13**, **14**). The images showed that for all the groups almost complete closure was reached within 5 days. The presence of the two hydrogels did not inhibit cell migration to the wound area, and the recovery rate was found to be very similar for the two hydrogels and the control, i.e., keratinocytes growth medium only. After 2 days, the scratched area started to be covered with keratinocytes, proving that the cells were alive and active from both migratory and proliferative point of view.

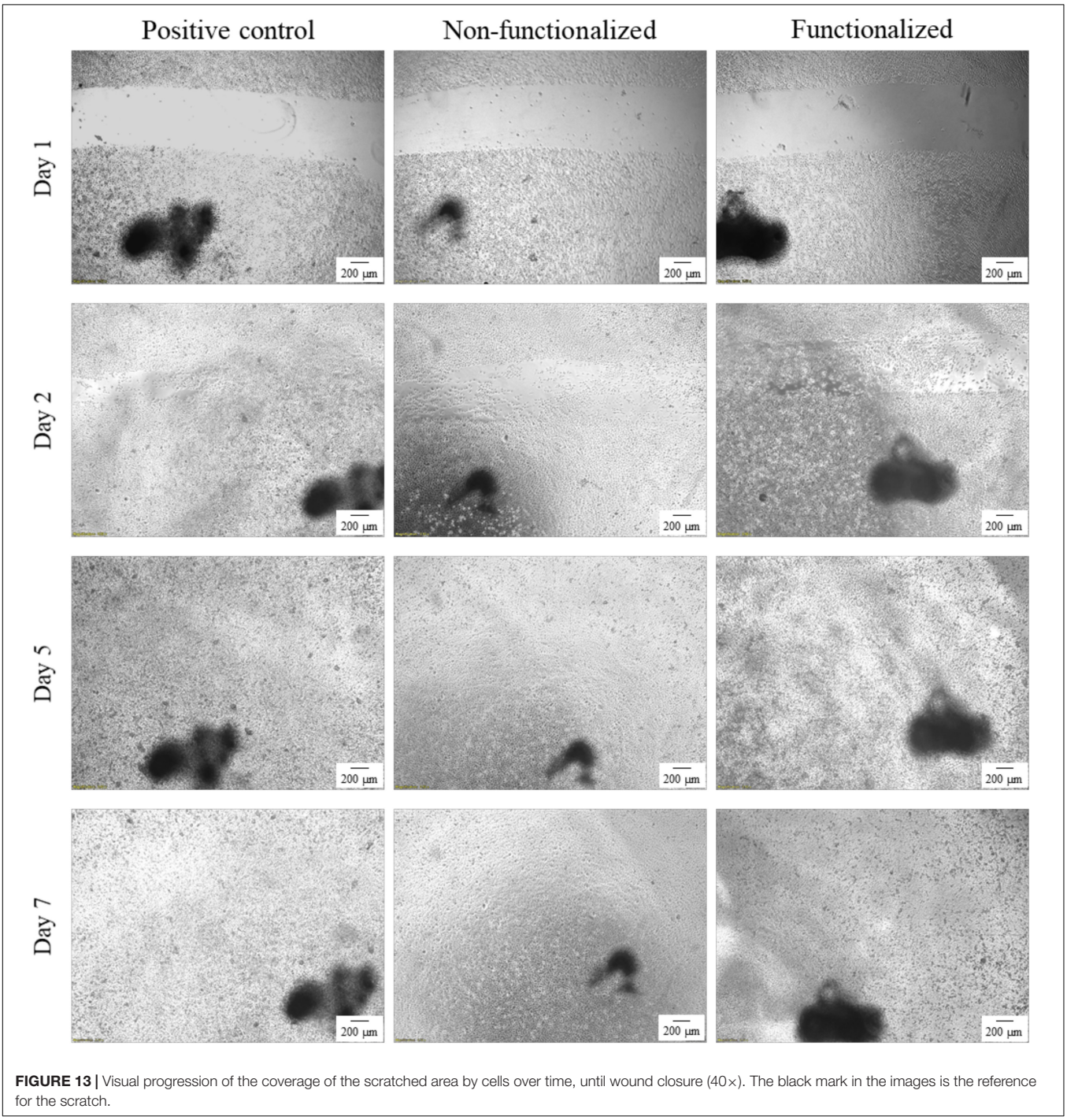

FIGURE 13 | Visual progression of the coverage of the scratched area by cells over time, until wound closure (40×). The black mark in the images is the reference for the scratch.

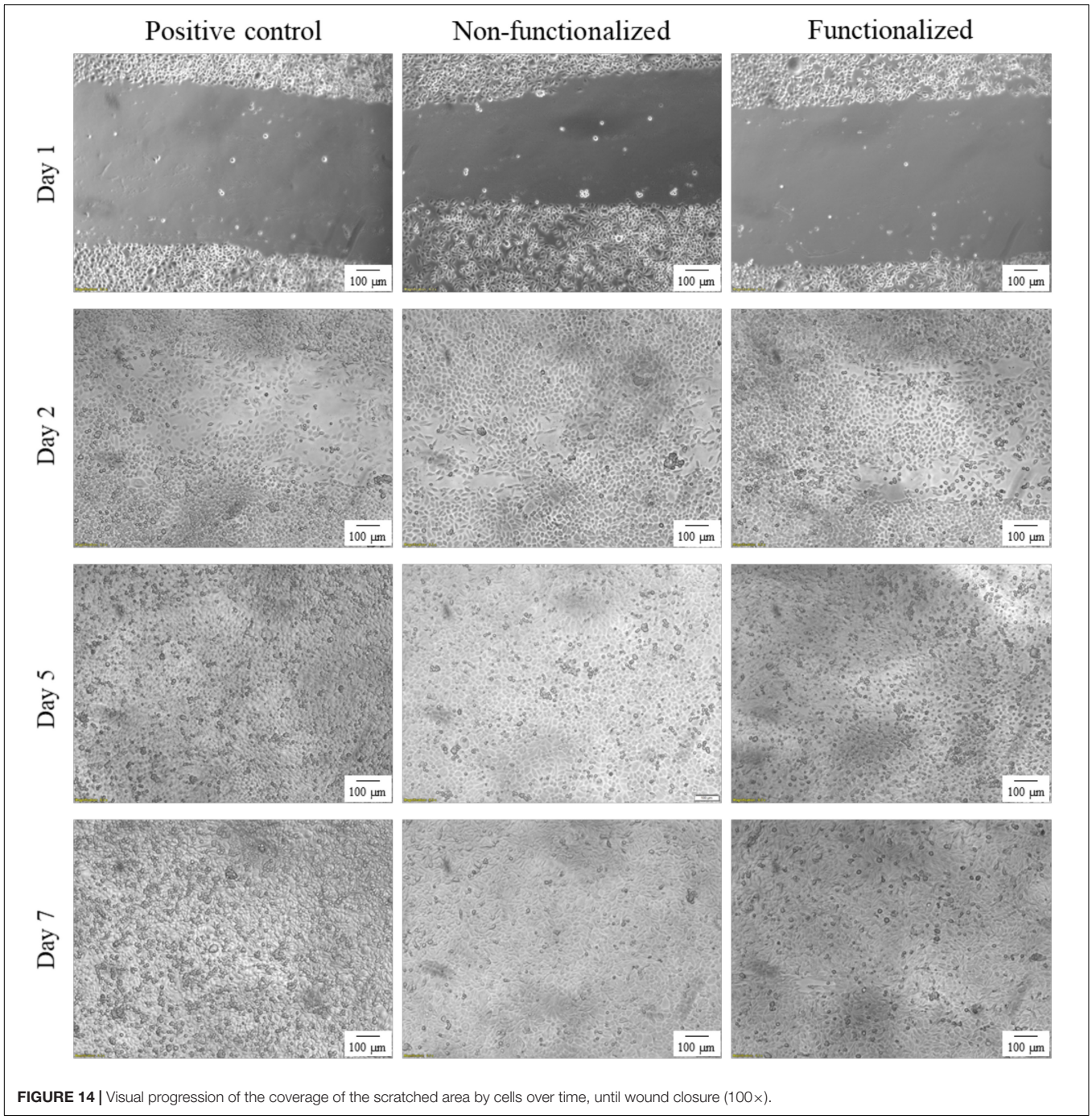

FIGURE 14 | Visual progression of the coverage of the scratched area by cells over time, until wound closure (100×).

After a first qualitative assessment, the images were analyzed in order to quantitatively evaluate the rate of wound closure in the presence of unmodified and modified cellulose and in comparison with the control. The percent of the scratched area covered by cells over time was quantified using an image processing software by considering the extension of the area covered by cells (white pixels) and the area not covered by cells (black pixels) (**Figure 15**). As expected, the calculations confirmed that the three groups showed similar behavior and wound progression trend, with a linear decrease of the scratch and almost complete coverage by the cells within 5 days. In particular, for the unmodified cellulose wound closure of 100% was reached, whereas both the modified and the positive control presented a value of ≈90%. The statistical analysis carried out for the values obtained at each time point showed no significant difference between the functionalized hydrogel and the control at any time point. A similar trend was observed for the non-functionalized sample, although this was found to significantly differ from the control on day 1 and day 2 (p = 0.03 and p = 0.04, respectively).

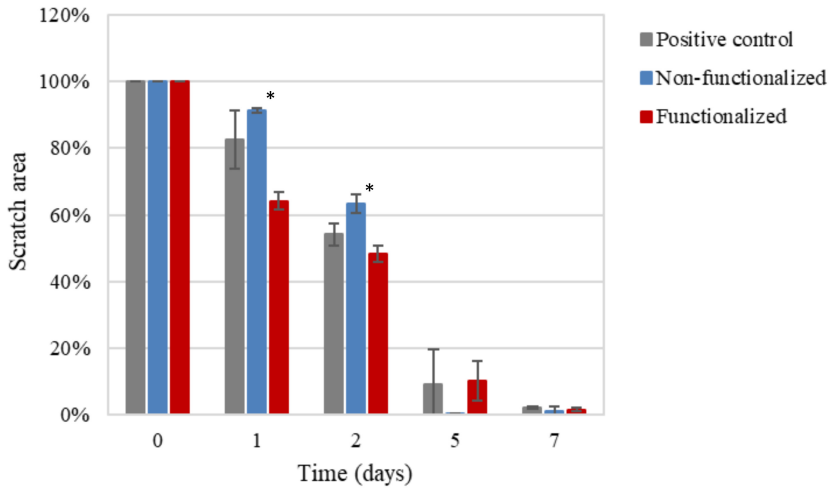

FIGURE 15 | Progression of the closure of the scratch area over time as the ratio between black pixels at time × and black pixels at time 0 (set as 100%, i.e., no coverage by cells). The non-functionalized cellulose group was found to be significantly different as compared to the positive control, i.e., keratinocytes growth medium, at day 1 and 2 (*$p < 0.05$), whereas no significant difference was observed between the functionalized cellulose and the control at any time point.

DISCUSSION

In this study, a water-based green method for the surface modification of bacterial cellulose was proposed to impart antibacterial activity. To achieve so, BC pellicles were produced through static fermentation of *Gluconacetobacter xylinus* in the presence of glucose as the main carbon source. More specifically, a modified HS medium was used, which consisted of glucose, yeast extract and $CaCO_3$. Although several sugars such as mannitol, sucrose and fructose have been successfully used as carbon sources, it was observed that glucose resulted in higher yield under the conditions applied in this study. Similarly, yeast extract was found to give higher yield as compared to other nitrogen sources, including corn steep liquor and beef extract (Son et al., 2001; Jia et al., 2004; Castro et al., 2012). Finally, calcium carbonate was chosen as the metal ions source, as recent studies evidenced that the introduction of ions such as calcium and magnesium results in an increase of the polymer production yield (Son et al., 2003; Hungund and Gupta, 2010; Hong et al., 2011).

The heterogeneous reaction was then conducted in one step upon deprotonation of the hydroxyl groups of the glucose units in the presence of sodium hydroxide. The derivatization of the hydroxyl groups was carried out through a base-catalyzed ring-opening reaction of two epoxides involving the alkylation of the oxygen, thus resulting in the etherification of the hydroxyl groups. The reaction is believed to proceed as a regioselective nucleophilic attack (probably via a S_N2 mechanism) of the oxygen to the less hindered electrophilic carbon of the epoxide ring (Padwa and Murphree, 2000; Smith, 2010). The functionalization was performed using water as the solvent, both because of the high original water content of the substrate, as this polysaccharide is naturally biosynthesized as a hydrogel with a minimum water content of 97% (even higher values might be obtained through harsher drying techniques such as freeze-drying or oven-drying), as well as to ensure that no traces of toxic volatile solvents that could alter the crystalline organization of the fibrils would remain in the network. Due to the intrinsic insolubility of cellulose in most solvents, solid-state techniques were used to characterize the modified material. In particular, EDX and XPS were carried out on the hydrogel before and after functionalization to evaluate the degree of substitution. The presence of the nitrogen and chlorine peaks in the EDX spectrum indicated successful incorporation of GTMAC. In addition to this, the increase in the nitrogen content as well as the decrease in the superficial carbon to oxygen ratio detected by the XPS further confirmed the attachment of both GTMAC and GHDE. As compared to the EDX analysis, however, XPS did not detect chlorine in the area considered. This result might be related to the ability of XPS to give information only for the most external layer of the sample, i.e., 0.8–5 nm, whereas in the case of EDX the elemental composition of the outer 0.2–8 μm region can be observed (Walzak et al., 1998). It is possible, in fact, that chlorine (a counterion) was not visible as it had been displaced before/during the analysis due to the non-covalent nature of the bond with the quaternary ammonium. In addition to this, it is also possible that the XPS analysis did not detect chlorine in the area of analysis due to the inhomogeneity of the reaction, which was conducted under heterogeneous conditions. Nevertheless, the analyses showed that the epoxides were permanently bonded to the polymer backbone, as the washing procedure to which the pellicles were subjected prior to the characterization did not affect the result. This finding is particularly important with respect to the antibacterial properties of the dressing. A permanent modification of the structure can in fact ensure long-term activity against bacteria, as opposed to the physical absorption of leachable agents, which is limited by the maximum loading amount that can be incorporated into the matrix and released over time (Poverenov et al., 2013; Giano et al., 2014).

The effect of the reaction on the mechanical properties of BC was investigated through rheological studies. The storage and loss moduli (respectively, G' and G'') of the hydrogels were measured through frequency sweep and temperature ramp assays. As regards the frequency sweep assay, similar trends were observed for the two samples, with increasing storage modulus as a response to increased oscillation rate and lower degree of variation for the loss modulus in the interval of frequencies applied. This is a common feature for hydrogels, as they typically present a more solid-like response at increased frequencies, i.e., higher stiffness upon fast movement in a short time-scale (Sanabria-DeLong et al., 2007; Yan and Pochan, 2010). The results obtained for the functionalized sample evidenced a slight decrease in the storage and loss moduli. The effect could probably be ascribed to the high temperature and basic treatment required for the reaction, which might have caused a certain degree of degradation due to alkaline hydrolysis of the polymer (Shibazaki et al., 1997; Reiniati et al., 2016). Nevertheless, the hydrogel presented a predominantly elastic response with $G' > G''$ at all the conditions tested. Similar results were observed for the temperature ramp test, with only 1–2% variation for both dynamic moduli even at higher temperatures. Overall, the membranes presented good mechanical properties as compared to previously published results based on cellulose hydrogels as well as synthetic polymers-based substrates. It was found, in fact, that most hydrogels exhibit a more viscous behavior at temperatures over 35–40°C, probably due to the degradation of the crystalline regions that results in the disruption of the 3D-network (Van Den Bulcke et al., 2000; Huang et al., 2010; Roy et al., 2010; Smith et al., 2010; Zuidema et al., 2014). This effect was not observed in this study, as the membranes retained a solid structure and good stiffness even at 60°C. This is a crucial feature for wound healing applications, as a dressing needs to be easy to handle and to remove (for dressing change), stiff enough to sustain the cell growth and the tissue surrounding the wound while able to adapt to its shape (Boateng et al., 2008; Kocen et al., 2017). Furthermore, a stability study was conducted on BC in order to assess the degradation of the pellicles in liquid media in terms of weight loss. The test did not evidence major degradation over 7 days, as both samples retained circa 85–90% of their initial weight in PBS solution and keratinocytes growth medium with no statistically significant difference between them except for one time point.

Finally, the hydrogels were characterized from the biological point of view to assess both their antibacterial properties and their biocompatibility. In particular, as the agents were covalently bonded to the backbone of the polymer, the antibacterial activity was studied following a direct contact protocol. For both *S. aureus* and *E. coli*, the functionalized material caused a decrease by circa half in the cell count as compared to plain cellulose. More specifically, a 53% reduction was observed for *S. aureus* vs. 43% in the case of *E. coli*. This difference in the activity can be ascribed to the structure of the cell membrane of Gram-negative bacteria as well as the mechanism of action of the groups involved. Gram-negative strains possess an outer membrane in addition to the peptidoglycan layer. This membrane consists of a lipid bilayer containing phospholipids and glycolipids and acts as a permeability barrier, making the cell less susceptible to the penetration of biocidal agents (Silhavy et al., 2010; Malanovic and Lohner, 2016; Miller, 2016; Exner et al., 2017). Due to this additional layer, Gram-negative bacteria are considered a greater threat in the medical field since they show higher degree of resistance toward traditional antibiotics. In this context, few substances have been found to be active against Gram-negative bacteria. Among these, quaternary ammonium groups have demonstrated to act against a broad spectrum of microorganisms thanks to their non-selective mechanism of action. As mentioned in the introduction, it is commonly acknowledged that the biocidal activity of these compounds is related to the cationic nature of the nitrogen, which is able to electrostatically interact with the negative charges of the bacterial cell membrane. Zeta potential and electrophoretic mobility studies on *E. coli* and *S. aureus* showed in fact a net negative charge on the bacterial cell envelope, although higher values were registered for *E. coli* (Sonohara et al., 1995; Halder et al., 2015). These results indicated that the presence of the additional negatively charged layer in Gram-negative strains caused an increase in the anionic potential of the membrane, suggesting that achieving a higher cationic charge density on the polymer might have a stronger impact against such bacteria (Silhavy et al., 2010). In addition to this, the alkyl chains attached to the backbone probably contributed to the overall antibacterial activity thanks to their lipophilic nature. It has been proven that such groups can penetrate through the lipid regions of the membrane through hydrophobic interactions, thus causing its disruption with consequent leakage of intracellular components. In particular, the activity was found to be dependent on the chain length, with the optimal carbon chain in the range between C_{12} and C_{14} (Kubo et al., 1993; Wiener and Horanyi, 2011; Zheng et al., 2016). In light of the results obtained, it is also worth mentioning that an increase in the effectiveness of the reaction would probably lead to higher antibacterial action. It has been reported that the presence of water can decrease the degree of substitution in ring-opening reactions due to the hydrolysis of the alkylating agent under basic conditions (Zaman et al., 2012). This effect, together with the solid-liquid reaction kinetics, could have caused an anisotropy in the bactericidal activity. It is in fact possible that the heterogeneous conditions applied led to the non-homogeneous distribution of the functional groups, causing some differences in the surface structure and, therefore, the antibacterial effect (Ramsden, 2011; Salmi et al., 2013).

The biocompatibility of the modified hydrogel was studied using the human epidermal keratinocyte cell line (HaCaT) and compared to pristine BC. First, the cytotoxicity upon indirect contact was evaluated to investigate the presence of residual leachable compounds that could cause an adverse reaction toward cells. A direct cytotoxicity assay was then carried out over a period of 6 days, as the average time between two consecutive dressing changes has been reported as 1–3 days (Purser, 2010; Sood et al., 2014). In all cases, cell viability of about 90% was obtained for both materials, with no statistically significant difference between BC and the positive control at any timepoint. The results obtained were in line with previously published

literature on the cytotoxicity of various polymers derivatized with quaternary ammonium compounds. No inhibitory effect was in fact observed toward various types of cells including fibroblasts and human dental pulp cells, confirming the biocompatibility of such groups toward eukaryotic cells even when compared with well-established antibacterial agents such as silver (Ding et al., 2009; Li et al., 2013; Huang et al., 2018). After 6 days, the morphology of the cells was visually assessed through staining of the nuclei and the cytoplasm using DAPI and phalloidin. In all cases, the presence of an adherent monolayer of cells was observed, with the typical polygonal morphology of keratinocytes and a "cobblestone" growth pattern (Koehler et al., 2011). The size of the cells was also in accordance with previous studies. The diameter was in fact in the range of 15–20 μm, which has been indicated as the average size for young keratinocyte cells (Sun et al., 2007; Soroka et al., 2008). In addition to this, it is possible that a certain degree of penetration of the cells into the polymer matrix occurred. Previous works evidenced in fact the ability of BC to support the infiltration of cells throughout the third dimension of the scaffold, in a proportional manner with respect to the cells size and the pore size of the nanofibrillar structure (Luo et al., 2019; Ul-Islam et al., 2019b).

An *in vitro* scratch assay was also carried out in the presence of the cellulose-based hydrogels using keratinocyte cells. Despite the functionalization performed, the quantitative assessment of the scratch coverage by the cells evidenced no statistically significant difference between the modified cellulose and the control at any of the timepoints considered. In addition to this, the wound closure rate was found to be in agreement with the literature: after only 12 h, the wound started to be re-populated, showing a pattern of growth comparable with previously published research. Studies on the mechanism of wound healing indicated in fact that keratinocytes start migrating after 6–24 h upon wounding and express keratin after 8–24 h. This is a crucial step in the healing process, as cell migration is the rate-limiting event, with keratinocytes presenting lower migration rates as compared to dermal fibroblasts. In particular, fibroblasts are believed to be the first type of cells that migrate to the wound site together with endothelial cells, followed by keratinocytes that induce re-epithelialization. Finally, a remodeling stage takes place involving a second migration of fibroblasts (Usui et al., 2008; Walter et al., 2010). These encouraging findings prove that the reaction carried out induced an adverse effect against bacteria without affecting the wound healing process, as the cells presented good migratory ability in the short term as well as active proliferative behavior after various days of contact with the samples.

CONCLUSION

In this study, for the first time, a one-step method for the modification of never-dried bacterial cellulose was developed in order to introduce antibacterial features. The procedure proposed included a green-chemistry approach for the derivatization of the hydroxyl groups of glucose without using any toxic organic solvent. The functionalization was in fact carried out in water through base-catalyzed heterogeneous reaction with two different epoxides, without affecting the hydrogel structure of the biopolymer. The material was then chemically characterized to investigate the incorporation of the active groups. The viscoelastic behavior before and after the modification was also studied to assess the mechanical properties of the hydrogels. The tests highlighted that no major degradation occurred as a result of the chemical treatment, with very similar storage and loss moduli for both the frequency sweep and the temperature ramp assays. The stability studies confirmed these findings, as the samples retained good structural features for up to 7 days of incubation in liquid media. A biological evaluation was conducted to investigate the antiproliferative ability and cytotoxicity of the samples. First, the activity upon direct contact with *S. aureus* and *E. coli* was determined, and for both strains a reduction by circa half in the bacterial cell population was observed within 24 h in the case of the functionalized material as compared to the unmodified one. In addition to this, cytotoxicity studies evidenced that no adverse effect was caused by the cellulose hydrogels upon indirect or direct contact with keratinocytes even after 6 days of contact. The staining of the cells, in fact, did not reveal any difference in the morphology, growth pattern and size of the cells in the three groups. Finally, the *in vitro* scratch assay highlighted that the presence of the samples did not interfere with the healing process, with wound closure rates comparable to the control. Future works can focus on better characterizing the material developed from the chemical point of view, for instance by performing a solid-state NMR for the quantitative evaluation of the reaction yield as well as by assessing the elemental distribution related to the functional groups introduced in the structure. In addition to this, the mechanical properties of the modified pellicles can be further investigated with respect to their application as wound dressings, for instance through compressive dynamic mechanical analysis (DMA) and nanoindentation.

Overall, this work represents a promising strategy for the use of bacterial cellulose as a wound dressing platform with tailorable properties. Its innate hydrogel-like nature can in fact provide a high level of moisture to dry wounds and great biocompatibility, while the functionalization carried out can ensure an inhibitory effect against both Gram-positive and Gram-negative bacteria through an environmentally friendly procedure. Furthermore, this versatile methodology can also be applied to other polysaccharides such as hyaluronic acid and chitosan to introduce inherent antibacterial features or improve their efficiency.

DATA AVAILABILITY STATEMENT

All datasets generated for this study are included in the article/supplementary material.

AUTHOR CONTRIBUTIONS

IO performed the experiments, analyzed the data, and wrote the manuscript. PB developed and optimized the BC production method. RN contributed to the reaction design. WW supervised the scratch assay performed in this work. JCK was involved

in the SEM/EDX and confocal microscopy. IR supervised the experimental work and corrected the manuscript. All authors contributed to the article and approved the submitted version.

FUNDING

This work has received funding from the European Union's Horizon 2020 Research and Innovation Programme under the Marie Skłodowska-Curie actions (HyMedPoly project, Grant Agreement No. 643050). RN was supported by the FP7 Neurimp project (Grant Agreement No. 604450). PB was supported by the FP7 project Neurimp (Grant Agreement No. 604450) and the BBI/JU H2020 project PolyBioSkin (Grant Agreement No. 745839). IR was supported by the BBI/JU H2020 projects PolyBioSkin (Grant Agreement No. 745839) and ECOAT (Grant Agreement No. 837863).

REFERENCES

Abdelrahman, T., and Newton, H. (2011). Wound dressings: principles and practice. *Surgery* 29, 491–495. doi: 10.1016/j.mpsur.2011.06.007

Abid, C. K. V. Z., Chattopadhyay, S., Mazumdar, N., and Singh, H. (2010). Synthesis and characterization of quaternary ammonium PEGDA dendritic copolymer networks for water disinfection. *J. Appl. Polym. Sci.* 7, 23–42. doi: 10.1002/app.31510

Anderson, D. J., Podgorny, K., Berríos-Torres, S. I., Bratzler, D. W., Dellinger, E. P., Greene, L., et al. (2014). Strategies to prevent surgical site infections in acute care hospitals: 2014 update. *Infect. Control Hosp. Epidemiol.* 35, 605–627. doi: 10.1086/676022

Antonucci, J. M., Zeiger, D. N., Tang, K., Lin-Gibson, S., Fowler, B. O., and Lin, N. J. (2012). Synthesis and characterization of dimethacrylates containing quaternary ammonium functionalities for dental applications. *Dent. Mater.* 28, 219–228. doi: 10.1016/j.dental.2011.10.004

Aravamudhan, A., Ramos, D. M., Nada, A. A., and Kumbar, S. G. (2014). Natural polymers: polysaccharides and their derivatives for biomedical applications. *Nat. Synth. Biomed. Polym.* 2014, 67–89. doi: 10.1016/B978-0-12-396983-5.00004-1

Boateng, J. S., Matthews, K. H., Stevens, H. N. E., and Eccleston, G. M. (2008). Wound healing dressings and drug delivery systems: a Review. *J. Pharm. Sci.* 97, 2892–2923. doi: 10.1002/jps.21210

Castro, C., Zuluaga, R., Álvarez, C., Putaux, J.-L., Caro, G., Rojas, O. J., et al. (2012). Bacterial cellulose produced by a new acid-resistant strain of *Gluconacetobacter genus*. *Carbohydr. Polym.* 89, 1033–1037. doi: 10.1016/j.carbpol.2012.03.045

Chawla, P. R., Bajaj, I. B., Survase, S. A., and Singhal, R. S. (2009). Microbial cellulose: fermentative production and applications. *Food Technol. Biotechnol.* 47, 107–124.

Chen, H., Cheng, R., Zhao, X., Zhang, Y., Tam, A., Yan, Y., et al. (2019). An injectable self-healing coordinative hydrogel with antibacterial and angiogenic properties for diabetic skin wound repair. *NPG Asia Mater.* 11:3. doi: 10.1038/s41427-018-0103-9

Cheng, L., Weir, M. D., Limkangwalmongkol, P., Hack, G. D., Xu, H. H. K., Chen, Q., et al. (2012). Tetracalcium phosphate composite containing quaternary ammonium dimethacrylate with antibacterial properties. *J. Biomed. Mater. Res. Part B Appl. Biomater.* 100B, 726–734. doi: 10.1002/jbm.b.32505

DeBoer, T. R., Chakraborty, I., and Mascharak, P. K. (2015). Design and construction of a silver(I)-loaded cellulose-based wound dressing: trackable and sustained release of silver for controlled therapeutic delivery to wound sites. *J. Mater. Sci. Mater. Med.* 26:243.

Deka, S., Sharma, A., and Kumar, P. (2015). Cationic polymers and their self-assembly for antibacterial applications. *Curr. Top. Med. Chem.* 15, 1179–1195. doi: 10.2174/1568026615666150330110602

Denis, O., Rodriguez-Villalobos, H., and Struelens, M. J. (2010). "The problem of resistance," in *Antibiotic and Chemotherapy*, eds R. G. Finch, D. Greenwood, S. R. Norrby, and R. J. Whitley (Amsterdam: Elsevier), 24–48. doi: 10.1016/B978-0-7020-4064-1.00003-8

Devínsky, F., Kopecka-Leitmanová, A., Šeršeň, F., and Balgavý, P. (1990). Cut-off effect in antimicrobial activity and in membrane perturbation efficiency of the homologous series of N,N-Dimethylalkylamine Oxides†. *J. Pharm. Pharmacol.* 42, 790–794. doi: 10.1111/j.2042-7158.1990.tb07022.x

Dharmalingam, K., and Anandalakshmi, R. (2020). Functionalization of cellulose-based nanocomposite hydrogel films with zinc oxide complex and grapefruit seed extract for potential applications in treating chronic wounds. *Polymer* 202:122620. doi: 10.1016/j.polymer.2020.122620

Dhivya, S., Padma, V. V., and Santhini, E. (2015). Wound dressings - a review. *Biomedicine* 5:22. doi: 10.7603/s40681-015-0022-9

Dincă, V., Mocanu, A., Isopencu, G., Busuioc, C., Brajnicov, S., Vlad, A., et al. (2020). Biocompatible pure ZnO nanoparticles-3D bacterial cellulose biointerfaces with antibacterial properties. *Arab. J. Chem.* 13, 3521–3533. doi: 10.1016/j.arabjc.2018.12.003

Ding, M., Li, J., Fu, X., Zhou, J., Tan, H., Gu, Q., et al. (2009). Synthesis, degradation, and cytotoxicity of multiblock Poly(ε-caprolactone urethane)s containing gemini quaternary ammonium cationic groups. *Biomacromolecules* 10, 2857–2865. doi: 10.1021/bm9006826

Exner, M., Bhattacharya, S., Christiansen, B., Gebel, J., Goroncy-Bermes, P., Hartemann, P., et al. (2017). Antibiotic resistance: what is so special about multidrug-resistant Gram-negative bacteria? *GMS Hyg. Infect. Control* 12:Doc05. doi: 10.3205/dgkh000290

Faisul Aris, F. A., Mohd Fauzi, F. N. A., Tong, W. Y., and Syed Abdullah, S. S. (2019). Interaction of silver sulfadiazine with bacterial cellulose via ex-situ modification method as an alternative diabetic wound healing. *Biocatal. Agric. Biotechnol.* 21:101332. doi: 10.1016/j.bcab.2019.101332

Fan, L., Yang, J., Wu, H., Hu, Z., Yi, J., Tong, J., et al. (2015). Preparation and characterization of quaternary ammonium chitosan hydrogel with significant antibacterial activity. *Int. J. Biol. Macromol.* 79, 830–836. doi: 10.1016/j.ijbiomac.2015.04.013

Farah, S., Aviv, O., Laout, N., Ratner, S., Beyth, N., and Domb, A. J. (2015). Quaternary ammonium polyethylenimine nanoparticles for treating bacterial contaminated water. *Coll. Surf. B Biointerf.* 128, 614–619. doi: 10.1016/j.colsurfb.2015.03.006

Fierheller, M., and Sibbald, R. G. (2010). A clinical investigation into the relationship between increased periwound skin temperature and local wound infection in patients with chronic leg ulcers. *Adv. Skin Wound Care* 23, 369–379. doi: 10.1097/01.ASW.0000383197.28192.98

Gao, C., Yan, T., Du, J., He, F., Luo, H., and Wan, Y. (2014). Introduction of broad spectrum antibacterial properties to bacterial cellulose nanofibers via immobilising ε-polylysine nanocoatings. *Food Hydrocoll.* 36, 204–211. doi: 10.1016/j.foodhyd.2013.09.015

Giano, M. C., Ibrahim, Z., Medina, S. H., Sarhane, K. A., Christensen, J. M., Yamada, Y., et al. (2014). Injectable bioadhesive hydrogels with innate antibacterial properties. *Nat. Commun.* 5:4095. doi: 10.1038/ncomms5095

Gupta, A., Low, W. L., Radecka, I., Britland, S. T., Mohd Amin, M. C. I., and Martin, C. (2016). Characterisation and in vitro antimicrobial activity of biosynthetic silver-loaded bacterial cellulose hydrogels. *J. Microencapsul.* 33, 725–734. doi: 10.1080/02652048.2016.1253796

Halder, S., Yadav, K. K., Sarkar, R., Mukherjee, S., Saha, P., Haldar, S., et al. (2015). Alteration of Zeta potential and membrane permeability in bacteria: a study with cationic agents. *Springerplus* 4:672. doi: 10.1186/s40064-015-1476-7

Helenius, G., Bäckdahl, H., Bodin, A., Nannmark, U., Gatenholm, P., and Risberg, B. (2006). In vivo biocompatibility of bacterial cellulose. *J. Biomed. Mater. Res. Part A* 76, 431–438. doi: 10.1002/jbm.a.30570

Hong, F., Zhu, Y. X., Yang, G., and Yang, X. X. (2011). Wheat straw acid hydrolysate as a potential cost-effective feedstock for production of bacterial cellulose. *J. Chem. Technol. Biotechnol.* 86, 675–680. doi: 10.1002/jctb.2567

Horue, M., Cacicedo, M. L., Fernandez, M. A., Rodenak-Kladniew, B., Torres Sánchez, R. M., and Castro, G. R. (2020). Antimicrobial activities of bacterial cellulose - Silver montmorillonite nanocomposites for wound healing. *Mater. Sci. Eng. C* 116:111152. doi: 10.1016/j.msec.2020.111152

Huang, H.-C., Chen, L.-C., Lin, S.-B., Hsu, C.-P., and Chen, H.-H. (2010). In situ modification of bacterial cellulose network structure by adding interfering

substances during fermentation. *Bioresour. Technol.* 101, 6084–6091. doi: 10.1016/j.biortech.2010.03.031

Huang, Q., Huang, S., Liang, X., Qin, W., Liu, F., Lin, Z., et al. (2018). The antibacterial, cytotoxic, and flexural properties of a composite resin containing a quaternary ammonium monomer. *J. Prosthet. Dent.* 120, 609–616. doi: 10.1016/j.prosdent.2017.12.017

Hungund, B. S., and Gupta, S. G. (2010). Production of bacterial cellulose from *Enterobacter* amnigenus GH-1 isolated from rotten apple. *World J. Microbiol. Biotechnol.* 26, 1823–1828. doi: 10.1007/s11274-010-0363-1

Iguchi, M., Yamanaka, S., and Budhiono, A. (2000). Bacterial cellulose - A masterpiece of nature's arts. *J. Mater. Sci.* 35, 261–270. doi: 10.1023/A

Ioannou, C. J., Hanlon, G. W., and Denyer, S. P. (2007). Action of disinfectant quaternary ammonium compounds against *Staphylococcus aureus*. *Antimicrob. Agents Chemother.* 51, 296–306. doi: 10.1128/AAC.00375-06

Janpetch, N., Saito, N., and Rujiravanit, R. (2016). Fabrication of bacterial cellulose-ZnO composite via solution plasma process for antibacterial applications. *Carbohydr. Polym.* 148, 335–344. doi: 10.1016/j.carbpol.2016.04.066

Jia, S., Ou, H., Chen, G., Choi, D., Cho, K., Okabe, M., et al. (2004). Cellulose production from *Gluconobacter oxydans* TQ-B2. *Biotechnol. Bioproc. Eng.* 9, 166–170. doi: 10.1007/BF02942287

Kavitha, K. V. (2014). Choice of wound care in diabetic foot ulcer: a practical approach. *World J. Diabetes* 5:546. doi: 10.4239/wjd.v5.i4.546

Khalid, A., Khan, R., Ul-Islam, M., Khan, T., and Wahid, F. (2017). Bacterial cellulose-zinc oxide nanocomposites as a novel dressing system for burn wounds. *Carbohydr. Polym.* 164, 214–221. doi: 10.1016/j.carbpol.2017.01.061

Khan, S., Ul-Islam, M., Khattak, W. A., Ullah, M. W., and Park, J. K. (2015). Bacterial cellulose-titanium dioxide nanocomposites: nanostructural characteristics, antibacterial mechanism, and biocompatibility. *Cellulose* 22, 565–579. doi: 10.1007/s10570-014-0528-4

Kim, Y., Ullah, M. W., Ul-Islam, M., Khan, S., Jang, J. H., and Park, J. K. (2019). Self-assembly of bio-cellulose nanofibrils through intermediate phase in a cell-free enzyme system. *Biochem. Eng. J.* 142, 135–144. doi: 10.1016/j.bej.2018.11.017

Kingkaew, J., Kirdponpattara, S., Sanchavanakit, N., Pavasant, P., and Phisalaphong, M. (2014). Effect of molecular weight of chitosan on antimicrobial properties and tissue compatibility of chitosan-impregnated bacterial cellulose films. *Biotechnol. Bioprocess Eng.* 19, 534–544. doi: 10.1007/s12257-014-0081-x

Kocen, R., Gasik, M., Gantar, A., and Novak, S. (2017). Viscoelastic behaviour of hydrogel-based composites for tissue engineering under mechanical load. *Biomed. Mater.* 12:025004. doi: 10.1088/1748-605X/aa5b00

Koehler, M. J., Zimmermann, S., Springer, S., Elsner, P., König, K., and Kaatz, M. (2011). Keratinocyte morphology of human skin evaluated by in vivo multiphoton laser tomography. *Ski. Res. Technol.* 17, 479–486. doi: 10.1111/j.1600-0846.2011.00522.x

Kubo, I., Muroi, H., Masaki, H., and Kubo, A. (1993). Antibacterial activity of long-chain alcohols: the role of hydrophobic alkyl groups. *Bioorg. Med. Chem. Lett.* 3, 1305–1308. doi: 10.1016/S0960-894X(00)80336-4

Legge, R. L. (1990). Microbial cellulose as a speciality chemical. *Biotechnol. Adv.* 8, 303–319. doi: 10.1016/0734-9750(90)91067-Q

Li, F., Weir, M. D., Chen, J., and Xu, H. H. K. (2013). Comparison of quaternary ammonium-containing with nano-silver-containing adhesive in antibacterial properties and cytotoxicity. *Dent. Mater.* 29, 450–461. doi: 10.1016/j.dental.2013.01.012

Lin, W.-C., Lien, C.-C., Yeh, H.-J., Yu, C.-M., and Hsu, S. (2013). Bacterial cellulose and bacterial cellulose-chitosan membranes for wound dressing applications. *Carbohydr. Polym.* 94, 603–611. doi: 10.1016/j.carbpol.2013.01.076

Liu, T., Liu, Y., Liu, M., Wang, Y., He, W., Shi, G., et al. (2018). Synthesis of graphene oxide-quaternary ammonium nanocomposite with synergistic antibacterial activity to promote infected wound healing. *Burn. Trauma* 6, 115. doi: 10.1186/s41038-018-0115-2

Luo, H., Cui, T., Gan, D., Gama, M., Zhang, Q., and Wan, Y. (2019). Fabrication of a novel hierarchical fibrous scaffold for breast cancer cell culture. *Polym. Test.* 80:106107. doi: 10.1016/j.polymertesting.2019.106107

Malanovic, N., and Lohner, K. (2016). Gram-positive bacterial cell envelopes: the impact on the activity of antimicrobial peptides. *Biochim. Biophys. Acta Biomembr.* 1858, 936–946. doi: 10.1016/j.bbamem.2015.11.004

McCarthy, R. R., Ullah, M. W., Booth, P., Pei, E., and Yang, G. (2019). The use of bacterial polysaccharides in bioprinting. *Biotechnol. Adv.* 37:107448. doi: 10.1016/j.biotechadv.2019.107448

Miller, S. I. (2016). Antibiotic resistance and regulation of the gram-negative bacterial outer membrane barrier by host innate immune molecules. *mBio* 7:e01541-16. doi: 10.1128/mBio.01541-16

Nayak, R., and Padhye, R. (2015). "Antimicrobial finishes for textiles," in *Functional Finishes for Textiles*, ed. R. Paul (Amsterdam: Elsevier), 361–385. doi: 10.1533/9780857098450.2.361

Okajima, K., Matsuda, Y., and Kamide, K. (1991). Study on change in the degree of polymerisation of bacterial cellulose produced by *Acetobacter xylinum* during its cultivation. *Polym. Int.* 25, 145–151. doi: 10.1002/pi.4990250303

Olatunji, O. (2016). "Biomedical application of natural polymers," in *Natural Polymers*, ed. O. Olatunji (Cham: Springer International Publishing), 93–114. doi: 10.1007/978-3-319-26414-1_4

O'Neill, J. (2018). *Tackling Drug-Resistant Infections Globally: Final Report and Recommendations*. Singapore: Straits Times.

Padwa, A., and Murphree, S. S. (2000). Three-membered ring systems. *Prog. Heterocyc. Chem.* 12, 57–76. doi: 10.1016/S0959-6380(00)80006-9

Picheth, G. F., Pirich, C. L., Sierakowski, M. R., Woehl, M. A., Sakakibara, C. N., de Souza, C. F., et al. (2017). Bacterial cellulose in biomedical applications: a review. *Int. J. Biol. Macromol.* 104, 97–106. doi: 10.1016/j.ijbiomac.2017.05.171

Poverenov, E., Shemesh, M., Gulino, A., Cristaldi, D. A., Zakin, V., Yefremov, T., et al. (2013). Durable contact active antimicrobial materials formed by a one-step covalent modification of polyvinyl alcohol, cellulose and glass surfaces. *Coll. Surf. B Biointerf.* 112, 356–361. doi: 10.1016/j.colsurfb.2013.07.032

Power, G., Moore, Z., and O'Connor, T. (2017). Measurement of pH, exudate composition and temperature in wound healing: a systematic review. *J. Wound Care* 26, 381–397. doi: 10.12968/jowc.2017.26.7.381

Purser, K. (2010). Wound dressing guidelines. *Royal United Hospital Bath NHS Trust*, 747, 1–25.

Ramsden, J. J. Ed. (2011). "The Nanoscale," in *Nanotechnology*, (Amsterdam: Elsevier), 15–34. doi: 10.1016/B978-0-08-096447-8.00002-8

Reardon, S. (2014). Antibiotic resistance sweeping developing world. *Nature* 509, 141–142. doi: 10.1038/509141a

Reiniati, I., Hrymak, A. N., and Margaritis, A. (2016). Recent developments in the production and applications of bacterial cellulose fibers and nanocrystals. *Crit. Rev. Biotechnol.* 37, 510–524. doi: 10.1080/07388551.2016.1189871

Roy, N., Saha, N., Kitano, T., and Saha, P. (2010). Development and characterization of novel medicated hydrogels for wound dressing. *Soft Mater.* 8, 130–148. doi: 10.1080/15394451003756282

Salmi, T., Grénman, H., Wärnå, J., and Murzin, D. Y. (2013). New modelling approach to liquid-solid reaction kinetics: from ideal particles to real particles. *Chem. Eng. Res. Des.* 91, 1876–1889. doi: 10.1016/j.cherd.2013.08.004

Sanabria-DeLong, N., Agrawal, S. K., Bhatia, S. R., and Tew, G. N. (2007). Impact of synthetic technique on PLA-PEO-PLA physical hydrogel properties. *Macromolecules* 40, 7864–7873. doi: 10.1021/ma071243f

Shahmohammadi Jebel, F., and Almasi, H. (2016). Morphological, physical, antimicrobial and release properties of ZnO nanoparticles-loaded bacterial cellulose films. *Carbohydr. Polym.* 149, 8–19. doi: 10.1016/j.carbpol.2016.04.089

Shao, W., Liu, H., Wang, S., Wu, J., Huang, M., Min, H., et al. (2016). Controlled release and antibacterial activity of tetracycline hydrochloride-loaded bacterial cellulose composite membranes. *Carbohydr. Polym.* 145, 114–120. doi: 10.1016/j.carbpol.2016.02.065

Shibazaki, H., Kuga, S., and Okano, T. (1997). Mercerization and acid hydrolysis of bacterial cellulose. *Cellulose* 4, 75–87. doi: 10.1023/A:1024273218783

Siddhan, P., Sakthivel, K., and Basavaraj, H. (2016). Biosynthesis of bacterial cellulose imparting antibacterial property through novel bio-Agents. *Res. J. Biotechnol.* 11, 86–93.

Silhavy, T. J., Kahne, D., and Walker, S. (2010). The bacterial cell envelope. *Cold Spring Harb. Perspect. Biol.* 2:a000414. doi: 10.1101/cshperspect.a000414

Smith, M. B. Ed. (2010). "CD disconnect products," in *Organic Synthesis*, (Amsterdam: Elsevier), 623–779. doi: 10.1016/B978-1-890661-40-3.50008-9

Smith, T. J., Kennedy, J. E., and Higginbotham, C. L. (2010). Rheological and thermal characteristics of a two phase hydrogel system for potential wound healing applications. *J. Mater. Sci.* 45, 2884–2891. doi: 10.1007/s10853-010-4278-x

Son, H.-J., Heo, M.-S., Kim, Y.-G., and Lee, S.-J. (2001). Optimization of fermentation conditions for the production of bacterial cellulose by a newly isolated *Acetobacter* sp.*A9* in shaking cultures. *Biotechnol. Appl. Biochem.* 33:1. doi: 10.1042/BA20000065

Son, H.-J., Kim, H.-G., Kim, K.-K., Kim, H.-S., Kim, Y.-G., and Lee, S.-J. (2003). Increased production of bacterial cellulose by *Acetobacter* sp. V6 in synthetic media under shaking culture conditions. *Bioresour. Technol.* 86, 215–219. doi: 10.1016/S0960-8524(02)00176-1

Sonohara, R., Muramatsu, N., Ohshima, H., and Kondo, T. (1995). Difference in surface properties between *Escherichia coli* and Staphylococcus aureus as revealed by electrophoretic mobility measurements. *Biophys. Chem.* 55, 273–277. doi: 10.1016/0301-4622(95)00004-H

Sood, A., Granick, M. S., and Tomaselli, N. L. (2014). Wound dressings and comparative effectiveness data. *Adv. Wound Care* 3, 511–529. doi: 10.1089/wound.2012.0401

Soroka, Y., Ma'or, Z., Leshem, Y., Verochovsky, L., Neuman, R., Brégégère, F. M., et al. (2008). Aged keratinocyte phenotyping: morphology, biochemical markers and effects of Dead Sea minerals. *Exp. Gerontol.* 43, 947–957. doi: 10.1016/j.exger.2008.08.003

Sun, T., Norton, D., Ryan, A. J., MacNeil, S., and Haycock, J. W. (2007). Investigation of fibroblast and keratinocyte cell-scaffold interactions using a novel 3D cell culture system. *J. Mater. Sci. Mater. Med.* 18, 321–328. doi: 10.1007/s10856-006-0696-3

Tan, H., Ma, R., Lin, C., Liu, Z., and Tang, T. (2013). Quaternized chitosan as an antimicrobial agent: antimicrobial activity, mechanism of action and biomedical applications in orthopedics. *Int. J. Mol. Sci.* 14, 1854–1869. doi: 10.3390/ijms14011854

Tenover, F. C. (2006). Mechanisms of antimicrobial resistance in bacteria. *Am. J. Infect. Control* 34:219. doi: 10.1016/j.ajic.2006.05.219

The PEW charitable trust (2016). *A Scientific Roadmap for Antibiotic Discovery*. Philadelphia, PA: The Pew Charitable Trusts.

Ul-Islam, M., Khan, S., Ullah, M. W., and Park, J. K. (2019a). Comparative study of plant and bacterial cellulose pellicles regenerated from dissolved states. *Int. J. Biol. Macromol.* 137, 247–252. doi: 10.1016/j.ijbiomac.2019.06.232

Ul-Islam, M., Subhan, F., Islam, S. U., Khan, S., Shah, N., Manan, S., et al. (2019b). Development of three-dimensional bacterial cellulose/chitosan scaffolds: analysis of cell-scaffold interaction for potential application in the diagnosis of ovarian cancer. *Int. J. Biol. Macromol.* 137, 1050–1059. doi: 10.1016/j.ijbiomac.2019.07.050

Ullah, M. W., Ul-Islam, M., Khan, S., Kim, Y., Jang, J. H., and Park, J. K. (2016). In situ synthesis of a bio-cellulose/titanium dioxide nanocomposite by using a cell-free system. *RSC Adv.* 6, 22424–22435. doi: 10.1039/C5RA26704H

Ullah, M. W., Ul-Islam, M., Khan, S., Kim, Y., and Park, J. K. (2015). Innovative production of bio-cellulose using a cell-free system derived from a single cell line. *Carbohydr. Polym.* 132, 286–294. doi: 10.1016/j.carbpol.2015.06.037

Usui, M. L., Mansbridge, J. N., Carter, W. G., Fujita, M., and Olerud, J. E. (2008). Keratinocyte migration, proliferation, and differentiation in chronic ulcers from patients with diabetes and normal wounds. *J. Histochem. Cytochem.* 56, 687–696. doi: 10.1369/jhc.2008.951194

Van Den Bulcke, A. I., Bogdanov, B., De Rooze, N., Schacht, E. H., Cornelissen, M., and Berghmans, H. (2000). Structural and rheological properties of methacrylamide modified gelatin hydrogels. *Biomacromolecules* 1, 31–38. doi: 10.1021/bm990017d

Wahid, F., Duan, Y.-X., Hu, X.-H., Chu, L.-Q., Jia, S.-R., Cui, J.-D., et al. (2019a). A facile construction of bacterial cellulose/ZnO nanocomposite films and their photocatalytic and antibacterial properties. *Int. J. Biol. Macromol.* 132, 692–700. doi: 10.1016/j.ijbiomac.2019.03.240

Wahid, F., Hu, X.-H., Chu, L.-Q., Jia, S.-R., Xie, Y.-Y., and Zhong, C. (2019b). Development of bacterial cellulose/chitosan based semi-interpenetrating hydrogels with improved mechanical and antibacterial properties. *Int. J. Biol. Macromol.* 122, 380–387. doi: 10.1016/j.ijbiomac.2018.10.105

Walsh, C. (2000). Molecular mechanisms that confer antibacterial drug resistance. *Nature* 406, 775–781. doi: 10.1038/35021219

Walter, M. N. M., Wright, K. T., Fuller, H. R., MacNeil, S., and Johnson, W. E. B. (2010). Mesenchymal stem cell-conditioned medium accelerates skin wound healing: an in vitro study of fibroblast and keratinocyte scratch assays. *Exp. Cell Res.* 316, 1271–1281. doi: 10.1016/j.yexcr.2010.02.026

Walzak, M. J., Davidson, R., and Biesinger, M. (1998). The Use of XPS, FTIR, SEM/EDX, contact angle, and AFM in the characterization of coatings. *J. Mater. Eng. Perform.* 7, 317–323. doi: 10.1361/105994998770347747

Wiener, M. C., and Horanyi, P. S. (2011). How hydrophobic molecules traverse the outer membranes of Gram-negative bacteria. *Proc. Natl. Acad. Sci. U.S.A.* 108, 10929–10930. doi: 10.1073/pnas.1106927108

Yan, C., and Pochan, D. J. (2010). Rheological properties of peptide-based hydrogels for biomedical and other applications. *Chem. Soc. Rev.* 39:3528. doi: 10.1039/b919449p

Yin, N., Du, R., Zhao, F., Han, Y., and Zhou, Z. (2020). Characterization of antibacterial bacterial cellulose composite membranes modified with chitosan or chitooligosaccharide. *Carbohydr. Polym.* 229:115520. doi: 10.1016/j.carbpol.2019.115520

Zaman, M., Xiao, H., Chibante, F., and Ni, Y. (2012). Synthesis and characterization of cationically modified nanocrystalline cellulose. *Carbohydr. Polym.* 89, 163–170. doi: 10.1016/j.carbpol.2012.02.066

Zhao, T., and Sun, G. (2008). Hydrophobicity and antimicrobial activities of quaternary pyridinium salts. *J. Appl. Microbiol.* 104, 824–830. doi: 10.1111/j.1365-2672.2007.03616.x

Zheng, Z., Xu, Q., Guo, J., Qin, J., Mao, H., Wang, B., et al. (2016). Structure-antibacterial activity relationships of imidazolium-type ionic liquid monomers, Poly(ionic liquids) and Poly(ionic liquid) membranes: effect of alkyl chain length and cations. *ACS Appl. Mater. Interf.* 8, 12684–12692. doi: 10.1021/acsami.6b03391

Zuidema, J. M., Rivet, C. J., Gilbert, R. J., and Morrison, F. A. (2014). A protocol for rheological characterization of hydrogels for tissue engineering strategies. *J. Biomed. Mater. Res. Part B Appl. Biomater.* 102, 1063–1073. doi: 10.1002/jbm.b.33088

Conflict of Interest: The authors declare that the research was conducted in the absence of any commercial or financial relationships that could be construed as a potential conflict of interest.

frontiers in Bioengineering and Biotechnology

REVIEW
published: 20 October 2020
doi: 10.3389/fbioe.2020.539319

The Open Challenge of *in vitro* Modeling Complex and Multi-Microbial Communities in Three-Dimensional Niches

Martina Oriano[1,2,3†], Laura Zorzetto[4†], Giuseppe Guagliano[5], Federico Bertoglio[1,6], Sebastião van Uden[5], Livia Visai[1,7] and Paola Petrini[5]*

[1] Molecular Medicine Department (DMM), Center for Health Technologies (CHT), UdR INSTM, University of Pavia, Pavia, Italy, [2] Department of Pathophysiology and Transplantation, University of Milan, Milan, Italy, [3] Internal Medicine Department, Respiratory Unit and Adult Cystic Fibrosis Center, Fondazione IRCCS Ca' Granda Ospedale Maggiore Policlinico, Milan, Italy, [4] Department of Biomaterials, Max Planck Institute of Colloids and Interfaces, Potsdam, Germany, [5] Department of Chemistry, Materials and Chemical Engineering "Giulio Natta" and UdR INSTM Politecnico di Milano, Milan, Italy, [6] Technische Universität Braunschweig, Institute of Biochemistry, Biotechnology and Bioinformatic, Department of Biotechnology, Braunschweig, Germany, [7] Department of Occupational Medicine, Toxicology and Environmental Risks, Istituti Clinici Scientifici (ICS) Maugeri, IRCCS, Pavia, Italy

OPEN ACCESS

Edited by:
Antonia Nostro,
University of Messina, Italy

Reviewed by:
Liangju Kuang,
Harvard Medical School,
United States
Brendan M. Leung,
Dalhousie University, Canada

***Correspondence:**
Livia Visai
livia.visai@unipv.it

[†] These authors share first authorship

Specialty section:
This article was submitted to Biomaterials, a section of the journal Frontiers in Bioengineering and Biotechnology

Received: 29 February 2020
Accepted: 28 September 2020
Published: 20 October 2020

Citation:
Oriano M, Zorzetto L, Guagliano G, Bertoglio F, van Uden S, Visai L and Petrini P (2020) The Open Challenge of in vitro Modeling Complex and Multi-Microbial Communities in Three-Dimensional Niches. Front. Bioeng. Biotechnol. 8:539319. doi: 10.3389/fbioe.2020.539319

The comprehension of the underlying mechanisms of the interactions within microbial communities represents a major challenge to be faced to control their outcome. Joint efforts of *in vitro*, *in vivo* and ecological models are crucial to controlling human health, including chronic infections. In a broader perspective, considering that polymicrobial communities are ubiquitous in nature, the understanding of these mechanisms is the groundwork to control and modulate bacterial response to any environmental condition. The reduction of the complex nature of communities of microorganisms to a single bacterial strain could not suffice to recapitulate the *in vivo* situation observed in mammals. Furthermore, some bacteria can adapt to various physiological or arduous environments embedding themselves in three-dimensional matrices, secluding from the external environment. Considering the increasing awareness that dynamic complex and dynamic population of microorganisms (microbiota), inhabiting different apparatuses, regulate different health states and protect against pathogen infections in a fragile and dynamic equilibrium, we underline the need to produce models to mimic the three-dimensional niches in which bacteria, and microorganisms in general, self-organize within a microbial consortium, strive and compete. This review mainly focuses, as a case study, to lung pathology-related dysbiosis and life-threatening diseases such as cystic fibrosis and bronchiectasis, where the co-presence of different bacteria and the altered 3D-environment, can be considered as worst-cases for chronic polymicrobial infections. We illustrate the state-of-art strategies used to study biofilms and bacterial niches in chronic infections, and multispecies ecological competition. Although far from the rendering of the 3D-environments and the polymicrobial nature of the infections, they

represent the starting point to face their complexity. The increase of knowledge respect to the above aspects could positively affect the actual healthcare scenario. Indeed, infections are becoming a serious threat, due to the increasing bacterial resistance and the slow release of novel antibiotics on the market.

Keywords: polymicrobial cultures, chronic infections, antimicrobial, antibiotic resistance, *in vitro* models, ecological models, lung dysbiosis, biofilm

THE NEED FOR PLATFORMS FOR POLYMICROBIAL CULTURE

Pure bacteria cultures are an unnaturally occurring scenario. Like all organisms, bacteria live as part of an ecosystem, sharing, exchanging and competing for resources with other microorganisms present in their environment (Freilich et al., 2010). This fact is combined with the mechanical, morphological and biochemical conditions of the microenvironment, leading to a biochemical action-reaction effect that changes the way bacteria communities respond to drastic events (Raimbault, 1998; Tuson et al., 2012). Specifically, bacterial ecosystems are mainly organized in three-dimensional matrices, either self-produced, like biofilms, either otherwise produced, like mucus. As a result, for example, *in vitro* pure bacteria culture in suspension in a medium (planktonic conditions) is significantly more susceptible to antibiotic treatment than an *in vivo* infection where the same bacterial strain is the dominant pathological agent. So much so that when a certain antibiotic is screened to be potentially effective to treat a patient, the needed antibiotic concentration to be delivered to the infection site must be 100 to 1000 times higher than the antibiotic concentration assessed in the susceptibility test (Macià et al., 2014).

These factual cues reveal the inability of *in vitro* culturing methods to provide the means for hosting the complexity of natural microbial environments. New technological and methodological tools are quested to enable the study of microbial communities in a reproducible and controlled manner, either *in vitro* or *in silico*. The aim of this is boosting the understanding of the dynamic mechanisms underlying the way that bacterial communities react and evolve in response to external stimuli and to study their delicate equilibrium within any environment, including the human body. These methods could work in synergy with proper *in vivo* models. Diverse applicative fields can benefit from the new methodological tools: the study of the effect of drugs, nutrients, prebiotics and probiotics on the gastrointestinal microbiota, or the effectiveness of antimicrobial treatments. The understanding of the underlying mechanisms precedes the deliberate control and modulation of the response, avoiding trial-and-error approaches based on phenomenological observations.

Abbreviations: BBC, Biofilm Bactericidal Concentration; BHI, Brain Heart Infusion; BPC, Biofilm Preventing Concentration; CF, cystic fibrosis; CFU, colony forming units; CL, closed system; CLSM, Confocal Laser Scanning Microscope; FISH, fluorescence *in situ* hybridization; LB, Lysogeny Broth; MBC, Minimal Bactericidal Concentration; MBEC, Minimal Biofilm Eradication Concentration; MBIC, Minimal Biofilm Inhibitory Concentration; MEM, Minimal Essential Medium; MIC, Minimal Inhibitory Concentration; MTT, 3-(4,5-dimethylthiazol-2-yl)-2,5-diphenyltetrazolium bromide; OP, open system; qPCR, Real Time-PCR; TSB, Tryptic Soy Broth; XTT, sodium 3′-[1- (phenylaminocarbonyl)- 3,4-tetrazolium]-bis (4-methoxy6-nitro) benzene sulfonic acid hydrate.

The development of new methods originates from the parallel study of the natural microbial environments that are still mainly unexplored. We will address the bacterial niches in the human body with a specific highlight on the lung environments and chronic and multiple infections, as they represent one of the most challenging issues to be addressed. In these cases, the changes in the microenvironment are related to the change of the dynamics of the multistrain interactions. This paper addresses the complexity of the polymicrobial systems in the human body, with a specific focus on challenging polymicrobial infections. We describe the state of the art of *in vitro* and mathematical models as powerful tools to investigate the natural complexity. Their multifaceted potential can influence diverse application fields. Among them, we focused on the fight against infectious diseases either by personalized testing of the efficacy of antimicrobial substances or the development of new therapeutic approaches.

3D-BACTERIAL NICHES IN THE HUMAN BODY

Each species in an ecosystem is thought to occupy a separate, unique niche. The ecological niche of a microorganism describes how it responds to the distribution of resources and competing species, as well as how it alters those same factors in turn. The niche is a complex description of how a microbial species uses its environment. In nature, bacteria interact in complex communities, with the contemporary presence of different species whose abundance fluctuates over time in response to their mutual interaction and to the surrounding environment. Their interaction can lead to competition or cooperation to achieve an evolutionary advantage. The complex microbial communities, also known as microbiota, are fundamental in the human body development and the presence of dysregulation of the microbial community is associated with different disease states. Human gut microbiota, for example, has important functions in the development of immunity, defenses against pathogens, host nutrition including the production of short-chain fatty acids, synthesis of vitamins, making it an essential component of the human body (Bauer et al., 1963; Amon and Sanderson, 2017). Moreover, the colonization from specific microorganisms can protect from parasites or other pathogens: *S. epidermidis* on the skin, for example, promotes the production of transmembrane proteins and cytokines involved in the immune response and ultimately protects against infection with the parasite Leishmania major (Naik et al., 2012).

Various biological environments in the human body host microbial communities (Costello et al., 2012), yet, for its clinical relevance, our focus is on the lung environment and its pathologies.

Lung Microbiota and Its Dysregulation in Pathological Conditions

Lungs were thought for many years as sterile, being the respiratory tract less charged in genetic material than other body districts, i.e., gastrointestinal or urinary tract. Nowadays, we know that the lungs have a physiological microbiome (Sze et al., 2015; Wang et al., 2016; Segal et al., 2017). Lungs are in constant communication with the external environment with continuous microbe immigration and elimination through mucociliary clearance, although a resident flora is present even in the lungs of healthy subjects (Hilty et al., 2010; Morris et al., 2013; Bassis et al., 2015; Dickson et al., 2015).

Lungs are not the ideal location for bacterial proliferation in comparison to the intestinal tract, because they are low-nutrient sites and their physiological conditions related to oxygen tension, pH, temperature and inflammatory cell infiltration can vary. These conditions determine a continuous change in the microbial pulmonary ecosystem (West, 1968; Ingenito et al., 1987).

The presence of lung microbiota was identified after the development of culture-independent techniques. The sequencing of highly conserved loci, like 16s rRNA gene, through high throughput sequencing, is the most common technique for microbiome identification. Moreover, the development of bacterial genomes databases allowed the scientific community to assign a relative abundance of bacteria and diversity (Costa et al., 2018).

Lung microbiota develops in early life and it is specific for the method of delivery. Vaginal-delivered children's microbiota resulted to be mainly composed of *Lactobacillus*, *Prevotella*, or *Sneathia* species, while cesarean section born children acquired *Staphylococcus*, *Corynebacterium*, and *Propionibacterium* species (Dominguez-Bello et al., 2010). The early microbiota acquisition protects the lungs from responses to possibly inhaled antigens. Healthy lungs microbiota composition is dynamic and among the multiple bacteria present in the lungs, whose abundance and composition vary in time, bacteroidetes and firmicutes constitute a retained core (Erb-Downward et al., 2011; Morris et al., 2013; Segal et al., 2013).

Microbial diversity in the lungs seems to be crucial in the homeostasis of the respiratory system. Dysbiosis situations result in both acute and chronic diseases (Boyton et al., 2013; Surette, 2014; Mammen and Sethi, 2017).

The level of dysregulation may be correlated to disease severity and the dominance of a specific microorganism seems to be linked to the disease state (Venkataraman et al., 2015) (**Figure 1**). The predominance of a bacterial species in the lungs and a decrease of richness in microbiota seems to be associated with diseases like cystic fibrosis (CF) (de Dios Caballero et al., 2017; Zemanick et al., 2017). In both acute and chronic (bronchiectasis) diseases, the disease state is associated with the loss of bacterial diversity and the dominance of a single or a small group of taxa (Tunney et al., 2013).

Interestingly, chronic infections are correlated with a change in mucus viscosity, indicating the interdependence of the three-dimensional matrix and the bacterial interspecies interactions. In the typical bacterial niches of CF and bronchiectasis, the chronic co-presence of different pathogens is a life-threatening issue. CF is a systemic disease caused by genetic mutations in which pulmonary implications are strictly related to disease severity and mortality. It involves airway surface liquid depletion producing mucus obstruction and chronic inflammation with persistent leukocyte accumulation at the pulmonary level (Cheung et al., 2008). Dehydrated, thickened secretions lead to endobronchial infection with a limited spectrum of distinctive bacteria, mainly *Staphylococcus*, *Pseudomonas,* and *Burkholderia*, an exaggerated inflammatory response leading to the development of bronchiectasis, progressive obstructive airways disease and frequent exacerbations (Guggino and Banks-Schlegel, 2004; Marshall et al., 2016). *P. aeruginosa,* which is one of the most frequent bacteria in CF, is also able to generate biofilm. Biofilm formation leads to further difficulty in antibiotic treatment. *Burkholderia* instead could be very dangerous in CF, due to their intrinsic antibiotic resistance, increasing lung disease severity. Infection from *Burkholderia cepacia* complex is also an exclusion criterion for lung transplants. Besides, continuous exposure to antibiotics is contributing to the insurgence of multidrug-resistant pathogens and studies are supporting a loss of microbiome diversity with age, due to antibiotics use with a parallel increase of disease severity (Knippenberg et al., 2015).

Bronchiectasis is a chronic respiratory disease characterized by permanent airway dilation with daily symptoms such as cough, sputum production, and recurrent exacerbations. The prevalence of bronchiectasis is up to 500/100,000 individuals increasing worldwide (Amati et al., 2017).

Bronchiectasis leads to a decreased mucus excretion and an overgrowth of microorganisms and this condition causes inflammation in the lungs. Infection and inflammation, that easily become chronic, leads to further damage to the airways and worsening of patients' conditions (Swenson et al., 2017). Bronchiectasis patients' lungs are colonized by several pathogens like *Pseudomonas aeruginosa*, *Haemophilus influenzae*, *Moraxella catarrhalis, Escherichia species, Klebsiella species* (Gram-negative) and Gram-positive as *Streptococcus pneumoniae* and *Staphylococcus aureus* detected though standard microbiology (Chalmers et al., 2014). Bronchiectasis etiology is very heterogeneous and identified as post-infectious in 20% of patients, caused by chronic obstructive pulmonary disease (COPD) in 15%, 10% as a cause of tissue diseases, 5.8% due to immunodeficiency and 3.3% linked to asthma. Identified causes cover 60% of patients, while in 40% of cases the cause of bronchiectasis is idiopathic (Amati et al., 2017). Microbiome analysis of low airways samples shows pronounced domination of proteobacteria including *Pseudomonas* and *Haemophilus* in association with neutrophil-mediated inflammation. In opposition, in the presence of lower neutrophilic inflammation and frequent exacerbations, the microbiome was dominated by firmicutes (Rogers et al., 2014; Taylor et al., 2015; Chalmers et al.,

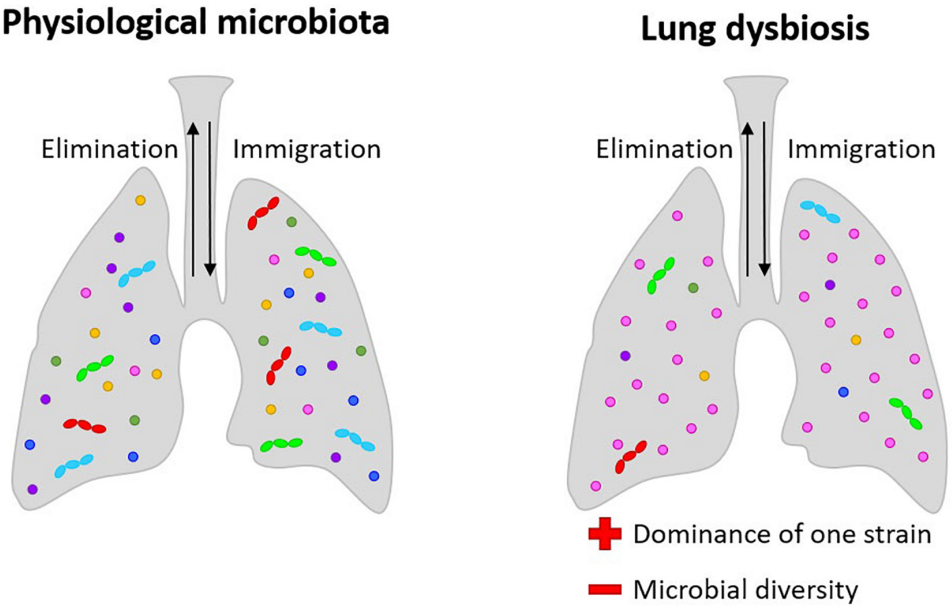

FIGURE 1 | Lung microbiota: in physiological conditions, its composition is dynamic and among the multiple bacteria present in the lungs; in pathological conditions, microbial diversity is lost, and dysbiosis situations result in both acute and chronic diseases, with the dominance of a single or a small group of taxa. In bronchiectasis, dehydrated, thickened secretions lead to endobronchial infection with a limited spectrum of distinctive bacteria, mainly *Staphylococcus*, *Pseudomonas,* and *Burkholderia*. In CF, the dominance of *Pseudomonas aeruginosa* and *Burkholderia cepacea* are related to the progression of the pathologies.

2017). Genera detected in lower airways through 16s rRNA gene sequencing during a stable state are usually *Prevotella*, *Veillonella Streptococcus*, *Moraxella*, *Neisseria*, *Flavobacterium*, *Leptotrichia*, *Fusobacterium* (Rogers et al., 2014; Lee et al., 2018).

Being interspecies interactions and the microbial niches crucial for the physiological conservation of the body homeostasis, both basic and translational studies in this field can result in clinical advances in the treatment of many diseases.

ANTIBIOTIC RESISTANCE AND DRUG DEVELOPMENT IN LUNG DISEASES

The lung microbiota is an ecosystem that can enter a state of dysbiosis when a pathological bacterium becomes dominant. Now the use of antibiotics is the traditional medical approach to treat this condition. Antibiotics are very useful in medicine, but aside their effect on target cause effects on the entire bacterial community that take time to recover. The remaining bacterial community becomes in severe need for rehabilitation until a new microbiota eubiosis is achieved.

Besides that, the awareness around the development of bacterial resistance to antibiotics is growing. Antibiograms are the tool used by clinicians and scientists to evaluate the susceptibility of bacterial isolates to antibiotics and are fundamental in diseases like CF or bronchiectasis where patients are constantly facing chronic respiratory infections (Swenson et al., 2017). In reality, susceptibility indicates that the tested antibiotic can neutralize the pathological bacteria culture in planktonic conditions at a concentration that is far lower than what would be required for infections in humans, and, as a consequence, its ability to control the infections is overestimated. Whether or not the treatment is effective, non-pathological bacteria communities, crucial for maintaining the symbiotic functions of the human microbiome, are severely debilitated or acquire the ability to resist such antibiotic class (Zhang et al., 2019).

Moreover, some bacteria are also able to form biofilms. Biofilms are bacterial communities that can develop in nature as well as in the human body, well-coordinated communities in which bacteria live in a self-produced extracellular matrix composed of exopolysaccharides, DNA and proteins (Costerton et al., 1995). CF lungs are a favorable place for biofilm formation given the properties of CF mucus. Biofilms in CF lungs can increase the spreading of antibiotic resistance among the community and also limit the bioavailability of drugs by inhalation creating a physical barrier. As mentioned above, *P. aeruginosa* is one of the most dangerous and frequent bacteria in CF, able to install very resistant chronic infection and able to initiate biofilm formation (Moreau-Marquis et al., 2008).

Development of Innovative Approaches for Combating Lung Infections

The use of antibiotics to fight bacterial infections seems not to be the only strategy to face this problem. An alternative strategy, which neutralizes the pathological bacteria while contemporaneously leading the lung microbiota toward eubiosis could revolutionize the way lung infections are treated. This is precisely what new approaches using pre- and probiotics are aiming at. Strategies that employ manipulation of distal (gut)

and local (lung) microbiomes to aid the host in combating a lung infection are proposed (Dumas et al., 2018). One strategy concerns the use of the immune-modulatory ability of the gut (distal) microbiome to allow the host to gain back control over the lung infection. Previous studies demonstrated the feasibility to recreate lung dysbiosis in mice, followed by seeding pathological bacteria – *K. pneumoniae*, *S. pneumoniae* and *Mycobacterium tuberculosis* – to model a severe lung infection *in vivo*. After delivering a fecal transplant, they noticed that the host restored control over the lung infection through increased immune system activity (Khan et al., 2016; Schuijt et al., 2016; Brown et al., 2017). This is one of the many surprising systemic effects of the intestinal microbiota. Not long ago it was assumed that a healthy lung was a sterile environment, now there is evidence indicating that not only it exists but also microbiome from distal body districts (e.g., gut) influences the stability of lung microbiota (Dumas et al., 2018).

The immunomodulation effect of certain bacteria, e.g., *Lactobacillus genus*, toward the well-being of their host is not restrained to a distal body district (Barbieri et al., 2013, 2017, 2019). These studies focus on the potential of administering probiotics directly over the infected region, to understand if these can establish a presence within the microbiota under a state of dysbiosis and assist in restoring control over the infection. They have infected the lungs of mice with *S. pneumoniae*, followed by nasal administration of *Lactobacillus rhamnosus*. It was observed that *L. rhamnosus* stimulates and increases the number of B cells (Barbieri et al., 2013), CD4 + T lymphocytes (Barbieri et al., 2017), macrophages and dendritic cells (Barbieri et al., 2019) in the lung, significantly improving the outcomes of pneumococcal infections. Although results are promising, clinical trials are needed to help understand if probiotics can be used as an aid to antibiotics in humans. Nevertheless, it provides another potential pathway to help solve the antibiotic crisis that is currently unfolding due to the rise of antimicrobial resistance (Hendriksen et al., 2019), led by the inability of antibiotic development stakeholders to bring new antibiotic classes to the market.

The health industry deals with bacterial infections by developing new testing methods and tailored strategies to fight infections; developing new bacterial culturing tools could increase their efficacy and broaden their range of applications. Improvement of *in vitro* efficacy screening seems to have the potential to enhance the development of new treatments.

IN VITRO MODELING THE THREE DIMENSIONAL AND MULTIMICROBIAL COMMUNITIES

In situ models would be the ideal solution to study biota and biofilm behavior in their native environment (Wimpenny, 1997) and test for novel antibiotics. Yet, in the case of bacterial related infection, such models are hardly attainable. Thus, researchers usually turn to *in vitro* and *in vivo* models. Focusing on the first type, there are two main approaches: a top-down approach, microcosms and a bottom-up approach, consortia (**Figure 2**) (Sissons, 1997; Wimpenny, 1997). In the microcosm approach, biological materials mimicking the target environment evolve *in vitro*: polymicrobial cultures from the natural biota, properly sampled from voluntary donors, are often used (Sissons, 1997; Lebeaux et al., 2013). In theory, this approach allows obtaining the most closely related model to the native conditions, but it is highly affected by inter- and intra-variability of donors and it can be easily influenced by the sampling methods (Sissons, 1997; Lebeaux et al., 2013). Moreover, among the sampled bacteria, strict anaerobes do not easily survive standard culture techniques (Woods et al., 2012) and the resulting flora of the model could be less well-representative of the native environment than initially thought. To study specific aspects of bacterial interactions, to exploit even simpler experimental models selecting the most relevant species to target a scientific question: this bottom-up approach can be labeled as 'consortium' because among the whole fauna, only a few species will be used. Well-established examples of bacterial consortia are the six and nine species 'Marsh' consortia to model dental plaque (Sissons, 1997; Brown et al., 2019). Both microcosms and consortia can be classified as open (continuous renovation of nutrients, removal of metabolic by-products and aerial exchanges allowed) or closed (bacteria grow on a limited supply of nutrients) (Lebeaux et al., 2013). Open models are sometimes referred to as 'dynamic models': this definition is widespread in microbiological studies [e.g., in studies using CDC biofilm reactor (Bilal et al., 2019)]. Yet, despite having a continuous medium flow, open bioreactors operate in a stationary state. Therefore, here we will refer to such systems as 'open' and will use the term 'dynamic' for the transient and unstable interactions between microorganisms that will ultimately lead to a new steady-state, different from the initial conditions of the system. The culture conditions deeply affect the response of bacteria to external stimuli, including the effect of antibiotics. The challenge is to produce realistic tools for the study of bacterial interactions and drug discovery. These tools should provide not the complete physiological situation, but the key features relevant for each aim. There is not "the ideal" *in vitro* model of lung microbiota, as it is strictly dependent on the feature to be tested. In antibiotic resistance studies, e.g., the 3D-matrix is relevant for permeability studies (Pacheco et al., 2019) but also to allow the formation of self-protecting clusters of bacteria (Melaugh et al., 2016). We propose a bottom-up approach in recapitulating the physiological complexity of the microbial niches within *in vitro* models. This approach implies to deconstruct in pieces the complex physiological situation by employing different tools, such as 3D models, the *in vitro* cultures of more than one bacterial species. Mathematical and ecological models complete the picture, by rendering the competing effects of the co-presence of different species.

Modeling the 3D-Microenvironment: *in vitro* Studies of Biofilm-Embedded Bacteria

Biofilm is the most common form of life of bacteria on Earth: it represents one of the most non-treatable and recalcitrant forms of infections when considering human health. As an example,

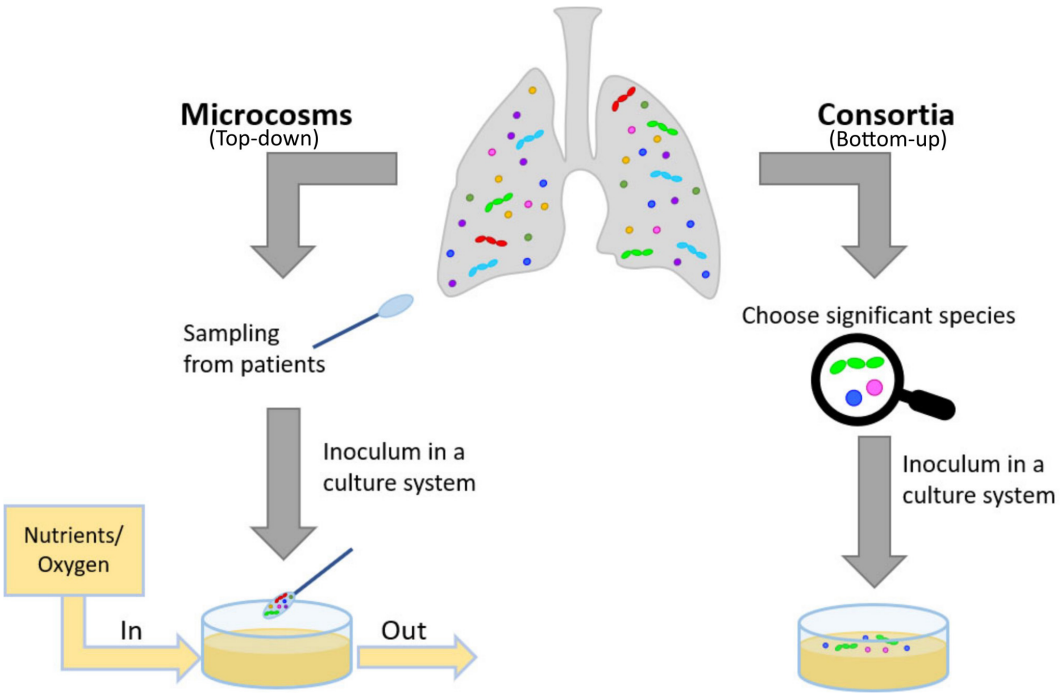

FIGURE 2 | Description of how to model *in vitro* physiological and pathological situations. In a top-down approach, the patient's pool of bacteria is collected and cultured, ideally preserving its multimicrobial nature. In a bottom-up approach, the complexity of the physiological or pathological situation is reduced by introducing the main features fundamental for the study, e.g., selecting significant species and culturing in an appropriate substrate, possibly reproducing the 3D-environment of the mucus.

P. aeruginosa, that is associated with clinical decline and severe outcomes both in cystic fibrosis and in bronchiectasis, is a biofilm-forming bacterium. The same strain is often involved in chronic wounds, together with *Staphylococcus aureus* and *Clostridium perfringens* (Woods et al., 2012; Bertesteanu et al., 2014). Experiences in the literature show resistance of these bacteria to eradication. The inefficacy of the treatment is often believed to be due to established antibiotic-resistant biofilms (Moreau-Marquis et al., 2008). The study of infections, in some cases, reflects a limited perspective, mainly analyzing the behavior of a few well-characterized, pure laboratory bacterial strains. The strategies employed to reproduce *in vitro* biofilms are examples of 3D-models for bacterial cultures. Pharmacodynamic parameters, as well as culturing devices and analytical methods, will be presented and discussed.

The main classical parameters (Macià et al., 2014), specifically used for planktonic bacteria, are still adopted to analyze the effect of different compounds on biofilm, namely the Minimal Inhibitory Concentration (MIC) and the Minimal Bactericidal Concentration (MBC) (**Table 1**). Minimal Biofilm Inhibitory Concentration (MBIC) and Biofilm Bactericidal Concentration (BBC) are indeed the two parameters that parallel MIC and MBC but specifically accounting biofilm. Two further parameters have been harnessed to analyze biofilm responses to external compounds: Biofilm Preventing Concentration (BPC) and Minimal Biofilm Eradication Concentration (MBEC) (**Table 1**). BPC refers to the preventive effect of an antibiotic in biofilm formation. Therefore, bacteria are seeded together with the compound under analysis and biofilm growth is monitored (Fernández-Olmos et al., 2012). Nevertheless, MBIC and BPC are reported as the lowest concentration of drug that resulted in an OD_{650} nm difference of $\leq$ 10% of the mean of two positive control well readings. Contrarily to BPC, the three parameters MBIC, BBC and MBEC are analyzed on biofilms already formed, subsequently challenged with the drug. MBEC represents the lowest concentration of an antibiotic that prevents visible growth in the recovery medium used to collect biofilm cells. These parameters are useful to compare results among different laboratories, but international guidelines on biofilm are missing, unlike for planktonic cultures (Clinical & Laboratory Standards Institutes [CLSI], 2019). Examples of reproducibility across different laboratories are available (Parker et al., 2014) but a general lack of standards in anti-biofilm compounds testing is evident.

Aside from the different parameters that can be tested, a panel of experimental setups can be deployed to investigate biofilm-embedded bacteria (**Table 2**). These culturing devices are in general divided into closed and open systems, the former being mostly related to microtiter plates, the latter involving dynamic systems underflow. Closed systems are in the vast majority of cases, static, batch cultures that are analyzed either during the experiment or at the endpoint. These systems allow scale-up of the analysis, involving more compounds at different concentrations at a single time,

thanks to the use of microtiter plates. Furthermore, these systems are inexpensive and allow quick readout of the test. Nevertheless, the main limitations of these approaches involve great variations between wells (therefore, usually, at least four replicates for each condition are tested), incomplete disruption of biofilm upon endpoint analysis and presence of exhausted nutrients in the well until the end of the test.

Three main supports have been harnessed to study biofilm-forming bacteria in closed systems: apart from plain 96-well tissue culture plates (O'Toole and Kolter, 1998; Stoodley et al., 2002; Ren et al., 2014; Pallavicini et al., 2017), Calgary Biofilm Device

TABLE 1 | Pharmacodynamic parameters employed to analyze the effect of antimicrobial substances, on both planktonic tests and tests accounting biofilm.

Effect	*Acronymous*	*Definition*	*Mode of growth*
Inhibitory effect	MIC	The lowest concentration of an antibiotic that inhibits the visible growth of a planktonic culture after overnight incubation	*Planktonic*
	MBIC	The lowest concentration of an antimicrobial substance at which there is no time-dependent increase in the mean number of biofilm viable cells when an early exposure time is compared with later exposure time (OD_{650} nm difference of $\leq$ 10% of the mean of two positive control well readings)	*Biofilm*
	BPC	The lowest concentration of an antimicrobial substance at which there is no time-dependent increase in the mean number of biofilm viable cells when bacterial inoculation and antibiotic exposure occur simultaneously (OD_{650} nm difference of $\leq$ 10% of the mean of two positive control well readings)	*Biofilm*
Bactericidal effect	MBC	The lowest concentration of an antibiotic able to produce a 99.9% CFUs reduction of the initial inoculum of a planktonic culture	*Planktonic*
	MBEC	The lowest concentration of antimicrobial agent that prevents visible growth in the recovery medium used to collect biofilm cells	*Biofilm*
	BBC	The lowest concentration of antimicrobial agent that killed 99.9% of the cells recovered from a biofilm culture compared to growth control	*Biofilm*

The Table was reformulated from reference 4 (Copyright Sep 11, 2020) with permission from Elsevier (licenses 4905821434139). CFU (Colony Forming Units).

TABLE 2 | Schematic overview of the strategies available to study biofilm communities.

Type	Main Features	Advantages	Drawbacks	Example systems	Evaluated aspects	Study
Closed	Static cultures. Realized within batches and microtiter plates	Low price. Possible scale-up of the analysis High throughput	Low adherence to *in vivo* situations High variance Exhaust medium hard to be eliminated. Incomplete disruption of the biofilm	Calgary Biofilm Device	Growth and shedding of biofilm on a bump, immersed in a bacterial suspension	Harrison et al., 2010; Chavant et al., 2007
				BioFilm Ring Test™	Early biofilm formation is quantified analyzing the precipitation kinetics of a paramagnetic bead through the biofilm itself	Peterson et al., 2015
Open	Dynamic cultures. Strong reliance on bioreactors and pump systems	Realistic experimental conditions Continuous refresh of the medium	High complexity Low throughput Expensiveness	Flow Chambers	Bacteria behavior in presence of physiological-like stimuli	Gómez-Suárez et al., 2001; Pamp et al., 2009; Jass et al., 1995
				Modified Robbins Device	Biofilm produced on a given specimen by a log-phase broth culture	Goeres et al., 2009
				Drip Flow Biofilm Reactor	Biofilm produced on a given specimen under low fluid shear	Donlan et al., 2004
				BioFlux	Long term bacteria-bacteria and bacteria-environment interactions	Lopes et al., 2018

(CBD) and BioFilm Ring Test™ belong to this category. CBD is composed of a microtiter reservoir plate that perfectly matches a lid with pegs that can be accommodated in the reservoir chamber (Ceri et al., 1999; Harrison et al., 2010). Biofilm grows on the suspended pegs. This system allows contemporary screening of many conditions, reduced volumes and contaminations since little handling is required upon lid transfer. The third set up, BioFilm Ring Test™, has been instead designed to investigate early biofilm stage formation (Chavant et al., 2007). Paramagnetic beads are co-inoculated upon biofilm seeding and depending on their precipitation or not after an initial incubation, they indicate if the biofilm has formed or not. If the community is starting to build its extracellular matrix, beads are trapped and cannot be therefore attracted toward the bottom of the microtiter plate by a magnet. Instead, if a visible spot appears at the bottom of the well, this indicates that beads can precipitate and therefore the biofilm formation has been hampered.

Concerning open systems, all the devices include a pump, which allows flux of nutrients, and bacterial cells, thus mimicking more realistic conditions, both for environmental and for healthcare-related biofilms. Shear forces are indeed one of the parameters that can induce stress and modify bacterial behavior (Stoodley et al., 2002; Purevdorj et al., 2002; Peterson et al., 2015). Furthermore, fresh medium is provided, while eliminating exhausted one, thus again increasing mimesis of natural environments. Compared to closed systems, open ones guarantee a more complex setup, having as a drawback a reduction in throughput, since not many conditions can be analyzed at the same time. In general, these systems require more expensive settings and maintenance.

Up to now, flow chambers are among the most convenient tools to understand how the embedded bacteria behave in the presence of flux because direct visualization of the samples is possible since the transparent devices can be coupled to microscopes (either optical, fluorescence or confocal) (Gómez-Suárez et al., 2001; Beyenal et al., 2004; Pamp et al., 2009). Other flow cells that allow parallel testing of different conditions exist, although, in this case, direct imaging is not allowed. These systems are the Modified Robbins Device (Jass et al., 1995) and the Drip Flow Biofilm Reactor (Goeres et al., 2009). Conditions during the experiment can be varied and samples collected thanks to the presence of different valves. Different surfaces can be accommodated within the devices, thus allowing investigation of anti-biofilm surfaces. Imaging is allowed only as an endpoint experimental measure.

The Center for Disease Control Biofilm reactor was named after their inventors (Donlan et al., 2004) and allows testing of up to 24 different coupons in high shear since the system is rotating. Coupons can be easily removed and thus analyzed at different intervals.

Finally, more recently, microfluidic devices have been developed. They can be, to some extent, designed and tailored to each experimental need. These systems are physiologically closer to the conditions that microbial communities may encounter, thus providing a more reliable experimental set up (Drescher et al., 2013; Rusconi et al., 2014). Besides reductions in equipment and reagents, microfluidics allow in-line analysis. Recent advances allowed designing a 96-well plate with connecting microfluidics channels, named BioFlux (Benoit et al., 2010), for throughput analysis.

Different techniques can be employed to analyze biofilm-embedded bacteria (**Table 3**). Viability is one of the first aspects that is analyzed in biofilms. To get quantitative data, the method that implies the count of viable bacteria able to form colonies when re-plated on agar (colony forming units, CFU) is still the most adopted yet laborious method. Especially in the multispecies community, recognition of single species ratios is challenging because it requires specific differential and selective agar media, which are not always available and may be expensive (Røder et al., 2016; Lopes et al., 2018). Other quantitative methods rely on metabolic assays in which viable bacteria can transform substrates that may change or turn into a colored product: examples are tetrazolium salts (e.g., XTT or MTT) or resazurin based products (Van den Driessche et al., 2014; Alonso et al., 2017). Other reagents are used to stain biofilms. Crystal violet unspecifically colors extracellular polymeric substance and cell, thus providing broad information on biofilm thickness and growth (Sharma et al., 2008). If instead general information of viable cells is required, staining with LIVE/DEAD BacLightTM Bacterial Viability Kit (Invitrogen) can be performed and visualization under a Confocal Laser Scanning Microscope (CLSM) would also provide the spatial distribution of bacteria. SEM (Golding et al., 2016; Gomes and Mergulhão, 2017; Huang et al., 2020) can provide useful information with a proper sample preparation. Innovative methods employ cryo-SEM and Environmental SEM to avoid dehydration. Approaches that may allow to specifically tag different components of the matrix, while advanced chip microfluidics are leading toward the development of methods with higher throughput (Di Poto et al., 2009; Hansen et al., 2019; Hartmann et al., 2019). Further methods can be applied to differentiate among species, e.g. probing the biofilm with specific Fluorescence *In Situ* Hybridization (FISH) or with species-specific primers with quantitative qPCR (Amann and Fuchs, 2008; Almeida et al., 2011; Azevedo et al., 2011; Ren et al., 2014; Lopes et al., 2018). These approaches are destructive and are carried out as endpoint analysis. An overview of the most used techniques to study biofilm embedded bacteria is reported in **Table 3**.

Among high-throughput techniques recently developed we can find the so-called –omics technologies. Some of these techniques are genomics, metagenomics, microbiomic, transcriptomics and proteomics, metabolomics (Yates et al., 2009; Sorek and Cossart, 2010; Moree et al., 2012; Krohn-Molt et al., 2013; Liu et al., 2019). These assays can give access to an extensive amount of information, considering bacteria and bacterial genomes, as well as the entire set of transcripts, proteins and metabolites in a target niche (Yates et al., 2009; Sorek and Cossart, 2010; Moree et al., 2012; Krohn-Molt et al., 2013; Liu et al., 2019). Schematic information on some of the most used -omics techniques to study bacterial communities are reported in **Table 3**. A multi-omics approach is very used in translational

TABLE 3 | Schematic overview of the strategies available to study biofilm embedded bacteria.

Assay	Type	Principle	Features	Advantages	Drawbacks	Study
CFU count	Viability	Diluted bacteria are plated on agar media and incubated until colonies growth; colonies formed are counted	Direct quantitative evaluation of viable cells	Quick and not expensive	Difficult to evaluate multispecies community Specific differential/selective media are needed to evaluate different bacteria The CFU countable range is relatively narrow, errors may arise from biofilms (high cell aggregation)	Røder et al., 2016; Alonso et al., 2017
XTT, MTT	Metabolic assays	Cells are incubated with a substrate that is metabolized by cells in a colorigenic compound	Indirect quantitative evaluation of viable cells	Mostly used with in planktonic situation, quantitative, relatively expensive	The use of specific compounds may interact with the substrate Biofilm embedded bacteria may have a different metabolic activity than planktonic bacteria usually used as standard	Van den Driessche et al., 2014; Sharma et al., 2008
Crystal violet	Biofilm staining	The compound stains the biofilm making it visible	Direct measure of biofilm mass	Provides broad information on biofilm thickness and growth	The entire biofilm mass is stained (extracellular matrix and cells), no information on cell viability is given	Golding et al., 2016
Live/dead staining	Biofilm staining	The compound differentially stains cells based on the integrity of the membrane	Direct quantitative measure of viable cells	Mostly used in planktonic situation, may provide the spatial distribution of bacteria in a biofilm	High-throughput quantification of biofilm viability may be difficult The use of CLSM is needed	Gomes and Mergulhão, 2017
FISH	Species differentiation	Species specific fluorescent probes hybridize with bacterial oligonucleotides making bacteria visible	Direct qualitative visualization of different strains	The use of a different probes specifically distinguishes among bacteria	If the probe target is low, the signal may be not detectable against the background	Parker et al., 2014; Røder et al., 2016; Hansen et al., 2019; Hartmann et al., 2019; Almeida et al., 2011
qPCR	Species differentiation	PCR amplification of a target release fluorescence proportional to the initial bacterial load	Direct quantitative or semi-quantitative visualization of bacteria	The use of a different probes specifically distinguishes among bacteria	It does not distinguish among viable and non-viable cells	Ceri et al., 1999; Røder et al., 2016
Microbiome	Next generation sequencing	Next-generation sequencing target amplification of 16s rRNA gene	Direct relative analysis of microbial community	Untargeted and relatively expensive, high-throughput	Not quantitative, bacteria identification to genus	Sorek and Cossart, 2010
Shotgun metagenomics	Next generation sequencing	Next-generation sequencing of genes in all bacteria	Direct relative analysis of microbial community and bacterial features	Untargeted, acquisition of all the genetic information in the bacteria	Very expensive High bioinformatic expertise needed for data-analysis	Amann and Fuchs, 2008; Sorek and Cossart, 2010
Metatran scriptomics	Next generation sequencing	Next-generation sequencing approach to study gene expression of profile of the whole bacterial community	Direct relative analysis of bacterial gene expression	Untargeted, acquisition of all the gene expression of sequenced bacterial community	Very expensive High bioinformatic expertise needed for data-analysis	Azevedo et al., 2011; Liu et al., 2019; Sorek and Cossart, 2010
SEM	Morphological observation	Scanning electron microscopy observations. Samples fixed and gold sputtered. Innovative preparative steps of the sample and alternatives to gold sputtering. Possible wet-SEM and cryo-SEM to avoid dehydration steps.	Morphological and spatial analysis of both the three-dimensional matrix and the embedded bacteria	High resolution and magnification. High depth of field Suitable for analyses on heterogeneous surfaces Possibility to identify the type (in some case the genus) of the microbe	No viability informations The use of fluorochromes is not allowed The output of the analysis is strictly dependent on not-obvious preparative steps Low sensitivity unless concentrated samples used	Golding et al., 2016; Gomes and Mergulhão, 2017; Huang et al., 2020

CFU, colony forming units; CLSM, Confocal Laser Scanning Microscope; FISH, fluorescence in situ hybridization; qPCR, Real time PCR; SEM, Scanning Electron Microscopy.

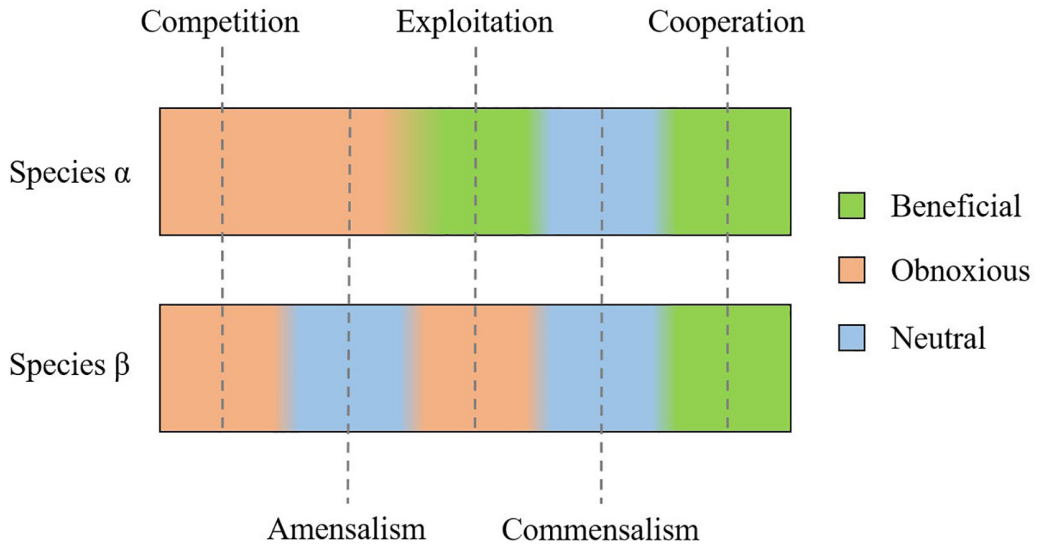

FIGURE 3 | Possible interaction between two bacterial species (α and β): competition and cooperation are respectively obnoxious or beneficial for both species. Exploitation is beneficial for species α, at the expense of species β; whereas amensalism and commensalism do not affect species β, but are respectively obnoxious or beneficial to species α.

research in the study of the interaction between bacterial niches and host response in human diseases (Hasin et al., 2017).

Modeling the Interactions of Different Bacterial Strains: Co-cultures

Bacteria are usually considered as single-cell organisms and their ability to interact and form monospecies biofilms is quite often overlooked. The use of *in vitro* co-culture, a family of laboratory techniques that aim at growing two or more different cell types on the same support, is the current strategy to study multistrain interactions. The general purpose of co-culture is to recapitulate *in vitro* key communication and interaction mechanisms, which might intervene *in vivo* among the target cell types (Bogdanowicz and Lu, 2013), thus enabling the uncovering of crucial phenomena to design new therapies. Three macro-groups of co-cultures are distinguished based on the kind of cultured cells. Firstly, co-cultures of eukaryotic cells are realized by growing different cell types to either study physiological interactive processes (Bam et al., 2015; Jia et al., 2017; Yin et al., 2017) or develop a functional construct to be used in tissue engineering approaches (Vuornos et al., 2019). Similarly, co-cultures of prokaryotic cells have also been realized, in which various bacterial strains are cultured for many objectives, spacing from the study of interspecies *quorum-sensing* occurrences (An et al., 2006) to the industrialized production of chemicals (Jones and Wang, 2018). Hybrid co-cultures have also been proposed, in which both eukaryotic and prokaryotic cells are cultured, in the attempt to understand physiological symbiosis relations (Haller et al., 2000), or pathological effects on tissues after the settlement of an infectious phenomenon (Kim et al., 2010).

Co-cultures of prokaryotic cells are crucial for the development of new therapies against threatening diseases that are characterized by the presence of complex infectious microbiomes (e.g., cystic fibrosis, bronchiectasis, tuberculosis). However, the realization of fully functional and effective models is still challenging due to both the complexity of the *in vivo* microbiome itself, and the compelling boundary conditions stated by the host organism. Moreover, due to the novelty of the topic, a consensus on one platform for the realization of bacterial co-cultures does not exist yet. As a result, in our opinion, different studies relate to different protocols to be developed in a time-consuming quest of the appropriate experimental conditions. Moreover, in consequence, the results are difficult to compare and the whole picture to be reconstructed is rendered in parts that, in some cases, are difficult to match. Up to now, it is not possible to culture the whole microbiota and this challenge is far to be met.

MATHEMATICAL AND ECOLOGICAL MODELS FOR MICROBIAL CO-CULTURES

Mathematical models have characterized single-strain bacterial genetic evolution (Hindré et al., 2012) and antibiotic resistance (Greulich et al., 2015). Once validated, such models allow us to explore many different scenarios in a cost-effective way (Hindré et al., 2012; Allen and Waclaw, 2016). This possibility becomes of interest when modeling polymicrobial consortia facing the fact that bacteria do not live in monocultures in nature. In mixed communities, the most common natural ecosystems, each and every species optimized for different functions (Kneitel and Chase, 2004), and the interaction between different species sharing metabolic resources, defined as cross-feeding (Estrela et al., 2012; Coyte et al., 2015), has been modeled. Ecological

theories in the framework of microbial consortia engineering aimed at designing efficient co-cultures for biofuel production or enhanced mineral recovery (Bernstein and Carlson, 2012). These theories have been applied also to human microbiota and polymicrobial infections (Costello et al., 2012; de Vos et al., 2017). In particular, it is possible to distinguish five different ecological interactions, when cross-feeding is involved (**Figure 3**; Coyte et al., 2015; Bernstein and Carlson, 2012; Faust and Raes, 2012):

- competition for space and resources;
- amensalism: one organism is inhibited or destroyed while the other organism remains unaffected;
- exploitation: one organism takes advantage of the other for resources scavenging and metabolism;
- commensalism: neither of the bacteria benefits from the other or provokes any harm;
- and cooperation: both the organisms benefit from the relation.

Mathematical models aim to relate the physical characteristics of the studied system and its dynamic evolution starting from the initial conditions until the system reaches an equilibrium. In case there are two bacterial strains and they coexist at the equilibrium, a bistability condition is reached (El Hajji et al., 2009; Wang and Wu, 2011; Assaneo et al., 2013). Considering the basic example of a chemostat, it is possible to model it with a system of five equations that describe the interaction between the bacteria and their nutrient support and consumption (Speirs et al., 1996). The outputs of the model are the variation in time of the bacterial population density and the nutrient concentration. The system of equations relates such variation with the system working conditions (e.g., initial population density of the bacterial species involved, growth rate, nutrient flow and intake) (Speirs et al., 1996). In this case, however, the relation between stability condition and model parameters is not straightforward, for the high the number of parameters required to solve the system of equations. To simplify it, it is possible to use the Lodka-Volterra equations that were initially designed to describe just the prey-predator competitive interaction (Lotka, 1922; Volterra, 1928), but they were generalized to all kinds of ecological interactions (May, 1973; Solé and Bascompte, 2012). This model consists of fewer equations than the physical model and a limited number of parameters that retain a physical interpretation of the model characteristics (Vet et al., 2018). Indeed, the Lodka-Volterra model will consist of as many equations as many are the species involved in the chemostat (e.g., two competing species will result in a model with two equations). Thanks to this simplification, it is easier to explore the relation between the initial conditions and the possible multiple species coexistence at the equilibrium (Vet et al., 2018). The model relies on some simplifying hypothesis: it ignores the mechanisms of interaction (like predator preferences) and it is based on the additivity assumption (Momeni et al., 2017). The latter assumes that pairwise interactions are sufficient to describe microbial community dynamics: the fitness of the polymicrobial system results from the sum of the fitness of each individual species, given by the interaction of the aforementioned species and the other interacting species (Momeni et al., 2017). Since it has been recently proven that the additivity assumption may fail, due to the complex non-linear interactions present in microbial communities (Dormann and Roxburgh, 2005; Momeni et al., 2017), it is possible to use higher-order models (Bairey et al., 2016) or models closer to the physical systems they want to describe (Vet et al., 2018), but at the expense of model simplicity.

Considering a relevant case of polymicrobial infections as Cystic Fibrosis, clinical data has been gathered regarding the microbial populations present under different conditions (age, use of antibiotics) (Klepac-Ceraj et al., 2010; Sherrard et al., 2019). In the near future, these databases could be exploited to validate mathematical models able to predict the development of infections in CF patients, knowing the patient history and, therefore, to choose the best treatment for each clinical case.

FOCUS ON *IN VITRO* MODELS FOR CYSTIC FIBROSIS

Cystic fibrosis (CF) is one notable example of how the absence of well-established laboratory protocols for the realization of bacterial co-cultures drives researchers to choose and optimize different methods and culture conditions that are case-dependent systems, which challenges the comparison of data among different laboratories. One of the most pernicious aspects of this disease resides in the high number of species composing the infectious microbiome (Huang and LiPuma, 2016), resulting in a dynamic evolution of the chronic pulmonary infections throughout the life of the patients. Such behavior is one of the main factors causing the inefficiency of a classical antibiotic therapy in completely eradicating lungs-resident pathogens. Various *in vivo* models have been developed to test antibiotics efficacy: an essential requirement for such a model is the progression from a spontaneous bacterial infection to a chronic stage associated with biofilm formation (Lebeaux et al., 2013). *In vitro* models, on the other hand, can be useful to elucidate different aspects, such as the competitive effects of the different species on their viability and the modification of genic expression due to gain resistance to antibiotic treatments. The factors promoting the coexistence of different pathogens, such as phenotype modification, and their adaptive evolution to accommodate different species are also complex aspects that need to be understood and controlled. Most of the studies are conducted by dual cultures, with *S. aureus* and *P. aeruginosa*.

It is well known that *S. aureus* is the main colonizer of lung mucosa from the childhood of the cystic fibrosis patients, until the establishment of *P. aeruginosa* colonies, which tend to prevail in *S. aureus*. Despite the majority of *in vitro* models assuming *P. aeruginosa* to carry on complete eradication of *S. aureus*, it is uncommon to isolate both bacterial species from Cystic Fibrosis-infected lungs. In an *in vitro* model, it has been demonstrated that the culture in dual-species biofilm led to a consistent decrease of *S. aureus* relative abundance without achieving its complete eradication (Woods et al., 2018). This study exploits both a relatively simple closed multiwell model and a microfluidic system based on the culture of the strains on silicon tubes with a continuous circulation of fresh medium (Woods

et al., 2018). The same model was previously used by the same authors to study the effect of signaling molecules on the genetic expression of *P. aeruginosa* monocultures (Davies and Marques, 2009; Marques et al., 2014). In the open model, bacteria grow at the liquid/solid interface: this configuration is gradually adding complexity concerning the basic multiwell closed model, but it is still far from the lung environment.

Two different co-culture systems were able to provide a deeper and more specific model for the early interaction of the two strains. It was supposed that *P. aeruginosa* genes, responsible to produce substances inducing the elimination of *S. aureus,* were downregulated when grown in dual-species biofilm. Both single and dual-species biofilms of *S. aureus* and *P. aeruginosa* were grown. To test this hypothesis, two experimental conditions were considered. In the first one *P. aeruginosa* was introduced at a specific proportion, that could mimic the *in vivo* situation in which a small amount of *P. aeruginosa* encounters a bigger and well-established amount of *S. aureus*, after the development of *S. aureus* biofilm. In the second, bacterial biofilms were co-cultured since the beginning of the experiment. While the previous example investigated the responses produced by the co-culture of bacteria in the mid-term (days), another research studied the reactions triggered at a genetic level during a short period (hours) of co-culture. In particular, various genomic analyses revealed how the competition for resources drives the first responses. The encounter of the two pathogens stimulated the up-regulation of genes related to the optimization of all those factors functional to the adaptation of metabolism, to excel in the competition for resources (Tognon et al., 2019). Pure cultures of *P. aeruginosa* and *S. aureus* were thus produced, and co-cultures were prepared by mixing the previously formed monocultures. Genomic analysis to evaluate changes in genic expressions of both organisms subsequently performed via RNA extraction, RNA-seq assays, and quantitative. Real Time-PCR (qPCR) (Tognon et al., 2019). In this case, a closed multiwell system was implemented, and single and co-cultures were seeded on solid agar plates enriched with nutrients and ions to sustain bacterial growth and mimic physiological conditions. The medium was tailored in previous studies to ensure a similar growth rate of both species (Tognon et al., 2017). Despite being elementary, the growth of the biofilms at the solid/air interface reproduces the pulmonary environment more than a microfluidic system.

The realization of *in vitro* co-cultures recently also played a key role in studying the causes of several evolutive changes observed in *P. aeruginosa* adaptation to the CF lung environment, like downregulation of lipopolysaccharide (LPS) and quorum sensing (QS) factors. *P. aeruginosa* might undergo two highly represented mutations (Tognon et al., 2017). The first one (WSP-level mutation, negatively correlated with *S. aureus* survival rates) was supposed to be caused by the culture condition (growth in a low oxygen environment) since it was present in both mono-cultured and co-cultured bacteria. The second mutation (a mutation at LPS level, increasing *P. aeruginosa* antibiotic resistance) appeared instead only in co-cultured *P. aeruginosa*, thus it has been thought to be an adaptive response to the presence of *S. aureus*. Such an experiment has been performed

TABLE 4 | Main features of recent experiments designed to explore bacterium–bacterium interactions in the case of cystic fibrosis.

Model type	Approach	Species	Culture Conditions	Physical Parameters	Aim	Study
CL (multiwell) and OP (continuous flow in silicon tubes bioreactor)	Consortium	*P. aeruginosa* *S. aureus* (1:250)	Medium: BHI 20% (CL), BHI 10% (OP) Seeding: 7×10^7 cells/ml (*S. aureus*) (OP and CL)	T: 37°C (CL), 22°C (OP) Replenishing rate (CL): 12 h Medium flow (OP): 10.8 ml/h Duration (*S. aureus*): 5 days Duration (coculture): 14 days Sampling Rate: 24 h	Dynamic competition	Woods et al., 2018
CL: multiwell, solid agar medium	Consortium	*P. aeruginosa* *S. aureus* (1:1)	Medium: (tailored) M14 Seeding: 10^8 CFU/ml	T: 37°C Duration: 3 h (mono and cocultures)	Dynamic competition Genetic expression	Tognon et al., 2019
CL: multiwell, liquid medium	Consortium	*P. aeruginosa* *S. aureus* (1:100 and 1:1000)	Medium: (tailored) M14 Seeding: 5 (@#105 CFU per well (*P. aeruginosa*	T: 37°C Duration: 15 days Sampling rate: 24 h.	Adaptation to lung environment	Tognon et al., 2017
CL: solid agar medium	In between consortium and microcosm	*P. aeruginosa* (clinical isolate) *S. aureus* (lab strain) (1:1)	Medium: LB (*P. aeruginosa*), TSB (*S. aureus*) Seeding: [0.5;1] x 10^8 CFU/ml	T: 37(°C Duration: 16 h	Genetic expression	Limoli et al., 2017
CL: multiwell, liquid	Consortium	*P. aeruginosa* *S. aureus*	Medium: LB (*P. aeruginosa*), TSB (*S. aureus*), MEM + L-Gln Seeding: 50 μl of 0.05 OD_{600} cell suspension (*S. aureus*), ans *P. aeruginosa* supernatant	T: 37°C CO_2: 5% Duration: 30 h	Antibiotic resistance	Orazi and O'Toole, 2017
CL: bacteria cultured onto epithelial cell monolayers	Microcosm	*P. aeruginosa* (biofilm forming and non-forming strains) + epithelial cells	Medium: LB Seeding: 1.0 OD_{600} *P. aeruginosa* suspension diluted up to 1:500 and seeded on murine epithelial cells	T: 37°C Duration: 20 h	Biofilm formation	Woodworth et al., 2008; Cont et al., 2020

CL, closed system; OP, open system; BHI, Brain Heart Infusion; M14, is a tailored medium ([137]); LB, Lysogeny Broth; TSB, Tryptic Soy Broth; MEM, Minimal Essential Medium.

through the establishment of a peculiar protocol, in which *P. aeruginosa* has been evolved for at least 150 generations in liquid close multiwell cultures, both in the presence and absence of *S. aureus*, since interactions between *P. aeruginosa* and *S. aureus* are thought to be crucial in this process of adaptation. Serial dilutions of cellular suspensions were performed to mimic the *in vivo* situation in which a small amount of *P. aeruginosa* encounters pre-established large colonies of *S. aureus*.

Moreover, an interesting mutation of *P. aeruginosa* might take place in CF patients' lungs, characterized by a switch from the native phenotype toward the so-called "mucoid" phenotype, which owes its name to the overproduction of alginate (Pritt et al., 2007). *P. aeruginosa* was demonstrated to undergo this phenotypic shift, expressing the mucoid phenotype not only characterized by the up-regulation of genes responsible for alginate production, but also by the down-regulation of genes encoding for virulence factors responsible of killing *S. aureus* (Limoli et al., 2017). Their protocol relied on the "agar-plate cross streak assay" (Balouiri et al., 2016). More in detail, *P. aeruginosa* isolated from mono-infected and co-infected patients was cross-streaked to a laboratory strain of *S. aureus*. In the same way, *S. aureus* clinical isolation was cross-streaked to a laboratory strain of *P. aeruginosa* (Limoli et al., 2017). This model, therefore, is in between the consortium and microcosm classification, as it sources parts of the bacteria from patients and partially from laboratory culture.

Another field taking advantage of *in vitro* co-cultures is the research against antibiotics resistance. Clinical data supported the hypothesis that the exposure of *S. aureus* to *P. aeruginosa* by-product leads to a drastic decrease in vancomycin (frontline antibiotic to treat *S. aureus* infections) efficiency against *S. aureus* (Filkins et al., 2015). This phenomenon was examined and it was found out that in the presence of the *P. aeruginosa* supernatant, vancomycin activity was reduced, and more colonies were detected whether *S. aureus* was cultured in planktonic or as biofilms. Given that *P. aeruginosa* tends to over-compete *S. aureus* while co-cultured (both *in vivo* and *in vitro* models), co-cultures were prepared in a peculiar way called "biofilm disruption assay" (Orazi and O'Toole, 2017). This procedure relied on the preparation of *S. aureus* monocultures. Then the biofilm produced by *S. aureus* pure cultures was mechanically disrupted, and *P. aeruginosa* supernatant was joined. This method compared to the Minimal Bactericidal Concentration (MBC) assay for planktonic cultures and as an alternative to the other methods to assess antibiotic resistance in biofilms.

Eventually, considering the role played by biofilm formation, the ability of *P. aeruginosa* to form biofilm was studied. This ability was investigated through scanning electron microscopy and confocal microscopy of different *P. aeruginosa* strains on an airway epithelial cell (Woodworth et al., 2008). Biofilm-forming strains were able to produce viable biofilms on the surface of airway epithelial cell monolayer. Further, *P. aeruginosa* and *V. Cholerae* were cultured on a monolayer of endothelial cells to assess the mechanobiological effect on the cells (Cont et al., 2020). In these cases, the co-culture is represented by the simultaneous culture of prokaryotic and eukaryotic cells. Despite being far from the physiological environment, such systems can be considered a microcosm for the complexity introduced by this type of co-culture.

It is glaring how the realization of a reliable *in vitro* model represents nowadays a crucial point for better understanding, and, consequently, try to solve as many criticalities as possible of such a polyhedral disease. However, comparing the experiments considered, it is possible to notice a remarkable heterogeneity under various points of view (e.g., duration of cultures, culture medium, and seeding ratios) (**Table 4**). Moreover, most of the experiments refer to planktonic cultures, without considering the case of bacteria grown inside some three-dimensional matrix mimicking the pulmonary CF mucus, which is known to be crucial in influencing bacterial behaviors. Regrettably, the realization of both a standard procedure and support, allowing the realization of co-cultures, still represents a big challenge. This reason is pushing scientists to realize culture systems tailored for the experimental purpose.

CONCLUSIVE REMARKS

The study of the biological features of polymicrobial infections needs to be considered to develop effective antimicrobial strategies useful to treat complex and chronic diseases like CF and bronchiectasis. The available *in vitro* testing methods provide the state-of-the-art although they were not developed to study the crosstalk among different bacteria and the effect of the three-dimensional environment. They represent important but limited examples available up-to-now: two-species cultures and biofilms as unique examples of polymicrobial cultures and 3D-environments, respectively. New developments in co-cultures and the study of *in vitro* bacterial three-dimensional substrates are needed to overcome the frontier for the production of realistic tools to be employed in the study of bacterial interactions and drug discovery and to switch to the reproduction of 3D environments and polymicrobial cultures. Within this scenario, we envision the need for *in vitro* methods that could impact on diverse applicative sectors.

AUTHOR CONTRIBUTIONS

MO and LZ worked on the draft of the document and revised the manuscript with the help of GG. LZ organized the bibliography. FB and SVU wrote the first draft of some sections. PP organized and focussed the contributions and coordinated the revision and the answers to the reviewers. PP and LV designed the content and the structure of the review and critically revised the manuscript in all stages. All authors contributed to the final manuscript revision, read and approved the submitted version.

FUNDING

The research was also supported by a grant of the Italian Ministry of Education, University and Research (MIUR) to the Department of Molecular Medicine at the University of Pavia under the initiative "Dipartimenti di Eccellenza (2018–2022)."

ACKNOWLEDGMENTS

Authors are grateful to Ing. Anna Ziccarelli, since part of this manuscript stemmed from her master thesis work. PP., LV., GG. and SVU thank Switch to Product 2018 project, funded by Politecnico di Milano, which supported the increase of knowledge in this field.

REFERENCES

Allen, R., and Waclaw, B. (2016). Antibiotic resistance: a physicist's view. *Phys. Biol.* 13:045001. doi: 10.1088/1478-3975/13/4/045001

Almeida, C., Azevedo, N. F., Santos, S., Keevil, C. W., and Vieira, M. J. (2011). Discriminating multi-species populations in biofilms with peptide nucleic acid fluorescence in situ hybridization (PNA FISH). *PLoS One* 6:e14786. doi: 10.1371/journal.pone.0014786

Alonso, B., Cruces, R., Pérez, A., Sánchez-Carrillo, C., and Guembe, M. (2017). Comparison of the XTT and resazurin assays for quantification of the metabolic activity of *Staphylococcus aureus* biofilm. *J. Microbiol. Methods* 139, 135–137. doi: 10.1016/j.mimet.2017.06.004

Amann, R., and Fuchs, B. M. (2008). Single-cell identification in microbial communities by improved fluorescence in situ hybridization techniques. *Nat. Rev. Microbiol.* 6, 339–348. doi: 10.1038/nrmicro1888

Amati, F., Franceschi, E., Gramegna, A., Chalmers, J. D., and Aliberti, S. (2017). Investigating the etiology of bronchiectasis: you do not find what you do not look for. *Respiration* 93, 228–229. doi: 10.1159/000455880

Amon, P., and Sanderson, I. (2017). What is the microbiome? *Arch. Dis. Child Educ. Pract. Ed.* 102, 257–260.

An, D., Danhorn, T., Fuqua, C., and Parsek, M. R. (2006). Quorum sensing and motility mediate interactions between *Pseudomonas aeruginosa* and *Agrobacterium tumefaciens* in biofilm cocultures. *Proc. Natl. Acad. Sci. U.S.A.* 103, 3828–3833. doi: 10.1073/pnas.0511323103

Assaneo, F., Coutinho, R. M., Lin, Y., Mantilla, C., and Lutscher, F. (2013). Dynamics and coexistence in a system with intraguild mutualism. *Ecol. Complex.* 14, 64–74. doi: 10.1016/j.ecocom.2012.10.004

Azevedo, N. F., Jardim, T., Almeida, C., Cerqueira, L., Almeida, A. J., Rodrigues, F., et al. (2011). Application of flow cytometry for the identification of Staphylococcus epidermidis by peptide nucleic acid fluorescence in situ hybridization (PNA FISH) in blood samples. *Antonie Van Leeuwenhoek* 100, 463–470. doi: 10.1007/s10482-011-9595-9

Bairey, E., Kelsic, E. D., and Kishony, R. (2016). High-order species interactions shape ecosystem diversity. *Nat. Commun.* 7:12285.

Balouiri, M., Sadiki, M., and Ibnsouda, S. K. (2016). Methods for *in vitro* evaluating antimicrobial activity: a review. *J. Pharm. Anal.* 6, 71–79. doi: 10.1016/j.jpha.2015.11.005

Bam, R., Khan, S., Ling, W., Randal, S. S., Li, X., Barlogie, B., et al. (2015). Primary myeloma interaction and growth in coculture with healthy donor hematopoietic bone marrow. *BMC Cancer* 15:864. doi: 10.1186/s12885-015-1892-7

Barbieri, N., Herrera, M., Salva, S., Villena, J., and Alvarez, S. (2017). *Lactobacillus rhamnosus* CRL1505 nasal administration improves recovery of T-cell mediated immunity against pneumococcal infection in malnourished mice. *Benef. Microbes* 8, 393–405. doi: 10.3920/bm2016.0152

Barbieri, N., Salva, S., Herrera, M., Villena, J., and Alvarez, S. (2019). Nasal priming with *Lactobacillus rhamnosus* CRL1505 stimulates mononuclear phagocytes of immunocompromised malnourished mice: improvement of respiratory immune response. *Probiotics Antimicrob. Proteins* 12, 494–504. doi: 10.1007/s12602-019-09551-8

Barbieri, N., Villena, J., Herrera, M., Salva, S., and Alvarez, S. (2013). Nasally administered *Lactobacillus rhamnosus* accelerate the recovery of humoral immunity in B lymphocyte-deficient malnourished mice. *J. Nutr.* 143, 227–235. doi: 10.3945/jn.112.165811

Bassis, C. M., Erb-Downward, J. R., Dickson, R. P., Freeman, C. M., Schmidt, T. M., Young, V. B., et al. (2015). Analysis of the upper respiratory tract microbiotas as the source of the lung and gastric microbiotas in healthy individuals. *mBio* 6:e00037-15.

Bauer, H., Horowitz, R. E., Levenson, S. M., and Popper, H. (1963). The response of the lymphatic tissue to the microbial flora. Studies on germfree mice. *Am. J. Pathol.* 42, 471–483.

Benoit, M. R., Conant, C. G., Ionescu-Zanetti, C., Schwartz, M., and Matin, A. (2010). New device for high-throughput viability screening of flow biofilms. *Appl. Environ. Microbiol.* 76, 4136–4142. doi: 10.1128/aem.03065-09

Bernstein, H. C., and Carlson, R. P. (2012). Microbial consortia engineering for cellular factories: *in vitro* to *in silico* systems. *Comput. Struct. Biotechnol. J.* 3:e201210017. doi: 10.5936/csbj.201210017

Bertesteanu, S., Triaridis, S., Stankovic, M., Lazar, V., Chifiriuc, M. C., Vlad, M., et al. (2014). Polymicrobial wound infections: pathophysiology and current therapeutic approaches. *Int. J. Pharm.* 463, 119–126. doi: 10.1016/j.ijpharm.2013.12.012

Beyenal, H., Lewandowski, Z., and Harkin, G. (2004). Quantifying biofilm structure: facts and fiction. *Biofouling* 20, 1–23. doi: 10.1080/08927010420001916 28

Bilal, H., Bergen, P. J., Kim, T. H., Chung, S. E., Peleg, A. Y., Oliver, A., et al. (2019). Synergistic Meropenem-Tobramycin Combination Dosage Regimens against Clinical Hypermutable *Pseudomonas aeruginosa* at Simulated Epithelial Lining Fluid Concentrations in a Dynamic Biofilm Model. *Antimicrob. Agents Chemother.* 63:e01293-19.

Bogdanowicz, D. R., and Lu, H. H. (2013). Studying cell-cell communication in co-culture. *Biotechnol. J.* 8, 395–396. doi: 10.1002/biot.201300054

Boyton, R. J., Reynolds, C. J., Quigley, K. J., and Altmann, D. M. (2013). Immune mechanisms and the impact of the disrupted lung microbiome in chronic bacterial lung infection and bronchiectasis. *Clin. Exp. Immunol.* 171, 117–123. doi: 10.1111/cei.12003

Brown, J. L., Johnston, W., Delaney, C., Short, B., Butcher, M. C., Young, T., et al. (2019). Polymicrobial oral biofilm models: simplifying the complex. *J. Med. Microbiol.* 68, 1573–1584. doi: 10.1099/jmm.0.001063

Brown, R. L., Sequeira, R. P., and Clarke, T. B. (2017). The microbiota protects against respiratory infection via GM-CSF signaling. *Nat. Commun.* 8:1512.

Ceri, H., Olson, M. E., Stremick, C., Read, R. R., Morck, D., and Buret, A. (1999). The Calgary Biofilm Device: new technology for rapid determination of antibiotic susceptibilities of bacterial biofilms. *J. Clin. Microbiol.* 37, 1771–1776. doi: 10.1128/jcm.37.6.1771-1776.1999

Chalmers, J. D., Goeminne, P., Aliberti, S., McDonnell, M. J., Lonni, S., Davidson, J., et al. (2014). The bronchiectasis severity index. An international derivation and validation study. *Am. J. Respir. Crit. Care Med.* 189, 576–585. doi: 10.1164/rccm.201309-1575oc

Chalmers, J. D., Moffitt, K. L., Suarez-Cuartin, G., Sibila, O., Finch, S., Furrie, E., et al. (2017). Neutrophil Elastase activity is associated with exacerbations and lung function decline in bronchiectasis. *Am. J. Respir. Crit. Care Med.* 195, 1384–1393. doi: 10.1164/rccm.201605-1027oc

Chavant, P., Gaillard-Martinie, B., Talon, R., Hébraud, M., and Bernardi, T. (2007). A new device for rapid evaluation of biofilm formation potential by bacteria. *J. Microbiol. Methods* 68, 605–612. doi: 10.1016/j.mimet.2006.11.010

Cheung, J. C., Kim Chiaw, P., Pasyk, S., and Bear, C. E. (2008). Molecular basis for the ATPase activity of CFTR. *Arch. Biochem. Biophys.* 476, 95–100. doi: 10.1016/j.abb.2008.03.033

Clinical & Laboratory Standards Institutes [CLSI], (2019). CLSI Microbiology Standards Subcommittees & Resources Advancing the Field of Microbiology with Timely AST Standards. Available at: https://clsi.org/meetings/microbiology/ (accessed December 7, 2019).

Cont, A., Rossy, T., Al-Mayyah, Z., and Persat, A. (2020). Biofilms mechanically damage epithelia by buckling. *bioRxiv* [Preprint]. doi: 10.1101/2020.01.29.923060

Costa, A. N., da Costa, F. M., Campos, S. V., Salles, R. K., and Athanazio, R. A. (2018). The pulmonary microbiome: challenges of a new paradigm. *J. Bras. Pneumol.* 44, 424–432. doi: 10.1590/s1806-37562017000000209

Costello, E. K., Stagaman, K., Dethlefsen, L., Bohannan, B. J. M., and Relman, D. A. (2012). The application of ecological theory toward an understanding of the human microbiome. *Science* 336, 1255–1262. doi: 10.1126/science.1224203

Costerton, J. W., Lewandowski, Z., Caldwell, D. E., Korber, D. R., and Lappin-Scott, H. M. (1995). Microbial biofilms. *Annu. Rev. Microbiol.* 49, 711–745.

Coyte, K. Z., Schluter, J., and Foster, K. R. (2015). The ecology of the microbiome: networks, competition, and stability. *Science* 350, 663–666. doi: 10.1126/science.aad2602

Davies, D. G., and Marques, C. N. H. (2009). A fatty acid messenger is responsible for inducing dispersion in microbial biofilms. *J. Bacteriol.* 191, 1393–1403. doi: 10.1128/jb.01214-08

de Dios Caballero, J., Vida, R., Cobo, M., Máiz, L., Suárez, L., Galeano, J., et al. (2017). Individual patterns of complexity in cystic fibrosis lung microbiota, including predator bacteria, over a 1-year period. *mBio* 8:e00959-17.

de Vos, M. G. J., Zagorski, M., McNally, A., and Bollenbach, T. (2017). Interaction networks, ecological stability, and collective antibiotic tolerance in polymicrobial infections. *Proc. Natl. Acad. Sci. U.S.A.* 114, 10666–10671. doi: 10.1073/pnas.1713372114

Di Poto, A., Sbarra, M. S., Provenza, G., Visai, L., and Speziale, P. (2009). The effect of photodynamic treatment combined with antibiotic action or host defence mechanisms on *Staphylococcus aureus* biofilms. *Biomaterials* 30, 3158–3166. doi: 10.1016/j.biomaterials.2009.02.038

Dickson, R. P., Erb-Downward, J. R., Freeman, C. M., McCloskey, L., Beck, J. M., Huffnagle, G. B., et al. (2015). Spatial variation in the healthy human lung microbiome and the adapted island model of lung biogeography. *Ann. Am. Thorac. Soc.* 12, 821–830. doi: 10.1513/annalsats.201501-029oc

Dominguez-Bello, M. G., Costello, E. K., Contreras, M., Magris, M., Hidalgo, G., Fierer, N., et al. (2010). Delivery mode shapes the acquisition and structure of the initial microbiota across multiple body habitats in newborns. *Proc. Natl. Acad. Sci. U.S.A.* 107, 11971–11975. doi: 10.1073/pnas.1002601107

Donlan, R. M., Piede, J. A., Heyes, C. D., Sanii, L., Murga, R., Edmonds, P., et al. (2004). Model system for growing and quantifying *Streptococcus pneumoniae* biofilms in situ and in real time. *Appl. Environ. Microbiol.* 70, 4980–4988.

Dormann, C. F., and Roxburgh, S. H. (2005). Experimental evidence rejects pairwise modelling approach to coexistence in plant communities. *Proc. Biol. Sci.* 272, 1279–1285. doi: 10.1098/rspb.2005.3066

Drescher, K., Shen, Y., Bassler, B. L., and Stone, H. A. (2013). Biofilm streamers cause catastrophic disruption of flow with consequences for environmental and medical systems. *Proc. Natl. Acad. Sci. U.S.A.* 110, 4345–4350. doi: 10.1073/pnas.1300321110

Dumas, A., Bernard, L., Poquet, Y., Lugo-Villarino, G., and Neyrolles, O. (2018). The role of the lung microbiota and the gut-lung axis in respiratory infectious diseases. *Cell. Microbiol.* 20:e12966. doi: 10.1111/cmi.12966

El Hajji, M., Harmand, J., Chaker, H., and Lobry, C. (2009). Association between competition and obligate mutualism in a chemostat. *J. Biol. Dyn.* 3, 635–647. doi: 10.1080/17513750902915978

Erb-Downward, J. R., Thompson, D. L., Han, M. K., Freeman, C. M., McCloskey, L., Schmidt, L. A., et al. (2011). Analysis of the lung microbiome in the "healthy" smoker and in COPD. *PLoS One* 6:e16384. doi: 10.1371/journal.pone.0016384

Estrela, S., Trisos, C. H., and Brown, S. P. (2012). From metabolism to ecology: cross-feeding interactions shape the balance between polymicrobial conflict and mutualism. *Am. Nat.* 180, 566–576. doi: 10.1086/667887

Faust, K., and Raes, J. (2012). Microbial interactions: from networks to models. *Nat. Rev. Microbiol.* 10, 538–550. doi: 10.1038/nrmicro2832

Fernández-Olmos, A., García-Castillo, M., Maiz, L., Lamas, A., Baquero, F., and Cantón, R. (2012). *In vitro* prevention of *Pseudomonas aeruginosa* early biofilm formation with antibiotics used in cystic fibrosis patients. *Int. J. Antimicrob. Agents* 40, 173–176. doi: 10.1016/j.ijantimicag.2012.04.006

Filkins, L. M., Graber, J. A., Olson, D. G., Dolben, E. L., Lynd, L. R., Bhuju, S., et al. (2015). Coculture of *Staphylococcus aureus* with *Pseudomonas aeruginosa* Drives *S. aureus* towards Fermentative Metabolism and Reduced Viability in a Cystic Fibrosis Model. *J. Bacteriol.* 197, 2252–2264. doi: 10.1128/jb.00059-15

Freilich, S., Kreimer, A., Meilijson, I., Gophna, U., Sharan, R., and Ruppin, E. (2010). The large-scale organization of the bacterial network of ecological co-occurrence interactions. *Nucleic Acids Res.* 38, 3857–3868. doi: 10.1093/nar/gkq118

Goeres, D. M., Hamilton, M. A., Beck, N. A., Buckingham-Meyer, K., Hilyard, J. D., Loetterle, L. R., et al. (2009). A method for growing a biofilm under low shear at the air-liquid interface using the drip flow biofilm reactor. *Nat. Protoc.* 4, 783–788. doi: 10.1038/nprot.2009.59

Golding, C. G., Lamboo, L. L., Beniac, D. R., and Booth, T. F. (2016). The scanning electron microscope in microbiology and diagnosis of infectious disease. *Sci. Rep.* 6:26516.

Gomes, L. C., and Mergulhão, F. J. (2017). SEM analysis of surface impact on biofilm antibiotic treatment. *Scanning* 2017:2960194.

Gómez-Suárez, C., Busscher, H. J., and van der Mei, H. C. (2001). Analysis of bacterial detachment from substratum surfaces by the passage of air-liquid interfaces. *Appl. Environ. Microbiol.* 67, 2531–2537. doi: 10.1128/aem.67.6.2531-2537.2001

Greulich, P., Scott, M., Evans, M. R., and Allen, R. J. (2015). Growth-dependent bacterial susceptibility to ribosome-targeting antibiotics. *Mol. Syst. Biol.* 11:796. doi: 10.15252/msb.20145949

Guggino, W. B., and Banks-Schlegel, S. P. (2004). Macromolecular interactions and ion transport in cystic fibrosis. *Am. J. Respir. Crit. Care Med.* 170, 815–820. doi: 10.1164/rccm.200403-381ws

Haller, D., Bode, C., Hammes, W. P., Pfeifer, A. M., Schiffrin, E. J., and Blum, S. (2000). Non-pathogenic bacteria elicit a differential cytokine response by intestinal epithelial cell/leucocyte co-cultures. *Gut* 47, 79–87. doi: 10.1136/gut.47.1.79

Hansen, S. H., Kabbeck, T., Radtke, C. P., Krause, S., Krolitzki, E., Peschke, T., et al. (2019). Machine-assisted cultivation and analysis of biofilms. *Sci. Rep.* 9:8933.

Harrison, J. J., Stremick, C. A., Turner, R. J., Allan, N. D., Olson, M. E., and Ceri, H. (2010). Microtiter susceptibility testing of microbes growing on peg lids: a miniaturized biofilm model for high-throughput screening. *Nat. Protoc.* 5, 1236–1254. doi: 10.1038/nprot.2010.71

Hartmann, R., Jeckel, H., Jelli, E., Singh, P. K., Vaidya, S., Bayer, M., et al. (2019). BiofilmQ, a software tool for quantitative image analysis of microbial biofilm communities. *bioRxiv* [Preprint]. doi: 10.1101/735423

Hasin, Y., Seldin, M., and Lusis, A. (2017). Multi-omics approaches to disease. *Genome Biol.* 18:83.

Hendriksen, R. S., Bortolaia, V., Tate, H., Tyson, G. H., Aarestrup, F. M., and McDermott, P. F. (2019). Using genomics to track global antimicrobial resistance. *Front. Public Health* 7:242. doi: 10.3389/fpubh.2019.00242

Hilty, M., Burke, C., Pedro, H., Cardenas, P., Bush, A., Bossley, C., et al. (2010). Disordered microbial communities in asthmatic airways. *PLoS One* 5:e8578. doi: 10.1371/journal.pone.0008578

Hindré, T., Knibbe, C., Beslon, G., and Schneider, D. (2012). New insights into bacterial adaptation through *in vivo* and *in silico* experimental evolution. *Nat. Rev. Microbiol.* 10, 352–365. doi: 10.1038/nrmicro2750

Huang, Y., Chakraborty, S., and Liang, H. (2020). Methods to probe the formation of biofilms: applications in foods and related surfaces. *Anal. Methods* 12, 416–432. doi: 10.1039/c9ay02214g

Huang, Y. J., and LiPuma, J. J. (2016). The microbiome in cystic fibrosis. *Clin. Chest Med.* 37, 59–67.

Ingenito, E. P., Solway, J., McFadden, E. R., Pichurko, B., Bowman, H. F., Michaels, D., et al. (1987). Indirect assessment of mucosal surface temperatures in the airways: theory and tests. *J. Appl. Physiol.* 63, 2075–2083. doi: 10.1152/jappl.1987.63.5.2075

Jass, J., Costerton, J. W., and Lappin-Scott, H. M. (1995). Assessment of a chemostat-coupled modified Robbins device to study biofilms. *J. Ind. Microbiol.* 15, 283–289. doi: 10.1007/bf01569981

Jia, L., Gu, W., Zhang, Y., Ji, Y., Liang, J., Wen, Y., et al. (2017). The Crosstalk between HDPSCs and HUCMSCs on proliferation and osteogenic genes expression in coculture system. *Int. J. Med. Sci.* 14, 1118–1129. doi: 10.7150/ijms.19814

Jones, J. A., and Wang, X. (2018). Use of bacterial co-cultures for the efficient production of chemicals. *Curr. Opin. Biotechnol.* 53, 33–38. doi: 10.1016/j.copbio.2017.11.012

Khan, N., Vidyarthi, A., Nadeem, S., Negi, S., Nair, G., and Agrewala, J. N. (2016). Alteration in the gut microbiota provokes susceptibility to tuberculosis. *Front. Immunol.* 7:529. doi: 10.3389/fimmu.2016.00529

Kim, J., Hegde, M., and Jayaraman, A. (2010). Co-culture of epithelial cells and bacteria for investigating host-pathogen interactions. *Lab Chip* 10, 43–50. doi: 10.1039/b911367c

Klepac-Ceraj, V., Lemon, K. P., Martin, T. R., Allgaier, M., Kembel, S. W., Knapp, A. A., et al. (2010). Relationship between cystic fibrosis respiratory tract bacterial communities and age, genotype, antibiotics and *Pseudomonas*

aeruginosa. *Environ. Microbiol.* 12, 1293–1303. doi: 10.1111/j.1462-2920.2010.02173.x

Kneitel, J. M., and Chase, J. M. (2004). Trade-offs in community ecology: linking spatial scales and species coexistence. *Ecol. Lett.* 7, 69–80. doi: 10.1046/j.1461-0248.2003.00551.x

Knippenberg, S., Ueberberg, B., Maus, R., Bohling, J., Ding, N., Tort Tarres, M., et al. (2015). *Streptococcus pneumoniae* triggers progression of pulmonary fibrosis through pneumolysin. *Thorax* 70, 636–646. doi: 10.1136/thoraxjnl-2014-206420

Krohn-Molt, I., Wemheuer, B., Alawi, M., Poehlein, A., Güllert, S., Schmeisser, C., et al. (2013). Metagenome survey of a multispecies and alga-associated biofilm revealed key elements of bacterial-algal interactions in photobioreactors. *Appl. Environ. Microbiol.* 79, 6196–6206. doi: 10.1128/aem.01641-13

Lebeaux, D., Chauhan, A., Rendueles, O., and Beloin, C. (2013). From *in vitro* to *in vivo* models of bacterial biofilm-related infections. *Pathogens* 2, 288–356. doi: 10.3390/pathogens2020288

Lee, S. H., Lee, Y., Park, J. S., Cho, Y.-J., Yoon, H. I., Lee, C.-T., et al. (2018). Characterization of microbiota in bronchiectasis patients with different disease severities. *J. Clin. Med.* 7:429. doi: 10.3390/jcm7110429

Limoli, D. H., Whitfield, G. B., Kitao, T., Ivey, M. L., Davis, M. R., Grahl, N., et al. (2017). *Pseudomonas aeruginosa* alginate overproduction promotes coexistence with *Staphylococcus aureus* in a model of cystic fibrosis respiratory infection. *mBio* 8:e00186-17.

Liu, W., Jacquiod, S., Brejnrod, A., Russel, J., Burmølle, M., and Sørensen, S. J. (2019). Deciphering links between bacterial interactions and spatial organization in multispecies biofilms. *ISME J.* 13, 3054–3066. doi: 10.1038/s41396-019-0494-9

Lopes, S. P., Azevedo, N. F., and Pereira, M. O. (2018). Quantitative assessment of individual populations within polymicrobial biofilms. *Sci. Rep.* 8:9494.

Lotka, J. (1922). Natural selection as a physical principle. *Proc. Natl. Acad. Sci. U.S.A.* 8, 151–154. doi: 10.1073/pnas.8.6.151

Macià, M. D., Rojo-Molinero, E., and Oliver, A. (2014). Antimicrobial susceptibility testing in biofilm-growing bacteria. *Clin. Microbiol. Infect.* 20, 981–990. doi: 10.1111/1469-0691.12651

Mammen, M. J., and Sethi, S. (2017). Microbiome in chronic lung diseases. *BRN Rev.* 3, 102–120.

Marques, C. N. H., Morozov, A., Planzos, P., and Zelaya, H. M. (2014). The fatty acid signaling molecule cis-2-decenoic acid increases metabolic activity and reverts persister cells to an antimicrobial-susceptible state. *Appl. Environ. Microbiol.* 80, 6976–6991. doi: 10.1128/aem.01576-14

Marshall, B. E. A., Petren, K., Rizvi, S., Fink, A., Ostrenga, J., Sewall, A., et al. (2016). *Annual Data Report 2015. Cystic Fibrosis Foundation Patient Registry*. Available at: https://www.cff.org/our-research/cf-patient-registry/2015-patient-registry-annual-data-report.pdf (accessed August 5, 2019).

May, R. M. (1973). Stability and complexity in model ecosystems. *Monogr. Popul. Biol.* 6, 37–78.

Melaugh, G., Hutchison, J., Kragh, K. N., Irie, Y., Roberts, A., Bjarnsholt, T., et al. (2016). Shaping the growth behaviour of biofilms initiated from bacterial aggregates. *PLoS One* 11:e0149683. doi: 10.1371/journal.pone.0149683

Momeni, B., Xie, L., and Shou, W. (2017). Lotka-Volterra pairwise modeling fails to capture diverse pairwise microbial interactions. *eLife* 6:e25051.

Moreau-Marquis, S., Stanton, B. A., and O'Toole, G. A. (2008). *Pseudomonas aeruginosa* biofilm formation in the cystic fibrosis airway. *Pulm. Pharmacol. Ther.* 21, 595–599. doi: 10.1016/j.pupt.2007.12.001

Moree, W. J., Phelan, V. V., Wu, C.-H., Bandeira, N., Cornett, D. S., Duggan, B. M., et al. (2012). Interkingdom metabolic transformations captured by microbial imaging mass spectrometry. *Proc. Natl. Acad. Sci. U.S.A.* 109, 13811–13816. doi: 10.1073/pnas.1206855109

Morris, A., Beck, J. M., Schloss, P. D., Campbell, T. B., Crothers, K., Curtis, J. L., et al. (2013). Comparison of the respiratory microbiome in healthy nonsmokers and smokers. *Am. J. Respir. Crit. Care Med.* 187, 1067–1075.

Naik, S., Bouladoux, N., Wilhelm, C., Molloy, M. J., Salcedo, R., Kastenmuller, W., et al. (2012). Compartmentalized control of skin immunity by resident commensals. *Science* 337, 1115–1119. doi: 10.1126/science.1225152

Orazi, G., and O'Toole, G. A. (2017). *Pseudomonas aeruginosa* Alters *Staphylococcus aureus* sensitivity to vancomycin in a biofilm model of cystic fibrosis infection. *mBio* 8:e00873-17.

O'Toole, G. A., and Kolter, R. (1998). Flagellar and twitching motility are necessary for *Pseudomonas aeruginosa* biofilm development. *Mol. Microbiol.* 30, 295–304. doi: 10.1046/j.1365-2958.1998.01062.x

Pacheco, D. P., Butnarasu, C. S., Briatico Vangosa, F., Pastorino, L., Visai, L., Visentin, S., et al. (2019). Disassembling the complexity of mucus barriers to develop a fast screening tool for early drug discovery. *J. Mater. Chem. B Mater. Biol. Med.* 7, 4940–4952. doi: 10.1039/c9tb00957d

Pallavicini, P., Arciola, C. R., Bertoglio, F., Curtosi, S., Dacarro, G., D'Agostino, A., et al. (2017). Silver nanoparticles synthesized and coated with pectin: An ideal compromise for anti-bacterial and anti-biofilm action combined with wound-healing properties. *J. Colloid Interface Sci.* 498, 271–281. doi: 10.1016/j.jcis.2017.03.062

Pamp, S. J., Sternberg, C., and Tolker-Nielsen, T. (2009). Insight into the microbial multicellular lifestyle via flow-cell technology and confocal microscopy. *Cytometry A* 75, 90–103. doi: 10.1002/cyto.a.20685

Parker, A. E., Walker, D. K., Goeres, D. M., Allan, N., Olson, M. E., and Omar, A. (2014). Ruggedness and reproducibility of the MBEC biofilm disinfectant efficacy test. *J. Microbiol. Methods* 102, 55–64.

Peterson, B. W., He, Y., Ren, Y., Zerdoum, A., Libera, M. R., Sharma, P. K., et al. (2015). Viscoelasticity of biofilms and their recalcitrance to mechanical and chemical challenges. *FEMS Microbiol. Rev.* 39, 234–245.

Pritt, B., O'Brien, L., and Winn, W. (2007). Mucoid *Pseudomonas* in cystic fibrosis. *Am. J. Clin. Pathol.* 128, 32–34.

Purevdorj, B., Costerton, J. W., and Stoodley, P. (2002). Influence of hydrodynamics and cell signaling on the structure and behavior of *Pseudomonas aeruginosa* biofilms. *Appl. Environ. Microbiol.* 68, 4457–4464.

Raimbault, M. (1998). General and microbiological aspects of solid substrate fermentation. *Electron. J. Biotechnol.* 1, 174–188.

Ren, D., Madsen, J. S., de la Cruz-Perera, C. I., Bergmark, L., Sørensen, S. J., and Burmølle, M. (2014). High-throughput screening of multispecies biofilm formation and quantitative PCR-based assessment of individual species proportions, useful for exploring interspecific bacterial interactions. *Microb. Ecol.* 68, 146–154.

Røder, H. L., Sørensen, S. J., and Burmølle, M. (2016). Studying bacterial multispecies biofilms: where to start? *Trends Microbiol.* 24, 503–513.

Rogers, G. B., Zain, N. M. M., Bruce, K. D., Burr, L. D., Chen, A. C., Rivett, D. W., et al. (2014). A novel microbiota stratification system predicts future exacerbations in bronchiectasis. *Ann. Am. Thorac. Soc.* 11, 496–503.

Rusconi, R., Garren, M., and Stocker, R. (2014). Microfluidics expanding the frontiers of microbial ecology. *Annu. Rev. Biophys.* 43, 65–91.

Schuijt, T. J., Lankelma, J. M., Scicluna, B. P., de Sousa e Melo, F., Roelofs, J. J. T. H., de Boer, J. D., et al. (2016). The gut microbiota plays a protective role in the host defence against pneumococcal pneumonia. *Gut* 65, 575–583.

Segal, L. N., Alekseyenko, A. V., Clemente, J. C., Kulkarni, R., Wu, B., Gao, Z., et al. (2013). Enrichment of lung microbiome with supraglottic taxa is associated with increased pulmonary inflammation. *Microbiome* 1:19.

Segal, L. N., Clemente, J. C., Wu, B. G., Wikoff, W. R., Gao, Z., Li, Y., et al. (2017). Randomised, double-blind, placebo-controlled trial with azithromycin selects for anti-inflammatory microbial metabolites in the emphysematous lung. *Thorax* 72, 13–22.

Sharma, M., Visai, L., Bragheri, F., Cristiani, I., Gupta, P. K., and Speziale, P. (2008). Toluidine blue-mediated photodynamic effects on staphylococcal biofilms. *Antimicrob. Agents Chemother.* 52, 299–305.

Sherrard, L. J., Einarsson, G. G., Johnston, E., O'Neill, K., McIlreavey, L., McGrath, S. J., et al. (2019). Assessment of stability and fluctuations of cultured lower airway bacterial communities in people with cystic fibrosis. *J. Cyst. Fibros* 18, 808–816.

Sissons, C. H. (1997). Artificial dental plaque biofilm model systems. *Adv. Dent. Res.* 11, 110–126.

Solé, R. V., and Bascompte, J. (2012). *Self-Organization in Complex Ecosystems*. Princeton, NJ: Princeton University Press.

Sorek, R., and Cossart, P. (2010). Prokaryotic transcriptomics: a new view on regulation, physiology and pathogenicity. *Nat. Rev. Genet.* 11, 9–16.

Speirs, D. C., Smith, H. L., and Waltman, P. (1996). The theory of the chemostat: dynamics of microbial competition. *J. Appl. Ecol.* 33:651.

Stoodley, P., Cargo, R., Rupp, C. J., Wilson, S., and Klapper, I. (2002). Biofilm material properties as related to shear-induced deformation and detachment phenomena. *J. Ind. Microbiol. Biotechnol.* 29, 361–367.

Surette, M. G. (2014). The cystic fibrosis lung microbiome. *Ann. Am. Thorac. Soc.* 11(Suppl. 1), S61–S65.

Swenson, C., Schraufnagel, D., and Sadikot, R. (2017). What is Bronchiectasis? *Am. J. Respir. Crit. Care Med.* 195, 15–16.

Sze, M. A., Dimitriu, P. A., Suzuki, M., McDonough, J. E., Campbell, J. D., Brothers, J. F., et al. (2015). Host response to the lung microbiome in chronic obstructive pulmonary disease. *Am. J. Respir. Crit. Care Med.* 192, 438–445.

Taylor, S. L., Rogers, G. B., Chen, A. C.-H., Burr, L. D., McGuckin, M. A., and Serisier, D. J. (2015). Matrix metalloproteinases vary with airway microbiota composition and lung function in non-cystic fibrosis bronchiectasis. *Ann. Am. Thorac. Soc.* 12, 701–707.

Tognon, M., Köhler, T., Gdaniec, B. G., Hao, Y., Lam, J. S., Beaume, M., et al. (2017). Co-evolution with *Staphylococcus aureus* leads to lipopolysaccharide alterations in *Pseudomonas aeruginosa*. *ISME J.* 11, 2233–2243.

Tognon, M., Köhler, T., Luscher, A., and van Delden, C. (2019). Transcriptional profiling of *Pseudomonas aeruginosa* and *Staphylococcus aureus* during *in vitro* co-culture. *BMC Genomics* 20:30. doi: 10.1186/s12864-018-5398-y

Tunney, M. M., Einarsson, G. G., Wei, L., Drain, M., Klem, E. R., Cardwell, C., et al. (2013). Lung microbiota and bacterial abundance in patients with bronchiectasis when clinically stable and during exacerbation. *Am. J. Respir. Crit. Care Med.* 187, 1118–1126.

Tuson, H. H., Renner, L. D., and Weibel, D. B. (2012). Polyacrylamide hydrogels as substrates for studying bacteria. *Chem. Commun.* 48, 1595–1597.

Van den Driessche, F., Rigole, P., Brackman, G., and Coenye, T. (2014). Optimization of resazurin-based viability staining for quantification of microbial biofilms. *J. Microbiol. Methods* 98, 31–34.

Venkataraman, A., Bassis, C. M., Beck, J. M., Young, V. B., Curtis, J. L., Huffnagle, G. B., et al. (2015). Application of a neutral community model to assess structuring of the human lung microbiome. *mBio* 6:e02284-14.

Vet, S., de Buyl, S., Faust, K., Danckaert, J., Gonze, D., and Gelens, L. (2018). Bistability in a system of two species interacting through mutualism as well as competition: Chemostat vs. Lotka-Volterra equations. *PLoS One* 13:e0197462. doi: 10.1371/journal.pone.0197462

Volterra, V. (1928). Variations and fluctuations of the number of individuals in Animal species living together. *ICES J. Mar. Sci.* 3, 3–51.

Vuornos, K., Ojansivu, M., Koivisto, J. T., Häkkänen, H., Belay, B., Montonen, T., et al. (2019). Bioactive glass ions induce efficient osteogenic differentiation of human adipose stem cells encapsulated in gellan gum and collagen type I hydrogels. *Mater. Sci. Eng. C Mater. Biol. Appl.* 99, 905–918.

Wang, Y., and Wu, H. (2011). A mutualism-competition model characterizing competitors with mutualism at low density. *Math. Comput. Model.* 53, 1654–1663.

Wang, Z., Bafadhel, M., Haldar, K., Spivak, A., Mayhew, D., Miller, B. E., et al. (2016). Lung microbiome dynamics in COPD exacerbations. *Eur. Respir. J.* 47, 1082–1092.

West, J. B. (1968). Regional differences in the lung. *Postgrad. Med. J.* 44, 120–122.

Wimpenny, J. W. (1997). The validity of models. *Adv. Dent. Res.* 11, 150–159.

Woods, J., Boegli, L., Kirker, K. R., Agostinho, A. M., Durch, A. M., Delancey Pulcini, E., et al. (2012). Development and application of a polymicrobial, *in vitro*, wound biofilm model. *J. Appl. Microbiol.* 112, 998–1006.

Woods, P. W., Haynes, Z. M., Mina, E. G., and Marques, C. N. H. (2018). Maintenance of S. *aureus* in co-culture with *P. aeruginosa* while growing as biofilms. *Front. Microbiol.* 9:3291. doi: 10.3389/fmicb.2018.03291

Woodworth, B. A., Tamashiro, E., Bhargave, G., Cohen, N. A., and Palmer, J. N. (2008). An *in vitro* model of *Pseudomonas aeruginosa* biofilms on viable airway epithelial cell monolayers. *Am. J. Rhinol.* 22, 235–238.

Yates, J. R., Ruse, C. I., and Nakorchevsky, A. (2009). Proteomics by mass spectrometry: approaches, advances, and applications. *Annu. Rev. Biomed. Eng.* 11, 49–79.

Yin, L., Wei, H., Liang, S., and Yu, X. (2017). From the cover: an animal-free *in vitro* three-dimensional testicular cell coculture model for evaluating male reproductive toxicants. *Toxicol. Sci.* 159, 307–326.

Zemanick, E. T., Wagner, B. D., Robertson, C. E., Ahrens, R. C., Chmiel, J. F., Clancy, J. P., et al. (2017). Airway microbiota across age and disease spectrum in cystic fibrosis. *Eur. Respir. J.* 50:1700832.

Zhang, K., Fujita, Y., Chang, L., Qu, Y., Pu, Y., Wang, S., et al. (2019). Abnormal composition of gut microbiota is associated with resilience versus susceptibility to inescapable electric stress. *Transl. Psychiatry* 9:231.

Conflict of Interest: The authors declare that the research was conducted in the absence of any commercial or financial relationships that could be construed as a potential conflict of interest.

frontiers in Bioengineering and Biotechnology

ORIGINAL RESEARCH
published: 07 April 2021
doi: 10.3389/fbioe.2021.647007

Antibacterial Composite Materials Based on the Combination of Polyhydroxyalkanoates With Selenium and Strontium Co-substituted Hydroxyapatite for Bone Regeneration

*Elena Marcello[1], Muhammad Maqbool[2,3,4], Rinat Nigmatullin[1,5], Mark Cresswell[3], Philip R. Jackson[3], Pooja Basnett[1], Jonathan C. Knowles[6,7,8], Aldo R. Boccaccini[2] and Ipsita Roy[1,9]**

[1] School of Life Sciences, College of Liberal Arts and Sciences, University of Westminster, London, United Kingdom, [2] Institute of Biomaterials, Department of Materials Science and Engineering, University of Erlangen-Nuremberg, Erlangen, Germany, [3] Lucideon Ltd., Stoke-on-Trent, United Kingdom, [4] CAM Bioceramics B.V., Leiden, Netherlands, [5] Bristol Composites Institute (ACCIS), University of Bristol, Bristol, United Kingdom, [6] Division of Biomaterials and Tissue Engineering, Faculty of Medical Sciences, University College London Eastman Dental Institute, London, United Kingdom, [7] Department of Nanobiomedical Science and BK21 Plus NBM, Global Research Center for Regenerative Medicine, Dankook University, Cheonan, South Korea, [8] The Discoveries Centre for Regenerative and Precision Medicine, University College London, London, United Kingdom, [9] Department of Materials Science and Engineering, Faculty of Engineering, The University of Sheffield, Sheffield, United Kingdom

OPEN ACCESS

Edited by:
Liqiang Wang,
Shanghai Jiao Tong University, China

Reviewed by:
Maria P. Ferraz,
Fernando Pessoa University, Portugal
T. S. Sampath Kumar,
Indian Institute of Technology Madras, India
Sudip Mondal,
Pukyong National University, South Korea
Moorthi Ambigapathi,
Chettinad University, India

***Correspondence:**
Ipsita Roy
i.roy@sheffield.ac.uk

Specialty section:
This article was submitted to Biomaterials, a section of the journal Frontiers in Bioengineering and Biotechnology

Received: *28 December 2020*
Accepted: *04 March 2021*
Published: *07 April 2021*

Citation:
Marcello E, Maqbool M, Nigmatullin R, Cresswell M, Jackson PR, Basnett P, Knowles JC, Boccaccini AR and Roy I (2021) Antibacterial Composite Materials Based on the Combination of Polyhydroxyalkanoates With Selenium and Strontium Co-substituted Hydroxyapatite for Bone Regeneration. Front. Bioeng. Biotechnol. 9:647007. doi: 10.3389/fbioe.2021.647007

Due to the threat posed by the rapid growth in the resistance of microbial species to antibiotics, there is an urgent need to develop novel materials for biomedical applications capable of providing antibacterial properties without the use of such drugs. Bone healing represents one of the applications with the highest risk of postoperative infections, with potential serious complications in case of bacterial contaminations. Therefore, tissue engineering approaches aiming at the regeneration of bone tissue should be based on the use of materials possessing antibacterial properties alongside with biological and functional characteristics. In this study, we investigated the combination of polyhydroxyalkanoates (PHAs) with a novel antimicrobial hydroxyapatite (HA) containing selenium and strontium. Strontium was chosen for its well-known osteoinductive properties, while selenium is an emerging element investigated for its multi-functional activity as an antimicrobial and anticancer agent. Successful incorporation of such ions in the HA structure was obtained. Antibacterial activity against *Staphylococcus aureus* 6538P and *Escherichia coli* 8739 was confirmed for co-substituted HA in the powder form. Polymer-matrix composites based on two types of PHAs, P(3HB) and P(3HO-co-3HD-co-3HDD), were prepared by the incorporation of the developed antibacterial HA. An in-depth characterization of the composite materials was conducted to evaluate the

effect of the filler on the physicochemical, thermal, and mechanical properties of the films. *In vitro* antibacterial testing showed that the composite samples induce a high reduction of the number of *S. aureus* 6538P and *E. coli* 8739 bacterial cells cultured on the surface of the materials. The films are also capable of releasing active ions which inhibited the growth of both Gram-positive and Gram-negative bacteria.

Keywords: antibacterial, composites, polyhydroxyalkanoates, selenium, strontium, hydroxyapatite

INTRODUCTION

Bone tissue has a dynamic structure with high capacity of regeneration. However, its healing capability is linked with the proximity of the bone segments and, in the case of large-size defects, mechanical fixation on its own is not able to induce bone healing, requiring the use of additional material. These critical-size defects can be caused by a variety of scenarios including trauma, tumor resection, or bacterial infections (De Witte et al., 2018; Hasan et al., 2018). Moreover, external intervention is also required in the presence of fractures that have failed to heal completely (i.e., non-unions) (Stewart, 2019). In clinical practice, autologous osseous material is still considered the gold standard, thanks to its inherent osteogenic, osteoconductive, and osteoinductive properties. However, the restricted availability of this material combined with possible donor-site morbidity limits autograft applications, especially for the treatment of large bone defects (Fernandez de Grado et al., 2018; Zeng et al., 2018). Allografts and xenografts represent possible alternatives but are associated with the risk of an immunogenic response and disease transmission correlated with a reduction in the osteoinductive properties and a lack of viable cells (Baldwin et al., 2019).

In light of the limitations of the current transplanted osseous grafts, the use of tissue engineering has emerged as one of the main alternatives to restore or regenerate the damaged tissue through the combination of cells with a scaffold able to provide a suitable environment for cell anchorage and proliferation (Fernandez de Grado et al., 2018; Hasan et al., 2018). Among the characteristics of an ideal material for bone regeneration, increasing interest has been placed on the antibacterial properties. Infections represent a major complication in the orthopedic field, as bone repair is associated with a high risk of infections, especially in the presence of open fractures. If infection occurs, the tissue healing process might be impaired and, if not treated, can result in chronic infection, leading to bone necrosis and spreading to adjacent soft tissues (Thomas and Puleo, 2011). The main strategies applied in clinic to prevent the rise of or fight possible infections are based on antibiotics. For prevention, systemic delivery of antibiotics is employed which can be ineffective due to low drug concentration at the infected site and can lead to systemic toxicity (Mouriño and Boccaccini, 2010). Alternatively, grafts loaded with antibiotics are used, allowing a controlled release of the therapeutics at the targeted site and lowering possible side effects (Johnson and García, 2015). However, the increasing rise of antibiotic-resistant species due to the overuse or misuse of antibiotics has become a primary concern worldwide, posing a serious threat to global health and economy. Such a scenario requires the investigation of new materials for bone regeneration able to provide appropriate antibacterial features without the use of antibiotics to inhibit bacterial growth and reduce bacterial adhesion.

Composite materials are one of the best candidates for scaffolds for bone regeneration due to their ability to closely mimic the intrinsically heterogeneous composite architecture of such tissue, composed of cells, an organic phase (the extracellular matrix containing mainly collagen fibrils), an inorganic phase [mainly hydroxyapatite (HA)], and water (Chocholata et al., 2019; Qu et al., 2019). The most investigated combination in scaffold design involves the use of polymers to provide elasticity and biodegradability, mimicking the role of the extracellular matrix, and ceramics to increase the mechanical strength and improve the interactions between the tissue and the final constructs (Kashirina et al., 2019).

Hydroxyapatite $Ca_{10}(PO_4)_6(OH)_2$ is a versatile member of the calcium phosphate family with a stoichiometric composition similar to natural bone, Ca/P ratio 1.67. It is the main ceramic material used in the fabrication of composite scaffolds for bone regeneration thanks to its exceptional biocompatibility and bioactivity, in addition to osteoconductive properties (Ratnayake et al., 2017; Kaur et al., 2019). Moreover, the compressive strength of HA is similar to that of native bone, but the material possesses a brittle nature with low fracture toughness, limiting its use in load-bearing applications and requiring its combination with polymeric materials (Rezwan et al., 2006; Chocholata et al., 2019). Natural apatite has superior physical and biological properties as compared to synthetic HA because of a considerable hetero-ionic exchange (Eliaz and Metoki, 2017). For this reason, increasing research is being conducted to improve the physiochemical, biological, and mechanical properties of HA through the substitution of various metallic ions in the crystal structure of HA (Ratnayake et al., 2017). Among the ions investigated for substitution, selenium, an essential trace element, has attracted attention only in the last decade. Selenium plays a crucial role in the human body as an antioxidant through its incorporation in selenoproteins (proteins containing selenocysteine residues), specifically the glutathione peroxidase family, which are essential for protection against oxidative stress (Rodríguez-Valencia et al., 2013). Its deficiency has been associated with two diseases, the Kashin–Beck syndrome, which is characterized by cartilage and long bone degeneration, and the Keshan illness, which affects the heart in children (Moreno-Reyes et al., 2001; Rodríguez-Valencia et al., 2013). Moreover, selenium-containing biomaterials have shown an anticancer activity, inducing apoptosis of bone cancer cells *in vitro* and inhibiting the growth of bone tumors *in vivo* (Yanhua et al., 2016; He et al., 2019). Finally, recently, selenium

has been shown to possess antibacterial activity against a range of bacteria (Kolmas et al., 2014; Huang et al., 2019). Strontium is one of the most studied elements for bone regeneration. Thanks to its osteoconductive and osteoprogenic properties, this ion has been incorporated into a range of materials for bone regeneration, such us titanium implant coatings, bone cements, and synthetic HA (Wong et al., 2004; Gritsch et al., 2019). Strontium has been shown to elicit a bone remodeling effect through the increase of osteoblast activity inducing bone formation and the reduction of osteoblast proliferation and activity, therefore reducing bone reabsorption (Nielsen, 2004; Ratnayake et al., 2017).

As regards the polymeric matrix for composite materials for bone regeneration, polyhydroxyalkanoates (PHAs) have been considered promising candidates due to their biocompatibility, biodegradability, easy processability, and versatile and tuneable physical and mechanical properties (Rai et al., 2011; Możejko-Ciesielska and Kiewisz, 2016). PHAs are bioderived polyesters, naturally produced by bacteria as intracellular compounds. The production from natural and renewable resources makes PHAs a good alternative to petrol-derived plastics. Moreover, PHAs have shown to possess less acidic degradation products than other synthetic polyesters such as PLA, PLGA, and PGA, limiting the possibility of developing a late or chronic inflammation (Bonartsev et al., 2019). Compared to other natural-derived materials (e.g., collagen and chitosan), PHAs show better mechanical features and higher thermal stability making them suitable for a wider range of processing techniques (Puppi et al., 2019). Depending on the bacteria and the carbon source utilized in the fermentation process, two types of PHAs can be obtained, short chain length PHAs (scl-PHAs), characterized by up to five carbon atoms in their monomeric unit, and medium chain length PHAs (mcl-PHAs), with more than six carbon atoms in their monomeric unit. These two classes of PHAs usually exhibit distinctive properties. Scl-PHAs are stiff and brittle materials, with a high melting temperature (160–180°C) and glass transition close to 0°C (Możejko-Ciesielska and Kiewisz, 2016; Puppi et al., 2019). On the contrary, mcl-PHAs usually show a higher elongation at break and a lower elastic modulus, melting temperature (40–60°C), and glass transition (−50 to 25°C) compared to scl-PHAs (Rai et al., 2011; Możejko-Ciesielska and Kiewisz, 2016; Basnett et al., 2018). Scl-PHAs are the main polyesters of the PHAs family investigated for bone regeneration due to their high crystallinity and mechanical properties (i.e., Young's modulus and ultimate tensile strength), close to those of native bone (Karageorgiou and Kaplan, 2005). However, the *in vivo* application of these materials is limited by their brittle nature (Obat et al., 2013). Therefore, recently mcl-PHAs have also been investigated as an alternative material for bone regeneration in non-load bearing applications (Ansari et al., 2016).

In this work, we investigated the development of novel antibacterial materials based on the combination of PHAs with a novel co-substituted HA to be used as starting materials for the development of scaffolds for bone regeneration. In the first part of this research, we reported the synthesis and physiochemical characterization of novel selenium and strontium co-substituted HA (Se-Sr-HA) prepared by the co-precipitation method. *In vitro* characterization of the antibacterial properties of Se-Sr-HA was conducted to validate its utilization for the development of antimicrobial composites. The combination of the novel co-substituted HA with PHAs was then investigated. Two PHAs were selected as the bulk materials: P(3HB) as an scl-PHA and P(3HO-co-3HD-co-3HDD) as an mcl-PHA. The polyesters were combined with the novel co-substituted HA using three loading compositions, and the effect of the incorporation of the filler on the physical, thermal, mechanical, and antibacterial properties of the composite films was investigated.

MATERIALS AND METHODS

Bacterial Strains and Culture Conditions

Pseudomonas mendocina CH50 and *Bacillus subtilis* OK2 were obtained from the University of Westminster culture collection. The strains were cultured at 30°C at 200 r/min for 16 h in a shaking incubator and stored as a glycerol stock at −80°C. For the antibacterial characterization, *Staphylococcus aureus* 6538P and *Escherichia coli* 8739 were bought from the American Type Culture Collection (ATCC). They were cultured in sterile nutrient broth at 37°C and 200 r/min for 16 h in a shaking incubator and stored as a glycerol stock at −80°C.

Chemicals

All the chemicals were purchased from Sigma Aldrich Ltd., United Kingdom and VWR international, United Kingdom.

Synthesis of Selenium-Strontium-Hydroxyapatite

Selenium-strontium-HA was synthesized by wet precipitation method, using diammonium hydrogen phosphate $(NH_4)_2HPO_4$, calcium nitrate tetrahydrate $Ca(NO_3)_24H_2O$, sodium selenite $Na_2SeO_3{\cdot}5H_2O$, and strontium nitrate $Sr(NO_3)_2{\cdot}6H_2O$ as precursors. Two solutions coded A and B were prepared for this reaction. Solution A was prepared my dissolving $Ca(NO_3)_2{\cdot}4H_2O$ (0.668 M) and $Sr(NO_3)_2{\cdot}6H_2O$ (0.167 M) in 250 mL deionized water and adjusted to pH 11 using 1 M NH_4OH. Solution B was prepared by dissolving $(NH_4)_2HPO_4$ (0.4 M) and $Na_2SeO_3{\cdot}5H_2O$ (0.1 M) in 250 mL deionized water and adjusted to pH 9.5 using 1 M NH_4OH. The level of reactants used was calculated in order to keep the (Ca+Sr):(P+Se) ratio constant at 1.667 and Sr:(Sr+Ca) and Se:(Se+P) molar ratio constant at 0.2. The aimed chemical composition of the produced Se-Sr-HA was $Ca_{10-x}Sr_x(PO_4)_{6-y}(SeO_3)_y(OH)_{2-y}$, where x = 2 and y = 1.2 (Ravi et al., 2012; Pajor et al., 2018). Solution B was added dropwise to solution A. After mixing of the solutions, the pH value was maintained at 10.75 by adding NH_4OH, and the final solution was stirred for 16 h at 400 r/min followed by the aging of precipitates for 24 h. The obtained precipitates were washed with de-ionized water and then centrifuged (three times). The samples were dried at 80°C in an oven and sintered at 900°C for 6 h (at the heating rate of 5°C/min). Non-substituted HA was prepeared with the same method without the addition of $Na_2SeO_3{\cdot}H_2O$ and $Sr(NO_3)_2{\cdot}6H_2O$.

Physicochemical Characterization of Se-Sr-HA

X-Ray Diffraction (XRD) Analysis

X-ray diffraction (XRD) analysis was conducted on a Bruker D8 Advance using Bragg-Brentano parafocusing geometry. Data were collected for the 2θ range from 10° to 70° (step size of 0.01° and count time 1 s per step). Collected data were qualitatively examined using the Bruker diffract+ and EVA search-match software for compounds identification (using the ICDD database).

X-Ray Fluorescence Analysis (XRF)

For compositional analysis by XRF, the samples were prepared and reported in accordance with ISO standard 12677. The substituted HA samples were ignited at 1200°C for 1 h to examine the loss on ignition. Then approximately, 1.5 g powdered sample was mixed up with 7.5 g of $Li_2B_4O_7$ (lithium tetraborate) and heated in a platinum crucible at 1025°C for 20 min followed by 1200°C for 5 min. Then the glass melt was cast into a glass disc to get a glassy bead which was analyzed by using Axios' Panalytical X-Ray Fluorescence (XRF) spectrometer.

Production of Polyhydroxyalkanoates

P(3HO-co-3HD-co-3HDD) was produced by *P. mendocina* CH50 using 20 g/L of coconut oil as previously described by Basnett et al. (2018). P(3HB) was produced by the controlled fermentation of *B. subtilis* OK2 using 35 g/L of glucose as the carbon source as described by Lukasiewicz et al. (2018). Both fermentation processes were carried out in 15 L bioreactors, with 10 L working volume (Applikon Biotechnology, Tewkesbury, United Kingdom). The polymers were extracted using a two-stage method Soxhlet extraction (Lukasiewicz et al., 2018).

Composite Films Preparation and Characterization

Polyhydroxyalkanoates/Se-Sr-HA composite films were obtained by solvent casting technique. P(3HO-co-3HD-co-3HDD) or P(3HB) was first dissolved in chloroform (5% w/v) at room temperature and stirred for 24 h. The desired amount of filler (i.e., 10, 20, and 30 wt% of Se-Sr-HA) was added in the polymer solution, and the mixture was then sonicated in an ultrasonic water bath (XUBA3 Ultrasonic Bath, Grant Instruments) for 15 min. The obtained suspension was then poured in petri-dishes and left to evaporate at room temperature. Samples were kept for 5 weeks to allow complete crystallization of the samples before conducting the following characterizations (Lukasiewicz et al., 2018; Lizarraga Valderrama et al., 2020).

Attenuated Total Reflectance Fourier Transform Infrared (ATR-FTIR) Spectroscopy

Attenuated total reflectance Fourier transform infrared (ATR-FTIR) was carried out to investigate the functional groups of the composite films. The analyses were performed in a spectral range of 4000 to 400 cm^{-1} with a resolution of 4 cm^{-1} using PerkinElmer FT-IR spectrometer Spectrum Two (PerkinElmer Inc., United States).

Differential Scanning Calorimetry (DSC)

Thermal analysis of the films was conducted using differential scanning calorimetry (DSC) 214 Polyma (Netzsch, Germany) equipped with Intracooler IC70 cooling system. Approximately 5 mg of the sample was heated at a heating rate of 20°C per minute from −70 to 130°C for P(3HO-co-3HD-co-3HDD)-based samples and from −70 and 200°C for P(3HB)-based samples (Lukasiewicz et al., 2018; Lizarraga Valderrama et al., 2020). The data were analyzed using the Proteus 7.0 Analysis Software (Netzsch, Germany). The enthalpy of fusion (ΔHm) of the composite samples was normalized (ΔH^n_m) to take into account the weight fraction of the filler (w_f):

$$\Delta H^n_m = \frac{\Delta H\mathrm{m}}{(1-w_f)}$$

For P(3HB)-based samples, the percentage crystallinity of the materials (X_c%) was calculated according to the following formula:

$$X_c\% = \frac{\Delta H\mathrm{m}}{\Delta H^\circ} * 100$$

Where ΔHm is the enthalpy of fusion of the material and ΔH° is the enthalpy of fusion for the material with 100% crystallinity, which for P(3HB) is 146 J/g (Ho et al., 2014). In case of composite films, ΔHm was replaced with ΔH^n_m.

Scanning Electron Microscopy (SEM) and Energy-Dispersive X-Ray (EDX) Spectroscopy

The surface topography of the composite samples was analyzed through scanning electron microscopy (SEM) using a beam of 5 keV at 10 cm working distance (JEOL 5610LV-SEM). Energy-dispersive X-ray (EDX) analysis was used to perform a qualitative elemental analysis of the materials developed with a beam of 20 keV at 10 cm working distance. The data were analyzed using the software IncaEDX Energy System. For both analyses, all the samples were coated with gold for 2 min using an EMITECH-K550 gold sputtering device. The analyses were carried out at the Eastman Dental Hospital, University College London.

Mechanical Analysis

Tensile testing was performed on the composite films using Instron 5940 testing system equipped with 500 N load cell. Solvent casted films of 5 mm width and 35 mm length were used for the analysis, and six specimens were used for each sample. A deformation rate of 10 mm/min was applied for mcl-PHAs, while 5 mm/min was used for scl-PHAs following the ASTM D882–10 "Standard Test Method for Tensile Properties of Thin Plastic Sheeting" (Lukasiewicz et al., 2018; Lizarraga Valderrama et al., 2020). The data were acquired and analyzed using a BlueHill 3 software.

Antibacterial Characterization

Minimal Inhibitory Concentration (MIC)

The antibacterial activity of Se-Sr-HA in powder form was investigated using the ISO 20776 against *S. aureus* 6538P and *E. coli* 8739. A range of concentration of the material in powder form (5–100 mg/mL) prepared in Mueller Hinton broth was

mixed with a microbial suspension adjusted to achieve a final concentration of 5×10^5 CFU/mL and incubated at 37°C for 24 h at 100 r/min in 96 multi-well plates (final volume 100 μL). After the incubation time, the OD_{600} of the wells was measured to determine the concentration of the Se-Sr-HA able to inhibit the growth [minimal inhibitory concentration (MIC)] of each bacterial strain.

Direct Contact Test—ISO 22196

The antibacterial properties of the composite films were evaluated following the ISO 22196 against *S. aureus* 6538P and *E. coli* 8739. Samples of 6 mm in diameter were sterilized by UV light for 15 min, placed onto agar plates, inoculated with 10 μL of a bacterial culture adjusted to a concentration of $3–5 \times 10^5$ CFU/mL and incubated in static conditions at 37°C for 24 h. After the incubation time, the bacteria were recovered from the sample using a PBS solution and the number of viable cells was determined through the colony-forming unit method using the drop plate technique (Herigstad et al., 2001). P(3HO-co-3HD-co-3HDD) or P(3HB) neat samples were used as controls. The antibacterial activity (R%) was expressed as the % reduction of the number of cells, which was calculated using the formula:

$$R(\%) = \frac{U-T}{U} * 100$$

Where U is the number of viable bacteria normalized to the surface area of the sample, in CFU/cm^2, recovered from the control samples, and T is the number of viable bacteria, in CFU/cm^2, recovered from samples containing Se-Sr-HA.

Antibacterial Ion Release Studies

Antibacterial ion release studies were performed on composite films against *S. aureus* 6538P or *E. coli* 8739, following an adapted method described by Cao et al. (2017). Samples of 6 mm in diameter were incubated in 1 mL of Mueller Hinton broth at 37°C for 1, 3, 6, and 24 h. After each time point, the media with the eluted ions were collected and replaced with fresh media. The obtained eluates were incubated with a microbial suspension adjusted to $3–5 \times 10^5$ CFU/mL and incubated for 24 h at 37°C in 96 multi-well plates (final volume 100 μL). The control consists of Mueller Hinton broth incubated for the same time period with P(3HO-co-3HD-co-3HDD) or P(3HB) neat samples. The antibacterial activity was calculated as the % reduction of the OD at 600 nm compared to the control using the following formula:

$$\%OD_{600}\ reduction = \frac{(OD_c - OD_s)}{OD_c} * 100$$

OD_c is the optical density at 600 nm of the control samples and OD_s is the optical density at 600 nm of the sample.

Statistical Analysis

All measurements were made in triplicate unless otherwise specified, and data are presented as mean values ± standard deviation. Statistical analysis was performed using GraphPad Prism 7 software by one-way analysis of variance (ANOVA) with Tukey *post hoc* test to determine statistically significant differences between two or more groups. The differences were considered statistically significant when the p-values resulted lower than 0.05 [p-value < 0.05 (*), p-value < 0.01 (**), p-value < 0.001 (***), and p-value < 0.0001 (****)].

RESULTS

Se-Sr-HA Characterization

XRD Analysis

Figure 1 shows powder X-ray diffractograms of HA and Se-Sr-HA. Both diffractograms were characteristic of highly crystalline materials that matched the standard diffractogram of HA (JCPDS. 09-432). The characteristic diffraction peaks for hexagonal HA could be detected in both HA and Se-Sr-HA samples. The co-substituted HA showed broadening of the peaks and slight reduction in the peak intensities, indicating the incorporation of ions in the HA lattice structure. Moreover, a minor shift in the diffraction peaks of Se-Sr-HA toward lower angle values (2θ) as compared to reference HA peaks was also detected, a further confirmation of ion doping (Ozeki et al., 2014).

Measurements of the lattice parameters of HA and Se-Sr-HA were performed by Rietveld refinement, and are reported in **Table 1**. The substitution of selenium and strontium ions caused the increase in a-axis and c-axis lattice parameters of Se-Sr-HA as compared to reference HA. An expansion of the unit cell volume of Se-Sr-HA as compared to pure HA was also detected.

XRF Analysis

Table 2 shows the mol.% of the elements present in HA and Se-Sr-HA calculated through semi-qualitative XRF analysis. For the co-substituted HA, the presence of strontium and selenium could be detected along with calcium and phosphorus, confirming the substitution of both the selenium and strontium ions into the lattice structure of HA. Se-Sr-HA samples showed a Ca/P molar ratio 1.53, slightly lower than the stoichiometric Ca/P molar ratio in pure HA which is equal to 1.667. The slight difference might be the semi-quantitative mode of analysis.

Antibacterial Characterization of Se-Sr-HA

To evaluate whether the novel Se-Sr-HA possessed any antibacterial properties, a preliminary *in vitro* characterization was conducted following the ISO 20776 to determine the MIC (i.e., the lowest concentration of an antimicrobial agent that inhibits the visible growth of the bacteria) using the broth dilution test against *S. aureus* 6538P and *E. coli* 8739. **Figure 2** shows the variation of the optical density at 600 nm as a function of the Se-Sr-HA concentration against the two bacterial species. In both curves, a similar trend could be detected characterized by the inhibition of bacterial growth with increasing concentration of Se-Sr-HA. The MIC against *S. aureus* 6538P was 40 mg/mL, while the value for *E. coli* 8739 was 60 mg/mL.

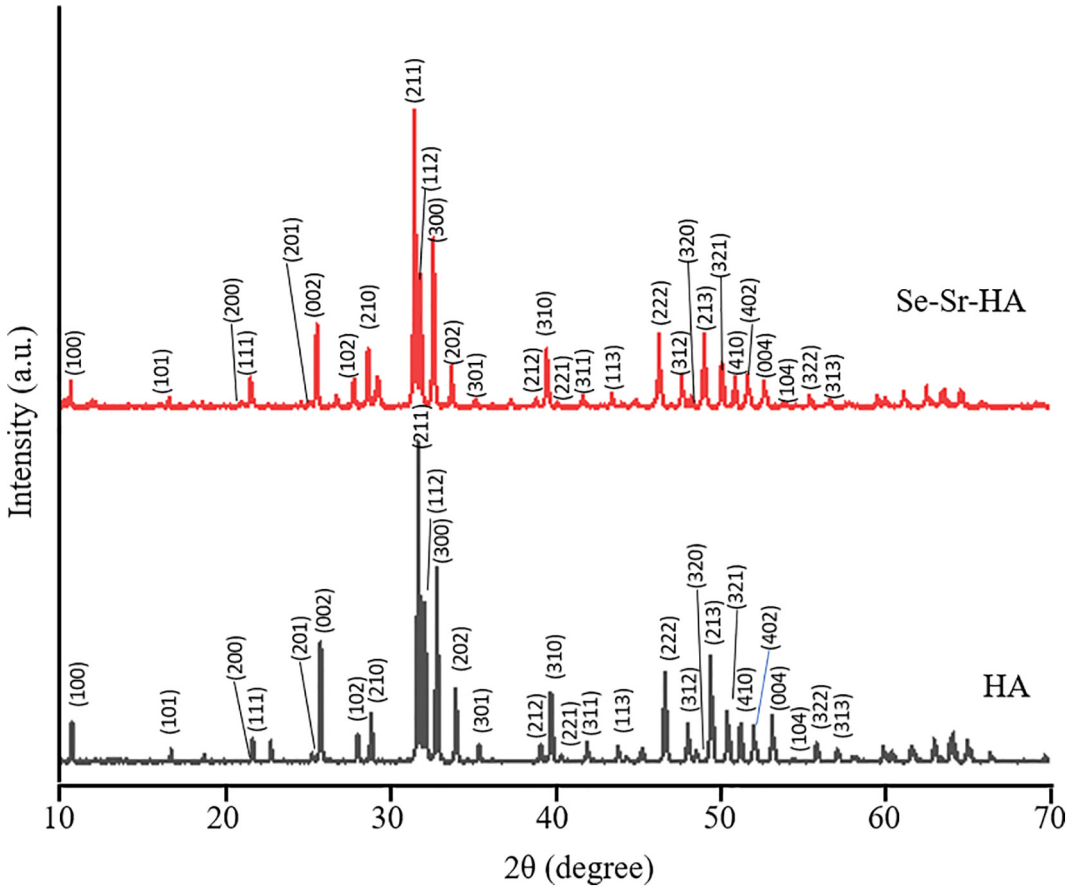

FIGURE 1 | X-ray diffractograms of non-substituted hydroxyapatite (HA) and selenium ion substituted hydroxyapatite (Se-Sr-HA) synthesized by the wet precipitation method and sintered at 900°C. The characteristic diffraction peaks for hexagonal HA could be detected in both HA and Se-Sr-HA samples. Reflections originating from hexagonal HA phase are labeled with their corresponding Miller indices.

Physicochemical Characterization of 2D Antibacterial Composite Scaffolds

To obtain 2D antibacterial composite scaffolds, three different loading compositions of Se-Sr-HA were investigated, 10, 20 and 30 wt% using P(3HB) or P(3HO-co-3HD-co-3HDD) as the matrix material. **Figure 3** shows the appearance of composite films of different compositions and corresponding FTIR spectra. From macroscopic observation the presence of HA in the films could be detected, as the material looked white and opaque.

ATR-FTIR Analysis

Qualitative characterization of P(3HB) and P(3HO-co-3HD-co-3HDD) composites was conducted by ATR-FTIR and the spectra are shown in **Figures 3C,D**, respectively. In all the spectra, the characteristic peak of PHAs related to the stretching of the carbonyl group (1720–1740 cm^{-1}) in the ester bond was identified. For scl-based composites, this peak is at 1720 cm^{-1}, while for mcl-based films at 1727 cm^{-1}. The mcl-PHA-based composites also showed more prominent peaks around 2900 cm^{-1} [i.e., stretching of carbon–hydrogen bond of methyl and methylene group (CH_3, CH_2)] compared to the scl-PHAs (Randriamahefa et al., 2003; Kann et al., 2014). The spectra of all the composite films showed new bands at 1072–1032, 601, 571, and 474 cm^{-1}, which were assigned to the vibrations of the phosphate group, PO_4^{-3}, present in the HA. In particular, the area between 1072 and 1032 cm^{-1} is related to the stretching mode of the phosphorus oxygen (P–O) bond in the phosphate group, while the area below 600 cm^{-1} is due to the bending mode of the O–P–O bond in the phosphate group (Koutsopoulos, 2002; Li et al., 2007).

TABLE 1 | Lattice parameters of HA and Se-Sr-HA.

Sample	α-axis (A°)	*c*-axis (A°)	Unit cell volume $(A^{\circ})^3$
HA	9.443	6.865	528.03
Se-Sr-HA	9.506	6.961	536.91

SEM and EDX Analyses

Scanning electron microscopy and EDX analyses of the surface of P(3HB) and P(3HO-co-3HD-co-3HDD) composite films are reported in **Figures 4**, **5**, respectively. For both types of PHAs, the surface of the composite films appeared less uniform than

TABLE 2 | The measured elemental composition of HA and Se-Sr-HA.

Samples	Calcium	Phosphorus	Selenium	Strontium	Ca+Sr/P+Se ratio	
	(mol.%)	(mol.%)	(mol.%)	(mol.%)	Theoretically calculated	XRF
HA	1.09	0.65	0	0	1.67	1.67
Se-Sr-HA	0.82	0.55	0.0441	0.0897	1.67	1.53

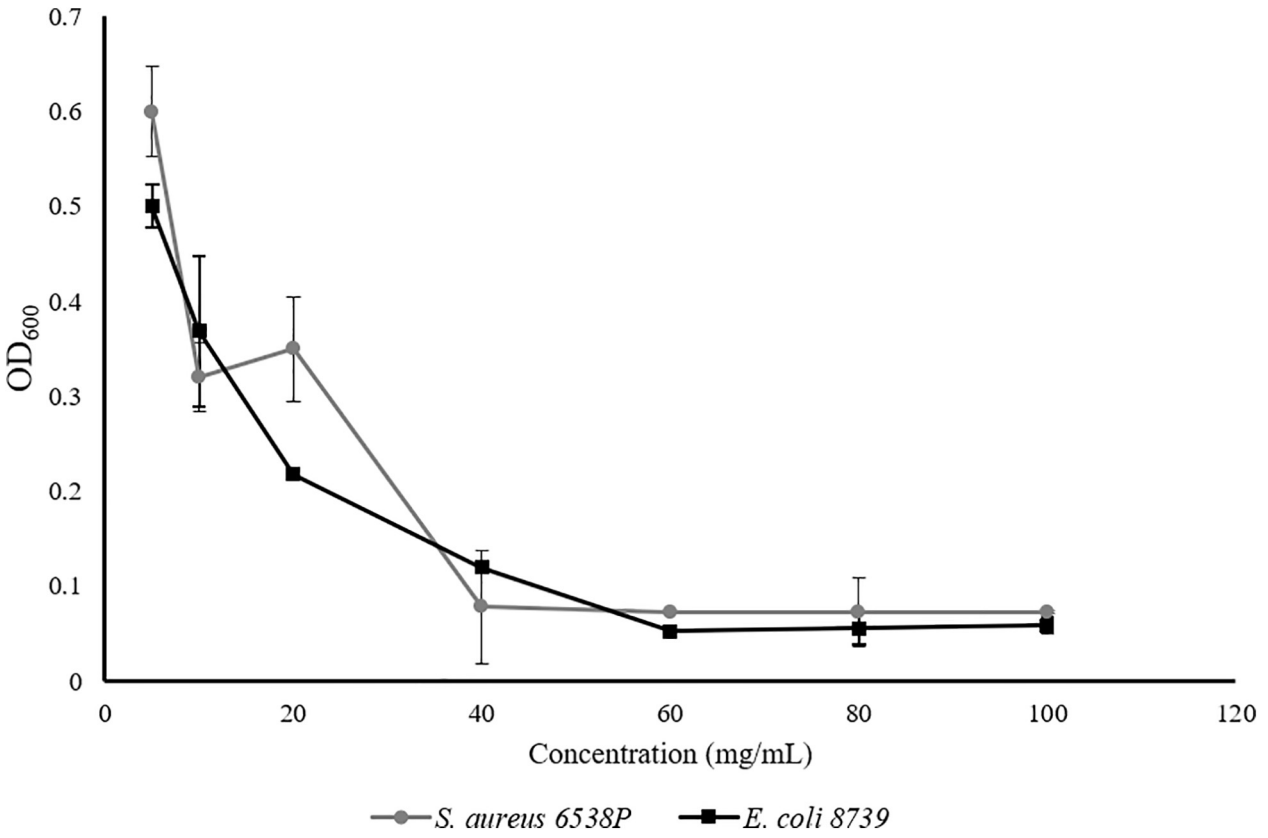

FIGURE 2 | MIC analysis of Se-Sr-HA powders against *S. aureus 6538P* (in grey) and *E.coli 8739* (in black). For both bacteria, the variations of the OD_{600} with an increase in the concentration of Se-Sr-HA are plotted.

that of the neat samples due to the presence of HA particles. EDX analyses confirmed the presence of Se-Sr-HA particles in the materials. The spectra of the neat samples showed only the presence of peaks assigned to carbon and oxygen, while for all the composite films, the presence of the other four elements (i.e., calcium, phosphorus, selenium, and strontium) associated with Se-Sr-HA was detected.

Thermal Characterization

The effect of the incorporation of Se-Sr-HA on the thermal properties of the composite films was evaluated by DSC analysis (**Table 3**). For both P(3HO-co-3HD-co-3HDD) and P(3HB) composite samples, the loading of HA did not induce statistically significant differences in the melting temperature and the glass transition values of the composite films as compared to the neat samples. Interestingly, none of the P(3HB)-based films showed the presence of a glass transition phase, including the neat samples. Such result indicates the transformation of the amorphous fraction of the polymer into a rigid amorphous phase due to vitrification during storage of the films at room temperature for 5 weeks (Lukasiewicz et al., 2018). The loading of the antibacterial HA into both types of polymeric matrices led to a significant reduction of the enthalpy of fusion (normalized to the content of the polymer) for both types of PHAs considered. For P(3HB)-based samples, the sample with 30 wt% of Se-Sr-HA showed a statistically significant reduction in the enthalpy of fusion and consequently the percentage crystallinity of the composite samples as compared to the neat samples

(p-value < 0.01). Moreover, the sample with 30 wt% of filler showed a statistically significant reduction in the values of enthalpy of fusion as compared to both samples with 20 wt% (p-value < 0.05) and 10 wt% (p-value < 0.01) of Se-Sr-HA. For P(3HO-co-3HD-co-3HDD) films, the samples with the highest contents of filler (i.e., 20 and 30 wt%) showed statistically

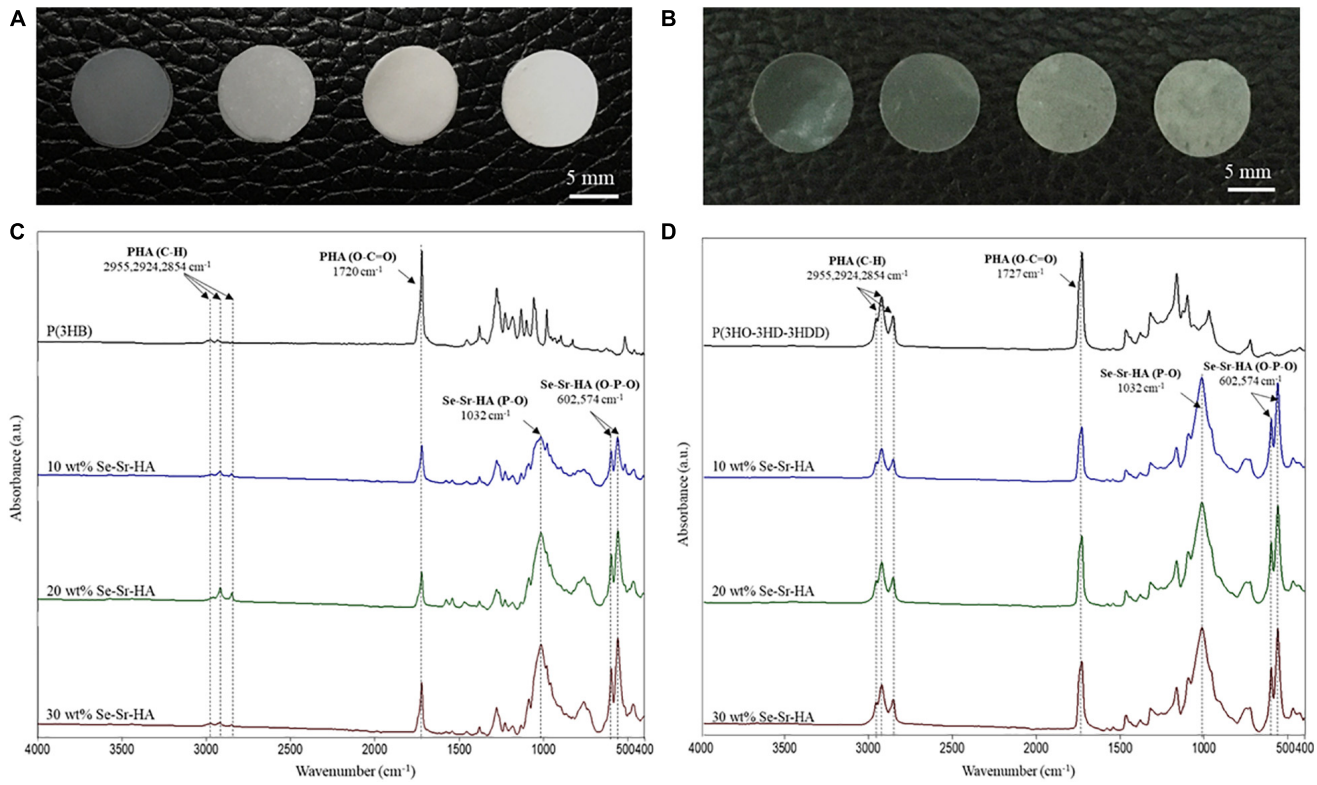

FIGURE 3 | Optical images of P(3HB) **(A)** and P(3HO-co-3HD-co-3HDD) **(B)** composite films. In each image, the samples are in the following order from left to right: neat film, 10 wt% Se-Sr-HA, 20 wt% Se-Sr-HA, and 30 wt% Se-Sr-HA composite films. ATR-FT-IR spectra of P(3HB) **(C)** and P(3HO-co-3HD-co-3HDD) **(D)** composite films. In each spectrum, neat samples are in black, 10 wt% Se-Sr-HA in blue, 20 wt% Se-Sr-HA in green, and 30 wt% Se-Sr-HA in red.

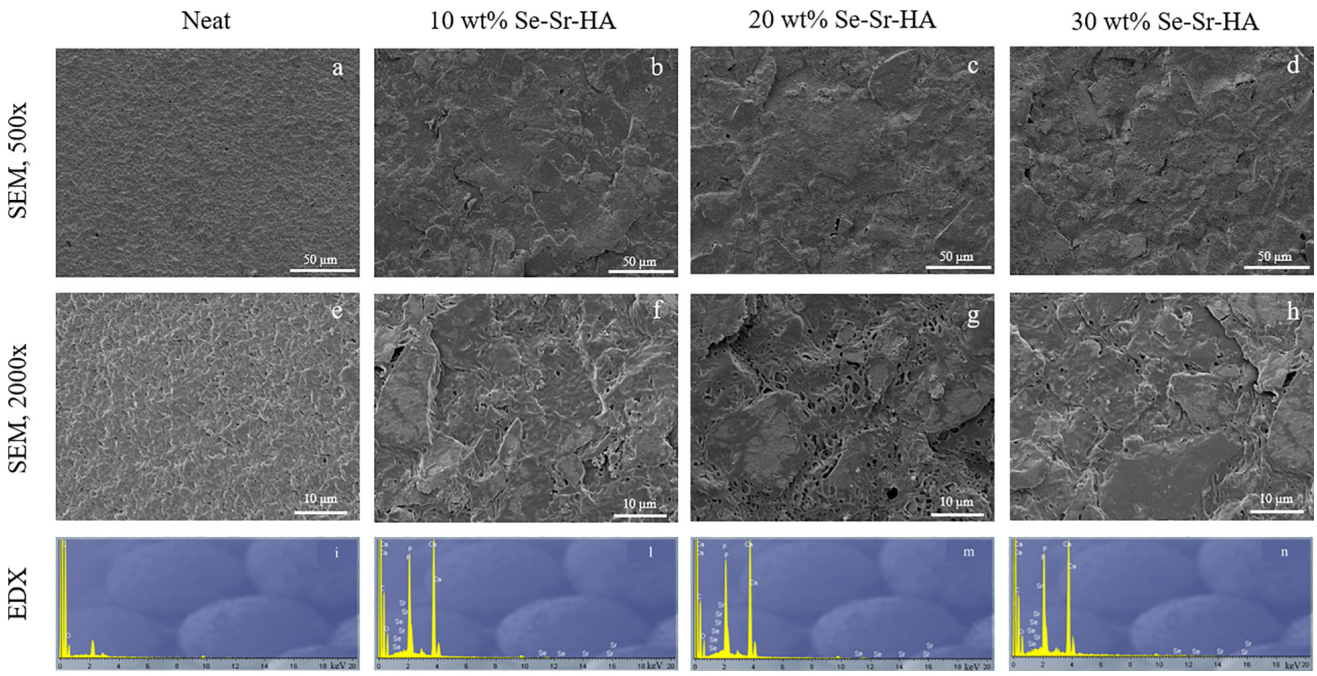

FIGURE 4 | SEM image at 500× **(a–d)** and 2000× **(e–h)** and EDX spectra **(i–n)** of P(3HB) based composite films. The samples are in the following order from left to right: neat film, 10 wt% Se-Sr-HA, 20 wt% Se-Sr-HA, and 30 wt% Se-Sr-HA composite films.

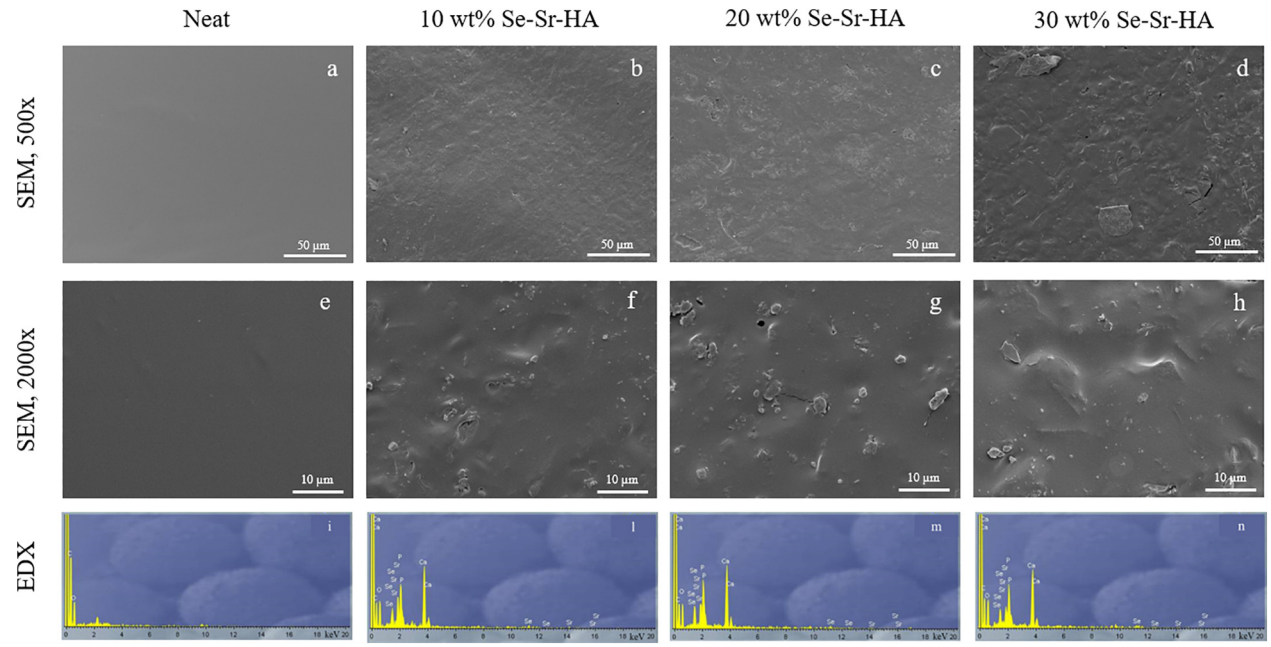

FIGURE 5 | SEM image at 500× **(a–d)** and 2000× **(e–h)** and EDX spectra **(i–n)** of P(3HO-co-3HD-co-3HDD) based composite films. The samples are in the following order from left to right: neat film, 10 wt% Se-Sr-HA, 20 wt% Se-Sr-HA, and 30 wt% Se-Sr-HA composite films.

TABLE 3 | Thermal properties of P(3HB) and P(3HO-co-3HD-co-3HDD) composite samples.

Sample		T_m(°C)	T_g(°C)	ΔH^n_m(J/g)	X_c(%)
PHA	**Wt% of Se-Sr-HA**				
P(3HB)	0 (neat)	169 ± 2	n.d.	82 ± 4	56 ± 4
	10	169 ± 1	n.d.	83 ± 4	57 ± 3
	20	170 ± 1	n.d.	78.5 ± 4	54 ± 3
	30	169 ± 1.5	n.d.	61 ± 4.5	42 ± 3
P(3HO-3HO-3HDD)	0 (neat)	53 ± 5	−44 ± 2	24.5 ± 1	–
	10	52 ± 0.5	−40.5 ± 2	21.5 ± 1.5	–
	20	52.5 ± 0.5	−42 ± 2	19 ± 1.5	–
	30	52 ± 0.5	−42 ± 0.5	18 ± 2	–

T_m is the melting peak, T_g is the glass transition, ΔH^n_m is the enthalpy of fusion normalized to the mass fraction of the polymer, and X_c is the % polymer crystallinity.

lower values of enthalpy of fusion as compared to the neat films (p-value < 0.05 for 20 wt% and p-value < 0.01 for 30 wt%). However, no statistically significant differences in the enthalpy of fusion were detected between the composite films (i.e., 10 wt% vs 20 wt% vs 30wt%). For mcl-PHA-based materials, it was not possible to calculate the value of crystallinity from the enthalpy of fusion as the reference enthalpy of fusion (i.e., the enthalpy of fusion for a 100% crystalline polymer) is not known (Suchitra, 2004). Since the enthalpy of fusion is directly proportional to the degree of crystallinity, the decrease in the enthalpy of fusion of the composite indicated that the presence of the filler affected P(3HO-co-3HD-co-3HDD) crystallization.

Mechanical Characterization

Tensile testing of the composite films was conducted to assess the influence of the incorporation of Se-Sr-HA on the mechanical properties of the materials, and the results are reported in **Table 4**. Overall, for both types of PHAs, the addition of HA leads to an increase in the elastic modulus and a decrease of the elongation at break of the composite samples as compared to the neat ones. For P(3HB) samples, the film containing 20 wt% of Se-Sr-HA showed the highest increase in the Young's modulus, which was almost double that of the neat samples (p-value < 0.01). Also, the ultimate tensile strength increased by 1.5 times as compared with the neat films (p-value < 0.001). In terms of elongation at break, all the composite films showed a three to seven times decrease in the average values, without statistically significant difference between the three different compositions. As regards the mcl-PHA-based composites, Se-Sr-HA filler induced an increase in the elastic modulus by two to three times for all the compositions tested as compared to neat P(3HO-co-3HD-co-3HDD) samples, but no statistically significant differences were detected between

TABLE 4 | Mechanical properties of P(3HB) and P(3HO-co-3HD-co-3HDD) composite films and corresponding neat polymers (n = 6).

Sample		Young's modulus (MPa)	Ultimate tensile strength (MPa)	Elongation at break (%)
PHA	**Wt% of Se-Sr-HA**			
P(3HB)	0 (neat)	900 ± 120	20 ± 1.5	16 ± 8
	10	1100 ± 100	23.5 ± 1.0	5 ± 2
	20	1700 ± 200	30 ± 3	2.5 ± 1.0
	30	900 ± 200	24 ± 2	3 ± 1
P(3HO-3HO-3HDD)	0 (neat)	5 ± 2	6.5 ± 1.0	414 ± 32
	10	14 ± 4	7.0 ± 1.5	299 ± 44
	20	14 ± 6	6.0 ± 1.5	284 ± 31
	30	16 ± 2	4 ± 1	173 ± 32

the samples with different Se-Sr-HA content. In terms of the ultimate tensile strength, the samples with 30 wt% of filler showed a significant decrease in the average values compared to the neat films (p-value < 0.5), while for the other two filler contents (i.e., 10 and 20 wt%), no variation could be detected. Finally, a significant reduction of the elongation at break was detected for all the composite samples, with the highest average reduction of almost 2.5 times observed for the films with 30 wt% of Se-Sr-HA.

Antibacterial Characterization

The antibacterial properties of the composite films developed were investigated using two tests, a direct contact test (i.e., ISO 22196) and an indirect one (i.e., antibacterial ion release). The former is a standard well-established procedure used for the quantification of the antimicrobial properties of the surfaces of materials (Molling et al., 2014). The latter one was chosen to evaluate whether the materials produced release ions possessing antimicrobial activity. The 2D composite films developed are expected to exhibit an antibacterial activity by two mechanisms: contact activity when bacteria adhere to the material surface containing HA with selenite ions incorporated in its structure and due to an action of solubilized ions released in the surrounding environment. The two selected tests enable analysis of the contribution of the two mechanisms independently of each other.

Direct Contact Test—ISO 22196

The ISO 22196 was performed to investigate the antimicrobial activity of the composite films against *S. aureus* 6538P and *E. coli* 8739, seeded directly on the surface of the materials. P(3HB) and P(3HO-co-3HD-co-3HDD) composite samples showed to be active against both bacterial species at all the three loading contents investigated, inducing a reduction of the bacterial cell number as compared to the respective neat samples (**Figure 6**). For the scl-PHA-based composites, all the films showed a high efficacy, causing a 100% killing of *S. aureus* 6538P and *E. coli* 8739 for all the compositions tested. The P(3HO-co-3HD-co-3HDD) composite films showed a bactericidal effect against *S. aureus* 6538P, increasing with the increase in the HA content. The samples with the lowest contents of filler (i.e., 10 and 20 wt% of Se-Sr-HA) induced a 90 and 94% average reduction of the number of bacterial cells, respectively, while the highest efficacy was obtained with the highest content of the filler (i.e., 30 wt% of Se-Sr-HA), causing an average 96% reduction of bacterial cells. The mcl-PHA-based composites showed a higher effect against *E. coli* 8739, as all the compositions investigated led to at least a 99.5% reduction of the bacterial cell count.

Antibacterial Ion Release Studies

The antibacterial release study was performed against *S. aureus* 6538P and *E. coli* 8739 to investigate the capability of the developed 2D antibacterial composite films to release ions with antibacterial properties. In this indirect method, the bacterial cells were with the eluates obtained by incubating the polymeric samples in Mueller Hinton broth. The antibacterial activity was calculated as the reduction in the OD of the bacterial suspension in contact with the eluates obtained from the composite samples as compared to bacteria cultured with the eluates from the neat films. Overall, P(3HB) and P(3HO-co-3HD-co-3HDD) composite samples showed activity against both bacterial species, as shown in **Figure 7**. In the case of *S. aureus* 6538P, both materials showed at least a 30% average reduction of the OD for all the time points evaluated. Moreover, the composite with the highest content of HA (i.e., 20 and 30 wt%) showed a higher antibacterial activity than that of samples with 10 wt% of filler at all the time points evaluated. Finally, both materials induced a reduction of the OD of *E. coli* 8739 cells, even though the efficacy was lower as compared to *S. aureus* 6538P.

DISCUSSION

The use of HA doped with metal ions in bone regeneration has attracted great interest in recent years thanks to the possibility of enhancing its mechanical and biological properties. In this work, a novel co-substituted HA was developed by wet precipitation with sodium selenite and strontium nitrate as the sources of selenium and strontium, respectively. In the literature, HA containing either strontium or selenium has been developed (Uskokovic et al., 2017; Zarins et al., 2019), but to our knowledge to date, no study regarding the simultaneous co-substitution of such ions has been published. Selenium was chosen to introduce antibacterial properties in the material. Only a few studies have been conducted on the antibacterial properties of selenium and the mechanism behind its efficacy has not been elucidated yet. The main hypothesis formulated is the induction of oxidative

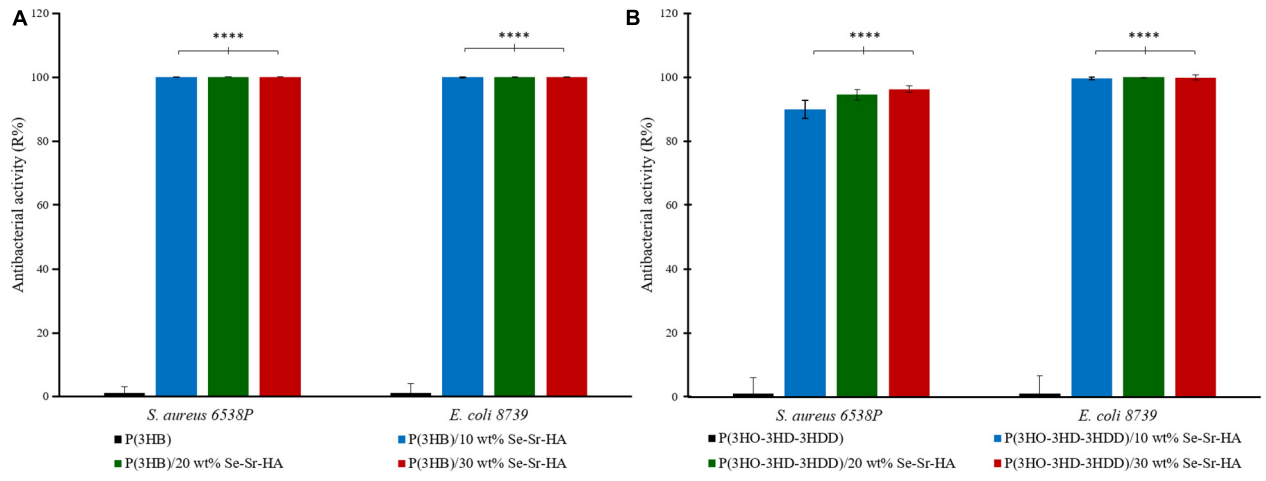

FIGURE 6 | Antibacterial activity (R%) (ISO 22196) of P(3HB) **(A)** and P(3HO-co-3HD-co-3HDD) **(B)** composite films against *S. aureus* 6538P and *E. coli* 8739. In each figure, neat films are in black, composite films with 10 wt% of Se-Sr-HA in blue, 20 wt% in green, and 30 wt% red. The control consists of bacteria cultured on neat films (inducing no reduction in the bacterial cell number, having an average R% of zero). ****p-value < 0.0001 indicates statistically significant difference between the composite films and the respective neat films.

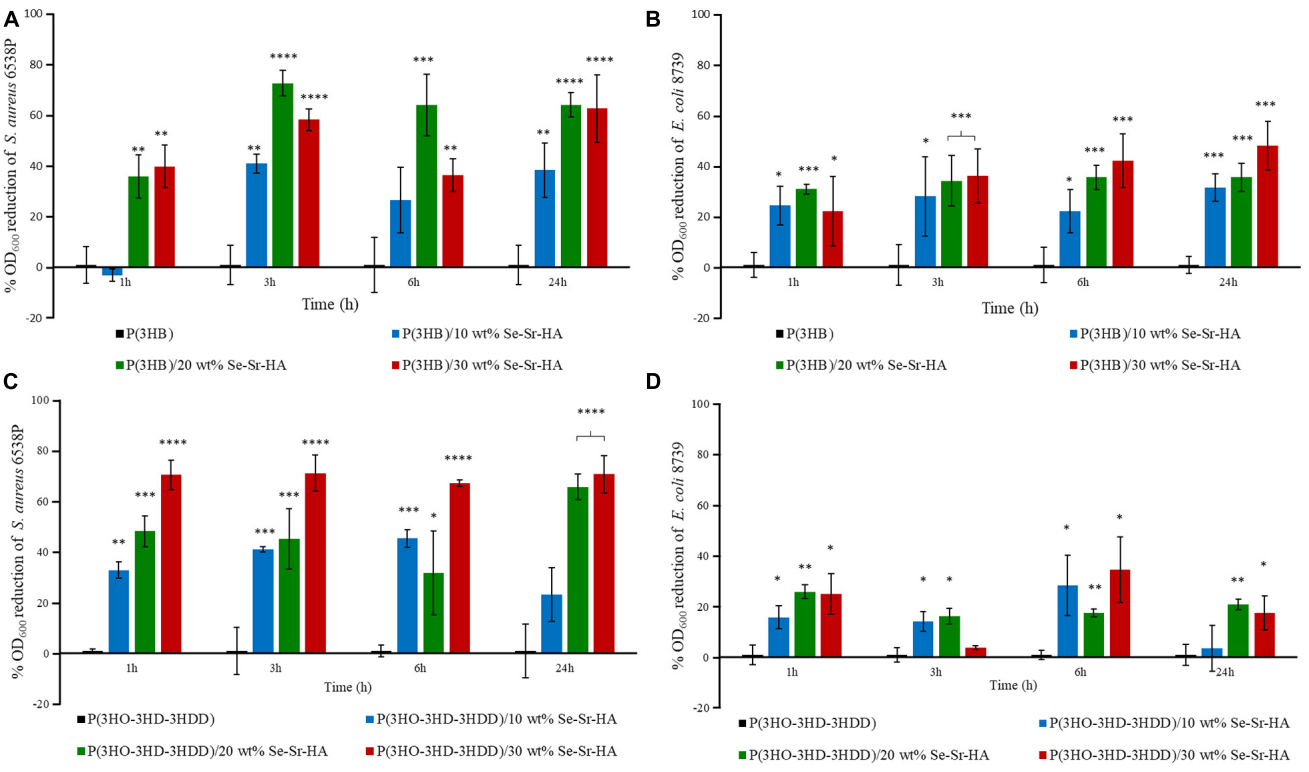

FIGURE 7 | Indirect antibacterial ion release study of the eluates from P(3HB) **(A,B)** and P(3HO-3HD-3HDD) **(C,D)** composite films *S. aureus* 6538P **(A,C)** and *E. coli* 8739 **(B,D)**. In each figure, neat films are in black, composite films with 10 wt% of Se-Sr-HA in blue, 20 wt% in green, and 30 wt% in red. The control is bacteria cultured with the eluates obtained from the neat films (inducing no antibacterial effect, having an average %OD_{600} reduction of zero).*p-value < 0.05, **p-value < 0.01, ***p-value < 0.001, and ****p-value < 0.0001 indicate statistically significant difference between the composite samples and the respective neat films.

stress through the production of reactive oxygen species and the depletion of thiol groups, inducing membrane and cell wall damage as well as permanent changes in cell components leading to bacterial death (Kolmas et al., 2014; Huang et al., 2019). However, the use of selenium has also been linked with cytotoxic effects (Wang et al., 2012; Uskokovic et al., 2017). For

this reason, in this work, its co-substitution with strontium was investigated to off-set its toxicity. Strontium ions were chosen as they have been shown to introduce osteoinductive and osteogenic properties, favoring bone remodeling (Nielsen, 2004; Ratnayake et al., 2017). Structural characterization through XRD and XRF confirmed the co-substitution of both ions in the crystalline lattice. From the literature, it is known that strontium ions partially substitute calcium ions through cationic substitutions, while anionic substitution occurs between selenite and phosphate groups (Ratnayake et al., 2017; Uskokovic et al., 2017). The introduction of such ions induced a change in lattice parameters and an increase in the unit cell volume. Sr^{2+} might have played a significant role in the expansion of the unit cell volume of Se-Sr-HA due to its larger ionic radius as compared to Ca^{2+}, 118 and 99 pm, respectively (Gritsch et al., 2019; Zarins et al., 2019). Nevertheless, Se-Sr-HA still maintained the crystalline structure of HA. In particular, the XRD results showed that selenite ions were substituted into the HA crystal lattice in the absence of secondary phase. Moreover, the XRD and XRF data confirmed the incorporation of selenium into the lattice structure of HA. If these ions were only adsorbed on the crystal surface, the content of selenium would have been negligible (as any soluble selenium salt would be removed during the washing step). The selenium and strontium content obtained in Se-Sr-HA samples was significantly lower than the anticipated values based on the stoichiometric ratio of components used in the synthesis (**Table 2**). Such a difference could be associated with the semi-quantitative mode of analysis used for XFR in this study. Moreover, the lower substitution of strontium ions at calcium sites could be related to the larger ionic radii of Sr^{2+}(118 pm) compared to Ca^{2+} (99 pm). Selenite and phosphate ions have similar ionic radii, but a different geometric arrangement, flat trigonal pyramid structure for SeO_3^{2-} compared to tetrahedral structure for PO_4^{3-} ions, which could be the reason for the lower substitution (Pajor et al., 2018). Consequently, the added ions were partially substituted in the HA lattice, while the excess selenium and strontium ions remained in solution were removed during the washing steps of the wet precipitation synthesis.

A preliminary *in vitro* characterization of the materials confirmed that the introduction of selenium conferred antibacterial properties to the HA. The Se-Sr-HA showed to be active against both *S. aureus* 6538P and *E. coli* 8739, inducing inhibition of the microbial cell growth. The composition of the Se-Sr-HA used in this work [i.e., produced considering Sr:(Sr+Ca) and Se:(Se+P) molar ratios of 0.2] was selected based on their antibacterial properties. Other compositions of Se-Sr-HA were prepared by varying the Se/(Se+P) and Sr/(Sr+Ca) ratios (i.e., 0.01, 0.03, 0.05, and 0.1) and they exhibited a lower antibacterial activity compared to the one used in this study (i.e., 0.2) against both bacterial species (data not shown). Limited research has been conducted in the literature to investigate the antibacterial properties of selenium-doped HA, and the few studies carried out vary in terms of content of selenium, form of HA, and test method utilized, making it difficult to compare the results obtained. Nevertheless, overall the materials produced have shown activity against both Gram-positive and Gram-negative bacteria, as shown in this study. In the study by Uskokovic et al., substituted HAs with four concentrations of selenium (0.1, 1.2, 1.9, and 3 wt%) in the form of powders showed activity against *E. coli*, *S. aureus*, *Salmonella enteritidis*, and *Pseudomonas aeruginosa*, inducing a zone of inhibition at all the concentrations investigated. Rodríguez-Valencia et al. produced Se-HA with 0.6 at% of selenium. The ceramic produced was used as a coating for titanium disc samples and showed activity against *P. aeruginosa* 19582 and *S. aureus* 6538P, by inducing a reduction in biofilm formation (Rodríguez-Valencia et al., 2013). Finally, a co-substituted HA with selenium (3.6 wt%) and manganese (0.6 wt%) was produced by Kolmas et al. The antimicrobial properties of the material were investigated by the incubation of the ceramic in the form of pellets with a microbial suspension of *S. aureus* 25293 and *E. coli* 2592 for 24 h. The material induced reduction in the cell count of *S. aureus* 25293, while it showed no activity against *E. coli* 2592 (Kolmas et al., 2015). The difference in the form of HA used, pellet discs, compared to the powder used in this study and in the work of Uskokovic et al. might be the reason for the discrepancy in the results obtained against *E. coli*, as the former might have led to a lower release of antimicrobial ions compared to the free powder form. Nevertheless, our study and published works are in agreement that Se-HA is less efficient against *E. coli* than *S. aureus*.

The Se-Sr-HA produced was combined with two types of PHAs, P(3HB) and P(3HO-co-3HD-co-3HDD) to produce antibacterial composite materials for their potential use as the starting materials for the fabrication of scaffolds for bone regeneration. The two polymers were produced by bacterial fermentation following optimized protocols previously developed by our group (Basnett et al., 2018; Lukasiewicz et al., 2018). These two polyesters were chosen as representative of scl and mcl-PHAs, respectively. As mentioned in Section "Introduction," P(3HB) has been explored in the literature as a material for bone tissue regeneration thanks to its mechanical properties, in the range of those of native bone (Karageorgiou and Kaplan, 2005; Misra et al., 2008). Little investigation has been conducted on the use of mcl-PHAs for bone regeneration. Ansari et al. (2016) developed a porous composite scaffold through the combination of P(3HHx-co-3HO) with non-substituted HA. The elastomeric nature of these polymers makes them attractive suitable candidates as materials for non-load bearing applications. In this work, we studied the combination of the two PHAs with Se-Sr-HA to produce novel composite materials with osteinductive and antibacterial properties, without the use of antibiotics.

Qualitative chemical analysis through FT-IR and EDX confirmed the incorporation of the Se-Sr-HA inside the polymer matrix. Analysis of the surface morphology evidenced differences between the P(3HB)-based and P(3HO-co-3HD-co-3HDD)-based samples. Mcl-PHA films obtained by solvent evaporation are usually characterized by a smooth surface, while scl-PHA films usually show a rougher surface with protrusions and pores (Rai et al., 2011; Anbukarasu et al., 2015). This distinctive feature can be attributed to the higher degree of crystallization and a

more rapid crystallization rate of scl-PHAs compared to mcl-PHAs (Kai et al., 2003; Li et al., 2016). The two types of composite films with Se-Sr-HA showed the same distinctive characteristics. For P(3HB) composites, the presence of a more porous surface led to a higher exposure of the HA compared to the P(3HO-co-3HD-co-3HDD) ones. Wang et al. reported a similar behavior between the surface of P(3HB) and P(3HB-co-3HHx) films loaded with HA. A higher amount of the filling could be detected on the surface of the former composites, which was attributed to the higher crystallinity of the bulk material (Wang et al., 2008).

The loading of Se-Sr-HA in the two types of PHA-based composites induced a decrease in the enthalpy of fusion (and consequently the crystallinity) of the materials with high content of filler compared to the neat samples. These results indicate that the introduction of high quantities of filler reduced the mobility of the chains, hindering the material crystallization (Misra et al., 2008). Such behavior can be associated with the micro-size dimension of the filler utilized in this study. In the literature, hindering of the crystallization has been shown when combining PHAs with micro-size HA (Bergmann and Owen, 2003; Ansari et al., 2016), while a nucleating effect was detected in the presence of nano-sized HA particles (Misra et al., 2008; Noohom et al., 2009; Sadat-Shojai et al., 2013). The increase in crystallinity has been associated with the better interface between the filler and the polymeric matrix created by the higher dispersion of nano-sized HA compared with micro-size particles (Misra et al., 2008; Sadat-Shojai et al., 2013).

One of the main reasons for the use of composites is to create a final material that has a higher strength and modulus than the polymeric component and at the same time better toughness and processability than the inorganic filler. For both types of PHAs, the introduction of the HA led to an improvement in the strength and stiffness of the material. Simultaneously, an embrittlement of the constructs was evidenced through the reduction of the elongation at break. In particular, in the case of P(3HB), a composite loading percentage of 20 wt% was found to be optimal to obtain the highest increment of Young's modulus (1.7 GPa) and tensile strength (30 MPa) compared with the neat P(3HB) films (0.9 GPa and 19 MPa, respectively). A higher content of filler (i.e., 30 wt%) induced a detrimental effect on the mechanical properties of the composite films with a decrease in both the elastic modulus and the tensile strength as compared to the samples with 20 wt% of Se-Sr-HA. Such behavior can be correlated to the decrease in the crystallinity of the material for the composites with the highest filler loading. Moreover, the higher particle agglomeration for samples with the highest filler loading is likely to increase filler–filler contacts which weaken the composite structure (Goonasekera et al., 2016; Grøndahl et al., 2017). For the P(3HO-co-3HD-co-3HDD) composite films, the sample with the lowest content of Se-Sr-HA showed the highest improvement of elastic modulus (14 MPa) and tensile strength (7 MPa) compared to neat P(3HO-co-3HD-co-3HDD) films (5.3 and 6.5 MPa, respectively). No increase in the elastic modulus was in fact evidenced for P(3HO-co-3HD-3HDD) samples containing 20 and 30 wt% of Se-Sr-HA compared to the ones with 10 wt% of filler and in parallel a reduction of the enthalpy of fusion (and consequently crystallinity) was obtained with the materials with 20 and 30 wt% of HA. The difference between the two types of PHAs might be related to the higher crystallinity of the scl-PHAs compared to the mcl ones. It has in fact been hypothesized that in polymers with high crystallinity, low quantities of filler present in the amorphous region do not impact significantly on the final bulk mechanical properties, therefore requiring higher filler amount compared to less crystalline materials (Kaur and Shofner, 2009; Grøndahl et al., 2017).

Overall, the P(3HB) composite containing Se-Sr-HA showed mechanical features similar to those of cancellous bone, making them good candidates for the development of materials for the reconstruction of defects of such type of tissue (Fernandez de Grado et al., 2018). However, future work should still be conducted to improve the brittleness of these materials, which might limit their *in vivo* application. On the other hand, P(3HO-co-3HD-3HDD) still showed a ductile behavior after the incorporation of the HA. Even though a drastic decrease in the deformation capability of the films was evidenced for the three filler contents analyzed, the composite samples with 30 wt% of Se-Sr-HA still showed a high elongation at break with an average value of 170%. Such a characteristic could make them a suitable candidate for the generation of scaffolds for non-load bearing applications, where their elastic nature might be an advantage for the development of flexible and easily shaped materials able to adapt to the defect site (Ural et al., 2000; Chen et al., 2012). Nevertheless, the final mechanical properties should be further optimized and could be achieved by improving the interface between the polymers and the filler with the use, for example, of nano-sized HA (Misra et al., 2008; Rai et al., 2008).

The main reason for the use of a co-substituted HA compared to traditional calcium phosphates was to develop a material possessing antibacterial properties to be used for the fabrication of the scaffold able to reduce and prevent the attachment and proliferation of bacteria in bone regeneration. The 2D composite films developed exhibited an antibacterial activity by two mechanisms, by direct contact between the bacteria and the selenite ions present in the HA structure (analyzed through the direct tests ISO 22196) and by action of the ions released in the surrounding environment (analyzed through the indirect contact test and antibacterial ions release). In particular, both composite types exhibited a high activity on contact, inducing at least a 90% reduction of bacterial cell number of both *S. aureus* 6538P and *E. coli* 8739. These results confirmed the activity of selenium containing compound against both Gram-positive and Gram-negative species, as already evidenced in MIC studies (Rodríguez-Valencia et al., 2013; Alam et al., 2016; Uskokovic et al., 2017). *S. aureus* 6538P and *E. coli* 8739 were chosen as representative organisms of Gram-positive and Gram-negative bacteria, respectively, as described by the ISO 22196. Future work will evaluate the antibacterial activity of the materials against other strains (e.g., *Staphylococcus epidermidis*, *Streptococci* sp., and *Pseudomonas* sp.) associated with bone

infection and antibiotic-resistant strains such as methicillin-resistant *S. aureus*.

P(3HB) composites showed a higher effect compared to the P(3HO-co-3HD-co-3HDD) ones, as they completely prevented the growth of both Gram-positive and Gram-negative cells. This higher activity might be due to the differences in the surface properties of the two types of composites that were evidenced in the SEM analyses. The scl-PHAs samples possessed in fact a more porous surface which might have led to a higher exposure of HA on surface of the films, therefore potentially increasing the amount of ions in contact with the bacterial cells.

Both P(3HB) and P(3HO-co-3HD-co-3HDD) composites showed a reduction in the growth of *S. aureus* 6538P and *E. coli* 8739 during the *in vitro* antibacterial indirect tests. Such results can be used as an indication of the capability of such materials to release ions. In particular, the release of the ions seemed to possess an early onset as a reduction of the number of bacteria could be detected with the eluates obtained after 1 h of incubation for both types of PHAs. Moreover, it appears that the release is extended over time, as the media obtained at 24 h of incubation still possessed an antimicrobial activity. As expected, the materials containing a higher percentage of HA showed a higher antimicrobial effect which could be associated with an increased amount of selenite ions. Moreover, P(3HB)-based composites exhibited a slightly higher activity against both bacterial strains compared with composites with mcl-PHA matrix polymer. The higher porosity of P(3HB) matrix might be the reason of the higher antibacterial activity due to more rapid release of antimicrobial ions. Nevertheless, further studies should be conducted to quantify the concentration of the ions released and to investigate release kinetics over a longer period of time. For both P(3HB) and P(3HO-co-3HD-co-3HDD) composites, the growth inhibition was slightly more effective against Gram-positive bacteria than negative ones. In a few studies in the literature, low concentrations of selenite ions did not induce significant reduction in *E. coli* cultures (Vasić et al., 2011; Alam et al., 2016). It is known in the literature that some species are capable of reducing inorganic selenite ions to elemental selenium nanoparticles which are then deposited within the cell (e.g., in the cytoplasm or in the periplasmic space) or pumped outside the cells (Turner et al., 1998; Gonzalez-Gil et al., 2016). *E. coli* has been shown to possess such features probably making them less susceptible to the antimicrobial activity of such ions at lower concentrations (Turner et al., 1998). These results are also in agreement with the slightly higher MIC value obtained for *E. coli* 8739 compared to the *S. aureus* 6538P for the Se-Sr-HA.

CONCLUSION

This work focused on tackling the worldwide threat posed by the rapid growth of antimicrobial resistance to antibiotics. In particular, we targeted bone regeneration, a biomedical application characterized by a high risk of bacterial infection which can significantly impair the correct regrowth of functional tissue. We reported, for the first time, the synthesis of a novel dual substituted HA containing selenium and strontium and its combination with two types of PHAs, both scl and mcl, to produce novel antibacterial materials for bone regeneration without the use of antibiotics. The loading of the filler in the polymer matrix induced an enhancement in the mechanical strength of both scl and mcl-PHA films, combined with a parallel reduction in the deformability of the materials. The developed composite materials possess high antibacterial activity against *S. aureus* 6538P and *E. coli* 8739 through two mechanisms, by direct contact between the bacteria and the materials surface and through the release of active ions at a concentration capable of inhibiting bacterial growth in a prolonged manner, up to 24 h. This study demonstrates the potential of these materials to provide antibacterial activity without the use of antibiotics, allowing them to be used as starting materials for the development of unique and effective antibacterial scaffolds for bone regeneration. Future work will focus on the development of these scaffolds and investigation of their biocompatibility properties using bone cell lines and further *in vivo* work.

DATA AVAILABILITY STATEMENT

The raw data supporting the conclusions of this article will be made available by the authors, without undue reservation.

AUTHOR CONTRIBUTIONS

EM produced the PHAs, performed all the experiments and data analysis related to the composite samples, and drafted the manuscript. MM produced the Se-Sr-HA, conducted the experiments and data analysis related to the Se-Sr-HA physiochemical characterization, and contributed to the drafting of the manuscript. RN contributed to the data analysis related to the characterization of the composite materials and the manuscript revision. MC, PJ, and PB contributed to the manuscript revision. JK was involved in the SEM/EDX analyses. AB and IR contributed to the planning and supervision of the project and manuscript revision. All authors contributed to manuscript revision and read and approved the submitted version.

FUNDING

This work was supported by the "Drug-Free Antibacterial Hybrid Biopolymers for Medical Applications" HyMedPoly project and the European Union's Horizon 2020 Research and Innovation Programme under the Marie Skłodowska-Curie Action MSCAITN-2014-EID: Marie Skłodowska-Curie Innovative Training Networks (Grant No. 643050).

ACKNOWLEDGMENTS

The authors would like to thank Dr. Nicola Mordan from Eastman Dental Institute, University College London for her contribution in SEM and EDX analyses.

REFERENCES

Alam, M. F., Safhi, M. M., Moni, S. S., and Jabeen, A. (2016). In vitro antibacterial spectrum of sodium selenite against selected human pathogenic bacterial strains. *Scientifica* 2016:9176273. doi: 10.1155/2016/9176273

Anbukarasu, P., Sauvageau, D., and Elias, A. (2015). Tuning the properties of polyhydroxybutyrate films using acetic acid via solvent casting. *Sci. Rep.* 5:17884. doi: 10.1038/srep17884

Ansari, N. F., Annuar, M. S. M., and Murphy, B. P. (2016). A porous medium-chain-length poly(3-hydroxyalkanoates)/hydroxyapatite composite as scaffold for bone tissue engineering. *Eng. Life Sci.* 17, 420–429. doi: 10.1002/elsc.201600084

Baldwin, P., Li, D. J., Auston, D. A., Mir, H. S., Yoon, R. S., and Koval, K. J. (2019). Autograft, allograft, and bone graft substitutes: clinical evidence and indications for use in the setting of orthopaedic trauma surgery. *J. Orthop. Trauma* 33, 203–213. doi: 10.1097/BOT.0000000000001420

Basnett, P., Marcello, E., Lukasiewicz, B., Panchal, B., Nigmatullin, R., Knowles, J. C., et al. (2018). Biosynthesis and characterization of a novel, biocompatible medium chain length polyhydroxyalkanoate by *Pseudomonas* mendocina CH50 using coconut oil as the carbon source. *J. Mater. Sci. Mater. Med.* 29, 179–190. doi: 10.1007/s10856-018-6183-9

Bergmann, A., and Owen, A. (2003). Hydroxyapatite as a filler for biosynthetic PHB homopolymer and P(HB-HV) copolymers. *Polym. Int.* 52, 1145–1152. doi: 10.1002/pi.1206

Bonartsev, A. P., Bonartseva, G. A., Reshetov, I. V., Kirpichnikov, M. P., and Shaitan, K. V. (2019). Application of polyhydroxyalkanoates in medicine and the biological activity of natural poly(3-hydroxybutyrate). *Acta Naturae* 11, 4–16. doi: 10.32607/20758251-2019-11-2-4-16

Cao, Z., Jiang, D., Yan, L., and Wu, J. (2017). In vitro and in vivo drug release and antibacterial properties of the novel vancomycin-loaded bone-like hydroxyapatite/poly amino acid scaffold. *Int. J. Nanomed.* 12, 1841–1851. doi: 10.2147/IJN.S122864

Chen, Q., Zhu, C., and Thouas, G. A. (2012). Progress and challenges in biomaterials used for bone tissue engineering: bioactive glasses and elastomeric composites. *Prog. Biomater.* 1:2. doi: 10.1186/2194-0517-1-2

Chocholata, P., Kulda, V., and Babuska, V. (2019). Fabrication of scaffolds for bone-tissue regeneration. *Materials* 12:568. doi: 10.3390/ma12040568

De Witte, T. M., Fratila-Apachitei, L. E., Zadpoor, A. A., and Peppas, N. A. (2018). Bone tissue engineering via growth factor delivery: from scaffolds to complex matrices. *Regen. Biomater.* 5, 197–211. doi: 10.1093/rb/rby013

Eliaz, N., and Metoki, N. (2017). Calcium phosphate bioceramics: a review of their history, structure, properties, coating technologies and biomedical applications. *Materials* 10:334. doi: 10.3390/ma10040334

Fernandez de Grado, G., Keller, L., Idoux-Gillet, Y., Wagner, Q., Musset, A. M., Benkirane-Jessel, N., et al. (2018). Bone substitutes: a review of their characteristics, clinical use, and perspectives for large bone defects management. *J. Tissue Eng.* 9, 1–18. doi: 10.1177/2041731418776819

Gonzalez-Gil, G., Lens, P. N. L., and Saikaly, P. E. (2016). Selenite reduction by anaerobic microbial aggregates: microbial community structure, and proteins associated to the produced selenium spheres. *Front. Microbiol.* 7:571. doi: 10.3389/fmicb.2016.00571

Goonasekera, C. S., Jack, K. S., Cooper-White, J. J., and Grøndahl, L. (2016). Dispersion of hydroxyapatite nanoparticles in solution and in polycaprolactone composite scaffolds. *J. Mater.Chem. B* 4, 409–421. doi: 10.1039/C5TB02255J

Gritsch, L., Maqbool, M., Mourin, V., Ciraldo, F. E., Cresswell, M., Jackson, P. R., et al. (2019). Chitosan/hydroxyapatite composite bone tissue engineering scaffolds with dual and decoupled therapeutic ion delivery: copper and strontium. *J. Mater. Chem. B* 7, 6109–6124. doi: 10.1039/C9TB00897G

Grøndahl, L., Jack, K., and Goonasekera, C. S. (2017). "*Composite materials for bone repair*," in *Biomedical Composites*, Second Edn, Ed. L. Ambrosio (Cambridge: Woodhead Publishing Limited), 101–126.

Hasan, A., Byambaa, B., Morshed, M., Cheikh, M. I., Shakoor, R. A., Mustafy, T., et al. (2018). Advances in osteobiologic materials for bone substitutes. *J. Tissue Eng. Regen. Med.* 12, 1448–1468. doi: 10.1002/term.2677

He, L., Li, H., Chen, X., Xu, T., Sun, T., Huang, H., et al. (2019). Selenium-substituted hydroxyapatite particles with regulated microstructures for osteogenic differentiation and anti-tumor effects. *Ceram. Int.* 45, 13787–13798. doi: 10.1016/j.ceramint.2019.04.075

Herigstad, B., Hamilton, M., and Heersink, J. (2001). How to optimize the drop plate method for enumerating bacteria. *J. Microbiol. Methods* 44, 121–129. doi: 10.1016/S0167-7012(00)00241-4

Ho, M. H., Li, S. Y., Ciou, C. Y., and Wu, T. M. (2014). The morphology and degradation behavior of electrospun poly(3- hydroxybutyrate)/Magnetite and poly(3-hydroxybutyrate-co-3-hydroxyvalerate)/ Magnetite composites. *J. Appl. Polym. Sci.* 131:41070. doi: 10.1002/app.41070

Huang, T., Holden, J. A., Heath, D. E., O'Brien-Simpson, N. M., and O'Connor, A. J. (2019). Engineering highly effective antimicrobial selenium nanoparticles through control of particle size. *Nanoscale* 11, 14937–14951.

Johnson, C. T., and García, A. J. (2015). Scaffold-based anti-infection strategies in bone repair. *Ann. Biomed. Eng.* 43, 515–528. doi: 10.1007/s10439-014-1205-3

Kai, Z., Ying, D., and Guo-Qiang, C. (2003). Effects of surface morphology on the biocompatibility of polyhydroxyalkanoates. *Biochem. Eng. J.* 16, 115–123. doi: 10.1016/S1369-703X(03)00029-9

Kann, Y., Shurgalin, M., and Krishnaswamy, R. K. (2014). FTIR spectroscopy for analysis of crystallinity of poly(3-hydroxybutyrate-co-4 -hydroxybutyrate) polymers and its utilization in evaluation of aging, orientation and composition. *Polym. Test.* 40, 218–224. doi: 10.1016/j.polymertesting.2014.09.009

Karageorgiou, V., and Kaplan, D. (2005). Porosity of 3D biomaterial scaffolds and osteogenesis. *Biomaterials* 26, 5474–5491. doi: 10.1016/j.biomaterials.2005.02.002

Kashirina, A., Yao, Y., Liu, Y., and Leng, J. (2019). Biopolymers as bone substitutes: a review. *Biomater. Sci.* 7, 3961–3983. doi: 10.1039/C9BM00664H

Kaur, G., Kumar, V., Baino, F., Mauro, J. C., Pickrell, G., Evans, I., et al. (2019). Mechanical properties of bioactive glasses, ceramics, glass-ceramics and composites: state-of-the-art review and future challenges. *Mater. Sci. Eng. C* 104:109895. doi: 10.1016/j.msec.2019.109895

Kaur, J., and Shofner, M. L. (2009). Surface area effects in hydroxyapatite/poly(ε-caprolactone) nanocomposites. *Macromol. Chem. Phys.* 210, 677–688. doi: 10.1002/macp.200800508

Kolmas, J., Groszyk, E., and Kwiatkowska-Rózycka, D. (2014). Substituted hydroxyapatites with antibacterial properties. *BioMed Res. Int.* 2014:178123. doi: 10.1155/2014/178123

Kolmas, J., Groszyk, E., and Piotrowska, U. (2015). Nanocrystalline hydroxyapatite enriched in selenite and manganese ions: physicochemical and antibacterial properties. *Nanoscale Res. Lett.* 10:989. doi: 10.1186/s11671-015-0989-x

Koutsopoulos, S. (2002). Synthesis and characterization of hydroxyapatite crystals: a review study on the analytical methods. *J. Biomed. Mater. Res.* 62, 600–612. doi: 10.1002/jbm.10280

Li, Z. Y., Lam, W. M., Yang, C., Xu, B., Ni, G. X., Abbah, S. A., et al. (2007). Chemical composition, crystal size and lattice structural changes after incorporation of strontium into biomimetic apatite. *Biomaterials* 28, 1452–1460. doi: 10.1016/j.biomaterials.2006.11.001

Li, Z., Yang, J., and Loh, X. J. (2016). Polyhydroxyalkanoates: opening doors for a sustainable future. *NPG Asia Mater.* 8:e265. doi: 10.1038/am.2016.48

Lizarraga Valderrama, L. D. R., Nigmatullin, R., Ladino, B., Taylor, C. S., Boccaccini, A. R., Knowles, J. C., et al. (2020). Modulation of neuronal cell affinity of composites scaffolds based on polyhydroxyalkanoates and bioactive glasses. *Biomed. Mater. (Bristol England)* 15:045024. doi: 10.1088/1748-605x/ab797b

Lukasiewicz, B., Basnett, P., Nigmatullin, R., Matharu, R., Knowles, J. C., and Roy, I. (2018). Binary polyhydroxyalkanoate systems for soft tissue engineering. *Acta Biomater.* 71, 225–234. doi: 10.1016/j.actbio.2018.02.027

Misra, S. K., Mohn, D., Brunner, T. J., Stark, W. J., Philip, S. E., Roy, I., et al. (2008). Comparison of nanoscale and microscale bioactive glass on the properties of P(3HB)/Bioglass® composites. *Biomaterials* 29, 1750–1761. doi: 10.1016/j.biomaterials.2007.12.040

Molling, J. W., Seezink, J. W., Teunissen, B. E. J., Muijrers-Chen, I., and Borm, P. J. A. (2014). Comparative performance of a panel of commercially available antimicrobial nanocoatings in Europe. *Nanotechnol. Sci. Appl.* 7, 97–104. doi: 10.2147/NSA.S70782

Moreno-Reyes, R., Egrise, D., Nève, J., Pasteels, J. L., and Schoutens, A. (2001). Selenium deficiency-induced growth retardation is associated with an impaired bone metabolism and osteopenia. *J. Bone Miner. Res.* 16, 1556–1563. doi: 10.1359/jbmr.2001.16.8.1556

Mouriño, V., and Boccaccini, A. R. (2010). Bone tissue engineering therapeutics: controlled drug delivery in three-dimensional scaffolds. *J. R. Soc. Interface* 7, 209–227.

Możejko-Ciesielska, J., and Kiewisz, R. (2016). Bacterial polyhydroxyalkanoates: still fabulous? *Microbiol. Res.* 192, 271–282. doi: 10.1016/j.micres.2016.07.010

Nielsen, P. S. (2004). The biological role of strontium. *Bone* 35, 583–588. doi: 10.1016/j.bone.2004.04.026

Noohom, W., Jack, K. S., Martin, D., and Trau, M. (2009). Understanding the roles of nanoparticle dispersion and polymer crystallinity in controlling the mechanical properties of HA/PHBV nanocomposites. *Biomed. Mater.* 4:015003. doi: 10.1088/1748-6041/25/1/015003

Obat, A., Iwata, T., Maeda, H., Hirata, H., and Kasuga, T. (2013). Preparation of poly(3-hydroxybutyrate-co-4-hydroxybutyrate)-based composites releasing soluble silica for bone regeneration. *J. Ceram. Soc. Jpn* 121, 753–758. doi: 10.1007/s00792-015-0735-4

Ozeki, K., Goto, T., Aoki, H., and Masuzawa, T. (2014). Characterization of Sr-substituted hydroxyapatite thin film by sputtering technique from mixture targets of hydroxyapatite and strontium apatite. *Biomed. Mater. Eng.* 24, 1447–1456. doi: 10.3233/BME-130949

Pajor, K., Pajchel, L., Kolodziejska, B., and Kolmas, J. (2018). Selenium-doped hydroxyapatite nanocrystals–synthesis, physicochemical properties and biological significance. *Crystals* 8:188. doi: 10.3390/cryst8050188

Puppi, D., Pecorini, G., and Chiellini, F. (2019). Biomedical processing of polyhydroxyalkanoates. *Bioengineering* 6:108. doi: 10.1016/j.nbt.2016.05.00

Qu, H., Fu, H., Han, Z., and Sun, Y. (2019). Biomaterials for bone tissue engineering scaffolds: a review. *RSC Adv.* 9, 26252–26262. doi: 10.1039/C9RA05214C

Rai, B., Noohom, W., Kithva, P. H., Grøndahl, L., and Trau, M. (2008). Bionanohydroxyapatite/poly(3-hydroxybutyrate-co-3-hydroxyvalerate) composites with improved particle dispersion and superior mechanical properties. *Chem. Mater.* 20, 2802–2808. doi: 10.1021/cm703045u

Rai, R., Keshavarz, T., Roether, J. A., Boccaccini, A. R., and Roy, I. (2011). Medium chain length polyhydroxyalkanoates, promising new biomedical materials for the future. *Mater. Sci. Eng. R Rep.* 72, 29–47. doi: 10.1016/j.mser.2010.11.002

Randriamahefa, S., Renard, E., Guérin, P., and Langlois, V. (2003). Fourier transform infrared spectroscopy for screening and quantifying production of PHAs by *Pseudomonas* grown on sodium octanoate. *Biomacromolecules* 4, 1092–1097. doi: 10.1021/bm034104o

Ratnayake, J. T. B., Mucalo, M., and Dias, G. J. (2017). Substituted hydroxyapatites for bone regeneration: a review of current trends. *J. Biomed. Mater. Res. Part B Appl. Biomater.* 105, 1285–1299. doi: 10.1002/jbm.b.33651

Ravi, N. D., Balu, R., and Sampath Kumar, T. S. (2012). Strontium-substituted calcium deficient hydroxyapatite nanoparticles: synthesis, characterization, and antibacterial properties. *J. Am. Ceram. Soc.* 95, 2700–2708. doi: 10.1111/j.1551-2916.2012.05262.x

Rezwan, K., Chen, Q. Z., Blaker, J. J., and Boccaccini, A. R. (2006). Biodegradable and bioactive porous polymer/inorganic composite scaffolds for bone tissue engineering. *Biomaterials* 27, 3413–3431. doi: 10.1016/j.biomaterials.2006.01.039

Rodríguez-Valencia, C., Lopez-Álvarez, M., Cochón-Cores, B., Pereiro, I., Serra, J., and González, P. (2013). Novel selenium-doped hydroxyapatite coatings for biomedical applications. *J. Biomed. Mater. Res. Part A* 101 A, 853–861. doi: 10.1002/jbm.a.34387

Sadat-Shojai, M., Khorasani, M. T., Jamshidi, A., and Irani, S. (2013). Nano-hydroxyapatite reinforced polyhydroxybutyrate composites: a comprehensive study on the structural and in vitro biological properties. *Mater. Sci. Eng. C* 33, 2776–2787. doi: 10.1016/j.msec.2013.02.041

Stewart, S. K. (2019). Fracture non-union: a review of clinical challenges and future research needs. *Malays. Orthop. J.* 13, 1–10. doi: 10.5704/MOJ.1907.001

Suchitra, M. (2004). Thermal analysis of composites using DSC. *Advanced Topics in Characterization of Composites* 11–33.

Thomas, M. V., and Puleo, D. A. (2011). Infection, inflammation, and bone regeneration: a paradoxical relationship. *J. Dent. Res.* 90, 1052–1061. doi: 10.1177/0022034510393967

Turner, R. J., Weiner, J. H., and Taylor, D. E. (1998). Selenium metabolism in *Escherichia coli*. *BioMetals* 11, 223–227. doi: 10.1023/a:1009290213301

Ural, E., Kesenci, K., Fambri, L., Migliaresi, C., and Piskin, E. (2000). Poly(D,L-cactide/ε-caprolactone)/hydroxyapatite composites. *Biomaterials* 21, 2147–2154. doi: 10.1016/S0142-9612(00)00098-3Get

Uskokovic, V., Iyer, M., and Wu, V. M. (2017). One ion to rule them all: combined antibacterial, osteoinductive and anticancer properties of selenite- incorporated hydroxyapatite. *J. Mater. Chem. B* 25, 1032–1057. doi: 10.1039/C6TB03387C

Vasić, S., Radojević, I., Pešić, N., and Čomić, L. (2011). Influence of sodium selenite on the growth of selected bacteria species and their sensitivity to antibiotics. *Kragujevac J. Sci.* 33, 55–61.

Wang, Y., Bian, Y. Z., Wu, Q., and Chen, G. Q. (2008). Evaluation of three-dimensional scaffolds prepared from poly(3-hydroxybutyrate-co-3-hydroxyhexanoate) for growth of allogeneic chondrocytes for cartilage repair in rabbits. *Biomaterials* 29, 2858–2868. doi: 10.1016/j.biomaterials.2008.03.021

Wang, Y., Ma, J., Zhou, L., Chen, J., Liu, Y., Qiu, Z., et al. (2012). Dual functional selenium-substituted hydroxyapatite. *Interface Focus* 2, 378–386. doi: 10.1098/rsfs.2012.0002

Wong, C. T., Lu, W. W., Chan, W. K., Cheung, K. M. C., Luk, K. D. K., Lu, D. S., et al. (2004). In vivo cancellous bone remodeling on a Strontium-containing hydroxyapatite (Sr-HA) bioactive cement. *J. Biomed. Mater. Res. Part A* 68, 513–521. doi: 10.1002/jbm.a.20089

Yanhua, W., Hao, H., Li, Y., and Zhang, S. (2016). Selenium-substituted hydroxyapatite nanoparticles and their in vivo antitumor effect on hepatocellular carcinoma. *Colloids Surf. B Biointerfaces* 140, 297–306. doi: 10.1016/j.colsurfb.2015.12.056

Zarins, J., Pilmane, M., Sidhoma, E., Salma, I., and Locs, J. (2019). The role of Strontium enriched hydroxyapatite and tricalcium phosphate biomaterials in osteoporotic bone regeneration. *Symmetry* 11:229. doi: 10.3390/sym11020229

Zeng, J. H., Liu, S. W., Xiong, L., Qiu, P., Ding, L. H., Xiong, S. L., et al. (2018). Scaffolds for the repair of bone defects in clinical studies: a systematic review. *J. Orthop. Surg. Res.* 13:33. doi: 10.1186/s13018-018-0724-2

Conflict of Interest: MM is currently employed by company CAM Bioceramics B.V. MC and PJ are employed by Lucideon Ltd. During this research MM was however affiliated as a Ph.D. student at the University of Erlangen-Nuremberg, Germany and Lucideon Ltd.

The remaining authors declare that the research was conducted in the absence of any commercial or financial relationships that could be construed as a potential conflict of interest.

frontiers in Bioengineering and Biotechnology

ORIGINAL RESEARCH
published: 20 April 2021
doi: 10.3389/fbioe.2021.652362

Synergistic and Antagonistic Effects of Biogenic Silver Nanoparticles in Combination With Antibiotics Against Some Pathogenic Microbes

*Kawther Aabed and Afrah E. Mohammed**

Department of Biology, College of Science, Princess Nourah Bint Abdulrahman University, Riyadh, Saudi Arabia

The latest advances in green nanoparticle synthesis have preserved natural and non-renewable resources and decreased environmental pollution. The current study was designed to evaluate silver nanoparticles (AgNPs) fabricated using aqueous extracts of two medicinal plants, *Anastatica hierochuntica* L. (Kaff Maryam) and *Artemisia absinthium*. The phytochemicals were detected by Fourier-transform infrared spectroscopy (FTIR) and Chromatography/Mass Spectrometry (GC-MS). The effects of the AgNPs on *Pseudomonas aeruginosa, Escherichia coli*, *Staphylococcus aureus*, and *Candida albicans* as well as the cytotoxicity against MDA-MB-231 cells were examined. The synergistic and antagonistic effects of the biogenic AgNPs in combination with standard antibiotics against several microbes were also investigated. The ability of the plant extracts to transfer silver ions to AgNPs was measured via dynamic light scattering, zeta potential measurement, and transmission electron microscopy. The most sensitive microbes to AgNP treatment were examined via scanning electron microscopy to assess morphological changes. Biogenic AgNPs showed significant antibacterial effects against most of the tested microbes and significant cytotoxicity was noted. Polysaccharides, proteins and Phenolic compounds are likely involved in AgNP biosynthesis since hydroxyl groups and amides were detected via FTIR as well as GC-MS. This study confirmed that plant-based AgNP fabrication with $AgNO_3$ as the Ag (I) delivering salt can be an economical and practical approach for large-scale production of particles with antimicrobial and cytotoxic potential. The synergistic effects of biogenic AgNPs in combination with some antibiotics support their potential as a safe therapeutic for bacterial infections because they are capped with organic biomolecules.

Keywords: ***Artemisia absinthium*, antimicrobial, cytotoxicity, *Anastatica hierochuntica*, silver nanoparticle**

OPEN ACCESS

Edited by:
Jochen Salber,
Ruhr-University Bochum, Germany

Reviewed by:
Rozhina Elvira,
Kazan Federal University, Russia
Luciana Dini,
Sapienza University of Rome, Italy

***Correspondence:**
Afrah E. Mohammed
AFAMohammed@pnu.edu.sa;
farhati@hotmail.com

Specialty section:
This article was submitted to Nanobiotechnology, a section of the journal Frontiers in Bioengineering and Biotechnology

Received: *12 January 2021*
Accepted: *11 March 2021*
Published: *20 April 2021*

Citation:
Aabed K and Mohammed AE (2021) Synergistic and Antagonistic Effects of Biogenic Silver Nanoparticles in Combination With Antibiotics Against Some Pathogenic Microbes. Front. Bioeng. Biotechnol. 9:652362. doi: 10.3389/fbioe.2021.652362

INTRODUCTION

Recently, nanotechnology has emerged as a rapidly developing research field in materials science with the potential to positively affect human health (Singh et al., 2010). In nanotechnology, silver nanoparticles (AgNPs) are the most important metal element with beneficial properties. AgNPs ranging in diameter from 1 to 100 nm are an attractive research target due to their antimicrobial and cytotoxic potential imparted by their ability to easily attach to the cell wall. This attachment leads to

effects on cellular respiration and permeability that result in cell death. Furthermore, AgNPs can also easily enter cells to interact with biomolecules, including DNA and protein via their phosphorus and sulfur groups, respectively. Because silver ions have been shown to have no significant effects on cell viability, silver-containing materials can be used in textiles and as additives in food and packaging to eliminate microbes. Due to their varied useful applications as antimicrobial and cytotoxic agents, multiple forms of silver, including silver ions and silver nanoparticles, have been developed (David et al., 2010). Silver ions have been successfully used as antimicrobial agents, although AgNPs have shown higher antimicrobial activity in comparative studies. Very small quantities of AgNPs may have higher antimicrobial effects compared to that for their bulk material. The increased prevalence of antibiotic-resistant microbes, currently considered a widespread health problem, is likely related to intensifying antibiotic use. Decreased antibiotic efficacy has been clearly documented (Huh and Kwon, 2011; El-Mokhtar and Hetta, 2018; El-Baky et al., 2019), triggering a surge in investigations into the antibacterial properties of other materials. Considerable attempts to develop antibiotic alternatives to prevent the rise of antibiotic-resistant microbes has highlighted the potential of nanomaterials. Silver nanoparticles are a promising approach for fighting microbial resistance since microbes are unlikely to accumulate the numerous mutations required to acquire nanoparticle resistance (Friedman et al., 2013). The delivery system for nano drugs involves the production, synthesis, and application of nanomaterials with sizes ranging from 1 to 100 nm (Madhuri et al., 2012; Abd Ellah et al., 2019a,b). Preparation of nanomaterials using chemical and physical approaches has multiple disadvantages, including the generation of toxic chemical byproducts and high energy consumption, making biological synthesis an excellent alternative. Biological systems for nanoparticle production have key advantages over other systems, including the production of more stable nanoparticles and increased control over size and shape. These advantages support the production of biogenic nanoparticles appropriate for various nanotechnology applications and provide nanoparticles with high compatibility for biomedical purposes since no toxic chemicals are used in their production. Various benign environmental agents have been used for AgNP production, including plant extract (Jain et al., 2009), fungi (Verma et al., 2010), bacteria (Saifuddin et al., 2009), and enzymes (Willner et al., 2007). Plants are a well known source of antimicrobial and antioxidant agents (Lewis and Ausubel, 2006; Tegos, 2006). In the current study, based on their various pharmacological applications, *Anastatica hierochuntica* and *Artemisia absinthium* have been used for AgNP fabrication. *A. hierochuntica* extracts showed antimicrobial, antifungal, antioxidant, hypolipidemic, and hypoglycemic effects (Rahmy and El-Ridi, 2002; Tayel and El-Tras, 2009; Mohamed et al., 2010; Al Gamdi et al., 2011; Salah et al., 2011; Daoowd, 2013; Abou-Elella et al., 2016). *A. absinthium*, which is as the main component in the infamous Absinthe drink, has been known for its medicinal benefits since the time of the ancient Greeks and in traditional medicine of western Europe. Furthermore, antimicrobial properties of essential oils from the flowers and aerial parts of *A. absinthium* are well documented (Juteau et al., 2003). *A. absinthium* contains caffeoyl and dicaffeoylquinic acids, which can prevent HIV-1 integrase from incorporating viral DNA into the host genome (Reinke et al., 2002). These properties inspired our rationale for using these plant sources as biomediators in AgNP formation with the expectation that the resulting AgNPs would have higher antimicrobial activity than the plant extracts and silver ions alone. Relevant to the increasing prevalence of antibiotic resistance, combinations of nanoparticles and antibiotics have been shown to have higher efficacy relative to antibiotics alone in clinical settings (Abo-Shama et al., 2020). Such combinations could limit the development of antibiotic resistance and reduce the duration and dose requirements for antibiotic treatment (Hwang et al., 2012a). Based on this framework, the current report describes the fabrication of AgNPs using two medicinal plants as biogenic agents. The efficacy of the resulting AgNPs in inhibiting the growth of bacterial and fungal pathogens alone and in combination with antibiotics was also investigated.

MATERIALS AND METHODS

Materials

Silver nitrate ($AgNO_3$) was obtained from Saudi Overseas Marketing and Trading Company (SOMATCO), Riyadh, Saudi Arabia. Nutrient agar plates and nutrient broth (Difco, Becton, Dickinson and Company, Sparks Glencoe, MD, United States) as well as potato-dextrose agar (PDA) plates (Difco, Becton, Dickinson and Company, Sparks Glencoe, MD, United States) were purchased from Wateen Alhaiah Company, Riyadh, Saudi Arabia. All clinical bacterial isolates were obtained from the Microbiology Laboratory of Princess Nourah bint Abdulrahman University, Riyadh, Saudi Arabia. Antibiotic discs were obtained from OXOID ™ United Kingdom at the following concentrations: bacitracin, 10 μg/mL; ciprofloxacin, 10 μg/mL; tetracycline, 30 μg/mL; and cefixime, 5 μg/mL.

Plant Materials

Complete *A. hierochuntica* L. (Kaff Maryam) plants and *A. absinthium* seeds were obtained from a local market in Riyadh, Saudi Arabia. Their identities were verified, and they were stored in polythene bags at 4°C prior to use. Plant parts were cleaned with distilled water, air dried, and then ground into a fine powder using a milling machine (IKA-Werke, GMBH and Co., Germany). The powder was stored at room temperature in plastic bags until use.

Preparation of Aqueous Extracts for AgNP Fabrication

Aqueous extracts of each plant were prepared via addition of water to the powder at a 10:1 (w:v) ratio. The mixtures were immediately heated to 80°C for 10 min for enzyme deactivation. Next, Whatman Grade No. 1 filter paper (diameter of 125 mm and mean pore size of 11 μm was used to filter the mixtures, and the supernatants were retained for use in AgNP synthesis. For

AgNP synthesis, 10 ml of plant extract was combined with 90 ml of $AgNO_3$ solution (1 mM) in a flask. The reaction was kept at room temperature in the dark for 48 h until a stable dark color developed. The mixture was then stored at 4°C.

Dynamic Light Scattering (DLS) and Zeta Potential Measurement

To characterize the prepared AgNPs, a Zetasizer nano device (Nano ZSP, Malvern Instruments Ltd., Serial Number: MAL1118778, ver. 7.11, United Kingdom) was used to determine the size distribution via DLS and the electrical charge via zeta potential measurement.

Transmission Electron Microscopy (TEM)

Transmission electron microscopy (JEM-1011, JEOL, Japan; 80 kV) was used to examine the AgNP morphology and size distribution. The tested materials were placed on carbon-coated (200 mesh) TEM grids via drop-coating.

Fourier-Transform Infrared Spectroscopy (FTIR)

Fourier-transform infrared spectroscopy spectroscopy is useful for analyzing the functional groups of biomolecules in a sample by measuring infrared absorption and emission spectra. FTIR (Spectrum100, Perkin-Elmer, United States) was performed with scanning data collected over a range of 450 to 3,500 cm^{-1}.

Microbial Analyses

Four different microbes were used to assess the antimicrobial activity of the biogenic AgNPs (*P. aeruginosa, E. coli, S. aureus*, and *C. albicans*). Microbial cultures were prepared in the Department of Biology, College of Science, Riyadh, KSA.

Antimicrobial Activity

The antibacterial effects of the biogenic AgNPs were assessed via agar well diffusion assays (Perez et al., 1990). Approximately 20 ml of Mueller-Hinton agar were placed in sterilized Petri dishes. Bacteria were cultured in nutrient broth for 24 h at 37°C. Approximately 0.2 ml of nutrient broth (containing 10^8 CFU/ml) were used to prepare bacterial lawns. On each agar plate, four wells were prepared using a sterilized 4-mm cork borer and then filled with the test materials. Sterile distilled water was used as a negative control, and $AgNO_3$ was used as a positive control.

The plates were then incubated for 18 h at 37°C for bacteria and for 48 to 96 h for fungi at 28°C; the zones of inhibition around the wells were then measured using a metric ruler and expressed as the mean value (in mm) for each plate (Cheesbrough, 2000).

Minimum Inhibitory Concentration (MIC) and Minimum Bactericidal Concentration (MBC) Determination

The MIC values were determined using the microdilution method. Approximately 10 μl of each bacterial culture (10^8 CFU/ml) was combined individually with 10 mL of nutrient broth (NB). Next, AgNPs were added to each tube of bacterial culture at various concentrations followed by incubation for 24 h at 37°C. Thereafter, the MIC values were determined by examining the turbidity in each tube. The MIC was defined as the minimum AgNPs concentration that prevented bacterial growth (Das et al., 2016). The minimum bactericidal concentration (MBC) was defined as the concentration that killed 99.9% of the bacteria (Basri and Fan, 2005).

Scanning Electron Microscopy (SEM)

Scanning electron microscopy (SEM) (Hitachi S-4500) was used to identify morphological changes to the external cell wall of AgNP-treated microbes. Thin layers of treated microbes were dropped onto carbon-coated copper grids, and the excess solution was removed with blotting paper. The thin layer on the SEM grid was dried by subjecting the grids to a mercury lamp for 5 min.

Synergistic Antibacterial Activity of AgNPs

Synergistic antibacterial effects of mixtures of AgNP and antibiotics (bacitracin, ciprofloxacin, tetracycline, and cefixime) were examined via a standard disk diffusion method. To assess synergism, bacteria were grown on nutrient agar plates. AgNPs (1 mg/mL) were mixed with each antibiotic (bacitracin, 10 μg/mL; ciprofloxacin, 10 μg/mL; tetracycline, 30 μg/mL; and cefixime, 5 μg/mL) at a 1:1 (v:v) ratio, and the solutions were sonicated at room temperature for 15 min. The synergistic antibacterial effects of the AgNP-antibiotic mixtures were assessed after 24 h of incubation at 37°C based on the diameters of the inhibition zones around the disks (expressed in mm).

Synergistic Anticandidal Activity of AgNPs

Synergistic anticandidal effects of mixtures of AgNPs and anticandidal agents (fluconazole and metronidazole) were examined via a standard disk diffusion method. AgNPs (2 mg/mL) and anticandidal agents (fluconazole, 150 μg/mL; metronidazole, 125 μg/mL) were combined at a 1:1 (v:v) ratio, and the solutions were sonicated at room temperature for 15 min. *C. albicans* (in liquid medium) was spread uniformly on potato-dextrose agar (PDA) plates. Disks containing the anticandidal agents were then placed on the plates followed by incubation for 48 h at 28°C. Synergistic anticandidal effects of the AgNP-anticandidal agent mixtures were assessed based on the diameters of the inhibition zones around the disks (expressed in mm).

MTT Assay

A 250 mg of MTT [3-(4,5-dimethylthiazol-2-yl)-2,5-diphenyl tetrazolium bromide] was used to assess cytotoxicity. MDA-MB-231 cells were treated with biogenic AgNPs, and the optical density (OD) was determined by measuring the absorbance at 595 nm using an ELISA reader (Anthos 2010 Microplate Reader, Biochrom Ltd., United Kingdom). Cell viability was calculated using following formula:

$$\text{Cellviability(in\%)} = (\text{ODsample}/\text{ODcontrol}) \times 100.$$

The IC_{50} (the half-maximal inhibitory concentration) is the concentration required to inhibit growth by 50%. IC_{50} values were calculated from regression curves.

Chromatography/Mass Spectrometry (GC-MS) Techniques

The chemical analysis of *A. hierochuntica* and *A. absinthium* was examined by GC-MS (AGILENT Technologies 220 Ion Trap GC/MS, United States) applying the alcoholic extract of both plant sources separately. Helium has been used as the carrier gas with a column (brand?) of the following specifications: Flow rate 1 mL/min; Pressure 8.2317 psi; Average velocity 36.623 cm/s; Holdup flow 1.3653 min; Post run 0.99996 mL/min; Column max. temperature 450°C, 30 m × 250 μm × 0.25 μm). Initial oven temperature was 70°C with run time is at 52 min to reach finally 250°C. The biomolecules were determined using the National Institute of Standards and Technology (NIST) chemical database.

Statistical Analyses

Results are stated as the mean ± standard deviation (SD) of three independent replicates (calculated using Excel Microsoft Office 2010). The IC_{50} values were computed using GRAPHPAD PRISM 8.1 to produce the cytotoxicity assay plots.

RESULTS

The current investigation aimed to examine the usefulness of *A. hierochuntica* and *A. absinthium* extracts as biomediators in AgNP formation, and the antibacterial and anticandidal activities of the resulting AgNPs were examined. In the current investigation, aqueous extracts of *A. hierochuntica* and *A. absinthium* were used for AgNP fabrication. Addition of the plant extracts to a solution of $AgNO_3$ yielded mixtures that changed from pale yellow to brown-yellow for An-AgNPs and Ar-AgNPs prepared from *A. hierochuntica* (An) (**Supplementary Files A,B**) and *A. absinthium* (Ar) extracts (**Supplementary Files C,D**). AgNP biosynthesis proceeded first via a slow color change in the reaction mixture (after approximately 1 h of incubation) after which the color intensity increased over the remainder of the reaction.

Characterization of Biogenic AgNPs

An-AgNPs and Ar-AgNPs showed mean sizes of 114 ± 2.04 and 125.5 ± 2.5 nm, respectively, as measured via DLS technique (**Table 1** and **Figures 1A,B**). Measurement of the zeta potential returned values of −1.2 and −0.4 mV for An-AgNPs and Ar-AgNPs, respectively. TEM imaging showed that the An-AgNPs were well dispersed and spherical with no significant aggregation (**Figure 2**). The Ar-AgNPs were semispherical or had no well-defined shape, but no aggregation was observed (**Figure 3**).

Differences in the FTIR data for An-AgNPs and Ar-AgNPs, as shown in **Figure 4**, provide information about the different biomolecules that might be involved in the reduction of silver ions into AgNPs. Absorption peaks were detected at 3278.55, 1633.70, 481.86, 429.90, and 413.89 cm^{-1} for An-AgNPs (**Figure 4A**), while absorption peaks were detected at 3286.15, 1633.99, 430.10, and 416.45 cm^{-1} for Ar-AgNPs (**Figure 4B**).

Biological Activity and Synergistic Antimicrobial Effects of AgNPs

Antimicrobial Activity of An-AgNPs

Antimicrobial activity was detected at 0.5 μg/well against all tested microorganisms as indicated by the diameters of the inhibition zones (**Figure 5**). The inhibition zone diameters for *S. aureus, E. coli,* and *P. aeruginosa* were 22.44 ± 0.4, 23.56 ± 3.8, and 23.56 ± 0.2 mm, respectively. As shown in **Figure 5**, anticandidal activity was observed against *C. Albicans* (14.78 ± 0.2 mm). On the other hand, the activity of An-AgNPs against *P. aeruginosa* and *C. Albicans* did not differ significantly from that of silver ions.

The Ability of An-AgNPs to Enhance Antibiotic Efficacy

The activity of An-AgNPs against several microbes was compared to those of standard antibiotics, i.e., bacitracin (BA), ciprofloxacin

TABLE 1 | DLS dimensions of NPs size (nm) and potential (mV) and the inhibition zone (mm) of the biogenic NPs as well as the antibiotics tested against different microbes.

Nano material	DLS Mean ± S.D. (nm)	Zeta Potential (m V)	Inhibition Zone Mean ± S.D. (mm)				IC_{50}
			E. coli	*S. aureus*	*P. aeruginosa*	*C. albicans*	MDA-MB-231 cells (μg/mL)
An-AgNPs	114 ± 2.04	−1.2	23.6 ± 3.8	22.4 ± 0.4	23.6 ± 0.2	14.8 ± 0.2	149.2
Ar-AgNPs	125.5 ± 2.5	−0.4	16.8 ± 0.5	16.4 ± 0.7	24.7 ± 0.3	0	585.2
An ions			15.8 ± 1.3	11.7 ± 0.7	24.4 ± 1.2	16.2 ± 2.2	
Bacitracin			0	6 ± 0	0	0	
Tetracycline			0	10 ± 0	15 ± 0	0	
Cefixime			0	10 ± 0	6 ± 0	0	
Ciprofloxacin			0	7 ± 0	35 ± 0	0	
Fluconazole			–	–	–	46.2 ± 0	
Metronidazole			–	–	–	15 ± 0	

Data represent the mean ± standard deviation of the mean (SD) of three independent experiments.

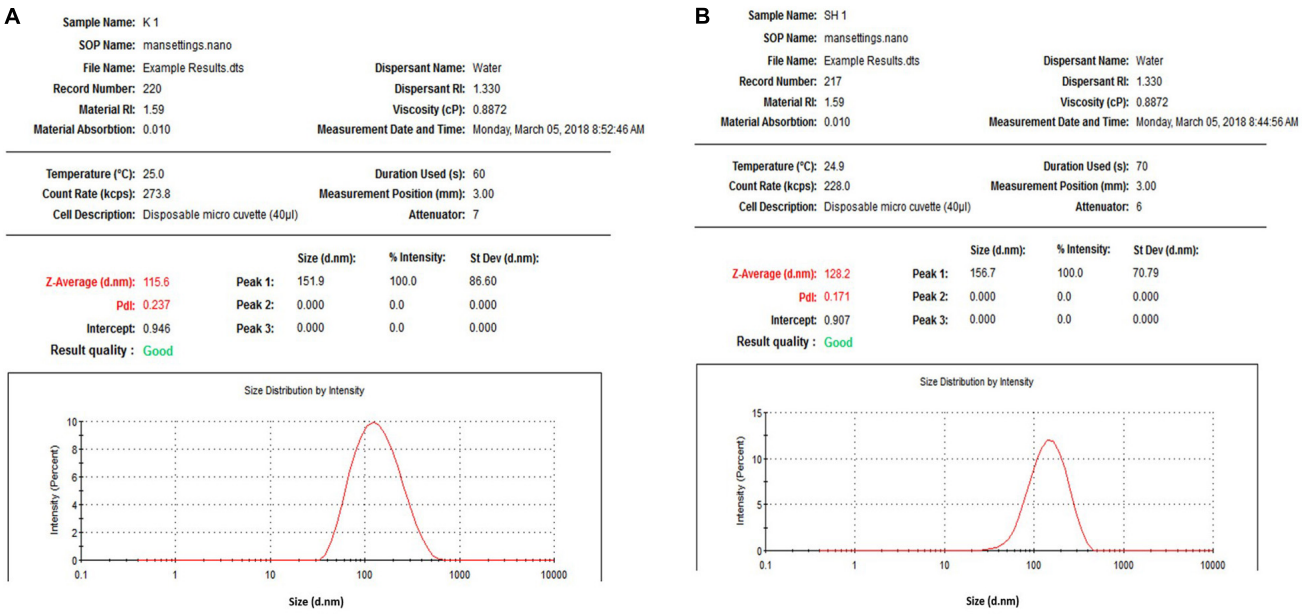

FIGURE 1 | Size distribution of AgNPs obtained using aqueous extracts of *A. hierochuntica* **(A)** and Size distribution of AgNPs obtained using aqueous extracts of *A. absinthium* **(B)**.

(CI), tetracycline (TE), and cefixime (CE) as shown in **Figure 5**. The activity of the An-AgNPs was higher than those of all tested antibiotics against *E. coli* and *S. aureus*. The same observations were made for *P. aeruginosa* with the exception of BA, whose activity was higher than that of the An-AgNPs. For *C. albicans*, An-AgNPs showed lower activity than fluconazole and metronidazole. For *E. coli,* mixtures of An-AgNPs and bacitracin, ciprofloxacin, tetracycline, or cefixime showed substantial synergistic effects relative to the activity of the antibiotic alone. Slight synergistic effects were noted for combinations of An-AgNPs and ciprofloxacin, tetracycline, or cefixime against *S. aureus*. By contrast, a slight decrease in antibiotic activity was observed against *S. aureus* when An-AgNPs were combined with bacitracin.

No antibacterial activity was detected for bacitracin against *P. aeruginosa*; however, a significant synergistic effect was

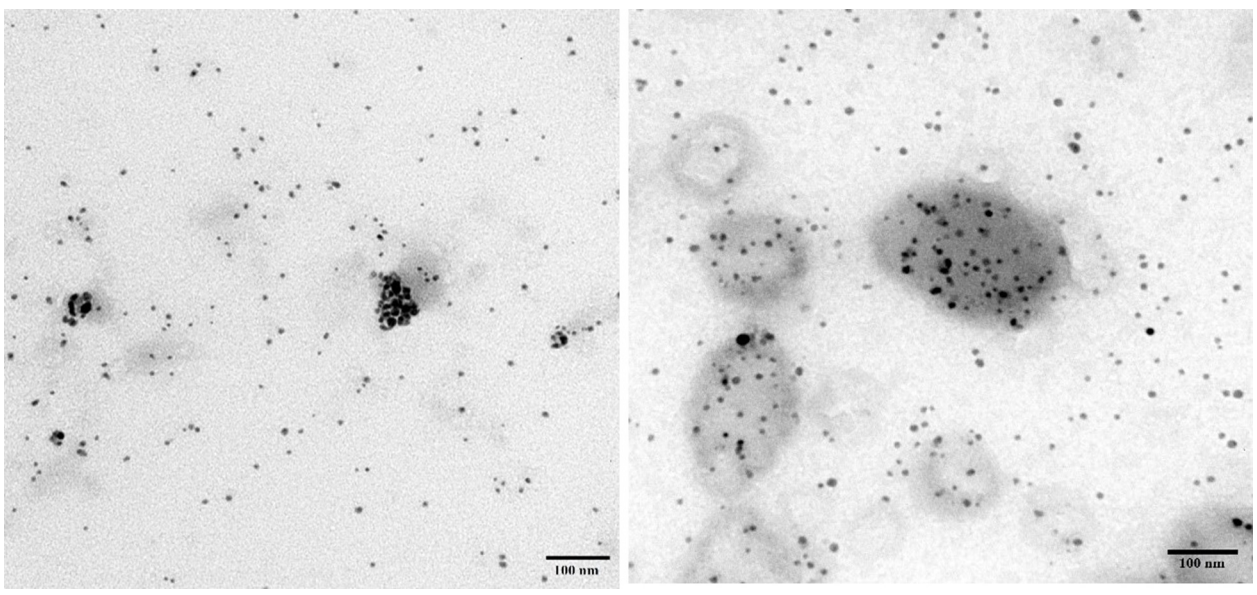

FIGURE 2 | TEM images of AgNPs obtained using aqueous extracts of *A. hierochuntica*.

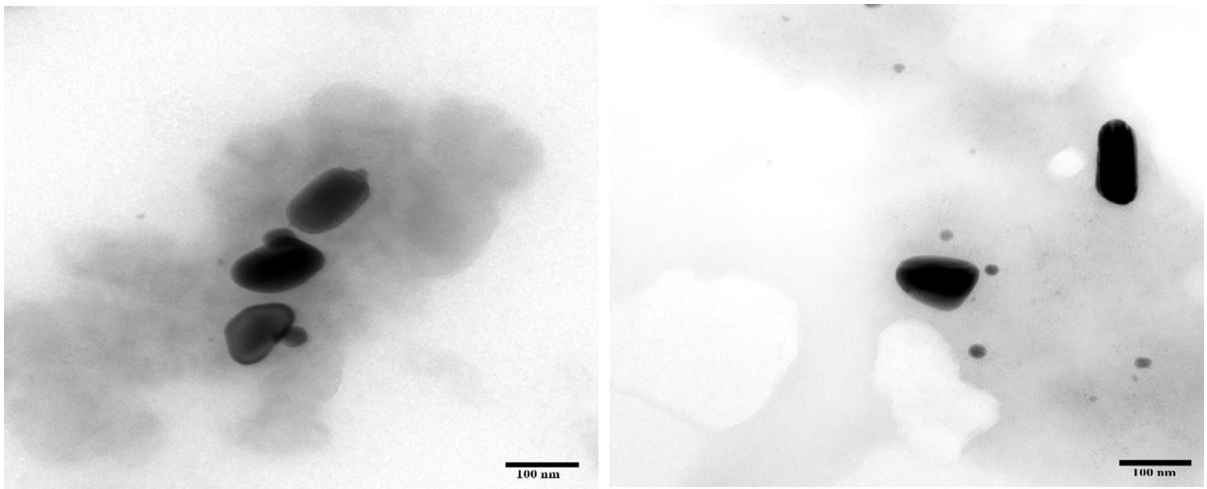

FIGURE 3 | TEM images showing the size of the AgNPs obtained using an aqueous extract of *A. absinthium*.

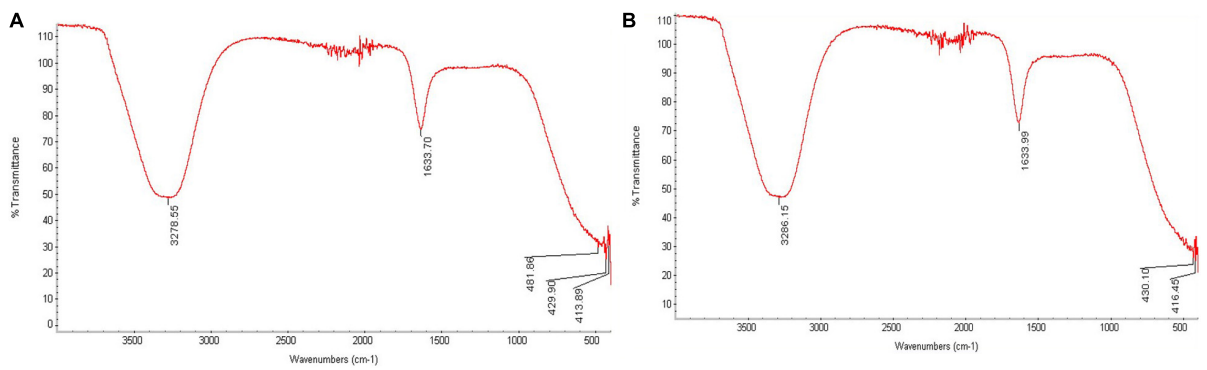

FIGURE 4 | FTIR analysis of An-AgNPs obtained using aqueous extracts of *A. hierochuntica* **(A)** and That for AgNPs obtained using an aqueous extract of *A. absinthium* **(B)**.

observed for a combination of bacitracin and AgNPs relative to the activity of AgNPs alone. Furthermore, An-AgNPs showed a synergistic effect against *P. aeruginosa* when combined with ciprofloxacin. Combinations of An-AgNPs and tetracycline or cefixime showed no effect on *P. aeruginosa* even though An-AgNPs, tetracycline, and cefixime were active against *P. aeruginosa* when tested separately. These observations suggest antagonistic effects in these antibiotic-AgNP combinations. For *C. albicans*, combinations of An-AgNPs and fluconazole or metronidazole reduced the effects of the anticandidal agents (**Figure 5**).

Antimicrobial Activity of Ar-AgNPs

Ar-AgNPs at 0.5 μg/well showed potential antibacterial effects against all tested bacteria, as revealed by inhibition zone diameters ranging from 16.44 and 24.67 mm, while no inhibitory activity against *C. Albicans* was observed (**Table 1** and **Figure 6**). Among the pathogenic microorganisms, Ar-AgNPs were more active against *P. aeruginosa* (24.67 mm) followed by *E. coli* (16.78 mm), and *S. aureus* (16.44 mm).

The Ability of Ar-AgNPs to Improve Antibiotic Efficacy

For *P. aeruginosa*, Ar-AgNP activity was higher than those of all tested antibiotics except for ciprofloxacin. In this case, the Ar-AgNP activity was approximately 69.4% of that of the antibiotic. Furthermore, combining of Ar-AgNPs with antibiotics resulted in a synergistic effect against *E. coli*; however, this activity was lower than that of Ar-AgNPs alone. For *S. aureus,* no significant differences were observed between the activities of tetracycline or cefixime alone or in combination with Ar-AgNPs; however, addition of Ar-AgNPs to ciprofloxacin or bacitracin suppressed their activities against *S. aureus*, suggesting antagonistic effects. Furthermore, significant synergistic effects on Ar-AgNP activity were observed against *P. aeruginosa* for cefixime, ciprofloxacin, and bacitracin; however, addition of Ar-AgNPs slightly decreased the activity of tetracycline. The activities of combinations of Ar-AgNPs and fluconazole or metronidazole were 86.5 and 85.9%, respectively, of the activities of the anti-fungal agents alone. Ar-AgNPs had no activity against *C. albicans*, but a clear synergistic effect was noted for Ar-AgNPs in combination with fluconazole

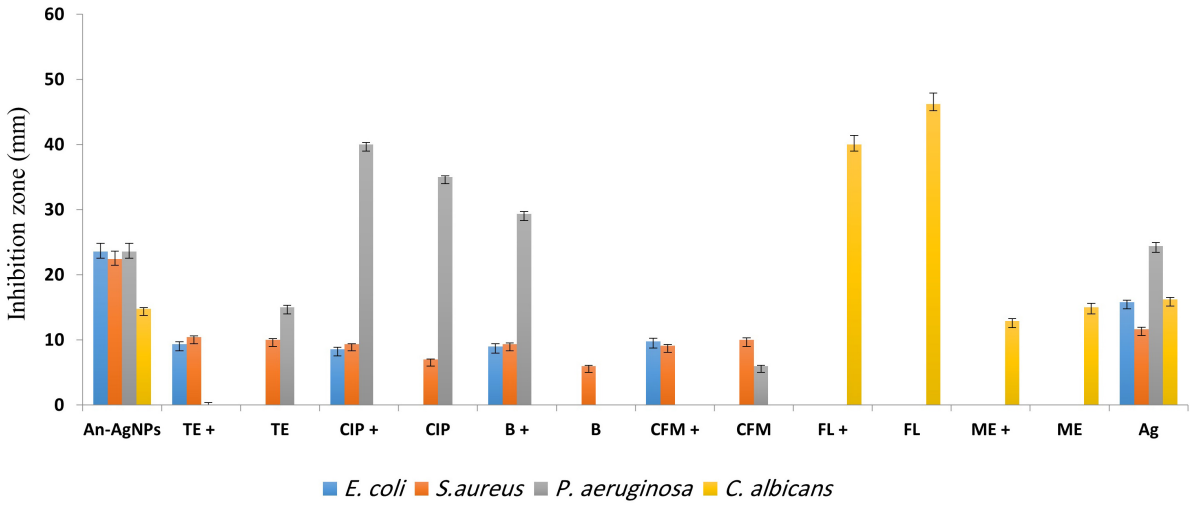

FIGURE 5 | Antibacterial activities of different antibiotics [bacitracin (B), ciprofloxacin (CIP), tetracycline (TE), cefixime (CFM), fluconazole (FL), and metronidazole (ME)] alone and in combination with An-AgNPs at the MIC (50 mg/L). Data are expressed as the means ± SD ($n = 3$ replicates).

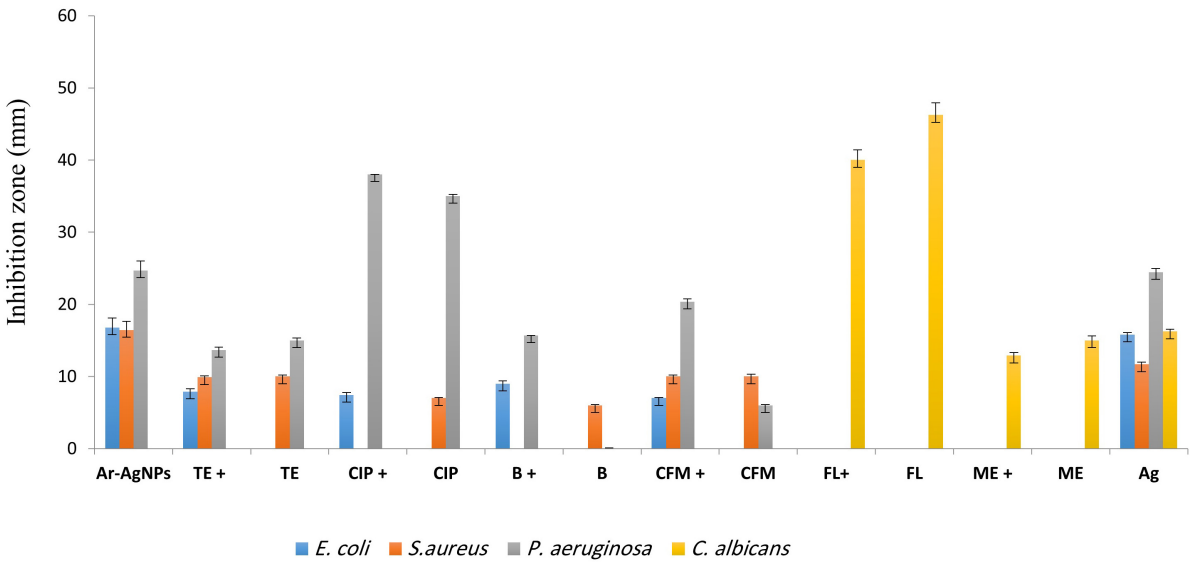

FIGURE 6 | Antibacterial activities of different antibiotics [bacitracin (B), ciprofloxacin (CIP), tetracycline (TE), cefixime (CFM), fluconazole (FL), and metronidazole (ME)] alone and in combination with Ar-AgNPs at the MIC (25–50 mg/L) against the tested microbes. Data are expressed as the means ± SD ($n = 3$ replicates).

or metronidazole (**Figure 6**). The MIC values of the AgNPs ranged from 25 to 50% against all tested microbes (**Table 2**). The highest activity was recorded for the Ar-AgNPs against *S. aureus* (25% MIC).

TABLE 2 | MIC (%) of aqueous extracts of An-AgNPs and Ar-AgNPs against clinical pathogens.

Treatment	*E. coli*	*S. aureus*	*P. aeruginosa*	*C. albicans*
An-AgNPs	50%	50%	50%	50%
Ar-AgNPs	50%	25%	50%	50%

Morphological Characterization of AgNP-Treated Microbes

An-AgNP-treated *C. albicans* showed abnormal morphology due to their effect by NPs (**Figure 7**). Variations in morphology, especially cellular elongation, were noticed in An-AgNP-treated *P. aeruginosa* cells compared with untreated control cells (**Figure 8**).

Cytotoxicity

To investigate the cytotoxicity of the biogenic AgNPs, cell viability assays were preformed using MDA-MB-231 cells (**Table 1**). Both An-AgNPs and Ar-AgNPs had dose-dependent

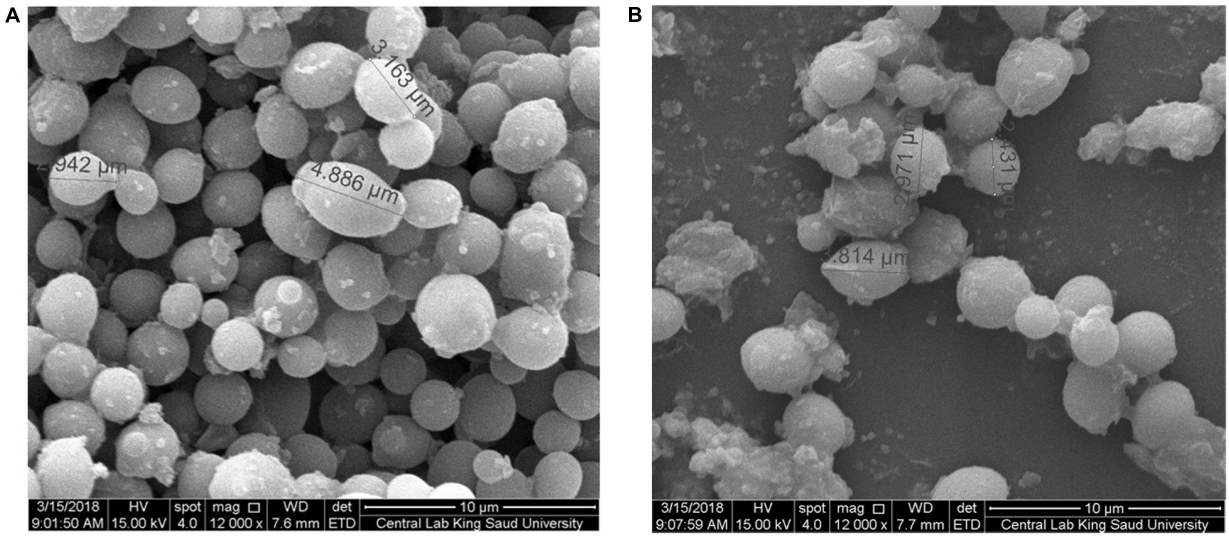

FIGURE 7 | (A) SEM image of *C. albicans*. **(B)** SEM image of An-AgNP-treated *C. albicans* showing abnormal cell size and morphology.

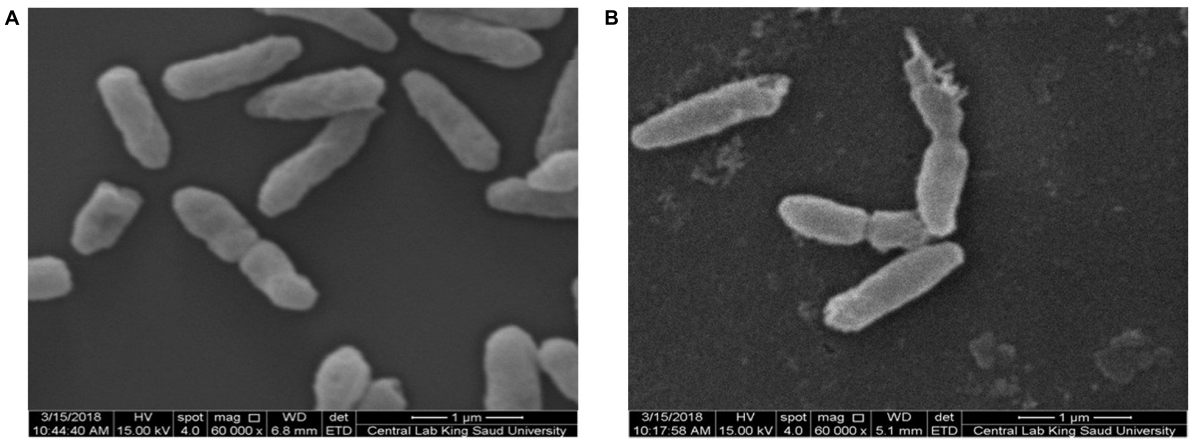

FIGURE 8 | (A) SEM image of normal *P. aeruginosa*. **(B)** SEM image of An-AgNP-treated *P. aeruginosa* showing abnormal cell morphology.

inhibitory effects on cell proliferation (**Figure 9A**). The potency of An-AgNPs was higher (IC_{50} 149.4 µg/mL) compared with that of Ar-AgNPs (IC_{50} 585.2 µg/mL) (**Figure 9B**).

Chromatography/Mass Spectrometry (GC-MS) Techniques

The chemical analysis of *A. hierochuntica* and *A. absinthium* were examined by GC-MS analysis and the active constituents are presented in **Tables 3**, **4**. GC-MS analysis of plants under investigation showed similar compounds from both plant origin such as Phenol, 2-methyl-5-(1-methylethyl) and O-xylene. However, from *A. hierochuntica*, 2,2-diethoxypropane, Alkenes and Alkanes such as 1-Pentadecene and Tridecane, respectively, as well as anthraquinone derivatives were also detected. On the other hand, Phenol, 2,4-bis-(1,1-dimethylethyl); TMS (Trimethylsilane); [1,1′-Biphenyl]-4-carbonitrile, 4′-pentyl-; 9-Tetradecen, Amabufotalin, octadecenoic acid methyl ester as well as colchicine were detected from *A. absinthium*.

DISCUSSION

Current developments in the field of nanomedicine have led to great opportunities for nanostructure formation using biogenic agents, providing a simple approach for producing particles with unique characteristics than can combat multidrug-resistant (MDR) bacteria. To the best of our knowledge, that this study is the first to report and analyze AgNP biosynthesis using *A. hierochuntica*, although (del Pilar Rodríguez-Torres et al., 2019) previously tested AgNP production using *A. absinthium*. AgNP biosynthesis proceeded first via a slow color change, after 24 h, the color intensity stabilized, and no further changes were observed, suggesting that color intensity was a time-dependent

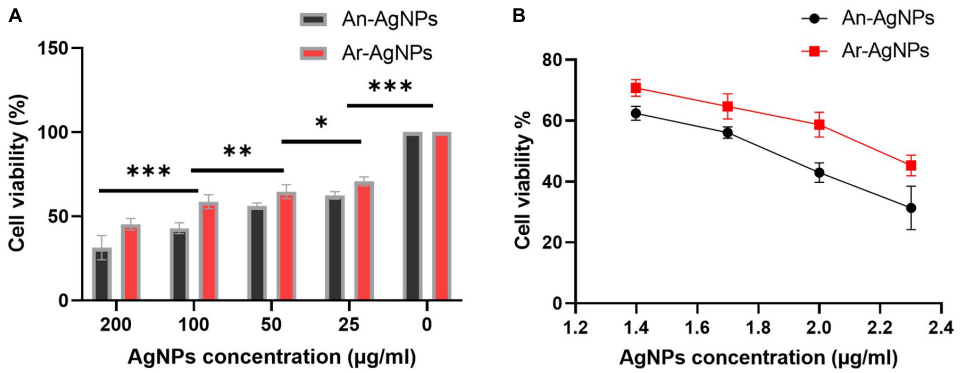

FIGURE 9 | (A) IC_{50} values for the AgNPs against MDA-MB231 cell lines after 48 h of treatment. Data are presented as the mean ± SD; *P* values have been calculated against control and $^{**}P < 0.001$ and $^{*}P < 0.01$. **(B)** The antiproliferative effect of AgNPs against MDA-MB-231 cells at logarithmic concentration. Data presented as % viability.

variable at room temperature. A relationship between the gradual color change and surface plasmon resonance (SPR) can reflect the reduction of silver ions into AgNPs (Algebaly et al., 2020). The exact mechanisms by which AgNPs form with the aid of the biogenic agents is not fully understood; however, plant secondary metabolites may act as reducing and capping agents in this process.

Characterization of Biogenic AgNPs

Varied sizes for An-AgNPs and Ar-AgNPs suggested that, different extracts can contain different plant metabolites; consistently, variations in their ability to support AgNP formation were indicated by the formation of particles of different sizes when different plant extracts were used for conversion. A recent study reported that AgNPs ranging in size from 2 to 80 nm were produced using *A. absinthium* (del Pilar Rodríguez-Torres et al., 2019) (smaller than those produced via our method described here). This variation might be explained by use of different plant parts because only plant leaves were used in the previous study. Use of different plant parts may lead to variations in the abundance of various biomolecules.

Negative values for zeta potentials for An-AgNPs and Ar-AgNPs, could be related to the organic biomolecules in the plant extract that cap the AgNPs. Negative values might reflect repulsion between the particles, suggesting high degrees of AgNP stability (Bélteky et al., 2019). Use of biological agents for AgNP fabrication normally result in particles with high stability and monodispersity (Iravani et al., 2014).

Regarding TEM imaging for AgNPs, since no washing was performed, the clear and white areas around the AgNPs could be due to biomolecules from the plant extract that cap the synthesized AgNPs. Undefined morphology has also been reported in AgNPs mediated by orange waste (de Barros et al., 2018).

TABLE 3 | GC-MS analysis results of *A. hierochuntica* ethanolic extract.

Name of compounds	Formula	Molecular weight	R time (min)
2,2-diethoxypropane	$C_7H_{16}O_2$	132	3.268
O-Xylene	C_8H_{10}	106	5.374
2-Cyclohexen-1-one,3,5,5-trimethyl	$C_9H_{14}O$	138	28.282
p-Pentylacetophenone	$C_{13}H_{18}O$	190	28.711
Phenol, 2-methyl-5-(1-methylethyl)-	$C_{10}H_{14}O$	150	31.851
1-Pentadecene	$C_{15}H_30$	210	32.488
Tridecane	$C_{13}H_{28}$	184	39.119
Phenol,2,4-bis(1,1-dimethylethyl)-	$C_{14}H_{22}O$	206	45.527
2,5-Cyclohexadiene-1,4-dione,2,6-bis(1,1-dimethylethyl)-	$C_{14}H_{20}O_2$	220	51.680
2-Ethylanthraquinone	$C_{16}H_{12}O_2$	236	69.512

TABLE 4 | GC-MS analysis results of *A. absinthium* ethanolic extract.

Phenolic Compound	Formula	Molecular weight	R time (min)
O-Xylene	C_8H_{10}	106	5.279
2-Cyclohexen-1-methyl-4-(1-methylethylidene)-	$C_{10}H_{16}$	136	13.513
9-Tetradecen-1-ol,(E)-	$C_{14}H_{28}O$	212	25.181
TMS (Trimethylsilane)	C_6H_8Si	108	28.319
Phenol,2-methyl-5-(1-methylethyl)-	$C_{10}H_{14}O$	150	31.889
[1,1′-Biphenyl]-4-carbonitrile, 4′-pentyl-	$C_{18}H_{19}N$	249	46.009
2,5-Cyclohexadiene-1,4-dione,2,6-bis(1,1-dimethylethyl)-	$C_{14}H_{20}O_2$	220	51.732
Gamabufotalin	$C_{24}H_{34}O_5$	402	78.808
9-Octadecenoic acid (Z)-, methyl ester	$C_{19}H_{36}O_2$	296	81.881
Colchicine	$C_{22}H_{25}NO_6$	399	89.234

The centers of the nanoparticles were darker than the particle edges, suggesting that organic plant biomolecules may cover and cap the AgNPs, leading to the reduction of silver ions in the AgNPs (Khandel et al., 2018). In general, the TEM data revealed smaller particles compared with the size predicted by DSL data, likely because impurities (e.g., bio-active molecules derived from the biogenic agents) surround the AgNPs. This property would have a stronger effect on the DLS readings due to the higher quantity of AgNP solution required for the measurement in contrast to the quantity normally used for TEM. Some cellular biomolecules have been shown to affect AgNP fabrication, including carbohydrates, amino acids, enzymes, proteins, and pigments (El-Naggar et al., 2016). Concentration of such biomolecules might be the main reason on the divergence of detected peaks using DLS. Furthermore, variations between NPs size detected by DLS and TEM technique is expected since the principles are varied for each instrument (Khandel et al., 2018). In general, the shape and size variation observed here might be expected since various reduction routes for silver ions are likely to exist in plant extracts due to the presence of multiple reducing and capping agents, which was verified by the FTIR analysis described below. FTIR is used to detect organic and inorganic compounds based on their infrared spectra (Leela and Anchana, 2017).

The spectra for both An-AgNPs and Ar-AgNPs ranged from 3300 to 3,500 cm^{-1}, suggesting the presence of polyphenolic hydroxyl (–OH) groups and N–H bond stretching in amine groups (Siddiqi et al., 2018). Absorption between 1,600 and 1,650 cm^{-1}, which can be attributed to the amide I band associated with carbonyl C = O stretching in proteins, was detected for both types of AgNPs (Khandel et al., 2018). Peaks in the 400 to 450 cm^{-1} range can be related to silver ions in both AgNPs. Polyphenolic and amide I absorption bands were noted for both types of AgNPs; however, such compounds might vary in concentration or type as indicated by slight differences in the FTIR spectra. The presence of peaks corresponding to hydroxyl and amide groups suggests that carbohydrates and proteins are involved in the reducing and capping of the AgNPs prepared using the two plant extracts. These findings suggest that these AgNPs are both safe and stable.

Biological Activity and Synergistic Antimicrobial Effects of AgNPs

Antimicrobial Activity of An-AgNPs

To determine whether the conversion of silver ions into AgNPs using plant extracts affected the biological characteristics of the biogenic-AgNPs, their effects on various microbes were tested. The activity of the An-AgNPs was higher than that of silver ions against *E. coli* and *S. aureus*, suggesting that their small particle size facilitated entry into the cells where they were more likely to induce damage (Pal et al., 2007). Use of AgNPs as antiseptics might be fueled by their broad-spectrum activity (Jones et al., 2004); however, interactions between sulfur groups in cell wall proteins and silver ions might specifically disrupt the bacterial cell wall (Rai et al., 2012; Abbaszadegan et al., 2015). The observed antibacterial effects of positively charged An-AgNPs might also be related to cell wall disruption driven by their ability to electrostatically adhere to the negatively charged bacterial membranes (Rai et al., 2012; Abbaszadegan et al., 2015). The catalytic oxidation of silver metal and monovalent silver ion interactions underly the bactericidal action of AgNPs (Abo-Shama et al., 2020).

The Ability of An-AgNPs to Enhance Antibiotic Efficacy

AgNPs are less likely than antibiotics to promote microbial resistance acquisition (Jones et al., 2004); therefore, the activity of An-AgNPs against several microbes was compared to those of standard antibiotics. Due to the increasing prevalence of antibiotic-resistant microorganisms, which threaten human health globally, we explored the efficacy of combinations of antibiotics and biogenic AgNPs. Microbial antibiotic resistance is rising more rapidly than silver resistance because acquisition of metal resistance requires accumulation of multiple mutations due to the multiple targets of metals (Herrera et al., 2001). In light of this trend, we examined potential synergism between the effects of AgNPs and antibiotics and the anticandidal agents fluconazole and metronidazole. Each antibiotic was mixed with AgNPs, and the antimicrobial effects of each mixture were tested.

A recent study confirmed the synergistic effects of combinations of some antibiotics and AgNPs against *E. coli* and *Salmonella* spp. (Abo-Shama et al., 2020). *Salmonella typhimurium* was synergistically inhibited by combinations of tetracycline and AgNPs and neomycin and AgNPs (McShan et al., 2015).

Antimicrobial Activity of Ar-AgNPs

Ar-AgNPs were more active than silver ions against the tested bacterial species, no activity was observed against *C. albicans*. By contrast, AgNPs prepared using *A. absinthium* have been shown to have significant activity against pathogenic yeasts of the *Candida* genus (del Pilar Rodríguez-Torres et al., 2019). This discrepancy might indicate that the smaller AgNPs prepared using *A. absinthium* in the earlier study (relative to the AgNPs prepared in our study) might confer increased activity against *Candida* spp. or that the activity of AgNPs fabricated using *A. absinthium* might be species specific. AgNPs and ZnNPs prepared using *Ulva fasciata* alga showed no anticandidal activity (Abo-Shama et al., 2020).

The Ability of Ar-AgNPs to Improve Antibiotic Efficacy

Combinations of antibiotics and AgNPs have been shown to exert an antibiofilm effect against mature bacterial biofilms (Hwang et al., 2012a). Furthermore, addition of AgNPs to antibiotics promotes an increase in the local antibiotic concentration around the site of action in bacteria, thus facilitating a strong antibiotic-microbe interaction (Allahverdiyev et al., 2011). Sharma et al. (2016) demonstrated synergistic effects of ZnO nanoparticles combined with ciprofloxacin against *S. aureus*, *E. coli*, and *Klebsiella pneumoniae*. Increased penetration of the antibiotic active ingredients facilitated by nanoparticles could explain the synergistic effect of AgNP-antibiotic combinations; however, antagonistic effects were also observed. Such effects

could be related, at least to some extent, to effects of the biomolecules capping the AgNPs; for example, these molecules might interfere with antibiotic components and limit their availability.

In general, the activity of the An-AgNPs was higher than that of the Ar-AgNPs against *E. coli*, *S. aureus*, and *C. albicans*, while no significant differences were observed between their activities against *P. aeruginosa*. These observations might be related to the smaller particle size of the An-AgNPs compared with that of Ar-AgNPs, which would result in a higher surface-to-volume ratio. This effect might support nanoparticle entry into the cells via the larger contact area with the microbial cell wall. The tolerance level for all tested AgNPs was bactericidal since the MBC:MIC ratio was $\leq$2 (Long, 2017).

Morphological Characterization of AgNP-Treated Microbes

To elucidate the antimicrobial mechanism of An-AgNPs, *P. aeruginosa* and *C. albicans* were treated with biogenic An-AgNPs and then observed under SEM to identify any differences in cell shape. TEM imaging has previously confirmed penetration and intracellular accumulation of AgNPs prepared using *Syzygium cumini* seed extract in *C. albicans* in addition to cell wall damage (Jalal et al., 2019), such information could support our findings in the abnormal morphology and cell elongation of An-AgNP-treated *C. albicans,* and *P. aeruginosa* cells, respectively. The precise antibacterial and anticandidal mechanisms of AgNPs are not fully understood. Various modes of action have been proposed, e.g., (1) induction of DNA and cytoplasmic leakage (Jun et al., 2000), (2) creation of holes in the cell membrane to induce death in *C. albicans* (Kim et al., 2009), and (3) induction of ROS production (Hwang et al., 2012b). Similar trends have been reported elsewhere (Gopinath et al., 2015; Hamouda et al., 2019).

The present observations of potential inhibitory activities against several pathogenic microbes suggests that An-AgNPs and Ar-AgNPs could be used as alternatives to antibiotics in various medical applications.

Cytotoxicity

To investigate the cytotoxicity of the biogenic AgNPs, cell viability assays were preformed using MDA-MB-231 cells. In general, anticancer activity in AgNPs prepared using green synthesis has been well documented (Jeyaraj et al., 2013; Paul et al., 2015; Al-Sheddi et al., 2018; Algebaly et al., 2020); however, different IC_{50} values and variations in cytotoxicity (which might be related to cell line and AgNP size, shape, and concentration) have been reported. The higher efficacy of An-AgNPs compared to Ar-AgNPs against MDA-MB-231 cells might be due to their smaller particle size; however, AgNPs generally have a high affinity for cell membranes that facilitates cell entry. Organic biomolecules derived from the plant extract that cap the AgNPs might also enhance their stability and facilitate cellular entry by stimulating cellular uptake. In general, various modes of action might enhance cancer cell suppression, including ROS generation, which leads to DNA damage and apoptosis via consequential caspase-3 activation (Siddiqi et al., 2018).

Chromatography/Mass Spectrometry (GC-MS) Techniques

Furthermore, the GC-MS investigation in the current study approved the incidence of various phytochemicals that could be responsible for the biological activity of AgNPs. Such molecules involving Phenolic compounds, the well-known antioxidant molecules with different biological activities. Antioxidant and antimicrobial effects were noted for the aromatic hydrocarbons, O-xylene (Tiwari et al., 2016) that detected for both currently investigated plants. A 2,2-diethoxypropane could has a main role as antimicrobial agent since it was also detected in *Mentha cervina* and *Origanum vulgare* essential oils that showed antimicrobial ability (Helal et al., 2019). Furthermore, anthraquinones could also contribute to the biological activity of *A. hierochuntica*. Antibacterial, anti-inflammatory and antioxidant effects were noted for *Ceratotheca triloba* from which anthraquinones were detected (Mohanlall and Odhav, 2013). Amabufotalin is a well-known cytotoxic agent (Yu et al., 2014). Presence of octadecenoic acid methyl ester and colchicine might also contribute to the activity of *A. absinthium*. Antimicrobial activity was noted for J. curcas leaf extracts that contain a component octadecenoic acid methyl ester (Asghar and Choudahry, 2011). The main alkaloid, colchicine, had cytotoxic activity (Kurek, 2018). Such Phenolic and other phytochemicals could be also essential in nanoparticle formation (Ouerghemmi et al., 2017).

CONCLUSION

The use of biogenic agents for nanoparticle formation is a remarkable advance in nanoscience that yields safe and stable nanostructures capped with biomolecules. The biogenic AgNPs in the current investigation were prepared using aqueous extracts from *A. hierochuntica* L. (Kaff Maryam) and *A. absinthium*. This method yielded biogenic nanoparticles with diameters ranging from 114 to 125.5 nm based on our DLS results. The current approach is simple, economical, and effective for producing AgNPs at room temperature using safe materials without the production of toxic byproducts. The AgNPs produced using both plant extracts demonstrated antimicrobial effects against multiple microorganisms, strong synergistic antibacterial activity in combination with some antibiotics, as well as cytotoxic effects against MDA-MB-231 cells. Based on our findings, we propose that the use of plant extracts for nanoparticle fabrication might be useful for large-scale production of nanomaterials. Combinations of AgNPs and antibiotics had synergistic antimicrobial effects, which might help to explain their mechanism of action. Furthermore, AgNPs capped and reduced by biomolecules such as carbohydrates and proteins are safe and stable nanoparticles that might be useful in antimicrobial drug formulations, making them potentially valuable for the pharmaceutical industry. Various levels of toxicity might be expected in different AgNP applications; therefore, it is important to carefully control and optimize the conditions needed to maintain an appropriate and safe concentration.

DATA AVAILABILITY STATEMENT

The raw data supporting the conclusions of this article will be made available by the authors, without undue reservation.

AUTHOR CONTRIBUTIONS

KA: conceptualization, funding acquisition, formal analysis, methodology, supervision, writing – original draft, writing, review, and editing. AM: conceptualization, formal analysis, methodology, visualization, writing – original draft, writing, review, and editing. Both authors contributed to the article and approved the submitted version.

ACKNOWLEDGMENTS

This research was funded by the Deanship of Scientific Research at Princess Nourah Bint Abdulrahman University through the Fast-Track Research Funding Program. Furthermore, we would like to express our special thanks and gratitude to Ms. Haifa Alawaad, Ms. Mada Alsaleh, Ms. Noura Alqahtani, Ms. Nourah Alanzan, Ms. Rawan Almahbub, Ms. Thekra Almashaan, Ms. Shrouq Alalwi, Ms. Samiah Aleanzi, and Ms. Yusra Almarshadi for their assistance with this study. Without their assistance and dedicated involvement in every step of the process, this research would never have been accomplished.

SUPPLEMENTARY MATERIAL

The Supplementary Material for this article can be found online at: https://www.frontiersin.org/articles/10.3389/fbioe.2021.652362/full#supplementary-material

Supplementary File 1 | (A) *A. hierochuntica* L. (Kaff Maryam) extract. **(B)** Silver nanoparticles prepared using *A. hierochuntica* L. (Kaff Maryam) extract. **(C)** *A. absinthium* extract. **(D)** Silver nanoparticles prepared using *A. absinthium* extract.

REFERENCES

Abbaszadegan, A., Ghahramani, Y., Gholami, A., Hemmateenejad, B., Dorostkar, S., Nabavizadeh, M., et al. (2015). The effect of charge at the surface of silver nanoparticles on antimicrobial activity against gram-positive and gram-negative bacteria: a preliminary study. *J. Nanomater.* 2015:720654. doi: 10.1155/2015/720654

Abd Ellah, N. H., Ahmed, E. A., Abd-Ellatief, R. B., Ali, M. F., Zahran, A. M., and Hetta, H. F. (2019a). Metoclopramide nanoparticles modulate immune response in a diabetic rat model: association with regulatory T cells and proinflammatory cytokines. *Int. J. Nanomed.* 14, 2383–2395. doi: 10.2147/IJN.S196842

Abd Ellah, N. H., Tawfeek, H. M., John, J., and Hetta, H. F. (2019b). Nanomedicine as a future therapeutic approach for Hepatitis C virus. *Nanomedicine* 14, 1471–1491. doi: 10.2217/nnm-2018-0348

Abo-Shama, U. H., El-Gendy H., Mousa W. S., Hamouda R. A., Yousuf W. E., Hetta H. F., et al. (2020). Synergistic and antagonistic effects of metal nanoparticles in combination with antibiotics against some reference strains of pathogenic microorganisms. *Infect. Drug Resist.* 13, 351–362. doi: 10.2147/idr.s234425

Abou-Elella, F., Hanafy, E. A., and Gavamukulya, Y. (2016). Determination of antioxidant and anti-inflammatory activities, as well as in vitro cytotoxic activities of extracts of *Anastatica hierochuntica* (Kaff Maryam) against HeLa cell lines. *J. Med. Plants Res.* 10, 77–87. doi: 10.5897/jmpr2015.6030

Al Gamdi, N., Mullen, W., and Crozier, A. (2011). Tea prepared from *Anastatica hierochuntica* seeds contains a diversity of antioxidant flavonoids, chlorogenic acids and phenolic compounds. *Phytochemistry* 72, 248–254. doi: 10.1016/j.phytochem.2010.11.017

Algebaly, A. S., Mohammed, A. E., Abutaha, N., and Elobeid, M. M. (2020). Biogenic synthesis of silver nanoparticles: antibacterial and cytotoxic potential. *Saudi J. Biol. Sci.* 27, 1340–1351. doi: 10.1016/j.sjbs.2019.12.014

Allahverdiyev, A. M., Kon, K. V., Abamor, E. S., Bagirova, M., and Rafailovich, M. (2011). Coping with antibiotic resistance: combining nanoparticles with antibiotics and other antimicrobial agents. *Expert Rev. Anti Infect. Ther.* 9, 1035–1052. doi: 10.1586/eri.11.121

Al-Sheddi, E., Farshori, N. N., Al-Oqail, M. M., Al-Massarani, S. M., Saquib, Q., Wahab, R., et al. (2018). Anticancer potential of green synthesized silver nanoparticles using extract of *Nepeta deflersiana* against human cervical cancer cells (HeLA). *Bioinorg. Chem. Appl.* 2018:9390784. doi: 10.1155/2018/9390784

Asghar, S. F., and Choudahry, M. I. (2011). Gas chromatography-mass spectrometry (GC-MS) analysis of petroleum ether extract (oil) and bio-assays of crude extract of *Iris germanica*. *Int. J. Genet. Mol. Biol.* 3, 95–100.

Basri, D. F., and Fan, S. (2005). The potential of aqueous and acetone extracts of galls of *Quercus infectoria* as antibacterial agents. *Indian J. Pharmacol.* 37, 26–29. doi: 10.4103/0253-7613.13851

Bélteky, P., Rónavári, A., Rónavári, A., Szerencsés, B., Tóth, I. Y., Pfeiffer, I., et al. (2019). Silver nanoparticles: aggregation behavior in biorelevant conditions and its impact on biological activity. *Int. J. Nanomed.* 14, 667–687. doi: 10.2147/ijn.s185965

Cheesbrough, M. (2000). *District Laboratory Practice in Tropical Countries, Low price Edition*. Cambridge: University of Cambridge, 157.

Daoowd, W. S. (2013). In vitro antifungal activity of extracts of *Anastatica hierochuntica*. *Kufa J. Vet. Med. Sci.* 4, 142–148.

Das, B., Dash, S. K., Mandal, D., Adhikary, J., Chattopadhyay, S., Tripathy, S., et al. (2016). Green-synthesized silver nanoparticles kill virulent multidrug-resistant *Pseudomonas aeruginosa* strains: a mechanistic study. *BLDE Univ. J. Health Sci.* 1, 89–101. doi: 10.4103/2468-838x.196087

David, E., Elumalai, E. K., Praad, T. N. V. K. V., Kambala, V., and Nagajyothi, P. C. (2010). Green synthesis of silver nanoparticle using *Euphorbia hirta* L and their antifungal activities. *Arch. Appl. Sci. Res.* 2, 76–81.

de Barros, C. H. N., Cruz, G. C. F., Mayrink, W., and Tasic, L. (2018). Bio-based synthesis of silver nanoparticles from orange waste: effects of distinct biomolecule coatings on size, morphology, and antimicrobial activity. *Nanotechnol. Sci. Appl.* 11, 1–14. doi: 10.2147/nsa.s156115

del Pilar Rodríguez-Torres, M., Acosta-Torres, L. S., Díaz-Torres, L. A., Padrón, G. H., García-Contreras, R., and Millán-Chiu, B. E. (2019). Artemisia absinthium-based silver nanoparticles antifungal evaluation against three *Candida* species. *Mater. Res. Express* 6:085408. doi: 10.1088/2053-1591/ab1fba

El-Baky, R. M. A., Sandle, T., John, J., Abuo-Rahma, G. E. A., and Hetta, H. F. (2019). A novel mechanism of action of ketoconazole: inhibition of the NorA efflux pump system and biofilm formation in multidrug-resistant *Staphylococcus aureus*. *Infect. Drug Resist.* 12, 1703–1718. doi: 10.2147/IDR.S201124

El-Mokhtar, M. A., and Hetta, H. F. (2018). Ambulance vehicles as a source of multidrug-resistant infections: a multicenter study in Assiut City, Egypt. *Infect. Drug Resist.* 11, 587–594. doi: 10.2147/IDR.S151783

El-Naggar, N. E.-A., Mohamedin, A., Hamza, S. S., and Sherief, A.-D. (2016). Extracellular biofabrication, characterization, and antimicrobial efficacy of silver nanoparticles loaded on cotton fabrics using newly isolated Streptomyces sp. SSHH-1E. *J. Nanomater.* 2016:3257359. doi: 10.1155/2016/3257359

Friedman, A. J., Phan, J., Schairer, D. O., Champer, J., Qin, M., Pirouz, A., et al. (2013). Antimicrobial and anti-inflammatory activity of chitosan–alginate nanoparticles: a targeted therapy for cutaneous pathogens. *J. Invest. Dermatol.* 133, 1231–1239. doi: 10.1038/jid.2012.399

Gopinath, V., Priyadarshini, S., Loke, M. F., Arunkumar, J., Marsili, E., Ali, M. D., et al. (2015). Biogenic synthesis, characterization of antibacterial silver nanoparticles and its cell cytotoxicity. *Arab. J. Chem.* 10, 1107–1117. doi: 10.1016/j.arabjc.2015.11.011

Hamouda, R. A., Hussein, M. H., Abo-elmagd, R. A., and Bawazir, S. S. (2019). Synthesis and biological characterization of silver nanoparticles derived from the cyanobacterium *Oscillatoria limnetica*. *Sci. Rep.* 9:13071. doi: 10.1038/s41598-019-49444-y

Helal, I. M., El-Bessoumy, A., Al-Bataineh, E., Joseph, M. R., Rajagopalan, P., Chandramoorthy, H. C., et al. (2019). Antimicrobial efficiency of essential oils from traditional medicinal plants of asir region, Saudi Arabia, over drug resistant isolates. *Biomed Res. Int.* 2019:8928306. doi: 10.1155/2019/8928306

Herrera, M., Carrion, P., Baca, P., Liebana, J., and Castillo, A. (2001). In vitro antibacterial activity of glass-ionomer cements. *Microbios* 104, 141–148.

Huh, A. J., and Kwon, Y. J. (2011). Nanoantibiotics: a new paradigm for treating infectious diseases using nanomaterials in the antibiotic's resistant era. *J. Controll. Release* 156, 128–145. doi: 10.1016/j.jconrel.2011.07.002

Hwang, I.-S., Hwang, J. H., Choi, H., Kim, K.-J., and Lee, D. G. (2012a). Synergistic effects between silver nanoparticles and antibiotics and the mechanisms involved. *J. Med. Microbiol.* 61, 1719–1726. doi: 10.1099/jmm.0.047100-0

Hwang, I. S., Lee, J., Hwang, J. H., Kim, K. J., and Lee, D. G. (2012b). Silver nanoparticles induce apoptotic cell death in *Candida albicans* through the increase of hydroxyl radicals. *FEBS J.* 27, 1327–1338. doi: 10.1111/j.1742-4658.2012.08527.x

Iravani, S., Korbekandi, H., Mirmohammadi, S. V., and Zolfaghari, B. (2014). Synthesis of silver nanoparticles: chemical, physical and biological methods. *Res. Pharm. Sci.* 9, 385–406.

Jain, D., Kumar Daima, S., Kachhwaha, S., and Kothari, S. L. (2009). Synthesis of plant mediated silver nanoparticles using papaya fruit extract and evaluation of their antimicrobial activities. *Dig. J. Nanomater. Biostruct.* 4, 557–563.

Jalal, M., Ansari, M. A., Alzohairy, M. A., Ali, S. G., Khan, H. M., Almatroudi, A., et al. (2019). Anticandidal activity of biosynthesized silver nanoparticles: effect on growth, cell morphology, and key virulence attributes of *Candida* species. *Int. J. Nanomed.* 14, 4667–4679. doi: 10.2147/ijn.s210449

Jeyaraj, M., Sathishkumar, G., Sathishkumar, G., MubarakAli, D., Rajesh, M., Arun, R., et al. (2013). Biogenic silver nanoparticles for cancer treatment: an experimental report. *Colloids Surf. B Biointerfaces* 106, 86–92. doi: 10.1016/j.colsurfb.2013.01.027

Jones, S. A., Bowler, P. G., Walker, M., and Parsons, D. (2004). Controlling wound bioburden with a novel silver-containing Hydrofiber dressing. *Wound Repair Regener.* 12, 288–294. doi: 10.1111/j.1067-1927.2004.012304.x

Jun, F., Jing, S., Sirimanne, S. R., and Mounier-Lee, C. E. (2000). Kinetic and stereochemical studies on novel inactivators of C-terminal amidation. *Biochem. J.* 350, 521–530. doi: 10.1042/0264-6021:3500521

Juteau, F., Jerkovic, I., Masotti, V., Milos, M., Mastelic, J., Bessière, J. M., et al. (2003). Composition and antimicrobial activity of the essential oil of *Artemisia absinthium* from Croatia and France. *Planta Med.* 69, 158–161. doi: 10.1055/s-2003-37714

Khandel, P., Shahi, S. K., Kanwar, L., Yadaw, R. K., and Soni, D. K. (2018). Biochemical profiling of microbes inhibiting silver nanoparticles using symbiotic organisms. *Int. J. Nano Dimens.* 9, 273–285.

Kim, K. J., Sung, W. S., Suh, B. K., Moon, S. K., Choi, J. S., Kim, J. G., et al. (2009). Antifungal activity and mode of action of silver nanoparticles on *Candida albicans*. *Biometals* 22, 235–242. doi: 10.1007/s10534-008-9159-2

Kurek, J. (2018). Cytotoxic colchicine alkaloids: from plants to drugs. *Cytotoxicity* 6:45. doi: 10.5772/intechopen.72622

Leela, K., and Anchana, D. C. (2017). A study on the applications of silver nanoparticle synthesized using the aqueous extract and the purified secondary metabolites of lichen *Parmelia perlata*. *Int. J. Pharm. Sci. Invent.* 6, 42–59.

Lewis, K., and Ausubel, F. M. (2006). Prospects for plant-derived antibacterials. *Nat. Biotechnol.* 24, 1504–1507. doi: 10.1038/nbt1206-1504

Long, T. E. (2017). Repurposing thiram and disulfiram as antibacterial agents for multi-drug 1 resistant *Staphylococcus aureus* infections. *Antimicrob. Agents Chemother.* 61:e00898-17. doi: 10.1128/AAC.00898-17

Madhuri, S., Maheshwar, S., Sunil, P., and Oza, G. (2012). *Nanotechnology: Concepts and Applications*. Boca Raton, FL: CRC Press.

McShan, D., Zhang, Y., Deng, H., Ray, P. C., and Yu, H. (2015). Synergistic antibacterial effect of silver nanoparticles combined with ineffective antibiotics on drug resistant *Salmonella* typhimurium DT104. *J. Environ. Sci. Health C* 33, 369–384. doi: 10.1080/10590501.2015.1055165

Mohamed, A. A., Khalil, A. A., and El-Beltagi, H. E. (2010). Antioxidant and antimicrobial properties of Kaff Maryam (*Anastatica hierochuntica*) and Doum Palm (*Hyphaene thebaica*). *Grasas Aceites* 61, 67–75. doi: 10.3989/gya.064509

Mohanlall, V., and Odhav, B. (2013). Antibacterial, anti-inflammatory and antioxidant activities of anthraquinones from *Ceratotheca triloba* (Bernh) Hook F. *J. Med. Plant Res.* 7, 877–886. doi: 10.5897/JMPR12.900

Ouerghemmi, I., Rebey, I. B., Rahali, F. Z., Bourgou, S., Pistelli, L., Ksouri, R., et al. (2017). Antioxidant and antimicrobial phenolic compounds from extracts of cultivated and wild-grown Tunisian *Ruta chalepensis*. *J. Food Drug. Anal.* 25, 350–359. doi: 10.1016/j.jfda.2016.04.001

Pal, S., Tak, Y. K., and Song, J. M. (2007). Does the antibacterial activity of silver nanoparticles depend on the shape of the nanoparticle? A study of the Gram-negative bacterium *Escherichia coli*. *Appl. Environ. Microbiol.* 73, 1712–1720. doi: 10.1128/AEM.02218-06

Paul, S., Singh, A. R., and Sasikumar, C. S. (2015). Green synthesis of bio-silver nanoparticles by *Parmelia perlata*, *Ganoderma lucidum* and *Phellinus igniarius* & their fields of application. *Indian J. Res. Pharm. Biotechnol.* 3:100.

Perez, C., Paul, M., and Bazerque, P. (1990). An antibiotic assay by the agar well diffusion method. *Acta Biol. Med. Exp.* 15, 113–115.

Rahmy, T. R., and El-Ridi, M. R. (2002). Action of *Anastatica hierochuntica* plant extract on Islets of Langerhans in normal and diabetic rats. *Egypt. J. Biol.* 4, 87–94.

Rai, M., Deshmukh, S., Ingle, A., and Gade, A. (2012). Silver nanoparticles: the powerful nanoweapon against multidrug-resistant bacteria. *J. Appl. Microbiol.* 112, 841–852. doi: 10.1111/jam.2012.112.issue-5

Reinke, R., King, P. J., Victoria, G. J., McDougall, R. B., Ma, G., Mao, Y., et al. (2002). Dicaffeoyltartaric acid analogues inhibit human immunodeficiency virus type 1 (HIV-1) integrase and HIV-1 replication at nontoxic concentrations. *J. Med. Chem.* 45, 3669–3683. doi: 10.1021/jm010359d

Saifuddin, N., Wong, C. W., and Yasumira, A. A. N. (2009). Rapid biosynthesis of silver nanoparticles using culture supernatant of bacteria with microwave irradiation. *Electron. J. Chem.* 6, 61–70. doi: 10.1155/2009/734264

Salah, S. A., Abdou, H. S., Azeem, A. S. A., and Abdel-Rahim, E. A. (2011). The antioxidative effects of some medicinal plants as hypoglycemic agents on chromosomal aberration and abnormal nucleic acids metabolism produced by diabetes stress in male adult albino rats. *J. Diabetes Mellitus* 1, 6–14. doi: 10.4236/jdm.2011.11002

Sharma, N., Jandaik, S., and Kumar, S. (2016). Synergistic activity of doped zinc oxide nanoparticles with antibiotics: ciprofloxacin, ampicillin, fluconazole and amphotericin B against pathogenic microorganisms. *An. Acad. Bras. Ciênc.* 88, 1689–1698. doi: 10.1590/0001-3765201620150713

Siddiqi, K. S., Rashid, M., Rahman, A., Husen, A., and Rehman, S. (2018). Biogenic fabrication and characterization of silver nanoparticles using aqueous-ethanolic extract of lichen (*Usnea longissima*) and their antimicrobial activity. *Biomater. Res.* 22:23. doi: 10.1186/s40824-018-0135-9

Singh, A., Jain, D., Upadhyay, M. K., Khandelwal, N., and Verma, H. N. (2010). Green synthesis of silver nanoparticles using *Argemone mexicana* leaf extract and evaluation of their antimicrobial activities. *Dig. J. Nanomater. Biostruct.* 5, 483–489.

Tayel, A. A., and El-Tras, W. F. (2009). Possibility of fighting food borne bacteria by Egyptian folk medicinal herbs and spices extracts. *J. Egypt. Public Health Assoc.* 84, 21–32.

Tegos, G. (2006). "Substrates and inhibitors of microbial efflux pumps; redefine the role of plant antimicrobilas," in *Naturally Occurring Bioactive Compounds: A New and Safe Alternative for Control of Pests and Microbial Diseases*, eds M. Rai, and C. M. Carpinella (Cambridge: Cambridge University Press).

Tiwari, S., Mishra, S., Misra, R. D., and Upadhyay, R. (2016). Identification of new bioactive compounds from fruit of *Abutilon indicum* through GC-MS analysis. *Biol. Forum Int. J.* 8, 548–554.

Verma, V. C., Kharwa, R. N., and Gange, A. C. (2010). Biosynthesis of antimicrobial silver nanoparticles by the endophytic fungus *Aspergillus clavatus*. *J. Nanomed.* 5, 33–40. doi: 10.2217/nnm.09.77

Willner, B., Basnar, B., and Willner, B. (2007). Nanoparticle–enzyme hybrid systems for nanobiotechnology. *FEBS J.* 274, 302–309. doi: 10.1111/j.1742-4658.2006.05602.x

Yu, Z., Guo, W., Ma, X., Zhang, B., Dong, P., Huang, L., et al. (2014). Gamabufotalin, a bufadienolide compound from toad venom, suppresses COX-2 expression through targeting IKKβ/NF-κB signaling pathway in lung cancer cells. *Mol. Cancer* 13:203. doi: 10.1186/1476-4598-13-203

Conflict of Interest: The authors declare that the research was conducted in the absence of any commercial or financial relationships that could be constructed as a potential conflict of interest.

frontiers in Bioengineering and Biotechnology

ORIGINAL RESEARCH
published: 16 November 2021
doi: 10.3389/fbioe.2021.742135

In situ Forming Hyperbranched PEG—Thiolated Hyaluronic Acid Hydrogels With Honey-Mimetic Antibacterial Properties

Jeddah Marie Vasquez[1,2,3†], Ayesha Idrees[1,4†], Irene Carmagnola[1], Aa Sigen[2,3], Sean McMahon[2,3], Lennart Marlinghaus[5], Gianluca Ciardelli[1], Udo Greiser[3], Hongyun Tai[2], Wenxin Wang[2,3], Jochen Salber[4‡] and Valeria Chiono[1*‡]*

[1]Department of Mechanical and Aerospace Engineering, Politecnico di Torino, Turin, Italy, [2]Blafar Ltd., Dublin, Ireland, [3]Wenxin Wang Research Group, Charles Institute of Dermatology, University College Dublin, Dublin, Ireland, [4]Department of Surgery, Universitätsklinikum Knappschaftskrankenhaus Bochum, Ruhr-University, Bochum, Germany, [5]Department of Medical Microbiology, Ruhr-University Bochum, Bochum, Germany

OPEN ACCESS

Edited by:
Giovanni Vozzi,
University of Pisa, Italy

Reviewed by:
Jennifer Patterson,
Instituto IMDEA Materiales, Spain
Khoon Lim,
University of Otago, Christchurch, New Zealand

***Correspondence:**
Jochen Salber
jochen.salber@rub.de
Valeria Chiono
valeria.chiono@polito.it

†These authors have contributed equally to this work and share first authorship

‡These authors have contributed equally to this work and share senior authorship

Specialty section:
This article was submitted to Biomaterials, a section of the journal Frontiers in Bioengineering and Biotechnology

Received: 15 July 2021
Accepted: 28 September 2021
Published: 16 November 2021

Citation:
Vasquez JM, Idrees A, Carmagnola I, Sigen A, McMahon S, Marlinghaus L, Ciardelli G, Greiser U, Tai H, Wang W, Salber J and Chiono V (2021) In situ Forming Hyperbranched PEG—Thiolated Hyaluronic Acid Hydrogels With Honey-Mimetic Antibacterial Properties. Front. Bioeng. Biotechnol. 9:742135. doi: 10.3389/fbioe.2021.742135

The rapidly increasing resistance of bacteria to currently approved antibiotic drugs makes surgical interventions and the treatment of bacterial infections increasingly difficult. In recent years, complementary strategies to classical antibiotic therapy have, therefore, gained importance. One of these strategies is the use of medicinal honey in the treatment of bacterially colonized wounds. One of the several bactericidal effects of honey is based on the *in situ* generation of hydrogen peroxide through the activity of the enzyme glucose oxidase. The strategy underlying this work is to mimic this antibacterial redox effect of honey in an injectable, biocompatible, and rapidly forming hydrogel. The hydrogel was obtained by thiol–ene click reaction between hyperbranched polyethylene glycol diacrylate (HB PEGDA), synthesized using reversible addition-fragmentation chain transfer (RAFT) polymerization, and thiolated hyaluronic acid (HA-SH). After mixing 500 µL HB PEGDA (10%, w/w) and 500 µL HA-SH (1%, w/w) solutions, hydrogels formed in ~60 s (HB PEGDA/HA-SH 10.0–1.0), as assessed by the tube inverting test. The HB PEGDA/HA-SH 10.0–1.0 hydrogel (200 µL) was resistant to *in vitro* dissolution in water for at least 64 days, absorbing up to 130 wt% of water. Varying glucose oxidase (GO) amounts (0–500 U/L) and constant glucose content (2.5 wt%) were loaded into HB PEGDA and HA-SH solutions, respectively, before hydrogel formation. Then, the release of H_2O_2 was evaluated through a colorimetric pertitanic acid assay. The GO content of 250 U/L was selected, allowing the formation of 10.8 ± 1.4 mmol H_2O_2/L hydrogel in 24 h, under static conditions. The cytocompatibility of HB PEGDA/HA-SH 10.0–1.0 hydrogels loaded with different GO activities (≤ 500 U/L) at a constant glucose amount (2.5 wt %) was investigated by *in vitro* assays at 24 h with L929 and HaCaT cell lines, according to DIN EN ISO 10993-5. The tests showed cytocompatibility for GO enzyme activity up to 250 U/L for both cell lines. The antibacterial activity of HB PEGDA/HA-SH 10.0–1.0 hydrogels loaded with increasing amounts of GO was demonstrated against various gram-positive bacteria (*S. aureus and S. epidermidis*), antibiotic-resistant gram-positive bacteria (MRSA and MRSE), gram-negative bacteria (*P. aeruginosa*, *E. coli*, *and A. baumanii*), and antibiotic-resistant gram-negative strains (*P. aeruginosa and E. coli*) using agar diffusion tests. For all gram-positive

bacterial strains, increasing efficacy was measured with increasing GO activity. For the two *P. aeruginosa strains*, efficacy was shown only from an enzyme activity of 125 U/L and for *E. coli* and *A. baumanii*, efficacy was shown only from 250 U/L enzyme activity. HB PEGDA/HA-SH 10.0–1.0 hydrogels loaded with ≤250 U/L GO and 2.5 wt% glucose are promising formulations due to their fast-forming properties, cytocompatibility, and ability to produce antibacterial H_2O_2, warranting future investigations for bacterial infection treatment, such as wound care.

Keywords: antibacterial, hyaluronic acid, hyperbranched PEG, thiol-ene click chemistry, honey-mimetic hydrogel, dressing, wound care

INTRODUCTION

The huge problem of antibacterial resistance to antibiotics has increased the demand for drug-free antimicrobial strategies, and this has led to reevaluation of ancient antibacterial remedies, such as those derived from natural products, including honey (Mandal and Mandal, 2011).

Research has been conducted on manuka (*L. scoparium*) honey, which has been demonstrated to be effective against several human pathogens, including *Escherichia coli* (*E. coli*), *Enterobacter aerogenes*, *Salmonella typhimurium*, *Staphylococcus aureus* (*S. aureus*), β-haemolytic streptococci, *vancomycin-resistant enterococci* (*VRE*), and *Pseudomonas aeruginosa* (*P. aeruginosa*) (Mandal and Mandal, 2011; Shenoy et al., 2012).

Honey has been widely studied for its bactericidal effects (Shenoy et al., 2012; Albaridi, 2019). Such antibacterial properties are attributed to many factors, including phytochemical components, osmotic effect of sugar on bacterial cells, acidic pH that helps macrophages in destroying bacteria, and the enzymatic activity of GO to produce *in situ* hydrogen peroxide from glucose (Bogdanov 1997; Abuharfeil et al., 1999; Cooper et al., 1999; Cooke et al., 2015). Particularly, hydrogen peroxide represents the main antimicrobial agent in honey: its concentration is determined by relative levels of glucose oxidase and glucose according to the following reaction (Wong et al., 2008; Mandal and Mandal, 2011):

$$\beta - D - Glucose + O_2 \xrightarrow{Glucose\ Oxidase} D - gluconolactone + H_2O_2.$$

Reactive oxygen species (ROS), such as hydrogen peroxide, play a pivotal role in the orchestration of the normal wound-healing response. They act as secondary messengers to many immunocytes and nonlymphoid cells, which are involved in the repair process (Dunnill et al., 2017). Harnessing the potential of ROS to be used within wound care devices, provides the ability to accelerate the healing process and to prevent bacterial infection (Loo et al., 2012). There are several ROS-based technologies currently available in the market or applied in research for wound applications. Among them is SurgihoneyRO™, a commercially available antibacterial product based on a bioengineered honey gel, which enzymatically produces H_2O_2 from glucose oxidase and glucose after application to a wound (Cooke et al., 2015). Another ROS-based commercially available wound dressing is Oxyzyme (Moffatt et al., 2014). It consists of one hydrogel patch embedded with glucose, that is called the "wound contact patch" and a smaller hydrogel patch, called the "secondary wound patch," embedded with GO enzyme. Such hydrogels are stacked on top of each other, then a cover dressing is applied to protect the wound from exposure. The *in situ* formed hydrogen peroxide from Oxyzyme allows the oxidation of loaded iodide ions into iodine, exerting antimicrobial activity, and the formation of oxygen, favoring wound healing (Brimson and Nigam, 2013).

Previously, a quick forming H_2O_2-releasing hydrogel was reported based on gelatin-hydroxyphenyl propionic acid, which triggered cross-linking by horseradish peroxidase enzyme (HRP)/ H_2O_2 (Lee et al., 2017). The amount of H_2O_2 not involved in hydrogel formation served as the antibacterial component and was gradually released. The hydrogel showed antimicrobial activity against gram-positive bacteria including *Staphylococcus aureus*, *S. epidermidis*, and clinical isolate of *methicillin-resistant S. aureus* (MRSA). As a drawback, residual H_2O_2 was only passively released by the system up to exhaustion, while the hydrogel was not able to continuously produce antimicrobial H_2O_2. Recently, Zhang et al. prepared a photocrosslinked antifouling hydrogel from polyethylene glycol diacrylate containing GO, to produce H_2O_2 in contact with glucose (Zhang et al., 2020). However, this hydrogel did not perfectly replicate antimicrobial honey-mimetic mechanisms as glucose was not added into the hydrogel.

Based on the current state of the art, this work aimed to produce an injectable, fast-forming, antibacterial hydrogel for future use in the treatment of wounds colonized or infected with bacteria that overcomes the limitations of other honey-mimetic products, such as the ability to adapt to each wound shape and release different amounts of H_2O_2 per hydrogel volume, depending on the individual wound situation. An ideal hydrogel for wound healing applications should form *in situ* within minutes under mild conditions. "Click" type chemical cross-linking was here exploited as a mechanism for rapid *in situ* formation of hydrogels (Kennedy et al., 2014). In detail, the hydrogel was formed by thiol–ene reaction between hyperbranched polyethylene glycol (PEG) diacrylate (HB PEGDA) and thiolated hyaluronic acid (HA-SH). HA was selected as it is one of the natural components of the dermal extracellular matrix (ECM) and has important functions during wound healing: it regulates inflammatory response and promotes fibroblast migration and proliferation (Dong et al., 2012; Loebel et al., 2017; Poldervaart et al., 2017). On the other hand, PEG is advantageous due to its nonimmunogenicity and resistance to

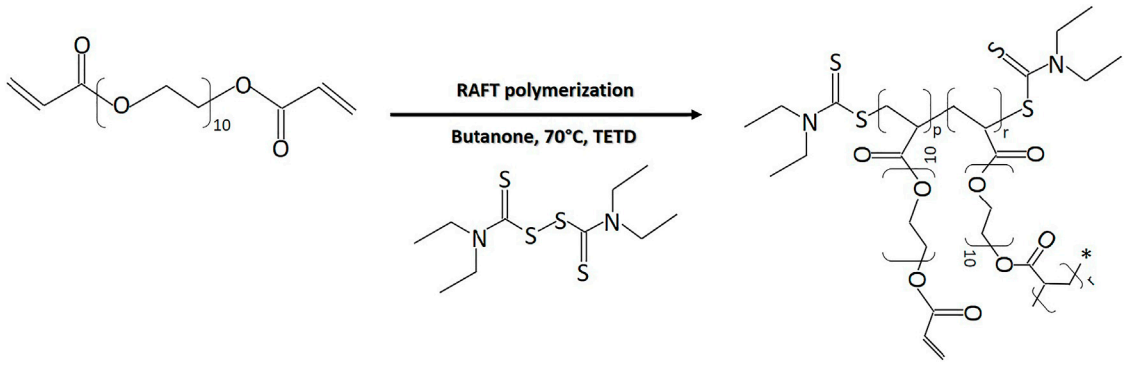

FIGURE 1 | RAFT polymerization reaction of PEG-diacrylate for HB PEGDA synthesis (p = 0.45) (r = 0.55).

protein adsorption (Dong et al., 2015). Thiol–ene crosslinking of the mixed system may impart to wound closure retard superior resistance to hyaluronidase-catalyzed degradation of HA and represents a tool to modulate hydrogel mechanical properties. Recently, Wenxin's lab has prepared HB PEGDA/HA-SH hydrogels and exploited them to support adipose stem cells-based therapy, demonstrating their biocompatibility (Zhang et al., 2018).

In this work, HB PEGDA/HA-SH hydrogels were prepared from HB PEGDA solution (containing GO) and HA-SH solution (containing glucose, G). Physical encapsulation of GO may protect the enzyme from degradation at the wound site with respect to topical application (Arul et al., 2012). The interaction between GO and G causes the formation of antibacterial H_2O_2. By manipulating the concentrations of GO at constant G content within the hydrogel, the rate of formation and release of H_2O_2 was controlled. Loo et al. previously demonstrated that daily topical application of H_2O_2 solution (15 µL) with varying concentrations (10–166 mM) on skin wounds in C57/BL6 mice for overall 10 days caused different effects, from enhanced angiogenesis (10 mM concentration, i.e., 0.15 µmol/wound) to wound closure retard (166 mM concentration, i.e., 2.5 µmol/wound) (Loo et al., 2012). In this work, tuning the amount of GO in HB-PEGDA/HA-SH hydrogels at fixed G content allowed the release of suitable H_2O_2 concentrations per hydrogel volume within 24 h, which were able to control various gram-positive and gram-negative bacterial strains while largely avoiding cytotoxic effects in 2D cultures of L929 mouse fibroblasts and HaCaT human keratinocytes.

MATERIALS AND METHODS

Materials

2,2′-Azobis(isobutyronitrile) (AIBN), tetraethylthiuram disulfide (TETD), polyethylene glycol diacrylate (PEGDA; Mw: 575 Da), butanone, hexane, diethyl ether, dimethyl formamide (DMF), acetone, lithium bromide (LiBr), glucose, glucose oxidase enzyme (E.C. 1.1.3.4), phosphate-buffered saline at pH 7.4 (PBS), Hank's buffer solution, high-glucose Dulbecco's modified Eagle's medium (DMEM), foetal bovine serum (FBS), resazurin sodium salt, and penicillin-streptomycin (PS) were supplied from Sigma-Aldrich, United Kingdom. Thiolated hyaluronic acid (HA-SH, 80% degree of thiolation, 400 kDa) was provided by Blafar, Ireland.

Synthesis of Hyperbranched PEG-Diacrylate

HB PEGDA was synthesized *via* reversible addition-fragmentation chain transfer (RAFT) polymerization, through the reaction illustrated in **Figure 1**. Briefly, in a 250 ml double-neck flask, the following reagents were dissolved in 160 ml butanone: 46 g PEGDA, 948.92 mg TETD (chain transfer agent), and 735.66 mg AIBN (reaction initiator). The double-neck flask was sealed and the reaction solution was purged with argon; afterward, the reaction vessel was placed into an oil bath at 70°C for 2–3 h.

Samples were taken hourly to be analyzed by gel permeation chromatography/size exclusion chromatography (Agilent 1260 Infinity GPC/SEC system, Agilent Technologies, Santa Clara, CA, United States) to monitor the molecular weight increase of the polymer and the molar conversion. When the molecular weight reached 10–20 kDa, polymerization was stopped by quenching the flask with ice water and exposed to the air. The polymer was purified by precipitation in diethyl ether: hexane solution (2:1 v/v) three times and then dried in a vacuum oven for 48 h to remove residual solvent.

Chemical Characterization of HB PEGDA

GPC/SEC Analysis

Samples were prepared for GPC analysis (Agilent PL-GPC50) by dissolving 3 mg of HB PEGDA in 1 ml of DMF. Each solution was filtered using a syringe filter type Sartorius Minisart™ (glass fibre upstream filter combined with a 0.45 µm pore size cellulose acetate filter, Fisher Scientific, United Kingdom) into a small amber GPC vial. The samples were analyzed by GPC/SEC to monitor number average molecular weight (Mn), weight average molecular weight (Mw), polydispersity index (PDI = Mw/Mn), and the degree of polymerization (PD) as the reaction proceeded. The system was equipped with a refractive index detector (RI). The columns in series (30 cm PLgel Mixed-C, two in series) were

eluted using DMF (containing 0.1% LiBr) as the mobile phase and calibrated with poly (methyl methacrylate) (PMMA) standards. All calibrations and analysis were performed at 60°C and with a flow rate of 1 ml min^{-1}.

^{1}H Nuclear Magnetic Resonance

For characterizing molecular structure, ^{1}H nuclear magnetic resonance (NMR) was used. The polymer samples were dissolved in chloroform-D ($CDCl_3$) and ^{1}H NMR analysis was carried out on a 400 MHz Varian NMR spectroscopy system. Data were analyzed using MesReNova 6.1 processing software. The chemical shifts were referenced to the lock chloroform ($CDCl_3$, 7.26 ppm).

The branching ratio, i.e. the ratio of the branched to all PEGDA units, was calculated by the following equation (Dong et al., 2015):

$$Branching\ ratio = 1 - \frac{Linear\ PEGDA\ units}{All\ PEGDA\ units} = 1 - \frac{Integral\ of\ y}{Integral\ of\ d/4},$$

with y indicating the chemical shifts of pendant acrylate groups (in the 5.8–6.4 ppm range) and d indicating the chemical shifts of PEG groups (3.95–4.34 ppm range).

Furthermore, vinyl ratio, i.e., the amount of vinyl groups (mol %) was also calculated (Zhang et al., 2018; Wang et al., 2015):

$$Vinyl\ ratio = \frac{Linear\ PEGDA\ units}{All\ PEGDA\ units} = \frac{Integral\ of\ y}{Integral\ of\ d/4}.$$

Preparation of the HB PEGDA/HA-SH 10.0–1.0 Hydrogel

HB PEGDA/HA-SH 10.0–1.0 hydrogel formulations for the different physicochemical and biological characterizations were always freshly prepared for each experiment by homogeneously mixing equal volumes of HB PEGDA/1X PBS solution (40% w/w) and HA-SH/1X PBS solution (4% w/w) by vortexing vigorously.

Gelation Time Measurement

The gelation time for HB PEGDA/HA-SH 10.0–1.0 hydrogels was measured by the vial tilt method (Deshmukh et al., 2010). Briefly, 500 µL HB PEGDA solution (40% w/w) was combined with 500 µL HA-SH solution (4% w/w). The vials were tilted upside down and observed for 5 s. Gelation was considered complete when no flow was observed within 5 s. Measurements of gelation time were carried out in triplicate (n = 3).

Water Uptake of Hydrogels

In order to determine the water uptake profile, 200 µL HB PEGDA/HA-SH 10.0–1.0 hydrogel was placed in a preweighed 20 ml scintillation vial and initially weighed. Then, 2 ml 1X PBS was added to the vial and incubated at 37°C. At different time points up to 6 weeks (every 2 h during the first 8 h, every 24 h for the first week, and every 2 days onward), PBS was removed and the vials were weighed again. After weight measurement, 2 ml fresh PBS solution was added again and the vial was replaced in the incubator. Measurements were performed in quadruplicates (n = 4).

Water uptake percentage was calculated as follows:

$$Water\ uptake\ (\%) = \frac{W_t - W_0}{W_0} \times 100,$$

where W_t is the weight of the hydrogel at time point t and W_0 is the initial weight of the hydrogel.

Preparation of Honey-Mimetic HB PEGDA/HA-SH Hydrogels by GO and G Encapsulation

The H_2O_2-releasing hydrogel samples were prepared by mixing HB-PEGDA solution (40% w/w), containing various GO concentrations, with HA-SH (4% w/w) solution, containing constant G concentration (**Supplementary Figure S1**).

In detail, HB-PEGDA was dissolved in 1X PBS to prepare a 80% (w/w) stock solution. 1 U is the amount of GO that catalyzes the conversion of 1 µM glucose into 1 µM H_2O_2 within 1 min [Nomenclature Committee of the International Union of Biochemistry (NC-IUB), 1979]. The purchased GO was a lyophilized product with 19.290 U/mg activity. Enzyme stock solution was prepared as 10,000 U/L in 1X PBS. Enzyme solutions (Solution A, shown in **Table 1**; **Supplementary Figure S1**) were prepared from the enzyme stock solution by dilution with PBS. Same volumes of Solution A and HB-PEGDA solution (80% w/w) were mixed to obtain Solution B (**Table 1**; **Supplementary Figure S1**). HA-SH solution (4% w/w, Solution D, **Supplementary Figure S1**) containing 5% (w/w) G (Solution C, **Supplementary Figure S1**) was prepared. HB PEGDA/HA-SH 10.0–1.0 hydrogels with various GO concentrations and 2.5% w/w content were prepared (**Table 1**; **Supplementary Figure S1**).

For further investigations, hydrogel test specimens were prepared by mixing equal volumes (e.g., 15 µL) of Solution B with Solution C. Afterward, properly dispersed mixture was completely pipetted onto a Teflon™ plate surface. Following this protocol, semispherical hydrogel beads with ~5 mm diameter were prepared. The HB PEGDA/HA-SH 10.0–1.0 hydrogel samples were named according to the concentration of encapsulated GO: PEGDA/HA-SH 10.0–1.0 500, 250, 125, 50, and 25 U/L GO, respectively.

Analysis of Hydrogen Peroxide Released From HB PEGDA/HA-SH 10.0–1.0 Hydrogels

Hydrogels with different compositions (**Table 1**) were formed by mixing a volume of 100 µL HB PEGDA/GO solution (Solution B) and 100 µL HA-SH/G solution (Solution C) into a 1 ml Eppendorf tube. After the hydrogel was formed, 800 µL of deionized H_2O was added to the 200 µL hydrogel sample and incubated at 37°C. The formation of H_2O_2 was monitored at different time points between 2 and 24 h. The production of H_2O_2 was quantified by a colorimetric pertitanic acid assay (Sigma-Aldrich, United Kingdom)

TABLE 1 | HB PEGDA/HA-SH 10.0–1.0 hydrogels containing GO and G.

GO solution in PBS (U/L) (Solution A)	GO concentration in HB PEGDA solution (40% w/w) (U/L) (Solution B)	G concentration in HA-SH solution (4% w/w) (w/w%) (Solution C)	GO concentration in the HB PEGDA/ HA-SH 10.0–1.0 hydrogel (U/L)
0	0	5	0
100	50	5	25
200	100	5	50
500	250	5	125
1,000	500	5	250
2,000	1,000	5	500

according to the method by Eisenberg (1943). Briefly, 100 µL of the release solution (containing *in situ* generated H_2O_2) was withdrawn at specific time points and placed in a 96-well plate. Then, 50 µL of the assay solution (2.5% w/w titanium oxysulfate in 2 M H_2SO_4 solution) was added. The color of the solution changed into yellow by H_2O_2 reaction with Ti(IV) (**Supplementary Figure S2**), according to the reaction:

$$Ti^{4+} + H_2O_2 + 2H_2O \rightarrow H_2TiO_4\left(pertitanic\,acid, yellow\right) + 4H^+.$$

The amount of pertitanic acid formed, corresponding to the amount of H_2O_2 released by hydrogels, was derived from the absorbance intensity of the pertitanic acid solution at 407 nm wavelength, measured in a SpectraMax M3 multi-mode microplate reader (Molecular Devices, San José, CA, United States) equipped with SoftMax Pro software for data collection and analysis. For obtaining the calibration curve, 100 µL of H_2O_2 solutions with 0–20 mM concentrations were pipetted into the wells of a 96-well plate. Then, 50 µL of the prepared ROS assay solution was added into each well. The plate was shaken in the plate reader for 15 s before the absorbance intensity was read at 407 nm wavelength. Based on the calibration curve (**Supplementary Figure S3**), H_2O_2 concentration in the release medium was calculated as follows:

$$H_2O_2\ [mM] = \frac{Absorbance\ -\ 0.0724}{0.1777}.$$

Considering that this is the H_2O_2 concentration released by 200 µL hydrogel in 800 µL release medium, H_2O_2 amount (mmol) per volume hydrogel was calculated through the following equation:

$$\frac{H_2O_2\ (mmol)}{Volume_{hydrogel}\,(L)} = \frac{Absorbance\ -\ 0.0724}{0.1777} \times 4.$$

Each measurement was performed in quadruplicate ($n = 4$). H_2O_2 concentration values were reported in mM, i.e., mmol H_2O_2 released per unit volume (L) of hydrogel.

Cytocompatibility Assessment of Hydrogels

Cell lines including L929 (a murine fibroblast cell line) and HaCaT (a transformed human keratinocyte cell line) were obtained from DSMZ (German Collection of Microorganisms and Cell Cultures). L929 cells were maintained in RPMI 1640 cell culture medium with stable glutamine without glucose (P04-18500, PAN Biotech, Germany), containing 10% foetal bovine serum (FBS; PAN Biotech, Germany) under physiological culture conditions (37°C, 5% CO_2), and subcultured using 0.25% trypsin (Gibco, ThermoFisher Scientific, Germany). HaCaT cells were maintained in Dulbecco's modified Eagle's medium (DMEM) cell culture medium (PAN Biotech, Germany) containing 10% FBS under physiological culture conditions (37°C, 5% CO_2), and subcultured using TrypLE™ Express (ThermoFisher Scientific, Germany).

Defined aliquots of cell suspensions for each cell type were used as follows: L929 [passage number (P) 7–P10] 0.7×10^5 cells/well and HaCaT (P35–P37) 2.5×10^5 cells/well were pipetted into 24-well plates. Cells were incubated at 37°C, with 5% CO_2 for 24 h. Cell culture subconfluency and cell morphology were verified before exposing the cells to hydrogel samples. The culture medium was removed and replaced with fresh medium (1 ml) before starting the assessment.

HB PEGDA/HA-SH 10.0–1.0 hydrogel samples (30 µL) containing G and GO (**Table 1**) were freshly prepared under sterile conditions right before exposing them to the cell monolayer culture either through direct or indirect contact method (according DIN EN ISO 10993-5). For direct contact test, freshly prepared hydrogel samples (**Table 1**) were equilibrated in respective cell culture media for 10 min and placed in the center of the cell monolayer culture without making unnecessary movements of the specimens. Thus, each hydrogel sample of ~5 mm diameter covered approx. 1/3rd growth area of the well surface of a 24-well cell culture plate.

For indirect contact test, the hydrogel samples were exposed to L929 and HaCaT cells through 24-well Transwell® inserts (PET membrane, 1 µm pore size, 6.5 mm diameter, Corning®, Sarstedt, Germany), in a 24-well cell culture plate. Cell culture media volumes at apical (250 µL) and basal sides (800 µL) of inserts were maintained at the same level outside and inside the Transwell inserts. Cells on tissue culture treated polystyrene (TCPS) wells, without the addition of hydrogel samples, were used as "TCPS control wells," while cells treated with lysis solution (9% Triton® X-100 in water from Promega, Germany) served as "lysis control." Cells treated with HB PEGDA/HA-SH 10.0–1.0 hydrogels neither containing GO (0 U/L GO) nor glucose were also used as "polymer control". The well plate was then incubated at 37°C, with 5% CO_2 for 24 h.

After 24 h, the supernatant culture medium and HB PEGDA/HA-SH 10.0–1.0 specimens were carefully removed, and the

CellTiter-Blue® assay (CTB, Promega, Germany) was performed for measuring the cell viability according to Promega's standard protocols (O'Brien et al., 2000).

To this aim, 400 µL CTB reagent (enough to cover the surface of each well in a 24-well plate) was pipetted into each well and left in incubation for 2 h at 37°C and 5% CO_2. The cell supernatant was transferred to black microtiter 96-well plates. Fluorescence intensity was measured at excitation (Ex) of 560 nm and emission (Em) of 590 nm using a TECAN microplate reader Infinite® 200 PRO (Tecan, Switzerland).

Morphological Analysis of Cells

Changes in morphological appearance and visualization of live and dead L929 and HaCaT cells were evaluated after a culture time of 24 h using bright field and fluorescent microscopy (Olympus IX51, Germany). Fluorescent staining was performed through Live/Dead imaging (Live/Dead Cell Staining Kit II, Promokine, VWR, Germany) using calcein-AM and ethidium homodimer III (EthD-III) to detect live (green-fluorescence for live cells by enzymatic conversion of nonfluorescent substrate calcein-AM, Ex/Em ~495 nm/ ~515 nm) and dead (red-fluorescence for dead cells upon binding to nucleic acid, Ex/Em ~530 nm/~635 nm) cells.

Antibacterial Activity

Staphylococcus aureus (ATCC 29213), *Staphylococcus epidermidis* (ATCC 12228), *Pseudomonas aeruginosa* (ATCC 27853), *Escherichia coli* (ATCC 25922), and *Acinetobacter baumannii* (as some of the most relevant bacteria in infected wounds) were used to evaluate antibacterial activity of H_2O_2-releasing HB PEGDA/HA-SH 10.0/1.0 hydrogels containing different amounts of GO (25–500 U/L, **Table 1**; **Supplementary Figure S1**) and constant 2.5% w/w G. Additionally, resistant strains with most commonly found resistance phenotypes were also tested including *methicillin-resistant Staphylococcus aureus* (MRSA), *methicillin-resistant Staphylococcus epidermidis* (MRSE), VIM-2–producing drug-resistant *Pseudomonas aeruginosa* (Verona integron-encoded metallo- (VIM-2) β-lactamases-producing multidrug-resistant *P. aeruginosa*) (Viedma et al., 2012), and KPC-2-producing drug-resistant *Escherichia coli* (Ben Tanfous et al., 2017). These clinically isolated and highly resistant gram-negative bacteria came from the state reference sample and database for gram-negative bacteria at the Department for Medical Microbiology, Ruhr-University Bochum. The disc-diffusion test was performed for antimicrobial susceptibility testing according to EUCAST (European Committee on Antimicrobial Susceptibility Testing) guidelines (EUCAST 2016). Bacterial strains were revived and cultured on fresh Mueller-Hinton (MH) agar 1 day before testing. The well-isolated colonies were suspended in 0.9% normal saline and adjusted to McFarland 0.5 (Weinstein 2021). The inoculum was spread evenly over the entire surface of MH agar using a sterile cotton swab. The freshly prepared hydrogel samples (30 µL), in the form of ~5 mm diameter bead-shaped discs, were applied on the agar plate within 15 min of bacterial inoculation. The plates were then incubated at 37°C for 16–20 h (within 15 min of disc application). The zone of inhibition (ZOI, in mm) was measured using a scale bar by reading the MH plates from the back against a dark background and zone edges were read at the point of complete inhibition.

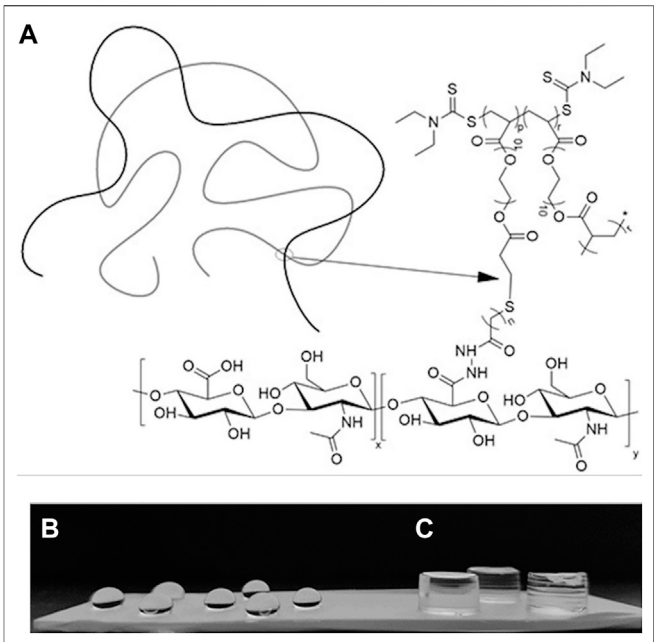

FIGURE 2 | (A): Schematic representation of the formation of a HB PEGDA/HA-SH hydrogel by thiol–ene cross-linking mechanism. **(B)**: HB PEGDA/HA-SH 10.0–1.0 hydrogel beads (30 µL) on the Teflon™ plate surface. **(C)**: HB PEGDA/HA-SH 10.0–1.0 hydrogels (200 µL) with cylindrical shape obtained by hydrogel cross-linking in a convenient mold. (p = 0.45) (r = 0.55) (n = 2) (x = 0.58) and (y = 0.42).

Statistical Analysis

Data are represented as mean ± standard deviation (SD) from two to four replicates depending on the analysis. Comparisons were made using one-way ANOVA or independent variable Student's t-test. Observations were considered to be significantly different for $p < 0.05$ and highly significant for $p < 0.01$.

All cell culture experiments and analyses of antibacterial activity were performed independently in duplicate (N = 2, number of independent experiments) and four technical replicates were made and examined per experiment (n = 4).

RESULTS

Chemical Characterization of HB PEGDA

The HB PEGDA polymer was synthesized with weight average molecular weight (Mw) of 16,656 Da, a number average molecular weight (Mn) of 11,060 Da, a polydispersity index (PDI) of 1.5, and a molar conversion of 32.5%, as assessed by GPC analysis.

^{1}H NMR spectra (**Supplementary Figure S4**) allowed the analysis of the branched structure and amount of pendant acrylate groups in HB PEGDA. The pendant acrylate groups were identified through the three characteristic chemical shifts at

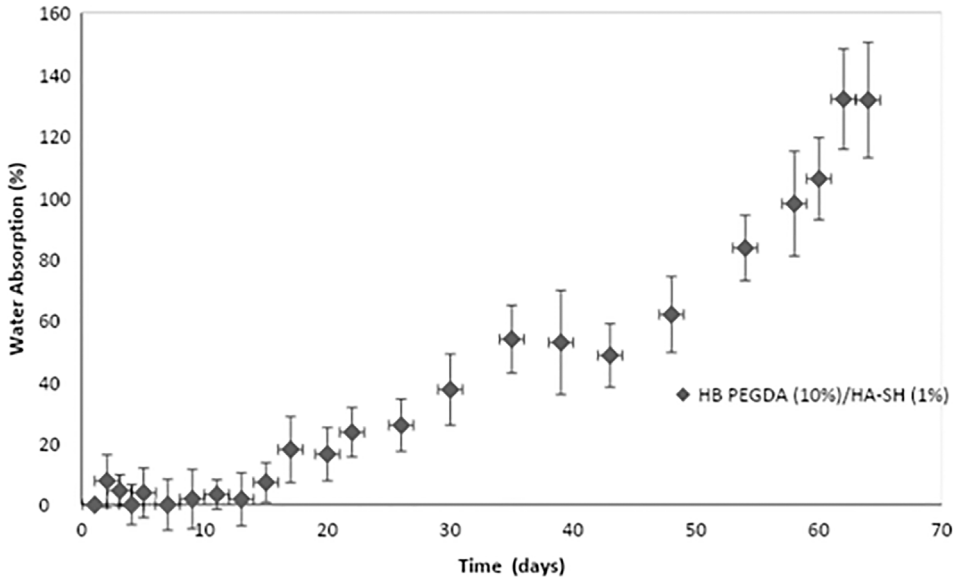

FIGURE 3 | Water uptake percentage of HB PEGDA/HASH 10.0–1.0 hydrogels as a function of time. Tests were performed using the HB PEGDA/HASH 10.0–1.0 hydrogel (200 μL) in 2 ml PBS solution at 37°C (n = 4).

6.4–5.8 ppm, while PEG groups were identified through the chemical shifts at 4.34–3.95 ppm. Vinyl ratio was measured to be 57 mol% with a vinyl content of 0.99 mmol vinyl groups/g polymer. On the other hand, branching ratio was 43 mol%.

HB PEGDA/HA-SH 10.0–1.0 Hydrogels: Formation Mechanism and Gelation Time

The HB PEGDA/HA-SH 10.0–1.0 hydrogel formed through the reaction of acrylate groups of HB PEGDA with thiol groups of HA-SH via Michael addition reaction. **Figure 2A** schematically illustrates HB PEGDA and HA-SH cross-linking while **Figures 2B,C** show photos of HB PEGDA/HA-SH 10.0–1.0 hydrogels with different shapes. A volume of 30 μL HB PEGDA/HA-SH 10.0–1.0 solution poured onto a hydrophobic Teflon™ plate surface formed hydrogel beads with ~5 mm size at their bottom side (**Figure 2B**). HB PEGDA/HA-SH 10.0–1.0 hydrogels with 200 μL volume and cylindrical shape were also formed using convenient molds (**Figure 2C**). The tube inverting test showed that HB PEGDA/HA-SH 10.0–1.0 hydrogels (with total volume of 1 ml) have an average gelation time of 63 s.

Water Uptake of HB PEGDA/HA-SH 10.0–1.0 Hydrogels

Figure 3 shows water uptake percentage as a function of time for HB PEGDA/HA-SH 10.0–1.0 hydrogels (200 μL). In the first 2 weeks, absorbed water was less than 10% of hydrogel initial mass. After 14 days, water uptake percentage tended to increase as a function of time. However, HB PEGDA/HA-SH 10.0–1.0 hydrogel did not dissolve up to 64 days, reaching a water uptake percentage of ~130%.

Hydrogen Peroxide Release From HB PEGDA/HA-SH 10.0–1.0 Hydrogels

The *in situ* production and release of hydrogen peroxide from HB PEGDA/HA-SH 10.0–1.0 hydrogels (with 200 μL volume) with varying GO concentrations from 25 to 500 U/L and constant G amount (2.5% w/w) (**Table 1**) was quantified over 24 h (**Figure 4**).

The amount of *in situ* released hydrogen peroxide increased continuously and significantly from 1.4 ± 0.2 to 10.8 ± 1.4 mmol per L hydrogel as a function of GO concentration (from 25 to 250 U/L). By further increasing the amount of GO to reach 500 U/L activity, no further increase in the amount of *in situ* released hydrogen peroxide was measured. In fact, the H_2O_2 released from the hydrogel HB PEGDA/HA-SH 10.0–1.0 with 500 U/L GO and 2.5% w/w G was 11.2 ± 0.7 mmol per L hydrogel, which was a nonsignificantly different amount with respect to what released from the hydrogel with 250 U/L GO and 2.5% w/w G ($p < 0.001$).

Cytotoxicity Analysis

Direct and Indirect Contact Test With L929 Fibroblasts

In the direct contact method with L929 cells, CTB assay results showed a decrease in cell viability with increasing GO amount, due to progressively higher H_2O_2 release (**Figure 5A**). The same type of hydrogel samples were also exposed to L929 cells via an indirect contact test. The viability of L929 cells (**Figure 5B**) was higher in indirect assays (~75–83%)—with cells exposed to the H_2O_2 amount released from hydrogel samples—than in direct assays (~37–100%)—with cells in contact with H_2O_2-releasing hydrogels (**Figure 5A**).

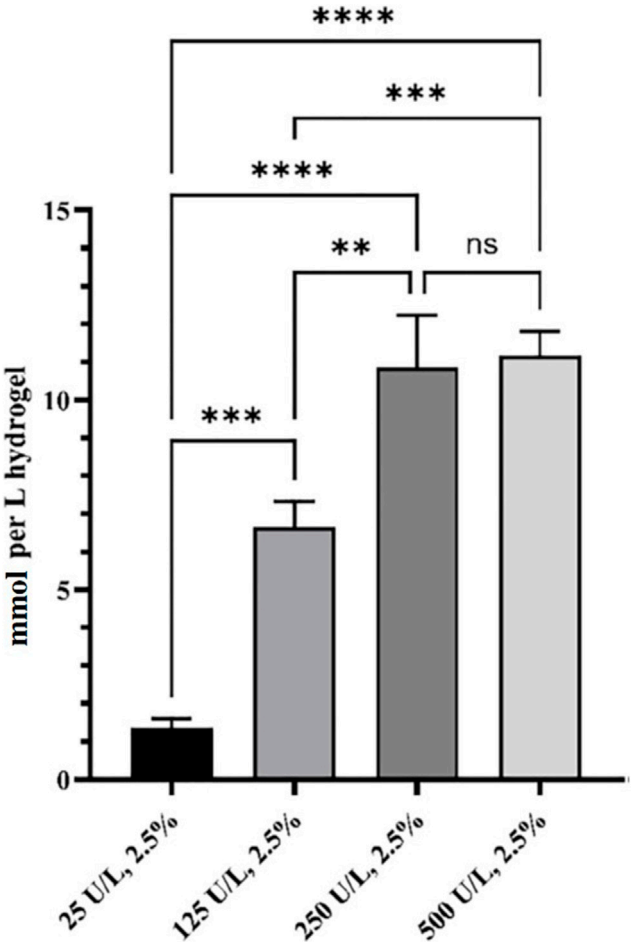

FIGURE 4 | Released H_2O_2 from HB PEGDA/HA-SH 10.0–1.0 hydrogels containing 2.5% w/w G and different amounts of GO (0–500 U/L), expressed as mmol/L of hydrogel. Release data were obtained under static conditions over 24 h (n = 4). (** indicates p value = 0.013; *** indicates p value = 0.0008; **** indicates p value < 0.0001).

Direct and Indirect Contact Test With HaCaT Keratinocytes

HaCaT cells in direct contact with hydrogels containing GO concentrations from 25 to 250 U/L showed similar viability to control cells. However, the viability of HaCaT cells in contact with hydrogels with GO concentration of 500 U/L decreased to approximately 80% with respect to control cells (**Figure 6A**). In indirect tests, the viability of HaCaT cells exposed to eluates from HB PEGDA/HA-SH 10.0–1.0 hydrogels with different GO concentrations was similar to control cells (**Figure 6B**).

Analysis of L929 and HaCaT Cell Morphology in Direct Contact Assays

Direct Contact Test With L929 Fibroblasts

On TCPS, after an incubation period of 24 h, the L929 fibroblasts showed a typical spread morphology with only a few rounded cell bodies that were either in division (in pairs) or apoptotic (isolated) (**Supplementary Figure S5A**). In the lysis control, significantly few cell bodies were seen compared to those on the TCPS surface, which were also more separated from each other and had fewer spread cell bodies (reduced nucleus–plasma relation) with mostly roundish morphology. Morphology was similar for cells in contact with control hydrogel samples (not containing GO and G), hydrogels containing 25–125 U/L GO at constant G content and control TCPS. In the case of HB PEGDA/HA-SH 10.0–1.0 sample with 250 U/L GO, most L929 fibroblasts showed similar morphology to TCPS controls; however, a few less densely packed cells with roundish morphology were also detected. Finally, in the case of HB PEGDA/HA-SH 10.0–1.0 sample with 500 U/L GO significantly fewer adherent cells were observed, and they almost exclusively exhibited a round morphology similar to those in the lysis control (**Supplementary Figure S5A**).

Live/dead assays served as evidence for almost 100% viability of L929 fibroblasts after 24 h cultivation on the control TCPS surface. Indeed, green-fluorescence results from the conversion of

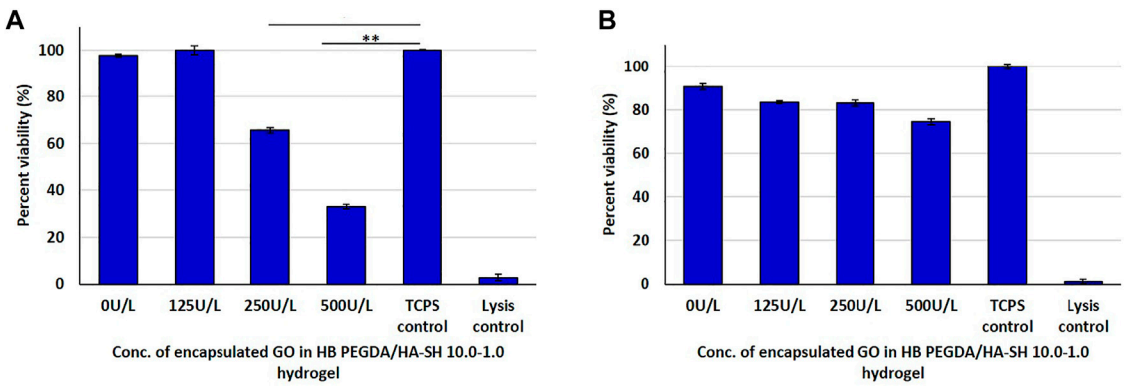

FIGURE 5 | Post 24 h cell viability data of L929 cells interacting with H_2O_2-releasing HB PEGDA/HA-SH 10.0–1.0 hydrogels containing different amounts of GO (25–500 U/L) and constant G amount (2.5% w/w) using the quantitative CTB assay: **(A)** direct contact: 250 U/L and TCPS control (* indicates p value = 0.0006); 500 U/L and TCPS control (** indicates p value = 0.0001); **(B)** indirect contact tests.

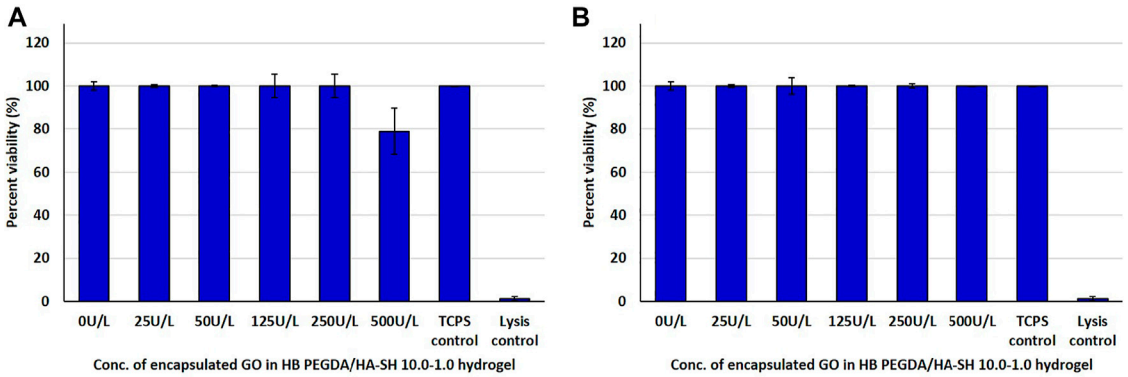

FIGURE 6 | Post 24 h cell viability data of HaCaT cells interacting with H_2O_2-releasing HB PEGDA/HA-SH 10.0–1.0 hydrogels containing different amounts of GO (25–500 U/L) and constant G amount (2.5% w/w) using the quantitative CTB assay: **(A)** direct contact and **(B)** indirect contact tests.

calcein-AM to calcein by esterase activity in viable cells. In contrast, only red-fluorescent avital cells were detected after treatment with Triton® X-100 (lysis control) (**Supplementary Figure S5B**). If the cell membrane integrity is disturbed or becomes porous and cells die, the intercalation dye EthD-III can penetrate the cells, enter their nucleus, and interact with their DNA. The Viability of L929 fibroblasts in contact with HB PEGDA/HA-SH 10.0–1.0 control hydrogel and TCPS controls was similar, showing rare red-fluorescent avital cells. However, L929 fibroblasts were slightly less close together than in control samples in some areas of the representative images. Similar results were obtained for cells in contact with HB PEGDA/HA-SH 10.0–1.0 hydrogel samples containing 25–50 U/L GO at constant G loading. On the contrary, only a few L929 fibroblasts in contact with hydrogel samples with 125 U/L GO activities showed prevalent green-fluorescent staining and normal size, while most cells showed reduced size and copresence of both staining. Finally, rare green-fluorescent cells were observed in contact with samples with 250 U/L GO activities, while most areas showed cells with double staining. When the amount of GO was further increased to 500 U/L, the removal of the hydrogel sample, the rinsing step and the staining showed a significantly reduced number of cells, with approximately equal number of vital and avital cells (**Supplementary Figure S5B**).

Direct Contact Test With HaCaT Keratinocytes

HaCaT keratinocytes showed typical spread morphology on TCPS controls after an incubation period of 24 h (**Supplementary Figure S6A**). A confluent monolayer of human HaCaT keratinocytes was observed, with relatively uniform nucleus–plasma ratio, forming a relatively uniform, hexagonal pattern in their entirety. Each cell was in very close contact with six neighboring cells. In the case of HaCaT cells treated with Triton® X-100, fewer cells remained on TCPS plates, separated from each other, showing clearly shrunken cell bodies. In contrast, the morphology of HaCaT keratinocytes in contact with control hydrogels and hydrogels with 25–250 U/L GO and constant G amount was similar to that of cells on control TCPS plates. On the other hand, only fewer adherent cells with the typical HaCaT morphology were observed after the contact with hydrogels containing 500 U/L GO (**Supplementary Figure S6A**).

Live/dead fluorescence staining confirmed viability of HaCaT cells in contact with hydrogels containing up to 250 U/L GO. In contrast, many attached, but avital cells were observed in the case of HaCaT cells in contact with hydrogels containing up to 500 U/L GO (**Supplementary Figure S6B**).

Antibacterial Testing

The antimicrobial activity or efficacy of the novel honey-mimetic H_2O_2-releasing HB PEGDA/HA-SH 10.0–1.0 hydrogels containing different amounts of GO (25–500 U/L) and constant G amount (2.5% w/w) was investigated against a variety of gram-positive (**Figure 7**) and gram-negative (**Figure 8**) bacteria that have significant clinical importance in wound colonization and infection.

In addition to *Staphylococcus aureus* (ATCC 29213), *Staphylococcus epidermidis* (ATCC 12228), *Pseudomonas aeruginosa* (ATCC 27853), *Escherichia coli* (ATCC 25922), *Acinetobacter baumannii* (some of the most relevant bacteria in infected wounds), and some of the most commonly found resistance phenotypes, including *methicillin-resistant Staphylococcus aureus* (MRSA), *methicillin-resistant Staphylococcus epidermidis* (MRSE), VIM-2-producing drug-resistant *Pseudomonas aeruginosa*, and KPC-2-producing drug-resistant *Escherichia coli*, were also tested.

All gram-positive bacteria types showed susceptibility (appearance of an inhibition zone, ZOI) to the *in situ* released hydrogen peroxide from the HB PEGDA/HA-SH 10.0–1.0 hydrogel containing the lowest amount of GO (25 U/L). As the amount of GO into the hydrogels increased (50–500 U/L), the ZOI values also increased continuously (**Figure 7**). This means, in detail, that for the sensitive *S. aureus* strain, for example, there was a highly significant increase in the ZOI with an increase in GO activity by a factor of five from 25 to 125 U/L ($p < 0.01$). While for all other gram-positive strains, highly significant ZOI enlargements were already shown with a doubling of GO activity from 25 to 50 U/L. A further increase in GO activity from 50 to 125 U/L for the gram-positive strains *S. epidermidis* and MRSA only showed a tendency to increase the

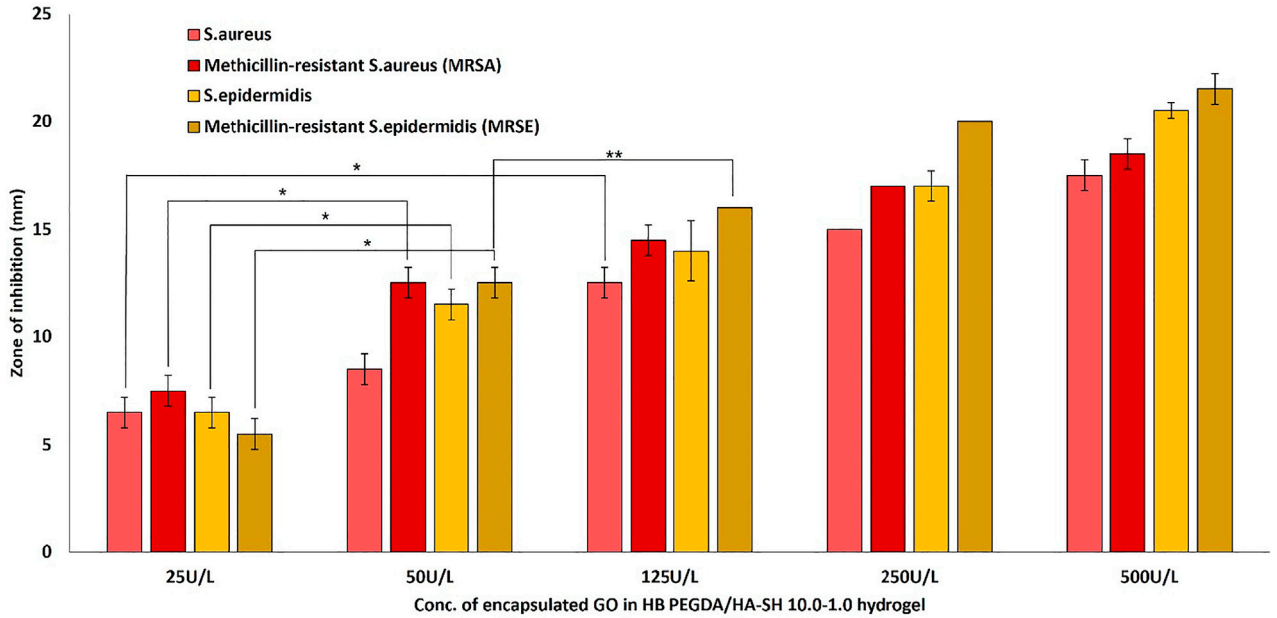

FIGURE 7 | Antibacterial activity of *in situ* H_2O_2-releasing HB PEGDA/HA-SH 10–1.0 hydrogels containing different GO activities (25–500 U/L) at constant G amount of 2.5 wt% against Gram-positive bacteria *S. aureus* and *S. epidermis* and two antibiotic-resistant clinical isolates of MRSA and MRSE. The graph shows the measured inhibition zones (ZOI) of the agar diffusion assays. (*$p < 0.01$; **$p < 0.05$).

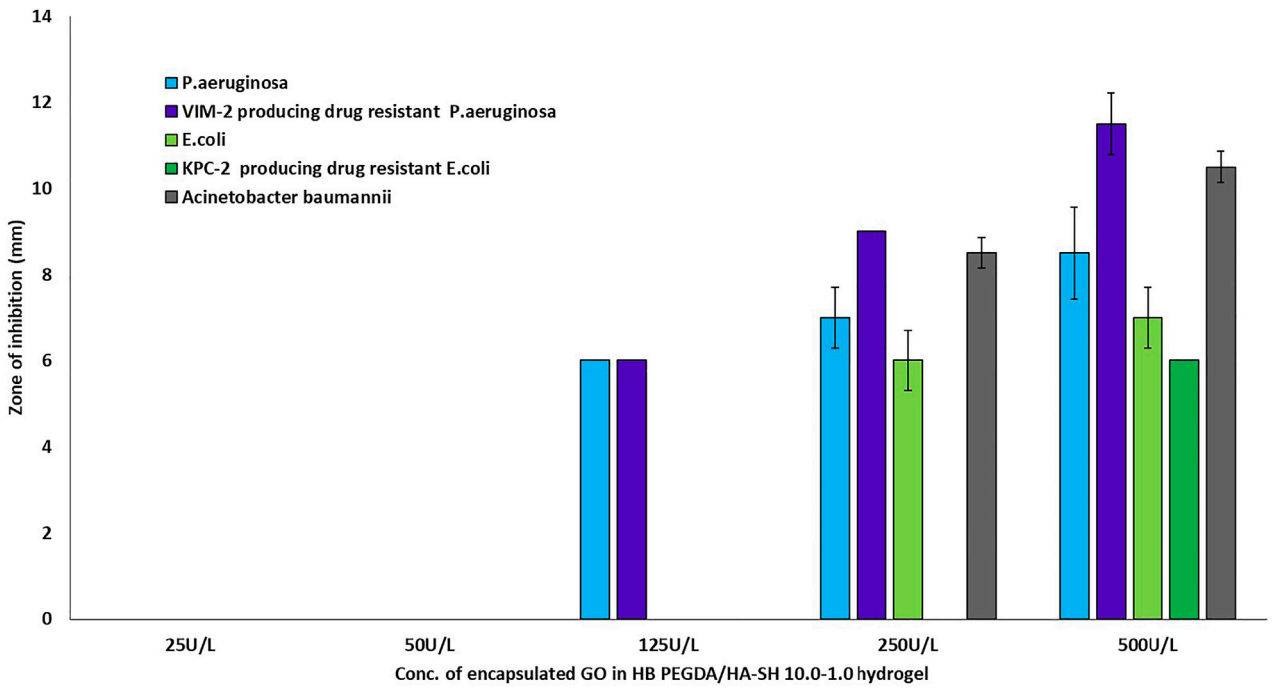

FIGURE 8 | Antibacterial activity of *in situ* H_2O_2-releasing HB PEGDA/HA-SH 10–1.0 hydrogels containing different GO activities (25–500 U/L) at constant G amount of 2.5 wt% against gram-negative bacteria *P. aeruginosa*, *E. coli*, and *A. baumanii*, and two highly antibiotic-resistant clinical isolates VIM-2-producing drug -resistant *Pseudomonas aeruginosa* and KPC-2-producing drug-resistant *Escherichia coli*. The graph shows the measured inhibition zones (ZOI) of the agar diffusion assays.

ZOI, but this was not significant. A slightly significant increase in ZOI could only be measured for MRSE ($p < 0.05$).

The two tested *P. aeruginosa* strains, the antibiotic-sensitive strain and the highly resistant strain VIM-2-producing drug-resistant *Pseudomonas aeruginosa*, were only susceptible to the hydrogen peroxide amount released from hydrogels with GO activity of 125 U/L. Although a tendency for ZOI to increase was measured for both strains when GO activity was increased from 125 to 250–500 U/L, these were not statistically significant (**Figure 8**). For the two antibiotic-sensitive strains *E. coli* and *A. baumanii*, a ZOI was only shown from hydrogels with a GO activity of 250 U/L, while for the highly resistant KPC-2-producing drug-resistant *Escherichia coli*, the ZOI was only shown for hydrogels with a GO activity of 500 U/L (**Figure 8**).

DISCUSSION

In this work, new antimicrobial hydrogels capable of releasing hydrogen peroxide *in situ* through a honey-inspired approach were designed, to be used as injectable or preformed hydrogels for future applications in the treatment of bacterially colonized or infected wounds. The hydrogels consisted of a chemically cross-linked polymeric network formed by the reaction of HB PEGDA and HA-SH components. HB PEGDA was a synthesized hyperbranched polymer (**Figure 1**) with a Mw of 16,656 Da, PDI of 1.5, vinyl ratio of 57 mol%, and a branching ratio of 43 mol% (**Supplementary Figure S4**). Thus the vinyl ratio was in the 40–60 mol% range typically reported for hyperbranched polymers suggesting a high degree of branching (Wang et al., 2015). On the other hand, the relatively high vinyl content (43 mol %) is beneficial for faster polymer cross-linking. The herein used HA-SH was produced and purchased from Blafar Ltd.

The HB PEGDA/HA-SH 10.0–1.0 hydrogel formed through reaction of acrylate groups of HB PEGDA and thiol groups of HA-SH *via* Michael addition reaction. Michael addition works by the weak sulfur-hydrogen bonds of HA-SH reacting with the electron-deficient acrylate groups in the HB PEGDA (Nair et al., 2014) (**Figure 2A**). The ability to achieve quantitative conversion without by-product formation, even under dilute conditions, makes thiol-Michael addition click reaction particularly suitable for biomedical applications (Nair et al., 2014).

In this work, one HB PEGDA/HA-SH hydrogel composition was explored for the design of injectable hydrogels for *in situ* formation and release of hydrogen peroxide: HB PEGDA/HA-SH 10.0/1.0 hydrogel, based on HB PEGDA/HA-SH blend with 91/9 w/w relative composition, and having 11% w_{blend}/v_{water} overall hydrogel concentration. This hydrogel showed a gelation time of around 60 s which ensured injectability. Proof-of-concept hydrogels with different and reproducible shapes were obtained, including hydrogel droplets on Teflon substrates and cylindrical hydrogels through molding (**Figures 2B,C**). Water uptake tests, performed on small volumes of hydrogels (200 µL) showed their limited swelling ability in the first 2 weeks of incubation in PBS and their resistance to loss of shape up to 64 days (**Figure 3**). Despite this observation, similar hydrogel systems composed of cross-links of PEG-diacrylates or PEG-diacrylamides with sulfhydryl group-containing peptides are known to exhibit hydrolytic instability not only at pH 8, but also more slowly at pH 7.4. Hydrolysis kinetics show that the hydrolysis half-life is a few days (Elbert and Hubbell, 2001). In this case, it is not the thioether group formed by Michael addition (click reaction) that is hydrolytically unstable, but the ester bond or amide bond located in the neighboring position with the amide bond being more stable than the ester bond. Other authors point out that the stability of such cross-links is strongly dependent on the neighboring groups and on the overall molecular structure of such hydrogel networks (Rydholm et al., 2011; Pérez-Madrigal et al., 2020). In the future, the biodegradability of the HB PEGDA/HA-SH system presented here will need to be investigated for application times greater than 24 h. Nevertheless, all the properties presented here are promising and ensure the possibility of long-term release of encapsulated drugs/molecules in case of drug delivery or long-term support of cells in case of cell delivery therapies. (Wechsler et al., 2019). Progressive increase in water uptake versus time is expected to enlarge hydrogel mesh radius increasing hydrogel permeability, favoring the release of drugs or the exchange of nutrients and metabolites, supporting cell viability in cell therapies, bioprinting applications, and other tissue engineering approaches (Richbourg et al., 2021). Indeed, previously, some of the coauthors employed HB PEGDA/HA-SH hydrogels as injectable systems for adipose stem cell therapy to treat diabetic wounds, preclinically validated in mice (Xu et al., 2018). As a next step, in this work, the hydrogel was proposed as an injectable system for the *in situ* formation and release of the antimicrobial agent hydrogen peroxide. As the antimicrobial mechanism of honey mainly depends on GO enzyme and G, allowing the formation of hydrogen peroxide, varying GO amounts were encapsulated into HB PEGDA component, keeping a fixed G content in the HA-SH component. Hydrogen peroxide production, determined under static conditions for a period of 24 h, increased as a function of GO concentration up to 250 U/L and then settled to an approximately constant value (10.8 ± 1.4 mmol per L hydrogel) (**Figure 4**). The amount of released H_2O_2 can be changed based on hydrogel volume (at fixed GO and G content) or by tuning GO content (at fixed G amount and hydrogel volume). A previous study by Loo et al. showed that daily topical application of 15 µL H_2O_2 solution with varying concentrations (10–166 mM) on skin wounds in C57/BL6 mice for overall 10 days caused different effects, from enhanced angiogenesis with 10 mM, i.e., 0.15 µmol/wound, to wound closure retard with 166 mM, i.e., 2.5 µmol/wound, (Loo et al., 2012).

A proper GO amount at constant G content should be selected to provide an antibacterial effect on a skin wound without causing simultaneous damage to dermal fibroblasts of the wound bed and to epidermal keratinocytes from wound edges. Therefore, initially *in vitro* investigations were performed in order to confirm the cytocompatibility of the HB PEGDA/HA-SH 10.0–1.0 hydrogel and to investigate the cytotoxic effect of the released amounts of hydrogen peroxide. Two internationally well-known fibroblast (L929) and epithelial (HaCaT) cell lines were used for the *in vitro* analysis, following DIN EN ISO 10993-5 standards. Furthermore, they represent typical starting cell lines for future investigations in the field of external wound treatment (Rajan et al., 2020; Ribeiro et al., 2020; De la Cruz-Concepción et al., 2021).

Before investigating the antibacterial activity and efficacy of the *in situ* hydrogen peroxide-releasing HB PEGDA/HA-SH hydrogel samples on certain gram-positive and gram-negative bacteria, quantitative direct and indirect cytotoxicity analyses were performed by the CTB assay on L929 and HaCaT cultures. Both tests are part of DIN EN ISO 10993-5 standards. Direct cytotoxicity tests allow the analysis of the behavior of cells in contact with or close to H_2O_2-releasing HB PEGDA/HA-SH hydrogel. In this test, results are affected by the release of H_2O_2 and the swelling of the hydrogel and its interaction with the cells. However, the direct test cannot separate the cytotoxic effect due to released H_2O_2 amount from that due to the hydrogel composition or its acting as a physical barrier in the diffusion of nutrients and catabolites. In contrast, in the indirect cytotoxicity test, the HB PEGDA/HA-SH sample itself is not in contact with the cells, and only H_2O_2 released in the medium may affect cell cytotoxicity.

Direct contact of the L929 fibroblasts with the HB PEGDA/HA-SH 10.0–1.0 hydrogels containing different amounts of GO (25–500 U/L) and constant G amount (2.5% w/w) showed a strong decrease in viability with increasing enzyme loading in the quantitative CTB assay (**Figure 5A**). In contrast, the indirect assay only showed a slight decrease in the viability of the fibroblasts with increasing GO amount (**Figure 5B**). L929 fibroblast viability decrease in the direct contact assay was probably due to an undersupply of nutrients and oxygen to the cells and additionally to the simultaneous H_2O_2 release and its accumulation below the hydrogel sample.

In contrast to fibroblasts, in direct tests, HaCaT keratinocytes showed no decrease in viability with increasing GO loading in the HB PEGDA/HA-SH 10.0–1.0 hydrogel, except for GO equal to 500 U/L, showing nonsignificant decrease in viability (**Figures 6A,B**). As compared to L929 fibroblasts, HaCaT keratinocytes were resistant to H_2O_2-induced cytotoxicity. Such findings are in agreement with *in vitro* data discussed in the study by Lee et al. who also showed that HaCaT keratinocytes gave slightly higher viability values than L929 fibroblasts (Lee et al., 2017).

Cell morphology studies (in direct contact tests) showed analogous differences in sensitivity to oxidative stress by released H_2O_2 between L929 fibroblasts and HaCaT keratinocytes when considering the hydrogel samples with 250 and 500 U/L GO activity (**Supplementary Figures S5A,B, S6A,B**). In the case of L929 cells interaction with hydrogels containing 125 U/L GO, the CTB assay showed a cell viability of 100% compared to those in the TCPS control and almost equal to the unmodified HB PEGDA/HA-SH hydrogel (**Figure 5A**). The corresponding fluorescence microscopic image after L/D staining suggested a large number of L929 cells showing esterase metabolism and converting calcein-AM into calcein (green fluorescence), and the copresence of cells with compromised membrane integrity allowing the intercalating dye EthD-III to penetrate L929 cells and interact with their DNA (red fluorescence) (**Supplementary Figure S5B**, 125 U/L). This finding suggested that the evaluation of real cytotoxic data is not sufficient by performing only one assay or measurement principle.

Figure 7 demonstrates the antibacterial activity of *in situ* H_2O_2-releasing HB PEGDA/HA-SH 10–1.0 hydrogels containing different GO activities (25–500 U/L) at constant G amount of 2.5 wt% against the gram-positive bacteria *S. aureus* and *S. epidermis* and two antibiotic resistant clinical isolates of MRSA and MRSE. In agar diffusion assays, ZOI—measured on hydrogel samples with the same volume (30 µL) as the ones used for cytocompatibility assays—increased with increasing the GO concentration and was also displayed in the case of methicillin-resistant gram-positive bacteria. However, in contrast to gram-positive bacteria, gram-negative bacteria *P. aeruginosa* and VIM-2-producing drug-resistant *P. aeruginosa* only showed ZOI at GO activity ≥125 U/L (**Figure 8**). For an antibiotic-sensitive *E. coli* and *A. baumanii* strain, the ZOI was only measured in the case of hydrogels with GO activity of 250 U/L. In addition, ZOIs of the hydrogel samples with higher GO activities were large for gram-positive compared to gram-negative bacteria, indicating that the gram-positive bacteria are much more susceptible to oxidative stress. There are various reasons for this significant difference between the measured ZOI for gram-positive compared to the gram-negative bacteria. One reason is the different structural composition of gram-positive and gram-negative bacteria: gram-negative bacteria have an outer lipid-based membrane that is additionally decorated with lipopolysaccharides (LPS), while gram-positive bacteria lack this outer lipid bilayer. The peptidoglycans of the outer layer of the gram-positive bacteria have been reported to be significantly more sensitive to oxidation (Rapacka-Zdończyk et al., 2021). In addition, Lee et al. showed that the LPS of the gram-negative bacteria have an antioxidant effect and thus eliminate part of the hydrogen peroxide produced and released *in situ* (Lee et al., 2017).

CONCLUSION

In summary, an *in situ* producing H_2O_2-PEGDA/HA-SH 10–1.0 hydrogel was developed that can be used as a drug-free antibacterial injectable hydrogel for the treatment of infected wounds. Based on the data so far, it can be said that GO activities of 125 U/L resulted in acceptable ZOIs for the gram-positive bacterial strains without affecting the viability of the fibroblasts too much within 24 h. This is a good indication that the hydrogel can be used for the treatment of infected wounds.

It was also shown that the keratinocytes were significantly less sensitive. To the extent possible based on this initial *in vitro* study, this honey-mimetic antibacterial hydrogel could also be used as a complementary system with some gram-negative bacteria such as *P. aeruginosa* and VIM-2-producing drug-resistant *P. aeruginosa*. Here, further studies with bacterially colonized 3D skin equivalents and over longer cultivation periods are required to assess the effective extent of cytotoxicity of the hydrogen peroxide released from this hydrogel. It is expected that the use of alternative antimicrobial solutions to antibiotics will help combat antimicrobial resistance. Considering its rapid formation, ability to produce H_2O_2 continuously, and antibacterial activity against susceptible and methicillin-resistant gram-positive bacteria while being cytocompatible for eukaryotic cells, this type of hydrogel represents a promising material for wound dressings and deserves further investigation.

DATA AVAILABILITY STATEMENT

The raw data supporting the conclusion of this article will be made available by the authors, without undue reservation.

AUTHOR CONTRIBUTIONS

JV synthesized HB PEGDA, prepared the hydrogels, and characterized them for their physicochemical properties. AI characterized hydrogels extensively for their biocompatibility and antimicrobial properties. IC supervised JV experimental activity at Politecnico di Torino. AS, SM, UG, HT, and WW supervised JV during her secondment period at Blafar Ltd. and WW Research Group. Additionally, the whole team was responsible for the development, production, and characterization of medical grade HA-SH. LM isolated, expanded, and characterized the used bacterial strains and supervised AI's microbiological experimental activity during her secondment period at Jochen Salber's lab. All cytocompatibility experiments were carried out at JS's lab. VC, WW, GC, and UG were JV supervisors during her doctorate. VC and JS were AI supervisors during her doctorate. GC, WW, and JS were unit coordinators, while HT was one of the industrial partners in the HyMedPoly project. The manuscript was written through main contribution by VC and JS with further help by the authors, particularly IC, AI, and JV. VC and JS cosupervised the work as senior authors. All authors have given approval to the final version of the manuscript.

FUNDING

This work has received funding from the European Union's Horizon 2020 research and innovation programme under the Marie Sklodowska-Curie actions (HyMedPoly project; Grant Agreement No. 643050).

ACKNOWLEDGMENTS

Contribution from the European Union's Horizon 2020 research and innovation programme under the Marie Sklodowska-Curie actions (HyMedPoly project; Grant Agreement No. 643050) is acknowledged. The authors thank some members of Wenxin Wang's research group, namely, Luca Pierruci, Sofia Kivotidi, Qian Xu, Xiao Lin Li, Hind Eddahani, and Manon Venet, for their kind help.

SUPPLEMENTARY MATERIAL

The Supplementary Material for this article can be found online at: https://www.frontiersin.org/articles/10.3389/fbioe.2021.742135/full#supplementary-material

Supplementary Figure 1 | Preparation of H_2O_2-releasing 10% HB-PEGDA/1% HA-SH hydrogel solution.

Supplementary Figure 2 | Colorimetric measurement of *in situ* generated H_2O_2.

Supplementary Figure 3 | Calibration curve of H_2O_2 obtained by the pertitanic acid assay.

Supplementary Figure 4 | ^{1}H NMR spectrum of synthesized HB PEGDA (Mw 16,656 Da).

Supplementary Figure 5 | (A) Bright-field micrographs of L929 cells after 24 h interaction with H_2O_2-releasing HB PEGDA/ HA-SH 10.0–1.0 hydrogels containing different amounts of GO (25–500 U/L) and constant G amount (2.5% w/w) versus controls (TCPS and lysis controls). **(B)** Fluorescent micrographs of Live/Dead-stained L929 cells after 24 h interaction with H_2O_2-releasing HB PEGDA/ HA-SH 10.0–1.0 hydrogels containing different amounts of GO (25–500 U/L) and constant G amount (2.5% w/w) versus controls (TCPS and lysis controls).

Supplementary Figure 6 | (A) Bright-field micrographs of HaCaT cells after 24 h interaction with H_2O_2-releasing HB PEGDA/ HA-SH 10.0–1.0 hydrogels containing different amounts of GO (25–500 U/L) and constant G amount (2.5% w/w) versus controls (TCPS and lysis controls). **(B)** Fluorescent micrographs of Live/Dead-stained HaCaT cells after 24 h interaction with H_2O_2-releasing HB PEGDA/ HA-SH 10.0–1.0 hydrogels containing different amounts of GO (25–500 U/L) and constant G amount (2.5% w/w) versus controls (TCPS and lysis controls).

REFERENCES

Abuharfeil, N., Al-Oran, R., and Abo-Shehada, M. (1999). The Effect of Bee Honey on the Proliferative Activity of Human B-And T-Lymphocytes and the Activity of Phagocytes. *Food Agric. Immunol.* 11 (2), 169–177. doi:10.1080/09540109999843

Albaridi, N. A. (2019). Antibacterial Potency of Honey. *Int. J. Microbiol.* 2019, 2464507. doi:10.1155/2019/2464507

Arul, V., Masilamoni, J. G., Jesudason, E. P., Jaji, P. J., Inayathullah, M., Dicky John, D. G., et al. (2012). Glucose Oxidase Incorporated Collagen Matrices for Dermal Wound Repair in Diabetic Rat Models: A Biochemical Study. *J. Biomater. Appl.* 26 (8), 917–938. doi:10.1177/0885328210390402

Ballal, M., Bairy, I., Shenoy, V., and Shivananda, P. (2012). Honey as an Antimicrobial Agent against Pseudomonas Aeruginosa Isolated from Infected Wounds. *J. Glob. Infect Dis.* 4 (2), 102–105. doi:10.4103/0974-777X.96770

Ben Tanfous, F., Alonso, C. A., Achour, W., Ruiz-Ripa, L., Torres, C., and Ben Hassen, A. (2017). First Description of KPC-2-Producing *Escherichia coli* and ST15 OXA-48-Positive *Klebsiella pneumoniae* in Tunisia. *Microb. Drug. Resist.* 23 (3), 365–375. doi:10.1089/mdr.2016.0090

Bogdanov, S. (1997). Nature and Origin of the Antibacterial Substances in Honey. *LWT - Food Sci. Technol.* 30 (7), 748–753. doi:10.1006/fstl.1997.0259

Brimson, C. H., and Nigam, Y. (2013). The Role of Oxygen-Associated Therapies for the Healing of Chronic Wounds, Particularly in Patients with Diabetes. *J. Eur. Acad. Dermatol. Venereol.* 27 (4), 411–418. doi:10.1111/j.1468-3083.2012.04650.x

Cooke, J., Dryden, M., Patton, T., Brennan, J., and Barrett, J. (2015). The Antimicrobial Activity of Prototype Modified Honeys that Generate Reactive Oxygen Species (ROS) Hydrogen Peroxide. *BMC Res. Notes* 8 (1), 20–28. doi:10.1186/s13104-014-0960-4

Cooper, R. A., Molan, P. C., and Harding, K. G. (1999). Antibacterial Activity of Honey against Strains of Staphylococcus Aureus from Infected Wounds. *J. R. Soc. Med.* 92 (6), 283–285. doi:10.1177/014107689909200604

De la Cruz-Concepción, B., Espinoza-Rojo, M., Álvarez-Fitz, P., Illades-Aguiar, B., Acevedo-Quiroz, M., Zacapala-Gómez, A. E., et al. (2021). Cytotoxicity of Ficus Crocata Extract on Cervical Cancer Cells and Protective Effect against Hydrogen Peroxide-Induced Oxidative Stress in HaCaT Non-tumor Cells. *Plants* 10 (1), 183–194. doi:10.3390/plants10010183

Deshmukh, M., Singh, Y., Gunaseelan, S., Gao, D., Stein, S., and Sinko, P. J. (2010). Biodegradable Poly(Ethylene Glycol) Hydrogels Based on a Self-Elimination Degradation Mechanism. *Biomaterials* 31 (26), 6675–6684. doi:10.1016/j.biomaterials.2010.05.021

Dong, Y., Saeed, A. O., Hassan, W., Keigher, C., Zheng, Y., Tai, H., et al. (2012). "One-step" Preparation of Thiol-Ene Clickable PEG-Based Thermoresponsive Hyperbranched Copolymer for *In Situ* Crosslinking

Hybrid Hydrogel. *Macromol. Rapid Commun.* 33 (2), 120–126. doi:10.1002/marc.201100534

Dong, Y., Qin, Y., Dubaa, M., Killion, J., Gao, Y., Zhao, T., et al. (2015). A Rapid Crosslinking Injectable Hydrogel for Stem Cell Delivery, from Multifunctional Hyperbranched Polymers via RAFT Homopolymerization of PEGDA. *Polym. Chem.* 6 (34), 6182–6192. doi:10.1039/c5py00678c

Dunnill, C., Patton, T., Brennan, J., Barrett, J., Dryden, M., Cooke, J., et al. (2017). Reactive Oxygen Species (ROS) and Wound Healing: The Functional Role of ROS and Emerging ROS-Modulating Technologies for Augmentation of the Healing Process. *Int. Wound J.* 14 (1), 89–96. doi:10.1111/iwj.12557

Eisenberg, G. (1943). Colorimetric Determination of Hydrogen Peroxide. *Ind. Eng. Chem. Anal. Ed.* 15 (5), 327–328. doi:10.1021/i560117a011

Elbert, D. L., and Hubbell, J. A. (2001). Conjugate Addition Reactions Combined with Free-Radical Cross-Linking for the Design of Materials for Tissue Engineering. *Biomacromolecules* 2 (2), 430–441. doi:10.1021/bm0056299

European Society of Clinical Microbiology and Infectious Diseases (2021). Disk Diffusion Method for Antimicrobial Susceptibility Testing. *Antimicrobial Susceptibility Testing (EUCAST)* Version 9.0, 1–22. Available at: http://www.eucast.org.

Kennedy, R., Ul Hassan, W., Tochwin, A., Zhao, T., Dong, Y., Wang, Q., et al. (2014). *In Situ* Formed Hybrid Hydrogels from PEG Based Multifunctional Hyperbranched Copolymers: A RAFT Approach. *Polym. Chem.* 5 (6), 1838–1842. doi:10.1039/c3py01513k

Lee, Y., Choi, K.-H., Park, K. M., Lee, J.-M., Park, B. J., and Park, K. D. (2017). *In Situ* Forming and H2O2-Releasing Hydrogels for Treatment of Drug-Resistant Bacterial Infections. *ACS Appl. Mater. Inter.* 9 (20), 16890–16899. doi:10.1021/acsami.7b03870

Loebel, C., Rodell, C. B., Chen, M. H., and Burdick, J. A. (2017). Shear-Thinning and Self-Healing Hydrogels as Injectable Therapeutics and for 3D-Printing. *Nat. Protoc.* 12 (8), 1521–1541. doi:10.1038/nprot.2017.053

Loo, A. E., Wong, Y. T., Ho, R., Wasser, M., Du, T., Ng, W. T., et al. (2012). Effects of Hydrogen Peroxide on Wound Healing in Mice in Relation to Oxidative Damage. *PLoS One* 7 (11), e49215. doi:10.1371/journal.pone.0049215

Mandal, M. D., and Mandal, S. (2011). Honey: Its Medicinal Property and Antibacterial Activity. *Asian Pac. J. Trop. Biomed.* 1 (2), 154–160. doi:10.1016/S2221-1691(11)60016-6

Moffatt, C. J., Stanton, J., Murray, S., Doody, V., Davis, P. J., and Franks, P. J. (2014). A Randomised Trial to Compare the Performance of Oxyzyme® and Iodozyme® with Standard Care in the Treatment of Patients with Venous and Mixed Venous/Arterial Ulceration. *Wound Med.* 6, 1–10. doi:10.1016/j.wndm.2014.08.002

Nair, D. P., Podgórski, M., Chatani, S., Gong, T., Xi, W., Fenoli, C. R., et al. (2014). The Thiol-Michael Addition Click Reaction: A Powerful and Widely Used Tool in Materials Chemistry. *Chem. Mater.* 26 (1), 724–744. doi:10.1021/cm402180t

O'Brien, J., Wilson, I., Orton, T., and Pognan, F. (2000). Investigation of the Alamar Blue (Resazurin) Fluorescent Dye for the Assessment of Mammalian Cell Cytotoxicity. *Eur. J. Biochem.* 267 (17), 5421–5426. doi:10.1046/j.1432-1327.2000.01606.x

Pérez-Madrigal, M. M., Shaw, J. E., Arno, M. C., Hoyland, J. A., Richardson, S. M., and Dove, A. P. (2020). Robust Alginate/hyaluronic Acid Thiol-Yne Click-Hydrogel Scaffolds with superior Mechanical Performance and Stability for Load-Bearing Soft Tissue engineeringAlginate/hyaluronic Acid Thiol-Yne Click-Hydrogel Scaffolds with superior Mechanical Performance and Stability for Load-Bearing Soft Tissue Engineering. *Biomater. Sci.* 8 (1), 405–412. doi:10.1039/c9bm01494b

Poldervaart, M. T., Goversen, B., De Ruijter, M., Abbadessa, A., Melchels, F. P. W., Öner, F. C., et al. (2017). 3D Bioprinting of Methacrylated Hyaluronic Acid (MeHA) Hydrogel with Intrinsic Osteogenicity. *PLoS ONE* 12 (6), e0177628–15. doi:10.1371/journal.pone.0177628

Rajan, M., Rajkumar, G., Farias Lima Guedes, T. J., Chagas Barros, R. G., and Narain, N. (2020). Performance of Different Solvents on Extraction of Bioactive Compounds, Antioxidant and Cytotoxic Activities in Phoenix Loureiroi Kunth Leaves. *J. Appl. Res. Med. Aromatic Plants* 17, 100247. doi:10.1016/j.jarmap.2020.100247

Rapacka-Zdończyk, A., Woźniak, A., Michalska, K., Pierański, M., Ogonowska, P., Grinholc, M., et al. (2021). Factors Determining the Susceptibility of Bacteria to Antibacterial Photodynamic Inactivation. *Front. Med. (Lausanne)* 8, 642609. doi:10.3389/fmed.2021.642609

Ribeiro, J. S., Barboza, A. d. S., Cuevas-Suárez, C. E., da Silva, A. F., Piva, E., and Lund, R. G. (2020). Novel In-Office Peroxide-free Tooth-Whitening Gels: Bleaching Effectiveness, Enamel Surface Alterations, and Cell Viability. *Sci. Rep.* 10 (1), 1–8. doi:10.1038/s41598-020-66733-z

Richbourg, N. R., Ravikumar, A., and Peppas, N. A. (2021). Solute Transport Dependence on 3D Geometry of Hydrogel Networks. *Macromol. Chem. Phys.* 222, 2100138: 1–7. doi:10.1002/macp.202100138

Rydholm, A., Anseth, K., and Bowman, C. (2007). Effects of Neighboring Sulfides and pH on Ester Hydrolysis in Thiol-Acrylate Photopolymers. *Acta Biomater.* 3 (4), 449–455. doi:10.1016/j.actbio.2006.12.001

Wang, D., Zhao, T., Zhu, X., Yan, D., Wang, W., et al. (2015). Bioapplications of Hyperbranched Polymers. *Chem. Soc. Rev.* 44 (12), 4023–4071. doi:10.1039/C4CS00229F

Viedma, E., Juan, C., and Villa, J. (2012). VIM-2-Producing Multidrug-Resistant Pseudomonas Aeruginosa ST175 Clone, Spain. *Emerg. Infect. Dis.* 18 (8), 1235–1241. doi:10.3201/eid1808.111234

Wechsler, M. E., Stephenson, R. E., Murphy, A. C., Oldenkamp, H. F., Singh, A., and Peppas, N. A. (2019). Engineered Microscale Hydrogels for Drug Delivery, Cell Therapy, and Sequencing. *Biomed. Microdevices* 21 (2), 31. doi:10.1007/s10544-019-0358-0

Weinstein, M. P. (2020). *Performance Standards for Antimicrobial Susceptibility Testing*, 30th edn. Clinical and Laboratory Standards Institute, CLSI supplement M100.

Wong, C. M., Wong, K. H., and Chen, X. D. (2008). Glucose Oxidase: Natural Occurrence, Function, Properties and Industrial Applications. *Appl. Microbiol. Biotechnol.* 78 (6), 927–938. doi:10.1007/s00253-008-1407-4

Xu, Q. A. S., Gao, Y., Guo, L., Creagh-Flynn, J., Zhou, D., Greiser, U., et al. (2018). A Hybrid Injectable Hydrogel from Hyperbranched PEG Macromer as a Stem Cell Delivery and Retention Platform for Diabetic Wound Healing. *Acta. biomaterialia.* 75, 63–74. doi:10.1016/j.actbio.2018.05.039

Zhang, J., Yong, H., A, S., Xu, Q., Miao, Y., Lyu, J., et al. (2018). Structural Design of Robust and Biocompatible Photonic Hydrogels from an *In Situ* Cross-Linked Hyperbranched Polymer System. *Chem. Mater.* 30 (17), 6091–6098. doi:10.1021/acs.chemmater.8b02542

Zhang, T., Qu, Y., Gunatillake, P. A., Cass, P., Locock, K. E. S., Blackman, L. D., et al. (2020). Honey-Inspired Antimicrobial Hydrogels Resist Bacterial Colonization through Twin Synergistic Mechanisms. *Sci. Rep.* 10 (1), 1–9. doi:10.1038/s41598-020-72478-6

Conflicts of Interest: JV, AS, SM, HT, and WW were employed by the company Blafar Ltd. The company provided the functionalized biomaterials for hydrogel fabrication in this paper.

The remaining authors declare that the research was conducted in the absence of any commercial or financial relationships that could be construed as a potential conflict of interest.

Publisher's Note: All claims expressed in this article are solely those of the authors and do not necessarily represent those of their affiliated organizations, or those of the publisher, the editors, and the reviewers. Any product that may be evaluated in this article, or claim that may be made by its manufacturer, is not guaranteed or endorsed by the publisher.

Advantages of publishing in Frontiers

OPEN ACCESS
Articles are free to read for greatest visibility and readership

FAST PUBLICATION
Around 90 days from submission to decision

HIGH QUALITY PEER-REVIEW
Rigorous, collaborative, and constructive peer-review

TRANSPARENT PEER-REVIEW
Editors and reviewers acknowledged by name on published articles

Frontiers
Avenue du Tribunal-Fédéral 34
1005 Lausanne | Switzerland

Visit us: www.frontiersin.org
Contact us: frontiersin.org/about/contact

REPRODUCIBILITY OF RESEARCH
Support open data and methods to enhance research reproducibility

DIGITAL PUBLISHING
Articles designed for optimal readership across devices

FOLLOW US
@frontiersin

IMPACT METRICS
Advanced article metrics track visibility across digital media

EXTENSIVE PROMOTION
Marketing and promotion of impactful research

LOOP RESEARCH NETWORK
Our network increases your article's readership